Late Quaternary to Holocene Geology, Geomorphology and Glacial History of Dawson Creek and Surrounding area, Northeast British Columbia, Canada

by

Adrian Scott Hickin
BSc, Simon Fraser University, 1999
MSc, University of Victoria, 2003

A Thesis Submitted in Partial Fulfillment
of the Requirements for the Degree of

Doctor of Philosophy

in the Faculty of Science/School of Earth and Ocean Science

© Adrian Scott Hickin, 2013
University of Victoria

All rights reserved. This thesis may not be reproduced in whole or in part, by photocopy or other means, without the permission of the author.

Supervisory Committee

Late Quaternary to Holocene Geology, Geomorphology and Glacial History of Dawson Creek and Surrounding area, Northeast British Columbia, Canada

by

Adrian Scott Hickin

BSc, Simon Fraser University, 1999

MSc, University of Victoria, 2003

Supervisory Committee

Dr. Eileen Van der Flier-Keller (School of Earth and Ocean Science)
Supervisor

Dr. Victor M. Levson (School of Earth and Ocean Science)
Co-Supervisor

Dr. Melvyn E. Best (School of Earth and Ocean Science)
Departmental Member

Dr. Dan Smith (Department of Geography)
Outside Member

Dr. Olav B. Lian (Department of Geography)
hdzŭăλŘŜ Member

Abstract

Supervisory Committee

Dr. Eileen Van der Flier-Keller (School of Earth and Ocean Science)

Supervisor

Dr. Victor M. Levson (School of Earth and Ocean Science)

Co-Supervisor

Dr. Melvyn E. Best (School of Earth and Ocean Science)

Departmental Member

Dr. Dan Smith (Department of Geography)

Outside Member

Dr. Olav B. Lian (Department of Geography)

Outside Member

Northeastern British Columbia was occupied by the Cordilleran (CIS) and the Laurentide (LIS) ice sheets, however, the timing and extent remains contentious. The late Quaternary and Holocene history of this area is examined by exploring geomorphic, stratigraphic, geochemical and geochronologic components of glacial, deglacial, paraglacial and non-glacial landsystems. New tools, such as GIS, LiDAR, and new geochronologic methods, such as optical dating are used to understand the Quaternary geology and geomorphology of the region.

Bedrock topography represents the base of the Quaternary section and modelling shows that paleovalleys, common in this region, host extensive Neogene sedimentary records. Stratigraphies from the Murray and Pine valleys indicate glaciation prior to the Mid-Wisconsinan (MIS 3) and during the Late Wiconsinan (MIS 2). Glacial landforms record Late Wisconsinan ice-sheet coalescence and reflect the complex interaction of the LIS and CIS margins.

During deglaciation, the LIS and CIS separated and glacial Lake Peace (GLP) formed. Shoreline features enable reconstruction of lake and ice configurations. Four phases of GLP are preserved. Optical ages from Phase II indicate GLP occupied the area some time between ca. 16 – 14 ka yrs ago. The apparent tilt on the shorelines provides a measure of isostatic adjustments and suggests asynchronous retreat of first the LIS, then the CIS.

The transition from paraglacial to boreal conditions was driven by climate change and is recorded by vegetation sucession and cessation of paraglacial processes. Optical ages from stabilized dunes and radiocarbon ages from organics date the transition between 12 – 11.5 ka yrs ago with full boreal conditions established by 10 ka yrs ago.

The Holocene is dominated by erosional processes, however some systems are aggrading. A case study on a floodplain demonstrates that resistivity (Ohmmapper) surveys provide a grain-size proxy to suppliant GPR studies, which is essential for geophysical fluvial architectural analysis. In the study, the discrepancy between planform style (classic meander model) and subsurface geophysical surveys (indicative of vertical accretion associated with braided and wandering fluvial styles) reiterates cautions that planform may not always be a functions of depositional process and one may not be used to predict the other.

Table of Contents

SUPERVISORY COMMITTEE ii

ABSTRACT iii

TABLE OF CONTENTS v

LIST OF TABLES x

LIST OF FIGURES xii

ACKNOWLEDGMENTS xxvii

DEDICATION xxix

CHAPTER 1: INTRODUCTION 1

CHAPTER 2: MAPPING QUATERNARY PALEOVALLEYS AND DRIFT THICKNESS USING PETROPHYSICAL LOGS, NORTHEAST BRITISH COLUMBIA, FONTAS MAP SHEET, NTS 94I 4

Abstract 5

2.1 Introduction 6

2.2 Methods 10

2.3 Results 17

2.3.1 Data 17

2.3.2 Model 17

2.3.3 Aquifers and natural gas occurrences in drift 19

2.4 Discussion 25

2.4.1 Data 25

2.4.2 Model 26

2.4.3 Implications 27

2.5 Conclusions 32

2.6 Acknowledgment 34

2.7 References 34

CHAPTER 3: MAPPING THE GEOMETRY AND LITHOSTRATIGRAPHY OF A PALEOVALLEY WITH A TIME-DOMAIN ELECTROMAGNETIC TECHNIQUE IN AN AREA WITH SMALL RESISTIVITY CONTRASTS, GROUNDBIRCH, BRITISH COLUMBIA, CANADA 39

Abstract 40
3.1 Introduction 41
3.1.2 Paleovalleys and Geologic Setting 43
3.1.3 Geology of the Paleovalley 46
3.2 Methods 46
3.2.1 Well Logging Method 46
3.2.2 Electromagnetic Method 49
3.3 Results 54
3.3.1 Well Log Data 54
3.3.2 Electromagnetic Interpretation 54
3.4 Discussion 56
3.5 Summary and Conclusion 63
3.6 Acknowledgements 65
3.7 References 65

CHAPTER 4: COALESCENCE OF LATE WISCONSINAN CORDILLERAN AND LAURENTIDE ICE SHEETS EAST OF THE ROCKY MOUNTAIN FOOTHILLS IN THE DAWSON CREEK REGION, NORTHEAST, BRITISH COLUMBIA, CANADA. 69

Abstract 70
4.1 Introduction 71
4.2 Previous Work 72
4.3 Methods 75
4.3.1 Geomorphology 75
4.3.2 Matrix Geochemistry 75
4.3.3 Stratigraphy 77
4.3.4 Chronology 78
4.4 Results 82
4.4.1 Geomorphology 82
4.4.2 Geochemistry 83
4.4.3 Stratigraphic Sections 87
4.4.4 Section 11 - Kiskatinaw River 111
4.4.5 Chronology 113

4.5 Discussion 120
4.6 Conclusion 130
4.7 References 132

CHAPTER 5: CAN THE ORIENTATION OF ELECTROMAGNETIC RESISTIVITY ANISOTROPY FROM TILL BE USED TO INFER PALEO-ICE FLOW? A COMPARISON OF RESISTIVITY ANISOTROPY AND STREAMLINED LANDFORM ORIENTATION..... 141

Abstract 142
5.1 Introduction 143
5.2 Methodology 147
5.3 Results 150
5.3.1 CCR Survey 150
5.3.2 Sediments and Landforms 152
5.3.3 Azimuthal Resistivity Data and Streamlined landforms 162
5.4 Discussion 167
5.4.1 Electrical anisotropy from alignment of sediment particles. 167
5.4.2 Electrical anisotropy from fractures in till 170
5.4.3 Electrical anisotropy from previous ice-flow inheritance 172
5.5 Conclusions 173
5.6 References 175

CHAPTER 6: HISTORY OF GLACIAL LAKE PEACE, NORTHEASTERN BRITISH COLUMBIA..... 182

Abstract 183
6.1 Introduction 184
6.2 Methods 187
6.3 RESULTS 197
6.3.1 SHORELINE MAPPING 197
6.3.2 ISOSTATIC ADJUSTMENT 201
6.3.3 OPTICAL DATING GEOCHRONOLOGY 204
6.4 Discussion 213
6.5 Conclusions 225
6.6 References 228

CHAPTER 7: GEOMORPHIC AND ECOLOGICAL AGE CONSTRAINTS FOR PARAGLACIAL TO BOREAL TRANSITION IN NORTHEASTERN BRITISH COLUMBIA 236

Abstract 237

7. 1 Introduction 238

7.2 Methods 240

7.2.1 Aeolian Landform Mapping 240

7.2.2 Organic Section 243

7.2.3 Chronology 245

7.3 Results 248

7.3.1 Kiskatinaw Dune Field 248

7.3.2 Organic Sections 260

7.4 Discussion 290

7.5 Conclusion 297

7.6 References 299

CHAPTER 8: USING GROUND-PENETRATING RADAR AND CAPACITIVELY COUPLED RESISTIVITY TO INVESTIGATE 3-D FLUVIAL ARCHITECTURE AND GRAIN-SIZE DISTRIBUTION OF A GRAVEL FLOODPLAIN IN NORTHEAST BRITISH COLUMBIA, CANADA 308

Abstract 309

8.1 Introduction 311

8.2 Study Area 313

8.3 Methods 318

8.4 Results and Interpretation 324

8.4.1 Trenching 324

8.4.2 Ground-Penetrating Radar 327

8.4.3 Resistivity 335

8.4.4 Combined GPR and Resistivity 339

8.5 Discussion 342

8.5.1 The Case Study 342

8.5.2 Methodology 346

8.6 Conclusion 348

8.7 Acknowledgments 349

8.8 References 350

CHAPTER 9: SUMMARY 356

References 365

APPENDIX 369

Appendix A: Bedrock Topography Database (Dawson Creek-Fort St John) Includes all data and interpretation of bedrock topography for the Montney Play area. ..... CD

Appendix B: Till Geochemistry Major oxide and elemental geochemistry from diamict samples ..... CD

Appendix C: PALEOTEC Macrofossil Report Macrofossil report from the Flatbed River Section ..... CD

List of Tables

Table 2.1. Gas well with tour sheets that report intersecting artesian aquifers or natural gas in the drift. 20

Table 4.1. Age dates from radiocarbon and OSL samples. 115

Table 4.2. K, U and Th concentration determined by neutron activation analysis 117

Table 4.3. Sample depth below the ground surface (d), equivalent dose (De), cosmic-ray dose rate (Dc), total dose rate (DT), Overdispersion, and apparent optical age. 118

Table 5.1. Descriptive statistics of the distribution of resistivity values from the inverted OhmMapperTM survey lines. 154

Table 5.2. Summary of the orientation of the electrical anisotropy ellipse, the landforms, and the pebble fabrics. 165

Table 6.1. Shoreline feature mapping by certainty. 200

Table 6.2. Regression surface analysis for very confident and confident data from each population of elevation data. 203

Table 6.3. OSL sample depths and locations. 206

Table 6.4. K, U, and Th concentrations determined from laboratory analyses and in situ γ-ray spectroscopy. 211

Table 6.5. Dosimetry results and optical ages. 212

Table 6.6. Radiocarbon dates related to GLP (from Hartman, 2005) 224

Table 7.1. Characteristics of Biomes (from Dyke, 2005) 241

Table 7.2. K concentrations and U and Th equivalent concentrations (U_e and Th_e)[1] determined from i*n-situ* γ-ray spectrometry. 246

Table 7.3. OSL sample site for the Kiskatinaw Dune Field. 257

Table 7.4. Sample depth below the ground surface (d), equivalent dose (D_e), cosmic-ray dose rate (D_c), total dose rate (D_T), and apparent optical age. 257

Table 7.5. Relative abundance of plant macrofossils from the Flatbed Peat Site (+ = taxon present, ++ = taxon common, +++ = taxon abundant). 262

Table 7.6. Relative abundance of animal macrofossils from the Flatbed Peat Site (+ = taxon present, ++ = taxon common, +++ = taxon abundant). 265

Table 7.T. Optical ages from sand dunes in Alberta and British Columbia. 293

Table 8.1. Summary of Trench Data 326

Table 8.2. Four Groups of Radar Facies and their interpretation. 330

Table 8.3. Combined radar facies and the distribution of resistivity values were interpreted in terms of grain size, sorting, and architecture. 341

List of Figures

Figure 2.1. The study area is located in northeastern British Columbia in NTS map sheet 94I (Shuttle Radar Topography Mission (SRTM) digital elevation model; 10x vertical exaggeration). 7

Figure 2.2. Generalized bedrock stratigraphy for the study area (after Stott, 1982 and Thompson, 1977). 8

Figure 2.3. The major stratigraphic units can be identified from gamma logs. The immediate base of drift is marked by an upward shift from a relatively high, uniform gamma response to a more varied, slightly reduced signal. Where the log extends off the scale it is shown as a "wrap-around" and is shaded grey. 12

Figure 2.4. (A) Drill chip samples are washed and collected during oil and gas well drilling. The recovered chips show a clear lithologic distinction between shale bedrock (left) and glacial sediments (right). (B) Closeup of glacial sediments from the chip sample archived (tick marks in mm). 13

Figure 2.5. The predicted surface was an interpolated surface that honoured only the ''hard'' data points (those that contain *x*,*y*,*z* information) and used spatial analysis to estimate the depth to bedrock between data points. However, in some cases, known information is available but cannot be represented as point data (e.g., the bedrock surface is known to be less than or greater than some depth below surface). To incorporate this additional information, estimated soft picks were established. In this example, there were no hard drift picks at well sites A and C because no contacts were present. Consequently, the predicted surface violated known information displayed in the well logs. At well site A, bedrock was observed to the top of the logged section of the well; therefore, the *z* value for the bedrock surface must pass above the logged portion of the well. The predicted surface over estimated the depth to bedrock because there was no contact to pull the predicted bedrock surface towards the ground elevation. A arbitrary soft pick (interpreted) was added between the top of the logged portion of the well and the ground surface forcing the new interpreted surface above the top of the well. At well site C, drift was logged to the base of the well, but the contact occurred below the logged section. Here, the depth of the predicted bedrock surface was under estimated. A soft pick was established below the logged section of the well, forcing the new interpreted

surface below the well. Because there is no hard data at wells A and C, when the new surface is interpolated from both the hard and the soft picks, it must be considered an interpretation. 16

Figure 2.6. The modelling process generated three working surfaces: (A) a predicted (kriged) bedrock topography surface incorporating only hard picks (similar to the predicted surface in Fig. 2.5); (B) a fitted interpolated surface based on hard picks, well cuttings, and water well data; (C) a fitted interpolated surface base on all hard and soft data; this model is the basis for combining isolated depressions into valleys by introducing paleovalley thalwegs (see Fig. 2.7); and (D) modern topography (Shuttle Radar Topographic Mission (SRTM) digital elevation model (DEM)). 18

Figure 2.7. The final model is achieved by linking the depressions in Fig. 2.5C to form paleovalleys (left). Additional data points were added to the working model (Fig. 2.5C) along proposed thalwegs interpreting the base of the valley between wells. The entire dataset was then reinterpolated using the software to produce a geological interpretation of the paleovalleys (includes hard, soft, and thalweg picks). Drift thickness was established by subtracting the geologically interpreted model from ground elevation (right). (A) Depressions are connected into four paleovalleys. (B) Because the thalwegs are established based on interpretation of the data, more than one bedrock topographic model is possible. For example an alternative interpretation can be generated if the single chip sample east of the Sikanni Chief River is eliminated and the thalwegs removed, resulting in a model with three paleovalleys. KCP, Kyklo Creek Paleovalley; KHP, Kotcho–Hoffard Paleovalley; NCP, Niteal Creek Paleovalley; RPV, Rainbow Paleovalley. 21

Figure 2.8. North-to-south cross sections show the modeled tops of the major stratigraphic boundaries, paleovalleys, and modern rivers (25x vertical exaggeration). KCP, Kyklo Creek Paleovalley; KHP, Kotcho–Hoffard Paleovalley; NCP, Niteal Creek Paleovalley. 28

Figure 2.9. Bedrock subcrop map based on the bedrock topography model (Fig. 2.7A). 30

Figure 3.1. The Groundbirch area in northeastern British Columbia, Canada. 42

Figure 3.2. The Groundbirch Paleovalley is one of 13 paleovalleys mapped from water well logs and exposures in the region (modified from Hickin, 2011). 44

Figure 3.3. The Groundbirch paleovalley-fill is exposed in the Coldstream River Canyon (located west of the survey area; see Fig. 3.1). 45

Figure 3.4. Stratigraphic section depicting the exposed geology of the Groundbirch Paleovalley at the Coldstream River Section (see Fig. 3.1). At this location, GPV is 135-m deep and consists of six units (C = Clay; S=Silt; S=Sand; G=Gravel; D=Diamict). 47

Figure 3.5. Sixty-five soundings were conducted in the Groundbirch area and two water wells were drilled and logged with borehole geophysical tools (digital elevation model has 2.5 x vertical exaggeration). 48

Figure 3.6. Station 14 on 269 Road (north end of line in Fig. 3.5) is an example of typical sounding data with the smooth model and best-fit 3-layer model. The final edited late-time apparent resistivity data versus time is on the left side (the squares are data points, the x values are masked data points, and the curves are the best-fit model). The interpreted 3-layer 1-D resistivity model is on the right side. The solid line is the best-fit 3-layer model (standard error of fit is 5.85 % RMS), and the broken line is from the smooth model. 51

Figure 3.7. Gamma and resistivity logs for the two water wells drilled and logged in the area (locations are shown in Fig. 3.5). There are two low gamma, high resistivity horizons in Well 1 that indicate medium- to coarse-grained sediment with fresh water (aquifers). Well 2 is entirely in interbedded mudstone and fine sandstone bedrock. 53

Figure 3.8. Resistivity-depth sections, from the 269 Road (north-south) and Stucky Road (east-west), show that when combined there is continuity between 1-D models. The resistivity variation in the sections is interpreted to reflect general grain-size differences. Medium- and coarse-grained units have aquifer potential. 55

Figure 3.9. The 4-layer model from the sounding at Station 3 on the 208 Road. The logs helped constrain the inversion and the results are comparable; A) Sounding data; b) 4-layer inversion model; c) Well #1 resistivity log; and d) Well #1 gamma log. 57

Figure 3. 10. Two-layer (left) and a 4-layer (right) best-fit inversion model from Station 3 on 208 Road are plotted with their equivalent error analysis. Both of these models have an RMS standard error fit of 4.48%. 59

Figure 3.11. Equivalence analysis can be used to provide a range of depths that a layer boundary can occur in inversions with the same standard error of fit. a) The resistivity ratio between adjacent layers at Station 6 on the Stucky Road is 3.49 and the resulting equivalent

analysis range is ± 13 m. b) The resistivity ratio between adjacent layers at Station 12 on the Stucky Road is 1.30 and the resulting equivalent analysis range is +31 m to -51 m..... 61

Figure 3.12. The resistivity depth-sections combined into a fence diagram show the likely 3-D continuity between lines. From these images, the geometry for the paleovalley and the potential aquifers can be determined (legend is the same as in Fig. 3.8)..... 62

Figure 4.1. The study area with the location of diamict samples (inset: location of diamict samples from northwest Alberta; Plouffe et al., 2006)(Datum: UTM NAD 83). 76

Figure 4.2. Radiocarbon samples were collected from Pine River Section 1. a) Disseminated organic fragments and wood. b) Close up view of the fossil wood and needles. c) Flattened wood fragment; d) Common silver weed (Potentillo anserine) achenes..... 79

Figure 4.3. Sections located along the Murray and lower Pine rivers in northeastern British Columbia. Streamlined landforms in the study area record ice flow patterns from western sourced (CIS/Montane) ice. 80

Figure 4.4. Streamlined landforms from high resolution DEM (4x vertical exaggeration; Datum: UTM, NAD 83, Zone 10); a) Streamlined landforms in the Swan Lake area indicate a north to north-northwest ice-flow direction; b) Streamlined land forms from the Noel area between the East and West Kiskatinaw rivers show a coherent arcuate and deflected flow path of Cordilleran ice; c) Streamlined landforms in the Redwillow area; d) Hummocky and reticulate terrain overlies the streamlined landforms; e) Discordant streamlined landforms indicating unimpeded ice-flow to the northeast occurred after northern flow deflection.84

Figure 4.5. Principal component analysis (PCA) bi-plots of major oxide geochemistry from diamict matrix from this study and Plouffe et al. (2006). 85

Figure 4.6. Diamict matrix major oxide discrimination plots from this study and from Plouffe et al. (2006). 86

Figure 4.7. Stratigraphy of a) Section 1: Tumbler Ridge; b) Section 2: Murray River; and c) Section 3: Salt Creek (see Fig. 4.3 for section locations). 88

Figure 4.8. Stratigraphy of Section 4: Nini Hill (see Fig. 4.3 for section locations; legend is the same as Fig. 4.7). 89

Figure 4.9. Stratigraphy of a) Section 5: Murray Terrace; and b) Setion 6; Serpents Head (see Fig. 4.3 for section locations; legend is the same as Fig. 4.7). 90

Figure 4.10. Stratigraphy of Section 7: Coldstream (see Fig. 4.3 for section locations; legend is the same as Fig. 4.7). 91

Figure 4.11. Stratigraphy of a) Section 8: Pine River 1; b) Section 9: Pine River 2 (see Fig. 4.3 for section locations; legend is the same as Fig. 4.7). 92

Figure 4.12. Stratigraphy of Section 10: Happy Hour Corner (see Fig. 4.3 for section locations; legend is the same as Fig. 4.7). 93

Figure 4.13. Highly deformed sand and gravel of Unit 1 is exposed at Section 2. a) Ductilely deformed sand and pebble gravel with subsequent brittle faulting; b) Large fold of laminated silt, sand and bedded sand and gravel; c) Folded cobble gravel bed. 94

Figure 4.14. a) Lower stratigraphy of Section 9; b) Unit 2 gravel conformably overlain by Unit 3 diamict (Section 9); c) Glaciotectonized rafts of sand, gravel and diamict preserved in Unit 3a at the base of Section 10; d) Mélange of facetted and striated clasts mixed with shale blocks from the lower contact of Unit 3a (Section 10); e) Sandy flame structures that originate at bedrock and terminate as sand filled thrusts from the contact between bedrock and Unit 3a (Section 6); f) Massive diamict typical of Unit 3b (Section 6). See Fig. 4.7 for legend. 96

Figure 4.15. Till genetic discrimination plots, based on clast macro fabrics (top of page), from sections in the Pine and Murray river valleys (MT = Murray Terrace, Section 5; PR2 = Pine River 2, Section 9; SH = Serpents Head, Section 6. a) Benn Diagram; b) May Diagram; and c) Hicock's Modality Diagram. Diamict definitions based on Hicock et al. (1996) and Dreimanis (1989). 98

Figure 4.16. a) Sand and gravel lenses in Unit 5 (Section 7); b) Non-glacial, imbricated gravel overlain by fining-upward sand to silt and clay of Unit 5 (Section 8); c) Upper stratigraphy of Section 9; d) Poorly-sorted pebble to cobble gravel of unit 6 (Section 7); e) Stratigraphy at the base of Section 10; f) Advance-phase glaciolacustrine sediments (Unit 7; glacial Lake Mathews) overlain by intercalated subaqueous debris assigned to Unit 8 (Section 4). See Fig. 4.7 for legend. 100

Figure 4.17. a) Clast and matrix-supported gravel (Unit 8a) interpreted to be an alluvial fan deposits overlain by massive diamict (Unit 9A; Section 5). Close-up of imbricated to flat-lying gravel (Unit 8a; Section 5); c) Flat-lying, clast-supported gravel interpreted to alluvial

fan deposit (Unit8a; Section 4); d) Silt (Unit 7; glacial Lake Mathews) overlain by normally graded, clast- to matrix-supported diamict interpreted to be a debris flow deposit (Unit 8b; Section 6). 104

Figure 4.18. a) Upper stratigraphy of the Section 6; b) Massive diamict with minor lenses of massive sand (Unit 9a; Section 6); c) Laminated and glaciotectonically folded sand and silt (Unit 9b; Section 6); d) Fractured sand clast in bedded diamict interpreted to be waterlain till (Unit 9b; Section 6); e) Massive diamict interpreted to be till (Unit 9a; Section 9); f) Massive, fissile diamict (Unit 9a; Section 6). Dmm = Matrix-supported, massive diamict. 106

Figure 4.19. a) Deltaic forset beds at a gravel pit near the confluence of Pine and Murray rivers (Unit 11a); b) Massive to crudely stratified gravel in gravel pit southwest of Section 8 in the paleo-Pine River Valley (see Fig. 4.3); c) Thick overbank sand (and possibly loess) over gravel (Unit 11b; Section 4); d) Gravel and overbank sand (Unit 11b) overlain by loess (Unit 12; Section 5); e) Oxidized silt interpreted to be loess (Unit 12; Section 7); f) Parabolic sand dunes (Unit 12) from above Section 10 in the Septimus area (see Fig. 4.3). 109

Figure 4.20. a) Stratigraphy of the Section 11, Kiskatinaw River (see Fig. 4.3 for section location); b) clast macrofabrics (numbers correspond to locations and elevations axis in 20a); c) Clast content proxy, matrix grain-size composition, and proportion of shield clasts (elevations axis same as 20a); d) Hicock modality till classification diagram (numbers refer to locations and elevations in 20a); e) May till classification diagram; f) Benn till classification diagram. 112

Figure 4.21. Major oxides geochemical trends from diamict matrix samples from Section 11. a) Major oxides in profile; b) Al_2O_3 verses SiO_2; c) Fe_2O_3 verses SiO_2 d) MgO versus SiO_2; e) CaO versus SiO_2; f) Na_2O versus SiO_2; K_2O versus SiO_2. Empirical discrimination fields are the same as those determined in Fig. 4.6. 114

Figure 4.22. Examples of the OSL response for each of the samples including, a typical shine down curve (photon counts per excitation time), associated growth curve (photon counts per Laboratory β dose) and a radial plot used to determine the statistical equivalent dose (De). The open circle on the growth curve plot is a duplicate dose point used to determine the recycling ratio. Since it is close to unity in these samples, the test dose procedures has successfully corrected for sensitivity changes. The grey region on the radial plots

represents the weighted-mean equivalent dose value of all the data. a) CS02 from Section 7; b) CS03 from Section 7; c) PR01 from Section 10; and d) PR02 from Section 8. OD = Overdispersion. 119

Figure 4.23. South to North correlated cross-section of the stratigraphy of the Murray-Pine rivers. 124

Figure 4.24. Summary of the stratigraphy and chronology from the study area (same legend Fig. 4.23). The optical ages for Units 6 and 9 are likely maximum ages, consequently, the depositional age for these units is younger. Correlation suggests they were deposited during the Late Wisconsinan (MIS 2). 126

Figure 5.1. Study area in northeast British Columbia, Canada with generalized ice-flow (arrows). 146

Figure 5.2. Digital elevation model of streamlined landforms within the Kiskatinaw streamlined landform field. Numbers refer to the landforms where electrical anisotropy was determined (detailed images shown in Figs. 5.7 – 5.13). Numbers preceded by “S” (e.g. S1) refer to sites where till matrix grain-size was determined (shown in Fig. 5.5c). Black lines represent capacitively coupled resistivity surveys (e.g. Fig. 5.3) and the west to east cross-section (blue line) is shown in Fig. 5.15 (2 x vertical exaggeration; Datum: UTM NAD 83). 148

Figure 5.3. An example of a typical capacitively coupled resistivity inversion along a portion of Line G (location shown on Fig. 5.2); Top: inversion model from RES2D software; Bottom: interpreted section showing till over shale. 151

Figure 5.4. The distribution of resistivity values along CCR sections for the west, east-central, and east portions of the study area. 153

Figure 5.5. Photographs of a) clay rich till common in the study area and b) gravel rich till typical of the east-central portion of the area; c) Ternary plot of matrix composition (locations shown in Fig. 5.2). 155

Figure 5.6. There is no correlation between the average resistivity at a station and the strength of the related anisotropy. 156

Figure 5.7. DEM of Landform 1 and 2 with resulting measurements for stations 1 – 8 (yellow circle = Station location; blue polygon = resistivity rose plot with black best-fit-ellipse;

green polygon = clast fabric rose plot with small arrow indicating average orientation; black arrow = orientation of the long axis of the landform). 157

Figure 5.8. DEM of landforms 3 (a) and 4 (b) with resulting measurements for stations 9 – 15 (yellow circle = Station location; blue polygon = resistivity rose plot with black best-fit-ellipse; black arrow = orientation of the long axis of the landform). 158

Figure 5.9. DEM of landforms 5 (a) and 6 (b) with resulting measurements for stations 15 – 18 (yellow circle = Station location; blue polygon = resistivity rose plot with black best-fit-ellipse; black arrow = orientation of the long axis of the landform). 159

Figure 5.10. DEM of landform 7 with resulting measurements for stations 19 and 20 (yellow circle = Station location; blue polygon = resistivity rose plot with black best-fit-ellipse; black arrow = orientation of the long axis of the landform). 160

Figure 5.11. DEM of landform 8 with resulting measurements for stations 21 and 22 (yellow circle = Station location; blue polygon = resistivity rose plot with black best-fit-ellipse; green polygon = clast fabric rose plot with small arrow indicating average orientation; black arrow = orientation of the long axis of the landform). 161

Figure 5.12. DEM of landforms 9 and 10 with resulting measurements for stations 23 – 26 (yellow circle = Station location; blue polygon = resistivity rose plot with black best-fit-ellipse; black arrow = orientation of the long axis of the landform). 163

Figure 5.13. DEM of landform 11 (a) and 12 (b) with resulting measurements for stations 27 – 30 (yellow circle = Station location; blue polygon = resistivity rose plot with black best-fit-ellipse; black arrow = orientation of the long axis of the landform). 164

Figure 5.14. There is a strong correlation between the orientation of the long axis of a landform (A_{max}) and average orientation of the maximum resistivity (ρ_{max}) for landforms with elongation ratios greater than 3 (top). The correlation is weaker for landforms with elongation ratios less than 3 (bottom). 166

Figure 5.15. A conceptual model for inferred subglacial conditions that may explain field observation and electrical anisotropy along a transect across the study area (Fig. 5.2). . 171

Figure 6.1. The study area in northeast British Columbia. Inset: Footprint of all phases of glacial Lake Peace (from Mathews, 1980). 185

Figure 6.2. Retreat phase glaciolacustrine sediments draping much of the terrain in the Peace River region of northeast British Columbia may be only a few metres thick in upland areas (e.g. a) North of the Dawson Creek) but are considerably thicker in paleovalleys and topographic lows (e.g. b) Coldstream Canyon). 188

Figure 6.3. Examples of grain-size and sedimentary structures within in GLP sediments: a) rhythmically bedded sand and silt; b) thin bedded, silty sand and clay; c) horizontally stratified, medium to coarse sand; d) medium sand with trough-cross bedding and climbing ripples; e) Hetrolithic silt, laminated silt and clay, bedded silt and diamict; and f) stratified sandy diamict with dropstones. 189

Figure 6.4. a) Gravel pit at the confluence of the Pine and Murray rivers (Highway 97; Fig. 6.1) revealing foreset beds of a prograding delta from a late stage of GLP (610 m); b) Wave cut benches revealed from high resolution DEM (2x vertical exaggeration) from south of Pouce Coupe (Phase III of GLP). 191

Figure 6.5. A gamma spectrometer and probe collecting (inserted) in situ measurements of U, Th, K and total gamma-ray counts used to calculate the environmental dose rate (D_e). . 194

Figure 6.6. Histogram of elevation points generated from mapping shoreline features; peaks represent elevations associated with relatively stable positions of GLP. 198

Figure 6.7. Best fit first-order polynomial surfaces, generated from the “very confident” and “confident” categories of shoreline (in all diagrams, north is to the top of the page). 199

Figure 6.8. Locations of shoreline data points and OSL samples. The lower chart is a projection of elevation points by population (Fig. 6.6) and the first order polynomial surfaces along transect A to A’. Mathews (1980) Bessborough phase is projected onto the chart (circle) within the Phase III population of this study. 202

Figure 6.9. OSL samples collected from 4 widely dispersed locations along Phase II features. Detailed DEMs (left), photograph of the shoreline sediments (centre) and topographic profiles (right) perpendicular to the shorelines. 205

Figure 6.10. Stratigraphic logs show the depth and OSL age of the four samples collected from the Phase II flight of shoreline features. 207

Figure 6.11. Examples of the OSL response for each of the samples from the Phase II shoreline including a typical shine down curve (photon count vs. excitation time) the associate growth curve (photon count vs. Laboratory β dose) and the radial plot. The open circle on the growth curve plot is a duplicate dose point used to determine the recycling ratio.

Since it is close to unity in these samples, the test dose procedures has successfully corrected for sensitivity changes. The grey region on the radial plots represents the weighted-mean equivalent dose value of all the data. a) GPBS-1; b) GPBS-2; c) GLP-03; and d) GLP-04. 209

Figure 6.12. The slope of the isostatically adjusted surfaces though time. Phase I, GLP formed between the LIS and the CIS. Phase II, Canadian Interior Plains initially rose in response to ice unloading, causing shorelines to dip to the southwest. After Phase III isostatic uplift in the Rocky Mountains outpaced uplift in the Canadian Interior Plains (not to scale). 216

Figure 6.13. Possible ice sheet and GLP configuration in the Late Wisconsinan with isostatically corrected topography (study area is marked by the dashed black box) (ice margins modified from Mathews, 1980 and St Onge, 1972). a) Ice Sheet Convergence; b) Early Ice Sheet Separation c) Phase I: Both the CIS and the LIS continue to retreat and meltwater coalesces to form GLP; d) Phase II: The first phase with well established shorelines, was established around <16.0 ± 2.5 ka to 14.2 ± 0.5 ka yrs BP (from OSL ages). e) Upper Phase III: Equivalent to Bessbough Phase, a stable phase with an outlet at Pass Creek; f) Lower Phase III: Equivalent to Mathews' unnamed Phase 3; It is possible as the lake receded, a topographic high separated the Peace River Basin from the Smokey River Basin causing emergence of land around Grande Prairie; Phase IV: Lowest phase of GLP that occupied mainly the Peace River Basin. 217

Figure 6.14. Phases of GLP from this study correlated with previous work. 221

Figure 7.1. Location map of the study area. 239

Figure 7.2. Regional vegetation history from ca. 13 ka to 8 ka (from Dyke et al., 2004); a) ~13 k ^{14}C yrs BP; b) 12 k ^{14}C yrs BP; c) 11 k ^{14}C yrs BP; d) 10 k ^{14}C yrs BP; e) 9 k ^{14}C yrs BP; f) 8 k ^{14}C yrs BP. 242

Figure 7.3. a) Peat ped from sample FBRP-06, (78 to 78.5 cm) with embedded *Chara* oogonia (black spheres); b) peat ped with embedded *Chara* oogonia (arrows; FBRP-08); c) close-up of embedded *Daphnia* ephippium in d) peat ped from FBRP-09; e) fossil ephippium of a water flea (*Daphnia* sp.; FBRP-09). 244

Figure 7.4. a) and b) Climbing ripple and cross-laminated silty sand from an exposure on the West Kiskatinaw River (black grains are coal fragments). These glaciolacustrine sediments are likely the source material for the Kiskatinaw Dune Field; c) an exposed dune mound from dune Area B (see Fig. 7b) and contoured stereo net showing poles to planes of the strata (near horizontal); d) a close up of horizontal to shallow dipping laminated medium sand from dune shown in Fig. 7.4c; e) low ridge from an elongated dune at sample site KDF-6 (Fig. 7.8); horizontally laminated medium sand overlain by planar cross stratified medium sand from within the arm of an elongated dune ridge at KDF-2 (see Fig. 7.9). .. 249

Figure 7.5. Four clusters of dunes (a-d) make up the Kiskatinaw Dune Field..... 251

Figure 7.6. a) Dune Area A (all images have 2x vertical exaggeration); b) composite parabolic dunes; c) sand accumulation and emerging dune along a gully; d) composite parabolic and zig-zag dunes with prominent dune heads; e) zig-zag dunes with well developed aprons rather than ridged dune heads. 252

Figure 7.7. a) Dune Area B (all images have 2x vertical exaggeration); b) dunes hummocks connected by subtle ridges; c and d) dune hummocks that form a eroded composite dune head. 253

Figure 7.8. a) Dune Area C (all images have 2x vertical exaggeration); b) Large (km-scale) u-shaped dune complex; c) Large (km-scale) u-shaped dune complex with subsequently remobilized head (not currently active). The luminescence stabilization age from a ridge on the southern shoulder is 10.6 ± 0.6 ka BP (KDF-5) and the northern arm is 11.0 ± 1.0 ka BP (see Fig. 7.8a for location). 254

Figure 7.9. a) Dune Area D (all images have 2x vertical exaggeration); b) a barchan dune with trailing arms partially preserved; c) elongated twined parabolic dune (optical ages: KDF-1 = 10.8 ± 0.6 ka BP; KDF-2 = 12.3 ± 0.7 ka BP); d) elongated parabolic dune with in succession arrangement (David, 1977) (optical ages: KDF-4 = 8.7 ± 0.5 ka BP; KDF-3 = 11.3 ± 0.7 ka BP); e) elongated parabolic dunes complex at the downwind (east) region of Dune Area D. 256

Figure 7.10. Dose response curves with example of a typical shine-down curve. The open circle on the growth curve is a duplicate dose point used to determine the recycling ratio. Since it is close to unity in these samples, the test dose procedures has successfully corrected for sensitivity changes. a) KDF-1; b) KDF-2; c) KDF-3; d) KDF-4; e) KDF-5; and f) KDF-6. .. 258

Figure 7.11. Radial Plots with central age modeled. The grey region on the radial plots represents the weighted-mean equivalent dose value of all the data. OD = Overdispersion; N = number of aliquots. a) KDF-1; b) KDF-2; c) KDF-3; d) KDF-4; e) KDF-5; and f) KDF-6. . 259

Figure 7.12. Organic section from the Flatbed River; a) summary stratigraphic log with radiocarbon dates; and b) photograph of the overbank and organic portion of the section; Overbank sand with paleosol (arrow) dated at 10 315 ± 25 ^{14}C yrs BP (12 183 ± 193 cal yrs BP); d) contact between overbank sand and compressed organics; e) contact between compressed organics and dense peat. 261

Figure 7.13. Examples of fossils recovered from FBRP-01. a) ostracode valve; b) calcium carbonate cylinder; c) Cretaceous reworked coal; d) moss; e) unknown seed (*Potamogeton?*); e) unknown partial seed; g) aged rhrizome. Note the poor preservation of the seeds and Fe staining (rust-coloured precipitate) on the fossils. 267

Figure 7.14. a and b) Opposite views of a conical (vertical coiled) snail from FBRP-01; Spruce (Picea sp.) macrofossil needle fragments from c) FBRP-01; d) FBRP-12; and e): FBRP-14 (charred). Charred and not charred spruce needle fragments from FBRP-14; f) a macrofossil fragment of a two-needle pine, Pinus contorta from sample FBRP-04. Pinus contorta occurs on a wide range of soils and sites, including wet depressions and easily colonizes recently burned areas (Farrar, 1999). 268

Figure 7.15. a) Fossil elytron from an *Aegialia* Sp. beetle (FBRP-05); b) fossil elytron of *Cytilus alternatus* fro sample FBRP-06. This elytron is one of three that were dated along with other beetle parts including *Morychus* elytron, *Lepidophorus lineaticolis* pronota, that yielded an age of 10 000 ± 35 ^{14}C yrs BP (11 490 ± 206 cal yrs BP). 272

Figure 7.16. a) fossil achene of *Typha latifolia* (Cattails) from sample FBRP-06.; b) fossil fruit of *Ruppia cirrhosa* (ditch grass) from FBRP-06; c) macrofossil achene of flatstem pondweed from FBRP-07; d)cross-section of same achene. 274

Figure 7.17. a) fossil seed likely of strawberry-blite (*Chenopodium catpitatum?*) from FBRP-08. Chenopodium seeds are abundant in this sample and not seen in other samples examined; b) *Chara* oogonium with calcium carbonate coating (FBRP-08); c) fossil achene of *Schoenoplectus tabernaemontani* (FBRP-09). Four achenes weighing 3.37 mg were dated yielding an age of 9770 ± 25 ^{14}C yr BP (11 207 ± 28 cal yrs BP); d) fossil fruit of mare's-tail (*Hippuris vulgaris*) from sample FBRP-09. 277

Figure 7.18. a, b, and c) fossil achene from Richard's pondweed (*Potamogeton richardsonii*) from FBRP-09; d) fossil of willow (*Salix* sp.) persistent bud from FBRP-09; e) a well preserved fossil achene enclosed in perigynium (outer seed coat) of Richard's pondweed, *Potamogeton richardsonii* (FBRP-10); f) fossil achene of *Ceratophyllum demersum* (FBRP-10). 280

Figure 7.19. Aquatic plant fragments from FBRP-10. 282

Figure 7.20. Fossil fauna from FBRP-11; a) fossil elytron fragment of a predaceous diving beetle (*Colymbetes* sp.); b and c) fossil statoblast of *Cristella mucedo*..... 283

Figure 7.21. Aquatic plants from FBRP-11; a) pondweed (*Potamogeton richardsonii*) leaf from felted peat layers; b) pondweed, *Potamogeton richardsonii?* From embedded leaf in felted peat layers. 284

Figure 7.22. Plant macrofossils from FBRP-11; a) fossil seed of water nymph (*Najas flexilis)*; b) flattened fossil seed of *Najas flexilis*; c) fossil seed of buckbean (*Menyanthes trifoliate*); d) freshwater algae stonewort (*Chara* sp.) oogonium; e) fossil seed of bearberry, *Arctostaphylos uva-ursi*. 285

Figure 7.23. a) fossil pronotum of *Acilius semisulcatus* from FBRP-12; b) fossil seed of snowberry (*Symphoricarpos albus*) from FBRP-12. Five seeds weighing 6.47 mg were dated yielding an age of 8845 ± 20 ^{14}C yr BP (UCIAMS-117271). 287

Figure 7.24. Moss from FBRP-13; a) felted, thin sheet, of compacted mosses; b) close-up of the moss sheet with modern root contamination (arrows). 289

Figure 7.25. a) Comparison of dune stabilization ages from the Kiskatinaw Dune Field (blue) and other published ages (red; from Wolfe et al. 2004; Wolfe et al., 2007 and Munyikwa et al., 2011; all K-Feldspar ages). Stabilization ages are considered to be from those samples collected from a depth of < 2m (arbitrary) below surface (NE BC = Northeast British Columbia; NNE BC = Northern Northeast British Columbia; NNW AB = Northern Northwest Alberta; NW AB = Northwest Alberta; NC AB = North-central Alberta; WC AB = West-central Alberta; C AB = Central Alberta; see Table 7.7); b) Comparison of the radiocarbon ages and the interpreted biome (following Dyke's, 2005 classification) from the Flatbed River Section and the stabilization ages for the Kiskatinaw Dune Field. 294

Figure 8.1. The study area is located at the Scobie Ranch on the Halfway River floodplain in northeast British Columbia. 314

Figure 8.2. This reach of the Halfway River is best described as a poorly organized wandering gravel-bed river. The study area is outlined. 315

Figure 8.3. Two hydrographs show the mean average monthly discharge of the Halfway River. Station 07FA003 is located downstream of the study area but above the confluence of the Graham and Halfway rivers. Station 07FA006 is located below the confluence towards the Peace River (Fig. 8.1). 316

Figure 8.4. Five aerial photographs of the Scobie Ranch show the evolution of the floodplain of the Halfway River in the study area (box indicates area in Figure 8.2). The numbers refer to bars, and letters to channels. From 1963 to 1987 subordinate channel b became the main channel when channel a was reduced to a subordinate status and eventually abandoned by 1999. Lateral bar 1 developed from the eastward migration of channel b. Bar 2 developed from a small lateral bar into a compound bar as channel c migrated to the east. Channel c eventually became choked with sediment by 1992 and avulsed to a western position by 1999, dissecting bar 2. The former positions of channel c were subsequently reduced to subordinate status after 1999. 317

Figure 8.5. Bar 2 (see Fig. 8.4) is a likely analog for the development of the features in this study. A, B) Migrating gravel sheets preserved on the top of bar 2. C) Gravel sheet preserved on top of the bar platform in Figure 8.6. D) Channel c is an abandoned channel of the Halfway River. E) The active channel in 1992 is now vegetated with organic mud overlying gravel. F) The organic mud in the former active channel. 319

Figure 8.6. The GPR and CCR surveys were conducted over a bar platform and channel bend. The numbers indicate trench locations, and the letters refer to morphostratigraphic units (BR = bar, CH = channel, TL = local topographic low, FP = undifferentiated floodplain). A) GPR survey lines (shown in white). B) The CCR survey lines (shown in white). C) Bar and channel viewed from the southeast end of Line 3 towards the northwest (arrow indicates people for scale). D) Topographic profile with morphostratigraphic units along GPR Line 2. 320

Figure 8.7. OhmMapper configuration with five dipoles and a transmitter (modified from Geometrics, 2001) 322

Figure 8.8. Trench stratigraphy of the bar platform and channel (locations in Fig. 8.6). 325

Figure 8.9. A portion of GPR Line 5 located across the bar platform. A) Raw data; B) filtered data; C) interpreted data (see Table 8.2). 328

Figure 8.10. A portion of GPR Line 2 located at the transition from the bar platform to the channel. A) raw data; B) filtered data; C) interpreted data (see Table 8.2). 329

Figure 8.11. Radar facies pairings and 3-D reflection orientations from the intersection of GPR lines. 333

Figure 8.12. Resistivity data from the 3-D model overlaid onto the GPR lines. The numbers refer to radar facies from Table 8.2, the dashed lines are facies boundaries, and the solid lines are storey boundaries. A) Upstream margin of bar platform and channel. B) Small subtle topographic low on bar platform. C) Upstream margin of bar platform. D) Well developed topographic low within bar platform. 334

Figure 8.13. The surface resistivity correlates well with the morphostratigraphic units derived from the aerial photographs (BR = bar, CH = channel, TL = local topographic low, FP = undifferentiated floodplain). 336

Figure 8.14. Example of combined the GPR and CCR from a portion of GPR Line 4 with resistivity distributions and corresponding grain size for several GPR facies. 338

Figure 8.15. Simplified Resistivity-value distribution shapes used as a proxy for grain size and sorting for each radar facies polygons (Table 8.3). a) log-normal low variability; b) log-normal moderate variability; c) log-normal highly variable; d) log-skewed left; e) log-skewed right; f) log-bimodal; and g) log-multimodal. 340

Figure 8.16. Two idealized vertical sections representing the stratigraphy of the channel fill and the bar platform from trench data. 343

Figure 8.17. The evolution of the bar and channel based on the combined sedimentology, GPR, and CCR data. 345

Acknowledgments

I would like to thank my wife, Dr. Leanne Pyle, and our sons Henry and James for permitting me the time to complete this work. I am eternally grateful to my father, Dr. Edward (Ted) James Hickin, for his mentoring, advice, nurturing and generosity. I would like to acknowledge my supervisor, Dr Vic Levson, who has taught me much and asked for very little in return.

During the course of this degree I have remained in the employment of the Government of British Columbia. During this period I have been fortunate to have risen through the License Science Officer ranks (LSO3-LSO5) and appointment to the Director of Cordilleran Geoscience at the British Columbia Geological Survey. This would not have been possible without the support of senior management in Oil and Gas Divison and the Mining and Mineral Divison. I would like to recognize executive directors Derek Brown, Vic Levson, and Linda Beltrano for allowing me to complete my thesis while attending to my other duties. During my studies I was supported by Pacific Leaders Scholarships for Public Servants.

Much of this work was completed as part of the Northeastern British Columbia Aggregate Program (2003-2010). This program was a partnership between the Province of British Columbia (Resource Development and Geoscience Branch), the Geological Survey of Canada, several universities, local communities, and many oil and gas operators. I would like to recognize all the program contributors and thank them. The success of the program was only possible because of the collaboration and sharing of information, data, and resources.

I appreciate the patients of my committee and thank them for the time and helpful guidance. I would particularly like to acknowledge the mentoring of Dr. Olav Lian and Dr. Mel Best who have been instrumental in my development as a scientist.

I have had the benefit of working, learning, and collaborating with some wonderful people over the years and would like to thank them all. In particular, my colleagues, collaborators and friends Roger Paulen, Travis Ferbey, Tom Barchyn, Dave Huntley, Ben Kerr, Fil Ferri, Marten Geertsma, Alice Telka, Chelton Van Geloven, Dave Wilford, Tania Demchuk, Chris Hugenholtz, and Rod Smith. My gratitude is extend to Roger Paulen, Travis Ferbey, Tom Barchyn, Derek Turner, Dave Sacco, Andrea Marich, Fil Ferri, Dave Huntley, and Janet Riddell for their capable assistance in the field. Many thanks to Justine Cullen (University of the Fraser Valley) for assisting with the laboratory processing and analysis of my optical samples.

Dedication

This thesis is dedicated to my family:

Dr. Leanne J. Pyle, Henry and James Hickin, Elaine Hickin and Dr. Edward J. Hickin

CHAPTER 1: INTRODUCTION

This thesis examines the late Quaternary and Holocene history of northeastern British Columbia through a series of papers that explore a number of independent, but related topics. Although the papers are intended to be stand-alone studies, collectively the research contributes to a better understanding of Quaternary geology and the evolution of the landscape in a region where two continental ice sheets (Cordilleran and the Laurentide) affected the area and likely interacted. Five of the studies included in this thesis occur in the Dawson Creek area, one occurs northwest of these studies along the Halfway River (a tributary of the Peace River), and one is farther north, east of Fort Nelson near the British Columbia-Alberta border. The thesis is organized into three parts, including: 1) introduction; 2) seven independent papers; and 3) summary.

The papers are presented in a broadly geochronological order starting with an investigation of the geometry of paleovalleys that represent ancient landscape features (chapters 2 and 3). Chapter 4 examines the late Quaternary stratigraphic record of several paleovalleys which provide the temporal context for glacial landforms preserved at surface in the modern landscape. Chapter 5 further examines surface landform features associated with an active glacial phase (streamlined landforms) and a stagnation phase (hummocky moraine) of the late Wisconsinan glaciation. Chapter 6 focuses on configuration, timing, and deglacial implication of glacial Lake Peace, the Late Wisconsinan ice marginal lake that occupied much of the Peace Region. Chapter 7 presents timing constraints for the transition from paraglacial to boreal conditions, using dating of stabilized sand dunes (geomorphic) and biome succession (biological) at the close of the Quaternary period. Chapter 8 explores the Holocene to modern landscape of the study area, specifically directed at linking river planform with subsurface architecture.

Chapters 2 and 3 include papers that examine bedrock topography and focus on paleovalleys, an important and ancient element of the landscape. These studies document bedrock surfaces and paleovalleys that either formed prior to glaciation and were then buried, or alternatively formed during glaciation but were subsequently filled with deglacial sediments. The sedimentary records preserved in these paleovalleys provide important stratigraphic information and chronological context for Quaternary studies.

The studies in chapters 2 and 3 are conducted in two physiographically distinct regions. Chapter 2 examines bedrock topography and paleovalleys from the Fort Nelson Lowlands physiographic region, a subdivision of the Alberta Plateau. A bedrock topography model, generated from oil and gas petrophysical logs, reveals a network of significant paleovalleys that have no relationship with subdued topography of the modern landscape. The study described in Chapter 3 is conducted in the Groundbirch region near Dawson Creek, a part of the Alberta Plateau physiographic region. Here, modern topography has more relief than in the area investigated in Chapter 2. Unlike the paleovalleys documented in Chapter 2, those in the Chapter 3 study area are coincident with modern valleys in this region. The bedrock topography model in Chapter 3 is based on water well drillers' logs. This model is used to test the applicability of a ground-based electromagnetic geophysical survey for mapping the geometry and lithostratigraphy of a paleovalley, in a setting with limited resistivity contrast between adjacent valley-fill units, as well as between the valley-fill and bedrock.

The study in Chapter 4 examines, documents, and correlates Quaternary stratigraphy within the Murray-Pine and Kiskatinaw paleovalleys as a means of providing the temporal context for paleo-ice flow landforms preserved at surface in the modern landscape. The age, origin and ice-flow direction interpreted from surface landforms is contentious in this area. Stratigraphy from 11 lithostratigraphic sections are described and correlated. The units are assigned to major climatostratigraphic intervals thereby providing the chronological context for glacial landforms at surface. Streamlined landforms are mapped to reconstruct various ice flow trajectories during major flow events.

The study in Chapter 5 evaluates a hypothesis that the orientation of electrical anisotropy in till is indicative of the direction of paleo-ice flow. It has been proposed that the principle axis of electrical anisotropy in till is coincident with the direction of ice flow. The orientation of the principal axes of resistivity ellipses generated from azimuthal electromagnetic data and the orientation of streamlined landforms (which are assumed to be parallel to ice flow) is, however, not consistent in northeast British Columbia. Several explanations are proposed to explain this inconsistency. Understanding the control on electrical anisotropy may provide a new tool that elucidates the preserved stress fields in sediments imparted by active or stagnant ice conditions.

Chapter 6 focuses on glacial Lake Peace, the retreat phase ice marginal lake whose sediments cover much of the Peace region. This study uses high resolution digital elevation

models such as those derived from light detection and ranging (LiDAR) surveys to map shorelines from glacial Lake Peace. These shorelines are first used to restore relative topography adjustment to pre-isostatic crustal position (the result of ice loading and unloading) and second, reconstruct glacial lake and ice-sheet configuration. Optical dating of quartz grains from a prominent shoreline provides temporal control of establishment of glacial Lake Peace, and therefore the separation of the Cordilleran and Laurentide ice sheets. This dating technique has not been widely applied to glacial lake settings.

The study in Chapter 7 focuses on establishing the timing for the transition from glacial and paraglacial conditions to a boreal setting similar to that of today's northeastern British Columbia. In this study, two independent proxies for climate amelioration are investigated. The first comes from the optical ages from sand dunes in the Kiskatinaw area, south of Dawson Creek. Optical ages are calculated by determining the amount of, and rate that ionizing energy is absorbed by a mineral grain after it is has been exposed to heat or sunlight (i.e. buried). These ages mark the stabilization of sand dunes that were likely active after the recession of glacial Lake Peace but prior to major forest colonization (i.e. while the area was still influenced by paraglacial conditions). The second proxy comes from radiocarbon ages and macrofossils from organic deposits. These deposits preserve flora and fauna that can be assigned to several biomes that mark the succession from Forest Tundra to the Boreal Forest conditions of the modern landscape.

The final paper in the thesis, Chapter 8, is directed at understanding the architecture of a modern river floodplain. Although incision is the dominant post-glacial geomorphic process in many river systems in this region, some systems along the foothills are in a state of limited aggradation. This case study investigates a poorly organized wandering gravel bed reach of the Halfway River and combines ground penetrating radar and capacitively-couple resistivity to examine the architecture and grain-size distribution of the floodplain deposits. This novel geophysical approach links fluvial style with subsurface sedimentology, two critical components to modern fluvial architectural analysis.

The thesis concludes with a summary chapter that discusses glacial history and landscape evolution in northeast British Columbia based on the major contributions of each of the papers.

CHAPTER 2: MAPPING QUATERNARY PALEOVALLEYS AND DRIFT THICKNESS USING PETROPHYSICAL LOGS, NORTHEAST BRITISH COLUMBIA, FONTAS MAP SHEET, NTS 94I

Adrian S. Hickin, Ben Kerr, Derek G. Turner, and Tom E. Barchyn

A version of this chapter was published in the Canadian Journal of Earth Science, 2008

Citation:

Hickin, A.S., Kerr, B., Turner, D.G., and Barchyn, T.E., 2008. Mapping Quaternary paleovalleys and drift thickness using petrophysical logs, northeast British Columbia, Fontas map sheet, NTS 94I; Canadian Journal of Earth Sciences, vol. 45, pages 577—591.

Abstract

The relatively subdued topography of British Columbia's northern interior plains does not reflect the irregular, buried bedrock surface. Many areas have been deeply incised by preglacial rivers that have subsequently filled with a succession of Quaternary sediments. In this study, oil and gas petrophysical logs, drill chip samples, water well logs, and surficial and bedrock outcrop maps were used to model the bedrock topography of the Fontas map sheet (NTS 94I). The modelled data produced several depressions that are interpreted to be paleovalleys incised into the soft Cretaceous shale of the Fort St. John Group. Understanding the geometry, thickness, and stratigraphy of the drift has considerable safety and resource management implications as artesian aquifers and natural gas were encountered in the drift during oil and gas well drilling. Four major paleovalleys are suggested. The most dominant paleovalley (Kotcho–Hoffard Paleovalley) is located south of the Etsho Plateau and trends west-southwest across the map area. A second depression occurs within the loop of the Hay River and may be a tributary of the Kotcho–Hoffard Paleovalley that links with the Rainbow Paleovalley in Alberta. A third paleovalley is mapped south of the Sahtaneh River (Kyklo Creek Paleovalley) and is either a tributary to, or crosscuts the Kotcho–Hoffard Paleovalley. The Niteal Creek Paleovalley is located between the Fontas and Sikanni Chief rivers. Its geometry is speculative as there are sparse data, but it may be a tributary of the Kotcho–Hoffard Paleovalley.

2.1 Introduction

Bedrock topography is often obscured in glaciated terrain. Sediment accumulates in pre-existing valleys, masking bedrock irregularities. Buried valleys are well known throughout Canada's Interior Plains (e.g., Stalker, 1960, 1967; Christiansen, 1961; Andriashek and Fenton, 1989; Horne and Seve, 1991; Pawlowicz et al., 2005). However, with the exception of the work of Mathews (1978) and Hartman (2005) on the Paleo-Peace River valley near Fort St. John, little bedrock topography and drift thickness information has been published for northeast British Columbia (NEBC). This study provides regional bedrock topography and drift thickness for the Fontas map sheet (National Topographic System (NTS) map sheet 94I). The merits and limitations of the mapping methods are discussed, and the major trends of paleovalleys in the study area are identified. Understanding the geometry and depth of these paleovalleys is becoming increasingly important for shallow gas exploration, drilling safety, casing depth estimates, aquifer management, and seismic processing and interpretation (Levson et al., 2006).

The study area is located in the British Columbian portion of Canada's Interior Plains (Holland 1976; Fig. 2.1). Much of the surface topography occurs at <610 m (2000 ft) above sea level (asl) and is part of the Fort Nelson Lowland physiographic region. Areas with elevations >610 m (2000 ft) asl, such as the Etsho Plateau, are arbitrarily assigned to the Alberta Plateau physiographic region (Holland 1976).

Much of the map area is underlain by Cretaceous age shale of the Fort St. John Group (late Albian to Cenomanian; Fig. 2.2). The Fort St. John Group is exposed along incised portions of the Sikanni Chief, Fontas, Kotcho, and Fort Nelson rivers and along portions of the Etsho Plateau escarpment. It consists of soft shale and siltstone with thin beds of fine-grained sandstone. In areas with elevation >610 m, Thompson (1977) mapped Upper Cretaceous Dunvegan Formation. Thompson (1977) did not encounter Dunvegan Formation in outcrop but inferred its presence based on topographic expression. Three areas are mapped as Dunvegan Formation in the map area, including the Etsho Plateau in the north, the uplands of the upper Fontas River in the southeast, and several prominent knobs in the southwest. Where exposed, west of the study area, the Dunvegan Formation is typically a cliff-forming succession of deltaic and pro-deltaic sandstone, conglomerate, and carbonaceous mudstones (Stott 1967).

In this study, major subsurface stratigraphic boundaries were picked from well logs, which include the Shaftesbury and Spirit River formations of the Fort St. John Group (Cretaceous),

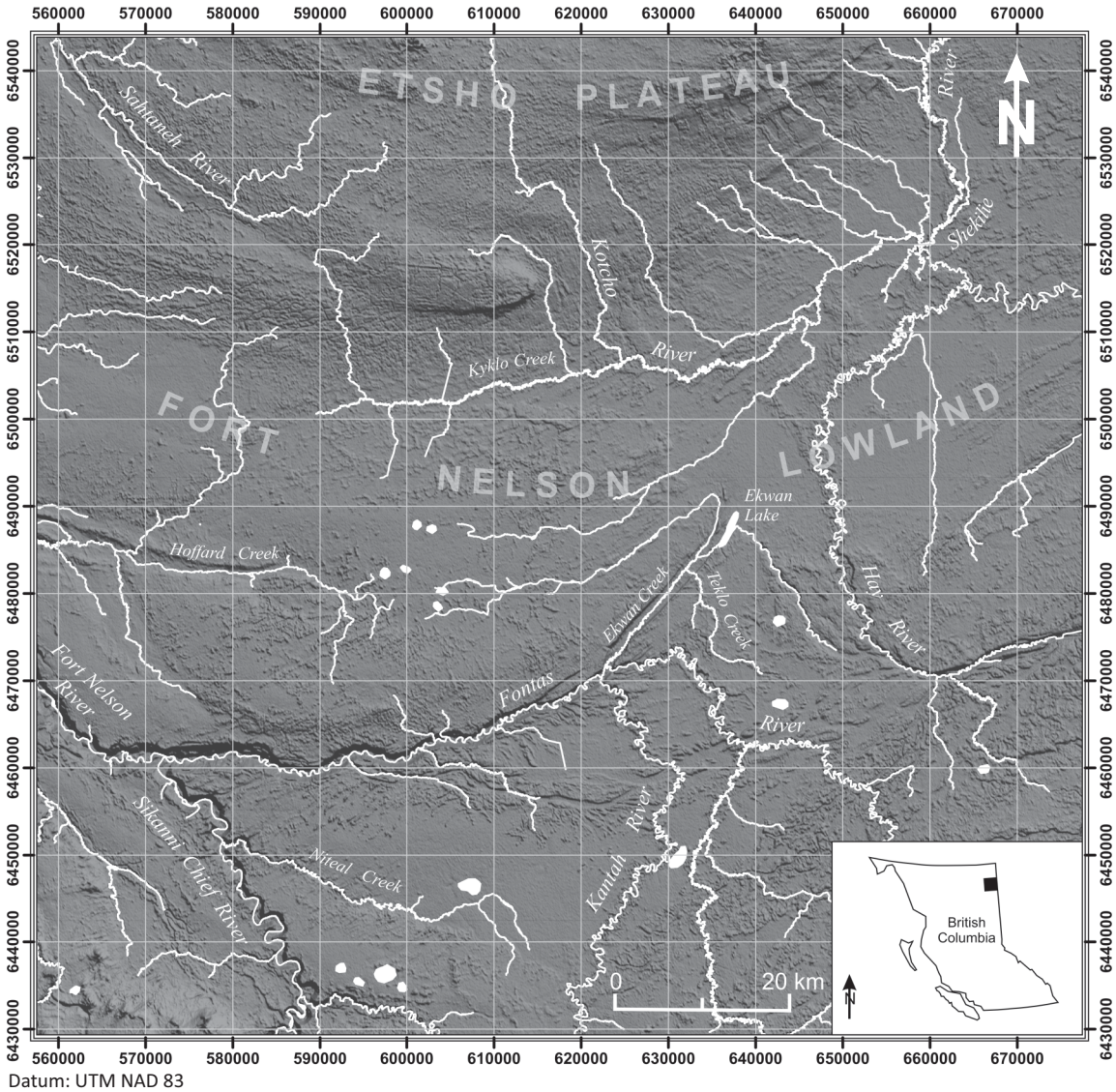

Figure 2.1. The study area is located in northeastern British Columbia in NTS map sheet 94I (Shuttle Radar Topography Mission (SRTM) digital elevation model; 10x vertical exaggeration).

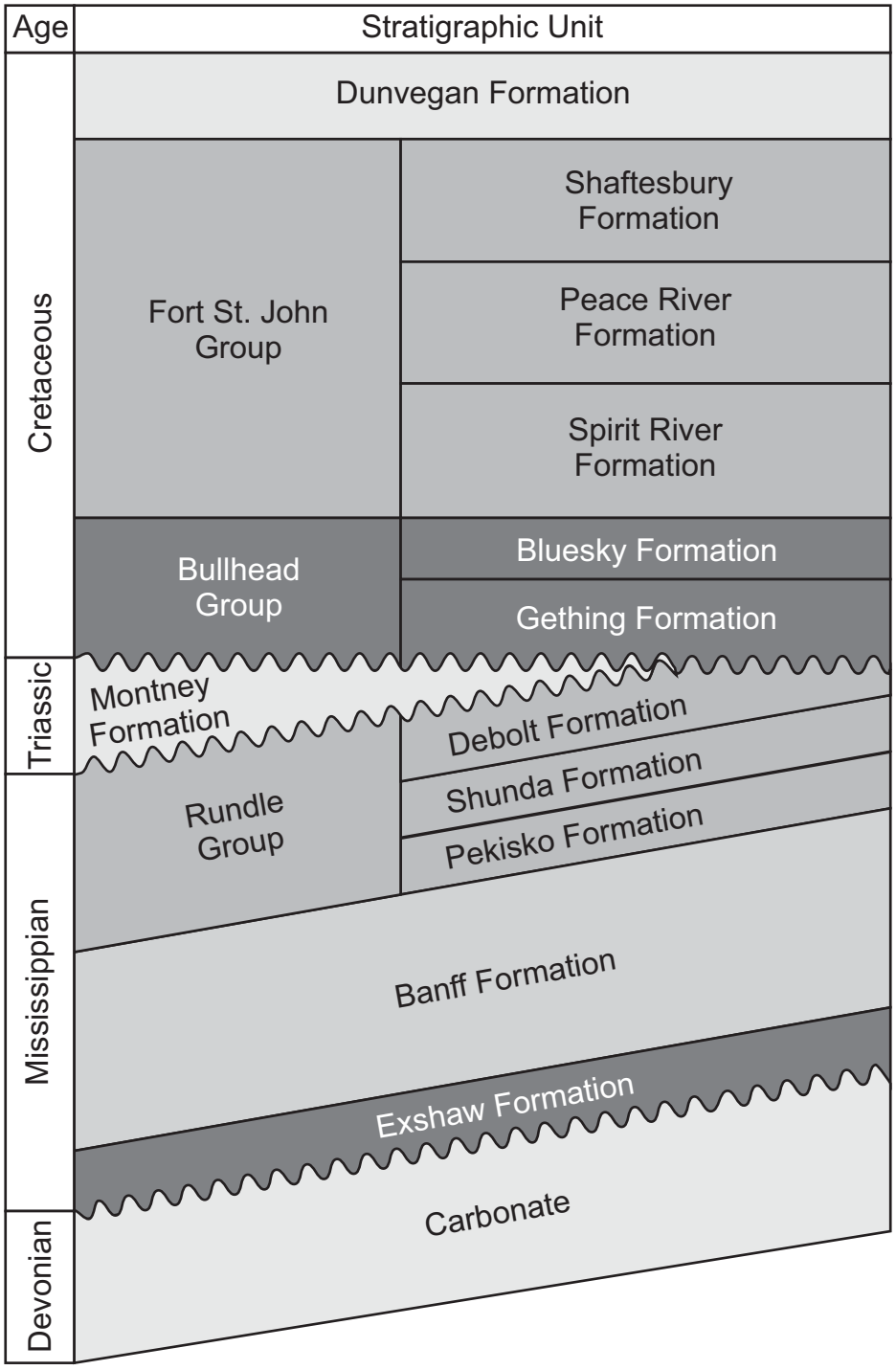

Figure 2.2. Generalized bedrock stratigraphy for the study area (after Stott, 1982 and Thompson, 1977).

Bullhead Group (Cretaceous), Diaber Group (Triassic), and Rundle Group (Mississippian; Fig. 2.2). Fort St. John Group, in the study area, is difficult to divide into its members as this succession represents distal basin facies, dominated by shale and siltstone, and minimal sandstone. Despite this, the Fort St. John Group can be separated into the Shaftesbury Formation and the Spirit River Formation. The lower Shaftesbury Formation contains a highly radioactive interval (condensed section), the base of which is marked by a sharp gamma drop separating the Shaftesbury from the underlying Spirit River Formation (W. Walsh, personal communication, 2007).

Where present, Bullhead Group strata underlie Fort St. John Group sediments. The Bullhead Group in 94I is represented by a thin wedge of siltstone and sandstone that thins to the northeast and pinches out to the west (Stott 1973). The base of the Bullhead Group in the area is coincident with the sub-Cretaceous unconformity.

The base of the Cretaceous is marked by a regionally extensive unconformity that eroded southwest dipping pre-Cretaceous sediments, forming erosional edges of the older Triassic and Mississippian units. The Triassic Diaber Group, represented by the Montney Formation, occurs in the southwest of the map area with an eastern margin near Kantah River. The Montney Formation consists of siltstone, shale, and sandstone and is an important gas-bearing unit (Glass 1997; British Columbia Ministry of Energy, Mines and Petroleum Resources 2006). Where the Triassic succession is absent, the Cretaceous package occurs directly above the Mississippian Rundle Group. The Rundle Group consists of crinoidal limestone (Pekisko Formation), interbedded limestone, dolostone, siltstone, sandstone, shale and breccia (Shunda Formation), and limestone with minor dolomite and shale (Debolt Formation). The Rundle Group also contains important gas-bearing units with several play styles including subcrop margin, distal ramp, and regional platform (Glass 1997; British Columbia Ministry of Energy, Mines and Petroleum Resources 2006).

The surficial geology of NEBC and northern Alberta is the result of Tertiary and Quaternary events. During the Tertiary, the Laramide Orogeny resulted in the uplift and subsequent erosion of the Canadian Rocky Mountains and adjacent areas. Erosion was the dominant geomorphic process through to the early Quaternary (Edwards and Scafe 1996). Paleodrainage during this time was likely eastward, down the regional slope towards Hudson Bay. Quartzite-rich gravels were transported from the Canadian Rocky Mountains, onto the Al-

berta Plateau as far east as central Alberta. These gravels armoured the relatively soft Cretaceous sediments and assisted in the formation of tablelands. Some of the major valleys (and paleovalleys) in NEBC are likely remnants of Tertiary drainage systems. Climatic deterioration at the end of the Tertiary, culminated in the glacial–interglacial cycles synonymous with the Quaternary. Much of the landscape of NEBC is attributed to the most recent cycle during the Late Wisconsinan (ca. 25–10 ka ^{14}C yrs BP). In British Columbia, this glaciation is referred to as the Fraser Glaciation (Clague and Ryder 1989).

The Wisconsinan glacial history in NEBC has been described by Mathews (1963, 1978, 1980), Bobrowsky and Rutter (1992), Catto et al. (1996), Bednarski and Smith (2007), and Bednarski (2008). NEBC was first glaciated prior to the Late Wisconsinan but only a limited, controversial record of these events exists (Mathews 1978, 1980; Reichmen 1980; Hartman 2005; Trommelen 2006). During the Late Wisconsinan, valley glaciers (montane), the Cordilleran Ice Sheet (CIS), and the Laurentide Ice Sheet (LIS) all interacted. The relationship of these glaciers is complex, with coalescence and nonsynchronous advances occurring along the ice margins (Bednarski and Smith 2007). In general, the LIS advanced from east to west up the regional slope, blocking drainage and developing large pro-glacial lakes along the margin (Mathews 1980). During this same interval, ice accumulated in the mountains and thickened to form large valley glaciers, which eventually combined to form the CIS that flowed east onto the plains from the Canadian Rocky Mountains (Rutter 1977; Clague 1989; Catto et al., 1996; Bednarski 2001; Bednarski and Smith 2007). The CIS and LIS likely coalesced for a period before receding (Jackson et al., 1997). As the CIS thinned to form valley glaciers, the LIS retreated, again forming large pro-glacial lakes along its margin (Mathews 1980; Dyke et al., 2003). Evidence for the advance and retreat of ice and the presence of glacial lakes is recorded in the thick sediment sequences and surface landforms that mask the underlying bedrock topography.

2.2 Methods

Bedrock topography mapping follows methods outlined by Hickin and Kerr (2005). The process can be summarized into four steps: (1) compile all available data sources; (2) standardize the data in a database; (3) spatially analyze the data and model subsurface horizons; and (4) add geological interpretation.

Several data sources were used to determine the base of the drift as well as the top of the

Spirit River Formation, Bullhead Group, Diaber Group, and Rundle Group. These sources include oil and gas petrophysical well logs, drill cuttings, water well logs, and available surficial and bedrock maps.

The most important and reliable source of data was from oil and gas petrophysical logs available from the British Columbia Ministry of Energy, Mines and Petroleum Resources. These contacts, or picks, are termed ‘‘hard picks.’’ The majority of the drift–bedrock contacts and all of the bedrock stratigraphy were compiled from these data. Gamma logs were the most common log used as they provided lithologic information for both cased and uncased portions of the wells. The drift contact was typically identified by a sharp upward shift from a uniform, relatively high gamma signal in the bedrock to a relatively low, fluctuating signal in the drift (Fig. 2.3). The uniform gamma signal is associated with thick sequences of dark, organic-rich shale and siltstone of the Fort St. John Group (Shaftesbury Formation). The fluctuating gamma signal is attributed to unconsolidated drift, containing a relatively low organic content and consisting of a variety of units including gravel, sand, diamict, silt, and clay (Fig. 2.3). Resistivity and conductivity logs were also used where the drift contact occurred below casing. Unfortunately, not all contacts were obvious. In some cases, the contrast between weathered shale and till was subtle and more speculative. In addition, not all wells were logged to surface so that only maximum depth to bedrock could be ascertained.

Drill cuttings were also used to provide an estimate of the depth to bedrock. All available drill cuttings with tops within 300 m of surface were examined and logged (Fig. 2.4). Glacial sediments have an abundance of exotic clasts that can be transported a considerable distance. In NEBC, these allochthonous lithologies include Canadian Shield granites and Omineca Belt phyllites (Mathews 1980), which presence in drill cuttings suggests glacial sediments.

In most wells where both a petrophysical log and drill cuttings were available, the contacts correlate within 10–15 m. However, there were some wells where the contact determined from the petrophysical log differed greatly from that determined from the drill cuttings. In some cases, granitic fragments were mixed with shale and siltstone over a lengthy interval (>100 m) or cuttings showed an inversion of glacial sediments under shale. Contamination must be considered. In addition, loss of circulating drilling fluids, gradational contacts, and the lag time for a sample to reach the surface all contribute to the ambiguity of the precise depth to the contact. Wherever possible, the cuttings contacts were verified with

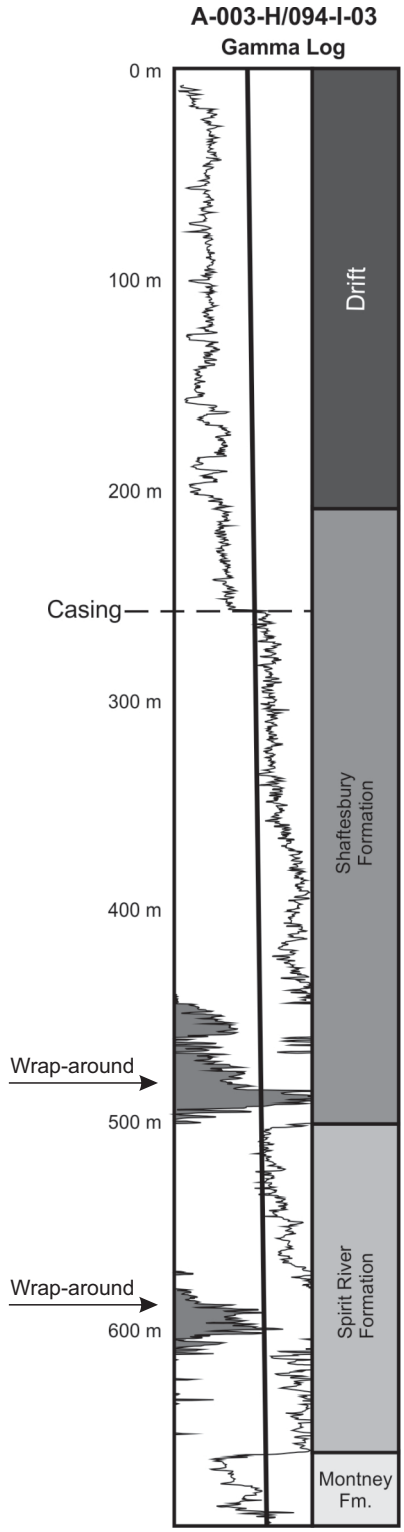

Figure 2.3. The major stratigraphic units can be identified from gamma logs. The immediate base of drift is marked by an upward shift from a relatively high, uniform gamma response to a more varied, slightly reduced signal. Where the log extends off the scale it is shown as a "wrap-around" and is shaded grey.

Figure 2.4. (A) Drill chip samples are washed and collected during oil and gas well drilling. The recovered chips show a clear lithologic distinction between shale bedrock (left) and glacial sediments (right). (B) Closeup of glacial sediments from the chip sample archived (tick marks in mm).

petrophysical data. The contacts determined solely from the lithology of the drill cutting were only used in the model where no other data were available. In some cases, driller's logs and tour sheets provided supplementary information regarding lithologic units encountered, drilling conditions, or problems associated with the penetration of aquifer- or gas-bearing units in both bedrock and drift. These noted intervals were incorporated into the model as ''soft picks'' where applicable.

The Province of British Columbia requests drill logs to be submitted to the British Columbia Ministry of Environment for all water wells drilled. The lithologic data from logs within the study area were compiled and incorporated into the model as soft picks. Unfortunately, many of the descriptions were colloquial and provide only limited information.

The final data set incorporated bedrock and surficial geological maps. Outcrop locations and elevations from Thompson (1977) were included as known depth to bedrock. In addition, bedrock and veneer (depth to bedrock <1 m) polygons from surficial maps were also digitized and included as known depths to bedrock (Trommelen 2006; Smith 2008*a*, 2008*b*, 2008*c*, 2008*d*). Data points were generated within the polygons in 100 m grid cells. Bedrock picks in bedrock polygons were coincident with surface elevations from a 90 m Shuttle Radar Topographic Mission[1] (SRTM) digital elevation model (DEM). Data points for veneer polygons were generated by subtracting 1 m from the DEM. These data are also considered soft picks.

All data were standardized and entered into a Microsoft Access database. Two classifications of data were established, lithologic and stratigraphic. Lithologic data refer to sediment types encountered (e.g., sand, gravel, shale, siltstone, etc.) but do not imply age or assignment of the sediment to a formation or group. These data were typically from oil and gas driller's logs and tour sheets, water well data, and drill cuttings. Stratigraphic data were derived from the petrophysical logs, and units were assigned to formations and groups implying an age relationship (e.g., Drift, Shaftesbury, Spirit River, etc.). All data were then available for query and display as logs in cross sections during the modelling and interpretation phase.

Once the data were compiled and sorted, point location and elevation below the surface data were extracted from the database for the major stratigraphic boundaries. These data provided the basis for generating interpolated surfaces that correspond to the major

[1]SRTM vertical datum is EGM96 and horizontal datum is WGS84.

stratigraphic boundaries. The quality of a predicted surface is closely linked to the quantity, reliability, and spatial distribution of inputs. The data distributions were spatially analyzed using histograms and semivariogram-covariance clouds in ArcMap and the Geostatistical Analyst extension. These characteristics provided insight into the most suitable interpolation method for predicting values between points (cf. Bailey and Gatrell 1995). The interpolation parameters were then fine-tuned through an iterative process in an attempt to minimize the root mean square error (i.e., the difference between the predicted value for the surface and the known data points).

To generate the bedrock topography map, two interpolation methods were used, a predicted and a fitted surface. The predicted (kriged) surface involved only the hard picks and was used as a working model into which the soft picks were incorporated (fitted). These were generated on cumulative combinations of samples from the three data sources in addition to geological interpretation.

Ordinary kriging was performed on the hard pick data, assuming general isotropy and using parameters generated from a semivariogram of elevation values. This provided statistically predicted bedrock topography in which to estimate soft picks. The next step in the process was to add nonpoint data (soft picks). All surfaces were imported into Viewlog software so that the data could be viewed and modified in cross section. The soft pick data were incorporated into the model by propagating a north–south cross section at 250 m intervals from the east side of the map sheet to the west, providing slices across the map area. This was repeated with an east–west cross section propagated from the north to the south. Posted on each cross section were the lithology and stratigraphy logs and the predicted surface. New points were added where the predicted surface violated some known information (Fig. 2.5).

The new combination of hard and soft elevation values were then interpolated using a radial basis function. This function honours the data at known points (now the hard and soft picks) and uses proximal points in a user-defined neighbourhood to predict values between known points. Points representing bedrock outcrop or surficial veneer were subsequently incorporated, and the interpolation was performed again. Density of elevation values from outcrop and veneer was much higher than from the other data sources. This affected the parameters used for modelling, but the results of the prediction were visually similar.

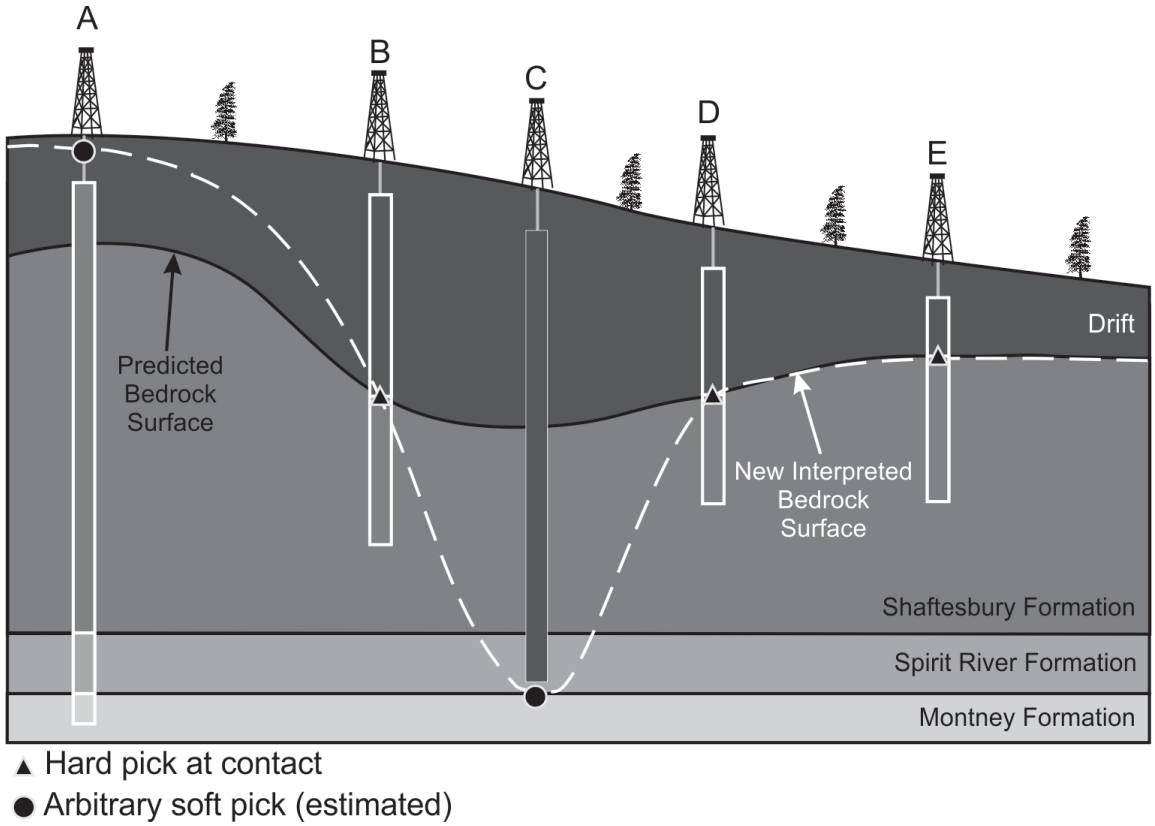

Figure 2.5. The predicted surface was an interpolated surface that honoured only the "hard" data points (those that contain *x*,*y*,*z* information) and used spatial analysis to estimate the depth to bedrock between data points. However, in some cases, known information is available but cannot be represented as point data (e.g., the bedrock surface is known to be less than or greater than some depth below surface). To incorporate this additional information, estimated soft picks were established. In this example, there were no hard drift picks at well sites A and C because no contacts were present. Consequently, the predicted surface violated known information displayed in the well logs. At well site A, bedrock was observed to the top of the logged section of the well; therefore, the *z* value for the bedrock surface must pass above the logged portion of the well. The predicted surface over estimated the depth to bedrock because there was no contact to pull the predicted bedrock surface towards the ground elevation. A arbitrary soft pick (interpreted) was added between the top of the logged portion of the well and the ground surface forcing the new interpreted surface above the top of the well. At well site C, drift was logged to the base of the well, but the contact occurred below the logged section. Here, the depth of the predicted bedrock surface was under estimated. A soft pick was established below the logged section of the well, forcing the new interpreted surface below the well. Because there is no hard data at wells A and C, when the new surface is interpolated from both the hard and the soft picks, it must be considered an interpretation.

The final process involved applying the radial basis function to the hard, soft, and outcrop-veneer points as well as incorporating a geologic interpretation. Points were added along cross section between depressions representing possible paleovalley thalwegs. The radial basis function was applied for a final time to include the thalweg data, resulting in a model of linear depressions considered more plausible as representing bedrock topography.

2.3 Results

2.3.1 Data

The data collection resulted in a total of 660 bedrock picks (hard picks), mainly from petrophysical logs. Picks from water wells and drill cuttings resulted in 130 data points. An additional 2984 points were generated from outcrop locations mapped by Thompson (1977) and from the grid cell points within mapped veneer and outcrop polygons from Trommelen (2006) and Smith (2008*a*, 2008*b*, 2008*c*, 2008*d*).

2.3.2 Model

Three working models were generated to illustrate the bedrock surface: (1) a predicted (kriged) bedrock topography surface incorporating only hard picks (Fig. 2.6A); (2) a fitted interpolated surface based on hard picks, drill cuttings, and water well data (Fig. 2.6B); and (3) a fitted interpolated surface base on all hard and soft data (Fig. 2.6C).

The predicted surface produces several significant depressions within the map area (Fig. 2.6A). The most prominent of these depressions form a northeast trend along the base of the Etsho Plateau. Several smaller depressions occur southwest of the Sahtaneh River, west of the Sikanni Chief River, and under the headwaters of Teklo Creek. An additional depression occurs within the loop of the Hay River along the British Columbia – Alberta border. The fitted surfaces reinforce these trends, partially constraining the topographic geometry (Figs. 2.6B, 2.6C).

The most significant relief in the map area occurred along the southern base of the Etsho Plateau. Here, three isolated lows (Fig. 2.6A) were present, with the lowest bedrock surface pick at an elevation of 90 m asl. In all of these depressions, multiple wells contained deep bedrock picks validating the depressions as real subsurface topographic lows.

Other significant depressions were present. A linear depression, consisting of >25 hard

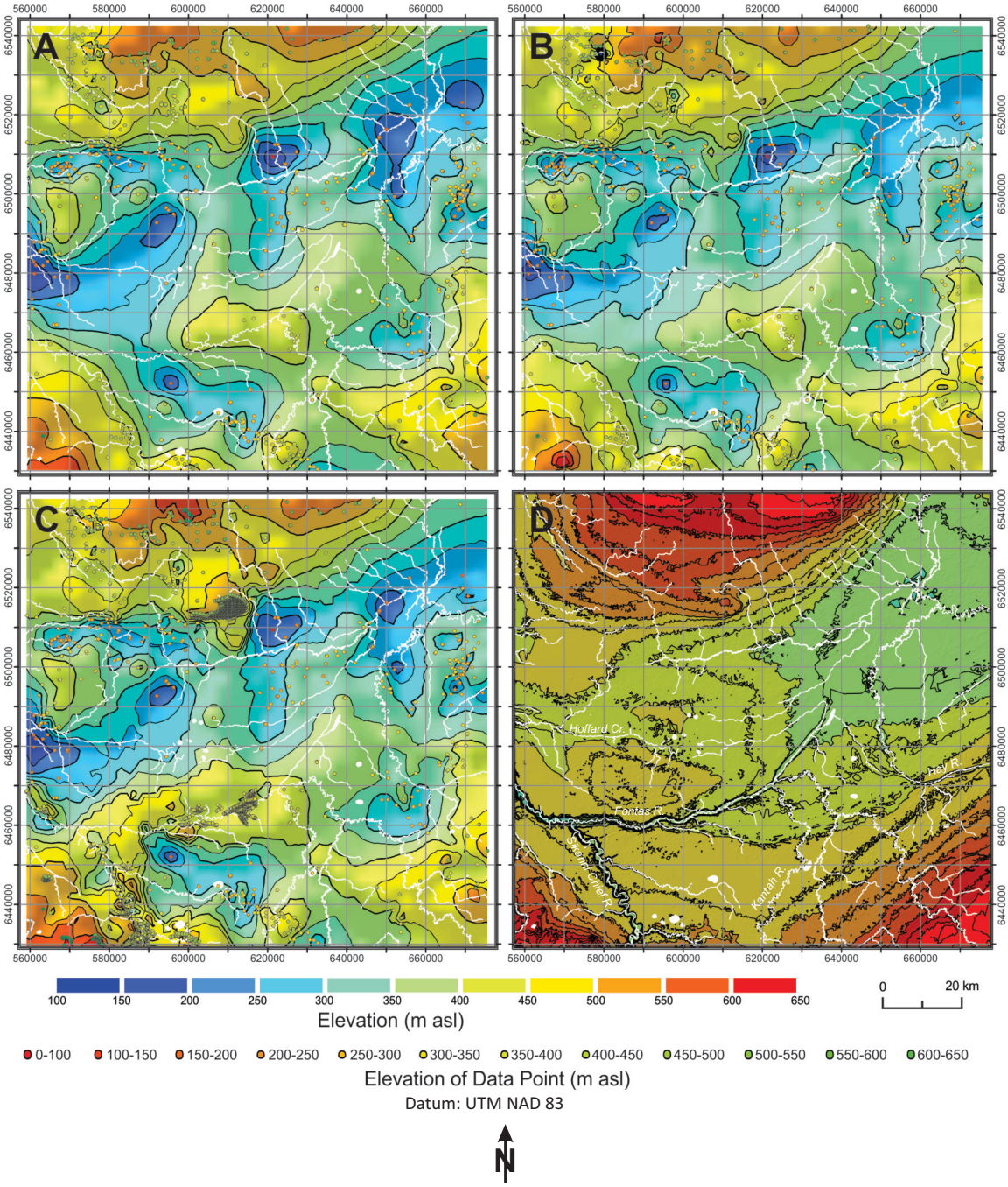

Figure 2.6. The modelling process generated three working surfaces: (A) a predicted (kriged) bedrock topography surface incorporating only hard picks (similar to the predicted surface in Fig. 2.5); (B) a fitted interpolated surface based on hard picks, well cuttings, and water well data; (C) a fitted interpolated surface base on all hard and soft data; this model is the basis for combining isolated depressions into valleys by introducing paleovalley thalwegs (see Fig. 2.7); and (D) modern topography (Shuttle Radar Topographic Mission (SRTM) digital elevation model (DEM)).

picks, occurred southwest of the Sahtaneh River. The depression trended to the east with a minimum elevation of 230 m asl. The depression east of the Sikanni Chief River had the bedrock surface at 250 m asl and a single data point at 130 m asl, based on logged chip samples (the petrophysical logs are inconclusive). This point occurred in isolation and lacked corroborating data; consequently, the certainty of the bedrock surface at this location is provisional. Another depression occurred along the British Columbia – Alberta border within the loop of the Hay River. This depression had a minimum elevation of 170 m asl. The last of the major depressions occurred under the headwaters of Teklo Creek with a minimum elevation of 265 m asl, corroborated by 11 other wells in the vicinity.

As noted, the soft picks were generated from subsidiary data such as drill chip samples, water well data, and mapped outcrops and drift veneers, which were used in conjunction with the predicted surface to estimate a new bedrock surface in some areas. Two fitted surfaces were generated, incorporating all known, predicted, and estimated data (i.e., hard and soft picks): (1) only the hard data, the logged chip samples, and water well data (Fig. 2.6B); and (2) all data (Fig. 2.6C). The first of these surfaces (Fig. 2.6B) did little to change the orientation of the depressions, which suggests that the subsidiary data are consistent with the predicted surface. However, two areas of the model were significantly affected by the outcrop and veneer data. A cluster of points in the northern portion of the map (Fig. 2.6C) pulled the bedrock surface closer to the current ground elevation and created a topographic high. The second area affected was near the Fort Nelson – Fontas River confluence, where bedrock outcrop was mapped. This added complexity to the bedrock topography and pulled the modelled surface closer to present ground elevation. The resulting surface closed the northern extent of the depression east of the Sikanni Chief River. There were no data at this location to confirm the true geometry of this topographic low.

2.3.3 Aquifers and natural gas occurrences in drift

During data compilation, oil and gas drilling records (tour sheets) were inspected for any indication of artesian flow or natural gas (location shown in Fig. 2.7). Fifteen records indicate wells that intersected artesian aquifers within the drift and two wells that encountered natural gas (Table 2.1). Location 1 (Table 2.1; Fig. 2.7) is an important site that encountered both natural gas and artesian water within the drift succession. The site is located over a depression that is

Table 2.1. Gas well with tour sheets that report intersecting artesian aquifers or natural gas in the drift.

Location (Fig. 2.7)	Well Name	Easting*	Northing*	WA Number	Depth (m)	Encountered
1	A-094-L/094-I-09	649399	6514608	15130	45-170	Gas/Water
2	D-075-C/094-I-16	655804	6522540	6162	92-121	Water
3	C-082-A/094-I-16	672024	652092	19164	49	Water
4	A-042-A/094-I-16	672533	6520216	7618	80	Water
5	D-051-J/094-I-09	666139	6512034	6188	91-105	Water
6	B-019-I/094-I-09	667604	6507717	10253	91	Water
7	C-029-I/094-I-09	667542	6509192	11820	110	Water
8	C-044-I/094-I-09	671061	6511075	12426	95	Water
9	B-002-J/094-I-09	665293	6506577	12648	97	Water
10	B-019-I/094-I-09	667502	6507738	12649	8-97	Water
11	C-021-J/094-I-09	666101	6508916	12663	110-123	Water
12	C-008-I/094-I-09	668196	6507136	12664	78-91	Water
13	D-052-B/094-I-09	666259	6493237	12749	100	Water
14	B-016-C/094-I-08	657046	6461030	9810	173-198	Water
15	D-093-J/094-I-01	667116	6459843	3934	0-163	Water
16	D-001-D/094-I-02	625490	6431230	8964	170-200	Water
17	D-085-K/094-I-12	569600	6511673	19810	203	Gas

*Universal Transverse Mercator (UTM) coordinates in North American Datum (NAD) 83, Zone 10.

Figure 2.7. The final model is achieved by linking the depressions in Fig. 2.5C to form paleovalleys (left). Additional data points were added to the working model (Fig. 2.5C) along proposed thalwegs interpreting the base of the valley between wells. The entire dataset was then reinterpolated using the software to produce a geological interpretation of the paleovalleys (includes hard, soft, and thalweg picks). Drift thickness was established by subtracting the geologically interpreted model from ground elevation (right). (A) Depressions are connected into four paleovalleys. (B) Because the thalwegs are established based on interpretation of the data, more than one bedrock topographic model is possible. For example an alternative interpretation can be generated if the single chip sample east of the Sikanni Chief River is eliminated and the thalwegs removed, resulting in a model with three paleovalleys. KCP, Kyklo Creek Paleovalley; KHP, Kotcho–Hoffard Paleovalley; NCP, Niteal Creek Paleovalley; RPV, Rainbow Paleovalley.

2.7A

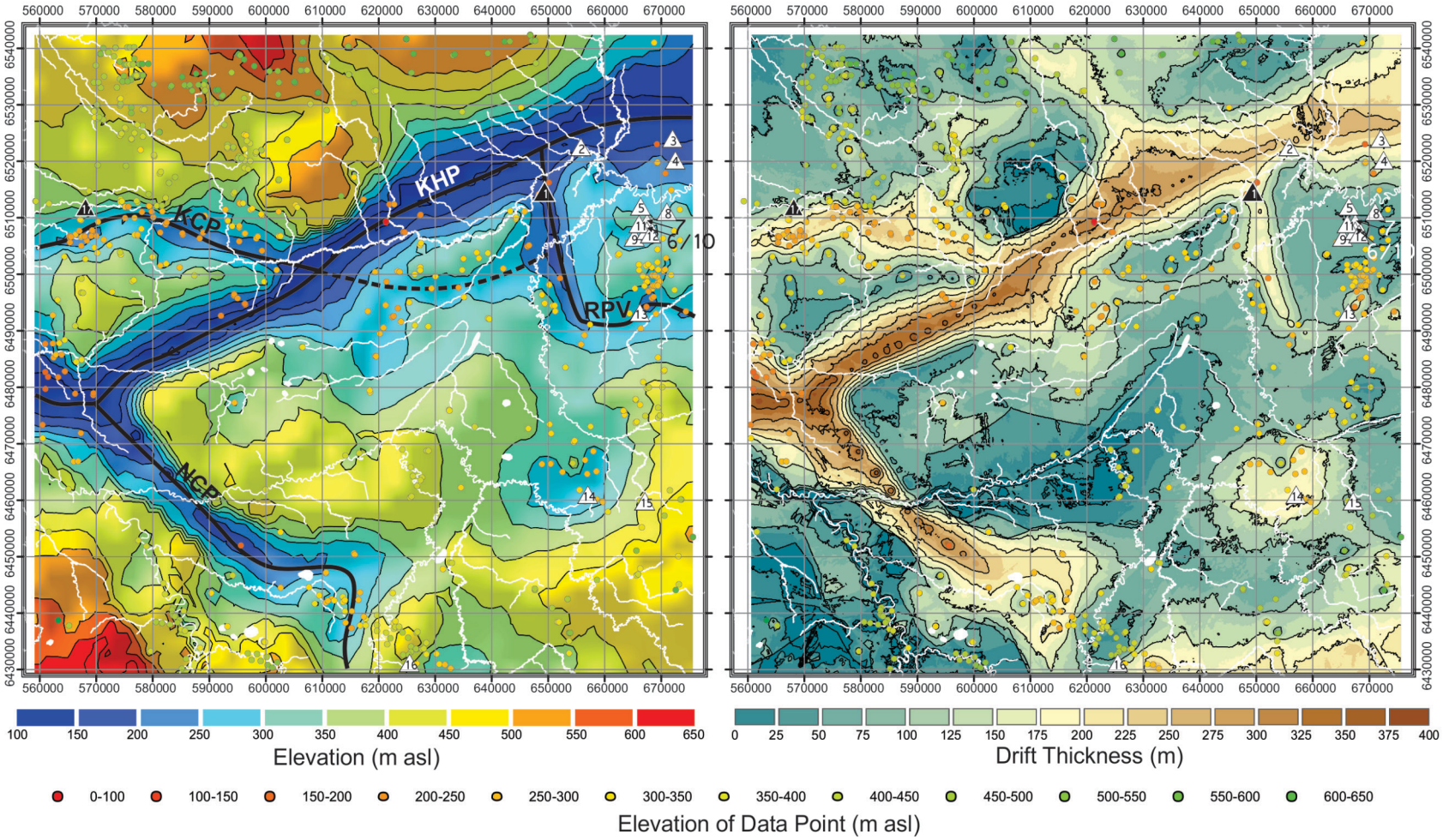

continues...

2.7B

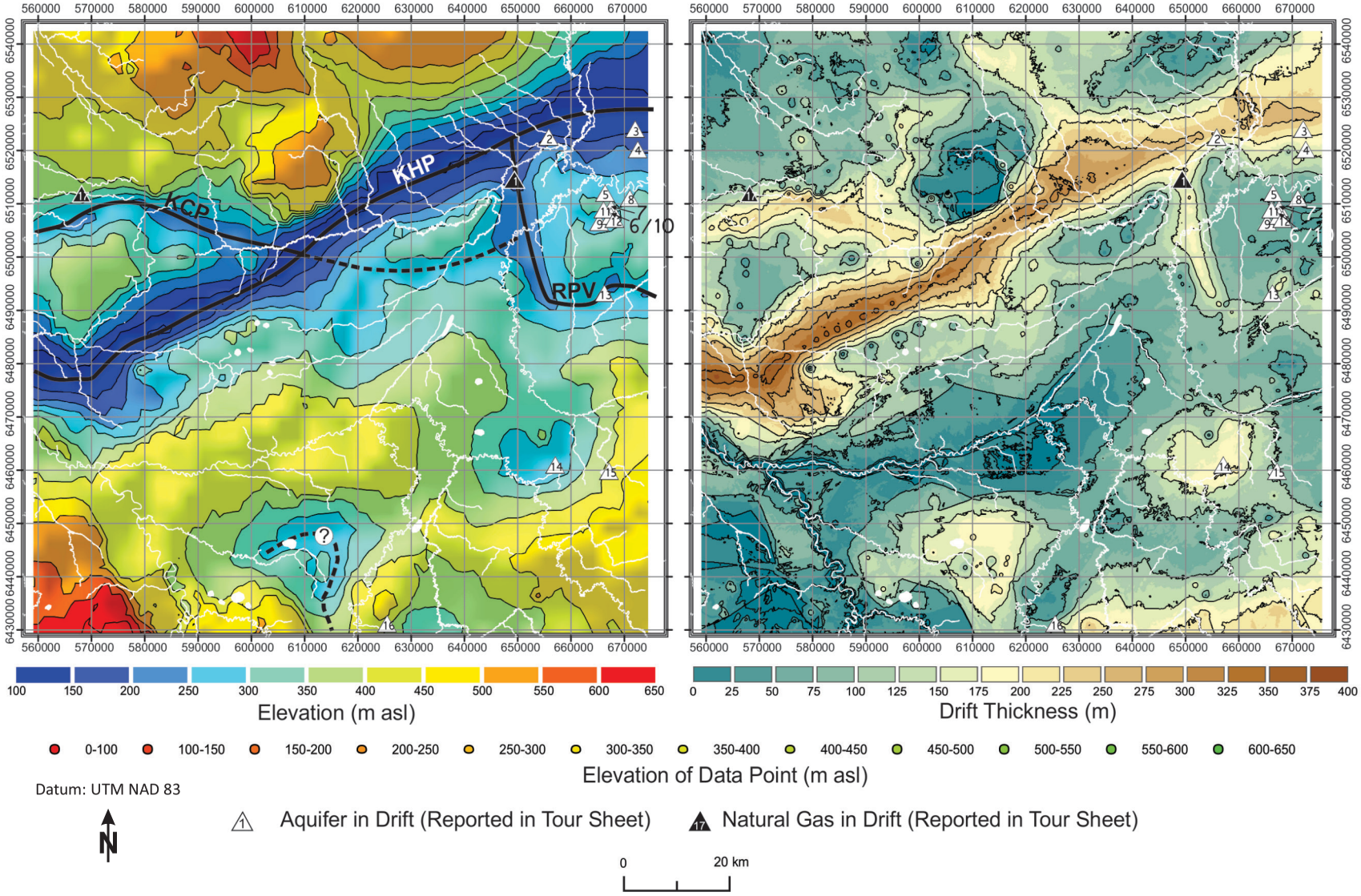
KHP
ACP
RPV
6/10
6/11
Elevation (m asl)
Drift Thickness (m)
0-100
100-150
150-200
200-250
250-300
300-350
350-400
400-450
450-500
500-550
550-600
600-650
Elevation of Data Point (m asl)
Datum: UTM NAD 83
N
Aquifer in Drift (Reported in Tour Sheet)
Natural Gas in Drift (Reported in Tour Sheet)
0
20 km

interpreted to be at the confluence of two paleovalleys, Rainbow Paleovalley (RPV) and Kotcho–Hoffard Paleovalley (KHP; see discussion section). Coarse-grained sediments were penetrated at 140 m with a gas show reported at 170 m below surface. Following the gas, water began to flow at a rate of 1–4 m^3/min. This eventually led to the abandonment of the well.

Three locations were noted within the eastern portion of KHP to have intersected aquifers (locations 2–4). A 32 m thick gravel to boulder deposit was encountered at 89 m below surface at location 2. The coarse-grained sediment hosted an artesian aquifer with an initial flow rate of 21 m^3/min. This high flow rate resulted in the abandonment of the original well, which was later redrilled with equipment capable of controlling water flow. Drill records at location 4 indicate an artesian aquifer at 80–86 m below surface. Flowing water delayed the drilling of the surface casing. No artesian flow was encountered at location 3. However, sloughing sand and gravel were reported to 140 m with an aquifer flow rate of 0.001–0.002 m^3/min. These wells suggest a portion of the KHP contains aquifers within coarse-grained units interpreted to be fluvial or glaciofluvial valley fill.

Eight other wells, located between RPV and the eastern portion of KHP (locations 5–12) encountered an aquifer between 70 and 110 m below surface, though typically around 100 m. This aquifer does not appear to be related to any deeply incised paleovalley, though the model would suggest drift thickness between 50–100 m with local variability.

The well at location 13 occurs within RPV where the model suggests bedrock to be 100–150 m below surface. This well encountered strong artesian flow at 100 m below surface (5 m^3/min) that caused abandonment of the first surface hole. The well was later redrilled with a diverter to control the water.

Locations 14 and 15 are near the depression that is situated at the headwaters of Teklo Creek. Records at location 14 document gravel between 173 and 198 m with limited water flow. However, there was sufficient flow to reduce the drilling mud viscosity, preventing proper well bore cleaning. Location 15 was abandoned after intersecting a sandy artesian aquifer at 115 m. Water flowed from the well at approximately 17 m^3/min, flooding the lease and flushing sand and silt into the surrounding forest.

Location 16 is in the southern area of the map sheet near the Kantah River. Water was encountered in gravel from 193 to 197 m below surface with a flow rate of approximately 1

m^3/min. This well is located on the edge of a depression that projects to the south or may join with Niteal Creek Paleovalley (NCP).

The final well of note in this study is location 17, situated along the edge of Kyklo Creek Paleovalley (KCP). This location is significant as natural gas was encountered between 80 and 203 m during surface hole drilling (i.e., a surface hole is drilled to set surface casing before drilling of the main gas well). The drill string was tripped at 200 m (brought to surface), and on the way out of the well, high gas levels were detected. The maximum reading was 6710 gas units (background for this well was 20–22 units)[2] that persisted for 12 min. The gas subsided before increasing a second time to a maximum of 348 gas units. The initial high reading may have been elevated owing to the vacuum caused by raising the drill stem with a mud ring seal. Nonetheless, this clearly indicates the presence of natural gas in the valley-fill sediments of KCP.

2.4 Discussion

2.4.1 Data

The spatial distribution of data in the study area does not exhibit stationarity (i.e., the distribution is not random). Wells are drilled based on geologic potential and proximity to infrastructure (pipelines, roads), and as such, first-order effects influence the distribution. Second-order effects are also present as there are clusters of development wells drilled around exploration wells that successfully identified gas reservoirs.

Comparison of the predicted and fitted surfaces shows similar trends. Given the present distribution of available data, the predicted and interpreted bedrock topography is only an approximation. Users of these data must be aware that the quality of prediction decreases as a function of distance from known elevation points used in the interpolation. Unfortunately, as the final model was created using an exact interpolator and included soft picks, no estimates of accuracy with any real meaning can be claimed from the final result.

---

[2]Gas unit: relative gas content of drilling mud reported from gas detectors at the mud tank. Typically 100 units equal *1% equivalent methane in air (EMA).

2.4.2 Model

The working models indicate that the bedrock surface differs significantly from the current topography of the map area. The isolated depressions are likely part of linear trends reflecting paleovalleys that have incised into the soft Cretaceous shale of the Fort St. John Group and subsequently buried. The final model results from the modification of the working models so that the final bedrock topographic surface represents both the point data as well as an imposed geological interpretation and, therefore, better represents a plausible surface. The data suggest several viable interpretations can be developed from these models, of which two examples are presented in Fig. 2.7.

In all interpretations, the three main depressions along the southern margin of the Etsho Plateau are combined to form a single paleovalley extending across the map sheet. This depression, referred to as KHP, extends to the west of the map area under Hoffard Creek and to the east into Alberta where it links with the Zama Paleovalley mapped by Pawlowicz et al. (2005). The small depression that occurs along the British Columbia – Alberta border within the loop of the Hay River may link to the RPV also mapped by Pawlowicz et al. (2005).

The depression southwest of Sahtaneh River is relatively well constrained and is interpreted to be a paleovalley that trends to the east. This depression is referred to as KCP. This depression either crosses or is a tributary to KHP. Because a depression of similar elevation and dimension occurs on the east side of KHP, it is possible this is the eastern extension of KCP and is of a different age than KHP. If this is the case, two scenarios are possible: (1) KCP is an older paleovalley that was incised by KHP to a lower base level, or (2) KCP is younger than KHP and developed subsequent to the infilling of KHP.

The remaining depressions are more problematic for interpretation. The depression below the headwaters of Teklo Creek has no obvious connection with the other topographic lows in the area. Consequently, there is insufficient data to link this depression with any of the paleovalleys.

Another depression located east of the Sikannni Chief River is referred to as the NCP. This paleovalley consists of several bedrock surface picks toward the southern edge of the map area between 250 and 270 m asl and a deep pick at 130 m asl (between Niteal Creek and the Fontas River). This suggests a northwest sloping valley, perhaps a tributary to KHP (Fig. 2.7A). This deep

well occurs in isolation and the pick is based mainly on the drill cuttings. If this pick is incorrect, the interpretation of NCP will be altered significantly (Fig. 2.7B). For the purposes of further discussion, the data are assumed correct and the former interpretation (Fig. 2.7A) is adopted, although the geometry of the NCP remains tentative.

2.4.3 Implications

The paleovalleys described in this study suggest that the present landscape masks a network of previously unreported buried valleys. The relief and the dimensions of the valleys are much larger than any contemporary fluvial systems in the area. The scale of these valleys, particularly KHP, suggests a lengthy duration of evolution, although the dimensions may, in part, be attributed to the limitations of the model. The modelled paleovalleys are wider, deeper, and have broader concave-up cross sections than contemporary river valleys in NEBC (Fig. 2.8). The morphology of modern valleys reflects two different origins: (1) occupation of incised meltwater channels (e.g., Fort Nelson River), or (2) post glacial incision through unconsolidated sediment or bedrock (e.g., Sikanni Chief River). Regardless of origin, modern valleys tend to be smaller, steeper walled, and narrower relative to the paleovalleys. Those valleys in the area with a melt-water origin formed during deglaciation likely from short catastrophic events with very high discharges and velocity. The meltwater valleys tend to be wide (though narrower than the paleovalleys) with flat bottoms and are occupied by under fit rivers. Postglacially incised valleys tend to form relatively narrow canyons. The modern valleys have developed since deglaciation (ca. 13–10 ka), over a relatively short time; and it is conceivable that, over a longer timescale, modern valleys may evolve to similar dimensions as the paleovalleys. Therefore, it is suggested that the paleovalleys may reflect long-lived Tertiary or Early Quaternary drainage systems. The paleovalleys may have been repeatedly excavated by cyclical glaciations throughout the Quaternary; and the paleovalleys reflect a complex origin of repeated incision and glacial over-deepening and widening associated with interglacial–glacial cycle, respectively. Therefore, paleovalleys may represent the culmination of geomorphic work from initiation to current dimensions. However, at any given time in the past, drainage geometries and dimensions may have been more comparable with modern systems. Stratigraphic control or exposure dates from the bedrock surface in the base of the valleys may elucidate the timing of incision; presently no definitive age(s) can be assigned. The crosscutting relationship between KCP and KHP suggests

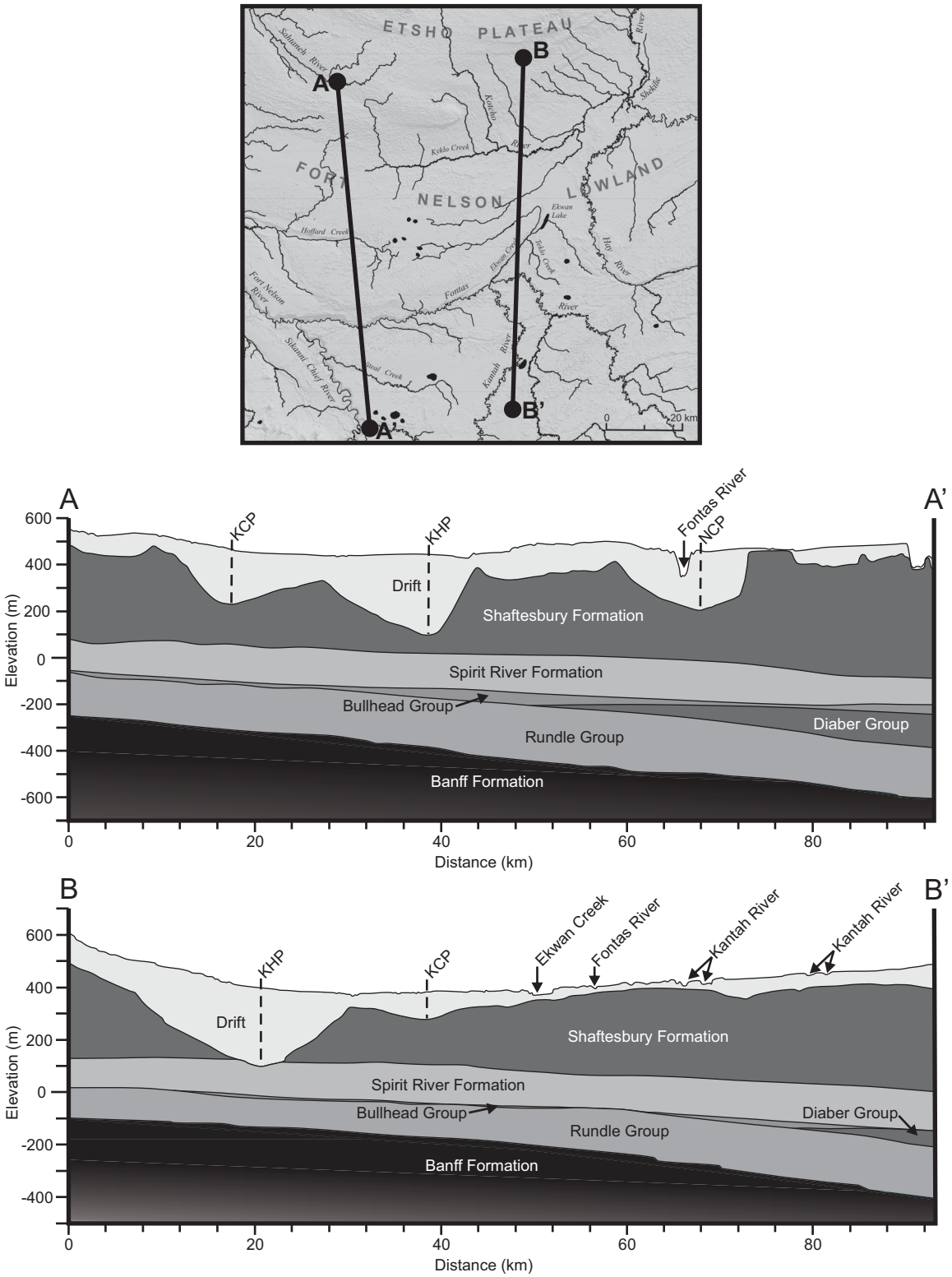

Figure 2.8. North-to-south cross sections show the modeled tops of the major stratigraphic boundaries, paleovalleys, and modern rivers (25x vertical exaggeration). KCP, Kyklo Creek Paleovalley; KHP, Kotcho–Hoffard Paleovalley; NCP, Niteal Creek Paleovalley.

that drainage patterns may have changed through time and that some valleys are superimposed, stacked, or incised through one another.

There is evidence that many modern valleys in NEBC are coincident with older paleovalleys that existed prior to the last glaciation. For example, the Prophet, Peace, Murray, and Kiskatinaw river valleys have pre-Late or Late Wisconsinan age sediments on the valley floor (J.M. Bednarski, personnel communication, 2007; Trommelen et al., 2008). The modern drainages may have become established where pre-existing valleys occur because the paleovalleys represent regional depressions, despite being masked by the valley-fill. The origin of the paleovalleys in this study remains unclear. There is no obvious relationship between paleovalley orientation and major structural trends or stress fields (Bell and Babcock 1986). In fact, the trend of KHP is oblique to the major structural trend of the Rocky Mountain Fold and Thrust Belt, west of the study area. The Cretaceous sediments in the study area are generally flat lying to slightly inclined, gently dipping to the southwest (Thompson 1977). There are two major fault systems that occur in northeast British Columbia and northwest Alberta, the Bovie Lake and Hay River faults (Great Slave Lake Shear Zone; Wright et al., 1994; Maclean and Morrow 2004). These structures occur several hundred kilometres from the study area and have no direct influence on the orientation of the paleovalleys. It is possible that subordinate structures associated with these major structural features have not been detected and could play a role in paleovalley development, particularly if the structures were active or present through the Tertiary and Quaternary.

Two of these paleovalleys link with buried valleys in Alberta, RPV and KHP (Pawlowicz et al., 2005). RPV is well constrained in Alberta and is narrower than the modelled RPV in British Columbia with a canyon like morphology. The canyon morphology suggests this valley may be younger than KHP and perhaps forming during the Quaternary. The direction of paleo-drainage is inconclusive.

KHP links with the Zama Valley and is less well constrained in Alberta. Pawlowicz et al. (2005) suggested it can be traced east, under Zama and Hay lakes to the Chinchaga River. The slope of KHP is speculative as the paleovalley floor shows little appreciable dip beyond the error associated with the model. But, if this paleovalley is indeed the western extension of the Zama Valley, then the paleo-slope of Zama–KHP from west of Zama Lake, Alberta, to the western edge of this study is approximately 0.05%, which tentatively suggests paleo-drainage to the west and

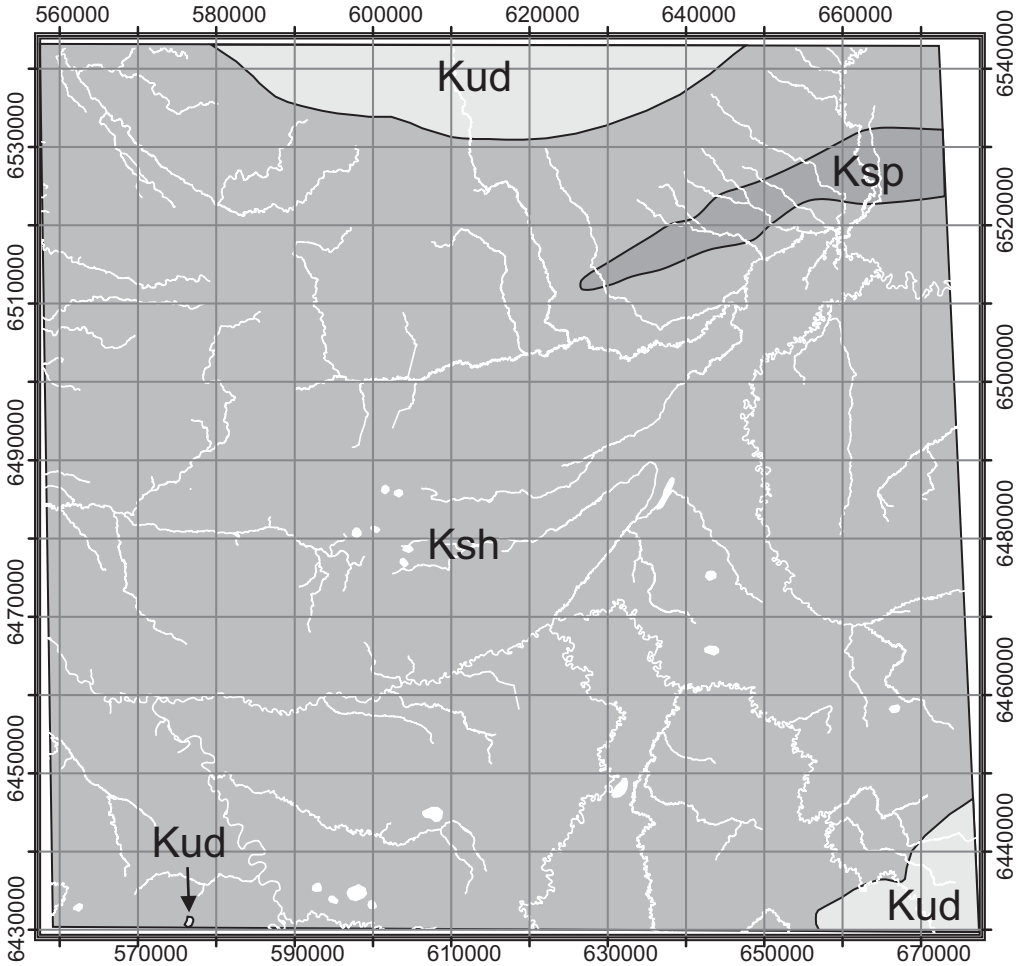

CRETACEOUS

Kud	DUNVEGAN FORMATION: conclomerate and coarse- to fine- grained sandstone, carbonaceous shale.
Ksh	SHAFTESBURY FORMATION: Dark marine shale with band of fish scale bearing silt.
Ksp	SPIRIT RIVER FORMATION: Dark grey shale, grey green clayey sandstone with interbeds of dark and light grey shale. greywacke, shale, and siltstone commonly glauconitic.

Figure 2.9. Bedrock subcrop map based on the bedrock topography model (Fig. 2.7A).

eventually to the north into the Arctic basin. The Zama–KHP has economic significance as shallow gas was discovered within its valley-fill sediments in Alberta in 1988 (Clare 1988) and has since been the target of natural gas exploration around the discovery (Sousa and Rainbow gas fields). Gas has been in production from shallow wells with Quaternary age reservoirs in the Zama–KHP valley-fill since 1993 (Levson et al., 2006). Although, there is no production of natural gas from Quaternary reservoirs in British Columbia, gas was noted in tour sheets in valley-fill sediments in both KHP and KCP.

The stratigraphy of valley-fills cannot be correlated from one well to the next. However, paleovalleys contain sequences of unconsolidated coarse-grained sediments (fluvial or glaciofluvial aquifers) interbedded within fine-grain sediments (diamict, lacustrine, or glaciolacustrine). These sequences are capped by Late Wisconsinan glacial and deglacial sediment at surface, which implies the paleovalleys, at least, predate the Late Wisconsinan. The valley-fills likely contain lengthy Quaternary stratigraphic records as other smaller preglacial valleys in NEBC contain records that extend to the Middle Wisconsinan and possibly older (Mathews 1978; Trommelen et al., 2008). Since the paleovalleys identified in this study are significantly deeper and perhaps older than others in NEBC, they may represent excellent sites for Quaternary age terrestrial records in western Canada.

Surface bedrock mapping relies on exposed outcrop, which is rare in the Fort Nelson Lowland, commonly restricted to incised river valleys. Bedrock topography mapping through petrophysical logs provides insight into the subcrop geology. In this study, the models show that the paleovalley network has incised up to 300 m into the Fort St. John Group shale (Fig. 2.8). The model also suggests the eastern portion of KHP has incised through the Shaftesbury Formation into the Spirit River Formation. Consequently, a wedge of the Spirit River Formation should appear on the bedrock subcrop geology map of 94I, reflecting the erosion of the upper Fort St. John Group sediments (Fig. 2.9).

As the oil and gas industry expands in NEBC, drilling practices and water and land management issues are becoming major concerns (Levson et al., 2006). Thick inhomogeneous Quaternary sediments associate with the deep paleovalleys have proven to be a safety issue for oil and gas, as well as the water well industry. Incidents have cost these industries millions of dollars in lost time, abandonment of wells, destruction of equipment, as well as injuries and in extreme cases fatalities (i.e., British Columbia Oil and Gas Commission 2005). Drilling within

paleovalleys requires the use of mitigative measures (e.g., blowout preventers or heavy mud) to reduce the impact of intersecting either artesian water or natural gas. In addition, protecting sources of potable water should be considered when drilling in the paleovalleys. In accordance with the British Columbia Petroleum and Natural Gas Act, surface casing is to be set into bedrock, which may be in excess of 300 m within the paleovalleys.

2.5 Conclusions

The objective of this study was to model the bedrock topography of the NTS map sheet 94I using oil and gas petrophysical logs, drill chip samples, water well logs, and surficial and bedrock geology maps. The models suggest that the bedrock topography has much more relief than modern topography because the bedrock topography is masked by thick accumulations of Quaternary drift. Several conclusions can be drawn from the results:

- The modeled data produced several depressions that likely represent paleovalleys when combined. These depressions are interpreted to be previously undocumented paleovalleys. The most prominent of these is KHP, which spans the map sheet along a west-southwest trend. The base of the valley is over 250 m below the modern surface and likely links with the Zama Paleovalley in Alberta (Pawlowicz et al., 2005). A tributary valley of KHP is mapped on the eastern side of the map sheet and is referred to as RPV. It can be traced into Alberta where it links with Rainbow Valley of Pawlowicz et al. (2005). The third paleovalley, KCP, trends east–west and may be a tributary to, or crosscut the KHP. KCP is well constrained on the northwest side of the KHP but is less well defined southeast of KHP. The fourth paleovalley, NCP, is considered speculative as its depth and geometry rely heavily on an isolated drill chip sample. If the chip sample is valid, NCP trends to the northeast and may be a tributary to KHP. Alternatively, the depression may be part of a paleovalley that extends to the south.
- There may be other geologically plausible ways to link the depressions. The geometry of the paleovalleys is limited by the quality, density, and distribution of the data. Data such as drill chip samples are less reliable than the petrophysical logs. Areas with a high density of wells provide the best confirmation of bedrock tops and verify less precise data such as drill chip samples. Some areas have many

wells and the geometry of paleovalleys can be constrained (e.g., western portion of KCP). Other areas have only a single data point and rely more on interpretation. The models generated here provide a regional–scale interpretation. The current density of wells is insufficient for high resolution interpretation, and new models should be developed as more wells are drilled or other techniques are developed that can better constrain the subsurface paleovalley geometry (e.g., geophysics such as shallow seismic or electromagnetic surveys).

- Understanding the geometry, thickness and stratigraphy of the drift has implications for the oil and gas industry. The presence of artesian aquifers or potential natural gas reservoirs poses a significant hazard to drilling. Subsurface modelling of the Quaternary succession and hydrogeology in NEBC should be a focus of further work.

2.6 Acknowledgment

The authors wish to thank J. Blackwell, S. Jones, and C. Peters for their initial work on the bedrock topography in NEBC. The authors would like to acknowledge the collaborative work of Northern Resource Development (NRD) project 4450 participants including Geological Survey of Canada and Alberta Geological Survey, particularly J. Pawlowicz, L. Andriashek, and A. Plouffe. Appreciation is extended to T. Ferbey for discussion and to V. Levson for reviewing an earlier manuscript. The authors thank critical reviewers J.M. Bednarski and C. Eyles and Associate Editor R. Gilbert for comments that improved the manuscript.

2.7 References

Andriashek, L.D., and Fenton, M.M. 1989. Quaternary stratigraphy and surficial geology of the Sand River area, 73L. Alberta Research Council, Bulletin 57.

Bailey, T., and Gatrell, T. 1995. Interactive spatial data. Addison– Wesley Longman Ltd., Essex, UK.

Bednarski, J.M. 2001. Drift composition and surficial geology of the Trutch map area (94G) northeastern British Columbia [CDROM]. Geological Survey of Canada, Open File D3815.

Bednarski, J.M. 2008. Landform assemblages produced by the Laurentide Ice Sheet in northeastern British Columbia and adjacent Northwest Territories — constraints on Glacial Lakes. Canadian Journal of Earth Sciences, **45**. 593 – 610.

Bednarski, J.M., and Smith, I.R. 2007. Laurentide and montane glaciation along the Rocky Mountain Foothills of northeastern British Columbia. Canadian Journal of Earth Sciences, **44**: 445– 457. doi:10.1139/E06-095.

Bell, J.S., and Babcock, E.A. 1986. The stress regime of the Western Canadian Basin and implications of hydrocarbon production. Bulletin of Canadian Petroleum Geology, **34**: 364–378.

Bobrowsky, P.T., and Rutter, N.W. 1992. The Quaternary geologic history of the Canadian Rocky Mountains. Géographie physique et Quatenaire, **46**: 5–50.

British Columbia Ministry of Energy, Mines and Petroleum Resources. 2006. Conventional natural gas play atlas, northeast British Columbia, British Columbia Ministry of Energy, Mines and Petroleum Resources. Petroleum Geology Publication 2006-1.

British Columbia Oil and Gas Commission. 2005. Alert to operators drilling in Quaternary gravels, particularly in Midwinter — Helmet North field areas but also in the rest of British Columbia. British Columbia Oil and Gas Commission, Information Letter #OGC 15-12.

Catto, N., Liverman, D.G.E., Bobrowsky, P.T., and Rutter, N.W. 1996. Laurentide, Cordilleran, and montane glaciation in the western PEACE River – Grande Prairie region, Alberta and British Columbia, Canada. Quaternary International, **33**: 21–32.

Christiansen, E.A. 1961. Geology and Ground-water Resources of the Regina Area, Saskatchewan. Saskatchewan Research Council, Geology Division, Report No. 2.

Clague, J.J. 1989. Cordilleran Ice Sheet. *In* Quaternary geology of Canada and Greenland. *Edited by* R.J. Fulton. Geological Survey of Canada, no. 1, Chap. 1, pp. 40–42.

Clague, J.J., and Ryder, J.M. 1989. British Columbia (Quaternary stratigraphy and history, Cordilleran Ice Sheet). *In* Quaternary geology of Canada and Greenland. *Edited by* R.J. Fulton. Geological Survey of Canada, no. 1, Chap. 1, pp. 48–58.

Clare, S. 1988. Water well test drilling and natural gas blowout – Zama Lake South observation well project; Alberta Environment, Report No. 577.

Dyke, A.S., Moore, A., and Robertson, L. 2003. Deglaciation of North America [CD-ROM]. Geological Survey of Canada, Open File, 1574, 2 map sheets.

Edwards, W.A.D., and Scafe, D. 1996. Mapping and resource evaluation of the Tertiary and preglacial sand and gravel formations of Alberta. Alberta Energy and Utilities Board, EUB/AGS Open File Report 994-06.

Glass, D. 1997 (*Editor*). Lexicon of Canadian Stratigraphy, Western Canada including Eastern British Columbia, Alberta, Saskatchewan and southern Manitoba. Canadian Society of Petroleum Geologist, Calgary, Alta. Vol. 4.

Hartman, G.M.D. 2005. Quaternary stratigraphy and geologic history of the Charlie Lake (NTS 94A) Map Area, British Columbia. M.Sc. thesis, Department of Earth Science, Simon Fraser University, Burnaby, B.C.

Hickin, A.S., and Kerr, B. 2005. Bedrock topography mapping and shallow gas in Northeastern BC. *In* Summary of activities 2005. B.C. Ministry of Energy and Mines, pp. 69–75.

Holland, S.S. 1976. Landforms of British Columbia, a physiographic outline. British Columbia Department of Mines and Petroleum Resources, Bulletin 48.

Horne, E., and Seve, G. 1991. Pleistocene ''buried valley'' outwash channels – east bank, Athabasca River. In 5th District five meeting, Canadian Institute of Mining and Metallurgy, Fort McMurray, Alta., 77-1 – 77-15.

Jackson, L.E., Jr., Phillips, F.M., Shimamura, K., and Little, E.C. 1997. Cosmogenic 36Cl dating of the foothills erratics train, Alberta, Canada. Geology, **25**: 195–198. doi:10.1130/0091-7613(1997)025<0195:CCDOTF>2.3.CO;2.

Levson, V.M., Hickin, A.S., Ferbey, T., and Best, M. 2006. Mapping high resistivity buried channel deposits with airborne electromagnetic surveys and other methods. *In* Proceedings of the 19th Annual Symposium on the Application of Geophysics to Engineering and Environmental Problems, Seattle, Wash., 2–6 April 2006, pp. 152–161.

Maclean, B.C., and Morrow, D.W. 2004. Bovie structure: its evolution and regional context. Bulletin of Canadian Petroleum Geology, **52**: 302–324. doi:10.2113/52.4.302.

Mathews, W.H. 1963. Quaternary stratigraphy and geomorphology of the Fort St. John area, northeast British Columbia. British Columbia Department of Mines and Petroleum Resources.

Mathews, W.H. 1978. Quaternary stratigraphy and geomorphology of Charlie Lake (94A) map area, British Columbia. Geological Survey of Canada, Paper 76-20.

Mathews, W.H. 1980. Retreat of the last ice sheets in northeastern British Columbia and adjacent Alberta. Geological Survey of Canada, Bulletin 331.

Pawlowicz, J.G., Hickin, A.S., Nicoll, T.J., Fenton, M.M., Paulen, R.C., Plouffe, A., and Smith, I.R. 2005. Bedrock topography of the Zama Lake Area, Alberta. Alberta Energy and Utility Board, Alberta Geological Survey, Map 328, scale 1 : 250 000.

Reichmen, T.H.F. 1980. Surficial Geology, Dawson Creek, British Columbia. Geological Survey of Canada, Map 1467A, scale 1 : 250 000.

Rutter, N.W. 1977. Multiple glaciations in the area of Williston Lake, British Columbia. Geological Survey of Canada, Bulletin 273.

Smith, I.R. 2008*a*. Surficial geology, Kyklo Creek, British Columbia (NTS 94I/11). Geological Survey of Canada, Open File 5307, British Columbia Ministry of Energy, Mines, and Petroleum Resources, surficial geology map 2006-1, 1 map, scale 1 : 50 000. In press.

Smith, I.R. 2008*b*. Surficial geology, Nogah Creek, British Columbia (NTS 94I/12). Geological Survey of Canada, Open File 5306, British Columbia Ministry of Energy, Mines, and Petroleum Resources, surficial geology map 2006-1, 1 map, scale 1 : 50 000. In press.

Smith, I.R. 2008*c*. Surficial geology, Gunnell Creek, British Columbia (NTS 94I/13). Geological Survey of Canada, Open File 5305, British Columbia Ministry of Energy, Mines, and Petroleum Resources, surficial geology map 2006-1, 1 map, scale 1 : 50 000. In press.

Smith, I.R. 2008*d*. Surficial geology, Lichen Creek, British Columbia (NTS 94I/14). Geological Survey of Canada, Open File 5309, British Columbia Ministry of Energy, Mines, and Petroleum Resources, surficial geology map 2006-1, 1 map, scale 1 : 50 000. In press.

Stalker, A.M. 1960. Buried valleys in central and southern Alberta. Geological Survey of Canada, Paper 60-32.

Stalker, A.M. 1967. Identification of Saskatchewan gravels and sands. Canadian Journal of Earth Sciences, **5**: 155–163.

Stott, D.F. 1967. Jurassic and Cretaceous stratigraphy between Peace and Tetsa rivers, northeast British Columbia. Geological Survey of Canada, Bulletin 2, Part 1.

Stott, D.F. 1973. Lower Cretaceous Bullhead Group between Bull-moose Mountain and Tetsa

River, Rocky Mountain Foothills, northeastern British Columbia. Geological Survey of Canada, Bulletin 219.

Stott, D.F. 1982. Lower Cretaceous Fort St. John Group and Upper Cretaceous Dunvegan Formation of the Foothills and Plains of Alberta, British Columbia, District of Mackenzie and Yukon Territory; Geological Survey of Canada, Bulletin 328.

Thompson, R.I. 1977. Geology of Beatton River, Fontas River and Petitot River map areas, northeastern British Columbia. Geological Survey of Canada, Paper 75-11.

Trommelen, M.S. 2006. Quaternary stratigraphy and glacial history of the Fort Nelson (southeast) and Fontas River (southwest) map areas (NTS 094J/SE and 094I/SW), northeastern British Columbia. M.Sc. thesis, University of Victoria, Victoria, B.C.

Trommelen, M.S., Levson, V.M., and Smith, I.R. 2008. Quaternary stratigraphy of the Prophet River. Canadian Journal of Earth Sciences, **45**. 565 – 575.

Wright, G.N., McMechen, M.E., and Potter, D.E.G. 1994. Structure and architecture of the western Canada sedimentary basin. *In* Geological atlas of the Western Canada Sedimentary Basin. *Edited by* G. Mossop and I. Shetsen. Canadian Society of Petroleum Geologists and the Alberta Research Council. Chap. 3, pp. 25–40.

CHAPTER 3: MAPPING THE GEOMETRY AND LITHOSTRATIGRAPHY OF A PALEOVALLEY WITH A TIME-DOMAIN ELECTROMAGNETIC TECHNIQUE IN AN AREA WITH SMALL RESISTIVITY CONTRASTS, GROUNDBIRCH, BRITISH COLUMBIA, CANADA

Adrian S. Hickin and Mel E. Best

A version of this chapter was published in the Journal of Environmental and Engineering Geophysics, 2013

Citation:

Hickin, A.S and Best, M.E., 2013. Mapping the Geometry and Lithostratigraphy of a Paleovalley with a Time-domain Electromagnetic Technique in an Area with Small Resistivity Contrasts, Groundbirch, British Columbia, Canada; Journal of Environmental and Engineering Geophysics, Vol. 18, pages 119—135.

Abstract

The purpose of this paper is to evaluate the effectiveness of large loop, ground-based, time-domain electromagnetic surveys for the modeling of paleovalley geometry and valley fills as a basis for determining groundwater potential. The electromagnetic (EM) survey was successful, despite limited resistivity contrast between adjacent valley-fill units, as well as limited contrast between the valley-fill and bedrock. Thin, coarse-grained units and low contrast in the resistivity present challenges for constraining 1-D inversions. Thin units could not be resolved and were merged, resulting in simplified models that reflect averaged apparent resistivity. Supplementary data (e.g., borehole resistivity logs) are useful for constraining complex multi-layer inversions, but where absent, complex models are not realistic. As the ratio of the resistivity of two layers decreases, there is more uncertainty in the placement of layer boundaries even though the root mean squared standard error of fit for the model may remain small (<6%). Nonetheless, when 1-D inversions are combined into resistivity-depth sections we interpret four generalized lithologies: 1) bedrock (~10-30 ohm-m); 2) fine-grained sediment (clay, silt, fine sand, and diamict; 30-50 ohm-m); 3) medium-grained sediment (silt and sand; 40-80 ohm-m); and 4) coarse-grained sediment (sand and possibly gravel; 90 to >350 ohm-m). When the 2-D resistivity-depth sections are combined, there is 3-D continuity and the geometry of the Groundbirch Paleovalley can be traced. The valley is approximately 3-4 km wide with a maximum depth of about 120 m. The data suggest a local basal aquifer (medium- to coarse-grained unit) in the central survey area and possibly an unconfined aquifer towards the northwest region of the survey area. The EM-based model is consistent with models based on water well logs and field observations. Although the EM data remain exploratory, the resulting EM models provide clear guidance for groundwater resource management strategies.

3.1 Introduction

Water is a valued resource and many rely on groundwater as their primary potable source. There is, however, increasing pressure on water supplies from a variety of stakeholders in various regions of British Columbia. In northeast British Columbia, water supports domestic, agricultural and industrial activities. As populations grow and industry expands, there is an increasing need to understand water systems and availability so that best management practices can be developed to ensure equitable use, economic development and sustainability of this valuable resource. This study is part of a larger joint project (Northeast British Columbia Aquifer Project) aimed at improving the understanding of the regional hydrogeology in northeast British Columbia.

Groundwater evaluation often relies on hydrogeological models, the accuracy of which is dependent on the quality and distribution of data from which they are derived. Critical inputs are the geological framework and lithologic characteristics, which are key parameters for groundwater storage and flow and define host aquifers and aquitards (Freeze and Cherry, 1979). In many places, the distribution and quality of well data may be insufficient to provide an appropriate geological framework. Under these circumstances, geophysical methods are an appropriate alternative for geological control.

Although electromagnetic (EM) surveys have been used in hydrological investigations since the 1970s (Reynolds, 1997), there are few specific large loop (>20 m) time-domain EM case studies, especially in settings where the paleovalley fills and the surrounding host bedrock have small resistivity contrasts, as is the case in this study. The purpose of this paper is to contribute to the understanding of the effectiveness of EM survey-based modeling of paleovalley geometry and valley fills as a basis for determining groundwater potential. The specific methodology adopted here is to test a geophysical model in an area where the general geometry and lithostratigraphy of the paleovalley are already known from independent well data and geological mapping.

The study area is located in the South Peace Region of British Columbia (Fig. 3.1). Cowen (1998) suggests that buried paleovalleys in the Peace Region are significant sources of ground water because they typically have higher yields than other potential aquifers. Buried paleovalleys are host to significant accumulations of heterogeneous sediment. Depending on the stratigraphy and hydrogeological constraints, coarse-grained units within the succession

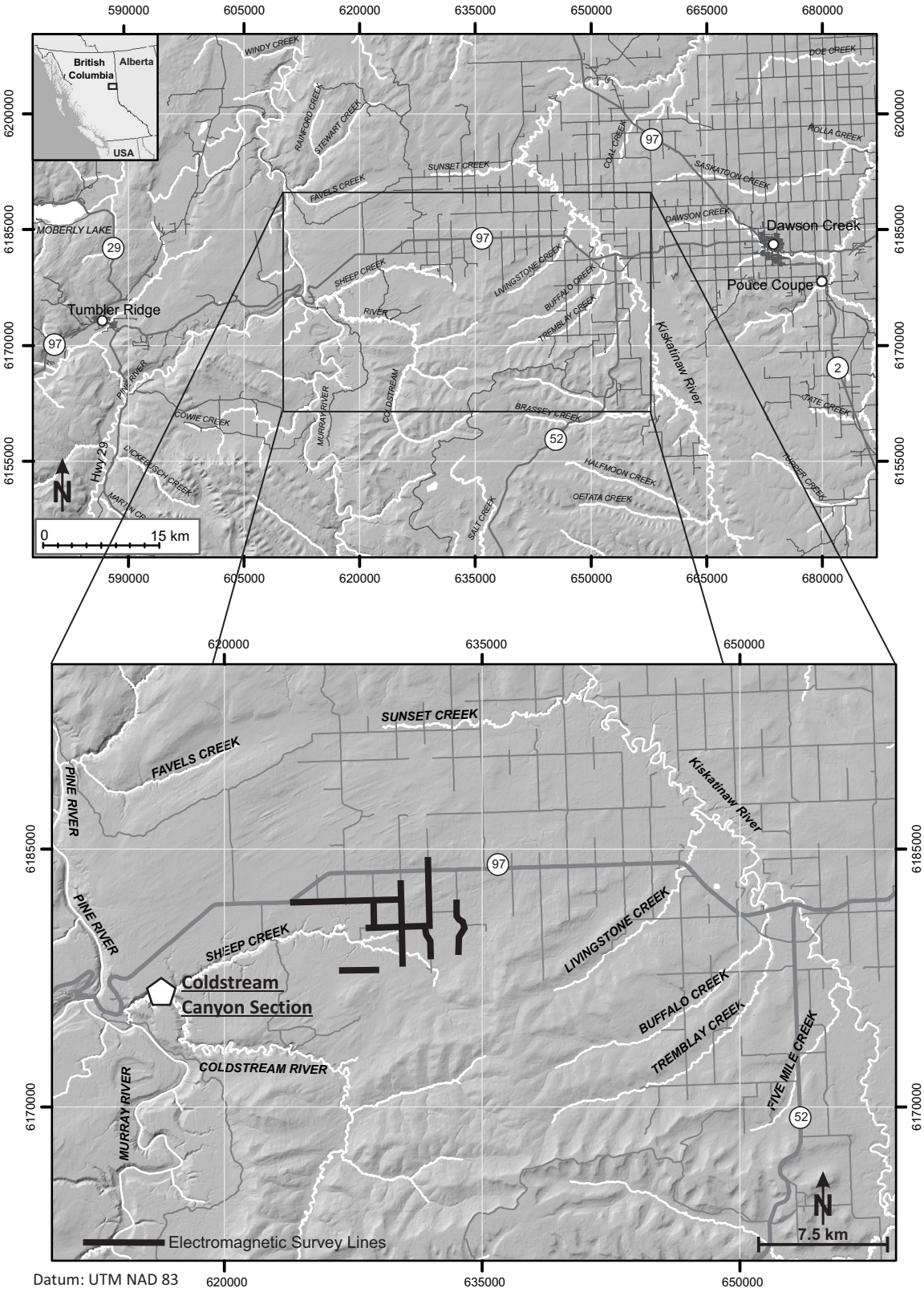

Figure 3.1. The Groundbirch area in northeastern British Columbia, Canada.

may constitute both confined and unconfined aquifers. The thickness, lateral extent, and connectivity of these horizons are integral to understanding groundwater availability.

Buried Late Cenozoic paleovalleys are relatively common in northeast British Columbia (Mathews, 1955, Hickin, 2011). In many cases, these paleovalleys may contain late Neogene and late Pleistocene sediments (Reimchen and Rutter, 1972; Mathews, 1978). Some paleovalleys in this region are buried with little or no surface expression (e.g., Pawlowicz et al., 2005, 2007; Hickin et al., 2008; Chapter 2), while others, like those within the study area, occur within modern bedrock-controlled valleys (Mathews, 1978). Since deglaciation, many of these paleovalleys have been incised 150-250 m by rivers, exposing the sediments of the paleovalley-fill succession and bedrock.

3.1.2 Paleovalleys and Geologic Setting

Thirteen paleovalleys were delineated in the region using mainly lithologic descriptions from water well drillers logs and surface exposures (Appendix A; Hickin, 2011; Hickin and Best, 2012) (Fig. 3.2). These data were modeled in a Geographic Information System (GIS) following the general method described by Hickin et al. (2008; Chapter 2). The Groundbirch Paleovalley (GPV), which was originally identified by Callan (1970), hosts a major aquifer for the local area and is the focus of this survey. The bedrock topographic model (Hickin, 2011) indicates that the GPV is approximately 6,000 m wide, 100 m deep, and trends east-northeast from the Kiskatinaw River to the Pine–Murray river confluence. This paleovalley has been described in part by Cowen (1998), but is depicted as a tributary of the Kiskatinaw Paleovalley to the west. Cowen (1998) reports good-quality fresh water hosted within “interglacial sand and gravel.” His test drilling indicates that the local stratigraphy differs from that presented by Callan (1970) and that the basal gravel (aquifer) expected at the bedrock-sediment interface is not present in drillholes. This interpretation suggests that the aquifer(s) may be discontinuous, may occur at various elevations within the valley-fill succession, and that the geology is complex. The GPV is exposed along the canyon sections of Coldstream River and Sheep Creek (Fig. 3.1). At the mouth of Coldstream River, there is a nearly continuous 170 m thick section of valley-fill sediments and underlying bedrock exposed along a 3 km stretch of the canyon (Fig. 3.3). This section exposes bedrock and six unconsolidated lithostratigraphic units (described below).

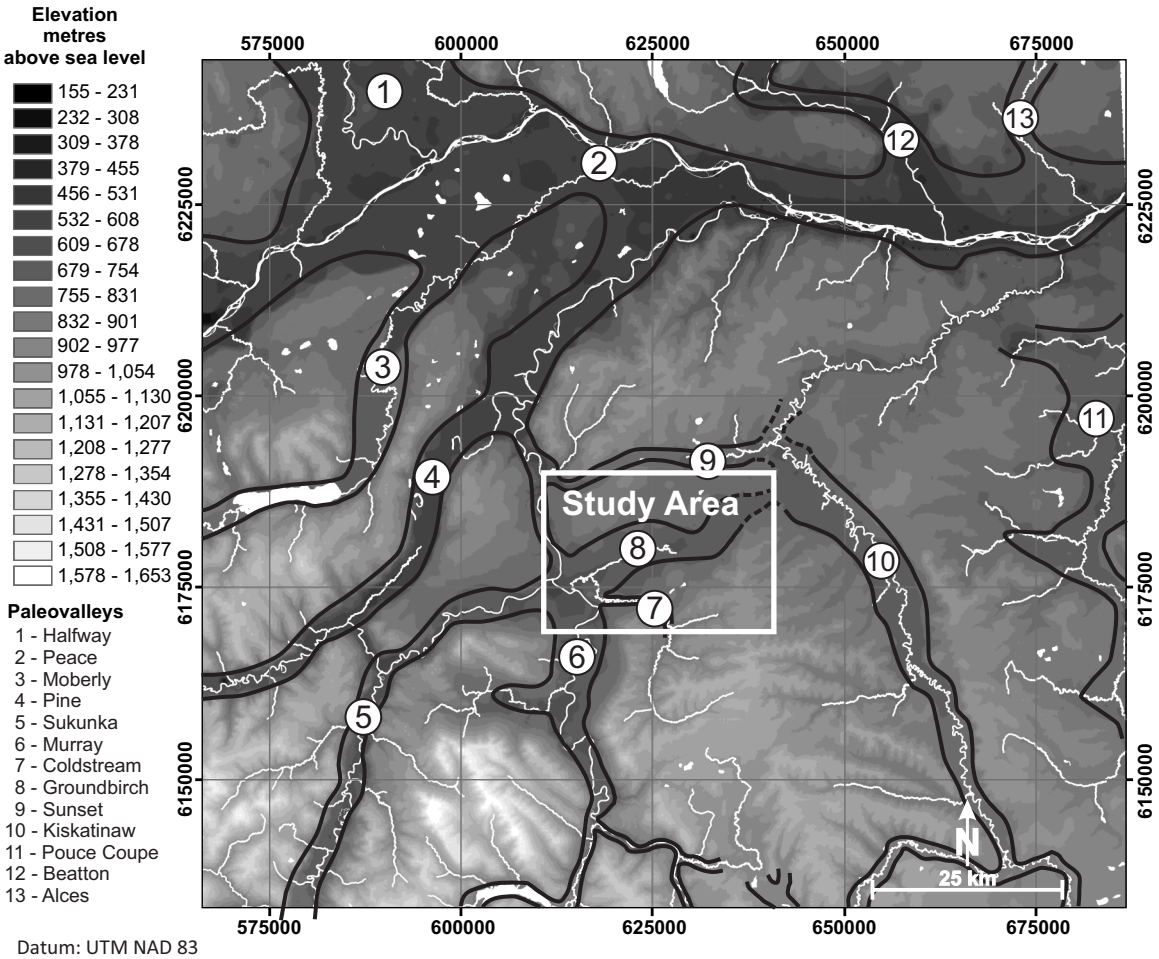

Figure 3.2. The Groundbirch Paleovalley is one of 13 paleovalleys mapped from water well logs and exposures in the region (modified from Hickin, 2011).

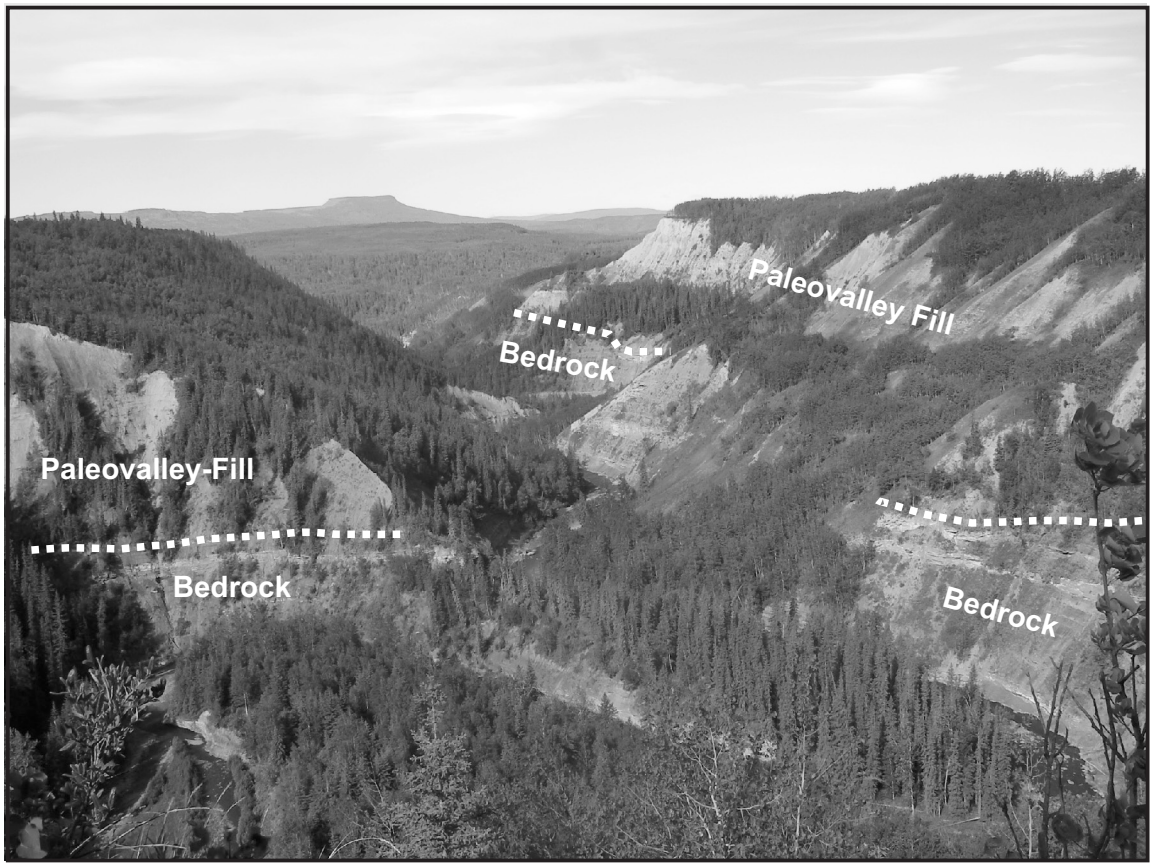

Figure 3.3. The Groundbirch paleovalley-fill is exposed in the Coldstream River Canyon (located west of the survey area; see Fig. 3.1).

3.1.3 Geology of the Paleovalley

The GPV is incised into Cretaceous bedrock, through shale of the Kaskapau Formation into the underlying Dunvegan Formation (Stott, 1961; McMechan, 1994). Dunvegan rocks at the base of the Coldstream River canyon include flat-lying, well-bedded, recessive fine-grained mudstone with interbedded 1-2 m thick resistant sandstone beds that represent a succession of shingled, nonmarine to marine deltaic sediments (Unit 1; Fig. 3.4) (Bhattacharya, 1993; Bhattacharya and Walker, 1991; Plint et al., 2001).

The lowest and oldest unconsolidated unit consists of fluvial sand and gravel, but it is poorly exposed in this section. Clast are of local sedimentary lithologies and are not striated or facetted. It is interpreted to have a pre-glacial or interglacial fluvial origin (Unit 2; Fig. 3.4). Where encountered, it consists of partially cemented, oxidized and indurated interbedded sand and gravel. Unit 3 (Fig. 3.4) consists of clast-supported, moderately oxidized, poorly sorted, pebble- to cobble-sized gravel in a silt to granule matrix. It is 6-m thick at its maximum, but swells and pinches laterally or is absent. This unit is interpreted to be a non-glacial fluvial deposit that transitions upwards into an advance-phase glaciofluvial deposit. Unit 4 (Fig. 3.4) is a matrix-supported, poorly sorted, granule to boulder diamict that is interpreted to be till associated with the last (Late Wisconsinan) glaciation. The unit is 12-20 m thick and is regionally extensive. Unit 5 (Fig. 3.4) is an approximately 10-m thick, laterally discontinuous medium sand that coarsens upward into gravel. These strata transition upwards into a fining-up succession of subhorizontally stratified pebble to small cobble gravel at the top of the unit. It is interpreted to be a glaciofluvial or subaqueous fan deposit associated with retreating ice in contact with glacial Lake Peace (Mathews, 1980). Unit 6 (Fig. 3.4) is a regionally extensive glaciolacustrine succession deposited in glacial Lake Peace that makes up the majority of the Coldstream section. It generally fines upwards and consists of well-bedded, horizontally stratified clay, silt, sand and diamict. The unit ranges from 70- to 100-m thick. Unit 7 (Fig. 3.4) is 6-m thick, occurs at the top of the section and is interpreted to have an aeolian origin.

3.2 Methods

3.2.1 Well Logging Method

Two wells were drilled and logged in this study. Well #1, located within the EM survey area (Fig. 3.5), is approximately 88-m deep, and was constructed with a steel casing in the upper

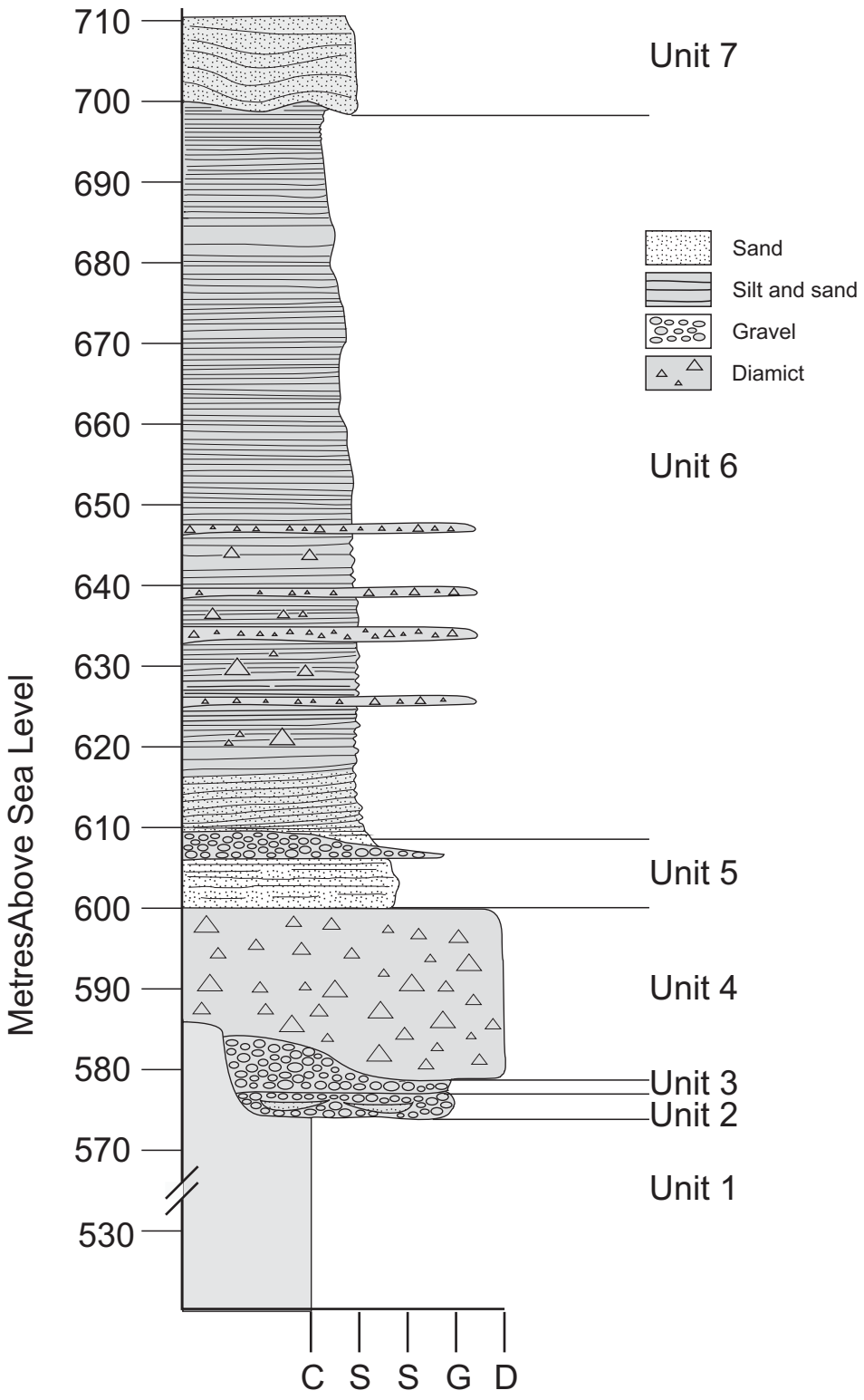

Figure 3.4. Stratigraphic section depicting the exposed geology of the Groundbirch Paleovalley at the Coldstream River Section (see Fig. 3.1). At this location, GPV is 135-m deep and consists of six units (C = Clay; S=Silt; S=Sand; G=Gravel; D=Diamict).

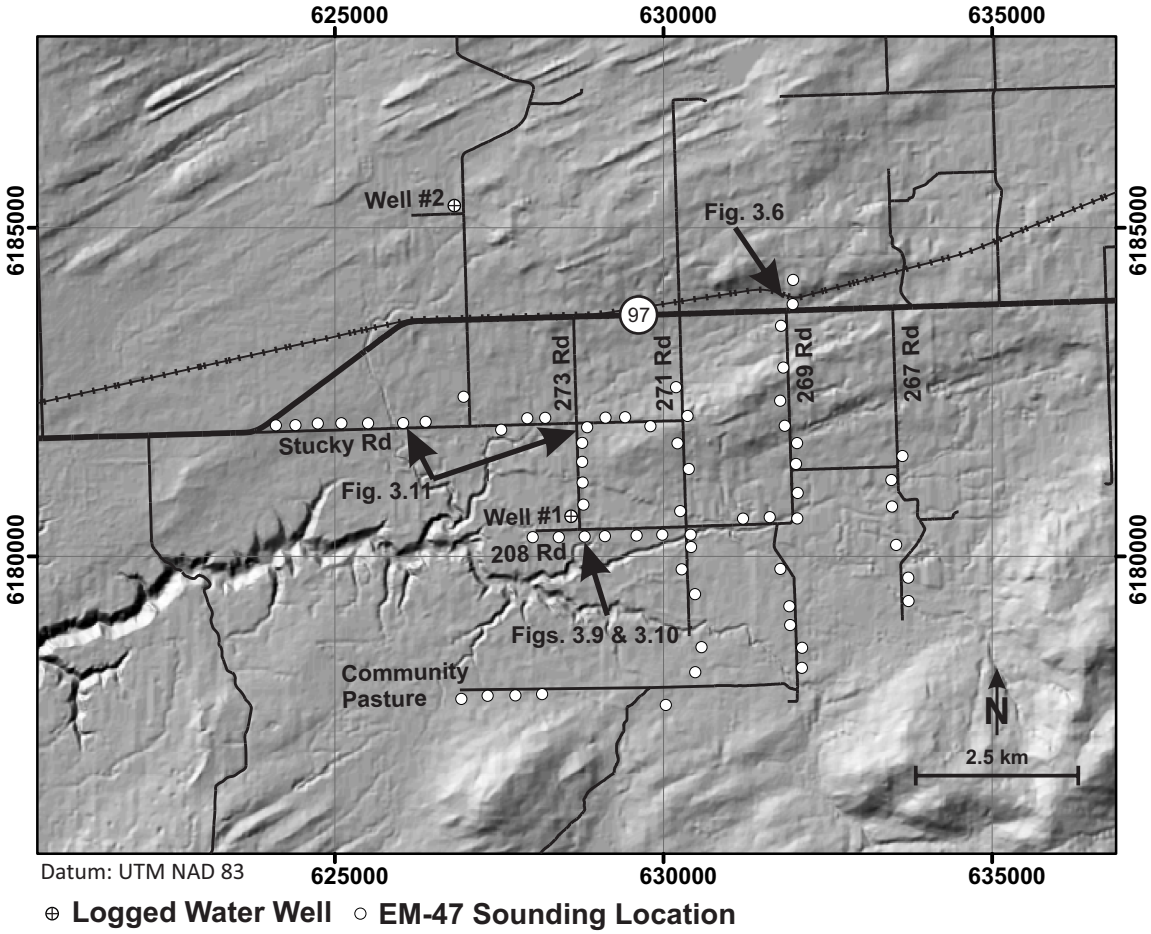

Figure 3.5. Sixty-five soundings were conducted in the Groundbirch area and two water wells were drilled and logged with borehole geophysical tools (digital elevation model has 2.5 x vertical exaggeration).

6 m and polyvinyl chloride (PVC) casing the length of the well bore to bedrock (at 80 m), below which the well is uncased. Well #2 is located north of the survey area (Fig. 3.5), is mainly in bedrock, and is approximately 30-m deep. The upper 6 metres consists of unconsolidated material and is cased with steel. The rest of the well is uncased. A Mount Sopris logging system was used to collect natural gamma and conductivity logs. The two logging tools were controlled by the Mount Sopris 5MCA-1000 MGX II console. The gamma tool was the 2PGA-1000, which measures the natural gamma radiation in counts per unit time. The conductivity tool was the 2PIA-1000, which is a Geonics EM-39 induction logging tool with a vertical resolution of about 20 cm and is tuned to respond to the geology between 20 and 80 cm from the center of the borehole (McNeill et al., 1990; Geonics 2006). The EM-39 logging tool provides both conductivity values (mS/m) and resistivity values (ohm-m), which is the reciprocal of conductivity. Measurements were collected every 5 cm. Editing of the raw data consisted of removing that portion of the EM-39 induction logs behind steel casing (the top 5-10 m), and the gamma logs were smoothed using a 5-point moving average.

3.2.2 Electromagnetic Method

3.2.2.1 Acquisition and initial processing.

The Geonics EM-47 time-domain electromagnetic system (Geonics, 2011) was used for this survey. It was set up in the central sounding mode with the receiver coil at the centre of a square transmitter loop (McNeill, 1994). The transmitter controls the shape and frequency of the transmitted current. The current was fed into a 100-m square loop consisting of a single turn of insulated copper wire. A reference cable is connected between the transmitter and the Protem 47D receiver to control the timing of the transmitted waveform and the length of time the receiver voltage is measured. The plane of the high frequency receiver coil is horizontal; hence the receiver coil measures the time derivative of the vertical component of the magnetic field (dBz/dt). Faraday's Law (Reitz and Milford, 1962) is then used to relate the time derivative to the voltage across the coil (measured in nV/Am2 since the voltage is normalized to the dipole moment of the transmitter loop).

The transmitter current approximates a square wave with a sine-wave rise time and a linear ramp at the end of the square wave when the current is turned off. The frequency of the square wave is equal to 1/T, where T is the period of the square wave pulse (in seconds). The

period consists of a positive square wave of duration T/4, followed by an off time of duration T/4. This is then reversed to give a total period equal to T. The frequencies used for this survey were: Ultra High frequency (UH) = 285 Hz, Very High frequency (VH) = 75 Hz, and High frequency (H) = 30 Hz. The receiver voltage was measured in 20 time windows during the transmitter off times for each of the three frequencies. The time windows are logarithmically spaced so they are larger at longer times. The time of the window centers range from about 6.8 µs to 7 ms (UH times, 6.8 µs – 696 µs; VH times, 35 µs – 2.79 ms; and H times, 88µs – 6.98 ms, thus providing overlap between the three different frequencies).

Voltages in each of the 20 time windows were time averaged and stored in the Protem 47D console. Three sets of time-averaged voltage measurements were recorded at each of the three frequencies (UH, VH and H), providing 180 values for each sounding. The data were downloaded each day to a computer using software supplied by Geonics. This software then averaged the three sets of time-averaged voltages at each frequency to yield a data set compatible with Interpex's IX1D.v3 software (Interpex, 2006).

Sixty-five soundings were made over a period of approximately 10 days. Soundings were recorded along several east-west and north-south roads within the Groundbirch area (Fig. 3.5). The center of the transmitter loop was located approximately 100 to 150 m away from roads and/or power lines to reduce cultural noise. Generally they were located in open fields, but a few were in heavily wooded areas. Spacing between sounding centers was nominally 400 m, but the actual spacing depended on the location of fences and other obstacles.

3.2.2.2 Manipulation of the EM data using Interpex IX1D.v3.

A one-dimensional (1-D) modeling and inversion software package (Interpex IX1D.v3) was used for final editing and processing of the data. The software package converted the voltage data to late-time apparent resistivity data. These data were then edited to remove saturated voltages at early times, i.e., voltages that were above the maximum voltage of the EM system (reflects the gain setting used during data acquisition). Late-time voltages within the noise envelope were masked, i.e., the values are shown with an x, but are not used for modeling (Fig. 3.6). The edited late-time resistivity versus time data were then used to interpret the soundings as 1-D layered earth resistivity models. There are several options within the software for carrying out the modeling: 1) a smooth multi-layer model with thicknesses computed on a

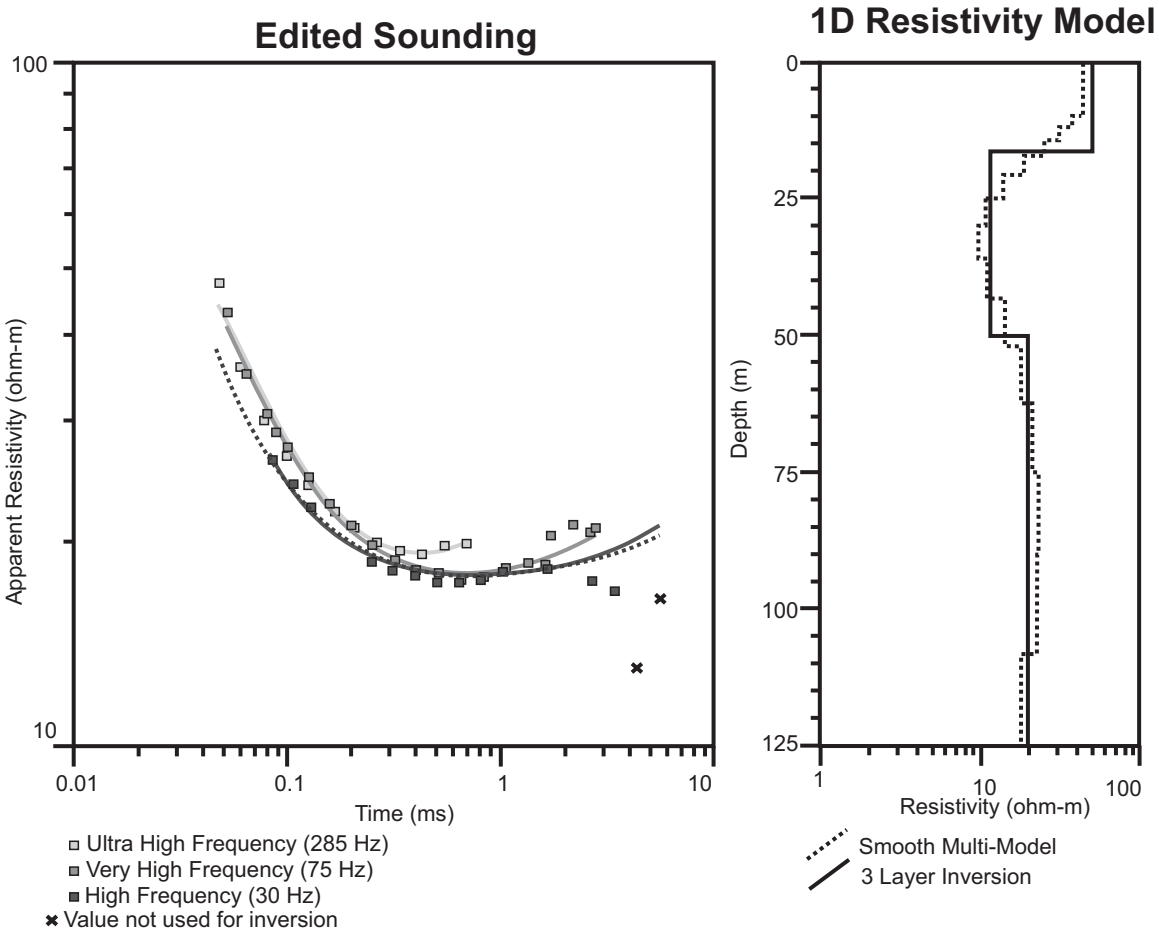

Figure 3.6. Station 14 on 269 Road (north end of line in Fig. 3.5) is an example of typical sounding data with the smooth model and best-fit 3-layer model. The final edited late-time apparent resistivity data versus time is on the left side (the squares are data points, the x values are masked data points, and the curves are the best-fit model). The interpreted 3-layer 1-D resistivity model is on the right side. The solid line is the best-fit 3-layer model (standard error of fit is 5.85 % RMS), and the broken line is from the smooth model.

logarithmic scale and the resistivity of each layer calculated using inversion (for example Occam's inversion; Constable et al., 1987); 2) a layer model with a relatively small number of layers which are inverted for thickness and resistivity; and 3) an error estimation option using "equivalence analysis."

3.2.2.3 Inversion and interpretation of EM data.

A smooth model inversion with layer thicknesses that increased logarithmically with depth was carried out for each sounding to determine the approximate variation of resistivity with depth (option 1 above). A 15-layer smooth model was selected because it provided enough detail to estimate significant resistivity variations. All inversions were arbitrarily limited to 130 m, as experience has suggested this is effectively the maximum depth of penetration given the low resistivity of the local ground conditions and the absence of any deep conductors. These inversions provided a preliminary estimate of the number of layers and their approximate resistivity values for multi-layered earth models. The preliminary model estimated from the smooth model was then inverted to produce the best-fit layered-earth model (option 2 above). The best-fit layered-earth models were then compared to the equivalence models (option 3 above) to assess the range of layer boundaries with similar standard errors (non-uniqueness of the inversion method). Where possible, boundaries were adjusted to reflect ancillary data or adjacent soundings, without exceeding the standard error achieved by the best-fit model.

3.2.2.4 Resistivity-depth sections.

The 1-D models were compiled into a database containing line number, station number, Universal Transverse Mercator (UTM; Zone 10, Datum: NAD 83) coordinates (x and y), elevation (z), and resistivity value (ρ). Elevations and the corresponding ρ value were assigned at surface, midpoint of thin modeled intervals (<40 m), or at approximately 40-m depth elevations within a thick modeled interval (>40 m). Data from lines in the x, z (north-south) and y, z (east-west) plane were introduced by line into ArcMap by ESRI. Data were contoured using inverse distance weighted interpolation and horizontal anisotropy with a major search radius of 800 m and minor search radius of 80 m (conducted with Geostatistical Analyst). This interpolation method was selected because it is an exact interpolator (honors data points) and the anisotropic search

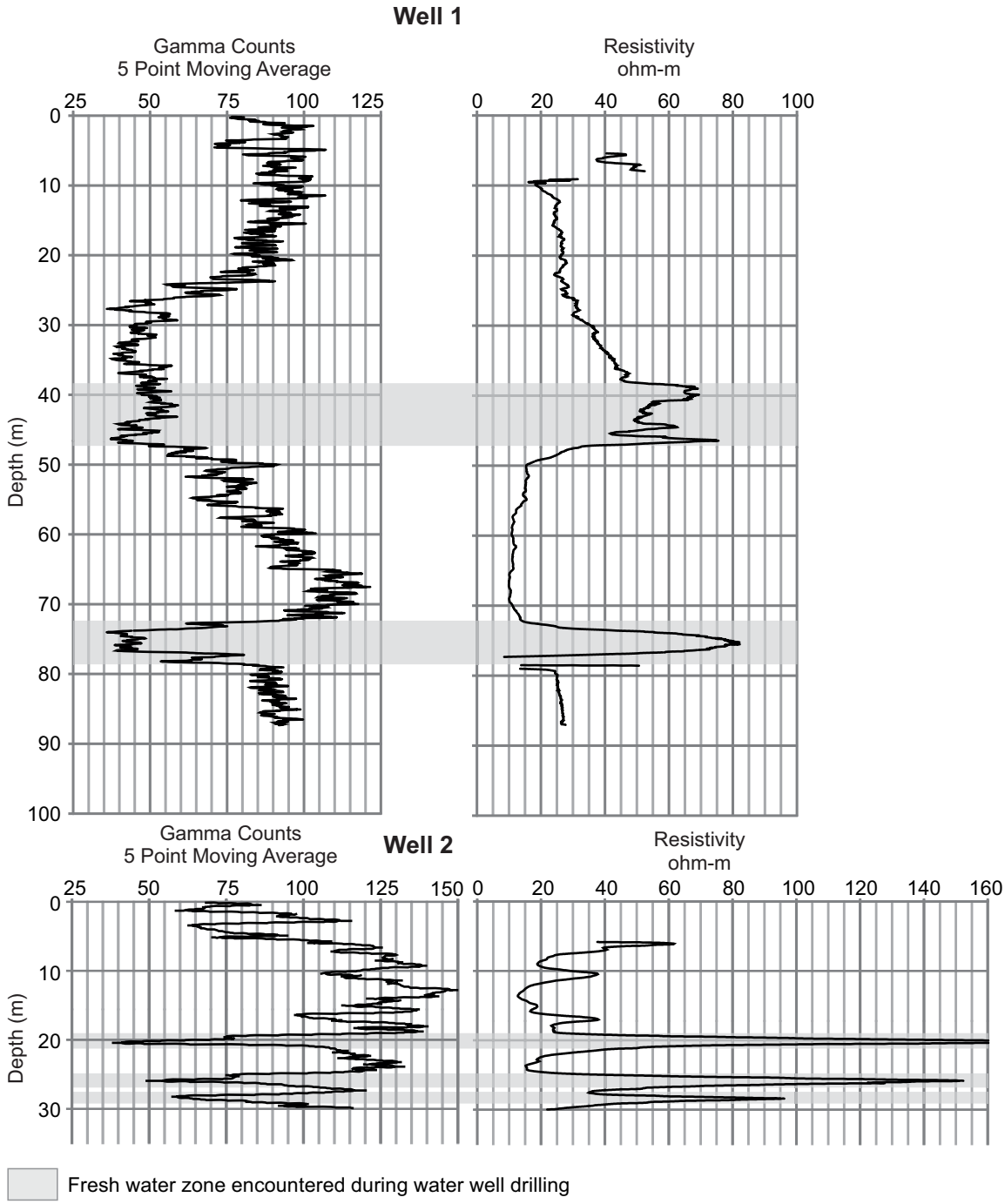

Figure 3.7. Gamma and resistivity logs for the two water wells drilled and logged in the area (locations are shown in Fig. 3.5). There are two low gamma, high resistivity horizons in Well 1 that indicate medium- to coarse-grained sediment with fresh water (aquifers). Well 2 is entirely in interbedded mudstone and fine sandstone bedrock.

radius accounts for higher vertical data density than horizontal data density and generates an image (Fig. 3.8) that adequately represents a layered earth.

3.3 Results

3.3.1 Well Log Data

Combined natural gamma and resistivity logging of the water well through the PVC casing was very effective at differentiating the lithology of the valley-fill sediments (Fig. 3.7). The higher resistivity zones correspond to zones with lower gamma counts, indicating high air or fresh water-filled porosity and low clay content. These intervals are likely coarse-grained, i.e., sand and/or gravel (Rider and Kennedy, 2011). The zones with lower resistivity and higher gamma counts are zones suggestive of higher clay content and lower air or fresh water-filled porosity, indicative of fine-grained intervals, i.e., silt, clay, diamict (till) and/or shale bedrock (Rider and Kennedy, 2011). The logs provide a detailed direct measure of the electrical properties of the bedrock and valley-fill units in well #1. The logs show that the ratio of high to low resistivity values is small (<3) for these geological units (Fig. 3.7). The logs and the Coldstream Canyon Section (Fig. 3.4) discussed earlier, indicate that the coarse-grained aquifer units are expected to be thin (<10 m) or absent.

3.3.2 Electromagnetic Interpretation

Because the coarse-grained valley-fill units are thin and have low-resistivity contrast, 1-D modeling of the specific units is a significant challenge, likely why there are few examples of this situation in the literature. As with most EM methods, it is generally difficult to resolve the lithostratigraphy to the same detail as is possible with downhole geophysical tools. It becomes even more difficult to model EM data when contrasts between layers are low. Because of this, the approach used in this study was to adopt the simplest model with the least number of layers that fit the data. In general, 2-layer models (valley-fill over bedrock) fit the data with a reasonable standard error of fit (root mean square error of 2-6%), but there were soundings where a 3-layer model provided a better standard error of fit than a 2-layer model. Despite the relatively few layers, resulting resistivity-depth sections generated from the 1-D models successfully show resistivity variation that can be attributed to distinct lithologic differences (e.g., Fig. 3.8). The resistivity values from all the survey lines are generally low, typically between

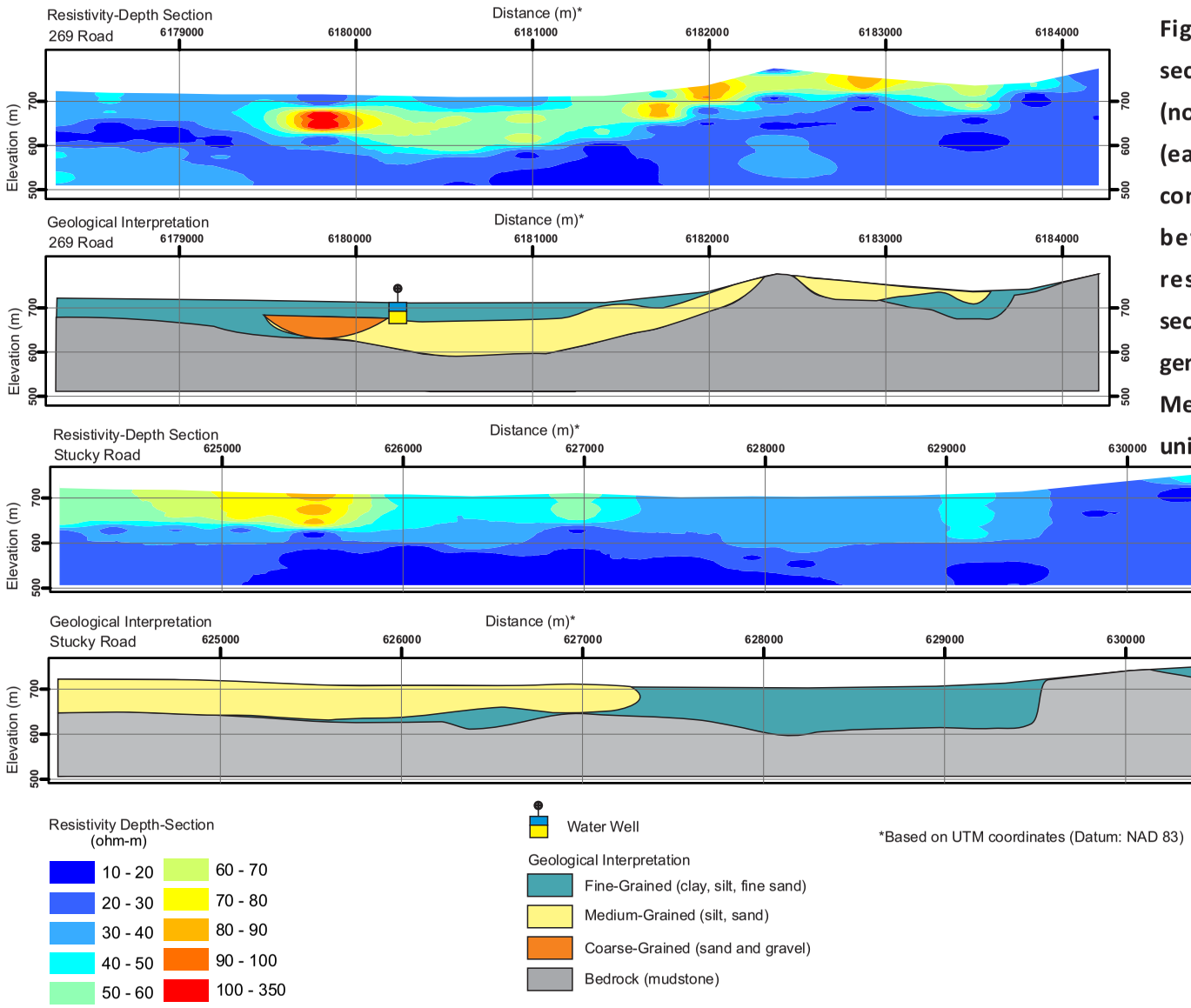

Figure 3.8. Resistivity-depth sections, from the 269 Road (north-south) and Stucky Road (east-west), show that when combined there is continuity between 1-D models. The resistivity variation in the sections is interpreted to reflect general grain-size differences. Medium- and coarse-grained units have aquifer potential.

10-~100 ohm-m. There are, however, rare places where values reach as high as >350 ohm-m. Four distinct resistivity zones are interpreted to represent generalized lithologic domains and likely reflect variations in clay content and air- and water-filled pore space. These zones are, therefore, inferred to correspond with sediment grain-size and were validated based on the natural gamma and resistivity logs (Well #1; Fig. 3.7), and from the expected stratigraphy (Coldstream Section; Fig. 3.4). The base of the sections typically includes a low resistivity (~10-30 ohm-m) zone that is consistent with values associated with fine-grained bedrock (shale or mudstone). Above this zone there is a region with resistivity values in the 30-50 ohm-m range that is likely fine-grained sediment (i.e., clay, silt, fine sand, diamict). Within this zone are regions with resistivity values that range from 40-80 ohm-m, suggesting medium-grained sediment (silt and sand). Locally, there are small areas with relatively elevated values (90 to >350 ohm-m) that are consistent with sand and possibly gravel.

3.4 Discussion

The Groundbirch paleovalley is identified in several studies as an important groundwater feature (Callan, 1970; Cowen, 1998; Lowen, 2011). These same studies suggest that there is a need for a more thorough groundwater evaluation to understand the aquifers in this groundwater system. There are numerous water-wells available in this area from the British Columbia Ministry of Environment's WELLS database (British Columbia Ministry of Environment, 2012), and the lithologic descriptions (drillers logs) are adequate only for differentiating bedrock from unconsolidated sediment. Unfortunately, the lithologic descriptions are not of a quality that enables confident correlation of the unconsolidated sediments between wells, even after significant effort has been made to standardize colloquial lithologic language. Discrepancies between the stratigraphy presented by Callan (1970) and that presented by Cowen (1998) indicate units vary from place to place and the geology is unpredictable. The logs from the WELLS database are, therefore, inadequate to provide confident information to generate an accurate geological framework for calibrating geophysical surveys or for hydrogeological modeling.

The gamma and resistivity logs are typically used to infer lithology (Rider and Kennedy, 2011), and the data collected in this study are effective and efficient for delineating high porosity, coarse-grained units that are potential water-bearing zones (Fig. 3.7). These data also

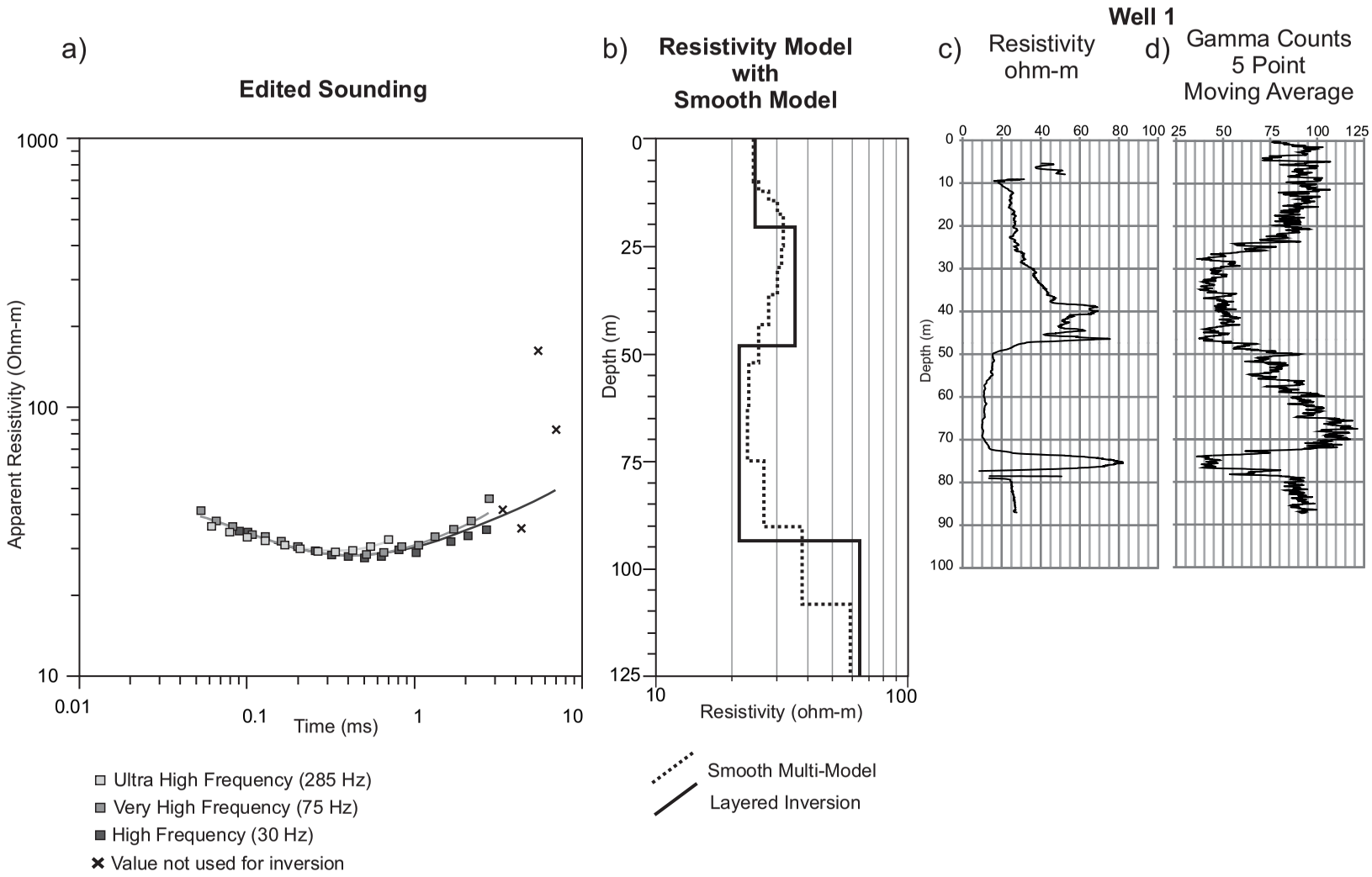

Figure 3.9. The 4-layer model from the sounding at Station 3 on the 208 Road. The logs helped constrain the inversion and the results are comparable; A) Sounding data; b) 4-layer inversion model; c) Well #1 resistivity log; and d) Well #1 gamma log.

provide a means to validate the 1-D models from the EM soundings (e.g., Fig. 3.9). The resistivity values from the well log (Well #1) and the resistivity values from a 4-layer best-fit layered-earth model from a sounding located approximately 200 m south of the well are generally comparable (Fig. 3.9). The two relatively higher resistivity zones on the resistivity log (25-48 m and 72-80 m; Fig. 3.9(c)) correspond to coarse units (sand and/or gravel aquifers) and the lower resistivity intervals correspond to fine-grained units (aquitards). Fresh water was encountered during drilling in both of these higher resistivity intervals (Fig. 3.7). The gamma log is consistent with these interpretations; low gamma counts occur where there is sand and/or gravel and higher gamma counts correspond to the finer sediments (Fig. 3.9(d)). From the bottom upwards, the deepest layer in the resistivity model (Fig. 3.9(b)) has a resistivity of 65 ohm-m, which appears to be an average of the underlying bedrock (25 ohm-m) and the narrow coarse-grained zone between 80 and 72 m in the well log (60 – 80 ohm-m; Fig. 3.9(c)). This interval is followed by a low resistivity layer between 80 and 48 m with a resistivity of 10-15 ohm-m in the log (Fig. 3.9(c)) and ~20 ohm-m in the model (Fig. 3.9(b)). The log shows the upper coarse-grained zone (48-25 m) includes a 10 m high resistivity zone (~50 ohm-m) between 48 and 38 m, overlain by a gradually decreasing resistivity zone (45 to 25 ohm-m) between 38-25 m (corresponds to a fining upward sequence; Fig. 3.9(c)). The layered-earth model averaged the interval between 25 and 48 m with a resistivity of 36 ohm-m (Fig. 3.9(b)). In both datasets, the upper 20 m of the profile has a resistivity value of 25 ohm-m (Figs. 3.9(b and c)). This comparison shows that where there are control points (i.e., logs or stratigraphy), a complex (i.e., 4-layer) model can be generated that retains geological meaning and has a reasonable standard error of fit. There are, however, limitations to inversions, even when ancillary information is available. Thin layers, particularly at depth, could not be resolved and resulted in an amalgamation of these horizons into an averaged apparent resistivity (e.g., low resistivity bedrock between 80 and 90 m and the high resistivity layer between 72 and 80 m shown in Fig. 3.9(c) were merged in the model shown in Fig. 3.9(b)). Upper layering is missing because of the voltage saturation at early times (affected by the gain used during data acquisition). This limits modeling of the top of the geological section (in this case 70 microseconds or approximately the top 10 m). The accuracy of boundary locations when adjacent layers have low resistivity contrasts is also affected (discussed in detail

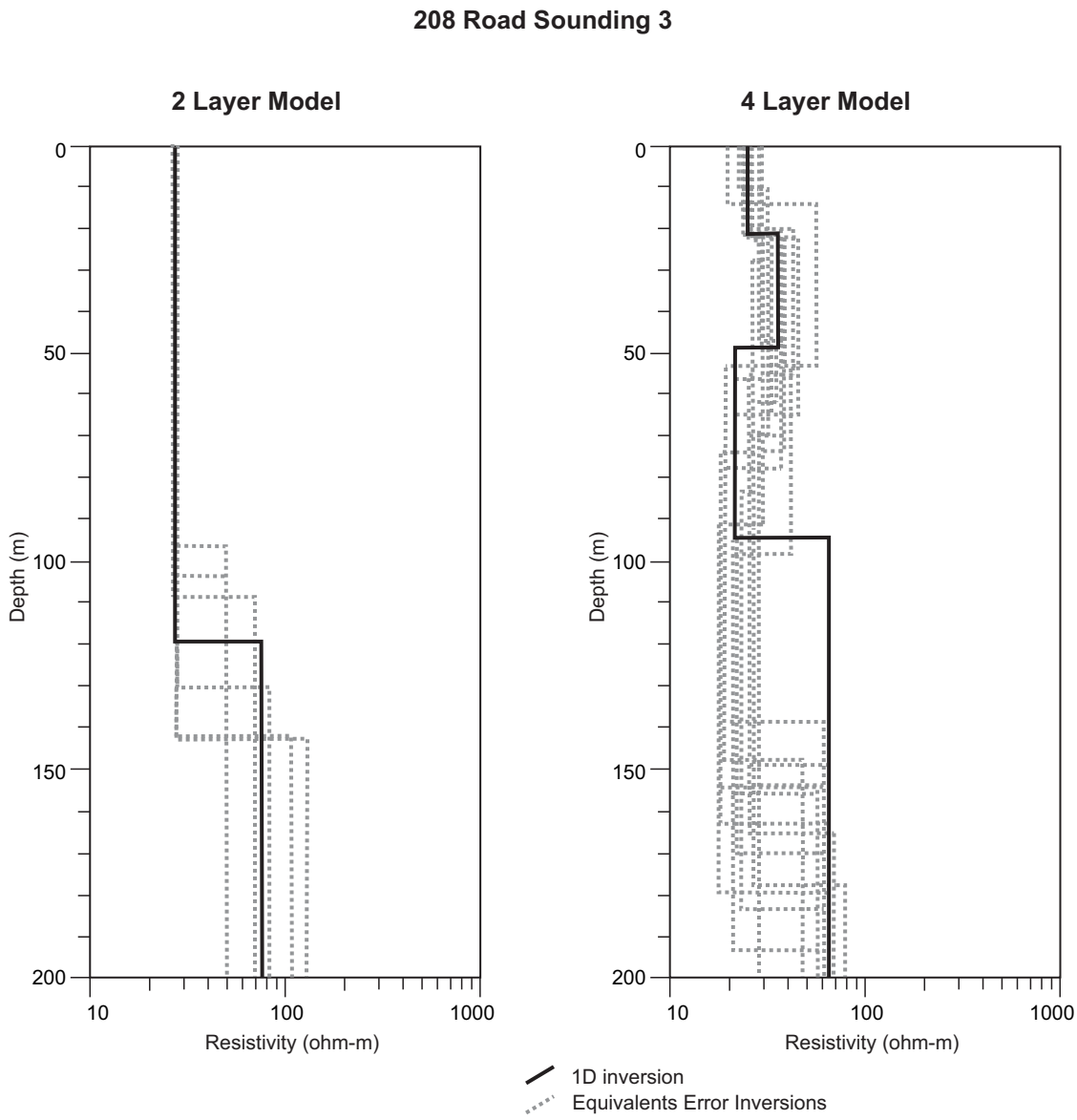

Figure 3. 10. Two-layer (left) and a 4-layer (right) best-fit inversion model from Station 3 on 208 Road are plotted with their equivalent error analysis. Both of these models have an RMS standard error fit of 4.48%.

below).

In the sounding described above, the water well logs offered some control in constraining a 4-layer inversion. There is, however, a considerable challenge when constraining (interpreting) soundings where control points are absent. For example, if we examine the same sounding as discussed above without considering the data from the water well, confidence in the 4-layer model breaks down. A simple 2-layer model for the same sounding has exactly the same root mean square (RMS) standard error of fit (4.48 %; Fig. 3.10). Without the additional knowledge provided by the resistivity log from the well (control point), any number of layers can be generated, but there is no way of knowing if the layers have geological meaning. It is therefore, unrealistic to model complex layered inversions without justification based on some kind of supplementary information.

What is particularly challenging in this study is generating appropriate inversions when low resistivity contrasts occur between the stratigraphy of the valley-fill succession and the surrounding rock. Equivalence analysis provides a series of alternative inversions (layer thicknesses and associated resistivity) with the same standard error of fit. An example of equivalence analysis for two soundings from Stucky Road (Fig. 3.5) illustrates the range of depths that a layer boundary will occur when a sounding is conducted over lithologic units with small resistivity contrasts between layers. They are both 2-layer models, but in one example (Station 6; Fig. 3.11(a)) the ratio of the resistivity of the two layers is 3.49 (standard error of fit = 6.18%) and in the other example (Station 12; Fig. 3.11(b)) the ratio of resistivity of the two layers is 1.30 (standard error of fit = 4.00%). The best-fit depth boundary for Station 6 is 107 m and the range of depths from the equivalence analysis is from 94 to 120 m (~± 13 m). The best-fit depth for Station 12 is 98 m and the range of depths from the equivalence analysis is from 65 to 148 m (~+31 m, ~-51 m). This demonstrates that the range of the equivalent inversions boundaries increases as the resistivity contrast ratio between layers diminishes. This range is the envelope where a boundary may occur and explains, in part, why there is often discrepancy between water well drill records and inversions.

Although this study has identified a number of limitations of this type of survey in regions with low resistivity contrast, it was successful in differentiating: 1) the valley-fill from bedrock; and 2) generalized lithologic units. When inversions are combined into resistivity-depth sections and the resistivity-depth sections are combined into fence diagrams (Fig. 3.12), there is

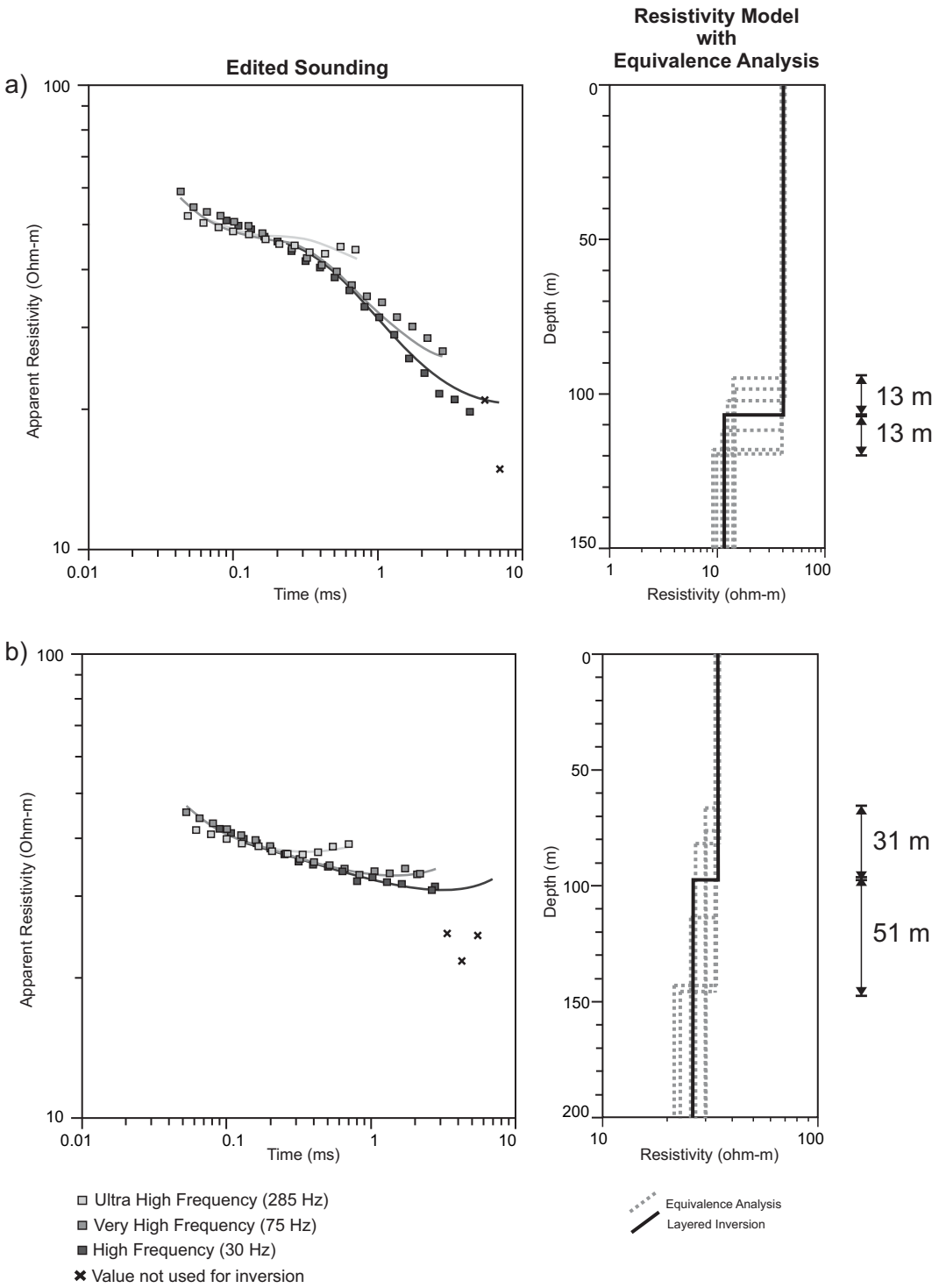

Figure 3.11. Equivalence analysis can be used to provide a range of depths that a layer boundary can occur in inversions with the same standard error of fit. a) The resistivity ratio between adjacent layers at Station 6 on the Stucky Road is 3.49 and the resulting equivalent analysis range is ± 13 m. b) The resistivity ratio between adjacent layers at Station 12 on the Stucky Road is 1.30 and the resulting equivalent analysis range is +31 m to -51 m.

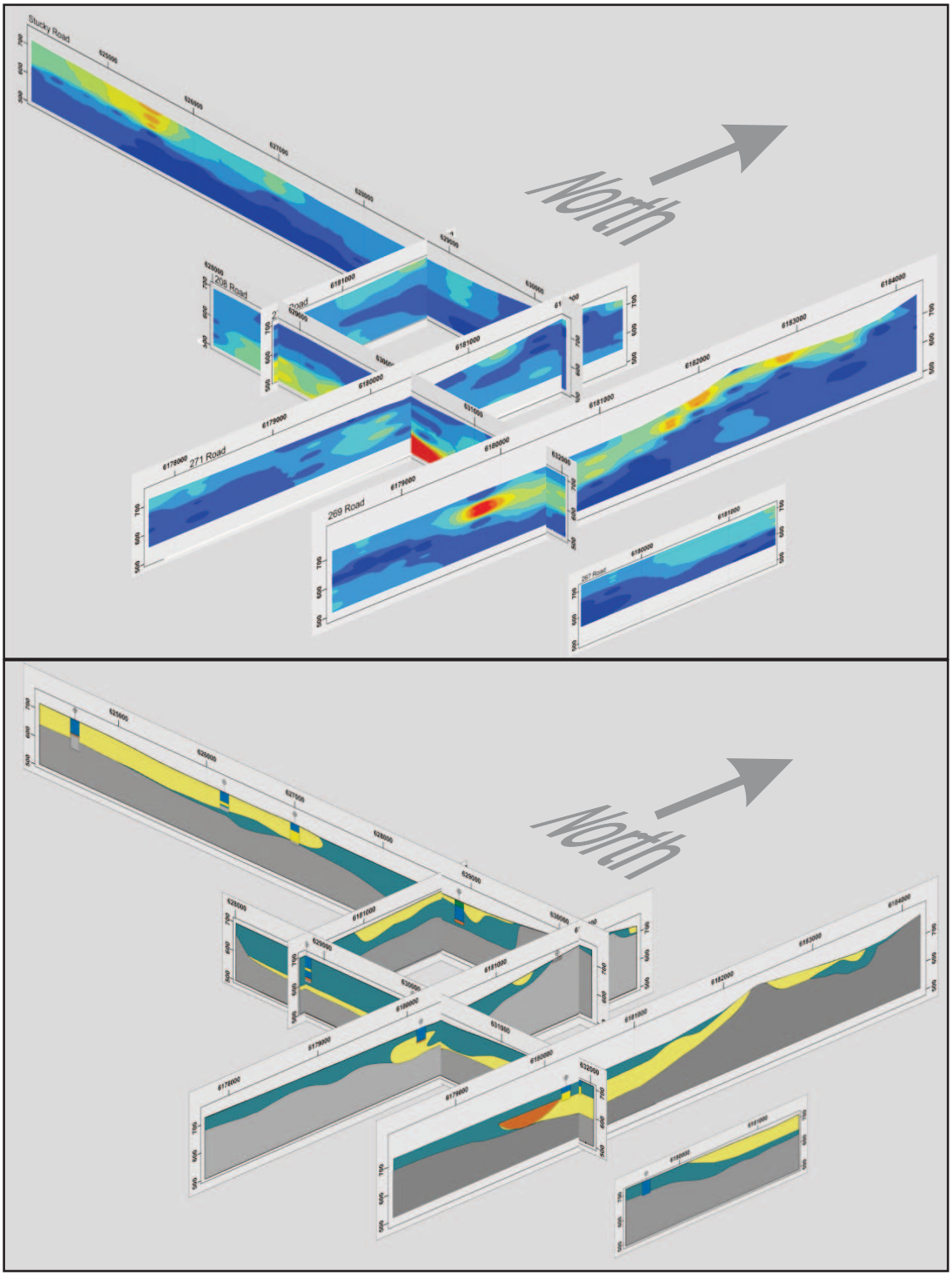

Figure 3.12. The resistivity depth-sections combined into a fence diagram show the likely 3-D continuity between lines. From these images, the geometry for the paleovalley and the potential aquifers can be determined (legend is the same as in Fig. 3.8).

considerable apparent continuity. Where the survey was conducted, the axis of the GPV thalweg (lowest part of the valley) was found to be generally parallel to, and under the 208 Road. The valley is constrained in the northwest by bedrock that underlies a small topographic high. The paleovalley shallows in the southern part of the study area where it is appears to be 20-40 m deep. This suggests that the GPV is no wider than about 3.5-4.0 km in the area near the 269 Road with a maximum depth below surface of approximately 120 m. The GPV is estimated to be approximately 70 m deep to the west where Highway 97 meets Stucky Road (Fig. 3.5). There is also inferred medium to coarse-grained valley-fill along the base of the paleovalley along the 208 Road between the 269 Road and the 271 Road, as indicated by a higher resistivity feature that might represent a channel immediately south of the 208 Road. This unit is likely the main aquifer for the region as most water wells in the area terminate at this depth. At the west end of Stucky Road the medium-grained unit (relatively high resistivity zone) occurs higher in the section and might represent an unconfined aquifer. Although these interpretations are speculative, they do refine the generalized bedrock topography (Hickin, 2011) and provide guidance for a drilling strategy to optimize the exploitation of the local groundwater resources.

3.5 Summary and Conclusion

A large loop, ground-based, time-domain electromagnetic survey (EM-47) was successfully used to map the geometry and valley-fill of a paleovalley. This was accomplished despite the limited resistivity contrast between adjacent valley-fill units, as well as the limited contrast between the valley-fill succession and the surrounding rock. The 1-D inversions were combined into resistivity-depth sections that were then combined into fence diagrams that show 3-D continuity. The resistivity data indicate the Groundbirch Paleovalley extends east-west under the survey area. The valley is approximately 3-4 km wide with a maximum depth of approximately 120 m. A local basal aquifer (medium- to coarse-grained unit) is inferred in the central survey area, but the true geometry and thickness is speculative. Another possibly unconfined aquifer may be present towards the northwest end of the survey area. Thus, the EM-based model of the GVP geometry and lithostratigraphy is broadly consistent with that established earlier from independent water well logs and section data observed in the field.

Thin, coarse-grained units and low contrast in the resistivity of the lithologic units present some challenges for constraining and interpreting inversions. Thin units cannot be

resolved and were merged in the inversions resulting in simplified inversion models that reflect averaged apparent resistivity. Ancillary data, such as borehole resistivity logs, are useful for justifying and constraining complex multi-layer inversion. Where ancillary data are absent, complex, multilayer inversions are inappropriate and simple 2- or 3-layer models are the most realistic in this area. If the ratio of the resistivity of two layers is low, there is more uncertainty (greater range) in the equivalence models. This range can be considered the envelope in which a geoelectrical boundary may occur.

3.6 Acknowledgements

The authors thank Les Beard (Associate Editor), D. Schmitt, and an anonymous reviewer for comments that improved the manuscript. This project is a contribution to the Northeast British Columbia Aquifer Project, a collaboration of the British Columbia Ministries of Energy and Mines and Natural Gas, Environment, and Forests, Lands and Natural Resource Operations. This project has received funding from the Ministry of Forests, Lands and Natural Resource Operations and the Climate Action, Clean Energy (CACE) Fund. The authors would like to express gratitude to Dave Wilford for agreeing to coordinate the project. The authors are grateful to Chelton van Geloven and the residents of the Groundbirch area for providing access to private land to accommodate the survey. Fil Ferri, David Wilford, and Matt Sakals provided capable and good-humored field support for the data acquisition. This project is a contribution to A.S. Hickin's PhD Thesis at the University of Victoria, which has been supported by the British Columbia Pacific Leaders Scholarship. The authors would like to thank V.M. Levson and E.J. Hickin for their helpful review of earlier versions of the manuscript.

3.7 References

Bhattacharya, J.P., 1993, The expression and interpretation of marine flooding surfaces and erosional surfaces in core; examples from the Upper Cretaceous Dunvegan Formation, Alberta foreland basin, Canada: in Posamentier, H.W., Summerhayes, C.P., Haq, B.U. and Allen, G.P., (eds.), Sequence stratigraphy and facies associations, International Association of Sedimentologists, Special Publication 18, pp. 125-160.

Bhattacharya, J.P., and Walker, R.G., 1991, Allostratigraphic subdivisions of the Upper Cretaceous Dunvegan, Shaftesbury, and Kaskapau formations in northwestern Alberta subsurface: Bulletin of Canadian Petroleum Geology, 39, 145-164.

British Columbia Ministry of Environment, 2012, The WELLS Database: https://a100.gov.bc.ca/pub/wells/public/indexreports.jsp, Accessed May 2012.

Callan, D.M., 1970, An investigation of a buried channel deposit in the Groundbirch area of northeastern British Columbia: Report No. 3 of 1969 Peace River Rotary Drilling Programme, British Columbia Ministry of Environment, Groundwater Division.

Constable, S.C., Parker, R.L., and Constable, C.G., 1987, Occam's inversion: A practical algorithm for generating smooth models from electromagnetic sounding data: Geophysics, 52, 289-399.

Cowen, A., 1998, BC Peace Region Groundwater Initiative Interim Report 1998: Prairie Farm Rehabilitation Administration.

Freeze, R.A., and Cherry, J.A., 1979, Groundwater: Prentice-Hall, Englewood Cliffs, NJ, USA.

Geonics, 2006, EM39 – Borehole Conductivity Logger: Geonics Limited, Mississauga, Ontario.

Geonics, 2011, Protem 47D operating manual for 20/30 gate model: Geonics Limited, Mississauga, Ontario.

Hickin, A.S., 2011, Preliminary bedrock topography and drift thickness of the Montney Play area: British Columbia Ministry of Energy and Mines, Energy Open File 2011-1 and Geoscience BC, Report 2011-07, 2 maps, 1:500 000 scale.

Hickin, A.S., and Best, M.E., 2012, Stratigraphy and proposed geophysical survey of the Groundbirch paleovalley: A contribution to the collaborative northeast British Columbia Aquifer Project: in Geoscience Reports 2012, British Columbia Ministry of Energy and Mines, 91-103.

Hickin, A.S., Kerr, B., Turner, D.G., and Barchyn, T.E., 2008, Mapping Quaternary paleovalleys and drift thickness using petrophysical logs, northeast British Columbia, Fontas map sheets, NTS 94I: Canadian Journal of Earth Sciences, 45, 577-591.

Interpex, 2006, IX1D.v3 tutorials: Interpex Limited, Golden, Colorado.

Lowen, D., 2011, Aquifer classification mapping in the Peace River region for the Montney Water Project: Lowen Hydrogeology Consulting Ltd., File 1026.

Mathews, W.H., 1955, Ground-water possibilities of the Peace River block, British Columbia: British Columbia Ministry of Energy and Mines, Groundwater Paper 3.

Mathews, W.H., 1978, Quaternary stratigraphy and geomorphology of the Charlie Lake (94A) map-area, British Columbia: Geological Survey of Canada, Paper 76-20.

Mathews, W.H., 1980, Retreat of the last ice sheets in northeastern British Columbia and adjacent Alberta: Geological Survey of Canada, Bulletin 331.

McMechan, M.E., 1994, Geology and structure cross-section, Dawson Creek, British Columbia: Geological Survey of Canada, Map 1858A.

McNeill, J.D., 1994, Principles and applications of time-domain electromagnetic techniques for resistivity sounding: Geonics Limited, Technical Note TN27.

McNeill, J.D., Bosnar, M., and Snelgrove, F.B., 1990, Resolution of an electromagnetic borehole conductivity logger for geotechnical and ground water applications, Technical Note TN-25: Geonics Limited, Mississauga, Ontario.

Pawlowicz, J.G., Hickin, A.S., Nicoll, T.J., Fenton, M.M., Paulen, R.C., Plouffe, A., and Smith, I.R., 2005, Bedrock topography of the Zama Lake Area, Alberta (NTS 84L): Alberta Energy and Utilities Board, Alberta Geological Survey, Map 328.

Pawlowicz, J.G., Nicoll, T.J., and Sciarra, J.N., 2007, Bedrock topography of Bistcho Lake area, Alberta (NTS 84M): Alberta Energy and Utilities Board, Alberta Geological Survey, Map 416.

Plint, A.G., McCarthy, P.J., and Faccini, U., 2001, Nonmarine sequence stratigraphy: updip expression of sequence boundaries and systems tracts in a high-resolution framework, Cenomanian Dunvegan Formation, Alberta Foreland Basin, Canada: American Association of Petroleum Geology, Bulletin, 85, 1967-2001.

Rider, M., and Kennedy, M., 2011, The geological interpretation of well logs (third edition): Rider-French, Scotland.

Reimchen, T.H.F., and Rutter, N.W., 1972, Quaternary geology, Dawson Creek, British Columbia: Geological Survey and Canada, Report of Activities, Part A, Paper 72-1, 176-177.

Reitz, J.R., and Milford, F.J., 1962, Foundations of electromagnetic theory: Addison-Wesley Publishing Company, Reading, MA., USA.

Reynolds, J.M., 1997, An Introduction to Applied Environmental Geophysics: John Wiley and Sons, New York.

Stott, D.F., 1961, Dawson Creek map-area, British Columbia, 93P: Geological Survey of Canada, Paper 61-10.

CHAPTER 4: COALESCENCE OF LATE WISCONSINAN CORDILLERAN AND LAURENTIDE ICE SHEETS EAST OF THE ROCKY MOUNTAIN FOOTHILLS IN THE DAWSON CREEK REGION, NORTHEAST, BRITISH COLUMBIA, CANADA.

Adrian S. Hickin, Victor M. Levson, Olav B. Lian, and Alice Telka

This manuscript has not yet been submitted for publication

Abstract

Geomorphic, stratigraphic and geochronological evidence from the Dawson Creek area of British Columbia (Canada) indicates that, during the Late Wisconsinan (marine isotope stage, MIS, 2), a major lobe of western-sourced ice (Cordilleran Ice Sheet or a montane ice lobe) flowed beyond the Rocky Mountain foothills and coalesced with the northeastern-sourced Laurentide Ice Sheet. The use of high-resolution digital elevation models (DEMs) from light detecting and ranging (LiDAR) technology, has enhanced delineation of geomorphic features that record former ice flow. Based on these data a continuous 75 km-long field of streamlined landforms has been mapped that records the flow path of a major lobe of east-flowing ice (Cordilleran Ice Sheet or montane ice lobe > 200 km wide) that was deflected from east-northeast to a north-northwest trajectory as it coalesced with the retreating Laurentide Ice Sheet. The streamlined landforms are composed of till with clasts of eastern provenance, implying that the Laurentide Ice Sheet must have reached its maximum extent before the western-sourced ice flow crossed the area. Since the Laurentide Ice Sheet did not reach this region until the Late Wisconsinan (MIS 2), the CIS/montane ice responsible for the streamlined landforms must also have occupied the area after the Laurentide Ice sheet withdrew. Stratigraphy from the Murray and Pine river valleys also supports a Late Wisconsinan age for the surface landforms. The stratigraphy indicates at least two glacial events separated by a non-glacial interval dated by radiocarbon and optically stimulated luminescence analyses to be of Middle Wisconsinan (MIS 3) age; this confirms that the surficial glacial sediments and landforms are of Late Wisconsinan (MIS 2) age.

4.1 Introduction

The timing and extent of the Cordilleran (CIS) and Laurentide (LIS) ice sheets in northeastern British Columbia has been the subject of debate for several decades. One view is that the two ice sheets coalesced during Marine Isotope Stage (MIS) 2 (Mathews, 1978; 1980, Dyke & Prest, 1987; Dyke et al, 2003; Bednarski & Smith, 2007; Hartman & Clague, 2008). Others have suggested, however, that coalescence, if it did occur, happened during an earlier glaciation (MIS 4 or older) and the CIS was of limited extent during MIS 2 (Reimchen, 1980; Bobrowsky, 1989; Bobrowsky & Rutter, 1992; Catto et al., 1996).

This study focuses on northeastern British Columbia (Fig. 4.1) and presents new geomorphic, stratigraphic, geochemical and geochronologic evidence to help resolve this debate. The study takes advantage of the recent increases in the resolution of digital elevation models (DEMs) constructed from light detecting and ranging (LiDAR) surveys in the study area. These techniques have enhanced considerably our ability to delineate geomorphic features (e.g. streamlined landforms) that record former ice sheet dynamics. They directly inform the model of ice sheet trajectory and interaction we propose here for northeastern British Columbia.

Stratigraphic evidence is drawn from sections exposed by river incision. The Murray-Pine drainage system and the Kiskatinaw River have incised paleovalley-fill successions revealing an extensive late Quaternary sedimentary record. These geological sections provide an excellent opportunity to examine stratigraphy in an area at the margins of two former, and potentially interacting, continental ice sheets.

Chronological control is based on radiocarbon and optical dating of sediments selected on the basis of their position within the geomorphic and/or stratigraphic record. The objective of this study is to reconstruct major paleo-ice flow from geomorphic features and establish temporal context for these surface landforms.

The study area is located in the region where the Rocky Mountain Foothills transition to the plains of the Alberta Plateau (Holland, 1976). It is generally agreed that the area was influenced by three glacial systems (Catto et al., 1996): 1) LIS (sourced from the northeast); 2) CIS (sourced from west of the Rocky Mountains; and 3) montane glaciers (mainly sourced within the Rocky Mountains). LIS deposits are generally differentiated from those of other glacial systems by the presence of allochthonous red, granitic and gneissic clasts derived from Proterozoic Canadian Shield (Beach & Spivak, 1943; Mathews, 1978). The presence of these very

durable clasts indicates transport from the Keewatin ice center in northern Canada (Dyke and Prest, 1987). Differentiating westerly derived CIS deposits can be more problematic as both local montane and Cordilleran sediments are dominated by sedimentary clast lithologies. The presence of low-grade schists and slate from the Rocky Mountain Trench, however, is considered diagnostic of CIS deposits (Mathews, 1978). Unfortunately, these rocks tend to be soft and may not survive subglacial transport. They will, therefore, be under-represented in till deposits sourced from distant localities. Nonetheless, the proportion of western and eastern-derived lithologies has been used by previous investigators to reconstruct the extent of former ice sheets in the area (e.g. Mathews, 1978; Hartman and Clague, 2008).

4.2 Previous Work

Quaternary studies in northeast British Columbia have been on-going for more than a century (Bobrowsky and Rutter, 1992). One of the earliest references to the Quaternary geology of the area was made by Dawson (1881) in which he proposed a water-lain origin for the silt covering much of the district. He speculated that the deposits were associated with submergence of the land below sea-level, but also acknowledged that the deposits may have resulted from water impounded by “glacier-dams”. Dawson (1888) coined the terms “Cordilleran” and “Laurentide” for the ice masses recognized as the two major continental ice sheets that occupied western Canada during glacial times.

Quaternary geology studies of the area proliferated after the 1940s because of increased access to the land following construction of the Alaska Highway (1942) and the W.A.C. Bennet Dam (1961-1968) and the subsequent settling of the Peace Region (Beach and Spivak, 1943; Bobrowsky and Rutter, 1992). Much of our knowledge of Quaternary history of the area comes from the extensive contributions of Mathews (1954, 1955, 1978, 1980). In his early work, Mathews (1954) proposed a twice-repeated succession of non-glacial gravel, advance-phase proglacial lacustrine sediments, till, and retreat-phase proglacial lacustrine sediments. He assumed the lower till to be of Early Wisconsinan (equivalent to MIS 4) age and the upper till to have been deposited during the Late Wisconsinan (equivalent to MIS 2). Mathews continued to develop his ideas over the next 25 years, culminating in a revised stratigraphy and glacial history (Mathews, 1978; 1980). He recognized three ice sources: LIS, CIS, and montane glaciers. He suggested that there were at least two Laurentide glacial events (Early and Late Wisconsinan)

and possibly a third (pre-Early Wisconsinan) event recorded by eastern provenance clasts in gravel, but he found no till in the area for this event. He assigned three western-sourced glacial events: two Cordilleran events (Early and Late Wisconsinan) and one (Late Wisconsinan) montane event (Portage Mountain). Rutter (1977), working along the Finlay, Parsnip, and Peace rivers, suggested that there was evidence of four western events, two representing full CIS development and two associated with later montane events. The oldest event, “Early Advance” is the penultimate Cordilleran event that pre-dates the Late Wisconsinan. This event is followed by the second CIS event, “Early Portage Mountain”, correlated to the Late Wisconsinan climatostratigraphic interval known as the Fraser Glaciation in British Columbia (Bobrowsky et al., 1987). Montane events, considered less extensive, are referred to as the “Late Portage Mountain” and the “Deserters Canyon” events. Mathews (1978) noted a gradual eastward increase in the proportion of LIS clast types in the upper till and suggested that this was evidence for Late Wisconsinan coalescence of the LIS and the CIS. Mathews' (1980) depiction of the retreat of LIS and CIS shows that after the ice sheets coalesced, a large region south of the Peace River valley remained occupied by CIS after the LIS retreated to the northeast.

A different interpretation emerged from the work of Reimchen and Rutter (1972), Reimchen (1980), Bobrowsky (1989), Bobrowsky and Rutter (1992) and Catto et al. (1996). This model suggests that an extensive CIS in the region was restricted to an Early Wisconsinan (MIS 4) or older event and that the Late Wisconsinan CIS was of limited extent. This model has important implications for the “Ice-Free Corridor” concept that was proposed as a potential migration route for the peopling of North America (Reeves, 1973). Surficial geology mapping in the Dawson Creek area (Reimchen, 1980) identified Cordilleran morainal deposits of Illinoisan (MIS 6), Early Wisconsinan (MIS 4) and Late Wisconsinan (MIS 2) age. The ages for these events were based on the interpretation of relative stratigraphy and cross-cutting relationships of so called “truncated” streamlined landforms. This work indicated that the maximum montane glaciation postdated the Laurentide advance (Reimchen & Rutter, 1972) but that the maximum CIS pre-dates the Late Wisconsinan. Furthermore, if coalescence occurred, it must have predated the Late Wisconsinan. Reimchen’s (1980) mapping showed that Late Wisconsinan Laurentide deposits to be restricted to the east side of the Dawson Creek map sheets (NTS 93P) and the dominant ice-flow direction for the LIS was to the south. Bobrowsky (1989) advocated for a limited Late Wisconsinan CIS based on his work in the Finlay River area. He simplified

Rutter's (1977) stratigraphy, suggesting that several of the diamicts have a sediment gravity-flow origin (based on sedimentology and clast macro-fabrics) and therefore are not primary till. He proposed a pre-Middle Wisconsinan Cordilleran event and a short Late Wisconsinan event (<5000 years long) of limited extent. His proposal was supported by two sub-till radiocarbon ages (TO-708: 15.18 ka BP; TO-709:18.75 ka BP). On the basis of these ages Bobrowsky (1989) argued that there would be little time for the CIS to grow and coalesce in the Late Wisconsinan. Liverman et al. (1989) working in western Alberta, concluded that only one Laurentide glacial event is recorded at Watino, Alberta (~175 km east of the study area) and that it was of a Late Wisconsinan age. Bobrowsky and Rutter (1992) summarized this work and suggested that, in the Peace River Valley: 1) Cordilleran and Laurentide events were asynchronous and maximum advance of the CIS predates the maximum extent of the LIS which is in turn postdated by the maximum extent of mountain ice; 2) the Late Wisconsinan Cordilleran event was of limited extent, 3) LIS only reached the area once in the Late Wisconsinan; and 4) there was no Late Wisconsinan ice sheet coalescence, an assertion supported by Catto et al. (1996).

Jackson et al. (1996, 1999) and Levson and Rutter (1996) contested the Late Wisconsinan "Ice-Free Corridor" concept. Jackson et al. (1996; 2009), using cosmogenic ^{36}Cl ages, confirmed that the Foothills erratic train in southern Alberta is Late Wisconsinan in age. These erratic were emplaced where CIS and LIS converged and deflected, flowing south along the Rocky Mountain Foothills. Levson and Rutter (1996) demonstrated that the CIS sourced from west of the continental divide, flowed through the Jasper area and was deflected south along the mountain front by the LIS during the Late Wisconsinan. Nonetheless, an "ice free corridor" likely did exist both before and after the late glacial maximum (Dyke et al., 2003; Bednarski and Smith, 2007).

Most recently, Hartman and Clague (2008) revisited the stratigraphy in the Peace River Valley between Hudson Hope and Fort St John and supported Mathews (1978) model of three Laurentide events and two Cordilleran events separated by interglacial intervals or lengthy interstadials. They conclude that the earliest Laurentide event (older than MIS 4) was less extensive than the penultimate (Early Wisconsinan (?)) event that in turn, was less extensive then the Late Wisconsinan event. They suggest that the penultimate Cordilleran event (Early Wisconsinan (?)) and the Late Wisconsinan event extended east, beyond the mountain front, but they did not speculate on the extent or if the ice sheets coalesced. They reconciled their

multiple Laurentide model with the single Late Wisconsinan Laurentide model (Westgate et al., 1971, 1972; Catto 1984; Liverman 1989; Liverman et al., 1989; Young et al., 1994) by suggesting that the pre-Late Wisconsinan LIS had a northwest trending ice front and southwest trajectory, so the ice sheet entered the region but terminated before Watino and Edmonton.

Bednarski and Smith (2007) found evidence of both Cordilleran and Laurentide deposits in the foothills around the Truch area (300 km north of the study area). They concluded that the CIS initially retreated from the foothills around 14 ka (based on cosmogenic ^{36}Cl ages) and that the CIS was therefore at its maximum around the same time the LIS was at its maximum. They further suggested that the CIS retreat was followed by an incursion of the LIS into the foothills. In the southern part of their study area, however, the CIS was still present at the mountain front, preventing the LIS from advancing into the mountains. In their sequence of events, the LIS then retreated and montane glaciers readvanced as far as the eastern edge of the foothills. They also argue that surface landforms that record deflection of the LIS are interpreted to be of a Late Wisconsinan age and indicated that the Late Wisconsinan CIS must have been present (i.e. coalescence) beyond the foothills to deflect the ice-flow trajectory of the LIS.

4.3 Methods

4.3.1 Geomorphology

Digital elevation models (DEMs) from a variety of sources were used within a geographic information system (GIS) to map streamlined glacial landforms, which are considered here to record former ice-flow direction. DEMs were generated from Shuttle Radar Topographic Mission (SRTM) data (~90 m resolution), Advanced Spaceborne Thermal Emission and Reflection Radiometer (ASTER) Imagery (30 m), British Columbia Terrain Resource Information Management (TRIM) data (25 m resolution), and Light Detection and Ranging (LiDAR) data (1 m resolution).

4.3.2 Matrix Geochemistry

To understand the composition and origin of till, diamict samples were collected from key stratigraphic sections and from a number of surface exposures (Fig. 4.1). Samples were categorized as: 1) Cordilleran (eastern provenance clast lithologies not present); 2) Transitional (samples with shield clasts from the zone where surface geomorphology suggest ice flowed

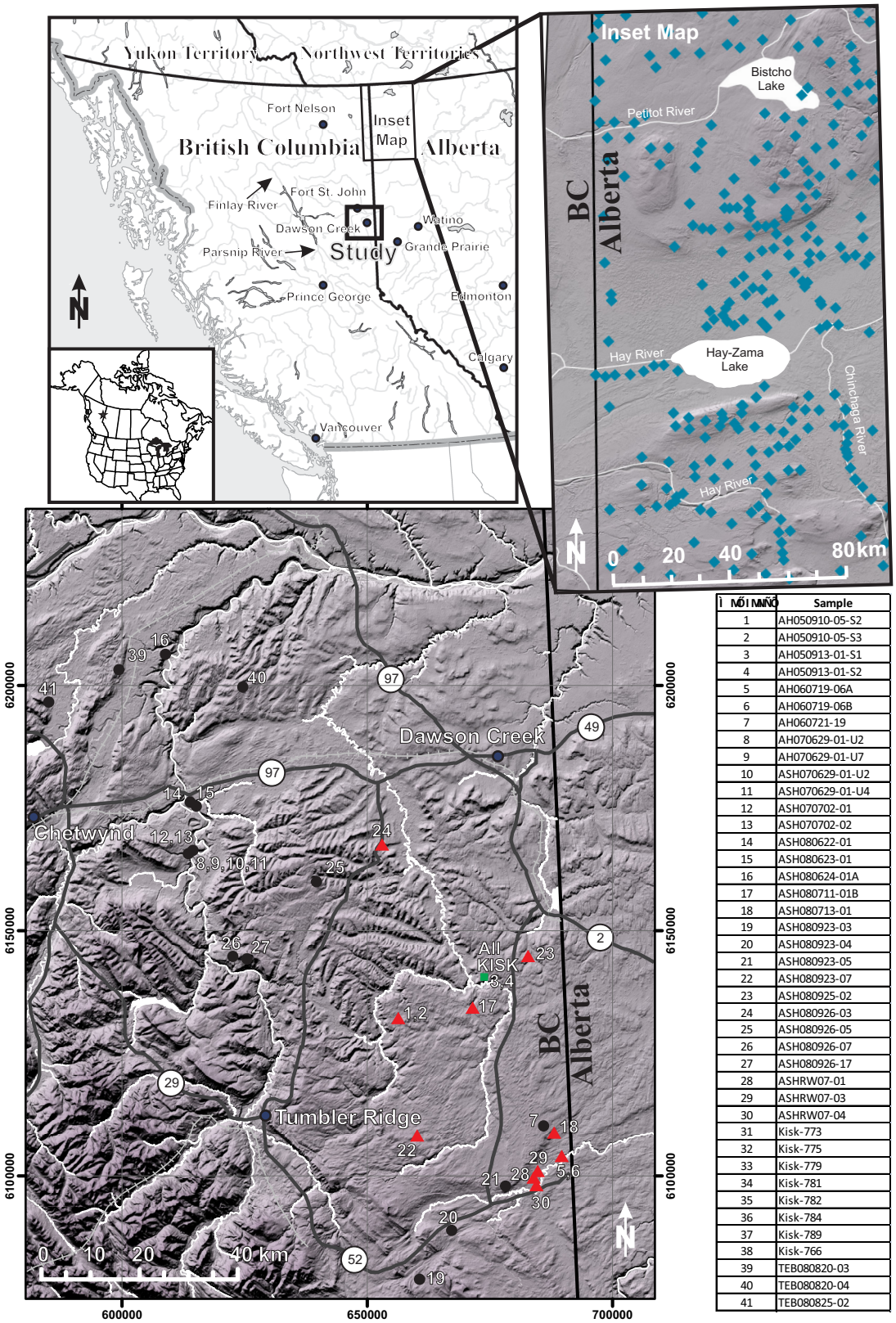

Number	Sample
1	AH050910-05-S2
2	AH050910-05-S3
3	AH050913-01-S1
4	AH050913-01-S2
5	AH060719-06A
6	AH060719-06B
7	AH060721-19
8	AH070629-01-U2
9	AH070629-01-U7
10	ASH070629-01-U2
11	ASH070629-01-U4
12	ASH070702-01
13	ASH070702-02
14	ASH080622-01
15	ASH080623-01
16	ASH080624-01A
17	ASH080711-01B
18	ASH080713-01
19	ASH080923-03
20	ASH080923-04
21	ASH080923-05
22	ASH080923-07
23	ASH080925-02
24	ASH080926-03
25	ASH080926-05
26	ASH080926-07
27	ASH080926-17
28	ASHRW07-01
29	ASHRW07-03
30	ASHRW07-04
31	Kisk-773
32	Kisk-775
33	Kisk-779
34	Kisk-781
35	Kisk-782
36	Kisk-784
37	Kisk-789
38	Kisk-766
39	TEB080820-03
40	TEB080820-04
41	TEB080825-02

Figure 4.1. The study area with the location of diamict samples (inset: location of diamict samples from northwest Alberta; Plouffe et al., 2006)(Datum: UTM NAD 83).

from west to the east); and 3) Laurentide which are a suite of samples from northwestern Alberta (Plouffe et al., 2006) that are known to be of LIS origin and not to have been influenced by Cordilleran ice (Fig. 4.1). An additional sub-set of transitional samples (from Section 11) was also distinguished to evaluate vertical variation within the transition area. Major oxide and element abundances were determined from the silt-clay size fraction (Acme Laboratory, Vancouver) of a 0.2 gram homogenized sample analysed by inductively coupled plasma emission spectrometry (ICP-ES) following a lithium metaborate/tetraborate fusion and dilute nitric acid digestion (Appendix B). The samples from Plouffe et al. (2006) were also analysed by the Acme Laboratory using the same method though the samples were analyzed several years before this study. Principal component analysis (PCA) on the major oxide data was performed on all analyzed samples using GCDkitTM to reduce and interpret the multivariate data set (Davis, 2002; Grunsky, 2006; Janoušek et al., 2006). The data are presented on a 2-D vector biplot (Gabriel, 1971).

4.3.3 Stratigraphy

Exposed Quaternary sections were noted along the rivers from a preliminary helicopter survey. Select sections were visited, examined and logged, recording stratigraphic unit attributes such as those described by Evans and Benn (2004). In most cases the units could be observed directly although there were cases where vertical cliffs prevented safe access, necessitating survey of these units from a distance through high-powered binoculars. For each unit, lithofacies were recorded using a similar system to that described by (Eyles et al., 1983). At key sections, long-axis (A-axis) clast macrofabrics were measured to aid in interpreting the genesis of diamict units (Dowdeswell & Sharp, 1986; Hicock et al., 1996). Only clasts with A/B axis length ratios of 1.5 or greater were recorded. Total clast content (> 2mm) was estimated in the field. Diamict samples (2-5 kg) were collected from selected units for geochemical and grain-size analysis. Clasts >100 mm were discarded in the field and we recognize that clast content established from sieving can only be considered a proxy as clasts >100 mm are not represented in the samples. Matrix content (<2 mm) was partitioned into sand (<2 mm – 0.063 mm), silt (<0.063 mm – 0.004 mm), and clay (<0.004 mm) size fractions. Samples were washed through graduated sieves, dried and weighed. The proportion of silt and clay was established using a hydrometer (Golder

Associates Ltd.) using procedures compliant with ASTM D 422-63 (2007). From the samples clasts >4 mm were inspected and the proportion of shield clasts determined.

4.3.4 Chronology

Two radiocarbon samples were collected and analysed from a 0.5 cm-thick organic-rich layer (Fig. 4.2a, b, c) at Pine River 1 (Section 8; Fig. 4.3). A flattened twig, approximately 5 cm long and 0.5 cm wide, was sent to Beta Analytical (Florida) for accelerator mass spectrometry (AMS) analysis. Four common silver weed (*Potentillo anserina*) achenes (Fig. 4.2d; total weight of 1.59 mg) were identified and extracted from the organic material by PALEOTEC Services (Ottawa) and sent for dating at the Keck AMS Dating Facility (University of California, Irvine). All calibrated ages reported are based on the online OxCal routine (Bronk Ramsey, 2001) using the IntCal 09 Calibration Curve (Reimer et al., 2009).

Four sand samples were collected for optical dating; a method that provides an estimate of the time elapsed since sand grains were last exposed to sunlight (i.e., deposited and buried). The method involves the measurement of an accumulation of ionized electrons in the lattice of a mineral grain (Huntley et al., 1985; Lian and Roberts, 2006; Lian, 2013). The assumption is that the traps in the crystal lattice that accumulate electrons will be vacated when the grain is exposed to sufficient energy such as light or heat. Exposure to sunlight will empty the traps and reset the luminescence clock. When the grain is deposited, buried, and consequently shielded from light, natural radiation within the environment immediately around the grain will be absorbed by the grain and stored as trapped electrons. The rate at which the mineral grain absorbs radiation energy (dose rate) is proportional to the concentration of radioisotopes and the intensity of cosmic rays at the site. The time elapsed since exposure to light is estimated by determining the laboratory dose of radiation that produces the same intensity of luminescence as the absorbed radiation in the natural environment (the equivalent dose), and a measure of the environmental dose rate (Huntley et al., 1985). Time since burial is determined by dividing the equivalent dose by the dose rate.

The environmental dose absorbed by the sand grains prior to sampling comes from alpha (α), beta (β), and gamma (γ) radiation produced by decay of U, Th, their daughter products, and by ^{40}K. The radiation is produced in the surrounding sediment and from the sampled grains themselves. The environmental dose rate was determined by laboratory analysis

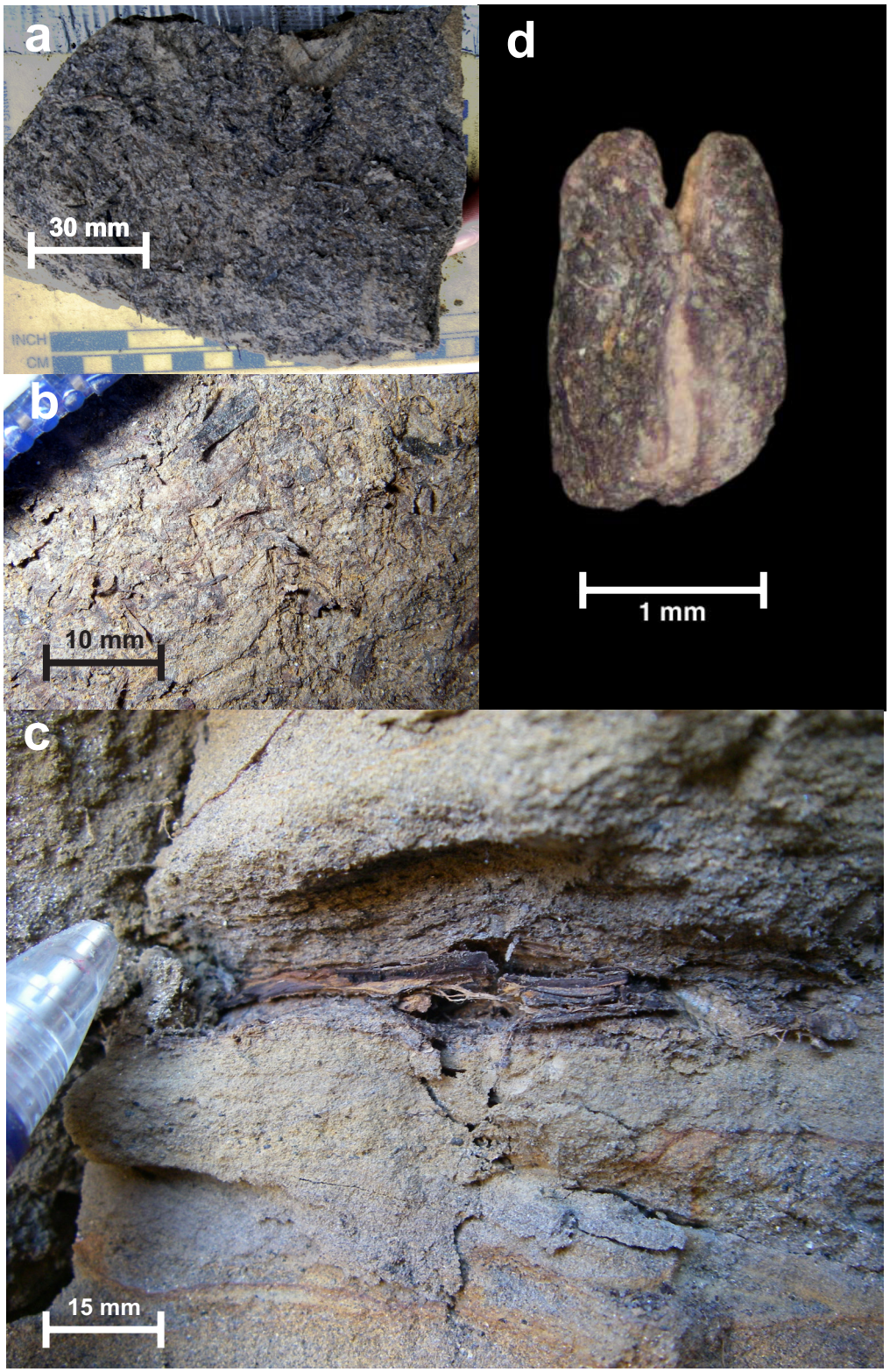

Figure 4.2. Radiocarbon samples were collected from Pine River Section 1. a) Disseminated organic fragments and wood. b) Close up view of the fossil wood and needles. c) Flattened wood fragment; d) Common silver weed (Potentillo anserine) achenes.

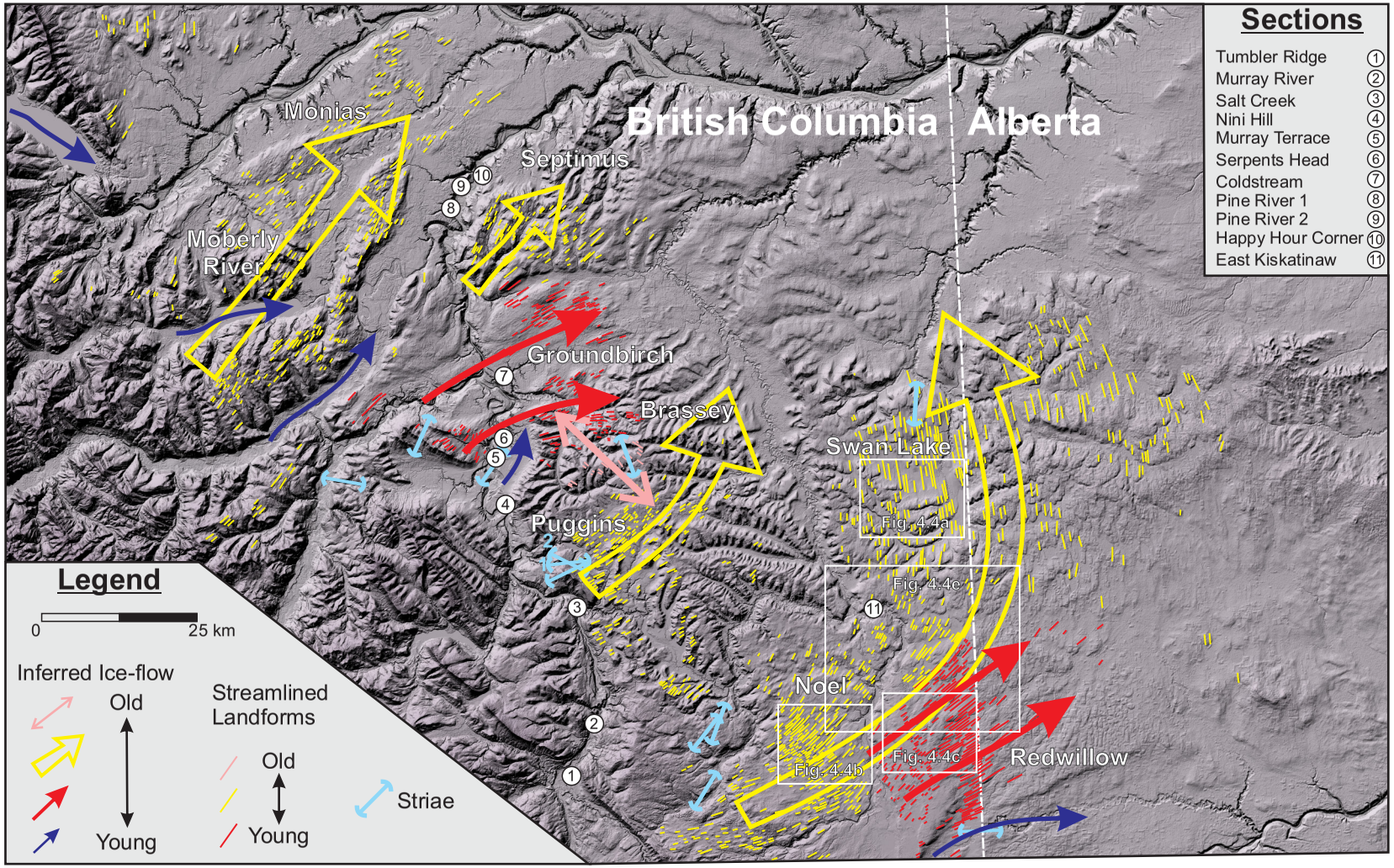

Figure 4.3. Sections located along the Murray and lower Pine rivers in northeastern British Columbia. Streamlined landforms in the study area record ice flow patterns from western sourced (CIS/Montane) ice.

of sediment samples collected adjacent to the OSL sample. Samples used for dosimetry were dried, milled, and sent to a commercial laboratory for instrumental neutron activation analysis (INAA; Becquerel Laboratories, Ontario) to determine ^{40}K, U, and Th contents. From these data, dose rates in grays per thousand years (Gy/ka) were calculated using standard formulae (Aitken, 1985; Berger, 1988; Lian et al., 1995) and the dose-rate conversion factors of Adamiec and Aitken (1998). In each case, it is assumed that the U and Th decay chains have been in secular equilibrium since deposition of the sediment. Prescott and Hutton (1995) and Olley et al. (1996) suggest that this assumption is generally valid for well-drained mineral sediments. Water in the sediment matrix attenuates or absorbs radiation differently from mineral matter, and therefore it has to be accounted for in the dose-rate calculations. Cosmic-rays can contribute significantly to the environmental dose rate, but their effect diminishes rapidly with burial depth. The contribution of cosmic rays was calculated using the method of Prescott and Hutton (1994).

Ages were determined from the luminescence measured from quartz grains using the single aliquot regenerative-dose (SAR) protocol (Murray and Wintle, 2000, 2003; Wintle and Murray, 2006). Aliquots were prepared and analyzed at the Luminescence Dating Laboratory at University of the Fraser Valley, British Columbia. In the laboratory, the light-exposed sediment was removed by discarding the outer 2-3 cm of the sediment from each end of the sample cylinders under controlled lighting conditions. Approximately 150 g of sample were extracted from the cylinder for preparation. The sand samples were treated with hydrochloric acid to dissolve carbonates and then sieved to isolate the 180-250 µm size fraction. Quartz grains were separated from heavier mineral grains using a sodium polytungstate solution with a density of 2.68 g/ml. Samples then were treated with concentrated hydrofluoric acid for 40 minutes to dissolve feldspar grains and to etch the outer surface of the quartz grains that had been affected by α radiation in the environment. Aliquots were then prepared by mounting 50-100 grains on 9.8 mm- diameter aluminum discs using silicone oil as an adhesive.

Luminescence intensity was measured using a Risø TL/OSL DA-20 reader. Aliquots were stimulated using light-emitting diodes that delivered 45 mW/cm^2 of blue (470 ± 20 nm) light to the sample. Ultraviolet emissions (~350 nm) were detected by a photomultiplier tube placed behind a 7.5 mm-thick Hoya U-340 optical filter. Laboratory irradiations were applied with a calibrated $^{90}Sr/^{90}Y$ β-source mounted on the reader that delivered 6.03 ± 0.11 Gy/min, 5.89 ± 0.11 Gy/min, 6.04 ± 0.11 Gy/min, and 5.78 ± 0.11 Gy/min for samples CS02, CS03, PR01, and

PR02, respectively. The equivalent dose of each sample was determined using the standard SAR protocol of Murray and Wintle (2000), but with the inclusion of an infrared wash to remove any luminescence resulting from K-feldspar contamination (Olley et al., 2004; Wintle and Murray, 2006).

Radial plots (Galbraith et al., 1999; Galbraith, 2010), which display the distributions of equivalent dose (De) values of each aliquot about weighted mean values, were prepared for each sample. The validity of the SAR protocol for dating quartz from the study area was tested through dose recovery experiments on all four samples (Roberts et al., 1999; Murray and Wintle, 2003). In each case the laboratory dose was sufficiently recovered, implying the quartz grains responded well to the technique and the method is suitable.

4.4 Results

4.4.1 Geomorphology

More than 1100 streamlined landforms were mapped from the DEMs (Fig. 4.3). Where there was LiDAR coverage, hundreds to thousands of subtle (<1 m height) streamlined features are detectable but were not specifically delineated because of scale limitations. Clusters of landforms have been grouped together and their relative age assigned based on cross-cutting relationship (Fig. 4.3). The flow direction is inferred from the shape of the streamlined landforms (Menzies and Rose, 1987).

The oldest mapped features, from the Brassey area (Fig. 4.3), are generally subtle and record either southeast or northwest ice flow. It is unclear if these features were formed from the CIS or LIS, however, thin (<0.5 m) till from these streamlined features at the highest elevations consists of local sandstone lithologies, with rare shield pebbles. Till from the flanks of the same hills contains abundant Canadian Shield clasts. Though this does not conclusively imply these Brassey landforms are related to the LIS, it does suggest that the LIS must have occupied the area during, or prior to the formation of these streamlined features.

The main ice flow features in the study area suggest ice from the west flowed onto the plains (yellow features; Fig. 4.3). Streamlined landforms in the Moberly River and Monias areas indicate unobstructed flow to the northeast. Landforms in the Septimus area record a general northeastern flow path, but preserve a subtle fanning pattern into, and along the Peace River Valley. Landforms in the Puggins and Noel areas are well developed and indicate deflection of

flow from an eastern trajectory to a northeastern trajectory (Fig. 4.4b), culminating in a northern to north-northwestern trajectory in the Swan Lake area (Fig. 4.4a).

A younger set of landforms (based on cross cutting relationships) in the Groundbirch area is generally parallel to major valley trends and suggests that topography influenced flow. Discordant streamlined features are preserved in a topographic low between the Septimus and Brassey areas. Streamlined landforms in the Redwillow area indicate that, following the northern deflection of ice, flow was unimpeded towards the northwest (Fig. 4.4e). The youngest Ice flow features (dark blue in Fig. 4.3), which occur in valleys, suggest ice probably occurred as valley glaciers during the late glacial/deglacial phase.

4.4.2 Geochemistry

The PCA of major oxide data differentiate Cordilleran from Laurentide samples (Fig. 4.5). The populations are distinct but overlap with transition samples plotting in the overlap zone. The CIS diamct samples are, therefore, geochemically distinct from LIS diamicts samples from Alberta and the transition samples are intermediate. In the biplots in Fig. 4.5, vectors of a consistent direction indicate positive correlation of variables; opposite vectors indicate negative correlation; and perpendicular vectors indicate weak correlation (Buccianti & Peccerillo, 1999). There is strong positive correlation between Al_2O_3, Fe_2O_3, and K_2O; TiO_2, Cr_2O_3 and P_2O_3; and MgO and CaO. There is a strong negative correlation between SiO_2 and both MgO and CaO. There is little correlation between SiO_2 and Al_2O_3, Fe_2O_3 and K_2O.

Elevated SiO_2 is associated with Cordilleran samples and generally lower SiO_2 together with relatively high levels of several of the other oxides, are associated with Laurentide samples. Bivariate plots show that the samples associated with CIS and LIS are distinct and plotting Al_2O_3, Fe_2O_3, CaO, K_2O and TiO_2 against SiO_2 are effective at defining unique geochemical domains for the two ice sheets. Although there is a strong trend in the MgO/SiO_2 relation in Fig. 4.6 there is also significant overlap between most of the LIS and CIS samples. The Na_2O/SiO_2 relation also has a substantial overlap envelope. Furthermore, the samples from section 11 plot outside the expected trend. There is also significant overlap in P_2O_5/SiO_2 values although the values for P_2O_5 are nearing the limit of measurement precision (as is the case of MnO and Cr_2O_3).

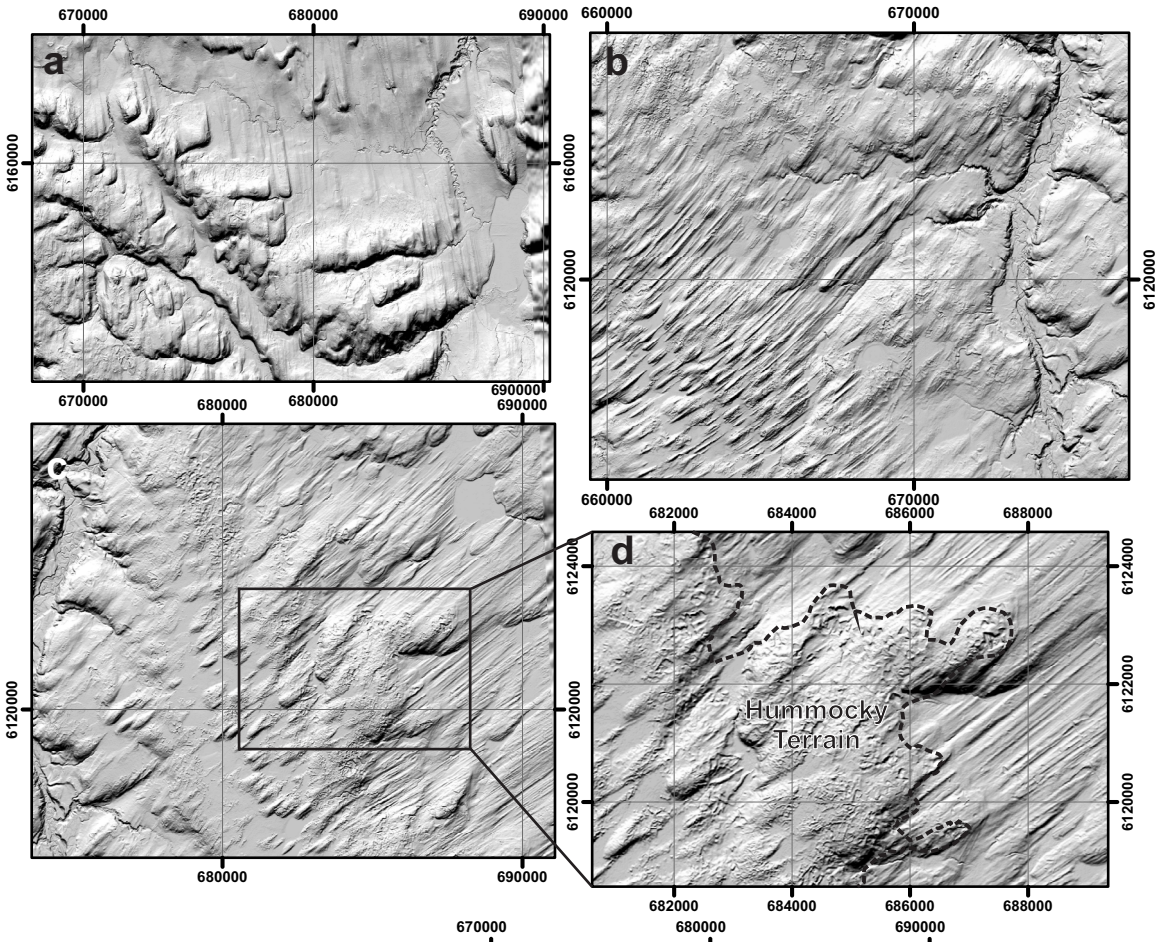

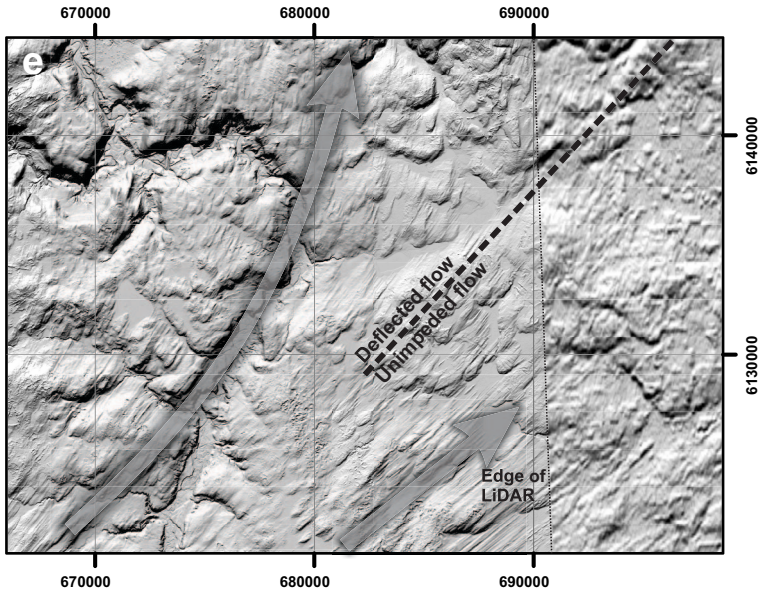

Figure 4.4. Streamlined landforms from high resolution DEM (4x vertical exaggeration; Datum: UTM, NAD 83, Zone 10); a) Streamlined landforms in the Swan Lake area indicate a north to north-northwest ice-flow direction; b) Streamlined land forms from the Noel area between the East and West Kiskatinaw rivers show a coherent arcuate and deflected flow path of Cordilleran ice; c) Streamlined landforms in the Redwillow area; d) Hummocky and reticulate terrain overlies the streamlined landforms; e) Discordant streamlined landforms indicating unimpeded ice-flow to the northeast occurred after northern flow deflection.

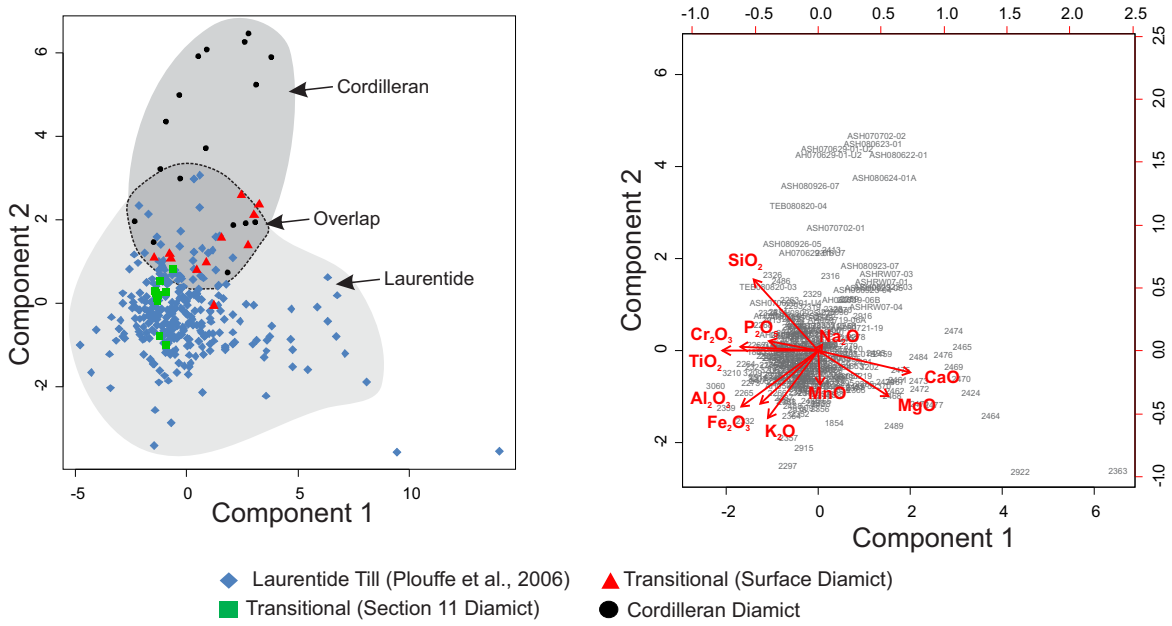

Figure 4.5. Principal component analysis (PCA) bi-plots of major oxide geochemistry from diamict matrix from this study and Plouffe et al. (2006).

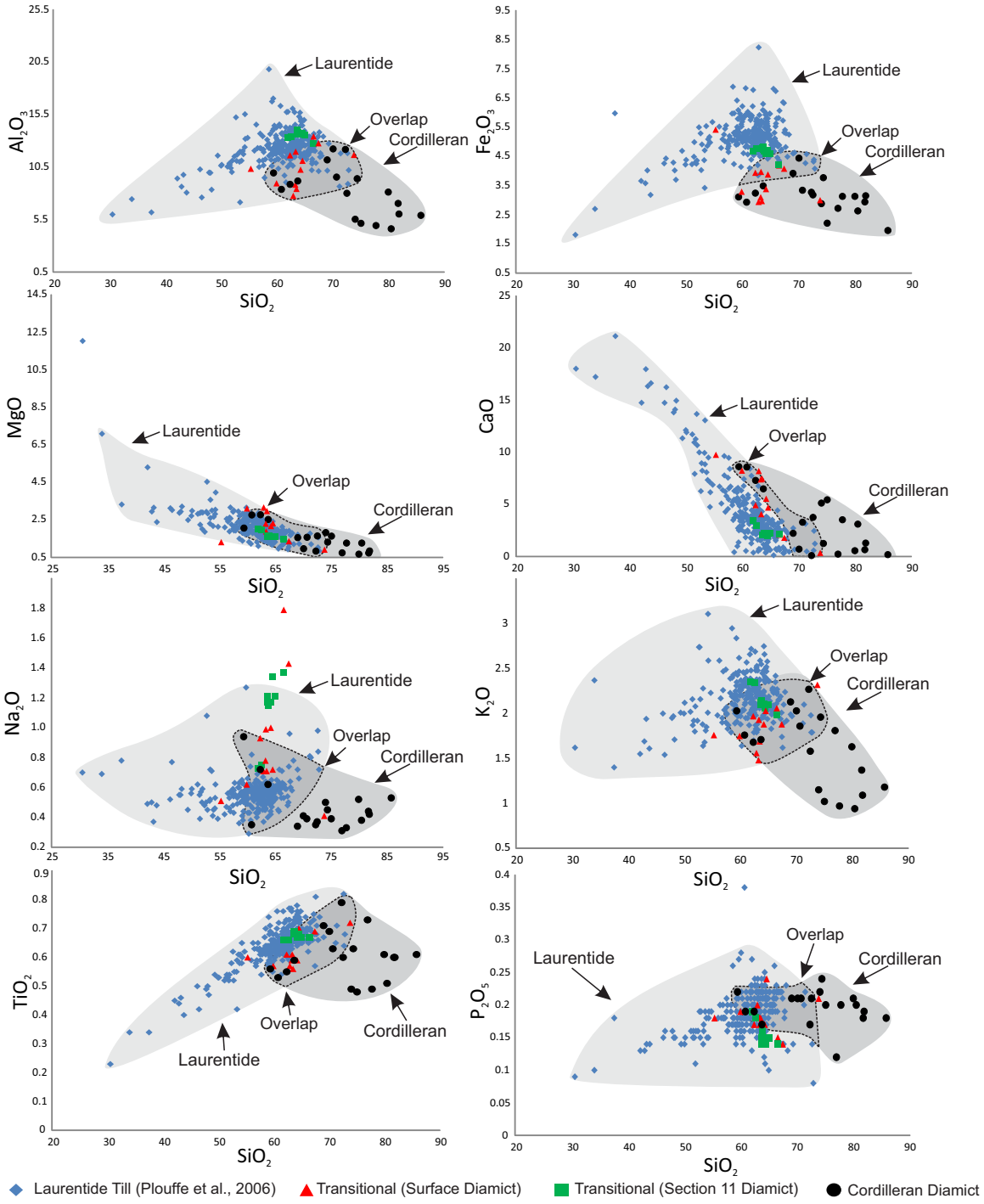

Figure 4.6. Diamict matrix major oxide discrimination plots from this study and from Plouffe et al. (2006).

4.4.3 Stratigraphic Sections

Eleven sections were logged including six from the Murray River, three from the lower Pine River, one from the Coldstream River, and one from the Kiskatinaw River (Fig. 4.3). Sections ranged in height from 15 m to more than 200 m. Units recorded in section from the Murray and Pine rivers are summarized and represented graphically in Figures 4.7—4.12. The section from the Kiskatinaw River (Section 11) is described and discussed separately. Detailed lithostratigraphic subdivisions are summarized into 12 units reflecting stratigraphic position and inferred genesis. Each unit is assigned to a climatostratigraphic interval and, for ease of global comparison, an equivalent Marine Isotopic Stage based on correlation (see discussion). In many sections more detailed lithofacies can be distinguished but these have been generalized for the purpose of this study. Descriptions of the 12 lithostratigraphic units follow.

4.4.3.1 Non-glacial (?) - MIS 5 (?)

4.4.3.1.1.1 Unit 1 – Description:

This unit is exposed along the Murray River around Section 2 (Murray River); its age and stratigraphic relationship is unclear. The unit is > 7 m thick and consists of bedded sand and gravel and laminated sand and silt. Clasts are well-rounded and dominantly resistant lithologies such as quartzite and siliceous sedimentary rocks. No shield clasts were observed in this unit. Striated and faceted clasts were not noted. Bedforms are not clearly recognized. The unit is over-consolidated with significant and large-scale soft sediment deformation (folding) that was subsequently offset 10—25 cm by high angle normal faults (Fig. 4.13). The basal contact is obscured below river level.

4.4.3.1.1.2 Unit 1 – Interpretation: Fluvial

The sediments of Unit 1 are deformed, however, well-developed stratification and well-rounded clasts indicates an alluvial setting. The absence of striated and facetted clasts implies the sediments are probably non-glacial. The unit likely represents deposition in a fluvial environment and the silt and sand over gravel is interpreted to be river gravel overlain by overbank sediments (Miall, 2006).

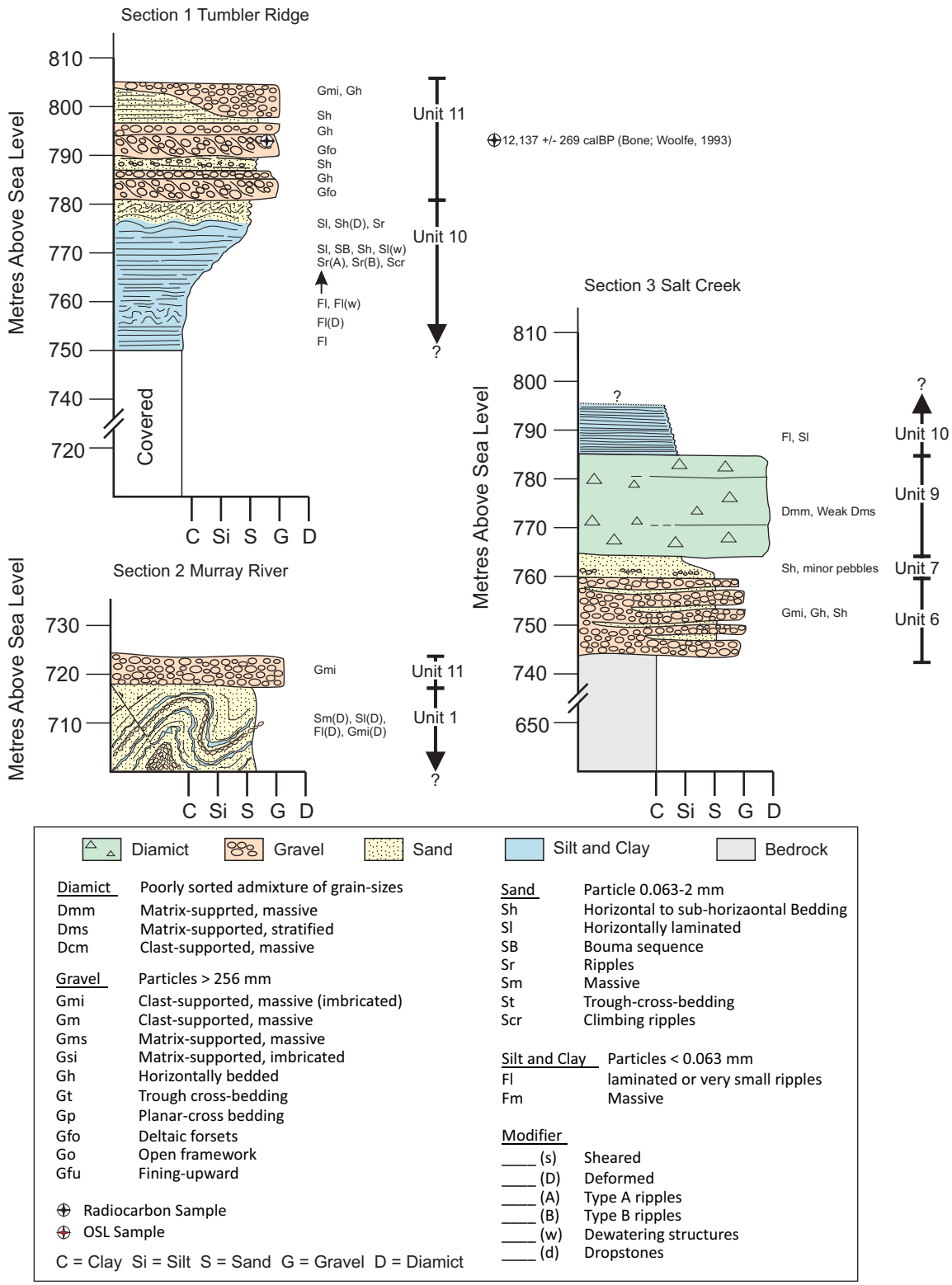

Figure 4.7. Stratigraphy of a) Section 1: Tumbler Ridge; b) Section 2: Murray River; and c) Section 3: Salt Creek (see Fig. 4.3 for section locations).

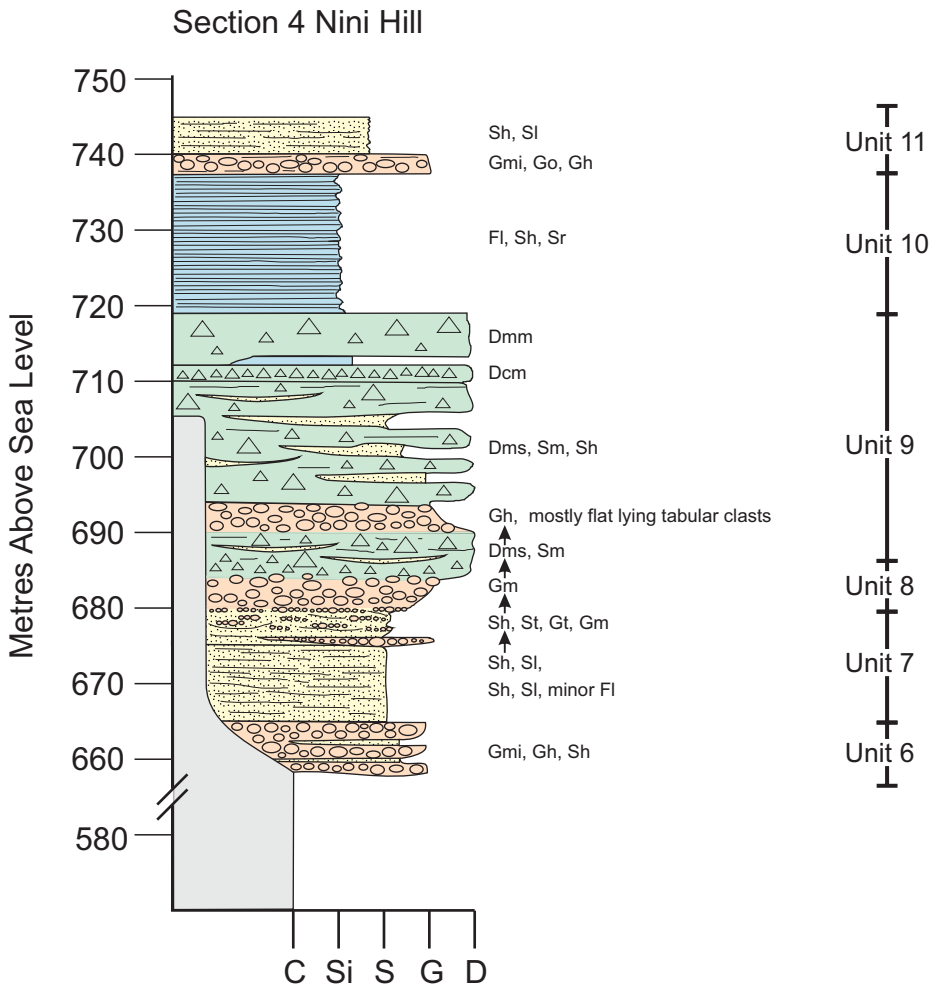

Figure 4.8. Stratigraphy of Section 4: Nini Hill (see Fig. 4.3 for section locations; legend is the same as Fig. 4.7).

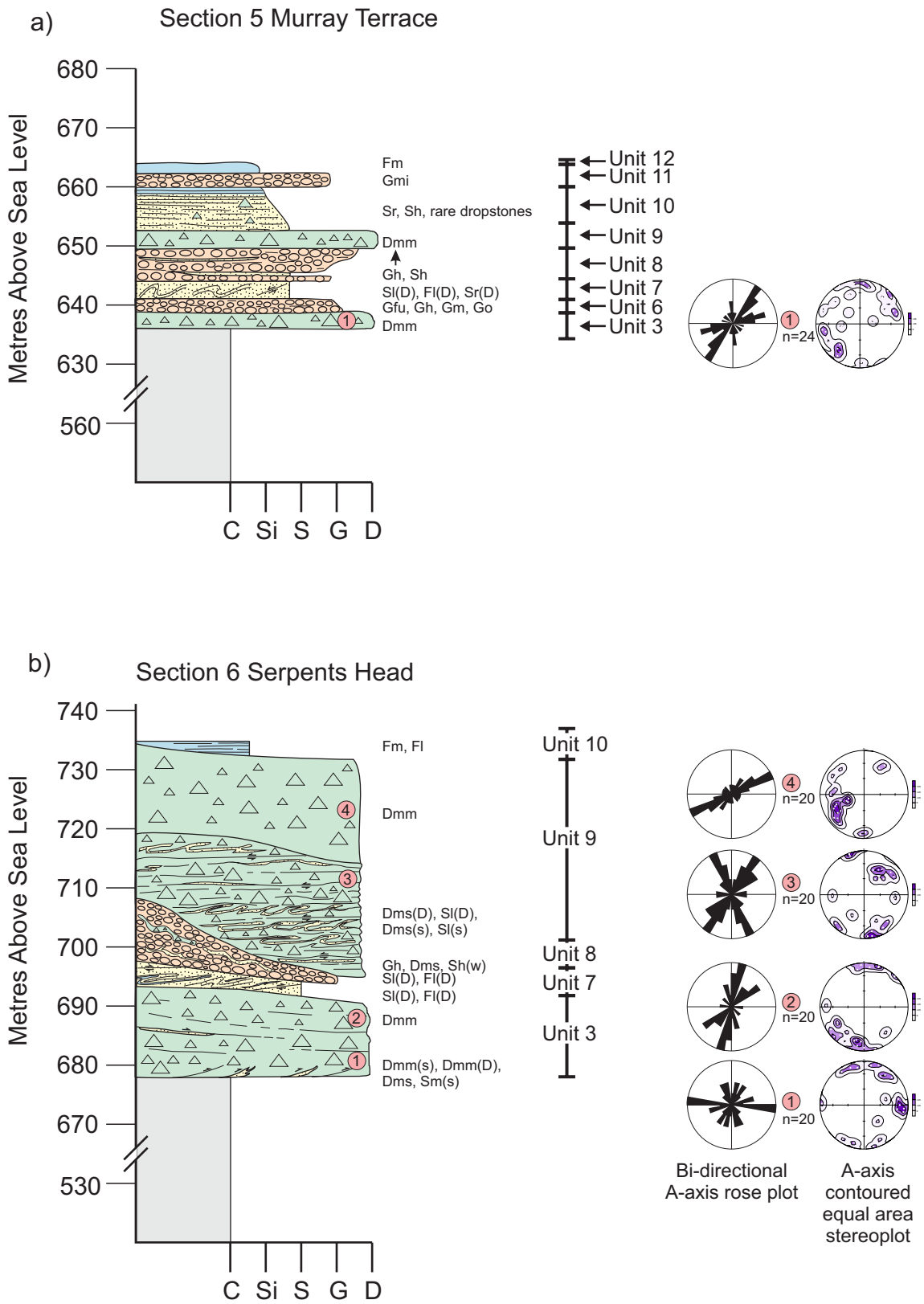

Figure 4.9. Stratigraphy of a) Section 5: Murray Terrace; and b) Setion 6; Serpents Head (see Fig. 4.3 for section locations; legend is the same as Fig. 4.7).

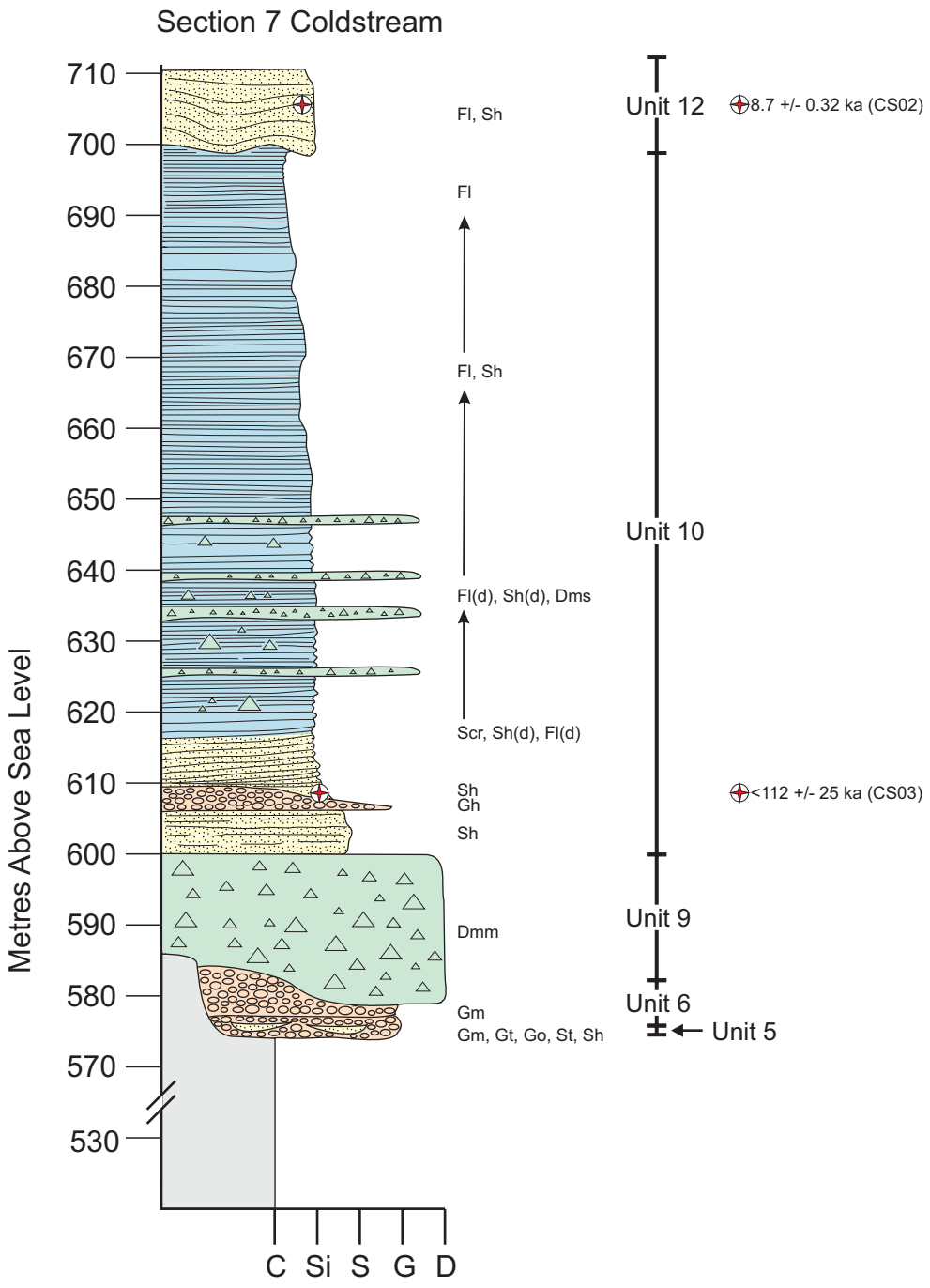

Figure 4.10. Stratigraphy of Section 7: Coldstream (see Fig. 4.3 for section locations; legend is the same as Fig. 4.7).

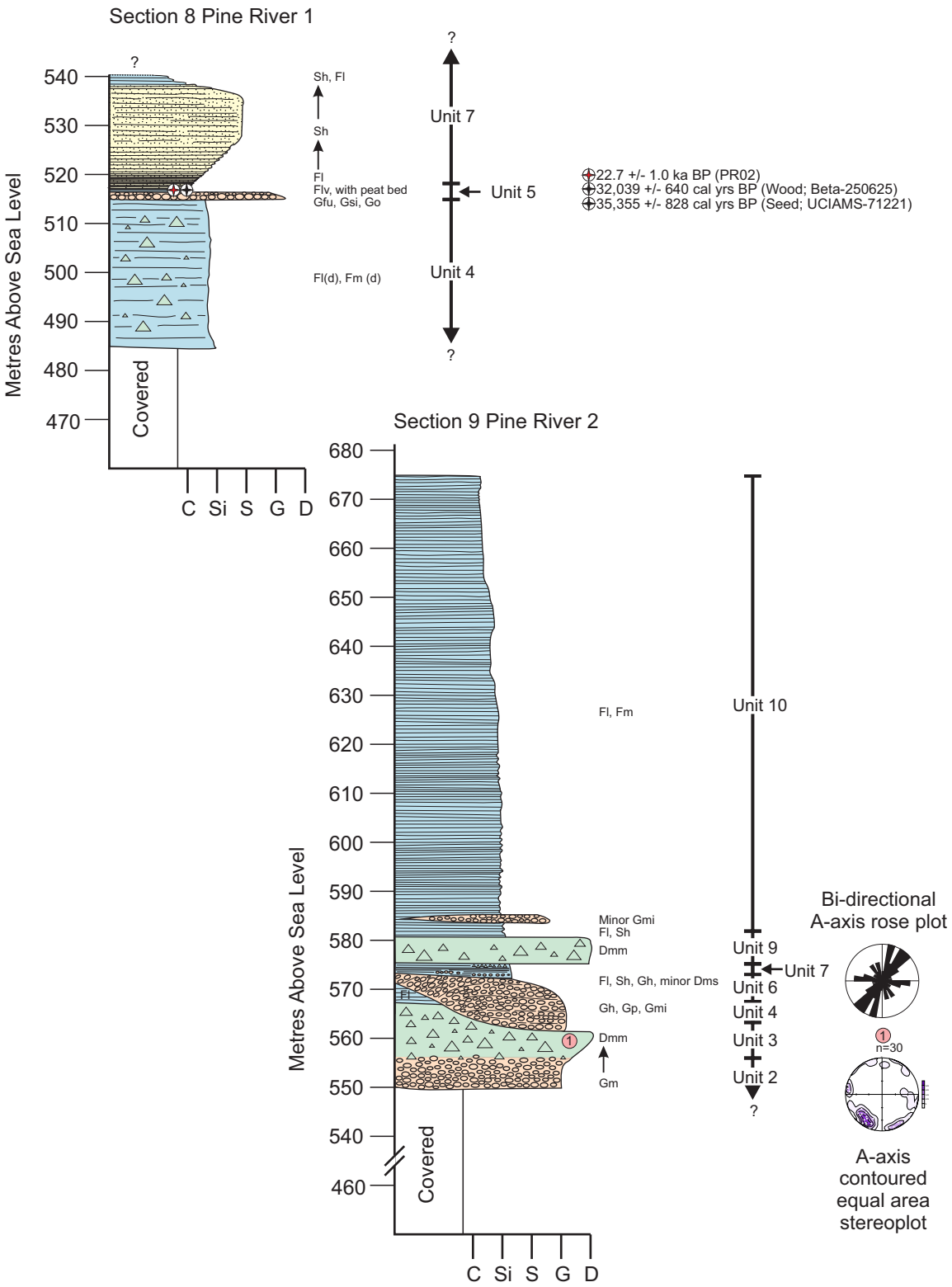

Figure 4.11. Stratigraphy of a) Section 8: Pine River 1; b) Section 9: Pine River 2 (see Fig. 4.3 for section locations; legend is the same as Fig. 4.7).

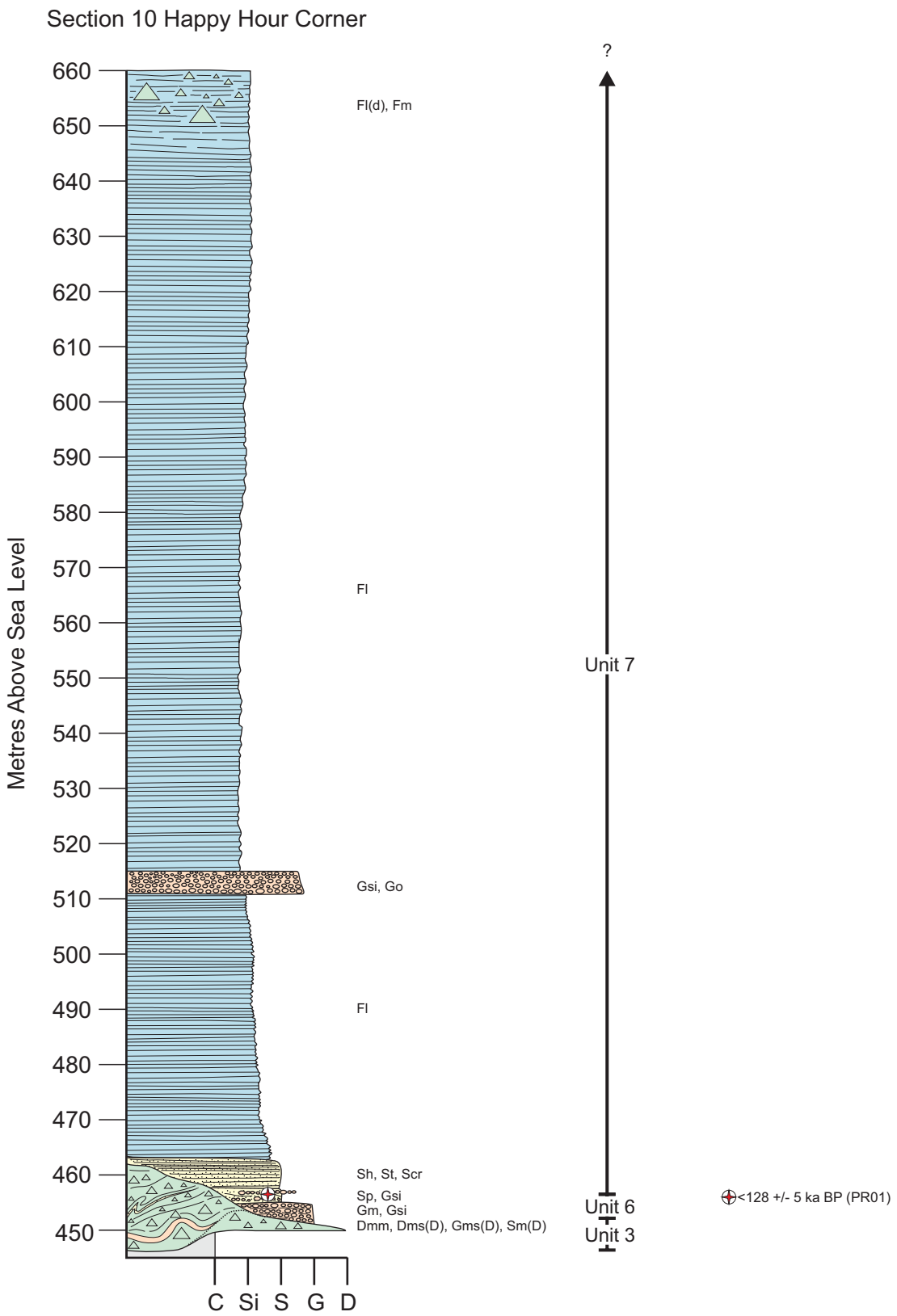

Figure 4.12. Stratigraphy of Section 10: Happy Hour Corner (see Fig. 4.3 for section locations; legend is the same as Fig. 4.7).

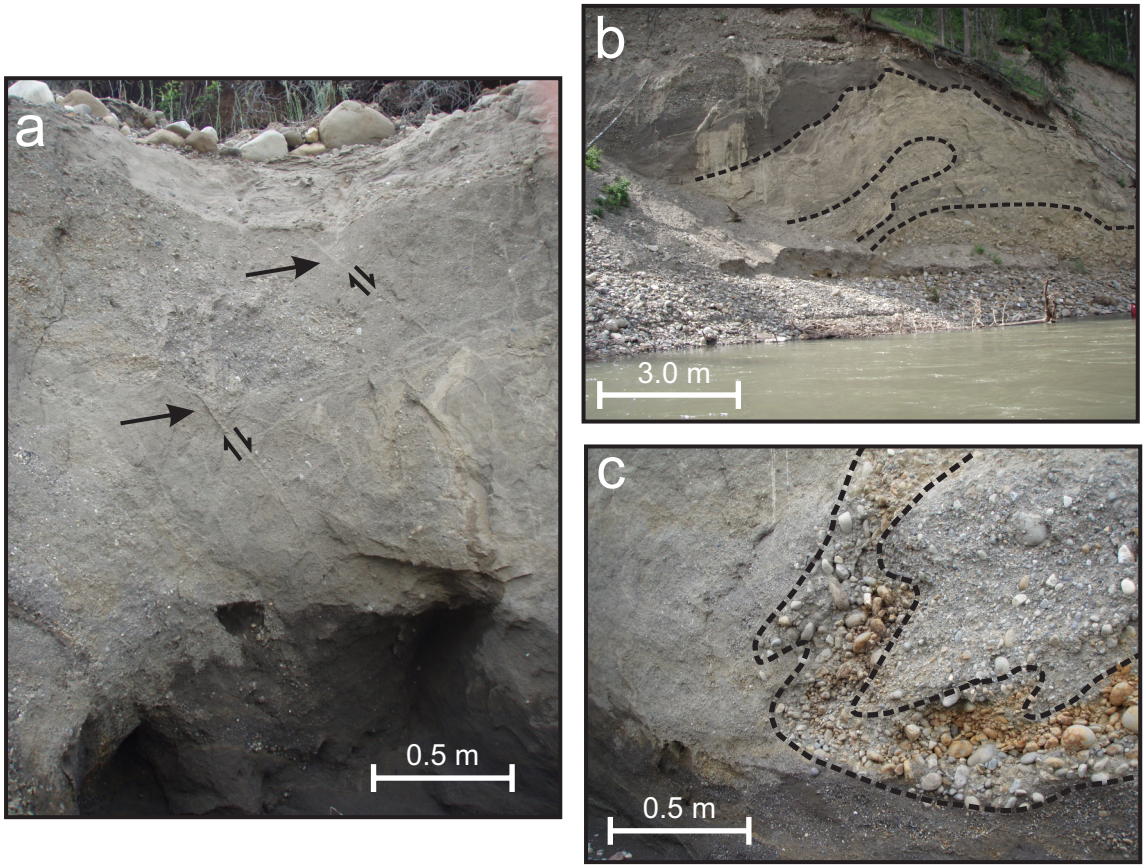

Figure 4.13. Highly deformed sand and gravel of Unit 1 is exposed at Section 2. a) Ductilely deformed sand and pebble gravel with subsequent brittle faulting; b) Large fold of laminated silt, sand and bedded sand and gravel; c) Folded cobble gravel bed.

4.4.3.2. Penultimate Glacial Event - MIS 4 (?)

4.4.3.2.1.1 Unit 2 – Description:

This unit is only recognized in Section 9 (Pine River 2) where it occurs at the base of the section and is partially covered by modern colluvium (Fig. 4.14a). The unit is > 5 m thick and is poorly sorted and massive to weakly horizontally stratified. The unit is pebble to cobble-sized gravel and as a unit, matrix content increases upwards from clast-supported to matrix-supported. Poorly developed beds are 1-2 m thick and are distinguished by subtle variation in modal clast-size. Clasts are sub- to well-rounded and many are striated and facetted. Clasts are of western provenance (sedimentary, no shield clasts) and consist of a mix of local lithologies (mainly Cretaceous) and Paleozoic(?) sedimentary rocks (quartzite and siliceous mudstones) likely from the main ranges of Rocky Mountains. Low-grade metamorphic clasts were not noted. The lower contact is covered and the unit grades conformably upward into Unit 3 (Fig. 4.14b).

4.4.3.2.1.2 Unit 2 – Interpretation: Advance-Phase Glaciofluvial

The unit likely has an alluvial origin, though poor sorting and massive to weak horizontal stratification implies textural immaturity. The presence of abundant striated and facetted clasts, the general stratigraphic position, and a conformable transition to diamict in unit 3b (interpreted to be till; see below) suggests a glaciogenic origin. The unit is interpreted to have been deposited initially in a distal glaciofluvial environment. The gradational transition from clast supported to a matrix supported gravel and the conformable contact with the overlying diamict implies an ice advance setting and transition is interpreted to reflect the proximity of the approaching glacier (Miall, 2006; Eyles and Eyles, 2010).

4.4.3.2.2.1 Unit 3 – Description:

Unit three consists of diamict deposits that can be assigned to two sub-units. Both sub-units contain abundant facetted and striated clasts. No shield lithologies of eastern provenance are present in either sub-unit.

Sub-unit 3a, present at sections 6 (Serpents Head) and 10 (Happy Hour Corner), has a maximum thickness of ~10 m but thins to <1 m at the south end of Section 6. The unit consists of massive to weakly stratified diamict with abundant sand and gravel lenses. Deformation is

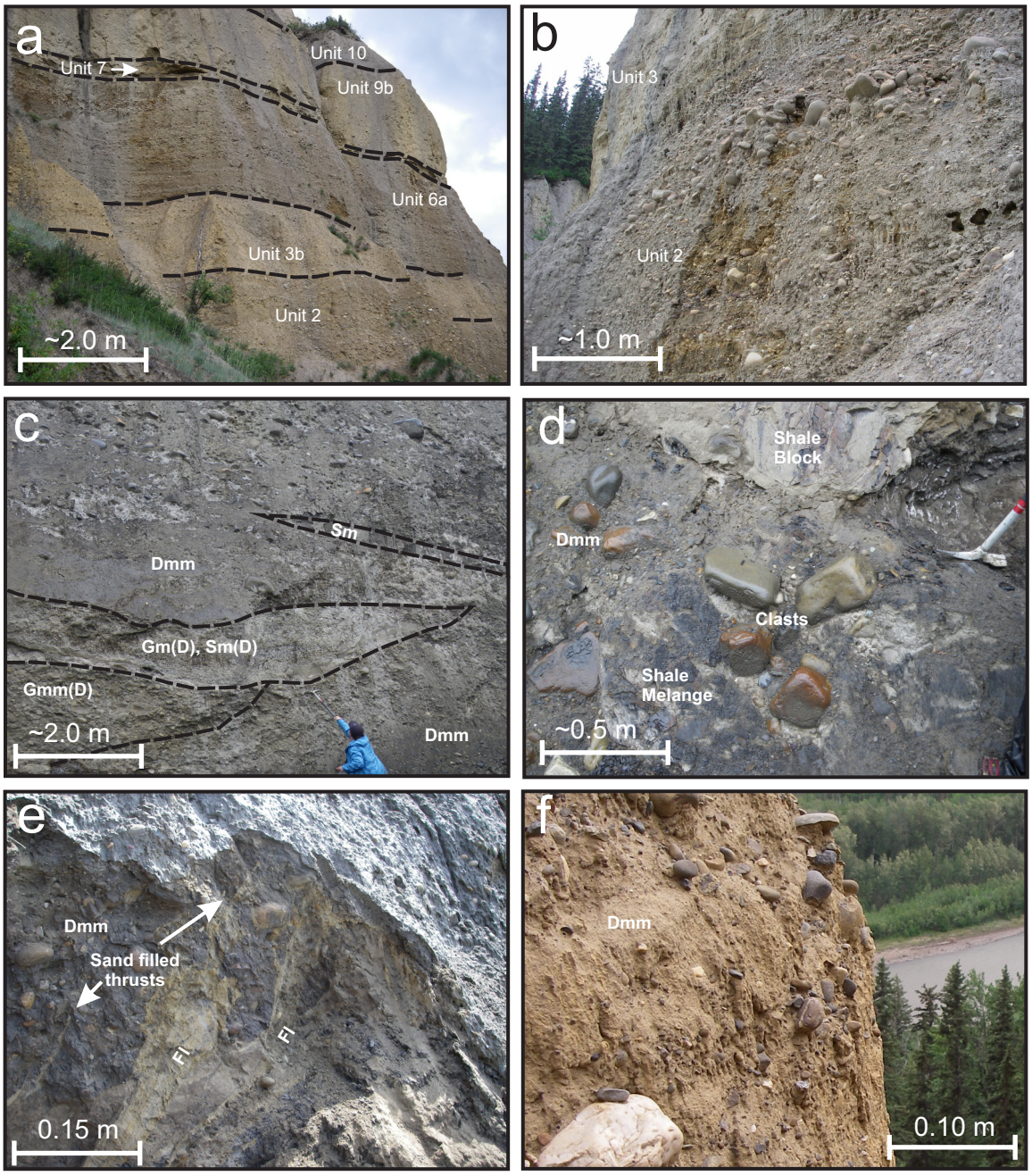

Figure 4.14. a) Lower stratigraphy of Section 9; b) Unit 2 gravel conformably overlain by Unit 3 diamict (Section 9); c) Glaciotectonized rafts of sand, gravel and diamict preserved in Unit 3a at the base of Section 10; d) Mélange of facetted and striated clasts mixed with shale blocks from the lower contact of Unit 3a (Section 10); e) Sandy flame structures that originate at bedrock and terminate as sand filled thrusts from the contact between bedrock and Unit 3a (Section 6); f) Massive diamict typical of Unit 3b (Section 6). See Fig. 4.7 for legend.

common with significant folding but also thrust faults (Fig. 4.14c). Diamict in this sub-unit is matrix supported, dense and blocky with well-developed fissility. The matrix is silt- and clay-rich. Clasts from the diamict range from pebbles to large boulders and are generally sub-rounded to well-rounded. Sedimentary rocks dominate the clasts lithologies and include a mix of local sandstone and more distantly sourced siliceous rocks from the west. Within the diamict there are large rafts of sand and gravel bodies, often deformed (Fig. 4.14c). At Section 10 this sub-unit is very dense and has large blocks and mélange of local bedrock incorporated at the lower contact (Fig. 14d). Sand beds 0.5—1.0 m thick are widespread and are typically horizontal to slightly inclined. Sand lenses 0.05—0.10 m thick are also common, often inclined up to 30° and follow inclined shear planes. Sand lenses frequently display ductile deformation resulting in flame-like structures that transition into thrusts (Fig. 4.14e). A pebble fabric from this unit at Section 6 (SH-1) plots in the glaciogenic sediment flow field of Benn's (Benn, 1994a, 1994b; Fig. 4.15a) and May's (May et al., 1980; Fig. 4.15b) discrimination diagrams. The fabric is multi-modal and plots in Hicock's deformation till field (Hicock et al., 1996; Fig. 4.15c). Sub-unit 3b, present at sections 5, 6, and 9, consists of massive, matrix supported diamict that has only rare, thin lenses (< 1 cm) of sand (Fig. 4.14a and 4.14f). Clasts range in size from pebbles to large boulders and include a variety of sedimentary lithologies. At Section 5, a pebble fabric (MT-1) plots in the glaciogenic sediment flow field of the Benn (4.15a) and May (Fig. 4.15b) diagrams. This fabric is multi-modal and plots in the deformation till field of the Hicock diagram (Fig. 4.15c). The fabric from this unit at Section 6 (SH-2) is spread unimodal and plots in the lodgement till field in all three of the discrimination diagrams (Fig. 4.15). At Section 9 the fabric (PR2-1) is bimodal and plots at the boundary of the glaciogenic sediment flow field in the May diagram (Fig. 4.15b) and the lodgement till fields in the Benn (Fig. 4.15b) and Hicock (Fig. 4.15c) diagrams.

4.4.3.2.2.2 Unit 3 – Interpretation: Glacial Complex

The striated and facetted clasts of these matrix supported diamicts suggest that these units have a glacial origin and the units are interpreted to be part of a glacial complex. Both sub-units probably have, in part, a subglacial origin. The rafts of sediment within Unit 3a likely have a mixed genetic origin (i.e. alluvium and colluvium) and have likely been incorporated in the

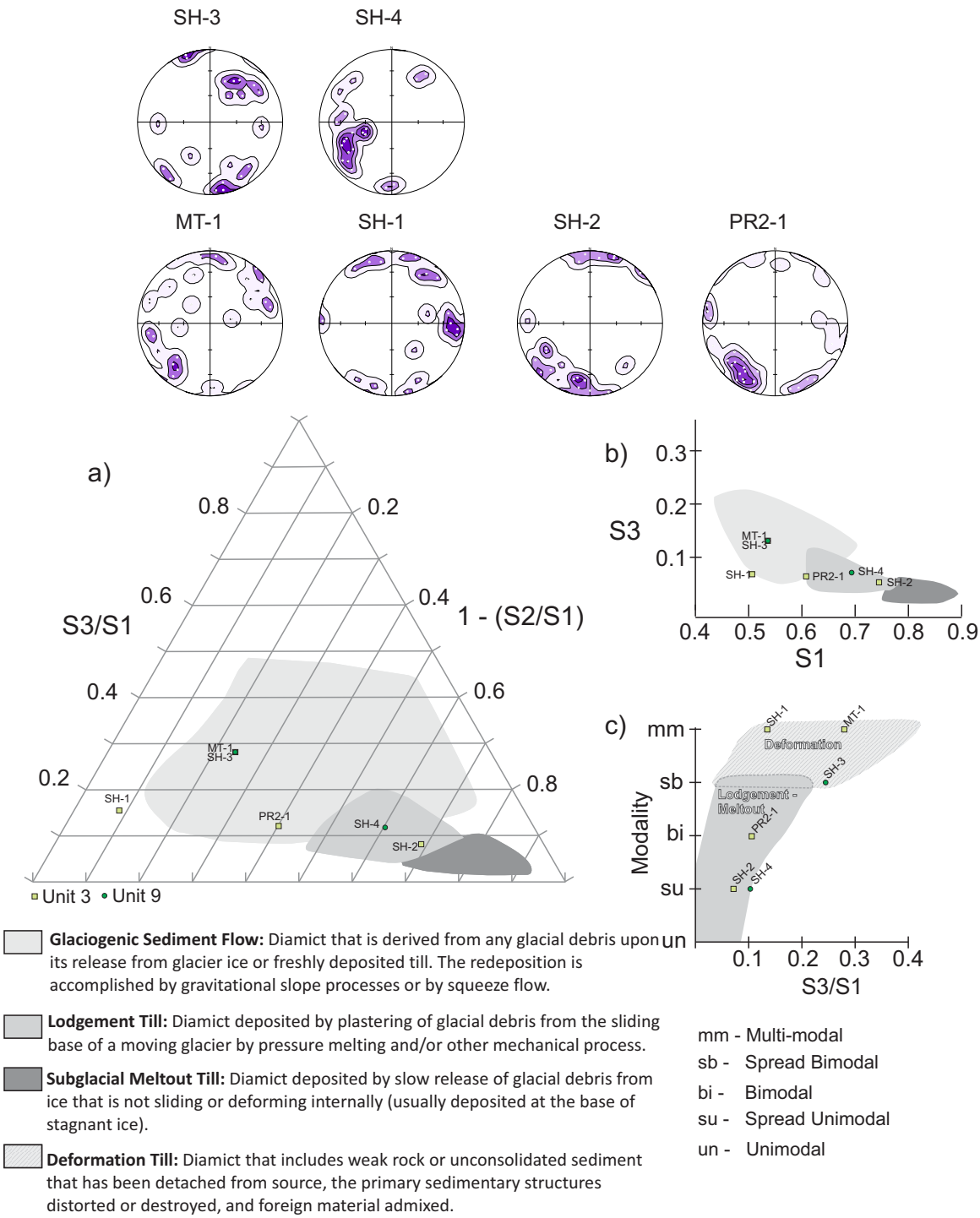

Figure 4.15. Till genetic discrimination plots, based on clast macro fabrics (top of page), from sections in the Pine and Murray river valleys (MT = Murray Terrace, Section 5; PR2 = Pine River 2, Section 9; SH = Serpents Head, Section 6. a) Benn Diagram; b) May Diagram; and c) Hicock's Modality Diagram. Diamict definitions based on Hicock et al. (1996) and Dreimanis (1989).

diamict by glaciotectonic processes (Occhietti, 1973; Aber and Ber, 2007). The pebble fabric classification from unit 3a implies it was deposited as a glaciogenic sediment flow or deformation till (see Fig. 4.15 for definitions). Although the diamict of unit 3a is interpreted to have a glacial origin it may have been significantly modified by other processes (i.e. gravitational) and consequently may not be primary till as defined by Dreimanis (1988). The massive diamict of Unit 3b is, however, likely primary till (Dreimanis, 1988). Although the pebble fabric data is not conclusive, it does suggest unit 3b has a subglacial origin, and is possibly lodgement till. Regardless of the specific genetic origin of these glacial deposits, the sediments of Unit 3 are interpreted to be associated with a major glacier in the valley and therefore represent the penultimate or older glacial climatostratigraphic interval.

4.4.3.2.3.1 Unit 4 – Description:

This unit is only present in sections 8 (Pine River 1) and 9 (Pine River 2). In Section 8 the unit is represented by 30 m of massive to laminated fine-sand, silt and clay with abundant, isolated, pebble sized clasts. The lower contact is covered and much of the unit is poorly exposed because of surface slumping. At Section 9, the unit is as thick as 4 m but thins, or is absent towards the north end of the section; a result of erosion (unconformity). At Section 9, the unit consists of blocky, well-laminated silt and sand with no clasts. The lower contact is sharp.

4.4.3.2.3.2 Unit 4 – Interpretation: Retreat-Phase Glaciolacustrine

The fine-grained nature and laminations in the unit imply deposition mainly from suspension. The clasts are interpreted to be dropstones, deposited as rain-out from melting ice bergs. The unit is interpreted to have been deposited in a glaciolacustrine setting. As the unit lies stratigraphically above the glacial sediments of unit 3, this unit is interpreted to be related to the retreat phase of the penultimate or older glacial interval.

4.4.3.3 Middle Wisconsinan Event - MIS 3

4.4.3.3.1.1 Unit 5 – Description:

Unit 5 is present at Section 7 (Coldstream) and 8 (Pine River 1). At Section 7, Unit 5 has a maximum thickness of 3 m but is laterally discontinuous. It occurs as a heavily oxidized, partially

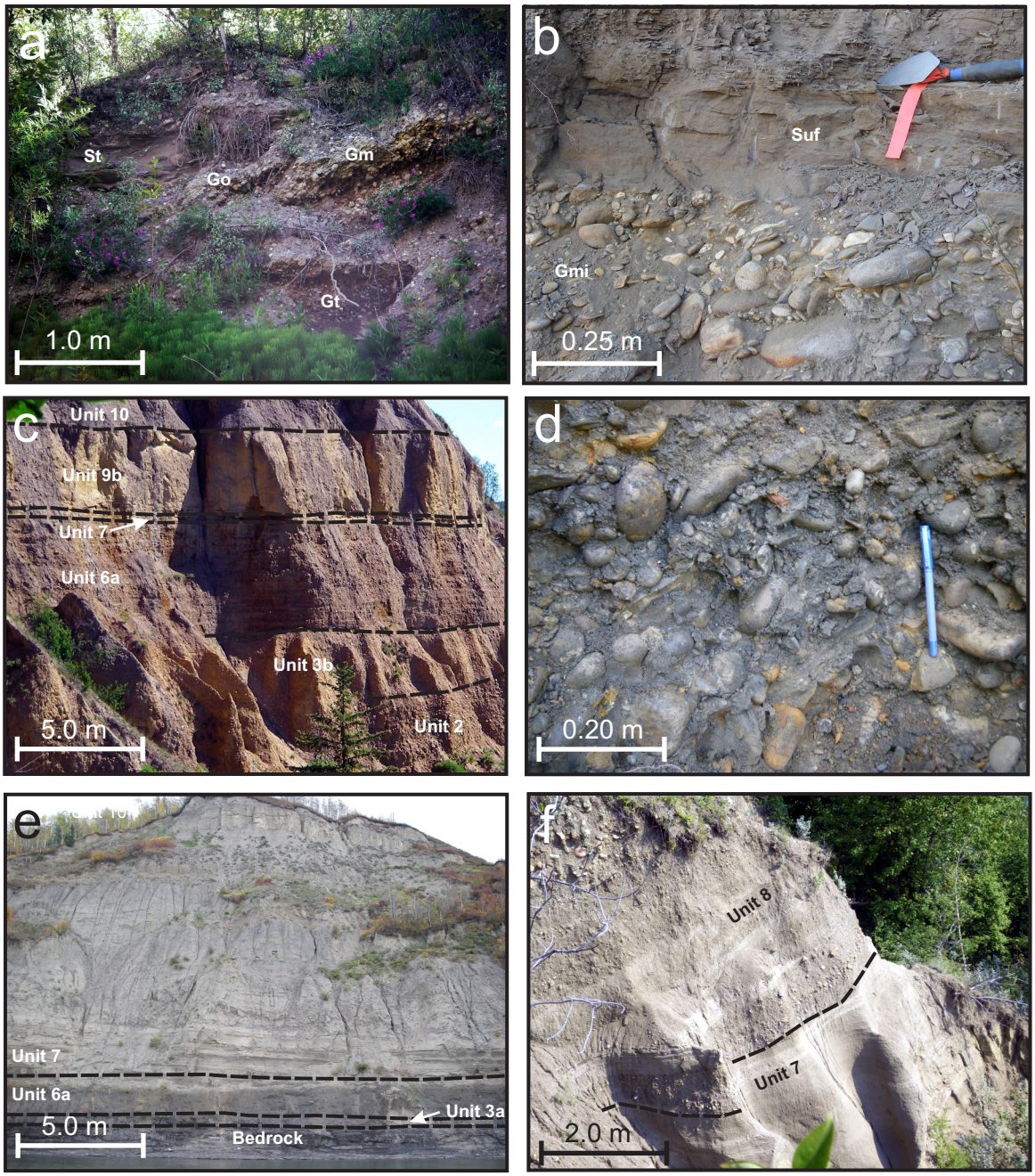

Figure 4.16. a) Sand and gravel lenses in Unit 5 (Section 7); b) Non-glacial, imbricated gravel overlain by fining-upward sand to silt and clay of Unit 5 (Section 8); c) Upper stratigraphy of Section 9; d) Poorly-sorted pebble to cobble gravel of unit 6 (Section 7); e) Stratigraphy at the base of Section 10; f) Advance-phase glaciolacustrine sediments (Unit 7; glacial Lake Mathews) overlain by intercalated subaqueous debris assigned to Unit 8 (Section 4). See Fig. 4.7 for legend.

cemented, massive to trough crossed-stratified (troughs 1-2 m wide and 0.5-1.0 m thick), open and closed-framework sand and poorly-sorted pebble to cobble gravel (Fig. 4.16a). Clasts, of a variety of sedimentary lithologies, are well rounded and are not striated. No shield clasts were noted. The lower contact is sharp and erosional over bedrock. At Section 8, Unit 5 consists of massive to imbricated, clast-supported, moderately-sorted, cobble-sized gravel overlain by fining-upward, laminated sand, silt and clay capped by a thin (0.5 cm) organic horizon (Fig. 4.16b). Clasts are well rounded and typically tabular and matrix is medium sand. Lithologies are sedimentary and typically siliceous and durable. No shield clasts were observed in this unit. The sand and silt that conformably overlies the gravel is horizontally laminated with major partings decreasing in thickness upwards from 4 cm to mm scale. The top of this unit is marked by a 0.5 cm thick organic horizon that contains plant fossils (Fig. 4.2).

4.4.3.3.1.2 Unit 5 – Interpretation: Fluvial

These deposits are alluvial and the absence of faceted and striated clasts suggests a non-glacial origin. The 1-2 m wide gravel and sand trough crossed beds at Section 7 imply a bedload dominated system and were likely deposited in a gravel-bed braided river with limited channel depth (Miall, 2006). The imbricated gravel overlain by fining upward sand and silt at Section 8 is suggestive of a gravel bar overlain by overbank deposits capped by organics within a floodplain (Miall, 2006). Luminescence and radiocarbon dating confirm that Unit 5 at Section 8 was deposited in the Mid-Wisconsinan (MIS 3; see Chronology Section).

4.4.3.4 Late Wisconsinan Glacial Event - MIS 2

4.3.4.1.1 Unit 6 – Description:

Two sub-units are assigned to Unit 6, both of which do not host eastern provenance clasts. Unit 6 is present in all sections except sections 1 (Tumbler Ridge), 3 (Salt Creek), 6 (Serpents Head) and 8 (Pine River 1). Unit 6a has a maximum thickness of 12 m and consists mainly of oxidized, massive to subhorizontally-stratified, imbricated, moderate to poorly-sorted, clast-supported, gravel with rare planar cross-bedding and minor subhorizontal sand beds (Fig. 4.16c). Matrix is coarse to medium sand. Major architectural elements are generally recognizable and are dominated by sheeted gravel deposits. The lower contact is erosional. Unit 6b has a maximum thickness of 6 m but laterally pinches and swells. It is generally oxidized,

weakly imbricated, massive to poorly stratified, poorly sorted, clast-supported pebble to cobble gravel with fine sand, silt and clay matrix (Fig. 4.16d). Clasts are well-rounded and are dominated by durable siliceous lithologies many of which are facetted and striated. The lower contact is sharp and erosional.

4.4.3.4.1.2 Unit 6 – Interpretation: Advance-Phase Glaciofluvial

Sub-unit 6a is interpreted as an alluvial deposit dominated by bedload transport. The substantial thickness (up to 12 m) of stacked sheeted gravel is indicative of vertical accretion (Miall, 2006). Unit 6a is interpreted to represent an aggrading braided or wandering gravel-bed fluvial system that reflects substantial sediment supply and lack of deep channels; typical of a meltwater dominated valley glaciofluvial system (Eyles and Eyles, 2010). The clast supported gravel of Unit 6b has well-rounded, facetted and striated clasts and is interpreted to have a glaciofluvial origin. It is, however, very poorly sorted with a fine-grained matrix which implies limited sorting due to transport. Consequently this unit is interpreted to have been deposited in an ice-proximal setting.

4.4.3.4.2.1 Unit 7 – Description:

Unit 7 is present in sections 3 to 6 and 8 to 10. It ranges in thickness from < 1m in the south of the study area to a maximum thickness of more than 200 m at Section 10 (Happy Hour Corner) in the north of the study area (towards the Peace River Valley). In the Murray River Valley, this unit tends to form vertical cliffs and is mainly horizontally bedded uniform medium sand without dropstones (Fig. 4.16e). The unit typically coarsens-up, commonly grading into gravel or diamict of overlying units (Fig. 4.16f). Beds are 1-3 metres thick, lenticular, and may extend for tens of metres laterally. The lower contact is conformable and gradational over approximately 1 m. In general, Unit 7 is finer grained in the Pine River Valley. It is best exposed at Section 10 (Happy Hour Corner) where the unit fines-up from horizontally laminated sand to laminated silt and sand (a 2-4 m thick gravel bed occurs at ~515 m asl). The unit continues to fine upward to laminated silt and clay to about 550 m asl at which point it begins to coarsen upward (laminated silt and sand). Towards the top of the section, dropstones and thin intercalated lenses of diamict (0.1-0.4 m thick) with shield clasts become common. At Sections 5 and 6, this unit is pervasively deformed showing both folding and faulting.

4.4.3.4.2.2 Unit 7 – Interpretation: Advance-Phase Glaciolacustrine (Glacial Lake Mathews)

This unit is dominantly horizontally laminated sand and fine-grained sediment that was likely deposited from suspension and is interpreted to be a glaciolacustrine deposit. The sandy component of the deposit typically occurs in the Murray River Valley and may represent sedimentation closer to the sediment supply from the mountains. The unit grades upwards into gravel or diamict of overlying units, which may represent the increased influence of the advancing ice. At the section 10, the unit fines upwards, perhaps representing the initial formation of the lake and its progressive deepening. The unit then coarsens upwards, culminating in abundant dropstones and thin diamict beds, suggesting that an advancing glacier is influencing sediment supply and depositional processes. This unit is interpreted to be the Late Wisconsinan advance-phase proglacial lake, referred to as glacial Lake Mathews in this area (Hartman and Clague, 2008).

4.4.3.4.3.1 Unit 8 – Description:

This unit occurs along the Murray River at sections 4 to 6 and consists of two sub-units. Clasts in both sub-units are of a western provenance and no shield clasts were noted. Unit 8a is 4—6 m thick and consists of low angle to subhorizontally-stratified, pebble to cobble-sized poorly sorted gravel with minor sand interbeds (Figs. 4.17a, b, c). In-places, it is an open framework though typically the unit has a coarse to fine sand matrix. Major beds are 1-3 m thick and are typically massive; however, where they transition to sand, they are normal graded. Clasts are typically, flat-lying to slightly imbricated. The unit is poorly sorted, dominantly clast-supported, with minor, matrix-support beds. Clasts are a mix of well-rounded to angular fragments. Many tabular clasts are local sandstone, but well rounded quartzite and siliceous mudstone clasts are common. The lower contact is gradational over 5-10 m, often intercalated with unit 7 (Fig. 4.16f). The unit has a sharp, conformable upper contact and is everywhere overlain by Unit 9. Unit 8b is 2—4 m thick and consists of massive to weakly normally graded, clast-supported pebble to boulder-sized diamict (Fig. 4.17d). Clasts are angular to sub-rounded and consist of a variety of lithologies. The matrix is clay, silt and sand and the lower contact is sharp and erosional.

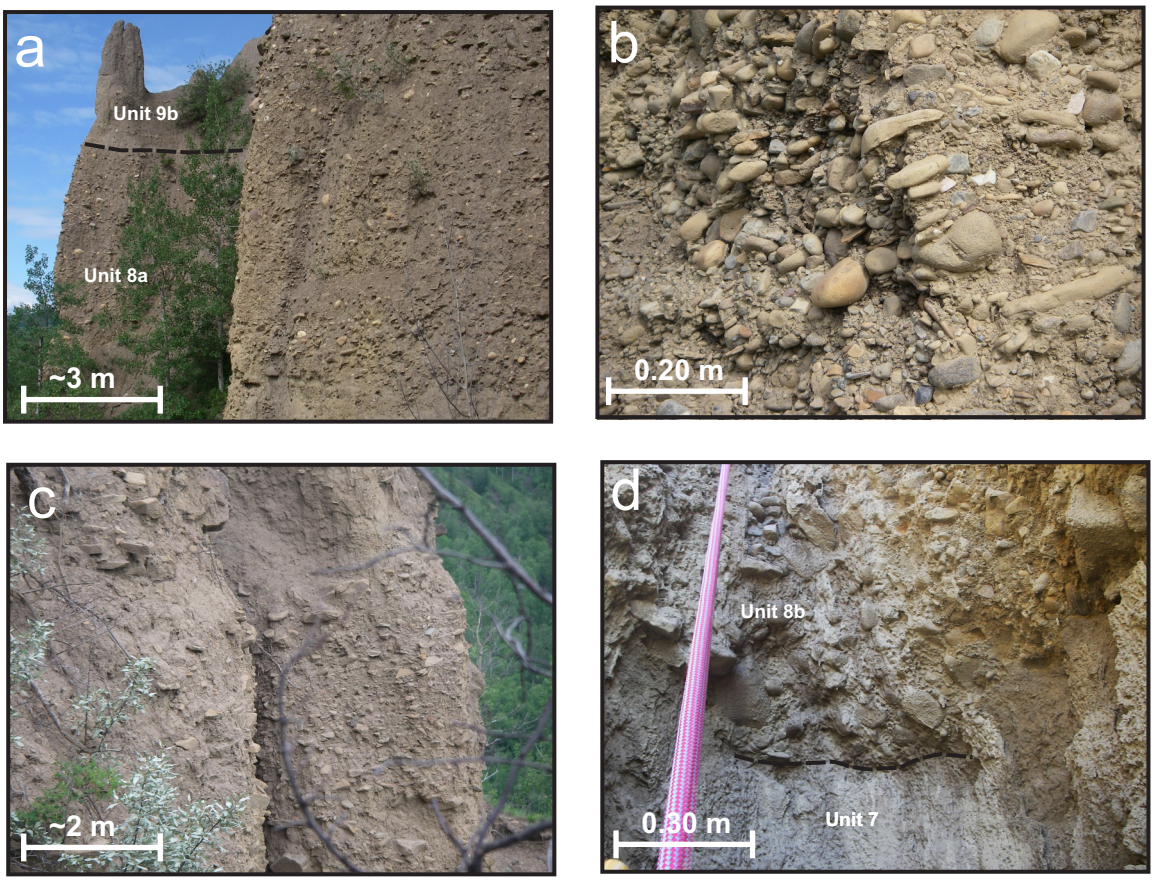

Figure 4.17. a) Clast and matrix-supported gravel (Unit 8a) interpreted to be an alluvial fan deposits overlain by massive diamict (Unit 9a; Section 5); b) Close-up of imbricated to flat-lying gravel (Unit 8a; Section 5); c) Flat-lying, clast-supported gravel interpreted to alluvial fan deposit (Unit 8a; Section 4); d) Silt (Unit 7; glacial Lake Mathews) overlain by normally graded, clast- to matrix-supported diamict interpreted to be a debris flow deposit (Unit 8b; Section 6).

4.4.3.4.3.2 Unit 8 – Interpretation: Advance-Phase Alluvial Fan/Subaqueous Fan/Debris Flow

Unit 8a consists of relatively thick beds of poorly sorted, clast-supported boulder to cobble gravel/diamicton that was probably deposited as rapidly aggrading, high energy sediment flows that are interpreted to represent sediment gravity flows or hyperconcentrated stream flows (Levson and Rutter, 2000). Unit 8a is interpreted to have been deposited as non-cohesive debris flows and likely was deposited mainly in an alluvial fan setting. The lower contact is, however, typically intercalated with Unit 7 (advance-phase glaciolacustrine), indicating a subaqueous component to this setting. The sharp erosional lower contact, large clast-size, and fine-grained matrix of unit 8b suggests these deposits may be cohesive gravity flows. Weak normal grading, and stratigraphic position and relationship with Unit 7 (advance-phase glaciolacustrine) suggest that Unit 8b may be, in part, a subaqueous deposit. Nonetheless, Unit 8 as a whole is interpreted to represent sediment gravity deposits (fans) associated with unstable valley slopes around a proglacial lake.

4.4.3.4.4.1 Unit 9 – Description:

This unit consists of two sub-units that, like unit 3, are genetically distinct but are grouped together because they belong to a continuum of genetically related deposits. There were no shield lithologies of eastern provenance identified in either of these sub-units within the Murray—Pine valley, however, the correlative unit in Section 11 (Kiskatinaw River; Fig. 4.3) contains abundant shield clasts (see below).

Unit 9a is well exposed at sections 4 (Nini Hill) and 6 (Serpents Head), occurs above Unit 8, and is stratigraphically lower than unit 9b (e.g. see Fig. 4.18a). The unit is up to 20 m thick and consists of stratified diamict, interbedded with horizontally laminated or massive sand. The diamict is poorly sorted, silt to clay-rich, and matrix supported (Fig. 4.18b). Clasts are generally sub-angular to well rounded and are commonly striated and facetted. Sand horizons range from a few mm up to more than 10 cm thick and exhibit a variety of bedforms, including subhorizontal stratification and ripples. This unit is intensely deformed at Section 6 where laminated sand, silt, diamict and pebble-gravel show recumbent, chevron, tight, and isoclinal folds that often merge into subhorizontal to low angle shear planes (Fig. 4.18c). A pebble fabric from this unit at section 6 (SH-3) plots in the glaciogenic sediment gravity flow field of the May

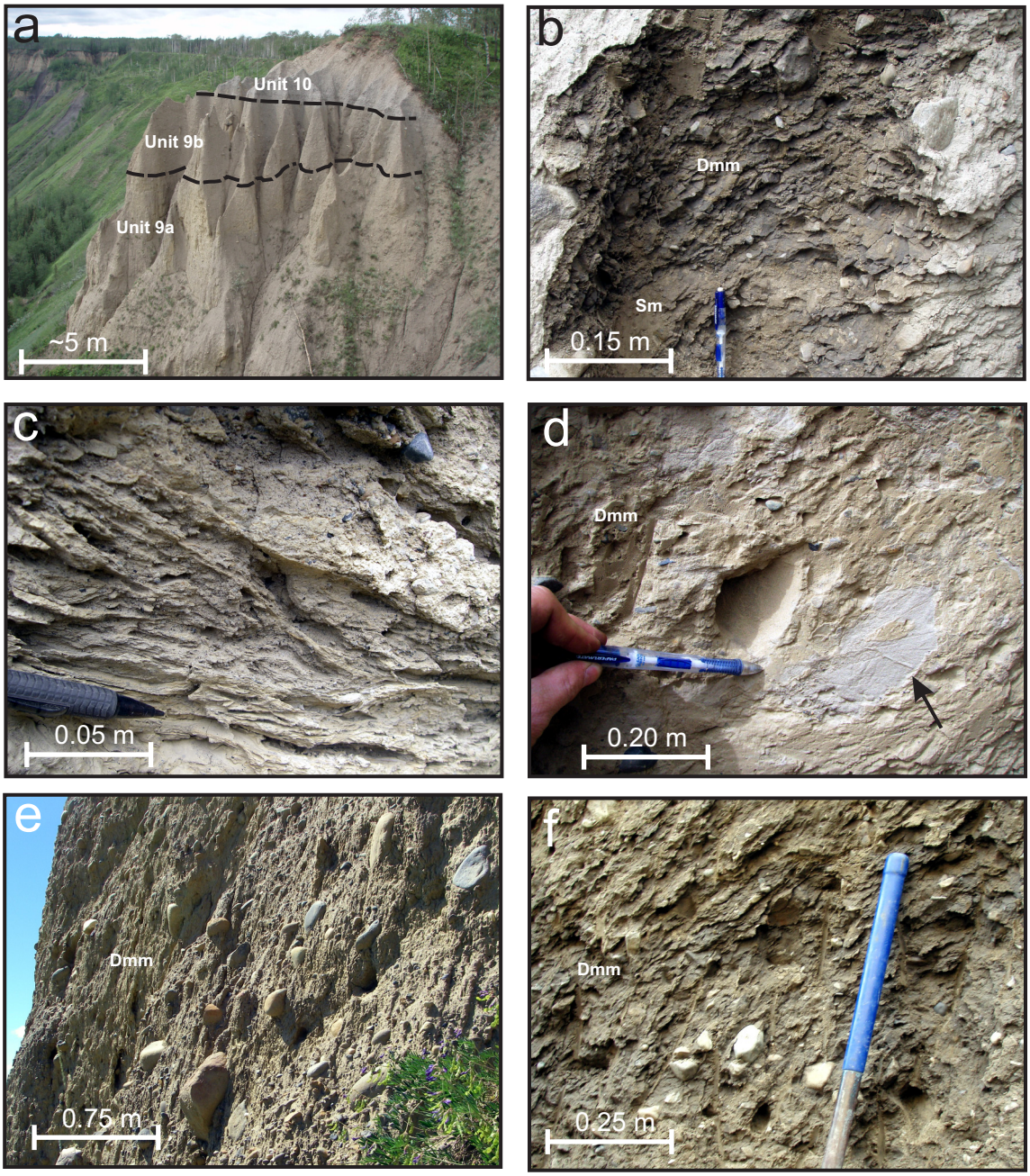

Figure 4.18. a) Upper stratigraphy of the Section 6; b) Massive diamict with minor lenses of massive sand (Unit 9a; Section 6); c) Laminated and glaciotectonically folded sand and silt (Unit 9b; Section 6); d) Fractured sand clast in bedded diamict interpreted to be waterlain till (Unit 9b; Section 6); e) Massive diamict interpreted to be till (Unit 9a; Section 9); f) Massive, fissile diamict (Unit 9a; Section 6). Dmm = Matrix-supported, massive diamict.

(Fig. 4.15a) and Benn (Fig. 4.15) diagrams. This spread bimodal fabric (Fig. 4.9b) plots in the transition between the deformation and lodgement-meltout fields of the Hicock et al. (1996) discrimination diagram (Fig. 4.15b). The lower contact of this unit is indistinct and gradational over 5-10 m and is often intercalated with unit 8. Unit 9b, the more common sub-unit, is present in sections 3—7 and Section 9. The unit is 20 m thick and consists of massive, poorly-sorted diamict that lacks sand and gravel interbeds (Fig. 4.18a). The unit generally has a silt- to clay-rich matrix with clasts that range in size from granules to boulders. Clasts are sub-angular to well-rounded, commonly striated and facetted, and are a mix of local sandstone and more remote quartzite and siliceous lithologies. No phyllitic or other low grade metamorphic clasts were noted. Well developed fissility is common. The lower contact is generally sharp and erosional at most locations but is conformable and intercalated where it overlies unit 8. A single pebble fabric from Section 6 is spread unimodal and plots in the lodgement till fields of all the discrimination plots (Fig. 4.15).

4.4.3.4.4.2 Unit 9 – Interpretation: Glacial Complex

The striated and facetted clasts in the stratified diamict of unit 9a imply a glaciogenic origin. Laminations and ripples in the silt and sand horizons demonstrate that water, both standing and flowing, has played a significant role in the genesis of this unit. The deformation at Section 6 is intense, yet the preserved folds and the presence of fragile coal and medium-grained sand clasts (Fig. 4.18d) suggest that comminution was not complete. Unit 9a is therefore interpreted to represent a waterlain glaciogenic diamict that was glaciotectonized (at least at Section 6). Unit 9b is a poorly sorted glaciogenic diamict with fissility and pebble fabric that suggests a subglacial till deposit.

4.4.3.4.5.1 Unit 10 – Description:

Unit 10 is regionally extensive and typically forms the surface unit in the Peace region below ~1000 m asl. It is present in all sections except 2, 8 and 10. Although the unit generally consists of clay, silt, and sand, grain-size varies across the region and within the succession. It ranges in thickness from a few metres to over 100 m. At the south end of the study area, the unit coarsens-up from rhythmically-laminated silt and clay to horizontally stratified and rippled sand. In the fine-grained lower part of this unit, local dewatering structures and partial and

complete turbidite sequences (Bouma) are common. Rare dropstones occur but typically are small (pebble sized). At some locations in the Murray River Valley, the upper part of the unit is sandy often with well developed Type A and Type B climbing ripples (Ashley et al., 1982). In the northern portion of the study area, Unit 10 generally fines upward. Here, the lower unit is dominantly sand with climbing ripples and some gravel, but fines upward to rhythmically-bedded silt and sand with abundant thinly-bedded diamict and common dropstones throughout. The proportion of diamict beds and dropstones decreases up section. In the northern sections, the top of unit 10 consists of clay, silt, and fine sand. Although dropstones in the top of the section are generally rare, at high- elevation outside of the paleovalleys they can be common. Shield clasts frequently occur in this unit north of Section 6.

4.4.3.4.5.1 Unit 10 – Interpretation: Retreat-Phase Glaciolacustrine (Glacial Lake Peace)

Sediment in Unit 10 has been deposited mainly from suspension settling, underflows, and turbidite currents. Diamict may also have been deposited by ice berg dumping and rain out. The unit is interpreted to represent deposition in a proglacial lake, and its stratigraphic position implies it is the retreat-phase of glacial Lake Peace (Mathews, 1980). In the southern Murray River Valley, coarsening upwards trends and a transition from suspension settling to underflow dominated sedimentation likely reflects the shallowing of the lake from regression or from the rapid progradation of deltas that developed from sediment laden meltwater as ice retreated. The fining upward trend and the decrease in diamict beds and dropstones noted north of Section 5 probably reflect retreating ice (becoming more distal up-section).

4.4.3.4.6.1 Unit 11 – Description:

Unit 11 is differentiated into two sub units, both of which consist of gravel and sand. The unit typically forms the surface unit on most terraces along the river valleys except where Unit 12 is present. Clasts of both sub-units have western sources. Unit 11a occurs in the Tumbler Ridge region and is also present at the confluence of the Murray and Pine rivers (Fig. 4.19a). The unit ranges in thickness from several metres to more than 20 m and consists of pebble to boulder gravel with interbedded sand. Clasts are moderately to well-rounded and commonly faceted. Striations are common on larger cobble to boulder clasts. The presence of large scale (2—4 m thick) planar tabular crossbeds distinguishes this unit from unit 11b (Fig. 4.19a).

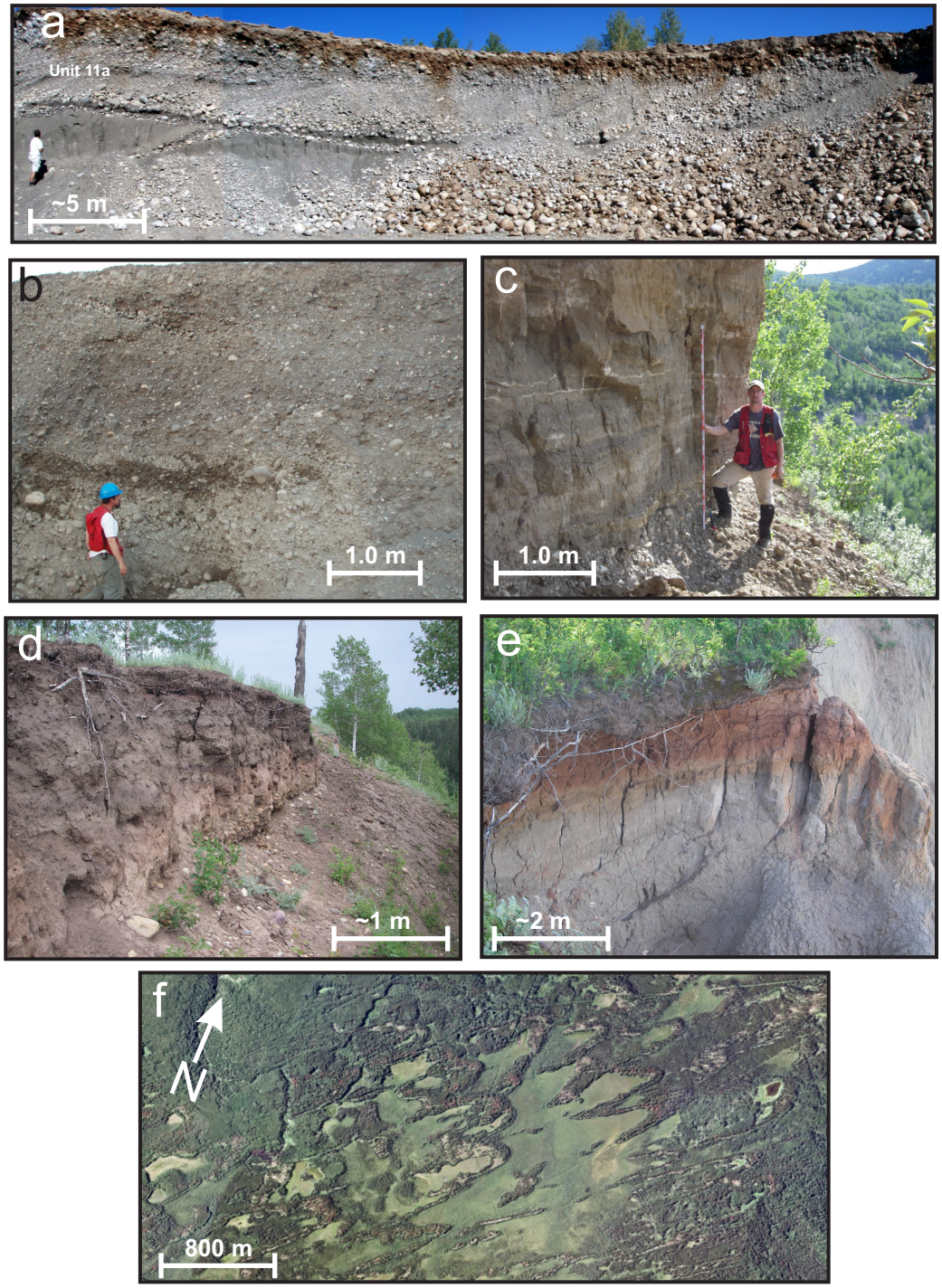

Figure 4.19. a) Deltaic forset beds at a gravel pit near the confluence of Pine and Murray rivers (Unit 11a); b) Massive to crudely stratified gravel in gravel pit southwest of Section 8 in the paleo-Pine River Valley (see Fig. 4.3); c) Thick overbank sand (and possibly loess) over gravel (Unit 11b; Section 4); d) Gravel and overbank sand (Unit 11b) overlain by loess (Unit 12; Section 5); e) Oxidized silt interpreted to be loess (Unit 12; Section 7); f) Parabolic sand dunes (Unit 12) from above Section 10 in the Septimus area (see Fig. 4.3).

Unit 11b ranges in thickness from 1—5m and consists of a succession of pebble to cobble gravel with interbedded sand, overlain by horizontally stratified silt and sand. The gravel can be massive or crudely bedded, poorly to well-sorted, has open and closed frameworks, and is poorly to well-imbricated (Fig. 4.19b). Clasts are moderately to well-rounded and facets are common. Like unit 11a, striations are generally restricted to large cobbles and boulders. In some large exposures large-scale downlapping clinoforms are recognized. Planar and trough cross-bedding is also common. At several gravel pits, crude bedding is disrupted by sand and gravel filled wedges that open upwards (ice wedge casts). The upper silt and sand portion of the unit is typically 1—2 m thick but can exceed 4 m in thickness (e.g. Section 4; Fig. 4.19c). The sand is horizontally laminated to thinly bedded.

4.4.3.4.6.2 Unit 11 – Interpretation: Retreat-Phase Glaciofluvial

The large scale planar cross strata in Unit 11a are interpreted to be foreset beds of glaciofluvial deltas that formed where high energy, sediment laden meltwater issued in to various stable phases of glacial Lake Peace. In Unit 11b, the clinoforms and cross-strata are interpreted to be architectural elements such as accretionary macroforms and bar forms (Miall, 2006) of a shallow braided or wandering gravel bed river. The fine-grained silt and sand that typically caps the gravel is interpreted to have been deposited during waning flow sedimentation (overbank deposit) on a floodplain (Miall, 2006). Unit 11b represent the terrestrial equivalent of Unit 11a and forms glaciofluvial outwash plains and terraces that developed between the retreating ice front and regressive glacial Lake Peace.

4.4.3.5 Holocene - MIS 1

4.4.3.5.1.1 Unit 12 – Description:

Unit 12 includes two sub-units and is present at sections 5 and 7. Unit 12a is 1—2 m thick and consists of massive to poorly stratified, moderately sorted silt and fine sand (Fig. 4.19d and 19e). At Section 7, unit 12a is oxidized and banded and poorly to moderately indurated. The banding does not reflect visible grain-size variation. Unit 12b is not represented in section, but is noted at several locations along terraces where Unit 12a is present. Unit 12b consist of oxidized, uniform medium sand and is associated with parabolic sand dunes (Fig. 4.19f).

4.4.3.5.1.2 Unit 12 – Interpretation: Post Glacial Aeolian

Unit 12a is generally massive and contains uniform silt to fine-sand size fractions. Where oxidation banding occurs there is no obvious grain-size variations, however, the banding may be related to groundwater exploitation of subtle grain-size variation or is pedogenic in origin. A luminescence age of 8.72 ± 0.32 ka BP was obtained from this unit (see Chronology Section). Unit 12a is interpreted as loess as defined by Muhs (2007). Unit 12b contains uniform medium sand and occurs in parabolic sand dunes and is of aeolian origin.

4.4.4 Section 11 - Kiskatinaw River

4.4.4.1 Stratigraphy

The Kiskatinaw River section is situated within the region occupied by both CIS and LIS, making it ideally located to examine the influence that each ice sheet may have imposed on the sedimentary record. Section 11 is 34 m thick (Fig. 4.20a) and consists of 30 m of diamict (Unit 9) and 4 m of glaciolacustrine sediments (Unit 10). Shield clasts are common in both units. Five pebble fabrics were measured and ten samples were collected from different elevations within the section (Fig. 4.20b). Pebble fabrics all plot in the deformation field of the till discrimination plots in the May (Fig. 4.20e; May et al, 1980) and the Benn diagrams (Fig. 4.20f; Benn 1994a, 1994b), although fabrics 3 and 4 plot close to the boundary of the lodgement field. The modality diagram (Fig. 4.20d; Hicock et al., 1996) suggests a transition from lodgement to deformation at the base of the section. Fabric 1 plots in the lodgment-deformation field (spread-bimodal) and Fabric 2 plots in the deformation field (multi-modal). The preservation of many soft coal fragments in this unit at the site of Fabric 2 further suggest limited strain during deposition as these clasts would not have survived otherwise. Fabrics 3 and 4 also plot in the transition envelope and are spread bimodal. At the site of Fabric 3 the dominant alignment of the long axis of the clasts is northern, whereas alignment in Fabric 4 is northeast. Fabric 5 plots in the deformation field and is multi-modal.

Clast content (2-100 mm fraction) has a strongly increasing trend from < 10% at the base of the section up to >30% at the top of the section (Fig. 4.20c). Matrix texture also has an increasing trend in the sand size fraction from 25% at the base to 36% at the top of the section. There is a marked change in the proportion of shield clasts from the lowest sample (15.6 % at Kisk-766) to the other samples which have proportions that range from 0.2—1.1%.

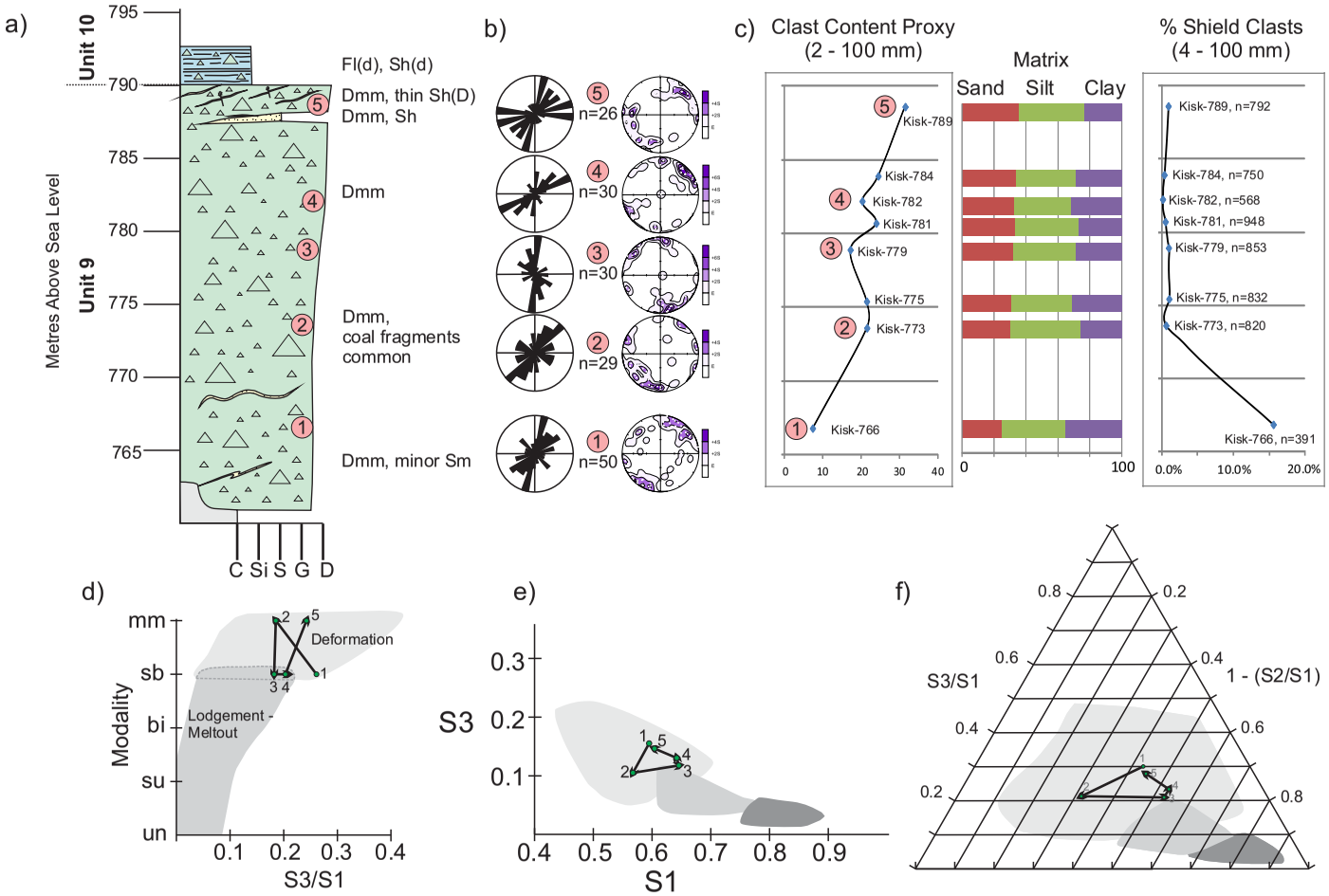

Figure 4.20. a) Stratigraphy of the Section 11, Kiskatinaw River (see Fig. 4.3 for section location); b) clast macrofabrics (numbers correspond to locations and elevations axis in 20a); c) Clast content proxy, matrix grain-size composition, and proportion of shield clasts (elevations axis same as 20a); d) Hicock modality till classification diagram (numbers refer to locations and elevations in 20a); e) May till classification diagram; f) Benn till classification diagram.

4.4.4.2 Major Oxide Geochemistry

There are several trends in the major oxide composition from the bottom to the top of Section 11 (Fig. 4.21a). There is a generally increasing up-section trend in SiO_2, Al_2O_3, Fe_2O_3, Na_2O, and TiO_2. There is however a slight deviation in the slope of the trend for SiO_2, Al_2O_3, Fe_2O_3, and TiO_2 in the top two samples (S2 and Kisk-789). There is a general decreasing up-section trend in MgO, CaO, K_2O, and P_2O_5. There is a significant composition deviation in sample Kisk-773 (i.e. SiO_2, Al_2O_3, Fe_2O_3, MgO, Na_2O, K_2O, P_2O_5).

There are consistent trends when the Section 11 samples are depicted in bivariate plots using the same classification field established for the matrix geochemical plots (Figs. 4.21b—g). All samples from Section 11 plot in the Laurentide and/or in the overlap fields and generally show an up-section trend from the Laurentide field towards the overlap field in the direction of the Cordilleran fields. Sample Kisk-773, however, plots farthest towards the Cordilleran field. Silica content remains the most significant control on the displacement of each sample towards the Cordilleran field. An up-section trend is poorly developed in Al_2O_3 and Fe_2O_3 (Fig. 4.21b and 4.21c). There is a well developed decreasing trend in MgO, CaO and K_2O from the bottom of the section to the top (Figs. 4.21d, e, and g). Na_2O has an increasing up-section trend that is directed away from all three discrimination field, an unexplained trend that is inconsistent with those of the other major oxides.

4.4.5 Chronology

Two radiocarbon ages and four optical ages were obtained to temporally anchor the stratigraphy (Table 4.1). The radiocarbon samples were both collected from the same horizon at Section 8. One sample consisted of a flattened piece of wood that yielded an accelerator mass spectrometry (AMS) radiocarbon age of 27 760 ± 230 BP (Beta-250625) calibrated to 32 039 ± 640 cal yrs BP (Bronk Ramsey, 2001). The other sample, Potentillo anserine achenes, yielded an older age of 30 380 ± 300 BP (UCIAMS-71221), calibrated to 35 355 ± 828 cal yrs BP. The ~3000 year discrepancy between the radiocarbon ages suggests that the organic horizon probably consist of reworked material. Alternatively, inconsistent ages result from differences in methodology and techniques used by the two laboratories (Scott et al., 1998).

Luminescence ages were determined for four quartz samples, collected from four separate horizons (Table 4.1). Environmental dose rate was determined from laboratory analysis

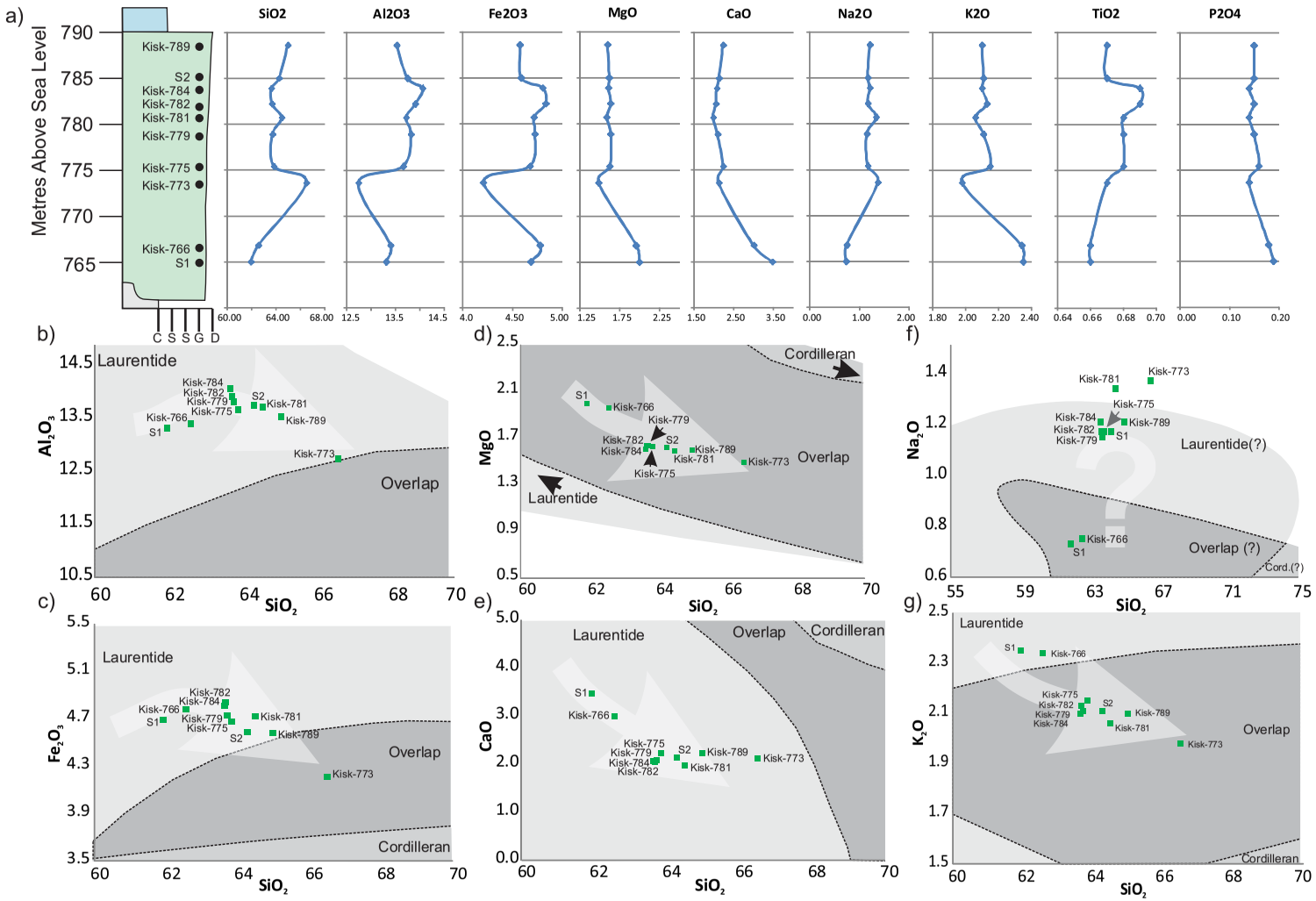

Figure 4.21. Major oxides geochemical trends from diamict matrix samples from Section 11. a) Major oxides in profile; b) Al_2O_3 verses SiO_2; c) Fe_2O_3 verses SiO_2 d) MgO versus SiO_2; e) CaO versus SiO_2; f) Na2O versus SiO_2; K_2O versus SiO_2. Empirical discrimination fields are the same as those determined in Fig. 4.6.

Table 4.1. Age dates from radiocarbon and OSL samples.

Sample	Lab Number	Material Dated	Section/ Unit	Method	^{14}C age BP	^{14}C cal yrs BP[1]
080929-03a	Beta-250625	wood	8/5	AMS ^{14}C	27 760 ± 230	32 039 ± 640
080929-03b	UCIAMS-71221	*Potentillo anserine* achenes	8/5	AMS ^{14}C	30 380 ± 300	35 355 ± 828
						Age (ka BP)
PR01	-	Quartz Sand	10/6	OSL - CAM	-	157 ± 9
				OSL - MAM	-	128 ± 5
PR02	-	Quartz Sand	8/5	OSL - CAM	-	22.7 ± 1.0
CS02	-	Quartz Sand	7/12	OSL - CAM	-	8.7 ± 0.32
CS03	-	Quartz Sand	7/10	OSL - MAM	-	112 ± 25

[1]Calibration based on OxCal 4.2 (Bronk Ramsey, 2001)

of the K, U, and Th from a representative subsample of that used for dating (Table 4.2). Parameters used for calculating the optical ages are summarized in Table 4.3. Most aliquots provided adequate luminescence and typical luminescence intensity vs. stimulation time (shine-down) curves show a significant fast component indicating that the desired thermally-stable component of luminescence signal was being measured (Fig. 4.22). Overdispersion in samples CS02 and PR02 is 12.5 ± 1.8 % and 12.0 ± 2.3 %, respectively indicating the central age model (CAM) is appropriate. Analysis returned ages of 8.7 ± 0.32 ka (CS02) and 22.7 ± 1.0 ka (PR02). Sample PR01 has an overdispersion of 26.1 ± 3.8 % which is at the threshold for applying either the CAM or the minimum age model (MAM) when its analytical uncertainty is considered. The CAM returned an age of 157 ± 9 ka whereas the age established from the MAM is 128 ± 5 ka. Consequently, it is only possible to state that sediment from sample PR01 was deposited during or after MIS 6 (based on time scale by Cohen and Gibbard, 2011). The natural luminescence measured from many of the aliquots from sample CS03 were close to saturation, so only 34 of 58 aliquots prepared were accepted. This, together with an overdispersion value of 30.5 ± 4.3 %, suggests that a significant proportion of grains were not exposed to sufficient sunlight to reset the “luminescence clock” prior to burial. The MAM age for this sample was 112 ± 25 ka, which implies that sediment sampled from PR01 was deposited during or after MIS 5 (based on time scale by Cohen and Gibbard, 2011).

The discrepancy between the luminescence age from PR02 and the radiocarbon ages from the same horizon is significant (>9 ka). It is possible that the radiocarbon ages are older than the deposition of the sediments and the organics are from reworked detritus that was transported and emplaced during deposition of Unit 5. If the ~3000 year difference between the two calibrated radiocarbon dates is valid then they support a detrital origin. Alternatively, the optical ages may be too young, which is possible if the unstable components of the luminescence signal (medium and slow components of the shine down curve) were inadvertently sampled. Additional radiocarbon sampling and analysis accompanied by further luminescence experiments (perhaps using feldspar) may elucidate these discrepancies. Nonetheless, both methods returned ages consistent with deposition during MIS 3 so we can be relatively confident that Unit 5 was deposited during the latter part of Mid-Wisconsinan.

Table 4.2. K, U and Th concentration determined by neutron activation analysis

Sample	K(%)	U ($\mu g \cdot g^{-1}$)	Th ($\mu g \cdot g^{-1}$)
PRO1	0.94 ± 0.06	1.93 ± 0.12	4.10 ± 0.14
PRO2	1.61 ± 0.08	2.93 ± 0.16	7.2 ± 0.23
CSO2	1.26 ± 0.06	2.74 ± 0.16	9.40 ± 0.29
CSO3	0.65 ± 0.04	1.57 ± 0.10	3.20 ± 0.11

Table 4.3. Sample depth below the ground surface (d), equivalent dose (De), cosmic-ray dose rate (Dc), total dose rate (DT), Overdispersion, and apparent optical age.

Sample	*d* (cm)	D_e (Gy)	D_c (Gy·ka^{-1})	D_T (Gy·ka^{-1})	Overdispersion (%)	Optical age (ka)
PRO1	20000	254 ± 12 207 ± 3[1]	negligible	1.62 ± 0.10	26.1 ± 3.8	157 ± 9 128 ± 5[1]
PRO2	1500	61.2 ± 1.7	0.0310	2.69 ± 1.70	12.0 ± 2.3	22.7 ± 1.0
CSO2	130	22.4 ± 0.5	0.168	2.57 ± 0.15	12.5 ± 1.8	8.7 ± 0.3
CSO3	8700	132 ± 29[1]	negligible	1.18 ± 0.07	30.5 ± 4.3	112 ± 25[1]

[1] using MAM; all others using CAM

Notes: uncertainties are analytical only, and are reported as ±1 standard deviation. An uncertainty was added to the "as-collected" water content values (±10%) for the dose rate calculation and is intended to account for any reasonable variation of the water content over the burial time.

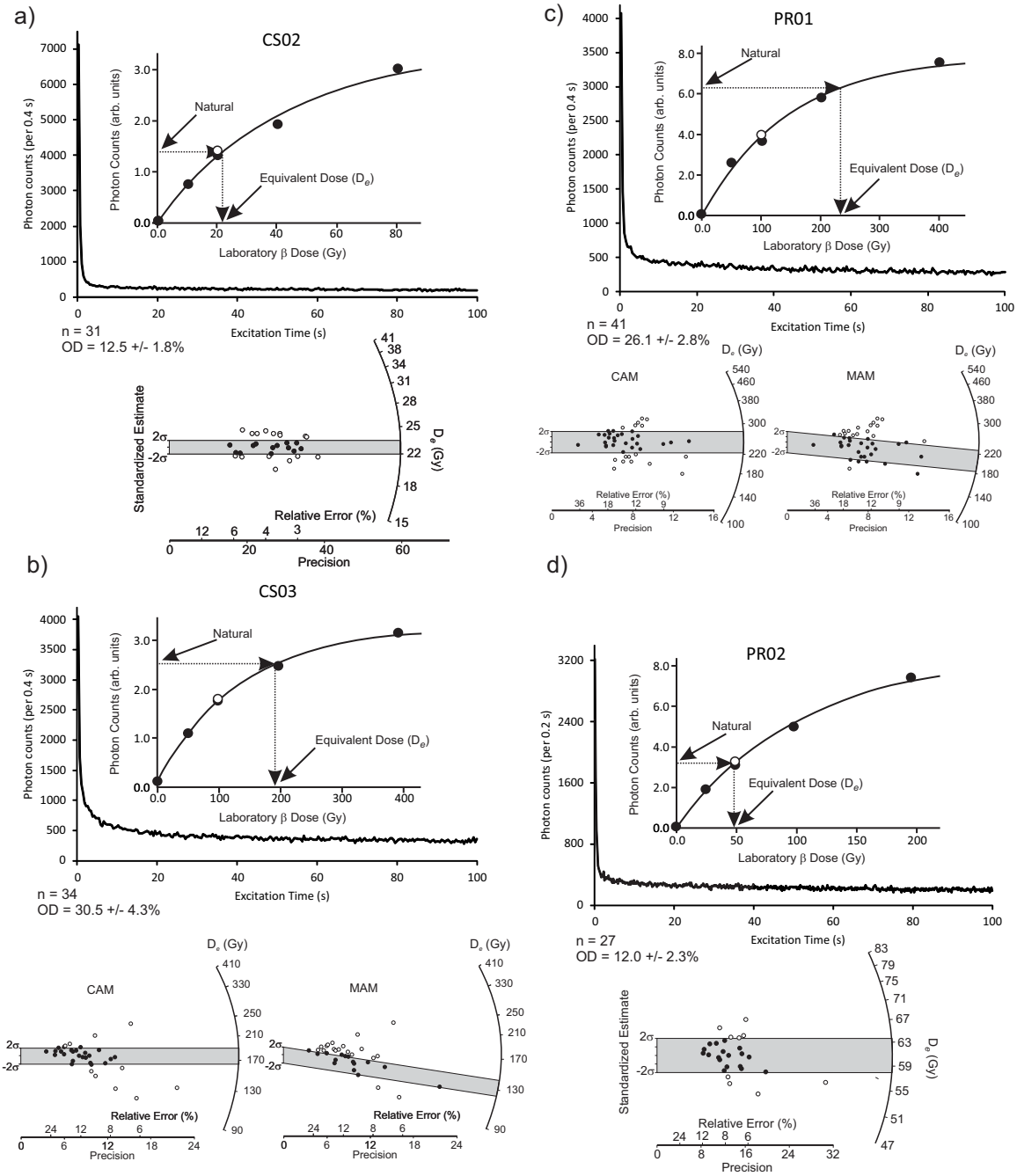

Figure 4.22. Examples of the OSL response for each of the samples including, a typical shine down curve (photon counts per excitation time), associated growth curve (photon counts per Laboratory β dose) and a radial plot used to determine the statistical equivalent dose (De). The open circle on the growth curve plot is a duplicate dose point used to determine the recycling ratio. Since it is close to unity in these samples, the test dose procedures has successfully corrected for sensitivity changes. The grey region on the radial plots represents the weighted-mean equivalent dose value of all the data. a) CS02 from Section 7; b) CS03 from Section 7; c) PR01 from Section 10; and d) PR02 from Section 8. OD = Overdispersion.

4.5 Discussion

This study provides evidence that, in the Dawson Creek area, an extensive Late Wisconsinan CIS coalesced with a contemporaneous LIS. This assertion is base on three main lines of reasoning: 1) a continuous field of curved streamlined landforms indicates a major lobe of east flowing ice was deflected by the LIS; 2) the ice lobe post-dates the maximum advance of the LIS and is, therefore, of Late Wisconsinan age; and 3) stratigraphy from the Murray and Pine river valleys support a Late Wisconsinan age for the surface glacial sediments and landforms.

Before this evidence is discussed, clarification of terms *montane ice* and *CIS* are necessary. Mathews (1980) and Catto et al. (1996) differentiate the CIS as ice originating west of the Rocky Mountain trench versus montane ice with sources from the Canadian Rocky Mountains. Although this is probably useful along the foothills, it becomes problematic in the interior plains. For example, Catto et al. (1996) infer that the Redwillow streamlined features are from a montane source, yet the scale and extent of the Redwillow streamlined field and the large flow tract depicted in the Noel and Swan Lake areas (Fig. 4.3) imply a glacier or ice lobe more than 100 km in width. It is possible that these glaciers or ice lobes were sourced from the main Rocky Mountain range (i.e. montane), but it is equally probable that they are associated with the CIS. Since it is the presence of soft low-grade schist and slate (which has limited preservation potential in far-travelled subglacially transported till) that differentiates the CIS from montane ice sources (Rocky Mountains), it is difficult to equivocally assign landforms to the CIS or montane ice sources. Furthermore, the bedrock host of these indicator lithologies is 200 km away. Consequently, in this study we can only imply a general western ice source and do not attempt to differentiate montane ice sources from the CIS.

The high-resolution LiDAR and other DEMs provide excellent imagery that show streamlined landforms in the Noel and Swan lake areas (Figs. 4.3 and 4.4b) form a continuous field of landform features that track more than 75 km. These features indicate that a substantive lobe of ice, nourished from a western source, flowed to the northeast but was deflected to a north-northwest flow trajectory. Since an eastern flow trajectory is down the general regional slope and there are no significant topographic barriers, this deflection is only possible if the LIS impeded the flow of western-sourced ice. Reimchen (1980) indicated that streamlined landforms within, and between the Puggins and Noel areas, (CIS origin), are truncated by landforms associated with the south flowing Late Wisconsinan LIS and that this truncation

implies that an extensive CIS pre-dated the maximum extent of the LIS. It is argued in this study that there is no geomorphic evidence of south-flowing ice in this area (mapped features are in fact indicative of northerly flow) and truncation has not occurred.

It has been established that the LIS only reached as far west as the Watino area in the Late Wisconsinan (Liverman et al, 1989). This implies that the Laurentide till in the Dawson Creek area must also be of Late Wisconsinan age. Although Hartman and Clague (2008) suggest three Laurentide events in the Fort St John area of the Peace River valley, they only have evidence of Laurentide till for what they interpreted to be of Late Wisconsinan age. Surface diamict samples (Fig. 4.1) and the absence of Laurentide till in the Murray and Pine rivers sections indicate the LIS did not extend into the foothills in this area, consistent with the observations of Bednarski and Smith (2007). Ice-rafted debris in the lower Pine River valley demonstrates that the Laurentide ice margin was supplying diamict to the western edge of the glacial Lake Peace basin.

If it is accepted that the LIS reached its maximum extent in the Late Wisconsinan and only reached the area during this time, then landforms occurring on this surface (that record eastern ice flow) must have formed after the LIS vacated the area. The fact that the features record deflection, but are comprised of eastern-provenance till with no distinct boundary, means that till emplacement from the LIS and its subsequent reworking from western ice probably occurred within a short timeframe (i.e. essentially contemporaneous). This supports the notion that both the LIS and the CIS/montane ice occupied the area in the Late Wisconsinan (first dominated by LIS and later by the CIS/montane ice) and coalesced (as described by Mathews, 1980). There is evidence for this sequence at the Section 11. The 30 m section of diamict shows geochemical, pebble counts and grain-size trends that tentatively imply that the base of the section has LIS affinity but becomes more transitional towards a CIS affinity at top of the section (Fig. 4.21). Although till classification based on pebble fabric data alone must be undertaken cautiously (e.g., Hicock et al., 1996; Bennett et al., 1999; Lian and Hicock, 2010), the classification diagrams suggest depositional conditions may have changed during emplacement of the diamict unit. The modality diagram suggests that there may be two depositional cycles, each including initial lodgement followed by deformation (i.e. Site 1 to 2; Sites 3 and 4 to 5). This may correspond with initial deposition from the LIS followed by reworking and deposition from the CIS/montane ice. The evidence from Section 11 must be considered exploratory, however,

and invites further study of other local sections. These thick diamict units in the mixing zone reflect the influences of both ice sheets and are complex. They are likely polygenetic and represent changes in subglacial dynamics as well as provenance.

Although truncation of CIS/montane ice flow features by the LIS is disputed in this study, discordant ice flow features do occur where the northeast trending Redwillow streamlined field overprints the main deflected ice flow trajectory (described above). It is asserted here that the Redwillow features record a younger CIS/montane surge-type event. This is consistent with Catto et al. (1996) although their conclusions imply that the glacial system that generated these features pre-dates the LIS. They suggest the LIS overrode these landforms, draping them in Laurentide till, but did not have the erosive power to modify the landscape (p. 28, Catto et al., 1996). They also suggest that the drop in the proportion of shield clasts noted southwest of Grande Prairie is the result of dilution of Laurentide provenance material by the incorporation of large amounts of bedrock and reworked montane derived sediments. We submit that it is unlikely that the very well preserved flutes (visible in LiDAR DEMs) that demarcate the Redwillow streamlined field (Figs. 4.4c and d) were overridden by the LIS. In fact, we imply that these features are indicative of CIS overriding the LIS till. The dilution of shield clasts southwest of Grande Prairie can be explained by the reworking of Laurentide till by a younger, Late Wisconsinan glacial system of either a CIS or montane origin (Mathews, 1980; Catto et al., 1996).

The results of this study suggest an alternative origin for the Redwillow streamlined landform field. The flow path of the ice lobe responsible for the streamlined features was established after recession of the LIS, allowing western-sourced ice to flow unimpeded into glacial Lake Peace (Mathews, 1980; Chapter 6). The narrow flutes associated with this field (Figs. 4.4c and d) probably represent a lake-terminating surge-type lobe (Paterson, 1994; Evans and Rea, 2005) or resulted from a draw-down effect as the ice entered glacial Lake Peace. Rapid ice flow was facilitated by a saturated and easily deformed glaciolacustrine substrate, reduced friction from ice made buoyant by deep proglacial lake water, and increased ablation from rapid calving. Surging would have a significant impact on the mass balance of the source region, draining the ice reservoir (Stokes and Clark, 2003). If the source area were depleted, the ice reservoir (Cordilleran or Montane) may have been unable to support continued ice flow. In many parts of the east side of the study area, well-developed streamlined features are overlain

by hummocky terrain that is interpreted to be stagnant ice moraine (e.g. Fig. 4.4d). These deposits represent a switch from an active ice phase that generated the streamlined forms to a stagnant ice phase. The stagnant phase would therefore represent the collapse of the ice surge.

The stratigraphy recorded in the Murray-Pine river valleys also supports an extensive Late Wisconsinan Cordilleran/Montane glacial event. The stratigraphy correlates well and spans at least two glacial cycles (Fig. 4.23). Rivers have incised though valley-fill successions and into Cretaceous bedrock so base level at the present time is at an all-time low elevation. Because the fill successions contain sediment possibly > 100,000 years in age, these major rivers valleys are ancient landscape elements established before the late Quaternary. The stratigraphy here is comparable with that of the Peace River valley suggested by Mathews (1980), Hartman and Clague (2008) and Morgan et al. (2012). A south-to-north cross-section (Fig. 4.23) shows that, towards the Peace River, there are at least two large nested paleovalleys. A number of the fill units are complex and represent several depositional settings and in some sections the units show significant modification by glacial tectonic deformation. There is, therefore, opportunity for additional detailed study of the precise genesis of these deposits. Here we discuss the units in terms of temporal context and climatostratigraphy and provide only general comment on their depositional settings.

There is no chronological control on Unit 1, and because the base of the unit is obscured and the top is unconformably bound, its relative stratigraphic position remains unclear. It is highly deformed, but is interpreted to have been deposited in a non-glacial fluvial setting. The sediment comprising the unit is over-consolidated and lithologically distinct from other fluvial units represented in this stratigraphy. The unit is tentatively assigned to the Sangamon (MIS 5) non-glacial interval. It is conceivable, however, that the unit is of an interglacial age, equivalent to Unit 5 (Middle Wisconsinan; MIS 3).

Units 2, 3, and 4 represent a glacial sequence and are interpreted as the penultimate glacial event of the Early Wisconsinan (MIS 4) or older. Unit 2 is interpreted to be a glaciofluvial deposit that conformably grades upwards into diamict interpreted to be deposited as a glaciogenic sediment flow (Fig. 4.15a) and lodgement till (Figs. 4.15b and c). This unit is overlain by glaciolacustrine sediment. The succession represents first, the deposition of glacial outwash followed by the arrival of a glacier resulting in the deformation, comminution and incorporation of existing substrate and deposition of glaciogenic diamict. The principal eigenvectors of pebble

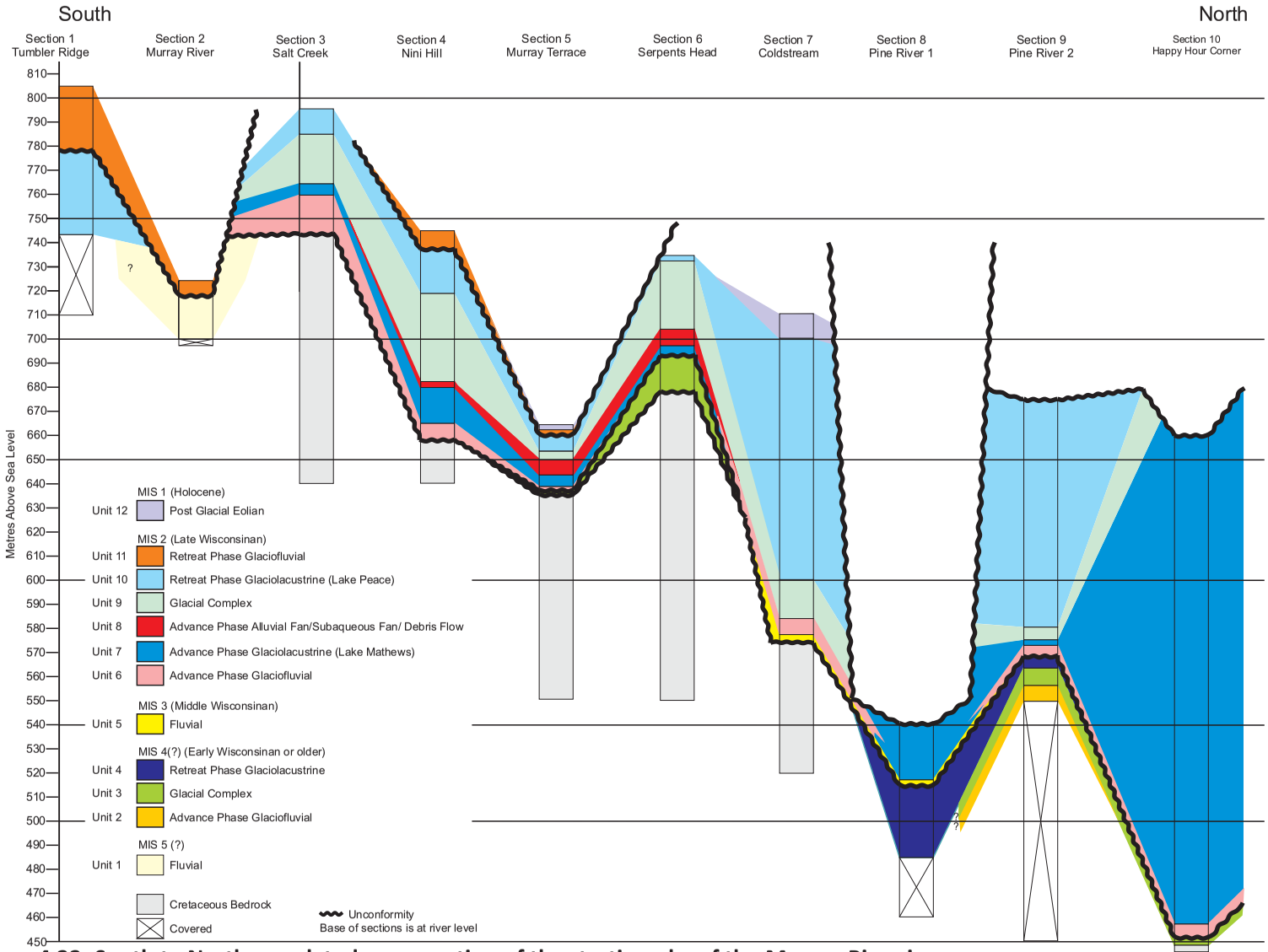

Figure 4.23. South to North correlated cross-section of the stratigraphy of the Murray-Pine rivers.

fabrics are typically parallel to the long axis of the valley. The glaciolacustrine sediments that cap the penultimate glacial succession likely represent a retreat-phase glaciolacustrine environment and demonstrate that water was impounded by a local valley obstruction such as a glacier or landslide in a downstream tributary valley, or by a regional barrier such as a penultimate LIS.

Unit 5 is a critical unit for the stratigraphy as it has been dated by radiocarbon and optical methods. At Section 8 this unit is represented by non-glacial fluvial gravel that fines upward to overbank sediments that were subsequently flooded resulting in the deposition of what is interpreted to be advance-phase glaciolacustrine sediments (Unit 7). A thin organic-rich horizon at the top of the overbank section returned radiocarbon ages of 27 760 ± 230 BP from a twig (32 039 ± 640 cal yrs BP) and 30 380 ± 300 BP from silverweed (Potentillo anserina) achenes (35 355 ± 828 cal yrs BP). The sand around this horizon returned an optical age of 22.7 ± 1.0 years (error value is 1σ) before present. As described previously (see Chronology Results), the discrepancy between the radiocarbon age and the luminescence age is unexplained and remains an avenue for more research. Regardless, both methods support a Middle Wisconsinan (MIS 3) age for this unit (Fig. 4.24). This is consistent with an age of 25 120 ± 140 years BP (29 927 ± 378 cal yrs BP) for a fluvial unit east of the study area in a similar stratigraphic position (Town of Peace River, Alberta; Morgan, et al., 2012). It is also consistent with the range of finite ages accepted in Hartman's (2005) summary for a correlative unit in the region (i.e. 27 400 ± 580 to 22 020 ± 450 BP or 32 112 ± 1127 to 26 525 ± 1296 cal yrs BP). Common silverweed typically grows in sandy or gravelly soil along the margins of streams, lakes and ponds, mudflats, and moist alkaline meadows and grasslands in the montane zone (Klinkenberg, 2013). The environment and climate was therefore probably very similar to that currently found in the lower Pine River valley. The implication is that this unit represents the Middle Wisconsinan nonglacial period (MIS 3) equivalent to the Olympia nonglacial climatostratigraphic interval recognized elsewhere in British Columbia (Clague, 1989).

Units 6—11 represent a succession assigned to the Late Wisconsinan (MIS 2) glacial interval equivalent to the Fraser Glaciation in the rest of British Columbia. Unit 6 represents an advance-phase glaciofluvial setting. It commonly precedes the advance-phase glaciolacustrine deposits associated with what is interpreted to be glacial Lake Mathews (Hartman and Clague, 2008). The transition from Unit 5 to Unit 6 represents the switch from non-glacial fluvial deposition to glaciofluvial deposition reflecting the increased influence of advancing glaciers in

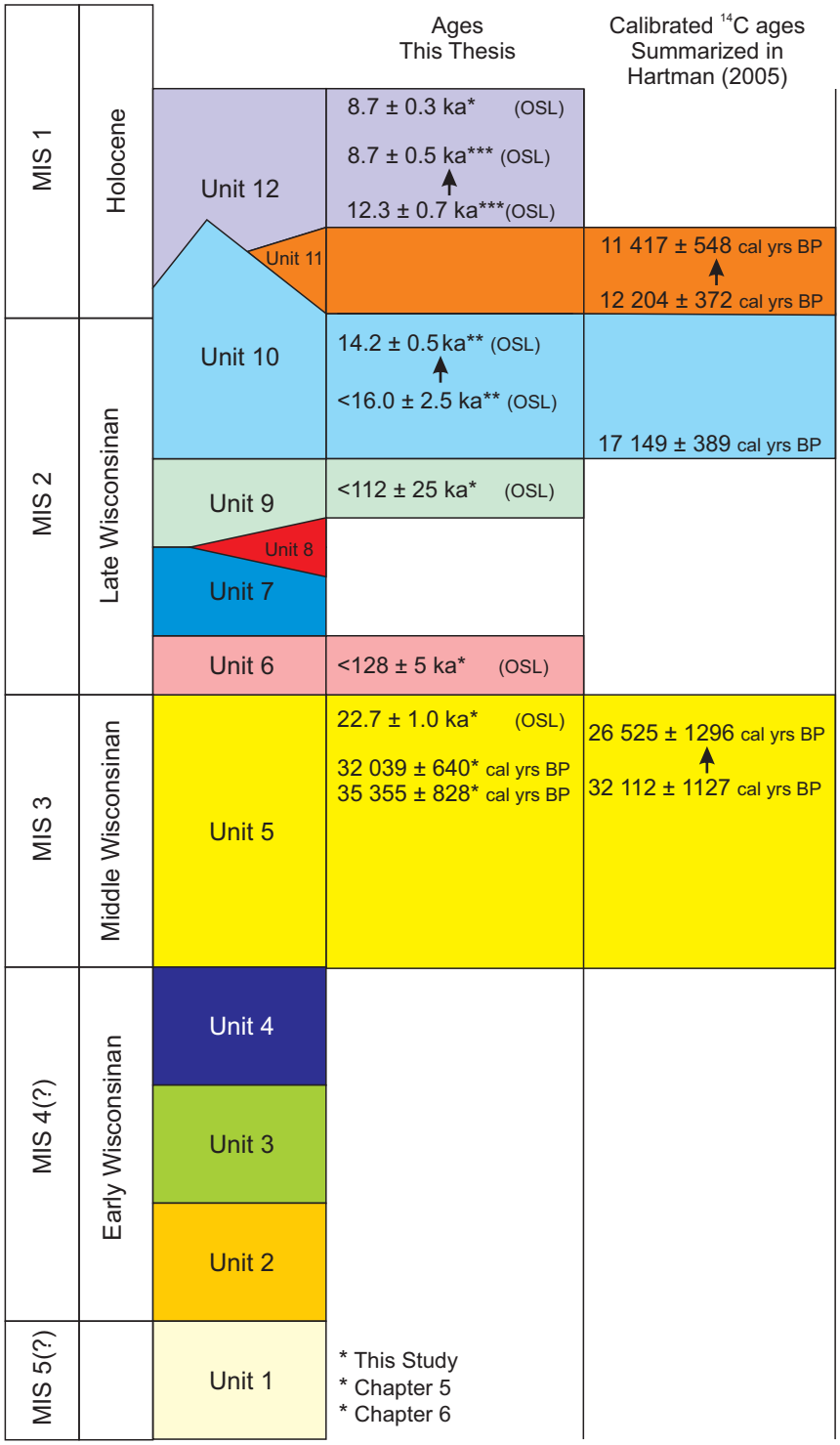

Figure 4.24. Summary of the stratigraphy and chronology from the study area (same legend Fig. 4.23). The optical ages for Units 6 and 9 are likely maximum ages, consequently, the depositional age for these units is younger. Correlation suggests they were deposited during the Late Wisconsinan (MIS 2).

the valley. Although Unit 6 (glaciofluvial) is stratigraphically lower than Unit 7 (glacial Lake Mathews) these units are probably, in part, time equivalent units and reflect transgression of Lake Mathews and the contemporaneous advance of valley glaciers. An OSL sample (PR01) collected from the contact between the glaciofluvial unit (Unit 6) and glacial Lake Mathews sediments (Unit 7) does not resolve the age of this succession. It returned a CAM age of 157 ± 5 ka and a MAM age of 128 ± 5 ka indicating it was deposited in a glacial interval during or after MIS 6. Because This age for this sample is surprisingly old so two possible conclusions may be drawn: 1) The unit from which this sample was collected not Unit 6 but is an older MIS 6 unit; or 2) the grains comprising sample PR01 were not exposed to sufficient light to reset the OSL clock and the unit is from either MIS 6, 4 or 2. The sample is from a glaciofluvial deposit, and since the overdispersion is relatively high, it is likely the grains were insufficiently exposed to enough light to reset the OSL clock. If this is the case the MAM age indicates that the unit is no older than 128 ± 5 ka and the sampled units if from glacial intervals: MIS 6 (pre-Wisconsinan); MIS 4 (Early Wisconsinan); or MIS 2 (Late Wisconsinan). Stratigraphic position, a conformable upper contact, and correlation favours a MIS 2 (Late Wisconsinan) age, but the age of the unit remains equivocal at this section.

Unit 7 represents an advance-phase glaciolacustrine deposit stratigraphically equivalent to deposits assigned to glacial Lake Mathews (Hartman and Clague, 2008). This is a regionally extensive unit that is recognized throughout the Peace River district. The unit marks the arrival of the LIS east of the study area where it blocked regional drainage. The transition from fluvial to glaciolacustrine environments occurs over < 1 m suggesting a very rapid rise in lake level (Hartman and Clague, 2008). Since this unit conformably overlies Unit 5 at Section 8, it is younger than MIS 3 (ca. 22.7 ± 1 ka based on the OSL age). This unit is recognized at an elevation of 760 m asl which raises the maximum elevation of glacial Lake Mathews (632 m asl; Hartman and Clague, 2008) by more than 130 m. In many of the sections this unit is deformed, likely reflecting glacial tectonism and loading associated with the arrival of the MIS 2 (Late Wisconsinan) glaciers.

Unit 8 consists of deposits interpreted to be associated with alluvial fans or sediments dominantly transported by gravitational processes. These deposits probably reflect deposition from the unstable slopes of the valley and debris-flows from advancing glaciers. These deposits

may, in part, represent ice-contact deposits where glacial debris was shed from the advancing ice front into glacial Lake Mathews.

Unit 9 is complex and represents a number of glaciogenic depositional settings. The succession at Section 6 provides a nearly complete summary of the Late Wisconsinan sequence for the Murray River valley. At Section 6, Unit 8 forms a 1 km-long wedge-shaped deposit and is likely a debris-flow fan deposited into glacial Lake Mathews in front of an advancing glacier. The lower part of Unit 9 (Unit 9a) is interpreted to be glacially tectonized waterlain diamict (SH-3; Fig. 4.15) that was deposited and over ridden by advancing ice. The main modes from the till fabric (Fig. 4.9) probably reflect 1) the valley parallel ice flow and 2) the near-orthogonal structural fabric resulting from deformation. Unit 9a is in turn overlain by lodgement or meltout till from Unit 9b (SH-44; Fig. 4.15) deposited directly from the ice. Pebble fabric from Unit 9a at Section 6 is perpendicular to the valley trend and is strongly aligned with the east-northeast regional flow pattern recorded in the surface streamlined landforms.

The retreat-phase glaciolacustrine Unit 10 is associated with the glacial Lake Peace. These sediments are ubiquitous across the Peace Region of northeast British Columbia and northwest Alberta. Glacial Lake Peace formed as a proglacial lake when regional (eastward) drainage was blocked by the LIS. Glacial Lake Peace followed the LIS margin as it retreated to the northeast (Chapter 6). An optical dated sample was collected from above diamict at the base of Unit 10 at Section 7. The MAM optical age for sample CS03 was 112 ± 25 ka years BP, but as noted earlier the luminescence measured from many of the aliquots was near saturation (could not provide equivalent doses). This indicates that many of the grains were not exposed to sufficient sunlight prior to burial. Although the time of formation of this unit is inconclusive (younger than 112 ka) the luminescence response does support the notion that this deposit was probably laid down in an environment not exposed to sunlight, consistent with the interpretation that the unit represents a subaqueous environment, probably from glacial ice in contact with glacial Lake Peace. Organic material from the base of Unit 10 in the Ft St John area provides an age of 13 970 ± 170 BP (17 149 ± 389 cal yrs BP; Catto et al, 1996) which is the oldest age for a unit over till from Hartman's (2005) summary (Fig. 4.24).

The youngest glacial unit in the succession is a retreat-phase glaciofluvial unit. It is common in terraces along the major river valleys and, in places occurs as relic deltas from stable periods of glacial Lake Peace (e.g. Town site of Tumbler Ridge or the confluence of the Pine and

Murray rivers; Fig. 4.19a). Numerous radiocarbon ages have been published for the glaciofluvial gravels in the Peace Region between Fort St John to Tumbler Ridge. Those in Hartman's (2005) summary range from 10 380 ± 100 to 9880 ± 130 ^{14}C yrs BP (12 204 ± 372 to 11 417 ± 548 cal yrs BP; Fig. 4.24).

The final unit in the stratigraphic sequence is an aeolian unit that is represented by sand dunes and loess (Muhs, 2007). Following glaciation, but before climate improved to support widespread forests, aeolian activity (i.e. in a paraglacial setting) occurred in northeast British Columbia (Wolfe et al., 2004; Wolfe et al., 2007). An optically dated sample returned an age of 8.7 ± 0.32 ka BP from what is interpreted to be loess from the Coldstream area. This age is consistent with 8 260 ± 80 BP (9232 ± 204 cal yrs BP) radiocarbon age from wood in the aeolian surface sediment at the Town of Peace River (Morgan et al., 2012), but is younger than optical ages from sand dunes in the Grand Prairie area reported by Wolfe et al. (2004) and Munyikwa et al. (2011) that range from 15.7 ± 1.6 to 14.2 ± 0.9 ka BP and range from 18.3 ± 1.2 to 1.31 ± 0.9 ka BP respectively. It is likely that aeolian deposition continued in local valleys after major dunes stabilized elsewhere in the region.

The Late Wisconsinan (MIS 2) glacial interval is well represented in the stratigraphy of the Murray-Pine river valleys. The chronology presented suggests that ice was present in the vicinity of the valleys between ca. 22 ka and ca. 17 ka. This is generally consistent with the conclusions of other studies in the region (e.g. Mathews 1980, Liverman 1989; Wolfe et al., 2004; Wolfe et al., 2007; Bednarski and Smith, 2007; Hartman and Clague, 2008; Morgan et al., 2012). Our interpretation of the stratigraphy implies that the surface landforms in the Dawson Creek map area are Late Wisconsinan in age.

We are, however, unable to reconcile our stratigraphy with several other studies. Bobrowsky (1989) and Bobrowsky and Rutter (1992) present an age of 15 180 ± 100 C^{14} yrs BP (18 345 ± 317 cal yrs BP) from a sub-till radiocarbon sample from the Finlay River area, which restricts the time available for the CIS to expand and flow onto the interior plains. Our ages also cannot be reconciled with bulk sample radiocarbon ages from Jull and Geertsema (2006) and Woolf (1993) that support limited ice coverage in the area during the Late Wisconsinan. Jull and Geetsema (2006) have a series of radiocarbon ages from an incised fan on a fluvial terrace above the Peace River (know as Bear Flats) that implies no glaciation after ca. 36,000 C^{14} yrs BP. There are, however, many age inversions in the succession and they state that dates older than

19,500 cal. yrs BP should be treated with caution. The abundance of coal in these sediments casts some doubt on the validity of the older ages. Woolf (1993) presented ages ranging from 38,106 ± 3911 (probably at the limit of C^{14} dating) and 19,601 ± 3394 for a lacustrine deposit under till in the Cache Creek Road area west of Fort St John. Woolf's (1993) dates have very large uncertainty, show inversions, and have abundant coal present in the sediments. He identifies a number of potential problems with the ages relating to contamination and consequently the validity of the dates are questioned.

4.6 Conclusion

This study seeks to address uncertainty and debate around the question: 'Did the Laurentide Ice Sheet (LIS) and Cordilleran Ice Sheet (CIS) coalesce or remain separated during the late Wisconsinan in northeastern British Columbia?'. We conclude that, indeed, there was ice-sheet coalescence at this time and we base our conclusion on three main lines of evidence:

(1) There exists in the Dawson Creek area a continuous field of streamlined landforms indicating that a major lobe of east flowing ice, sourced in, or west of the Rocky Mountains, was deflected from east-northeast to a north-northwest trajectory. There are no topographic features that could have caused this deviation to flow so it is inferred that the LIS must have been present to have caused this change in flow direction.

(2) The east to north-northeast flowing ice lobe post-dates the Late Wisconsinan (MIS 2) maximum advance of the LIS. The streamlined landforms that record the flow of western-sourced ice are constructed of till with clasts of eastern provenance (Proterozoic Canadian Shield clasts). This implies that the LIS must have reached its maximum extent before the western-sourced ice flowed across the area. It is tentatively interpreted that this sequence is recorded in the till (major oxide geochemistry, grain-size, and proportion of shield clasts) in this zone of overlap. Since it has been established by Liverman et al. (1989) that the LIS reached its maximum extent in this area during the Late Wisconsinan, the CIS/montane ice responsible for the streamlined landforms must also have occupied the area in the Late Wisconsinan (MIS 2).

(3) Stratigraphy from the Murray and Pine river valleys supports a Late Wisconsinan age for the surface landforms. The stratigraphy includes at least two glacial events separated by a non-glacial interval. Two radiocarbon ages (Beta-250625: 27 760 ± 230 BP; calibrated to 32 039 ± 640 cal yrs BP and UCIAMS-71221: 30 380 ± 300 BP; calibrated to 35 355 ± 828 cal yrs BP), and a

quartz optical age of 22.7 ± 1.0 ka BP indicate a Middle Wisconsinan (MIS 3) age for this unit. This confirms the regionally extensive glacial sediments that occur stratigraphically above this unit are assigned to the Late Wisconsinan (MIS 2).

4.7 References

ASTM Standard D422 - 63 2007. Standard test method for particle-size analysis of soils, ASTM International, West Conshohocken, PA, 8 pp.

Aber, J.S. and Ber, A. 2007. Glaciotectonism. Elsevier, 246 pp.

Adamiec, G. and Aitken, M.J. 1998. Dose-rate conversion factors Update. Ancient TL 16, 37—49.

Aitken, M.J. 1985. Thermoluminescence Dating. Academic Press, London, 359 pp.

Arnold, T.G. 2002.Radiocarbon dates from the ice-free corridor. Radiocarbon, 44, 437—454.

Ashley, G.M., Southard, J.B., and Boothroyd, J.C. 1982. Deposition of climbing-ripple beds: a flume simulation. Sedimentology, 29, 67—79.

Beach, H.H. and Spivak, J. 1943. The origin of the Peace River Canyon, British Columbia. American Joand & Smith, I.R. 2007. Laurentide and montane glaciations along the Rocky Mountain Foothills in northeastern British Columbia. Canadian Journal of Earth Sciences 44, 445—457.

Benn, D.I. 1994a. Fluted moraine formation and till genesis below a temperate valley glacier: Slettmrkbreen, Jotunheimen, southern Norway. Sedimentology 41, 279—292.

Benn, D.I. 1994b. Fabric shape and the interpretation of sedimentary fabric data. Journal of Sedimentary Research A64, 910—915.

Bennett, M.R., Waller, R.I., Glasser, N.F., Hambrey, M.J., and Huddart, D. 1999. Glacigenic clast fabrics: genetic fingerprint or wishful thinking? Journal of Quaternary Science 14, 120—135.

Berger, G.W. 1988. Dating Quaternary events by luminescence. In Easterbrook, D.J. (ed): Quaternary sediments; Geological Society of America Special Paper 227, 13—50.

Bobrowsky, P.T. 1989. Late Cenozoic geology of the northern Rocky Mountain Trench, British Columbia. Unpublished PhD. Thesis, University of Alberta, 463 pp.

Bobrowsky, P.T. and Rutter, N.W. 1992. The Quaternary geologic history of the Canadian Rocky Mountains. Géographie Physique et Quaternaire 46, 5—50.

Bobrowsky, P.T. 1987. Quaternary geology of northwestern Alberta and northeastern British Columbia; International Union for Quaternary Research, 12th international Congress (Ottawa, Ontario), Guidebook, Field Excursion A-24, 62 pp.

Bronk, R.C., 2001. Development of the radiocarbon calibration program OxCal. Radiocarbon, 43, 355—363.

Buccianti, A. and Peccerillo, A. 1999. The complex nature of potassic and ultrapotassic magmatism in Central–Southern Italy: a multivariate analysis of major element data. In: Lippard, S.J., Naess, A., Sinding-Larsen, R. (Eds), Proceedings of the 5th Annual Conference of the International Association for Mathematical Geology, Trondheim, Tapir, 145 – 150.

Catto, N.R. 1984. Glacigenic deposits at the Edmonton Convention Centre, Edmonton, Alberta. Canadian Journal of Earth Sciences, 21, 1473—1482.

Catto, N.R., Liverman, D.G.E., Bobrowsky, P.T., and Rutter, N. 1996. Laurentide, Cordilleran, and Montane glaciations in the western Peace River – Grande Prairie region, Alberta and British Columbia, Canada. Quaternary International 32, 21—32.

Clague, J.J. (compiler) 1989. Quaternary geology of the Canadian Cordillera. In Fulton, R.J. (ed.) Quaternary Geology of Canada and Greenland, Geological Survey of Canada, Geology of Canada no. 1, 17—96.

Cohen K.M. and Gibbard, P. 2011. Global chronostratigraphical correlation table for the last 2.7 million years. Subcommission on Quaternary Stratigraphy (International Commission on Stratigraphy), Cambridge, England.

Davis, J.C. 2002. Statistics and Data Analysis in Geology (Third Edition). John Wiley & Sons, New York, 678 pp.

Dawson, G.M. 1881. Report on exploration from Port Simpson on the Pacific Coast to Edmonton on the Saskatchewan; Geological Survey of Canada, Report of Progress, 1879-1880, Section B, 77 pp.

Dawson, G.M. 1888. Recent observations on the glaciations of British Columbia and adjacent regions. American Geologist, 3, 249—253.

Dowdeswell, J.A. and Sharp, M.J. 1986: Characterization of pebble fabrics in modern terrestrial glaciagenic sediments. Sedimentology 33, 699—710.

Dreimanis, A. 1988. Tills: Their genetic terminology and classification. In Goldthwait, R.P. & Matsch, C.L. (eds), Genetic classification of Glacigenic deposits, A.A. Balkema, Rotterdam, 17—68.

Dyke, A.S. and Prest, V.K. 1987. Paleogeography of northern North America, 18 000—5 000 years age. Geological Survey of Canada, Map 1703A, scale 1:12 500 000.

Dyke, A.S., Moore, A., and Robertson, L. 2003. Deglaciation of North America. Geological Survey of Canada, Open File 1574, CD ROM.

Evans, D.J.A. & Benn, D.I. 2004. Facies description and logging of sedimentary exposures. In Evans, D.J.A. and Benn, D.I. (eds.): A Practical Guide to the Study of Glacial Sediments; Oxford University Press, New York, 11—51.

Evans, D.J.A, and Rea, B.R. 2005. Surging glacier landsystem. In Evans, D.J.A (ed.): Glacial Landsystems, Holder Arnold, New York, 259—288.

Eyles, C.H. and Eyles, N. 2010. Glacial Deposits. In James, N.P. and Dalrymple, R.W. (eds.): Facies Models 4. Geological Association of Canada, St. John's, 73—104.

Eyles, N., Eyles, C.H., and Miall, A.D. 2003: Lithofacies types and vertical profile models: an alternative approach to the description and environmental interpretation of glacial diamict and diamictite sequences. Sedimentology 30, 393—410.

Galbraith, R.F. 2010. On plotting OSL equivalent doses. Ancient TL 28, 1—9.

Galbraith, R.F., Roberts, R.G., Laslett, G.M., Yoshida, H., and Olley, J.M. 1999. Optical dating of single and multiple grains of quartz from Jinmium rock shelter, northern Australia. Part I: experimental design and statistical models. Archaeometry 41, 339—364.

Grunsky, E.C. 2006. The evaluation of geochemical survey data: Data analysis and statistical methods using Geographic Information Systems. In Haris, J. (ed) GIS for Earth Sciences, Geological Association of Canada, Special Publication 44, 229—283.

Hartman, G.M.D. 2005. Quaternary Stratigraphy and Geologic History of the Charlie Lake (NTS 94A) map area, British Columbia. Unpublished MSc Thesis, University of Victoria, British Columbia, Canada, 166 pp.

Hartman, G.M.D. and Clague, J.J. 2008. Quaternary stratigraphy and glacial history of the Peace River valley, northeast British Columbia. Canadian Journal of Earth Sciences 45, 549—564.

Hicock, S.R., Goff, J.R., Lian, O.B., and Little, E.C. 1996: On the interpretation of subglacial till fabrics. Journal of Sedimentary Research 66, 928—934.

Holland, S.S. 1976. Landforms of British Columbia, A physiographic outline. British Columbia Department of Mines and Petroleum Resources, Bulletin 48, 138 pp..

Huntley, D.J., Godfrey-Smith, D.I., and Thewalt, M.L.W. 1985. Optical dating of sediments. Nature 313, 105—107.

Jackson, L.E., Jr., Phillips, F.M. and Little, E.C. 1999. Cosmogenic 36Cl dating of the maximum limit of the Laurentide Ice Sheet in southwestern Alberta. Canadian Journal of Earth Sciences, 36, 1347—1356.

Jackson, L.E., Jr., Phillips, F.M., Shimamura, K., and Little, E.C. 1997. Cosmogenic 36Cl dating of the foothills Erratic Train, Alberta, Canada. Geology, 25, 1995—198.

Janoušek, V. Farrow, C.M., and Erban, V. 2006. Interpretation of whole-rock geochemical data in igneous geochemistry: introducing geochemical data toolkit (GCDkit). Journal of Petrology, 47, 1255—1259.

Jull, T. G. and Geertsema, M. 2006. Over 16,000 years of fire frequency determined from AMS radiocarbon dating of soil charcoal in an alluvial fan at Bear Flat northeastern British Columbia. Radiocarbon, 48, 435—450.

Klinkenberg, B. (Editor) 2013. E-Flora BC: Electronic Atlas of the Plants of British Columbia [eflora.bc.ca]. Lab for Advanced Spatial Analysis, Department of Geography, University of British Columbia, Vancouver. [Accessed: 3/26/2013]

Levson, V.M. and Rutter, N.W. 1995. Pleistocene stratigraphy of the Athabasca River Valley region, Rocky Mountains, Alberta. Géographie Physique et Quaternaire 49, 381—399.

Levson, V.M. and Rutter, N.W. 1996. Evidence of Cordilleran late Wisconsinan glaciers in the 'Ice-Free Corridor'. Quaternary International, 32, 33—51.

Levson, V.M. and Rutter, N.W. 2000. Influence of bedrock geology on sedimentation in Pre-Late Wisconsinan alluvial fans in the Canadian Rocky Mountains. Quaternary International 68-71, 133—146.

Lian, O.B. 2013. Optical Dating. In: Elias S.A. (ed.) The Encyclopedia of Quaternary Science, vol. 2 (2nd ed.), Elsevier, Amsterdam, pages, 653—666.

Lian, O.B. and Roberts, R.G. 2006. Dating the Quaternary: progress in luminescence dating of sediments. Quaternary Science Reviews 25, 2449—2468.

Lian, O.B., Hu, J., Huntley, D.J., and Hicock, S.R. 1995. Optical dating of Quaternary organic-rich sediments from southwestern British Columbia and northwestern Washington State. Canadian Journal of Earth Sciences 32, 1194—1207.

Liverman, D.G.E. 1989. The Quaternary Geology of the Grande Prairie Area, Alberta. PhD thesis, University of Alberta, Edmonton Alberta, 360pp.

Liverman, D.G.E., Catto, N.R., and Rutter, N.W. 1989. Laurentide glaciations in west-central Alberta; a single (Late Wisconsinan) event. Canadian Journal of Earth Sciences, 26, 266—274.

Mathews, W.H. 1954. Quaternary stratigraphy and geomorphology of the Fort St John area, northeast British Columbia. Geological Society of America, Bulletin 65, 1345.

Mathews, W.H. 1955. Ground-water possibilities of the Peace River Block, British Columbia. British Columbia Department of Mines, Ground-water Paper No. 3, 7 pp.

Mathews, W.H. 1978. Quaternary stratigraphy and geomorphology of Charlie Lake (94A) Map-area, British Columbia. Geological Survey of Canada, Paper 76-20, 25 pp.

Mathews, W.H. 1980. Retreat of the last ice sheets in northeastern British Columbia and adjacent Alberta. Geological Survey of Canada, Bulletin 331, 22 pp.

May, R.W., Dreimanis, A., and Stankowski, W. 1980. Quantitative evaluation of clast fabrics within the Catfish Creek Till, Bradtville, Ontario. Canadian Journal of Earth Sciences 17, 1064—1074.

Menzies , J. and Rose, J.(eds). 1987. Drumlin Symposium. Proceedings of the Drumlin Symposium, 1st International Conference on Geomorphology, Manchester, 1985, Balkema, Rotterdam, 360 pp.

Miall, A.D., 2006.The Geology of Fluvial Deposits; Sedimentary Facies, Basin Analysis, and Petroleum Geology, 4th Printing. Springer, New York, 582 pp.

Morgan, A.J., Paulen, R.C., Slattery, S.R., and Froese, C.R., 2012. Geological Setting for Large Landslides at the Town of Peace River, Alberta (NTS 84C). Energy Resource Conservation Board/Alberta Geological Survey, Open File Report 2012-04, 33 pp.

Muhs, D.R. 2007. Loess deposits, origins and properties. In Elias, S.A. (ed): Encyclopedia of Quaternary Science, Elsevier, London, 1405—1418.

Murray, A.S. and Roberts, R.G. 1998. Measurement of the equivalent dose in quartz using a regenerative-dose single aliquot protocol. Radiation Measurements 29, 503—515.

Murray, A.S. and Wintle, A.G. 2000. Luminescence dating of quartz using an improved single-aliquot regenerative-dose protocol. Radiation Measurements 32, 57—73.

Murray, A.S. and Wintle, A.G., 2003. The single aliquot regenerative dose protocol: Potential for improvements in reliability. Radiation Measurements, 37, 377—381.

Occhietti, S. 1973. Les structure et déformations engendrées par les glacier – Essai de mise au point. Revue Géographique de Montréal, 27, 365—380.

Olley, J.M., Murray, A., and Roberts, R.G. 1996. The effects of disequilibria in the uranium and thorium decay chains on burial dose rates in fluvial sediments. Quaternary Science Reviews 15, 751—760.

Olley, J.M., Pietsch, T., and Roberts, R.G. 2004. Optical dating of Holocene sediments from a variety of geomorphic settings using single grains of quartz. Geomorphology, 60, 337—358.

Patterson, W.S.B. 1994. The physics of glaciers, 3rd Edition. Butterworth Heinemann, New York, 481 pp.

Plouffe, A., Paulen, R.C., and Smith, I.R. 2006. Indicator mineral content and geochemistry of glacial sediments from northwest Alberta (NTS 84L, M): new opportunities for mineral exploration. Geological Survey of Canada, Open File 5121, Alberta Energy and Utility Board, Alberta Geological Survey, Special Report 77, 29 pp.

Prescott, J.R. & Hutton, J.T. 1994. Cosmic ray contributions to dose rate for luminescence and ESR dating: Large depth and long-term time variations. Radiation Measurements, 23, 497—500.

Prescott, J.R. and Hutton, J.T. 1995. Environmental dose rate and radioactive disequilibrium from sediment grains: New experimental data. Quaternary Science Reviews 13, 439—448.

Reimchen, T.H.F. 1980. Surficial Geology, Dawson Creek, west of sixth meridian, British Columbia. Geological Survey of Canada, Map 1467A, scale 1:250 000.

Reimer, P.J., Baillie, M.G.L., Bard, E., Bayliss, A., Beck, J.W., Blackwell, P.G., Bronk Ramsey, C., Buck, C.E., Burr, G.S., Edwards, R.L., Friedrich, M., Grootes, P.M., Guilderson, T.P., Hajdas, I., Heaton, T.J., Hogg, A.G., Hughen, K.A., Kaiser, K.F., Kromer, B., McCormac, F.G.,

Manning, S.W., Reimer, R.W., Richards, D.A., Southon, J.R., Talamo,S., Turney, C.S.M., van der Plicht, J., and Weyhenmeyer, C.E. 2009. IntCal09 and Marine09 radiocarbon age calibration curves, 0-50,000 years cal BP. Radiocarbon, 51, 1111—1150.

Reeves, B.O.K. 1973. The nature and age of the contact between the Laurentide and Cordilleran ice sheets in the western interior of North America. Arctic and Alpine Research, 5, 1—16.

Roberts, R.G., Galbraith, R.F., Olley, J.M., Yoshida, H., & Laslett, G.M. 1999. Optical dating of single and multiple grains of quartz from Jinmium rock shelter, northern Australia. Part II: results and implications. Archaeometry 41, 365—395.

Rutter, N.W. 1977. Multiple glaciations in the area of Williston Lake, British Columbia. Geological Survey of Canada, Bulletin 273, 31 pp.

Scott, E.M., Harkness, D.D., and Cook, G.T. 1998. Interlaboratory comparisons: Lessons learned. Radiocarbon, 40, 331—340.

Smith, B.W. and Rhodes, E.J. 1994. Charge movements in quartz and their relevance to optical dating. Radiation Measurements, 23, 19—31.

Stokes, C.R. and Clark, C.D. 2003. The Dubawnt Lake palaeo-ice stream: evidence for dynamic ice sheet behaviour on the Canadian Shield and insights regarding the controls on ice-stream location and vigour. Boreas 32, 263–279.

Westgate J.A., Fritz, P., Matthews, J.V., Jr., Kalas, L., and Green, R. 1971. Sediment of mid-Wisconsinan age in west-central Alberta; Geochronology, insects, ostracodes, Mollusca, and the oxygen isotopic composition of mulluscan shells. Geological Society of America, 3, 419.

Westgate J.A., Fritz, P., Matthews, J.V., Jr., Kalas, L., Delmore, L.D., Green, R., and Aario, R. 1972. Geochronology and paleoecology of mid-Wisconsinan sediments in west-central Alberta, Canada. International Geological Congress, 24, 380.

Wintle, A.G. & Murray, A.S. 2006. A review of quartz optically stimulated luminescence characteristics and their relevance in single-aliquot regeneration dating protocol. Radiation Measurements, 41, 369—391.

Wolfe , S.A., Huntley, D.J., and Ollerhead, J. 2004. Relict Late Wisconsinan dune fields of the Northern Great Plains, Canada. Géographie Physique et Quaternaire, 58, 323—336.

Wolfe, S.A., Paulen, R.C., Smith, I.R., and Lamothe, M. 2007. Age and Paleoenvironmental significance of Late Wisconsinan dune fields in the Mount Watt (84-K) and Fontas River ((4-I) map sheets, northern Alberta and British Columbia. Geological Survey of Canada, Current Research, 2007-B4, 10 pp.

Woolf, K.E. 1993. Radiocarbon Chronology for Glacial Lake Peace. Unpublished MSc Thesis, Simon Fraser University, British Columbia, Canada, 93 pp.

Young, R.R., Burns, J.A., Smith, D.G., Arnold, L.D., and Rains, R.B. 1994. A single, late Wisconsinan Laurentide glaciations, Edmonton area and Southwestern Alberta. Geology, 22, 683—686.

CHAPTER 5: CAN THE ORIENTATION OF ELECTROMAGNETIC RESISTIVITY ANISOTROPY FROM TILL BE USED TO INFER PALEO-ICE FLOW? A COMPARISON OF RESISTIVITY ANISOTROPY AND STREAMLINED LANDFORM ORIENTATION.

Adrian S. Hickin and Melvyn E. Best

This manuscript has not yet been submitted for publication

Abstract

This study evaluates the hypothesis that the orientation of electrical anisotropy in till is indicative of the direction of paleo-ice flow. The orientation of the principal axes of resistivity ellipses generated from azimuthal electromagnetic data, the orientation of the streamlined landforms (which are assumed to be parallel to ice flow) and their clast fabrics are not always consistent. This study documents a 90° rotation of the electrical anisotropy between streamlined landforms with high elongation ratios (>3) and those with low elongation ratios (<3). Three explanations are proposed to elucidate these observations.

Electrical anisotropy may be coincident with the sediment fabric which could be parallel or transverse to ice flow, thus reflecting strain response to the local stress field. Two processes may account for the ~90° rotation in the electrical anisotropy. Firstly, the rotation may reflect modification of the subglacial sediment fabric during ice stagnation and the development of crevasse squeeze ridges. In this case, electrical anisotropy is consistent with the sediment particle fabric associated with the stress from stagnant ice. Alternatively, the rotation may be explained with the deforming bed mosaic concept. Highly elongated landforms are associated with highly deformable till and extensional ice flow. Landforms with lower elongation ratios form where a stiffer subglacial bed results in a “sticky-spot”, compressional ice flow, and rotation of the sediment particles towards a transverse fabric. The principle axis of the electrical anisotropy, therefore, corresponds with the sediment fabric, but would not necessarily be coincident with the paleo-ice flow direction.

Another explanation that merits further testing is that the electrical anisotropy results from fractures of various scales in till. Others have predicted that fractures and shear structures are responsible for electrical anisotropy. These structures are generally associated with a brittle or brittle-ductile bed response to stress fields. Small mesoscale structures (fissility) were observed at one location to be coincident with the principle axis of resistivity anisotropy, however these structures were not systematically evaluated in this study.

Inheritance may also be a viable explanation, though less favoured in this study. Streamlined landforms with low elongation ratios may be oriented in the direction of a younger flow event, but have unmodified cores that reflect earlier flow direction. This also remains untested.

5.1 Introduction

It has long been recognized that as glaciers move over sediments, the applied stress deforms these sediments into streamlined landforms (such as drumlins and flutes). These landforms often consist of till in which strain is recorded by various internal glaciogenic structures sensitive to the direction of ice movement (Benn and Evans, 1998). Analysis of the sediment fabric in tills can yield information about the ice-flow dynamics although such surveys can be very time consuming to undertake. The search for more efficient and faster measurement of strain in till has led to interest in the application of indirect geophysical techniques such as electrical resistivity. Indeed, it has been argued recently that the direction of electrical anisotropy from glacial diamict (till) is preferentially oriented parallel to the direction of ice flow and therefore, the direction of sediment transport (Penttinen et al., 1999; Sutinen et al., 2009; Sutinen et al., 2010). This assertion, however, is based on a limited set of observations relating primary deposition of glacial sediments to electrical anisotropy. If this geophysical method is to be accepted as a basis for inferring paleo-ice flow, the data base needs to be expanded in order to evaluate relations among the orientation of sediment fabrics, the alignment of elongated streamlined landforms, and the character of electrical anisotropy.

The purpose of this study is to present new data from northeastern British Columbia that allows a comparison of the orientation of the principal axes of electrical resistivity ellipses generated from azimuthal electromagnetic (EM) data to the orientation of flow-parallel streamlined landforms.

Rock and sediments have electrical anisotropy that can be measured by collecting oriented conductivity or resistivity data (e.g. Schlumberger and Leonardon, 1933; Keller and Frischknecht, 1966; Asten 1974; Habberjam, 1975; Taylor and Fleming, 1988). Watson and Barker (1999) describe two scales of anisotropy: micro and macro (Sauck and Zabik, 1992). Micro-anisotropy is commonly associated with the alignment of elongated mineral grains that result in a micro-fabric within the rock or sediment. This fabric develops from stress imparted on the grains during deposition (i.e. from moving water, wind, ice or gravity) or from the realignment of grains from external forces such as tectonism or metamorphism. Macro-anisotropy is attributed to alternating layers or beds of rock or is caused by fractures in an otherwise homogeneous rock or sediment.

Most electrical anisotropic studies use direct current geophysical methods and many are designed to evaluate groundwater resources. The application of this type of data is often directed at hydraulic transmissivity studies because it has been shown that there is a strong relationship between fracture orientation (and therefore the primary mechanism for hydraulic conductivity in low permeability media) and the principal directions of electrical anisotropy (e.g. Taylor and Fleming, 1988; Ritzi and Andolsek, 1992; Hagrey, 1994; Lane et al., 1995; Sandberg and Jagel, 1996; Watson and Barker, 1999; Guy et al., 2000; Skinner and Heinson, 2004).

Although most studies have focused on fractures in rock, a few have been directed at unconsolidated sediments. Taylor and Flemming (1988) presented sites from Wisconsin where azimuthal resistivity data were collected on till. They attributed the character of electrical anisotropy to the orientation of joints and joint sets, to joint set length, and to soil moisture content. Carpenter et al. (1990) also described resistivity anisotropy in till, noting that there was good correlation between azimuthal resistivity contrasts over prominent fractures, but they also stated that resistivity peaks may not necessarily correspond with the strike of fractures.

Only a few studies examine the relationship between electrical anisotropy and primary deposition of sediments. Sauck and Zabik (1992) noted that in some cases the orientation of joints in till did not match well the azimuthal resistivity and that this discrepancy was from unknown effects that were not evaluated in their study. They also imply that in stacked, braided stream channel deposits in a glaciofluvial fan, the maximum resistivity was perpendicular to the general direction of stream flow, and they concluded that the orientation of anisotropy was related to the direction of primary deposition. They suggested, however, that electrical anisotropy in this setting was associated with the meso-scale structure of the channel and interchannel areas as well as the channel fill, rather than micro- or macro-scale elements.

Penttinen et al. (1999) compared EM anisotropy to the orientation of clast fabrics in till. They suggested that, where till is thick, the maximum direction of resistivity will be perpendicular, and the maximum direction of conductivity will be parallel, to the principal orientation of clast fabric. They further suggested that EM anisotropy is directly related to primary deposition of till and that electrical anisotropy can be used to infer ice flow direction. They indicated that, where till is thin (<2 m), underlying sediments and bedrock will influence the EM anisotropy measured at surface. Sutinen et al. (2009) continued with this theme by investigating complex morainal ridges in south-central Finnish Lapland. This work showed that

the EM conductivity anisotropy was parallel or sub-parallel to the orientation of the morainal ridges and they implied that this orientation is perpendicular to ice flow. Based on sedimentological and this orientation data, they concluded that the ridges are not transverse bedforms (rogen moraines) formed directly from flowing ice, but are attributed to debris-flows deposited during sliding bed conditions.

Sutinen et al. (2010) examined the relationship between the orientation of streamlined landforms and EM anisotropy. They imply that electrical anisotropy is effective in delineating sediment anisotropy (fabric orientation). They consider the direction of the maximum EM conductivity (i.e. perpendicular to the maximum direction of resistivity anisotropy) to be indicative of the direction of sediment transport and deposition. They explain the discrepancy between the orientation of the streamlined landforms and the direction of anisotropy observed in their study, as the result of inheritance of a depositional fabric of an earlier ice-flow direction and argue that this inheritance is proof that the cores are unaltered and that the landforms are erosional.

The present study, located in northeastern British Columbia (Fig. 5.1), takes a similar approach to that of Sutinen et al. (2010) and seeks to test the notion that EM anisotropy can be used to infer ice flow direction. The study is conducted on flutes and drumlins (streamlined landforms) that make up the Kiskatinaw streamlined landform field. These streamlined landforms are associated with the Cordilleran Ice Sheet as it flowed out of the Rocky Mountains onto the interior plains (Mathews, 1980). Initially the flow was likely deflected to the north by the Laurentide Ice Sheet, but as the Laurentide Ice Sheet receded to the east, the Cordilleran ice flowed more towards the northeast (Fig. 5.1).

Though we recognize that there is no universally accepted explanation for the formation of streamlined landforms composed of sediment (e.g. Shaw, 1983, 2002, 2010; Shaw and Kvill, 1984; Menzies and Rose, 1987; Benn and Evans, 2006) we adopt the theory that the landforms in the Kiskatinaw streamlined landform field are subglacial bedforms that developed mainly as a result of a deforming bed, and whose morphometric characteristics (i.e. elongation) reflect ice flow dynamics involving shear stress and flow velocity as well as substrate conditions (e.g. Smalley and Unwin, 1968; Boulton, 1987; Boulton and Hindmarsh, 1987; Menzies and Rose, 1987; Boyce and Eyles, 1991; Benn, 1994a; Iverson et al., 1995; Hart, 1998; van der Meer et al., 2003; Stokes et al., 2007, Ó Cafaigh et al., 2013).

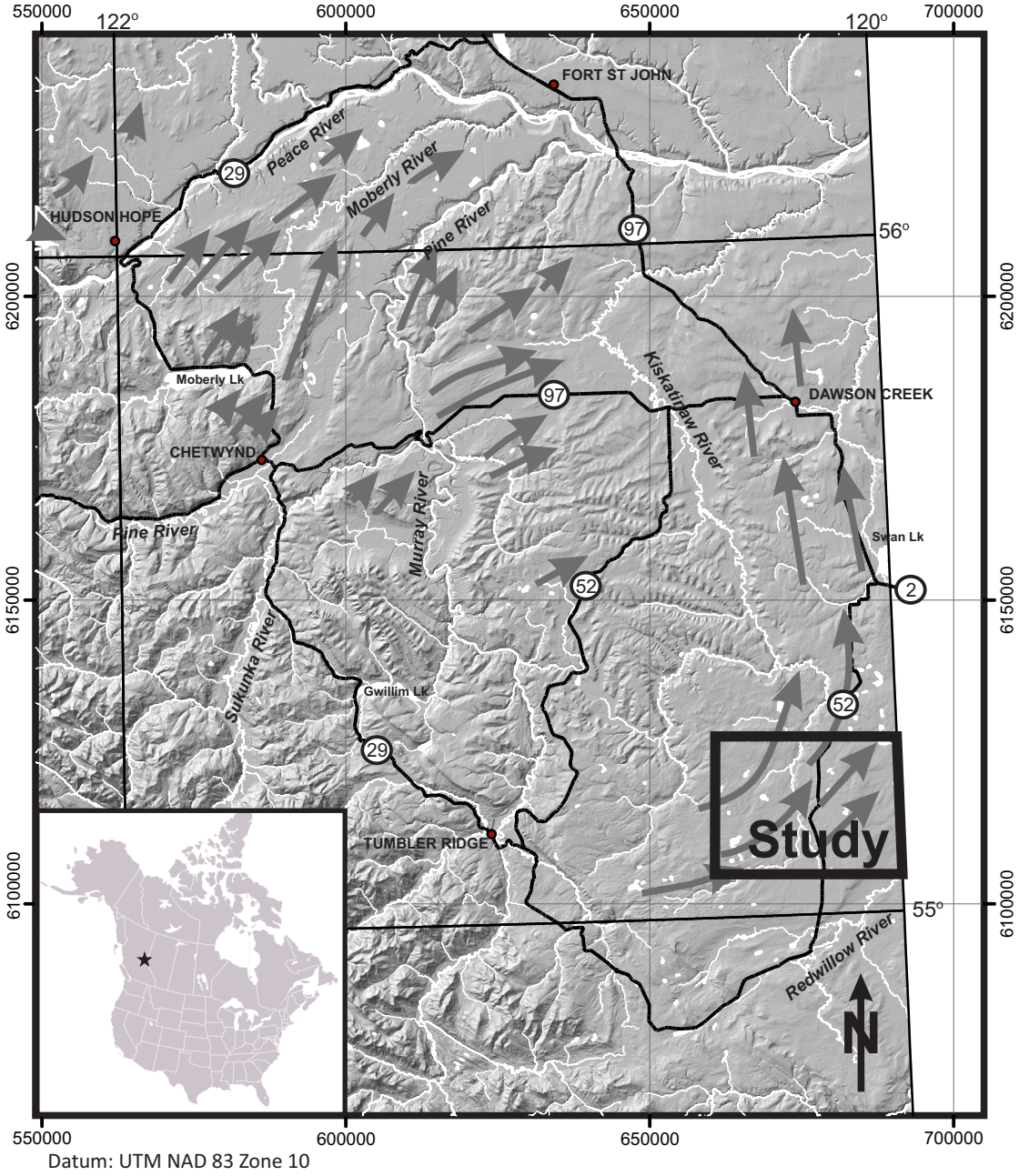

Figure 5.1. Study area in northeast British Columbia, Canada with generalized ice-flow (arrows).

5.2 Methodology

In order for this field experiment to be valid, resistivity data must be derived from a single homogeneous (though heterolithic) unit (till) and not from multiple stratigraphic units of various genetic origins or from bedrock (Penttinen et al., 1999). Where direct observations could be made, streamlined landforms in this study consisted only of diamict (interpreted as till). However, because there were relatively few exposures, the assumption that there was only one sedimentary unit present in the landforms was tested through a 2-D resistivity inversion model of the subsurface using capacitively coupled resistivity (CCR) data. CCR survey lines were collected in the winter with an OhmMapper^{TM} instrument (Geometrics Limited, San Jose, California) along seismic cutlines near the station where the azimuthal resistivity was measured (Fig. 5.2). Survey lines were inverted using RES2DINV^{TM} software (Geotomo Software; Griffiths and Barker, 1993; Loke and Barker, 1996). RES2DINV^{TM} provides a 2-D resistivity inversion of the subsurface for data obtained from electrical imaging surveys (deGroot-Hedlin and Constable, 1990; Griffiths and Barker, 1993; Loke and Barker, 1996). Each data point along the CCR lines was inspected and poor data points (data spikes) were removed.

The azimuthal EM conductivity data were collected with an EM31-MK2 conductivity meter (Geonics Limited, Mississauga Ontario). The instrument uses EM induction to measure the average ground conductivity (mS/m) over 5 to 6 m with the instrument oriented in its standard position (vertical dipole) or 2 to 3 m with the instrument on its side (horizontal dipole), depending on ground conductivity (McNeill, 1980).

Collection sites were on the crest of streamlined landforms located using a hand-held global positioning system (GPS). A piece of plywood marked at 10° increments was oriented with a compass so that 0° corresponded with north. The instrument was aligned to the north-south starting direction and rotated so that measurements were recorded every 10° from 0° to 360° (Taylor and Fleming, 1988; Cohn and Rudman, 1995; Sandberg and Jagel, 1996). Due to reciprocity, data values 180° apart should be identical but variation in readings occurs because of background signal noise. To limit the effects of noise, each paired value through 360° was averaged. Conductivity was converted to apparent resistivity and plotted on scaled radial plots to emphasize anisotropy (Taylor and Flemming, 1988).

Resistivity anisotropy was summarized using the least-squares fit of an ellipse to the data using the method and computer code (FITELLIPSE) from Hart and Rudman (1997). This code

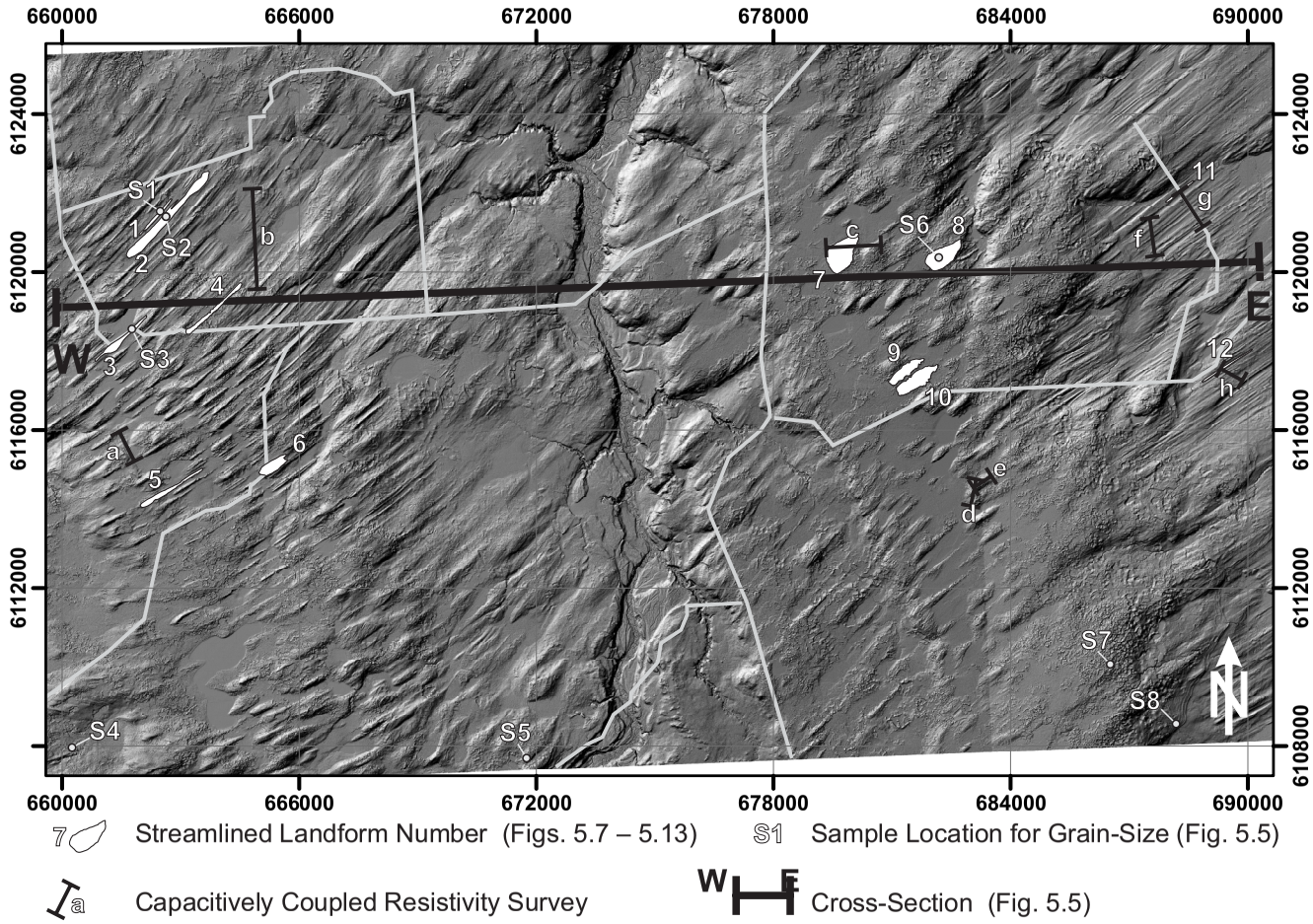

Figure 5.2. Digital elevation model of streamlined landforms within the Kiskatinaw streamlined landform field. Numbers refer to the landforms where electrical anisotropy was determined (detailed images shown in Figs. 5.7 – 5.13). Numbers preceded by "S" (e.g. S1) refer to sites where till matrix grain-size was determined (shown in Fig. 5.5c). Black lines represent capacitively coupled resistivity surveys (e.g. Fig. 5.3) and the west to east cross-section (blue line) is shown in Fig. 5.15 (2 x vertical exaggeration; Datum: UTM NAD 83).

establishes a best-fit ellipse with principle -axes ρ_{max} and ρ_{min} (i.e. the maximum and minimum perpendicular resistivity value, respectively), angle of rotation, coefficient of anisotropy, and a measure of fit (R^2) based on the percent reduction of variance from a best-fit circle ($\sigma^2_{(circle)}$) to a best-fit ellipse ($\sigma^2_{(ellipse)}$).The computer code accepts a sequence of paired data in the form of an angle (degrees) and a positive value (resistivity). Data must be "balanced" so that opposite vectors sum to zero, achieved in this study by assigning the averaged resistivity value of conjugate pairs to both angles (Φ and $\Phi + 180^o$). The program calculates a best fit circle from the mean resistivity value ($\bar{\rho}$), and the variance ($\sigma^2_{(circle)}$). The variance is a measure of the goodness-of-fit for the circular model and is later compared to the variance of the elliptical model ($\sigma^2_{(ellipse)}$). The program generates an elliptical model by the least-squares method (Gander et al., 1996; Varah, 1996). An ellipse centred at the origin is given in rectangular coordinates by an equation:

$$ax^2 + bxy + cy^2 = \bar{\rho}^2 \qquad (1)$$

Hart and Rudman (1997) explain that the use of $\bar{\rho}^2$ on the right hand side of the equation simplifies comparison of the circular versus elliptical models by making the scale the same. The data are converted from polar coordinates (Φ_i, ρ_i) to rectangular coordinates (x_i, y_i), and form the vector XX whose components are x_i^2 (similarly for YY and XY). The variance of the N data points from the model

$$\sigma^2_{(ellipse)} = \frac{1}{N}\sum(ax^2 + bxy + cy^2 - \bar{\rho}^2) \qquad (2)$$

is minimized by least-squares solution to

$$\mathbf{A}\chi = \beta \qquad (3)$$

where the three columns of matrix **A** are **XX**, **XY**, and **YY**, β is a vector whose components are all $\bar{\rho}^2$ and χ is the vector of unknown coefficients [a,b,c from Eq. 1]. The program solves for χ. The value of the variance that the elliptical model minimizes relative to the circular model is referred to by Hart and Rudman (1997) as the "reduction in variance" and is computed as the percentage of the variance from the circular model that is removed by the elliptical model:

$$R^2 \frac{\sigma^2{}_{(circle)} - \sigma^2{}_{(ellipse)}}{\sigma^2{}_{(circle)}} \; 100\%$$

The EM data are compared to the orientation of the landforms on which they were collected through high resolution (approximately 1 m) digital elevation model (DEM), generated from a light detection and ranging (LiDAR) survey. The landforms were digitized by hand at the

inflection of 1 m contours in a geographic information system (GIS). The length, width, and orientation of the landforms were determined by fitting a bounding rectangle to the outline of the landform and recording the maximum length (l: a-axis), minimum width perpendicular to the a-axis (w: b-axis), and the azimuthal orientation of these axes. The shape of the landform is expressed as an elongation ratio (l/w).

Three pebble fabrics were collected from opportune sites where excavation for road construction exposed the interior of the streamlined landform. The direction of the long axis (a-axis) and its dip were measured on each clast with a/b axis ratios of >1.5/1 (Holmes, 1941; Doweswell and Sharp, 1986; Benn, 2004). Clast a-axes were generally 2 to 4 cm in length with rare clasts as large as 25 cm. Fabric data were plotted as bidirectional rose plots and superimposed on resistivity diagrams from nearby stations.

The grain-size distribution of the matrix (< 2.0 mm) from eight till samples was determined for various sites in the study area. These samples were washed and sieved to Wentworth classifications (Wentworth, 1922) and the proportion of silt and clay from the <0.63 mm size fraction determined by the hydrometer method. These data were compared to the distribution of resistivity data from streamlined landforms included in the CCR inversions to develop a proxy for grain-size variations. Resistivity distribution data in till were compiled from the inverted CCR profiles using a GIS. Values interpreted to be from bedrock or swampy surficial materials were excluded.

5.3 Results

5.3.1 CCR Survey

Eight CCR survey lines were collected and processed (Fig. 5.2). The results from all lines were very similar and can be differentiated into two zones, a lower zone with values typically below 50 ohm-m and an upper zone typically between 50 and 300 ohm-m. The lower zone is interpreted to be fine grained bedrock, such as shale or siltstone. The upper zone is interpreted to be diamict (e.g. Fig. 5.3). If these interpretations are correct there are more than 4 m of diamict throughout the streamlined landform field. This thickness is sufficient for the oriented resistivity survey to reflect only the anisotropy of the diamict and not the underlying bedrock (Penttinen, 1999).

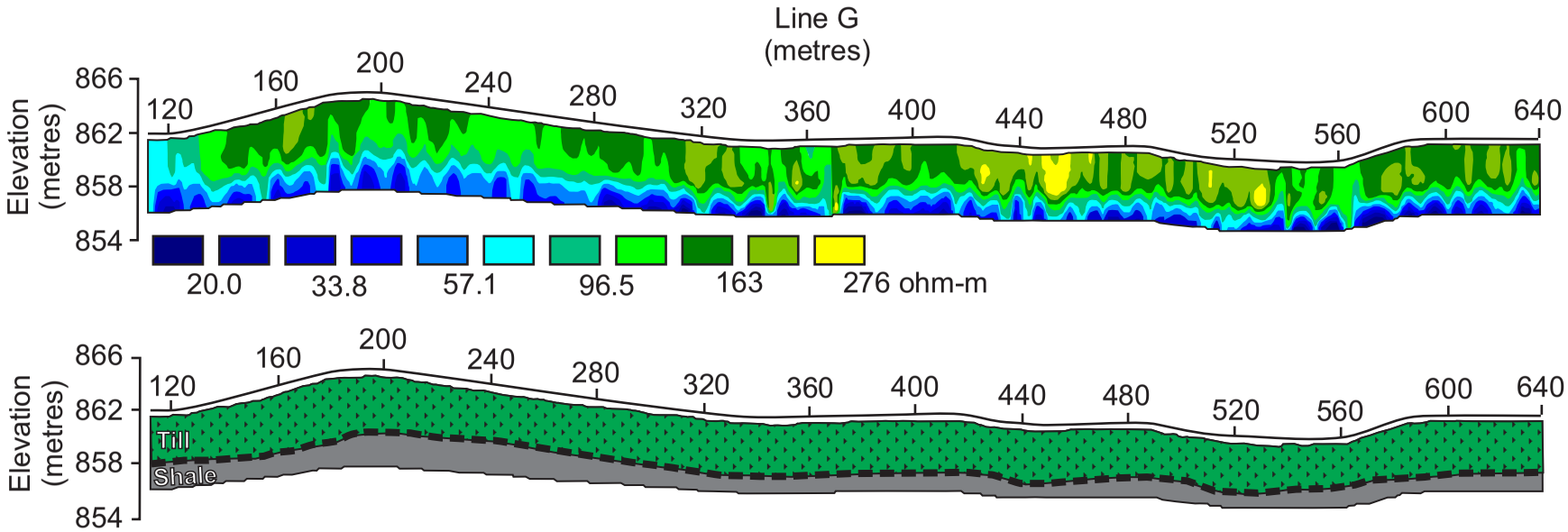

Figure 5.3. An example of a typical capacitively coupled resistivity inversion along a portion of Line G (location shown on Fig. 5.2); Top: inversion model from RES2D software; Bottom: interpreted section showing till over shale.

There is considerable variation in the distribution of resistivity values along the survey lines (Fig. 5.4; Table 1). In general, lines A, B, F, G, and H have near normal distribution and a more limited range in values. Lines C and D, collected in the east-central portion of the study area where streamlined landforms have low elongation ratios, have higher mean values, a wider range of values, more outliers, and are heavily skewed to the right. The distribution from Line E is intermediate between lines C and D and lines F, G, and H. This suggests that there is more variability in the grain size of the tills in the central region than in the rest of the field.

5.3.2 Sediments and Landforms

The landforms typically consist of silty-clay diamict with <25% clasts (visual field estimate; Fig. 5.5a). Clasts commonly are striated and facetted. The till at S6 is an exception and has much higher clast content (~55%) than the other tills in the area (Figs. 5.5a and 5.5b). Matrix grain-size analysis (Figs. 5.2 and 5.5) is relatively consistent (Fig. 5.5c), however, sample S1 and S6 have slightly higher sand components than other tills and samples S8 and S6 have the highest clay component.

The till fabrics (Figs. 5.7 and 5.11) show that the orientations of clasts are parallel to the orientations of the long axes of the elongate landforms. Landforms 1 and 2 have elongation rations of 15 and 11, respectively, and have a strong, narrow fabric (Fig. 5.7). Landform 8, with an elongation ratio of 2, has a fabric that is multi-modal though the principal eigenvector is oriented nearly parallel with the long axis of the landform (Fig. 5.11).

The shape of the streamlined landforms varies across the study area (see Fig. 5.2). Landforms in the northwest have high elongation ratios and show a long axis orientation that deviates from a east-northeast flow trajectory to a northeast trajectory and eventually to a northern flow trajectory (north of the study area). Landforms are 5 – 10 m high, 400 to > 1000 m long, and <50 to 400 m wide. Many also have abundant short rectilinear ridges superimposed, and commonly concentrated, on the flanks or tails of the landforms (Figs. 5.7 – 5.9). In the southwest, landforms are similar to those in the northwest, but tend to have lower elongation ratios and do not show a major change in trajectory. In the central region of the study area, landforms have low elongation ratios and indicate flow to the northeast. Landforms are typically

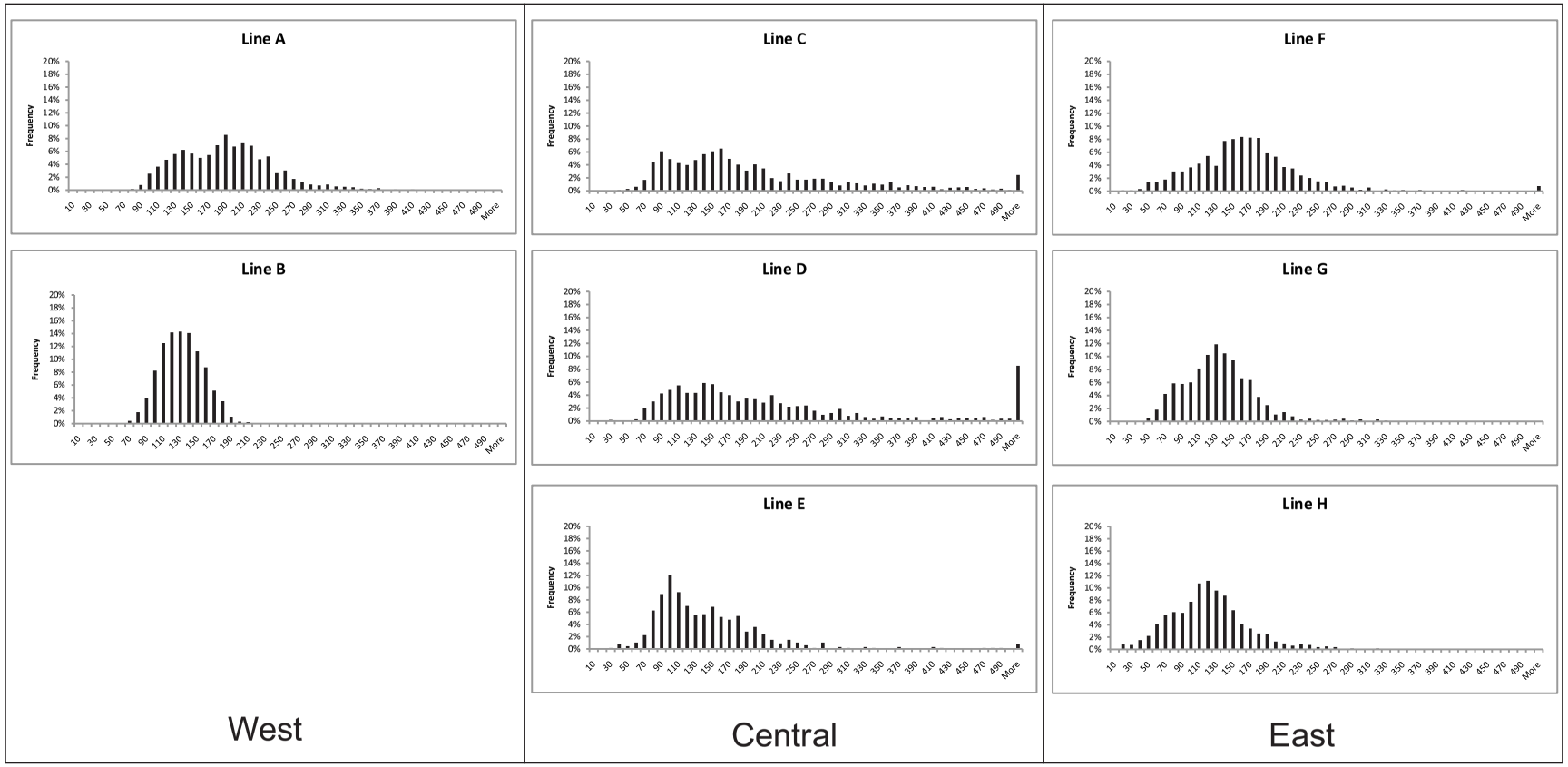

Figure 5.4. The distribution of resistivity values along CCR sections for the west, east-central, and east portions of the study area.

Table 5.1. Descriptive statistics of the distribution of resistivity values from the inverted OhmMapperTM survey lines.

	LineA	*LineB*	*LineC*	*LineD*	*LineE*	*LineF*	*LineG*	*LineH*
Mean	184.90	127.18	195.11	252.18	139.25	161.89	128.94	116.80
Standard Err.	1.45	0.37	2.54	8.08	2.69	1.70	0.95	1.13
Median	183.56	126.34	161.27	174.69	124.46	156.76	126.65	114.08
Mode	193.65	135.79	103.34	185.38	157.14	173.62	153.42	62.59
Standard Dev.	53.96	25.57	116.07	270.75	69.52	71.29	43.96	45.95
Sample Var.	2911.78	653.80	13471.68	73307.60	4833.54	5082.74	1932.71	2111.27
Kurtosis	0.32	0.43	4.19	30.43	10.80	15.79	4.92	1.39
Skewness	0.52	0.32	1.79	4.46	2.59	2.68	1.34	0.72
Range	327.81	231.78	783.36	3391.15	543.67	713.01	402.24	321.09
Minimum	77.47	50.77	31.96	18.75	28.10	18.49	41.74	12.30
Maximum	405.28	282.55	815.32	3409.90	571.77	731.50	443.98	333.39
Sum	254423	592781	406210	283448	93298	286388	276832	192601
Count	1376	4661	2082	1124	670	1769	2147	1649

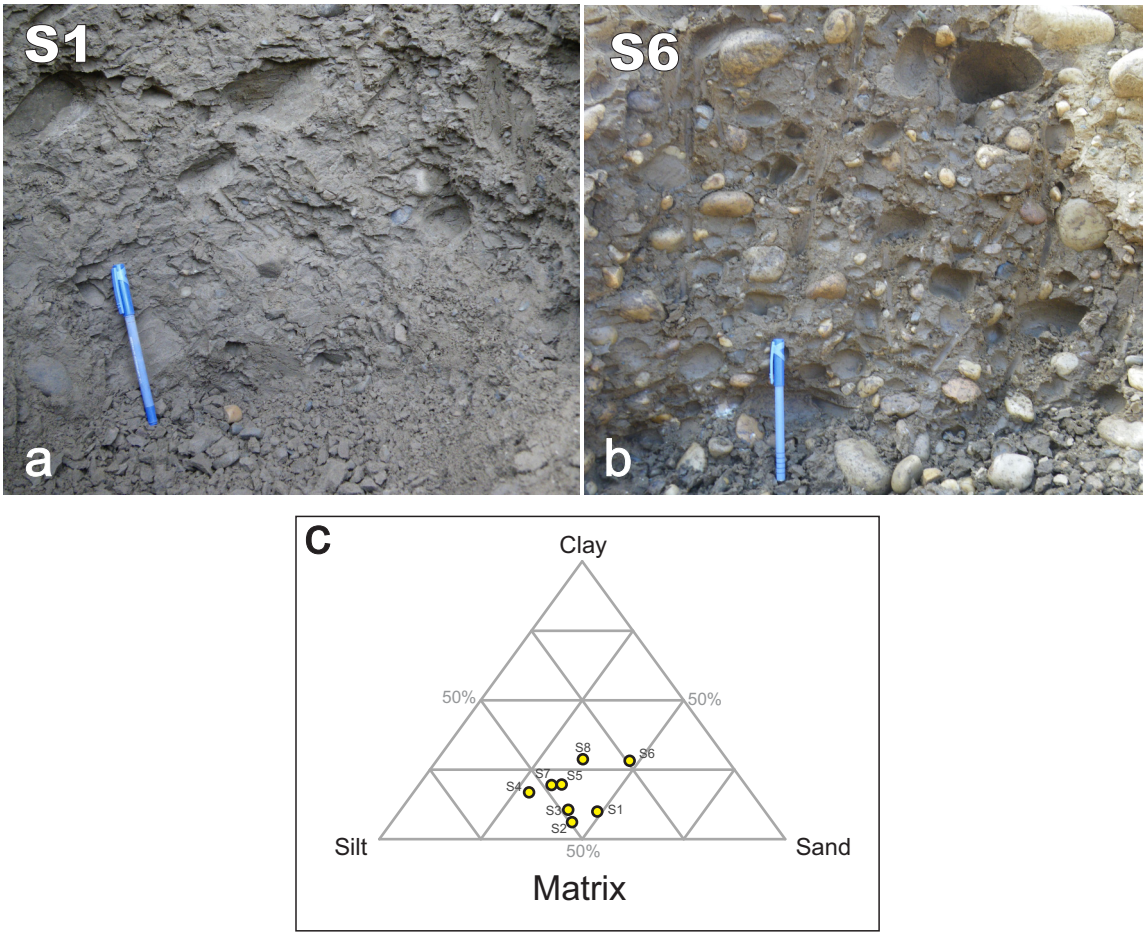

Figure 5.5. Photographs of a) clay rich till common in the study area and b) gravel rich till typical of the east-central portion of the area; c) Ternary plot of matrix composition (locations shown in Fig. 5.2).

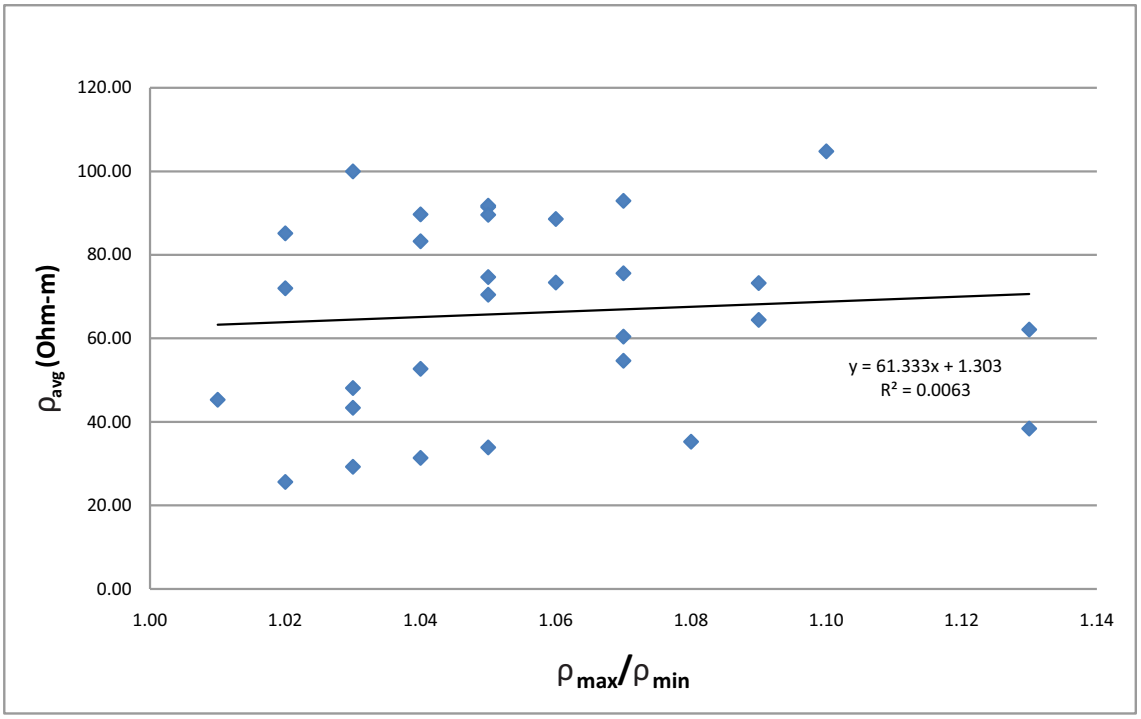

Figure 5.6. There is no correlation between the average resistivity at a station and the strength of the related anisotropy.

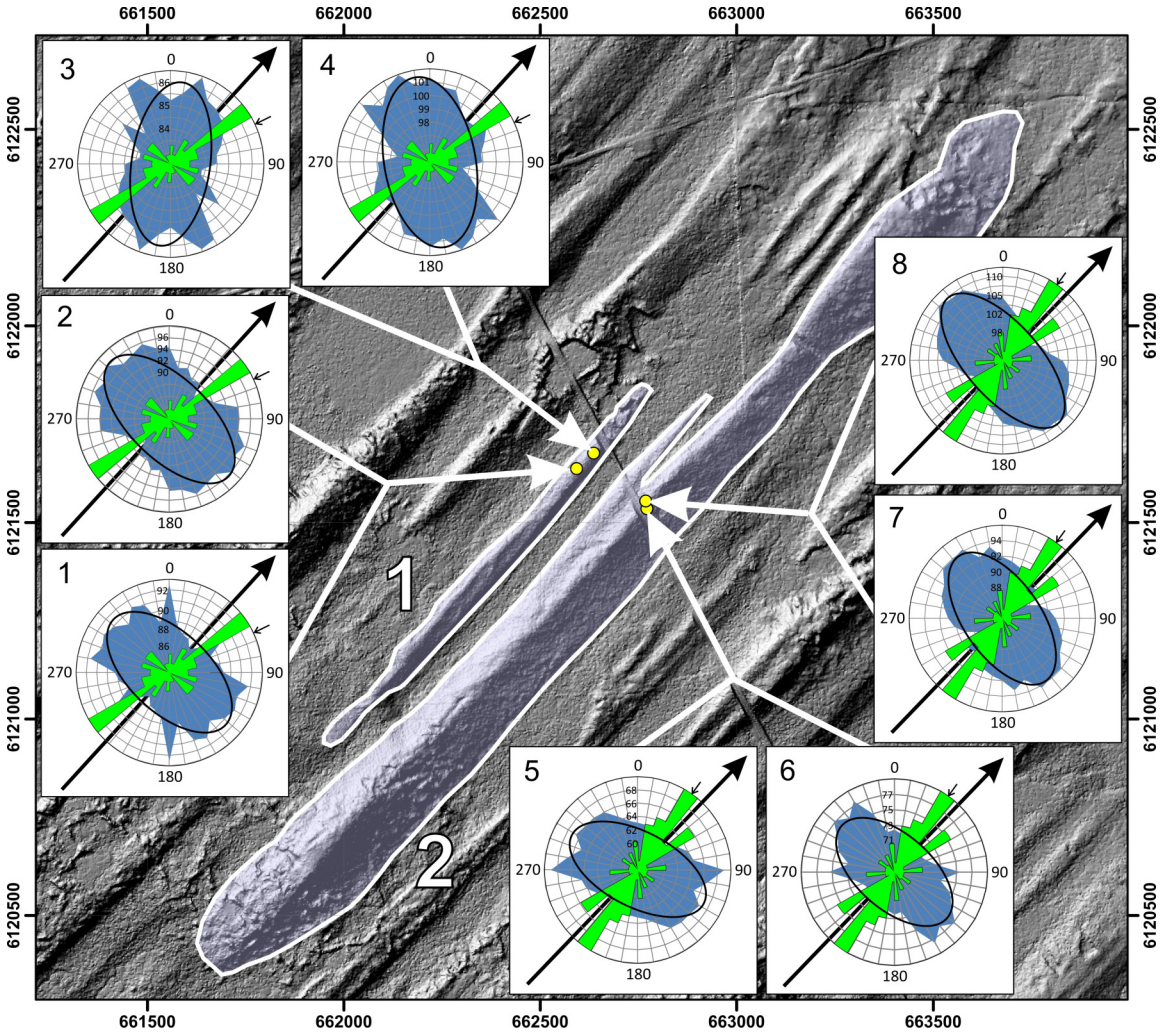

Figure 5.7. DEM of Landform 1 and 2 with resulting measurements for stations 1 – 8 (yellow circle = Station location; blue polygon = resistivity rose plot with black best-fit-ellipse; green polygon = clast fabric rose plot with small arrow indicating average orientation; black arrow = orientation of the long axis of the landform).

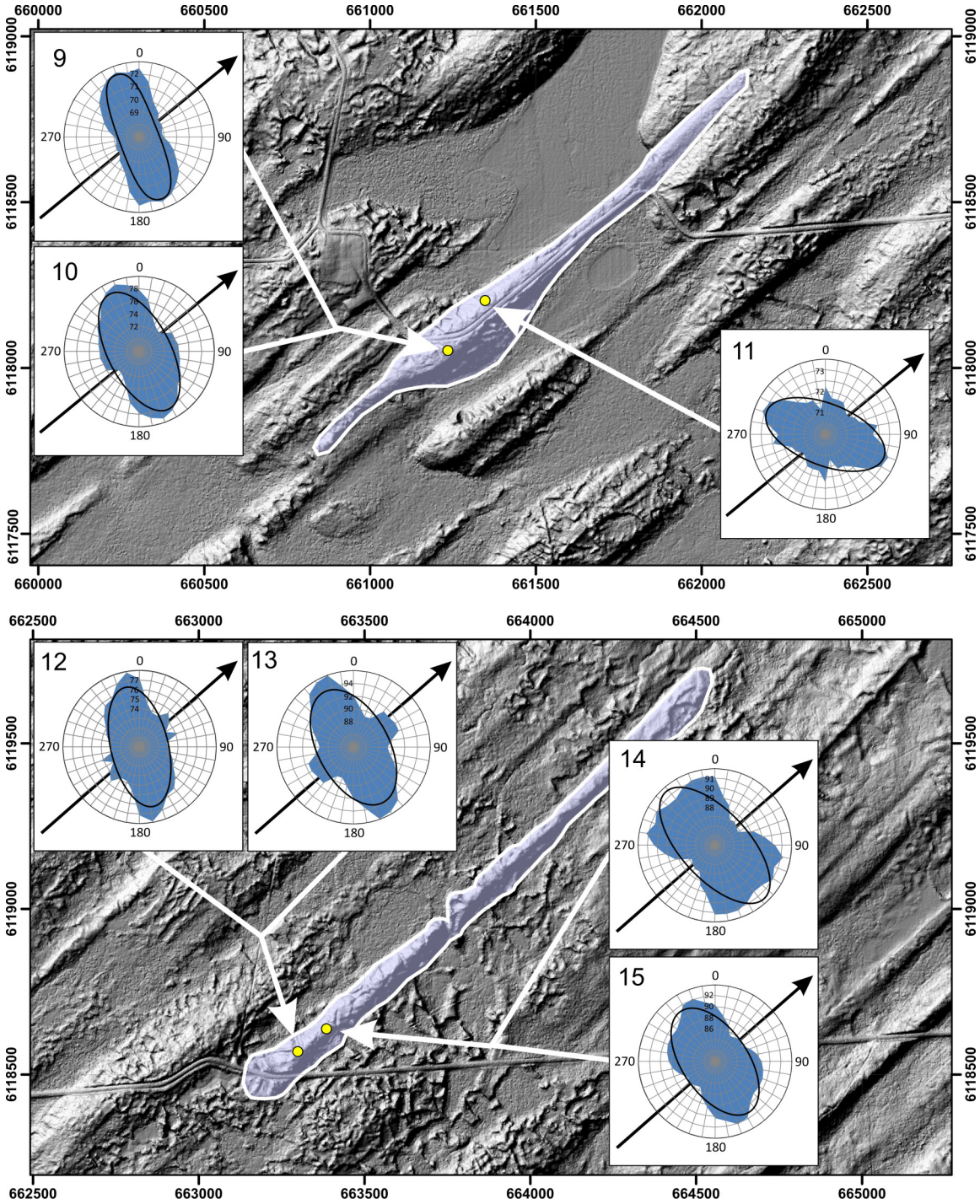

Figure 5.8. DEM of landforms 3 (a) and 4 (b) with resulting measurements for stations 9 – 15 (yellow circle = Station location; blue polygon = resistivity rose plot with black best-fit-ellipse; black arrow = orientation of the long axis of the landform).

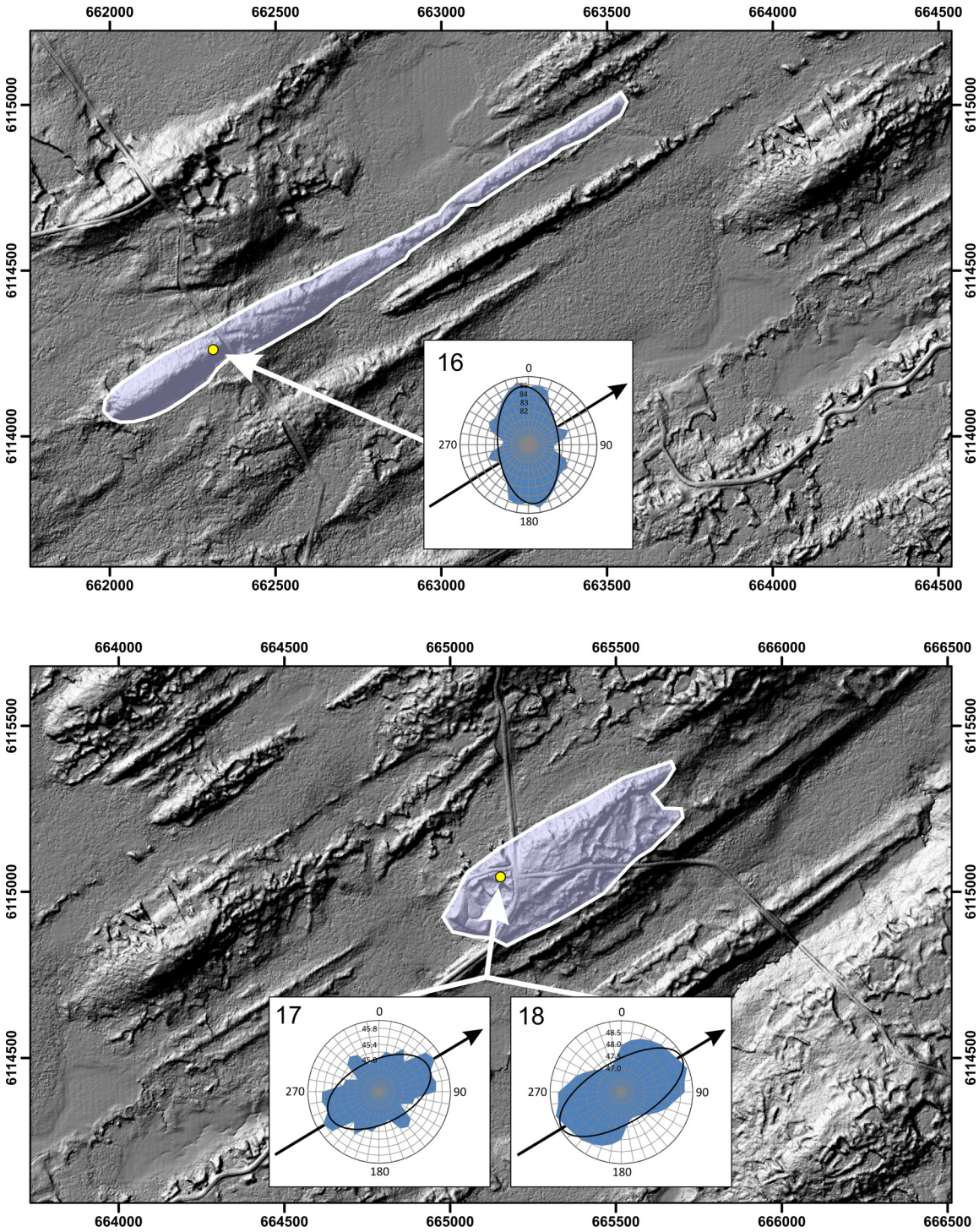

Figure 5.9. DEM of landforms 5 (a) and 6 (b) with resulting measurements for stations 15 – 18 (yellow circle = Station location; blue polygon = resistivity rose plot with black best-fit-ellipse; black arrow = orientation of the long axis of the landform).

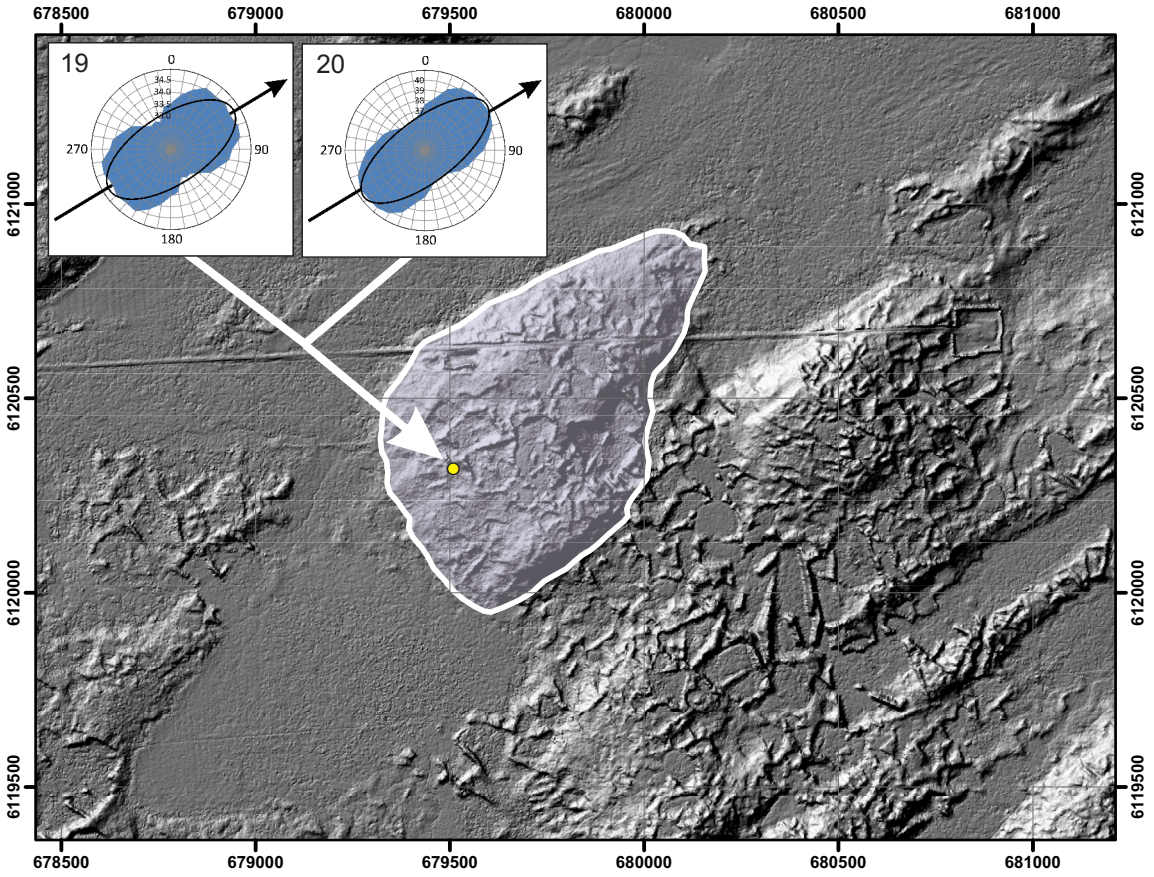

Figure 5.10. DEM of landform 7 with resulting measurements for stations 19 and 20 (yellow circle = Station location; blue polygon = resistivity rose plot with black best-fit-ellipse; black arrow = orientation of the long axis of the landform).

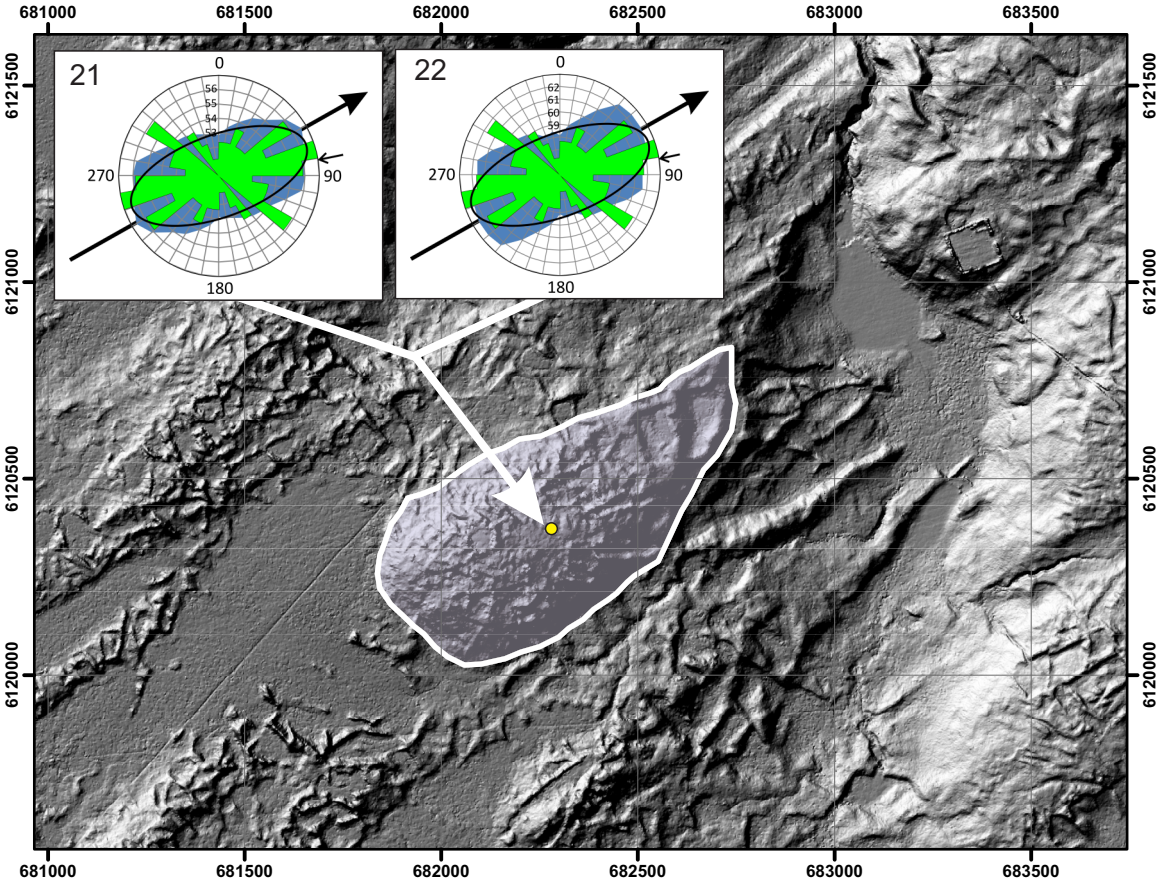

Figure 5.11. DEM of landform 8 with resulting measurements for stations 21 and 22 (yellow circle = Station location; blue polygon = resistivity rose plot with black best-fit-ellipse; green polygon = clast fabric rose plot with small arrow indicating average orientation; black arrow = orientation of the long axis of the landform).

about 10 m high, 400 to 800 m long, and 200 to 500 m wide. Landforms are ornamented with hummocky terrain and short rectilinear ridges and depressions are abundant (Figs. 5.10 – 5.12). Landforms on the west side of the area have very high elongation ratios and indicate a northwest flow trajectory. Landforms are low (2 – 10 m high), >1000 m long, and <100 m wide (Fig. 5.13). The hummocky terrain and rectilinear ridges are absent on these features.

5.3.3 Azimuthal Resistivity Data and Streamlined landforms

Thirty oriented resistivity surveys were conducted at 16 sites on 12 streamlined landforms (Fig. 5.2; Table 5.2). In general, resistivity values associated with the EM-31 instrument are slightly lower than the values associated with the OhmMapper^{TM} instrument. EM-31 values range from 25 – 110 ohm-m. In most cases there is an appreciable reduction in the variance between the elliptical model and the circular model, but there are cases where this reduction is low, i.e. <67% (e.g. surveys 1, 3, 4, 11, 13, and 17; Table 2). The data from stations 1, 3, and 4 are generally noisy, although the overall pattern is clear (Fig. 5.7). There is very little difference between the maximum and minimum resistivity in surveys 3, 11, 17, and 29, therefore, till at these locations is isotropic (Table 2). Survey 13 appears to be bimodal (Fig. 5.8b). In most surveys, there is measurable electrical anisotropy in the till, however, the difference between maximum resistivity (ρ_{max}) and the minimum resistivity (ρ_{min}) can be small (Table 2). The percent difference between ρ_{max} and ρ_{min} from the fit of the elliptical model averages 1.3% and ranges from 0.3 – 3.1%. There is no significant relationship between the average resistivity and the ratio of ρ_{max} and ρ_{min}, implying that the degree of anisotropy is not a function of resistivity/conductivity (Fig. 5.6).

Two clear relationships between the orientation of the resistivity ellipse and the long axis of the streamlined landforms emerge from the data (Figs. 5.7– 5.13). Where the elongation ratio (l/w) of the landform is 3 or less, the orientation of the principal axis of the resistivity ellipse is nearly parallel to the long axis of the landform (Fig. 5.14a). Where l/w is more than 3, the principal axis of the resistivity ellipse is nearly perpendicular to the long axis of the landform (Fig. 5.14b).

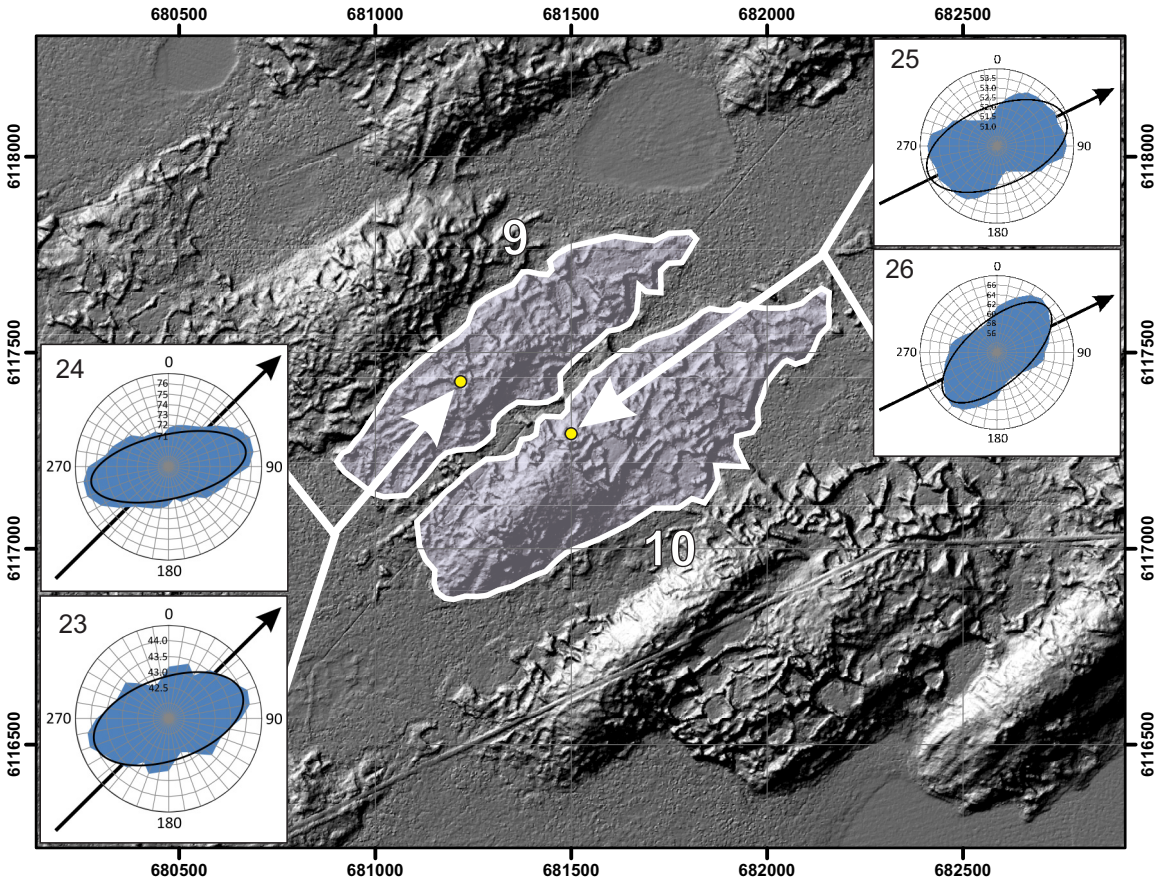

Figure 5.12. DEM of landforms 9 and 10 with resulting measurements for stations 23 – 26 (yellow circle = Station location; blue polygon = resistivity rose plot with black best-fit-ellipse; black arrow = orientation of the long axis of the landform).

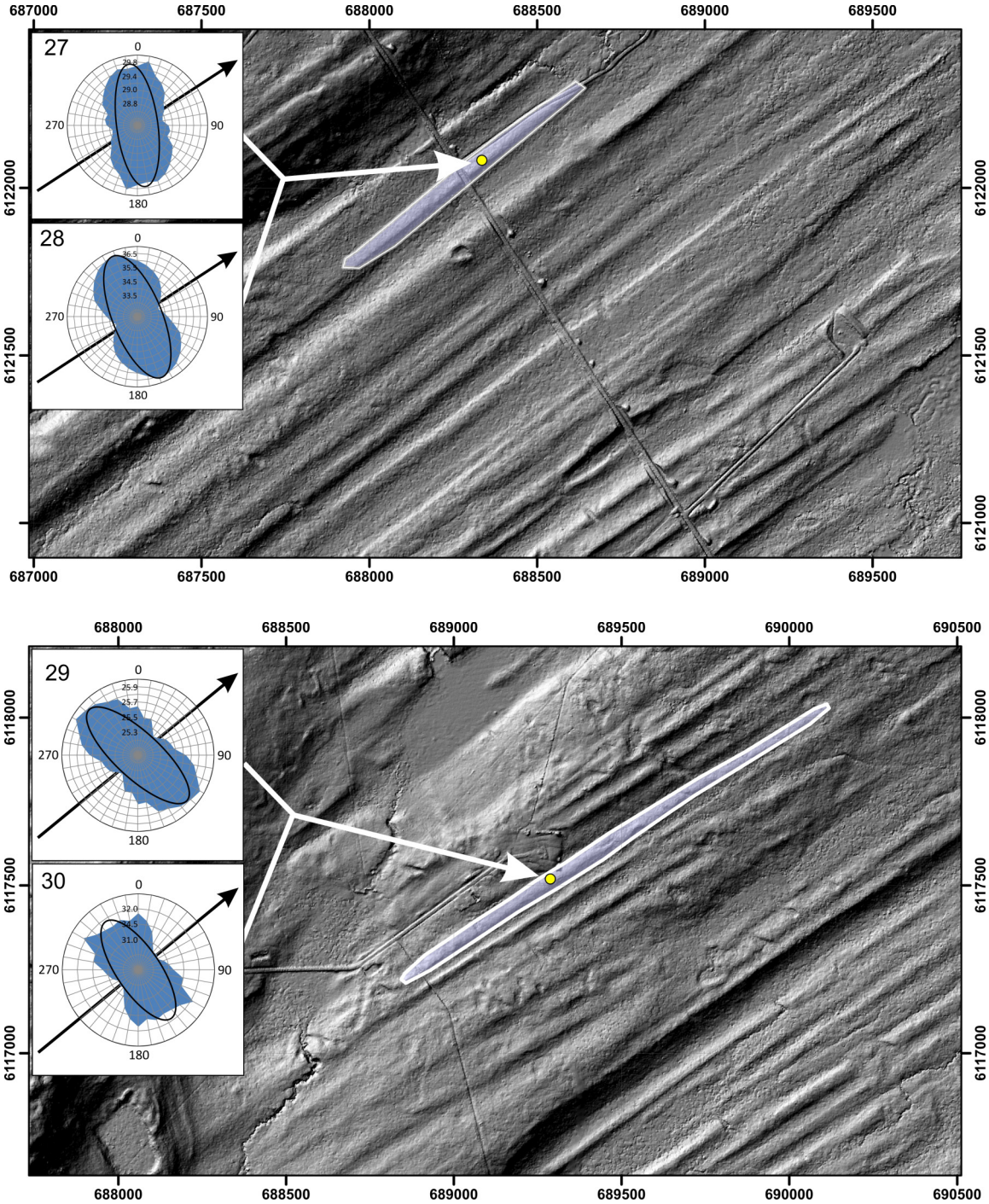

Figure 5.13. DEM of landform 11 (a) and 12 (b) with resulting measurements for stations 27 – 30 (yellow circle = Station location; blue polygon = resistivity rose plot with black best-fit-ellipse; black arrow = orientation of the long axis of the landform).

Table 5.2. Summary of the orientation of the electrical anisotropy ellipse, the landforms, and the pebble fabrics.

			Summary Ellipse							Landform Characteristics						Fabric
Station	Loop Position	Time Averaged	Variance (Elliptical Model)	Reduction in Variance (%)	ρ_{max} (ohm-m)	ρ_{min} (ohm-m)	ρ_{max}/ρ_{min}	Azimuth ρ_{max}	Azimuth ρ_{min}	Landform Number	Azimuth A_{max}	Azimuth A_{min}	A_{max} (m)	A_{min} (m)	A_{max}/A_{min}	Primary Azimuth
1	Vertical	No	1.08	58	91.42	87.96	1.04	133.3	43.3	1	42.5	132.5	1227	81	15	65
2	Horizontal	No	1.28	80	96.20	89.67	1.07	134.3	44.3							
3	Vertical	Yes	0.21	66	86.06	84.25	1.02	8.3	98.7							
4	Horizontal	Yes	0.50	67	101.39	98.57	1.03	169.8	79.8							
5	Vertical	No	0.96	79	67.12	61.73	1.09	117.5	27.5	2	44.1	134.1	2987	270	11	35
6	Horizontal	No	0.83	87	76.56	69.93	1.09	131.2	41.2							
7	Vertical	Yes	0.33	90	93.90	89.04	1.05	145.1	55.1							
8	Horizontal	Yes	0.71	94	109.57	100.01	1.10	138.7	48.7							
9	Vertical	No	0.07	96	72.28	68.63	1.05	160.6	70.6	3	50.7	140.7	1738	217	8	-
10	Horizontal	No	0.85	81	78.28	72.90	1.07	152.7	62.7							
11	Vertical	No	0.13	58	72.60	71.41	1.02	111.5	21.5							
12	Vertical	Yes	0.59	72	76.43	72.94	1.05	166.5	76.5	4	48.8	138.8	1892	154	12	-
13	Horizontal	Yes	2.12	51	93.84	89.72	1.05	151.7	61.7							
14	Vertical	Yes	0.61	77	91.59	87.59	1.05	137.4	47.4							
15	Horizontal	Yes	0.77	81	91.18	85.99	1.06	145.4	55.4							
16	Vertical	No	0.35	79	84.92	81.60	1.04	173.9	83.9	5	58.2	148.2	1833	148	12	-
17	Vertical	Yes	0.04	52	45.59	45.02	1.01	63.4	153.4	6	59.0	149.0	831	279	3	-
18	Horizontal	Yes	0.02	94	48.92	47.31	1.03	59.2	149.2							
19	Vertical	Yes	0.02	94	34.78	33.00	1.05	56.9	146.9	7	59.1	149.1	1028	695	1	-
20	Horizontal	Yes	0.04	99	40.69	36.12	1.13	53.0	143.0							
21	Vertical	Yes	0.05	97	56.40	52.89	1.07	70.1	160.1	8	60.8	150.8	1080	495	2	81
22	Horizontal	Yes	0.16	93	62.52	58.33	1.07	69.2	159.2							
23	Vertical	Yes	0.03	84	43.95	42.82	1.03	70.5	160.5	9	45.4	135.4	1058	311	3	-
24	Horizontal	Yes	0.22	92	75.64	71.12	1.06	77.3	167.3							
25	Vertical	Yes	0.05	92	53.75	51.66	1.04	67.9	157.9	10	64.0	154.0	1234	440	3	-
26	Horizontal	Yes	0.38	95	65.92	58.29	1.13	48.7	138.7							
27	Vertical	Yes	0.00	96	29.74	28.77	1.03	172.3	82.3	11	57.0	147.0	1511	58	26	-
28	Horizontal	Yes	0.02	98	36.64	33.88	1.08	158.0	68.0							
29	Vertical	Yes	0.00	96	25.90	25.35	1.02	132.8	42.8	12	50.7	140.7	898	63	14	-
30	Horizontal	Yes	0.03	84	31.92	30.84	1.04	146.0	56.0							

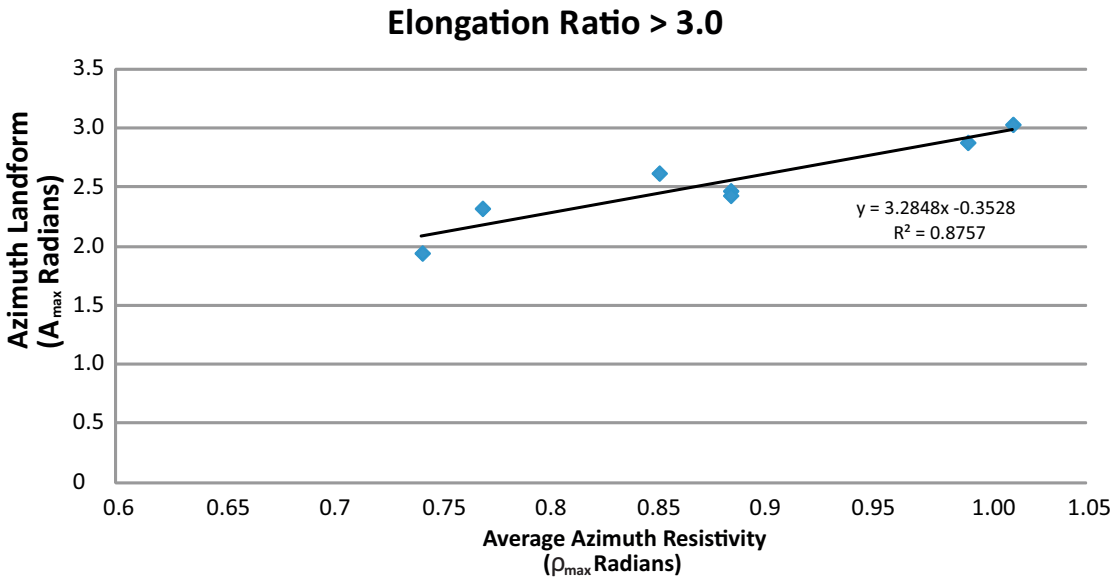

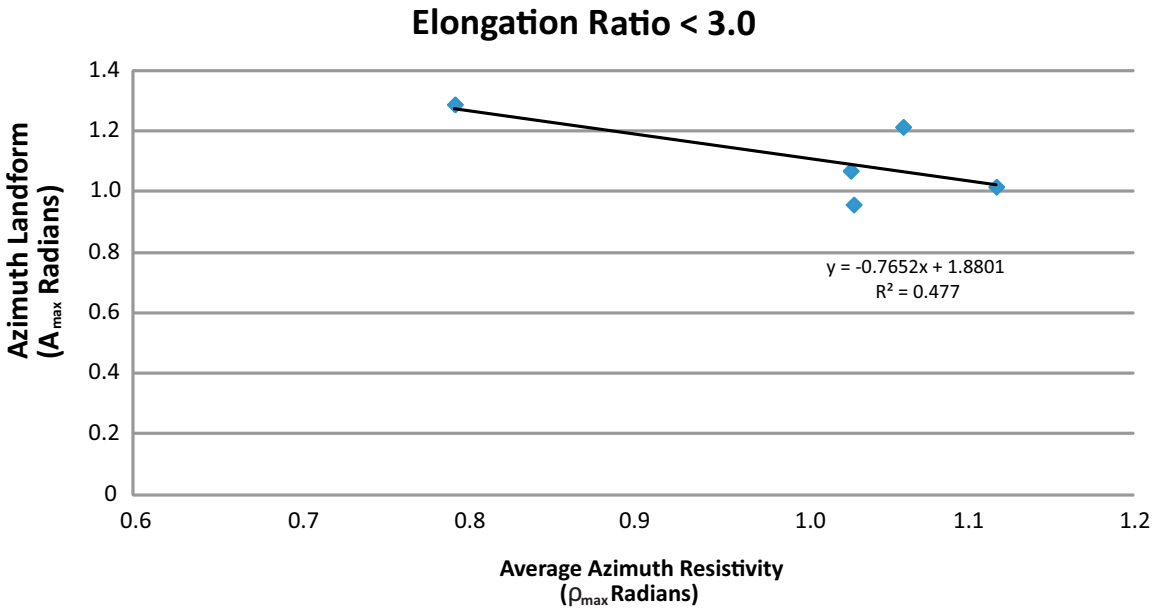

Figure 5.14. There is a strong correlation between the orientation of the long axis of a landform (A_{max}) and average orientation of the maximum resistivity (ρ_{max}) for landforms with elongation ratios greater than 3 (top). The correlation is weaker for landforms with elongation ratios less than 3 (bottom).

5.4 Discussion

The orientation of the principal axis of the resistivity ellipse is perpendicular to the orientation of the till fabrics and the long axis of the landforms where landforms have elongation ratios greater than 3. Thus, the till in these landforms is conductive in the direction of ice flow and in the inferred direction of sediment transport. The correlation between the orientation of the principle direction of electrical anisotropy (ρ_{max}) and the principle axis of landforms (A_{max}) with elongation ratios greater than 3 has an R^2 value of 0.87 (Fig. 5.14a). Therefore, where l/w>3, the orientation of ρ_{max} is an excellent predictor of the orientation of the A_{max}. This is consistent with the findings of Penttinen et al. (1999), Sutinen et al. (2009) and Sutinen et al. (2010). The orientation of the principal axis of the resistivity ellipse, however, comes close to parallel to the orientation of the till fabrics and the long axis of the landforms where l/w<3, a result inconsistent with previous studies. There is also a weaker correlation between the ρ_{max} and A_{max} where l/w<3 (R^2 = 0.48; Fig. 5.14b). This apparent ~90° rotation in the orientation of the resistivity ellipse suggests that the principal direction of resistivity/conductivity anisotropy may not simply reflect former flow direction at least where l/w<3. The origin of the anisotropy presented in this study remains somewhat equivocal, so we propose three working explanations (that may not be independent).

5.4.1 Electrical anisotropy from alignment of sediment particles.

This explanation implies that the electrical anisotropy is directly related to the alignment of sediment particles and the fabric developed from the stress field imposed on the mobile subglacial sediment by the glacier. The critical difference between our explanation and the general assertion that the orientation of electrical anisotropy is coincident with ice flow (Penttinen et al., 1999) is that, although it is implied that electrical anisotropy is associated with the sediment fabric, sediment fabric alignment does not necessarily equate to ice flow direction. Clast and sediment fabrics in glacially derived diamictons have long been studied and used as an important parameter for elucidating sediment genesis, stress and strain conditions, transport direction, and ice flow history (e.g. Holmes, 1941; Glen et al., 1957; Shimizu, 1966; Mark, 1973, 1974; Woodcock, 1974; Dowdeswell and Sharp, 1986; Hicock, 1990; Benn, 1994b, 1995; Ham

and Mickelson, 1994; Hart 1994; Benn and Evans, 1996; Hicock et al, 1996). Studies have shown that fabric orientation can be variable and this not always consistent with ice flow direction (e.g. Rose, 1989; Benn, 1994; Carr and Rose, 2003; Benn, 2004).

Penttinen et al. (1999) and Sutinen et al. (2010) suggest that the electrical anisotropy, determined from azimuthal measurements of resistivity or conductivity, is an effective geophysical method for determining fabric orientation. Evidence is convincing that this is indeed the case (particularly elongate landforms), but they imply that the alignment of the sediment fabric and the anisotropy reflect ice flow, which is not always valid (i.e. where transverse fabrics develop under comprssional stress fields; Car and Rose, 2003). This study confirms that there is a relationship between electrical anisotropy, landform elongation and orientation, and sediment fabric, however it appears more complex than simply indicating former ice flow direction. The results presented here show that the orientation of the principal direction of the resistivity anisotropy may be either perpendicular or parallel to the long axis of the landform (the inferred ice-flow direction). Thus the apparent rotation of the anisotropy on landforms with low elongation ratios in this study probably does not reflect a 90° rotation of the ice flow, but rather may indicate a rotation in the sediment fabric due to changes in the stress field at the subglacial bed.

Two mechanisms may be responsible for the change in sediment particle orientation including: 1) reorientation of sediments particles as a result of ice stagnation and sediment squeeze, or 2) sediment particle alignment in response to extensional and compressive ice flow dynamics.

The landforms at sites 6 – 10 (low elongation ratio; Fig. 5.2) all show a large number of superimposed ridges and depressions, many of which are rectilinear (Figs. 5.9b – 5.12). These features probably formed under stagnating ice and these structures likely reflect sediment squeeze up into crevasses with intervening depressions forming under ice blocks (Sharp, 1985). These features suggest that active ice flow was subsequently replaced by ice stagnation (Rea and Evans, 2011). The squeeze features are less well developed on the elongated landforms (e.g. sites 1 – 5 and sites 11 and 12; Figs. 5.7, 5.8, 5.9a, and 5.13). It is speculated that the reorientation of the electrical anisotropy may reflect remobilization of sediment particles as they were squeezed to form these features. Thus, this sediment alignment would reflect the

stress field of the stagnant ice, and not necessarily just the stress field associated with the actively flowing ice.

An alternative explanation for the correlation between highly elongated landforms and the orientation of electrical anisotropy involves sediment particle alignment in response to extensional and compressive ice flow dynamics. The deforming bed mosaic concept (Piotrowski and Kraus, 1997; van der Meer et al., 2003; Piotrowski et al., 2004; Evans et al., 2006) invokes variations in the local stress regime and bed conditions that result in a mosaic of bed deformation and stability fields which may be responsible for till formation, sedimentation, and landform development. This concept may be helpful in explaining the landforms and electrical anisotropy observed in this study. For example, high pore water pressure in dilatant till results in a decrease in cohesion, leading to deformation. Eventually, the till enters the liquid/fluid state and the applied stress of the ice is taken up by flow displacement. Under these conditions, ice would experience extensional flow and it would be expected that highly mobile sediment would produce elongated streamlined landforms such as those that are common in the western and eastern portions of the study area (Fig. 5.2).

Conversely, the landforms that have a lower elongation ratio likely had subglacial bed conditions that resisted deformation. For example, the till at S6 in the central portion of the area contains a higher proportion of clasts and is distinctly different from the till elsewhere in the study area (Fig. 5.5b). The distribution of the CCR data in the same region suggests that the till is coarser grained and variable. The abundant clasts in the till may have resulted in a stiffer, less ductile bed due to increased clast interactions and/or more efficient drainage of subglacial water (reduction in pore water pressure). A stiffer bed would behave as a so called “sticky-spot” as described by Stokes et al. (2007) and defined as a localised area of high basal drag surrounded by a well-lubricated lower shear stress bed (Alley, 1993). The increased drag/friction may have caused a local shift from extensional ice flow to compressional flow initiating the rotation of clasts towards a transverse fabric (Boulton, 1971; Stanford and Mickelson, 1985; Hicock, 1991; Hart, 1994; Stokes et al., 2008). The rotation of smaller particles (i.e. clay) may outpace the rotation of larger particles (Carr and Rose, 2003) and change the direction of electrical anisotropy, particularly if pore water pressure was dissipated laterally as might be expected under compressive flow conditions. Thus, the rotation of the resistivity/conductivity anisotropy may be a more sensitive measure of the alignment of sediment particles than macro

fabrics (clasts). Therefore, like clast fabrics, electrical anisotropy does correspond with the sediment fabric, but would not necessarily be indicative of the ice flow direction. If this is the case, electrical anisotropy may provide some insight into subglacial dynamics and bed strength (Fig. 5.15) and may be helpful in determining the orientation of the finite strain ellipse preserved in the sediment.

5.4.2 Electrical anisotropy from fractures in till.

Fractures can be grouped into a continuum of three scales: a) macroscale, 2) mesoscale, and 3) microscale. All scales involve deformation resulting in normal (tensile), thrust (shear), and/or decompression faulting. Macroscale manifestations may be related to large scale glaciotectonism (e.g. van der Meer et al., 2003; Aber and Ber, 2007) or to post depositional processes such as desiccation or mass movement fracturing. Mesoscale fractures include structures observed at the outcrop scale (e.g. Dreimanis, 1993; Lian and Hicock, 2000, 2010). Microscale deformation structures include small scale features such as fissility or those observable only in thin section (van der Meer et al., 2003; Menzies et al., 2005). This hypothesis is the basic premise of much of the early work on electrical anisotropy in sediment, where macroscale and large mesoscale fractures were considered primarily responsible for electrical anisotropy (e.g. Taylor and Flemming, 1988). The concept can be extended to smaller mesoscale and potentially microscale structures, if these structures generate fabrics that influence the electrical anisotropy.

No macroscale brittle deformation structures were observed in this study, but small mesoscale and microscale structures, in the form of fissility, are well developed at station S1 (Fig. 5.5). Here, 2-3 mm thick sand-filled shear planes striking 124° and dipping at 8° (SW), are essentially parallel with the orientation of the principal direction of the resistivity anisotropy at this location. Though not conclusive, the presence of fissility in the till at S1 and its coincidence with the orientation of the resistivity ellipse means that meso and microscale fractures cannot be ignored as a possible cause for the direction of electrical anisotropy. No clear fissility was observed at station S6 (streamlined landform 8) where the orientation of the resistivity anisotropy was rotated ~90° relative to the landform orientation.

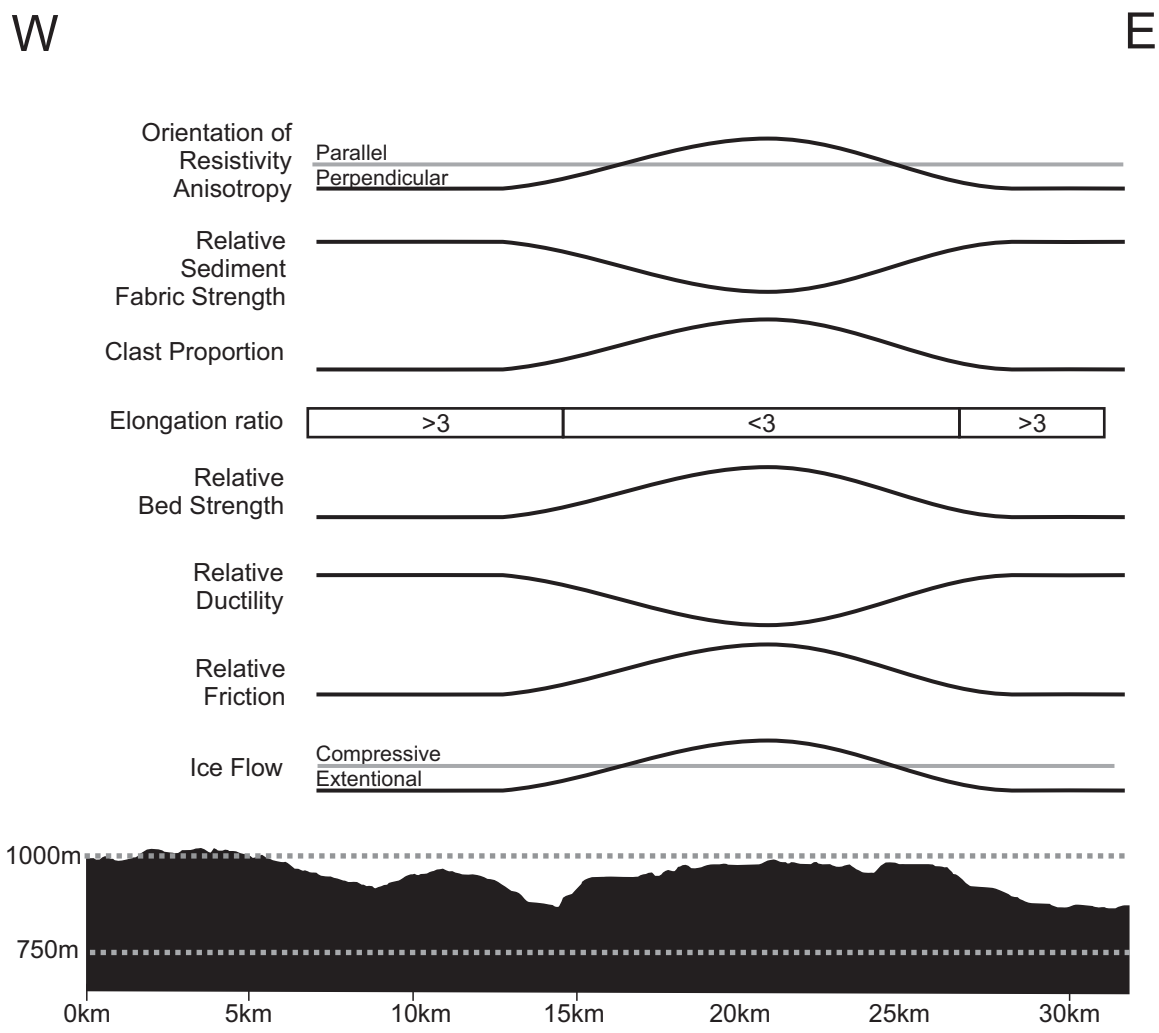

Figure 5.15. A conceptual model for inferred subglacial conditions that may explain field observation and electrical anisotropy along a transect across the study area (Fig. 5.2).

Previous work has shown that till deformation in the subglacial environment is complex and may change through time (Stokes et al., 2007). Factors such as composition, deforming bed thickness, temperature regime, and pore water pressure are important factors controlling deformation style. Temporal changes in subglacial environment can result in one style overprinting another as conditions change (ductile versus brittle; e.g. Hicock and Dreimanis, 1985; Hicock 1990, 1992; Benn and Evans, 1996; Stokes et al., 2008; and Lian and Hicock, 2000, 2010). The fabric alignment at sites S1 and S2 (Fig. 5.7) may have developed during ductile deformation and fissility developed later when the bed stiffened (location S1; Fig. 5.2). Alternatively, the fabric may have been generated through the process of brittle or brittle-ductile shearing, a till generation and deformation mechanism suggested by Boulton and Hindmarsh, (1987) and Benn (1995). Like clast fabrics, orientation of the brittle structures will reflect the principle stress directions created by the moving ice. Further detailed analysis of deformation structures at meso- and microscales was not undertaken in this study so the relationship between sediment fabric, fracture orientation and electrical anisotropy remains an avenue for further research.

5.4.3 Electrical anisotropy from previous ice-flow inheritance

Inheritance cannot be ruled out as a valid explanation for the apparent ~90° change in orientation of electrical anisotropy on streamlined landforms with elongation ratios less than 3. Inheritance was attributed to similar results found by Sutinen et al. (2010) where ρ_{max} was oblique to the orientation of the principle axis of the streamlined landforms. There is evidence, at least for part of the Kiskatinaw streamlined landform field that the Cordilleran Ice Sheet was deflected to the north by the Laurentide Ice Sheet during coalescence. As the ice sheets separated, unrestricted flow of the Cordilleran Ice Sheet resulted in a more northeastward flow trajectory. The early deflected flow is apparent in the orientation of the streamlined landforms in the northwest corner of the study area where the principle axes of landforms rotate towards the north (Fig. 5.2). This is even more pronounced north of the study area where the orientation of the landforms is approximately 355°. Though the orientation of streamlined landforms with low l/w ratios reflect the later northeast flow direction, it is possible that the cores of the landforms were not modified or the electrical anisotropy from the later flow event did not

develop sufficiently to mask the earlier record. In order for this explanation to be valid, the inherited fabric would be obliterated in highly elongate landforms, but preserved in less elongated landforms where the bed may have experienced less deformation.

5.5 Conclusions

This study was directed at testing the hypothesis that the orientation of electrical anisotropy in till indicates the direction of paleo-ice flow and sediment transport. For landforms with high elongation ratios (>3) the principal axis of electrical anisotropy is perpendicular the long axis of the landforms (inferred paleo-ice flow direction). There is, however, a 90° rotation of the electrical anisotropy between streamlined landforms with high elongation ratios (>3) and those with low elongation ratios (<3). Three explanations are proposed that may or may not be independent.

Electrical anisotropy in till may result from alignment of sediment particles. The alignment of the particles is however, a reaction to the subglacial stress, not necessarily the paleo-ice flow direction. This explanation implies that electrical anisotropy is coincident with the sediment fabric which may be parallel or transverse to ice flow depending on strain responses to local stress fields. This explanation is tentatively favoured, but the apparent 90° rotation of the electrical anisotropy may have resulted from two untested processes. The rotation may reflect modification of the subglacial sediment fabric during ice stagnation and the development of crevasse squeeze ridges. If this is the case, the electrical anisotropy on the low elongation ratio landforms is coincident with the strain ellipse associated with the stress from stagnant ice and mobilizing the sediment into subglacial crevasses. Alternatively, electrical anisotropy may be explained by the deforming bed mosaic concept. Highly deformable till takes up the stress from extensional flowing ice and subglacial sediments deform to produce elongated streamlined landforms. Landforms with lower elongation ratios form where stiffer subglacial beds occur. A stiffer bed would begin to behave as a so called “sticky-spot” where increased drag/friction results in a shift from extensional to compressional ice flow and initiates the rotation of the sediment fabric towards a transverse fabric. The anisotropy would, therefore, correspond with the sediment fabric, but would not necessarily be indicative of the ice flow direction.

Electrical anisotropy may also result from fractures of various scales in till. Brittle deformation structures (fractures) are mainly responsible for the electrical anisotropy. Brittle

structures exist as a continuum of three scales in glacial sediments including macro-, meso-, and micro-scales. These structures are generally associated with a brittle or brittle-ductile bed response to stress fields invoked by moving ice. Macro- and large meso-scale structures have been indicated in previous studies as the dominant influence on electrical anisotropy. No macroscale or large mesoscale structures were observed in this study, but small mesoscale structures (fissility) recorded at one location have a dip direction parallel to the principal axis of resistivity anisotropy. However, since mesoscale and microscale brittle structures were not systematically evaluated in this study, this explanation remains viable but requires further testing.

Inheritance may also be considered an explanation. There is evidence that an earlier ice-flow was towards the north for part of the study area. Streamlined landforms with low elongation ratios may have shapes that record the later flow, but have unmodified cores that reflect earlier flow direction. However, limited clast fabric data do not support this hypothesis.

This study has shown that, like sediment fabrics, electrical anisotropy may be an effective tool for understanding stress and strain conditions preserved in subglacial sediments. More case studies are required, however, to test the relationship between resistivity anisotropy and subglacial sediment deformation.

5.6 References

Aber, J.S. and Ber, A. 2007. Glaciotectonism; Elsevier, Amsterdam, 246 pp.

Alley, R.B. 1993. In search of ice-stream sticky spots; Journal of Glaciology, 39, 447—454.

Asten, M.W., 1974. The influence of electrical anisotropy on Mise-A-LaNasse Surveys; Geophysical Prospecting, 22, 238—245.

Benn, D.I. 1994a. Fluted moraine formation and till genesis below a temperate glacier Slettmarkbreen, Jotunheimen, Norway; Sedimentology, 41, 279-292.

Benn, D.I. 1994b. Fabric shape and interpretation of sedimentary fabric data; Journal of Sedimentary Research, A64, 910—915.

Benn D.I. 1995. Fabric signature of subglacial till deformation, Breidamerkurjokull, Iceland; Sedimentology, v. 42, 735—747.

Benn, D.I. 2004. Macrofabric; In Evans, D.J.A. and Benn, D.I., (eds), A practical guide to the study of glacial sediments; Arnold, London, 93—114.

Benn, D.I. and Evans, D.J.A. 1998. Glaciers and Glaciation; Arnold, London, 734 pp.

Benn, D.I. and Evans, D.J.A. 2006. Subglacial megafloods: outrageous hypothesis or just outrageous?; In Knight, P. (ed.) Glacier Science and Environmental Change, Blackwell, Oxford, 42—46.

Boulton, G.S. 1971. Till fabric and genesis in Svalbard, Spitsbergen; In Goldthwait, R.P. (ed), Till, a symposium; Ohio State University Press, 41—72.

Boulton, G.S. 1987. A theory of drumlin formation by subglacial sediment deformation; In Menzies, J. and Rose, J. (eds) 1987. Drumlin Symposium; A.A Balkema, Rotterdam, 25—80.

Boulton, G.S. and Hindmarsh, R.C.A. 1987. Sediment deformation beneath glaciers: Rheology and geological consequences; Journal of Geophysical, 92, 9059—9082.

Boyce, J. and Eyles N. 1991. Drumlins carved by deforming till streams below the Laurentide Ice Sheet; Geology, 19, 787—790.

Cars, S.J. and Rose, J. 2003. Till fabric patterns and significance: particle response to subglacial stress; Quaternary Science Reviews, 22, 1415—1426.

Carpenter, P.J., Keeley, M.C. and Kaufmann, R.S. 1990. Azimuthal resistivity, soil moisture and infiltration over a fractured glacial till landfill cover; EOS, 71, 519.

Cohn, M.E. and Rudman, A.J. 1995. Orientation of near-surface fractures from azimuthal measurements of apparent resistivity; Society of Exploration Geophysists, Extended Abstracts, Houston, Texas, 372—374.

DeGroot-Hedlin, C. And Constable, S. 1990. Occam's inversion to generate smooth two-dimensional models from magnetotelluric data; Geophysics, 55, 1613—1624.

Doweswell, J.A. and Sharp, M.J. 1986, Characterization of Pebble fabrics in modern terrestrial glacigenic sediments; Sedimentology, 33, 699—710.

Dreimanis, A. 1993 Small to medium-sized glacitectonic structures in till and in its substratum and their comparison with mass movement structures; Quaternary International, 18, 69—79.

Evans, D.J.A., Phillips, E.R., Hiemstra, J.F. and Auton, C.A. 2006. Subglacial till: Formation, sedimentary characteristics and classification; Earth-Science Reviews, 78, 115—176.

Gander, W., Golub, G.H. and Strebel, R. 1996. Least squares fitting of circles and ellipses; Bulletin of the Belgian Mathematical Society, 3, 63—84.

Glen J.W., Donner, J.J., and West, R.G., 1957. On the mechanism by which stones in till become oriented; American Journal of Science, 255, 194—205.

Griffiths, D.H. and Barker, R.D. 1993. Two-dimensional resistivity imaging and modelling in areas of complex geology; Journal of Applied Geophysics, 29, 211—226.

Guy, G., Best, M., Spence, G., Dosso, S. and Telmer, K. 2000. EM and GPR mapping of bedrock fractures as conduits for contaminated groundwater flow in a landfill; In Proceedings of the Symposium on the Application of Geophysics to Engineering and Environmental Problems (SAGEEP), Society of Engineering and Mining Geophysists, Arlington, Virginia, 1029—1035.

Habberjam, G.M. 1975. Apparent resistivity, anisotropy and strike measurements; Geophysical Prospecting, 23, 211—247.

Hagrey, S.A. 1994. Electrical study of fracture anisotropy at Falkenberg, Germany; Geophysics, 59, 881—888.

Hart, D. and Rudman, A.J. 1997. Least-squared fit of an ellipse to anisotropic polar data: application to azimuthal resistivity surveys in karst regions; Computers and Geosciences, 23, 189—194.

Hart, J.K. 1994. Till fabric associated with deformable beds; Earth Surface Processes and Landforms, 19, 15—32.

Hart, J.K. 1998. The deforming bed/debris-rich basal ice continuum and its implications for the formation of glacial landforms (flutes) and sediments (melt-out till); Quaternary Science Reviews, 17, 737—754.

Hicock, S.R. 1990. Genetic till prism; Geology, 18, 517—519.

Hicock, S.R. 1991. On subglacial stone pavements in till; Journal of Geology, 99, 607—619.

Hicock, S.R. 1992. Labal interactions and rheologic superposition in subglacial till near Bradtville, Ontario, Canada; Boreas, 21, 73—88.

Hicock, S.R. and Dreimanis, A. 1985. Glaciotectonic structures as useful ice-movement indictors in glacial deposits: four Canadian case studies; Canadian Journal of Earth Sciences, 29, 1565—1597.

Holmes, C.D. 1941. Till fabrics; Geological Society of America Bulletin, 52, 1299—1354.

Iverson, N.R., Hanson, B., Hooke, R.L. and Jansson, P. 1995. Flow mechanism of glaciers on soft beds; Science, 267, 80—81.

Keller, G.V. and Frischknecht, F.C. 1966. Electrical methods in geophysical prospecting. Pergamon Press, New York, 519 pp.

Lane, J.E.Jr.m Haeni, F.P. and Watson, W.M. 1995. Use of a square-array direct current resistivity method to detect fractures in crystalline bedrock in New Hampshire; Ground Water, 33, 476—485.

Lian, O.B. and Hicock, S.R. 2000. Thermal conditions beneath parts of the last Cordilleran Ice Sheets near its centre as inferred from subglacial till, associated sediments, and bedrock; Quaternary International, 68—71, 147—162.

Lian, O.B. and Hicock, S.R. 2010. Insight into the character of paleo-ice-flow in upland regions of mountain valleys during the last major advance (Vashon Stade) of the Cordilleran Ice Sheet, southwest British Columbia, Canada; Boreas, 39, 171—186.

Loke, M.H. and Barker, R.D. 1996. Rapid least-squares inversion of apparent resistivity pseudosections by a quasi-Newton method; Geophysical Prospecting, 44, 131—152.

Mathews, W.H., 1980. Retreat of the last ice sheets in northeastern British Columbia and Adjacent Alberta; Geological Survey of Canada, Bulletin 331, 22 pp.

McNeill, J.D., 1980. Electromagnetic terrain conductivity measurement at low induction numbers; Geonics Limited, Technical Note TN-6, 15 pp.

Menzies, J. And Rose, J. (eds) 1987. Drumlin Symposium; A.A Balkema, Rotterdam, 360 pages.

Menzies, J., van der Meer, J.J.M., Rose, J., 2005. Till – as a glacial “tectomict:, its internal architecture, and the development of a “typing” method for till differentiation; Geomorphology, 75, 172—200.

O Cofaigh, C., Stokes, C.R., Lian, O.B., Clark, C.D., Tulacyzk, S., 2013. Formation of mega-scale glacial lineations on the Dubawnt Lake Ice Stream bed: 2. Sedimentology and Stratigraphy; Quaternary Science Reviews, 77, 210—227.

Penttinen, S., Sutinen, R., and Hänninen, P. 1999. Determination of anisotropy of tills by means of azimuthal resistivity and conductivity measurements; Nordic Hydrology, 30, 317—332.

Piotrowski, J.A. and Kraus, A.M. 1997. Response of sediment to ice sheet loading in northwestern Germany: effective stresses and glacier bed stability; Journal of Glaciology, 43, 495—502.

Ritzi, R.W. and Andolsek, R.H. 1992. Relation between anisotropic transmissivity and azimuthal resistivity surveys in shallow fractured, carbonate flow systems; Ground Water, 30, 774—780.

Rose, J. 1989. Glacier stress patterns and sediment transfer associated with superimposed flutes; Sedimentary Geology, 62, 151—176.

Sandberg, S.K. and Jagel, D.L. 1996. The electromagnetic azimuthal resistivity method; Proceedings of the Symposium on the Application of Geophysics to Engineering and Environmental Problems (SAGEEP), Society of Engineering and Mining Geophysists, Keystone Colorado, 31—40.

Sauk, W.A. and Zabik, S.M. 1992. Azimuthal resistivity techniques and directional variations of hydraulic conductivity in glacial sediments; In Bell, R.S. (ed) Proceedings of the Symposium on the Application of Geophysics to Engineering and Environmental Problems (SAGEEP), Society of Engineering and Mining Geophysists, Golden, Colorado, 197—222.

Schlumberger, C.M. and Leonardon, E.G., 1933. Some observations concerning electrical measurements in anisotropic media, and their interpretation; American Institute of Mining and Metallurgical Engineers, Technical Paper, 505, 337 pp.

Sharp, M. 1985. “Crevasse-Fill” ridges: a landform type characteristic of surging glaciers?; Geografiska Annaler, Series A, Physical Geography, 67, 213—220.

Shaw, J. 1983. Drumlin formation related to inverted meltwater erosional marks; Journal of Glaciology, 29, 461—479.

Shaw, J. 2002. The meltwater hypothesis for subglacial bedforms; Quaternary International, 90, 5—22.

Shaw, J. 2010. In defence of the meltwater (megaflood) hypothesis for the formation of subglacial bedform fields; Journal of Quaternary Science, 25, 249—260.

Shaw, J. and Kvill, D. 1984. A glacialfluvial origin for drumlins of the Livingstone Lake Area, Saskatchewan; Canadian Journal of Earth Sciences, 21, 1442—1459.

Skinner, D. And Heinson, G. 2002. A comparison of electrical and electromagnetic methods for detection of hydraulic pathways in a fractured rock aquifer, Clare Valley, South Australia; Hydrogeology Journal, 12, 576—590.

Smalley, I.J., and Unwin, D.J. 1968. The formation and shape of drumlins and their distribution and orientation in drumlin fields; Journal of Glaciology, 51, 377—390.

Standford, S.D. and Mickelson, D.M. 1985. Till fabric and deformational structures in drumlins near Waukesha, Wisconsin, USA; Journal of Glaciology, 31, 220—228.

Stokes, C.R., Clarke, C.D., Lian, O.B., Tulaczyk, S. 2007. Ice stream sticky spots: A review of their identification and influence beneath contemporary and paleo-ice streams; Earth-Science Reviews, 81, 217—249.

Stokes, C.R., Lian, O.B., Tulaczyk, S. and Clark, C.D. 2008. Superimposition of ribbed moraines on a paleo-ice-stream bed: implications for ice stream dynamics and shutdown; Earth Surface Processes and Landforms, 33, 593—609.

Sutinen, R., Middleton, M., Liwata, P., Piekkari, M., and Hyvönen, E. 2009. Sediment anisotropy coincides with moraine ridge trend in south-central Finnish Lapland; Boreas, 38, 638—n 646.

Sutinen, R., Hyvönen, E., Närhi, P., Haavikko, P., Piekkari, M., Middleton, M. 2010. Sediment anisotropy diverges from flute trends in south-east Finnish Lapland; Sedimentary Geology, 232, 190—197.

Taylor, R.W. and Fleming, A.H. 1988. Characterizing jointed systems by azimuthal resistivity; Ground Water, 26, 464—474.

van der Meer, J.J.M., Menzie, J. and Rose, J. 2003. Subglacial till: the deforming glacier bed; Quaternary Science Reviews, 22, 1659—1685.

Varah, J.M. 1996. Least squares data fitting with implicit functions; BIT, 36, 842—854.

Wentworth, C.K. 1922. A scale of grade and class terms for clastic sediments; Journal of Geology, 30, 377—392.

Watson, K.A. and Barker, R.D. 1999. Differentiating anisotropy and lateral effects using azimuthal resistivity offset Wenner soundings; Geophysics, 64, 739—745.

CHAPTER 6: HISTORY OF GLACIAL LAKE PEACE, NORTHEASTERN BRITISH COLUMBIA

Adrian S. Hickin, Victor M. Levson, and Olav B. Lian

This manuscript has not yet been submitted for publication

Abstract

Recognition of positions of ancient glacial lakes along the margin of continental ice sheets is critical in reconstructing ice configuration and understanding the environments and ice dynamics that existed during deglaciation. Advances in remote sensing technology have enabled the generation of accurate digital-elevation models (DEMs) that reveal unprecedented geomorphic detail. Combined with geographic information systems, these new tools have enabled considerable advancement in mapping and correlation of geomorphic features such as relict shorelines.

This study examines the shorelines of glacial Lake Peace (GLP), an ice marginal lake that developed between the Laurentide and Cordilleran ice sheets in northeastern British Columbia and northwestern Alberta during early deglaciation. Shoreline mapping from high resolution DEMs produced more than 44,000 elevation data points generated from 3230 discrete shoreline features. These data enable the identification of four major phases of water surface elevation. Phase I ranges from 960 m to 990 m but is poorly constrained. Phase II consists of a flight of shorelines between 890 m and 910 m and represents the earliest unambiguous phase of GLP. Phase III is multi-modal and encompasses shorelines that span an elevation interval between 810 m and 865 m. The shoreline features from Phase IV between 724 m and 733 m developed as an isolated basin (now Swan Lake) as GLP retreated from the area.

The extensive mapping of the shorelines allow for measuring of isostatic adjustments during the various phases, as ice retreated. Results indicate slope aspect may have changed through time, reflecting the asynchronous retreat of the Cordilleran (CIS) and Laurentide (LIS) ice sheets. Initially the LIS in the Interior Plains retreated to the east allowing uplift to initiate in the northeast part of the study area. Later, the CIS receded west into the mountains and early uplift in the northeast was outpaced by uplift in the southwest.

Constraining the timing of the retreat of the ice sheets was attempted through optical dating of shoreline sediment associated with Phase II. Two optical ages of <16.0 ± 2.5 ka and 14.2 ± 0.5 ka provide a limiting age for this phase of GLP. These ages are consistent with the radiocarbon age ranges for GLP (17 to 12 ka Cal yrs BP) and overlap feldspar optical ages from sand dunes in the Grande Prairie region (14.9 ± 1.0 ka and 11.8 ± 0.8 ka).

6.1 Introduction

This study seeks to reconstruct the history of glacial Lake Peace (GLP) from relict shoreline features in the Dawson Creek area of northeast British Columbia (Fig. 6.1) and to evaluate previous reconstructions of GLP (Reimchen and Rutter, 1972; St-Onge, 1972; Mathews, 1980; Liverman, 1991; Woolf, 1993).

Understanding the distribution and timing of glacial lakes is central to modelling ice sheet configuration during deglaciation. Improved remote-sensing technology such as high-resolution satellite imagery and digital-elevation models (DEMs) generated from light detection and range (LiDAR) surveys have enabled geoscientists to image subtle geomorphic features previously obscured, unrecognized, or unresolved, in traditional topographic maps and aerial photographs (e.g. Webster et al., 2006; Yang and Teller, 2012). Such remotely sensed data, coupled with geographic information systems (GIS) and the relatively new geochronology tools such as optical dating, have recently yielded unprecedented detail for mapping and correlating geomorphic features such as raised shorelines.

Glacial Lake Peace was a proglacial lake that existed in northeast British Columbia and northwest Alberta during the retreat of the Cordilleran (CIS) and Laurentide (LIS) ice sheets. Large proglacial lakes were common along the margins of the LIS and are well documented in British Columbia, Arctic Canada, the Canadian Interior Plains, and in the Great Lakes regions (e.g. Craig, 1965; St-Onge, 1972; Alley and Harris, 1974; Mathews, 1980; Dyke and Prest, 1987; Teller, 1987; Smith, 1994; Lemmen et al., 1994; Teller, 1995; Fisher, 1999; Dyke et al, 2003; Leverington and Teller, 2003; Karrow, 2004; Yang and Teller, 2012).

In the western Canadian Interior Plains, GLP formed when the Laurentide Ice Sheet (LIS) blocked regional drainage and impounded a large lake that followed the ice margin as it retreated east across northeastern British Columbia and northwestern Alberta (Fig. 6.1; Taylor, 1958; Mathrews 1978, 1980, Liverman, 1991). The area has a complex Late Pleistocene glacial history involving three glacial systems that existed at various times (montane glaciation, CIS and LIS; Catto et al., 1996). Which event was most extensive, and when or if the CIS and LIS coalesced during the Late Wisconsinan (Marine Isotopic Stage 2) remain unresolved issues (Bednarski and Smith, 2007; Hartman and Clague, 2008). One model, based on the work of Reimchen and Rutter (1972), Rutter (1976, 1977) and Mathews (1978, 1980) suggests two or three Laurentide advances and three or four Cordilleran advances which coalescence during the

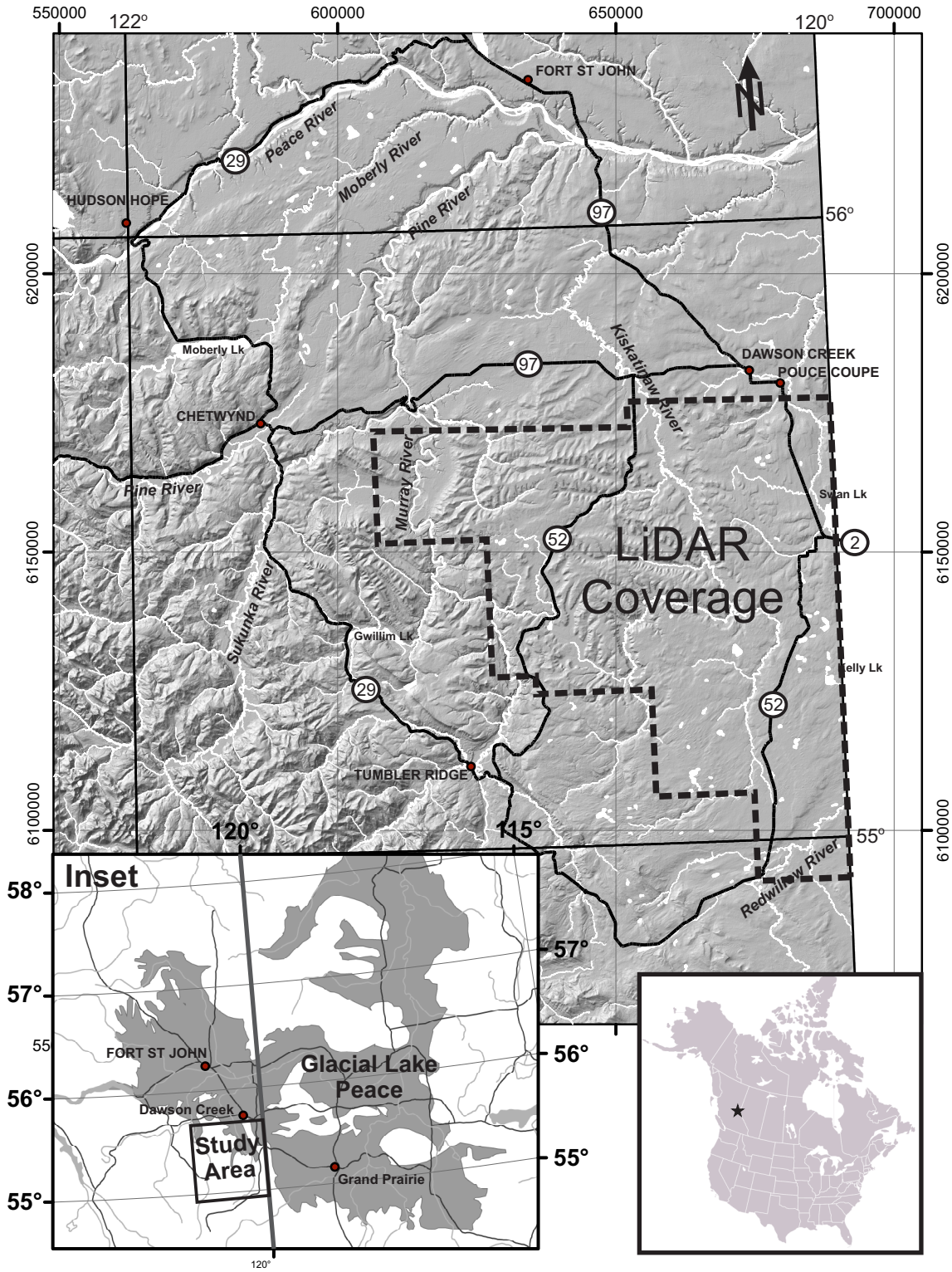

Figure 6.1. The study area in northeast British Columbia. Inset: Footprint of all phases of glacial Lake Peace (from Mathews, 1980).

Late Wisconsinan (late glacial maximum ca. 18,000 C^{14} yrs BP or 21 000 cal. yrs BP). Another model, based on the work of Bobrowsky (1989), suggests one Laurentide and two Cordilleran advances with pre-Late Wisconsinan coalescence (Catto et al., 1996; Hartman and Clague, 2008).

Dawson (1881) was first to recognize the water-lain origin of the silt that blankets much of the Peace River region. He postulated that these deposits resulted from submergence of the land below sea-level, but also suggested that the deposits may have been derived from water impounded by "glacier-dams". Taylor (1958) applied the name GLP to the body of water that occupied the Peace River region during deglaciation. St-Onge (1972) and Mathews (1978, 1980) provided interpretations of the configuration of lakes and ice sheets at various stages of GLP in British Columbia and Alberta. Their work suggests GLP formed during the separation of the LIS from the Rocky Mountain Foothills and perhaps from the CIS during the Late Wisconsinan.

Woolf (1993) summarized the documented lake stages from various studies. Reimchen and Rutter (1972) noted, while mapping in the area of the Dawson Creek map sheet (NTS 93P), beaches, wave-cut notches and wave-washed surfaces at 838 m (2750 ft), 738 m (2420 ft), 722 m (2370 ft), 710 m (2330 ft), 688 m (2260 ft), 664 m (2180 ft) and 655 m (2150 ft) above sea level (asl), but did not distinguish lake phases. Mathews (1978, 1980) suggested, from his work around Fort St John, that the highest elevation of GLP, his Phase 1, would have been >1130 m (all elevations are in m asl). As ice retreated down the regional slope to the east, the lake followed, shifting position with the ice margin and falling in elevation. His next major stage is the Bessborough phase, between 855-835 m, a stage equivalent to St-Onge's (1972) Iosegun I and II between 845-833 m from north-central Alberta and "Hudson Hope Phase" of Rutter (1977) during which the Portage Moraine complex was deposited. Mathews (1978, 1980) has an unnamed phase around 803 m, equivalent to St-Onge's (1972) Iosegun II and III between 792-833 m. The final two lake stages from Mathews in the study area include the Clayhurst (ca. 680 m) and Indian River (ca. 646 m) phases.

The physiography of the study area includes the transition from the Rocky Mountain Foothills in the west to the Canadian Interior Plains in the east (Fig. 6.1). The topography of the region reflects bedrock structure (Holland, 1976; McMechan, 1994). Much of the area is underlain by nearly flat lying, Upper Cretaceous sedimentary rock of the Dunvegan Formation, Smokey Group, and Wapiti Formation. These strata become warped in the southwest of the

study area, forming northeast dipping slopes at Tumbler Ridge (Fig. 6.1). The Rocky Mountain Foothills show progressively more intense deformation to the west, from gentle folding to complex thrusting. The topography generally rises from approximately 800 m on the plains to more than 1300 m in the foothills. Bedrock has been incised by Holocene and more ancient rivers and there is evidence of paleovalleys filled with Quaternary age sediments (Mathews, 1978; Hartman and Clague, 2008; Hickin et al., 2008, Hickin and Best, 2013). Many modern rivers, such as the Kiskatinaw, Murray, Pine, and Peace rivers have re-incised into their paleovalleys as much as 200 m below the surrounding terrain, dissecting the landscape and exposing older valley-fill sediments.

Exposures containing glaciolacustrine sediments are numerous in the study area and over 30 sections were visited in the field. In upland areas, glaciolacustrine sediments form a thin mantle a few centimetres to a few metres thick (Fig. 6.2a). In valleys, retreat phase glaciolacustrine deposits form widespread accumulations that can exceed 50 m in thickness (Fig. 6.2b). They typically consist of clay, silt, sand, and diamict and display numerous sedimentary structures related to various depositional processes (e.g. distal suspension settling, under flows, turbidity flows, rainout of ice rafted debris from icebergs; Fig. 6.3). Massive silt and clay is the most common of GLP sediments (Fig. 6.2b), however, 1-10 cm rythmites of silt and clay (Fig. 6.3a and 6.3b) or fine sand and medium sand (Fig. 6.3c) are also typical of GLP deposits. Sandy facies often contain a variety of bedfoms including climbing ripples (e.g. Type A, Type B and draped laminae; Ashely et al., 1982) and planar and trough crossed ripple laminae (Fig. 6.3d). In places the GLP sediments are hetrolithic and complex. For example, at an exposure south of Dawson Creek GLP sediments consist of interbedded massive silt with dropstones, overlain by laminated silt and clay, very thin-bedded silt, and a thin bed of diamict (Fig. 6.3e). Dropstones are also common (Fig. 6.3f). The diversity in the sedimentology reflects proximal to distal settings, distance from sediment supply, position of the glacier front, and lake level fluctuations around the GLP basin.

6.2 Methods

Paleogeographic reconstruction of various stages of early GLP and the related position of the ice margins can be established from the sedimentary and geomorphic record (Gray, 1983;

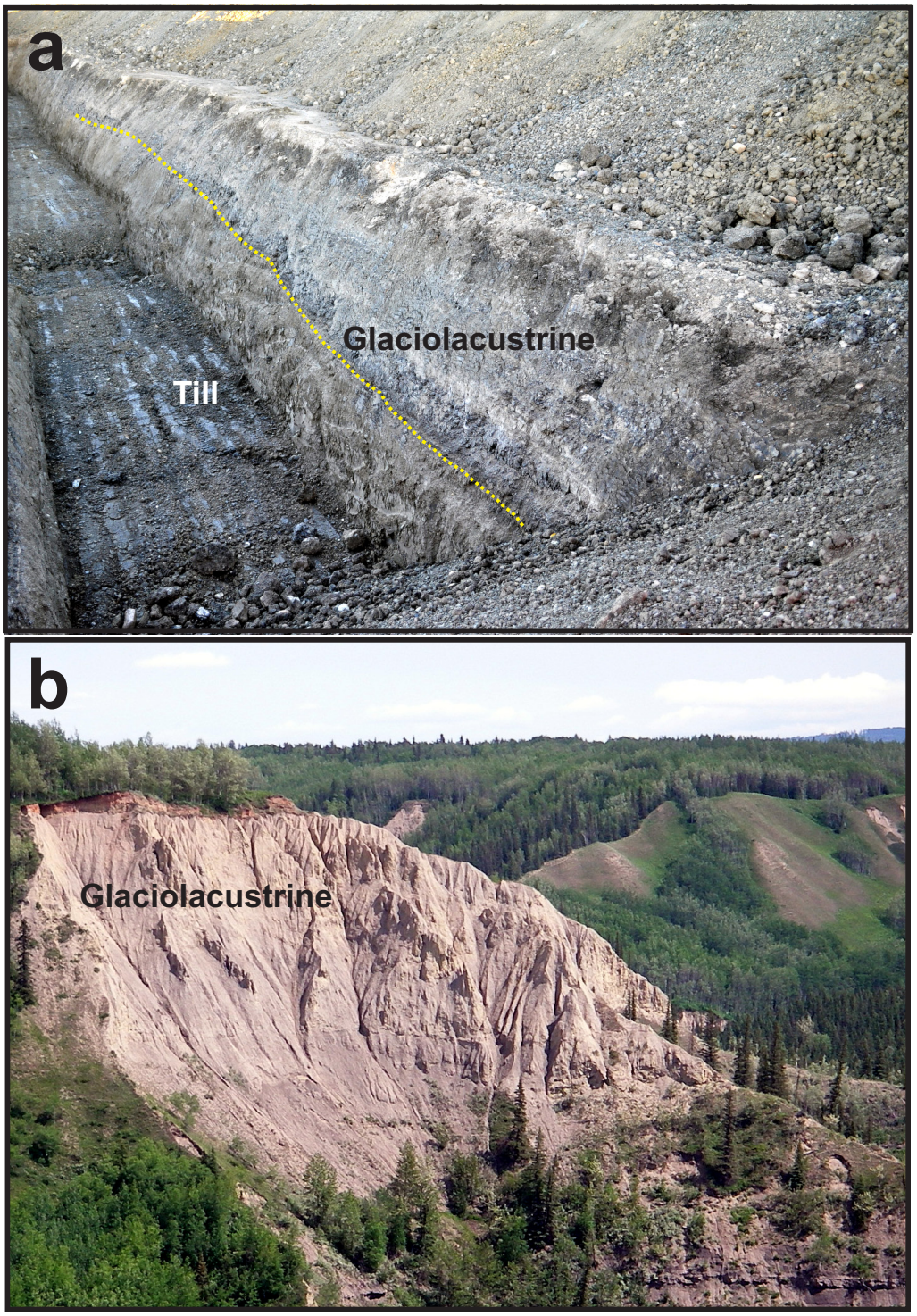

Figure 6.2. Retreat phase glaciolacustrine sediments draping much of the terrain in the Peace River region of northeast British Columbia may be only a few metres thick in upland areas (e.g. a) North of the Dawson Creek) but are considerably thicker in paleovalleys and topographic lows (e.g. b) Coldstream Canyon).

Figure 6.3. Examples of grain-size and sedimentary structures within in GLP sediments: a) rhythmically bedded sand and silt; b) thin bedded, silty sand and clay; c) horizontally stratified, medium to coarse sand; d) medium sand with trough-cross bedding and climbing ripples; e) Hetrolithic silt, laminated silt and clay, bedded silt and diamict; and f) stratified sandy diamict with dropstones.

Sack, 2001). Traditional studies of relict shorelines are based on the investigation of relatively few shoreline features (e.g. Mathews, 1978, 1980; Gray, 1983, Schaetzl et al., 2002; Johnson and Brennand, 2004). In contrast, the approach presented here uses thousands of points generated in a GIS from features associated with the margins of GLP, (e.g. strandlines, spits, and beach berms). Features were identified, examined and mapped from field observations (e.g. Fig. 6.4a) and from a high resolution 1 m DEM with vertical accuracy of ~20 cm generated from an airborne LiDAR survey (e.g. Fig. 6.4b). LiDAR is an optical remote sensing technology that measures the travel time between emitted and received pulses of light from a laser (Wehr and Lohr, 1999). When the position of the emitting and receiving instruments are known with high accuracy, the 3D position of the illuminated point of the earth surface can be computed. The result is a high resolution cloud of data points that can be processed into a DEM. In many applications multiple returns, variations in intensity, and backscatter can be used to filter and classify/separate objects. This enables features such as the tree canopy to be differentiated from the ground surface (Wehr and Lohr, 1999) allowing for the generation of a “bare earth” DEM. A bare earth model digitally strips the vegetation from the DEM revealing subtleties on the earth’s surface.

Shoreline features were mapped from a combination of hill shade models (with various sun orientations and angles) and slope models. The extents of individual shoreline features were captured in the GIS as line objects from manual digitization in ArcMap (ESRI, New York). Each line was assigned a qualitative confidence rating (very confident, confident, probable, possible, and uncertain). These ratings reflect the certainty that a given feature represents a landform associated with a paleo-water surface. For example, a well defined series of wave cut benches (such as those in Fig. 6.4b) would be assigned very confident designation, whereas a single berm/ridge with limited extent and questionable origin would be assigned uncertain designation.

Shoreline features typically occur as a series of closely spaced strandlines forming a “flight” of shoreline features. Though flights can extend for kilometres, individual strandlines are difficult to correlate over a short distance and impossible to trace over the entire map area. Groups of closely spaced shoreline features, however, represent relatively stable lake levels and can be traced over large areas. Each group of shoreline features is assumed to represent an average position of a continuous horizontal water-surface at the time of formation. Flights of

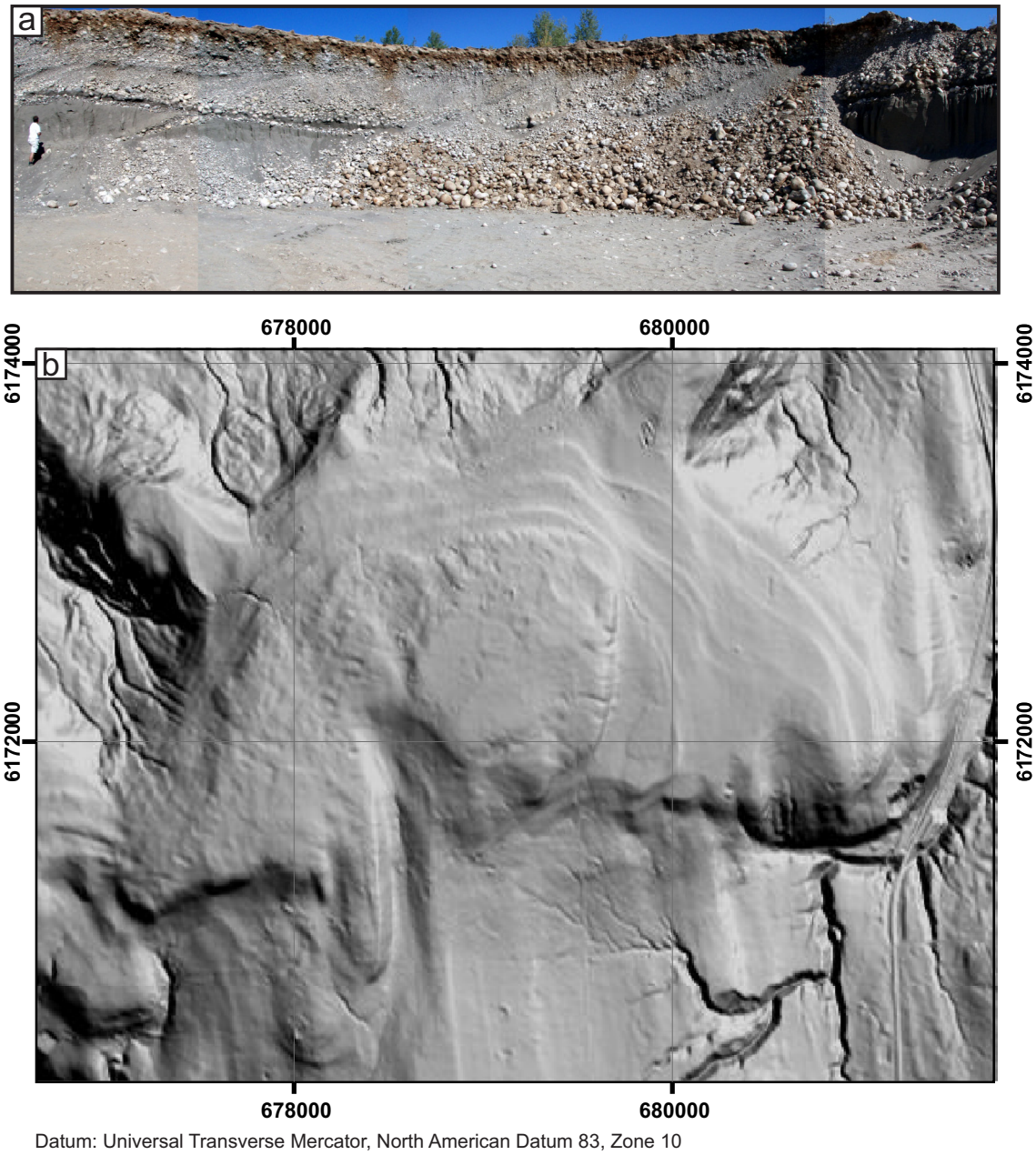

Figure 6. 4. a) Gravel pit at the confluence of the Pine and Murray rivers (Highway 97; Fig. 6.1) revealing foreset beds of a prograding delta from a late stage of GLP (610 m); b) Wave cut benches revealed from high resolution DEM (2x vertical exaggeration) from south of Pouce Coupe (Phase III of GLP).

shorelines were correlated across the study area by breaking digitized line segments into points every 25 m and assigning each point an elevation derived from the DEM. Elevation points from correlative stable lake levels cluster into populations in elevation-frequency histograms.

Isostatic adjustment following crustal unloading from ice retreat during deglaciation is common in continentally glaciated regions (Walcott, 1970, 1972; Peltier and Andrews, 1976). It is assumed that the study area was affected by glacial isostatic adjustment and the apparent slope observed along continuous shorelines is the consequence of differential uplift causing the shorelines to become deleveled. In order to reconstruct paleogeography, topography needs to be restored to its pre-isostatic position (McCann and Chorley, 1967; Leverington et al., 2002). This was achieved by assigning the "Very Confident" and "Confident" rated points to one of four dominant populations evident in the elevation histogram. Each population was then used to generate a best-fit, first-order, polynomial surface in Surfer® (Golden Software, Colorado). The general form of the first-order polynomial function describing each plane representing the average tilt associated with isostatic adjustment is:

$$Z_i = m_1(\text{easting}_i) + m_2(\text{northing}_i) + C_0$$

where Z_i is elevation in metres asl at point i with an x coordinate at easting_i and a y coordinate at northing_i. Coefficients m_1 and m_2 represent the slope of the surface with respect to the easting and the northing, and C_0 is a constant (base) elevation in metres above sea level. A gridded surface DEM was generated from each first order polynomial function with the base elevation (C_0) subtracted from each grid cell. This DEM was then subtracted from the modern DEM, producing a representative isostatically corrected DEM of topography when the shorelines were established (Johnston, 1946; Andrews, 1989; Leverington, et al., 2002).

Optical dating of sediments collected from the highest (oldest) well constrained shorelines (Phase II shoreline features), provides a limiting age for GLP. Optical dating, introduced by Huntley et al. (1985), involves the measurement of the accumulation of ionized electrons at structural defects and impurity sites that serve as electron traps in the crystal lattice of a mineral grain. The assumption is that these traps will be emptied when a grain is exposed to sufficient energy; freed electrons will almost immediately recombine at other sites which results in luminescence that can be measured. Exposure to sunlight will empty some of the traps and reset the luminescence clock. Therefore, when a grain is deposited, buried, and consequently shielded from sunlight, radiation resulting from the decay of radioisotopes within the grain and

in the immediate environment, and from cosmic rays, will be absorbed by the grain and stored as trapped electrons. The rate at which the mineral grain absorbs radiation energy (the dose rate) is proportional to the concentration of radioisotopes, and the intensity of cosmic rays, at the sample site. The time elapsed, since last exposure to sunlight, the optical age, is estimated by: (i) determining the laboratory dose of radiation that produces the same intensity of luminescence as did the dose of environmental radiation (the equivalent dose, De); and (ii) a measure of the environmental dose rate. The optical age (in ka) is simply the equivalent dose (measures in grays, Gy) divided by the dose rate (Gy/ka). Recent reviews of the methods used in this study can be found in Lian and Roberts (2006), Wintle (2008), and Lian (2013)

Four optical dating samples were collected from geographically dispersed sites on the well developed Phase II shorelines. Samples were collected by digging into the paleoshoreline sediments (using a mini excavator) and sampling a sand horizon below the surface. An aluminum cylinder 25 to 30 cm long was hammered into the face of the excavation, removed and the ends were sealed and taped to prevent grains from being exposed to light and to preserve water content. In order for an optical age to be accurate it is necessary, but not sufficient, that all of the grains comprising a multi-grain sample aliquot be exposed to sufficient sunlight to completely reset the luminescence signal before burial; this is a key assumption of the method. It is likely that sediments found in well developed beach ridges will have been exposed to sunlight for sufficiently long periods during their formation.

The environmental dose absorbed by the sand grains prior to sampling comes from alpha (α), beta (β), and gamma (γ) radiation produced by decay of U, Th, their daughter products, ^{40}K and cosmic rays. The radiation is produced in the surrounding sediment and in the sampled grains themselves. An in situ gamma-ray spectrometer was used to determine the concentrations of U, Th and ^{40}K at the sample sites for samples GPBS-1 and GPBS-2 (Fig. 6.5). The gamma-ray spectrometer probe was inserted into the hole augured at the sample location and allowed to collect data for 60 minutes. The gamma-ray spectrometer was unavailable during collection of samples GLP-03 and GLP-04 so the environmental dose rate was instead determined by laboratory analysis of sediment samples collected adjacent to the optical dating sample. Samples used for dosimetry were dried, milled, and sent to a commercial laboratory for instrumental neutron activation analysis (INAA; Bequerel Laboratories, Ontario) to determine ^{40}K, U, and Th contents. From these data, dose rates in grays/1000 years (Gy/ka) were calculated

Figure 6.5. A gamma spectrometer and probe collecting (inserted) in situ measurements of U, Th, K and total gamma-ray counts used to calculate the environmental dose rate (D_e).

using standard formulae (Aitken, 1985; Berger, 1988; Lian et al., 1995) and the dose-rate conversion factors of Adamiec and Aitken (1998). In each case, it is assumed that the U and Th decay chains have been in secular equilibrium since deposition of the sediment. This assumption generally has been found to be valid for well-drained mineral sediments (Prescott and Hutton, 1995; Olley et al., 1996). Water in the sediment matrix attenuates or absorbs radiation differently from mineral matter, and therefore it has to be accounted for in the dose rate calculations. For most of the time since deposition the shoreline sediments existed as well-drained sand so the contemporary ("as-collected") water contents, with an appropriate uncertainty, were used as an estimate of the average condition since burial.

Two samples were also collected from sand 15 cm above sample GLP-03 and from a diamict 25 cm below the sample site to check for the effect of inhomogeniety on the dose rate at the sample site. Concentrations of U, Th, and ^{40}K from above and below GLP-03 were very similar despite the upper sample being from sand and the lower sample being from diamict. The concentrations of U, Th, and ^{40}K from within the sample, were also very similar to those from around the sample location, so concentrations of U, Th, and ^{40}K from the sample were used in the calculation. Four samples were collected 15 cm from around GLP-04 (above, below, left and right of the optical dating sample site). Unfortunately, after the sample was retrieved, a granitic cobble was found to be in contact with the sample tube. The K-rich cobble contributed an elevated environmental dose rate at the sample site that needs to be accounted for in the calculations (using the method and information given in Appendix H of Aitken, 1985).

Where samples are collected near the ground surface, cosmic-rays can contribute significantly to the environmental dose rate, but their effect diminishes rapidly with burial depth. The contribution of cosmic rays was calculated using the formula of Prescott and Hutton (1994).

Aliquots were prepared and analyzed at the Luminescence Dating Laboratory at the University of the Fraser Valley, British Columbia. Ages were determined from the luminescence emitted from separated quartz grains using the single aliquot regenerative-dose (SAR) protocol (Murray and Roberts, 1998; Murray and Wintle, 2000, 2003; Wintle and Murray, 2006). Under controlled lighting conditions in the laboratory, 2-3 cm of the light-exposed sediment was removed and discarding from the end of the sample cylinder. Approximately 150 g of unexposed sediment was extracted from the cylinder for preparation. The bulk sand samples were treated

with hydrochloric acid to dissolve carbonates and then sieved to isolate the 180-250 µm size fraction. Samples then were treated with concentrated hydrofluoric acid for 40 minutes to dissolve feldspar grains and to etch the outer surface of the quartz grains that had been affected by α radiation in the environment. Quartz grains were separated from other mineral grains using a sodium polytungstate solution with a density of 2.68 g/ml. Aliquots were then prepared by mounting 50-100 grains on 9.8 mm- diameter aluminum discs using silicone oil as an adhesive.

Luminescence was measured using a Risø TL/OSL DA-20 reader. Aliquots were stimulated using light-emitting diodes that delivered 45 mW/cm2 of blue (470 ± 20 nm) light to the sample and a photomultiplier tube placed behind a 7.5 mm-thick Hoya U-340 optical filter detected the resulting ultraviolet emissions (~350 nm). Laboratory irradiations were applied with a calibrated $^{90}Sr/^{90}Y$ β-source mounted on the reader that delivered 6.26 Gy/min to each aliquot in sample GPBS-1 and GPBS-2 and 6.07 Gy/min for samples GLP-03 and GLP-04. The standard SAR protocol of Murray and Wintle (2000) was used to determine equivalent dose of each sample, but with the inclusion of an infrared wash to remove any luminescence resulting from K-feldspar contamination (Olley et al., 2004; Wintle and Murray, 2006). Aliquots were subjected to several regenerative doses in order to create a dose response curve and a zero-dose point was included to assess preheat-induced thermal transfer. One of the regenerative-dose points was repeated to test the efficacy of the test dose to correct for sensitivity change. The validity of the SAR protocol for dating quartz from the study area was tested through dose recovery experiments on all four samples (Roberts et al., 1999; Murray and Wintle, 2003). In each case the laboratory dose was sufficiently recovered, implying the quartz grains responded well to the technique and the method is suitable.

Radial plots (Galbraith et al., 1999; Galbraith, 2010), which display the distributions of equivalent dose (De) values of each aliquot about weighted mean values, were prepared for each sample. The central age model (CAM) of Galbraith et al. (1999) is appropriate for determining the De for samples with overdispersion (i.e. observed variance is higher than the variance of the theoretical model) of less than 20% (indicating the aliquots consisting of grains that were sufficiently exposed to sunlight to reset the OSL signal prior to burial). However, overdispersion above 20% in GPBS-01 and GLP-04 suggest that the sediment may contain some grains that may not have had their luminescence signal reset. In these cases the minimum age model (MAM) of Galbraith et al. (1999) was applied.

6.3 RESULTS

6.3.1 SHORELINE MAPPING

A total of 3230 linear features were interpreted and mapped as shoreline features. When converted to points at 25 m intervals, these segments yielded over 44,000 data points (Table 6.1). Of these, 155 segments (2,484 points) were considered to be uncertain and therefore eliminated from further analysis. The 42,338 usable elevation points display a frequency distribution with four distinct populations (Fig. 6.6). The highest group is relatively poorly constrained between 960 m and 990 m, and assigned to Phase I. A well constrained population occurs between 890 m and 910 m and is assigned to Phase II. A broad population exists between 810 m and 865 m all of which are assigned to Phase III. This population is multi-modal and consists of several peaks at approximately 815 m, 825 m, 835 m, 845m, 854 m, and 861 m. The population at the lowest elevation is between 724 m and 733 m and is assigned to Phase IV.

The data points are distributed across the mapped area with the most prominent shorelines occurring in the east and southeast region (Fig. 6.7). The highest elevation data points (Phase I) occur in the west and southwest where the topography rises above 1,000 m (includes data points with elevations >940m). These shorelines are poorly developed and generally do not extend over great distances. Where sediment is thin or absent there is extensive well-bedded sedimentary bedrock outcrop. Although there is ample evidence of wave-cut platforms in these rocks, some features mapped in this study may be resistant units that have differentially weathered and have been erroneously mapped as water-surface indicators. Field investigations east of the Murray River Valley, in the southwest part of the study area did, however, reveal glaciolacustrine sediment and washed till at elevations in excess of 1,100 m.

The population between 890 m and 910 m (Phase II) results from a very well developed flight of closely spaced shoreline features that typically span an elevation range of approximately 10 m to 15 m at any given location. Though present throughout the study area, this flight is best developed on the east side of the escarpment from the Redwillow River north to Kelly Lake (Fig. 6.1). Individual shorelines may extend for only several kilometres, but the flight of shorelines as a unit can be traced for more than 50 km. The multi-modal population between 810 m and 865 m (Phase III) has six distinct peaks within the distribution. These

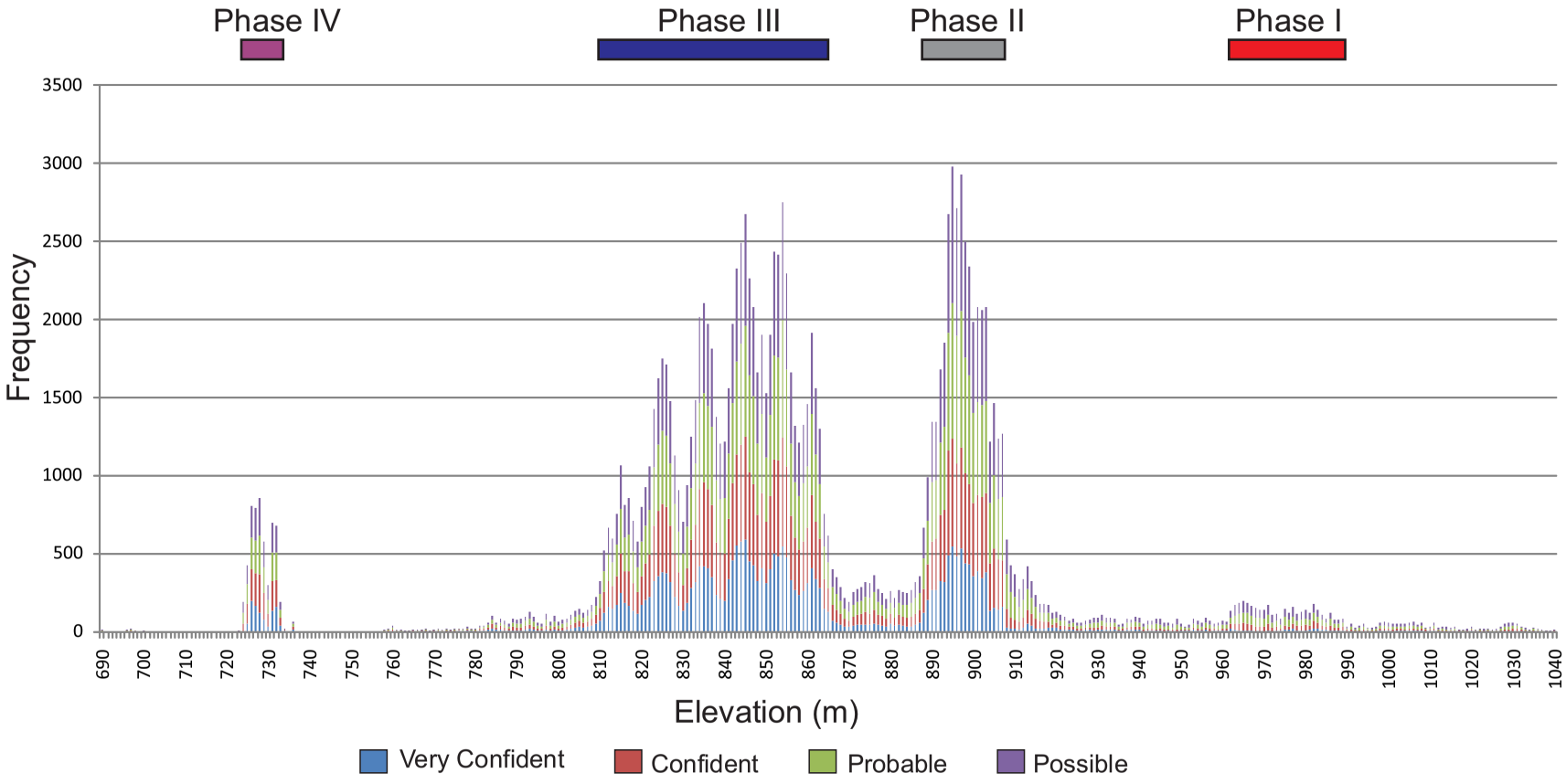

Figure 6.6. Histogram of elevation points generated from mapping shoreline features; peaks represent elevations associated with relatively stable positions of GLP.

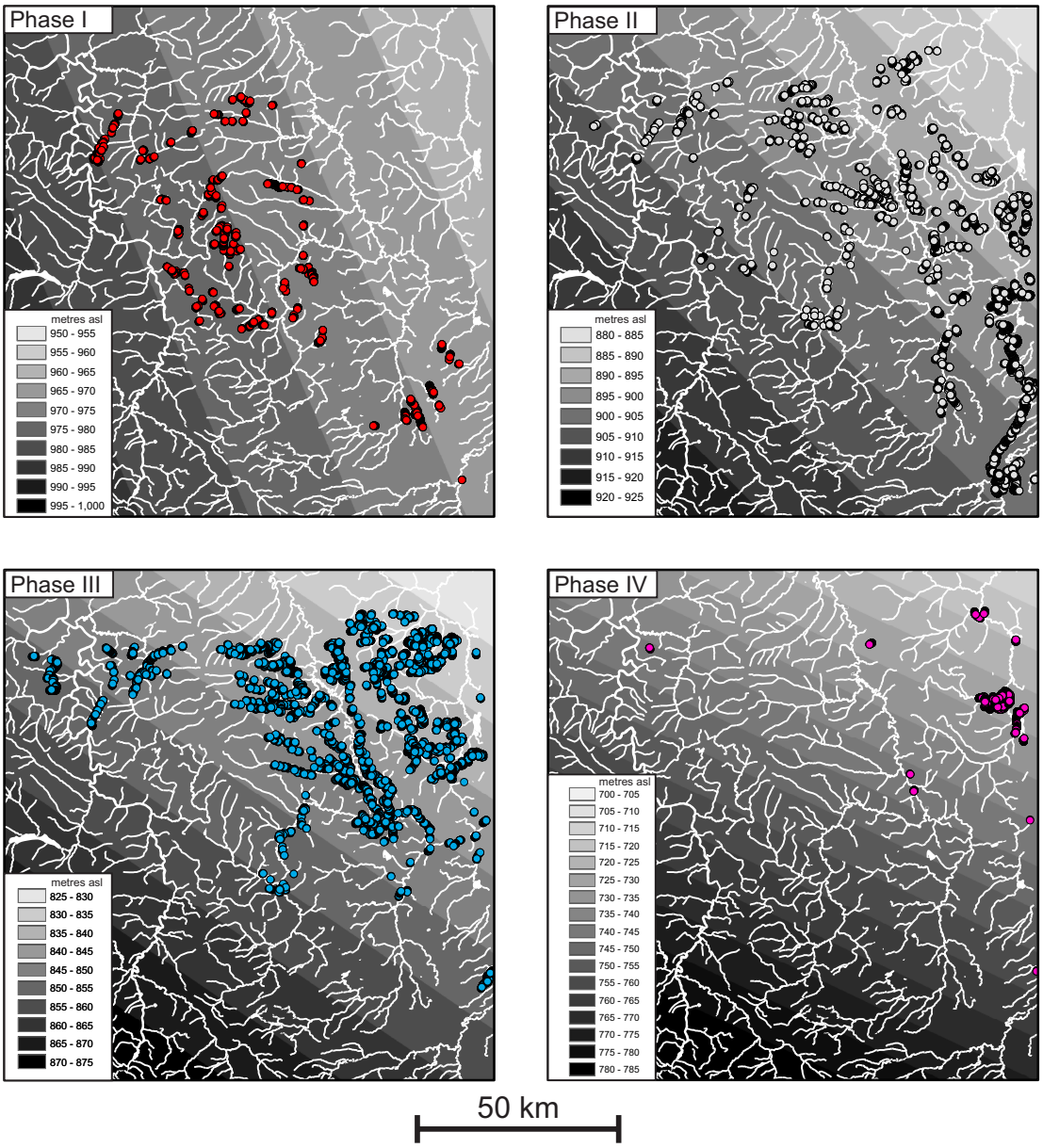

Figure 6.7. Best fit first-order polynomial surfaces, generated from the "very confident" and "confident" categories of shoreline (in all diagrams, north is to the top of the page).

Table 6.1. Shoreline feature mapping by certainty.

Certainty	No. Segments	Minimum Segment Length (m)	Maximum Segment Length (m)	Mean Segment Length (m)	Number of 25 m Points
Very Confident	1794	12.3	3109.1	365.7	27127
Confident	695	27.1	1646.5	294.3	8536
Probable	524	31.2	1444.3	274.2	6014
Possible	62	56.5	537.2	253.4	661
Uncertain	155	56	2584.5	387.7	2484
Total	3230				44822

correspond with the clearly developed shorelines south and west of Dawson Creek noted by Mathews (1980; Fig. 6.4). This flight of shorelines is well developed throughout the study area, constituting the bulk of the shorelines mapped. The Phase IV population (between 724 m and 733 m) are from well-developed shorelines clustered around Swan Lake basin in the northeast of the study area. There are two peaks in this population, one between 729 m and 734 m and another at 724 m and 729 m.

6.3.2 ISOSTATIC ADJUSTMENT

To reconstruct lake levels, elevation must be corrected for relative isostatic adjustment since deglaciation. A first order polynomial regression surface was generated for each of the phases (Figs. 6.7 and 6.8; Table 6.2). Data points between 960 m and 990 m were used to generate the regression surface for Phase I. There is large scatter in the distribution of the data >940 m. The regression surface was created from the dominant population between 960 m and 990 m. The resulting surface has an R^2 value of 0.154 and indicates a cumulative isostatic adjustment of a 0.26 m/km rise to the southwest (246°). Phase II data comes from a relatively narrow elevation interval and the resulting regression surface has an R^2 value of 0.567 and visually looks to fit well with the slope of the data (Fig. 6.8). This suggests that the cumulative isostatic adjustment since these shorelines developed has resulted in a relative south-westward (224°) rise of approximately 0.32 m/km. Phase III consists of 5 distinct and parallel shoreline stages (Fig. 6.8). All of the data between 770 m and 875 m were used to generate the regression surface for Phase III. Because the regression surface was not generated for each stage, no R^2 value is reported. This surface is, however, approximately parallel with the shoreline stages and is a reasonable representation of the overall isostatic adjustment for the whole population. The regression surface suggests a cumulative relative south-westward (213°) rise of approximately 0.43 m/km. The regression surface computed for Phase IV shows a poor fit (R^2 = 0.14 when all values in the population between 724 m and 733 m are used). When the two populations are separated, the R^2 values for Phase IVa (729m-734m) and Phase IVb (724 m-729 m) are 0.340 and 0.024, respectively. The regression surface for Phase IVa indicates a cumulative relative southern (180°) rise of approximately 0.23 m/km. The regression surface for Phase IVb has a relatively poor fit, but suggests a cumulative relative southwest (216°) rise of approximately 0.18 m/km.

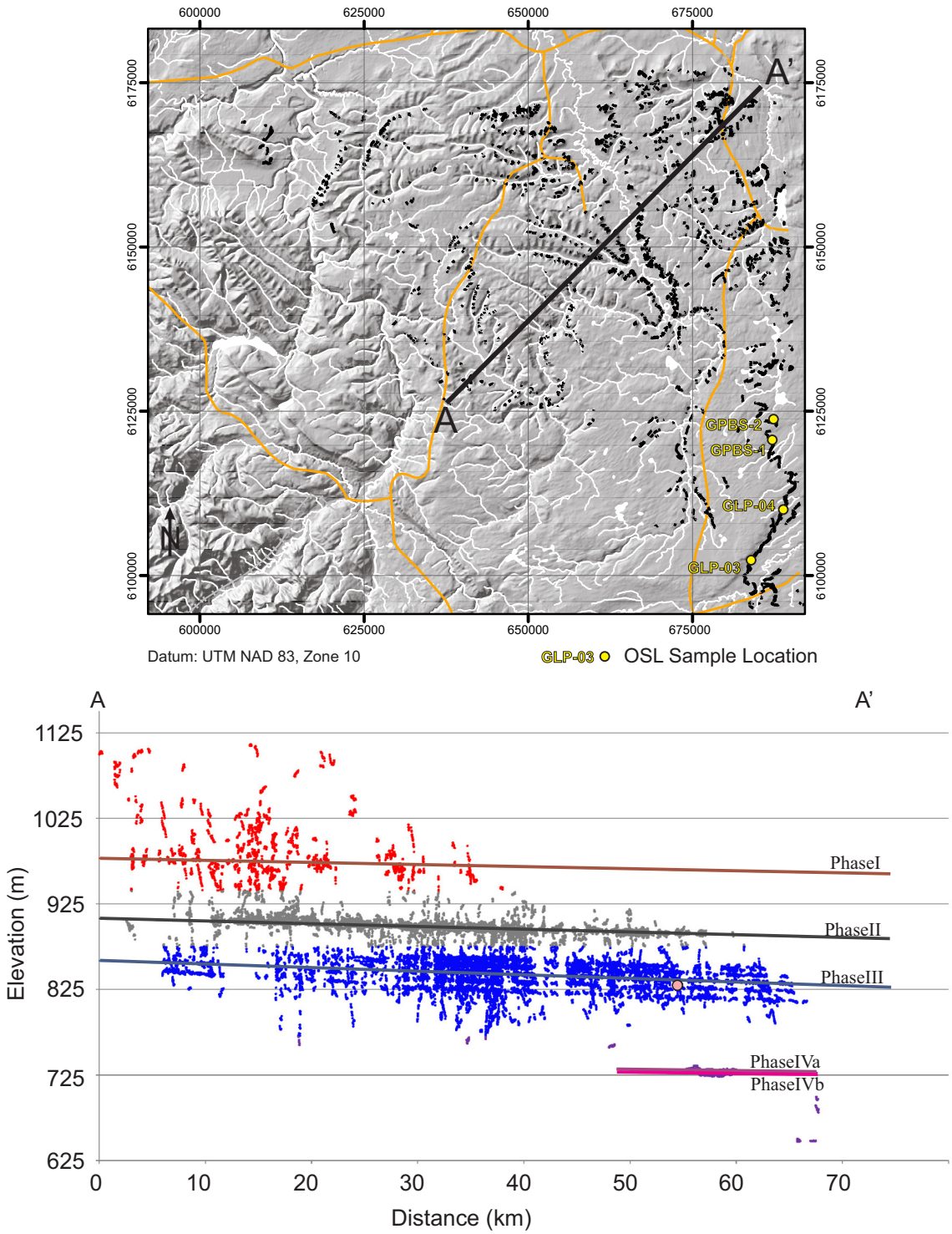

Figure 6.8. Locations of shoreline data points and OSL samples. The lower chart is a projection of elevation points by population (Fig. 6.6) and the first order polynomial surfaces along transect A to A'. Mathews (1980) Bessborough phase is projected onto the chart (circle) within the Phase III population of this study.

Table 6.2. Regression surface analysis for very confident and confident data from each population of elevation data.

	No. of points	Elevation (m asl)	Regresion Surface Equation z(x,y)	Aspect (azimuth)	Slope (m/km)
Phase I	899	960-990	-0.0002416(x) + -0.0001074(y) + 1789.8875	66.0	0.2645
Phase II	9145	>875-940	-0.0002256(x) + -0.0002293(y) + 2456.4429	44.0	0.3220
Phase III	20199	>770-875	-0.0002391(x) + -0.0003543(y) + 3181.2897	33.3	0.4269
Phase IVa	499	>729-734	-0.000002790(x) + -0.0002312(y) + 2157.0872	0.1	0.2314
Phase IVb	955	724-729	-0.0001055(x) + -0.0001438(y) + 1684.4369	36.2	0.1784

6.3.3 OPTICAL DATING GEOCHRONOLOGY

Four samples were collected for optical dating of the Phase II flight of shorelines (Fig. 6.9; Table 6.3). Each sample was collected from a prominent shoreline that contained near-shore or beach glaciolacustrine sediments (Fig. 6.10). Sample GPBS-1 was collected from an upper strandline on a northeast-facing slope. The local stratigraphy consists of a lower fine-grained sand unit with a small cobble-gravel interbed overlain by 95 cm of crudely stratified and dipping, poorly sorted, pebble to cobble sized gravel. This unit is overlain by 70 cm of poorly sorted, subhorizontally stratified, open-framework, granular to pebble sized gravel (Fig. 6.10a). The water table was present at 270 cm. The upper facies were too coarse to be dated so the first available sand bed was sampled from a depth of 210 cm below surface. Sand from this unit was initially interpreted to have been deposited in the littoral zone, however, the unit is probably from sublittoral or limnetic zones (limited light penetration; see discussion). GPBS-2 was collected from a lower strandline on a northeast facing slope, east of what would have been a headland (Fig. 6.9). The local stratigraphy consists of a lower laminated silt and sand unit with abundant coal granules (Fig. 6.10). This unit is overlain by 35 cm of poorly sorted pebbly sand and 30 cm of poorly sorted pebble to small cobble sized gravel with a sand matrix, separated by a 10 cm thick coaly sand horizon. This sequence, in turn, is overlain by another 10 cm coaly sand bed, followed by a poorly sorted pebble sand to the surface. The water table was present at approximately 2.0 m. The sample was collected 70 cm below the surface in a sandy portion of the pebble gravel interpreted to be deposited in a relatively high energy wave washed shoreface. In this environment it is expected that the wave action in the surf zone would (at least intermittently) expose sand grains to sufficient light energy to reset the optical clock. Sample GLP-03 was collected from an east-facing slope in approximately the middle of the flight of shorelines. The local stratigraphy consists of diamict overlain by 65 cm of poorly sorted, silty, fine to medium sized sand (Fig. 6.10). The lower contact is marked by a pebble lag. The sample was collected from 50 cm below the surface in a sandy unit interpreted to be deposited in a nearshore littoral zone. It is possible, however, that this unit is a aeolian (see discussion). Sample GLP-04 was collected from an upper strandline on a southeast-facing slope. The local stratigraphy consists of diamict overlain by 50 cm of sandy, pebble to cobble sized gravel (Fig. 6.10). The sample was collected from 45 cm below surface in a sandy lens immediately above

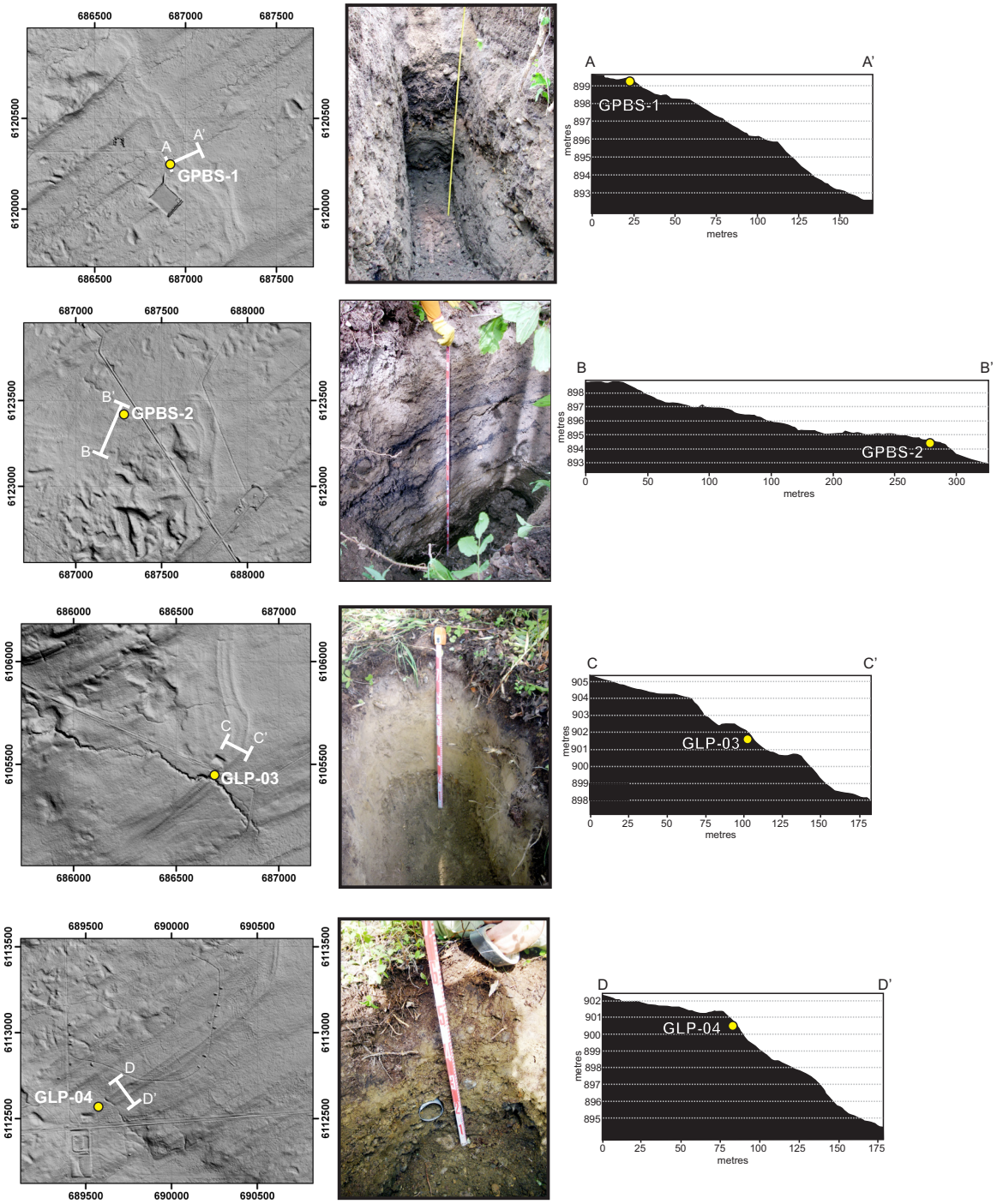

Figure 6.9. OSL samples collected from 4 widely dispersed locations along Phase II features. Detailed DEMs (left), photograph of the shoreline sediments (centre) and topographic profiles (right) perpendicular to the shorelines.

Table 6.3. OSL sample depths and locations.

Sample	Depth Below Surface (m)	Easting[1]	Northing[1]	Latitude	Longitude
GPBS-1	2.10	686892	6120327	55° 11' 39"	120° 03' 49"
GPBS-2	0.70	687316	6123417	55° 13' 18"	120° 03' 18"
GLP-03	0.50	686684	6105437	55° 03' 38"	120° 04' 36"
GLP-04	0.40	689598	6112576	55° 07' 24"	120° 01' 35"

[1] Universal Transverse Mercator coordinates in North American Datum (NAD) 83

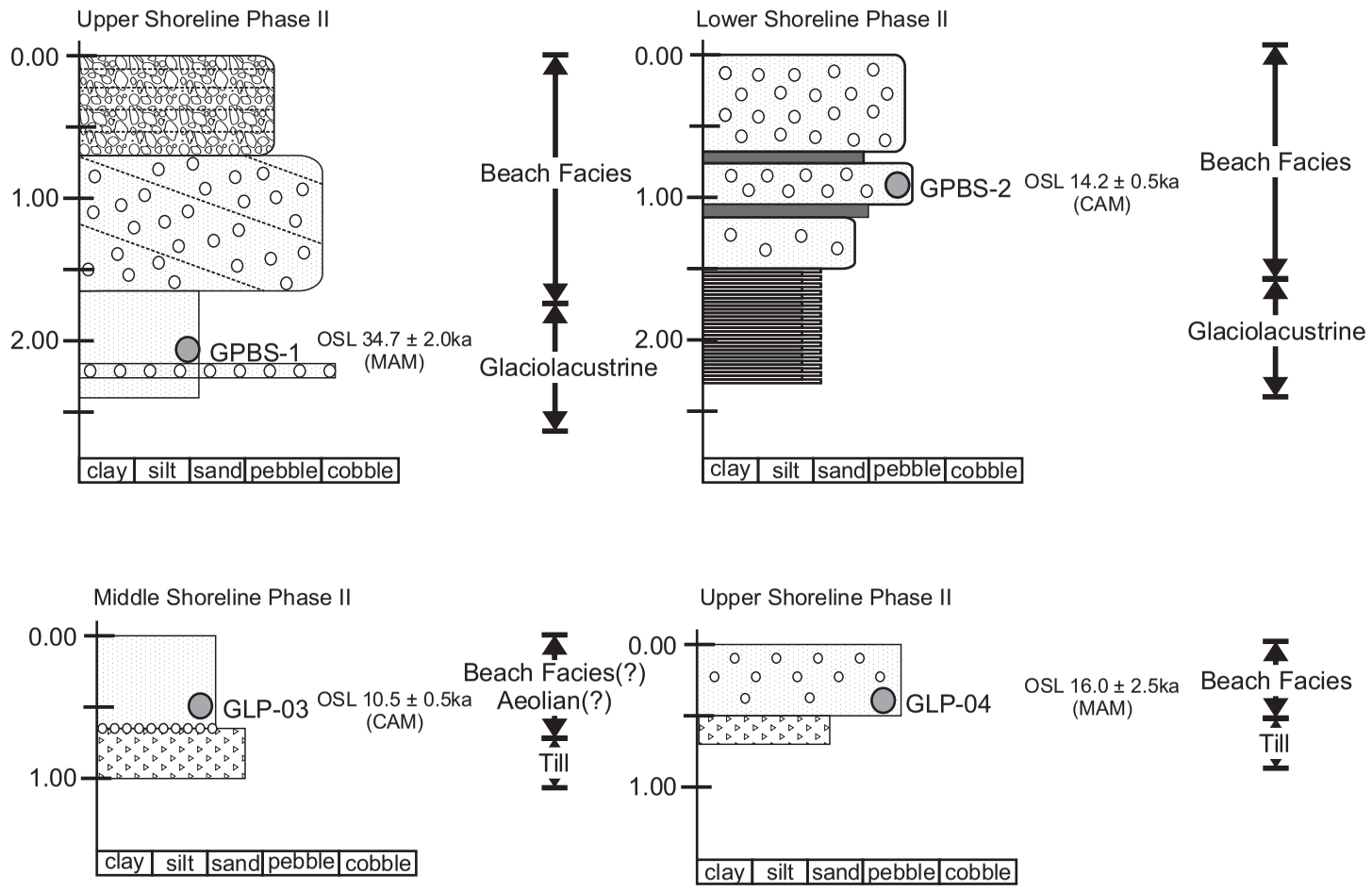

Figure 6.10. Stratigraphic logs show the depth and OSL age of the four samples collected from the Phase II flight of shoreline features.

the contact with the diamict, interpreted to be deposited in a relatively high energy wave washed shoreface.

The environmental dose rate was determined by in situ measurement for samples GPBS-1 and GPBS-2 and by laboratory analysis for samples GLP-03 and GLP-04. Dose rates are summarized in Table 6.4. Representative luminescence verses stimulation time curves ("shine down" curves) and dose-response curves for each sample are presented along with the radial plots showing all the accepted De values (Fig. 6.11). The calculated ages are presented in Table 6.5.

All but one of the samples returns Late Wisconsinan (MIS 2) optical ages; the exception being GPBS-1. Overdispersion for samples GPBS-2 (n = 85 aliquots) and GLP-03 (n = 35 aliquots) are 18.2 ± 1.5% and 19 ± 3%, respectively. The central age model (CAM) was, therefore, applied and optical age for GPBS-2 is 14.2 ± 0.5 ka and for GLP-03 is 10.5 ± 0.5 ka. Relatively low overdispersions and a significant fast component in the shine down curves, provides high confidence that the method is appropriate for these samples. GLP-03 returned a younger than expected age. The optical age maybe too young if the unstable components of the luminescence (medium and slow components of the shine down curve) were inadvertently sampled. Alternatively, the sediment sampled at this location may have been misidentified as glaciolacustrine and instead has an aeolian origin (c.f. Chapter 7). If this is the case, the optical age for GLP-03 is not related to GLP, but represents aeolian activity during paraglacial times (see Chapter 7)

The overdispersion for sample GLP-04 (n= 47 aliquots) was high (32.4 ± 3.4%) suggesting that a significant population of grains was not exposed to sufficient sunlight to reset the luminescence clock. A minimum age model (MAM) was instead applied and the resulting age indicates that GLP-04 was deposited and buried sometime after 16.0 ± 2.5 ka. The central age model (CAM) for GPBS-1 (32 aliquots) returned an age of 34.7 ± 2.0 ka which is significantly older than would be expected for deglacial sediments and is much older than the other samples. GPBS-1 has an overdispersion of 27 ± 3.1% which suggest that there may be a population of grains in this sample that were not exposed to sufficient sunlight to reset optical signal. Given the sample was collected from 2.10 m depth below surface in a fine-grained unit, it is likely that the sediment was not deposited in the shore facies associated with Phase II, but is probably from pelagic sediment deposited prior to phase II when the lake level was higher. Consequently,

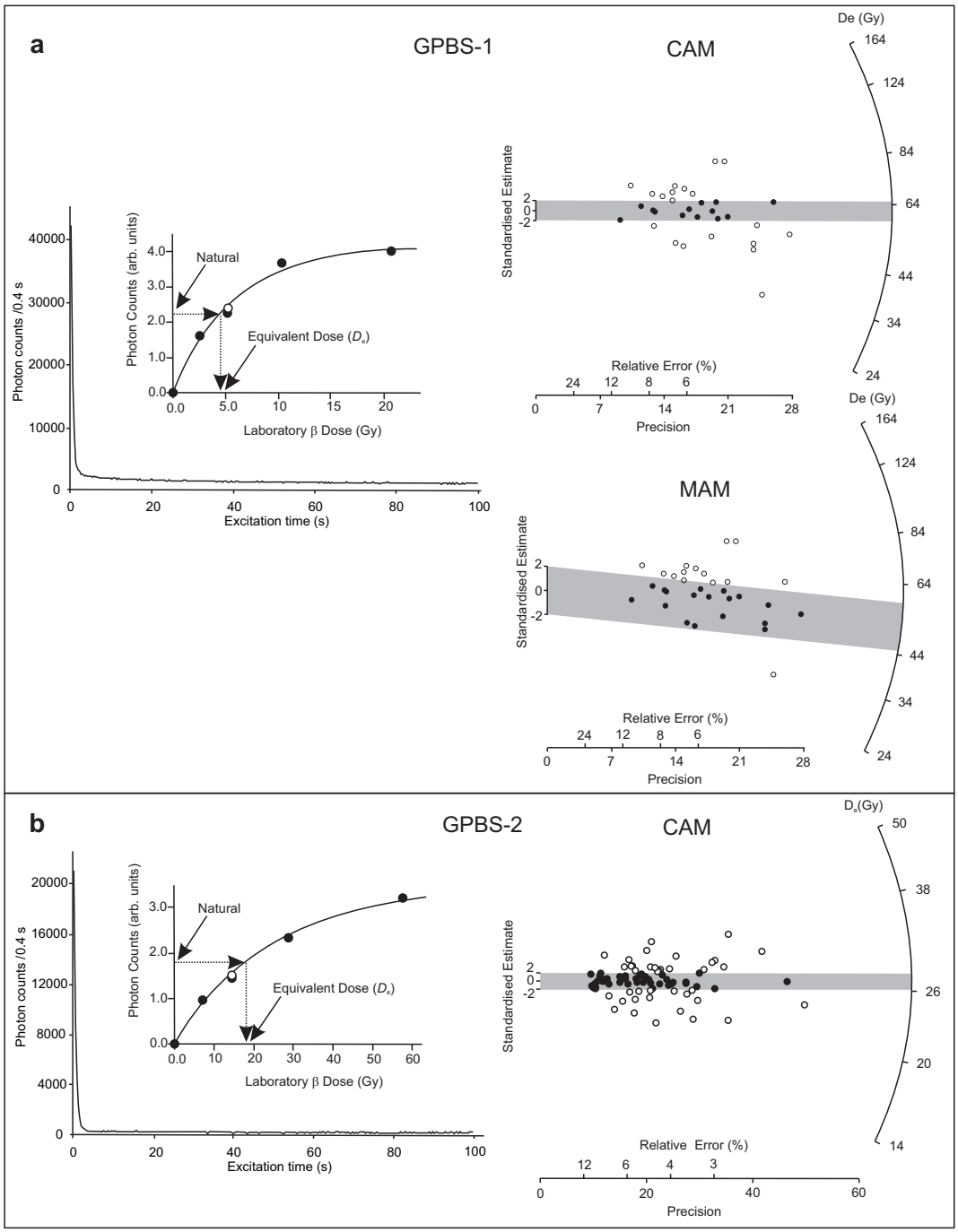

Figure 6.11. Examples of the OSL response for each of the samples from the Phase II shoreline including a typical shine down curve (photon count vs. excitation time) the associate growth curve (photon count vs. Laboratory β dose) and the radial plot. The open circle on the growth curve plot is a duplicate dose point used to determine the recycling ratio. Since it is close to unity in these samples, the test dose procedures has successfully corrected for sensitivity changes. The grey region on the radial plots represents the weighted-mean equivalent dose value of all the data. a) GPBS-1; b) GPBS-2; c) GLP-03; and d) GLP-04.

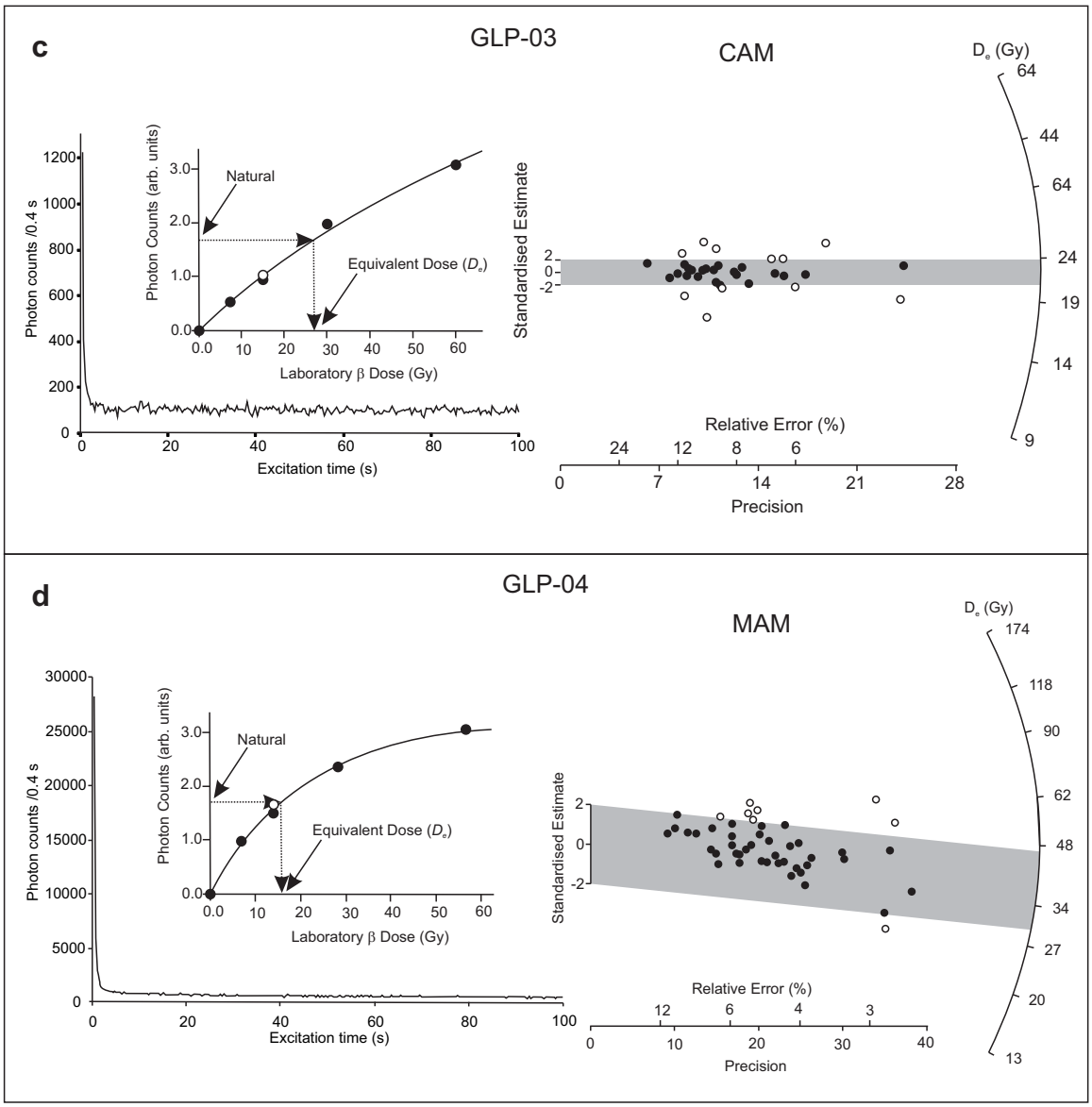

Figure 6.11. ***Continued***

Table 6.4. K, U, and Th concentrations determined from laboratory analyses and in situ γ-ray spectroscopy.

Sample	K (%)[1]	Th ($\mu g \cdot g^{-1}$)[1]	U ($\mu g \cdot g^{-1}$)[1]	From *in situ* γ-ray spectroscopy			
				K (%)	Th_e ($\mu g \cdot g^{-1}$)[2]	U_e ($\mu g \cdot g^{-1}$)[2]	γ dose rate ($Gy \cdot ka^{-1}$)[3]
GLP3	1.30 ± 0.07	7.20 ± 0.23	2.07 ± 0.13	–	–	–	–
GLP4	1.49 ± 0.08	7.20 ± 0.23	2.21 ± 0.41	–	–	–	–
GPBS1	–	–	–	0.933 ± 0.028	1.896 ± 0.150	3.722 ± 0.219	0.618 ± 0.021
GPBS2	–	–	–	0.982 ± 0.029	2.002 ± 0.164	4.700 ± 0.243	0.688 ± 0.023

[1] Concentrations calculated from dry sediment using atomic absorption.

[2] Equivalent concentrations calculated from the activities of ^{214}Bi for U and ^{208}Tl for Th, assuming secular equilibrium.

[3] From counts in the energy range 0.8–2.6 MeV, corrected for relative proportions of K, U, and Th. The values listed have not been corrected for water content.

Table 6.5. Dosimetry results and optical ages.

Sample	Depth (m)[1]	$\dot{D}_c$ (Gy/ka)[2]	$\dot{D}_T$ (Gy/ka)[3]	OD (%)	D_e (Gy)[4]	Optical age (ka)
GPBS-1	2.10	0.147 ± 0.007	1.81 ± 0.10	27 ± 4	62.7 ± 3.1 [5]	34.7 ± 2.0
					39.4 ± 7.6 [6]	21.8 ± 4.2
GPBS-2	0.70	0.186 ± 0.010	1.99 ± 0.11	18.2 ± 1.5	28.1 ± 0.6 [5]	14.2 ± 0.5
GLP-03	0.50	0.192 ± 0.010	2.25 ± 0.14	19 ± 3	23.7 ± 0.7 [5]	10.5 ± 0.5
GLP-04[7]	0.45	0.194 ± 0.010	2.39 ± 0.15	32.4 ± 3.4	38.2 ± 5.7 [6]	16.0 ± 2.5

O.D. = Overdispersion

[1] Sample depth below the ground surface.

[2] Dose rate due to comic ray radiation, calculated using present burial depths and the relationship of Prescott and Hutton (1994).

[3] Total dose rate, $\dot{D}_T = \dot{D}_c + \dot{D}_{\beta,\gamma}$ where $\dot{D}_c$ is the cosmic-ray dose rate and $\dot{D}_{\beta,\gamma}$ is the dose rate due to β and γ radiation, the α-affected surfaces of the grains having been removed by etching. *In situ* water contents were used for the dose rate calculations, with uncertainties that are expected to account for any reasonable fluctuation at two standard deviations.

[4] D_e found using luminescence measured during the first 0.4 s of excitation.

[5] Found using the central age model (CAM)

[6] Found using the minimum age model (MAM)

[7] Sample GLP-04 was collected adjacent to a potassium-rich granitoid boulder. The cobble was, therefore collected, a part milled, and analyzed by INAA. GLP-04 was treated as a sample that occurs at the boundary between media with two different dose rates (sand and cobble). The environmental dose rate was estimated by determining the contributing dose rate from the sand and the cobble using Aitken's (1985) method for dealing with layer to layer variation in radioactivity.

Concentrations, sample: [K] = 1.49 ± 0.08 %; [U] = 1.21 ± 0.14 μg/g; [Th] = 7.20 ± 0.23 μg/g.
Concentrations, boulder: [K] = 4.58 ± 0.19 %; [U] = 4.82 ± 0.20 μg/g; [Th] = 47.6 ± 1.4 μg/g.

The γ dose rate calculated for boulder is 3.93 ± 0.14 Gy/ka
The γ dose rate calculated for the sample is 0.838 ± 0.040 Gy/ka (using *in situ* water content)

Estimate that the sample was collected 5 cm from the boulder, and assume that both boulder and sample have a density, ρ, 2.5 g/cm^2. Using Table H.1 in Aitken (1985), scale the distance, *z*, by $2/\rho = 0.8$, so *z* effectively becomes 4 cm. At 4 cm the dose from the boulder drops by a factor of (1- 0.78) = 0.22. Therefore <u>estimate</u> γ dose contribution from boulder to be 0.865 ± 0.03 Gy/ka. The dose from the sample (imagining that the boulder is replaced by an inert medium) drops by a factor of 0.78 to be 0.653 ± 0.031 Gy/ka. Therefore the total γ dose rate at the sample is 0.865 + 0.653 ≈ 1.51 ± 0.06 Gy/ka.

the minimum age model (MAM) was applied and indicates that sediments deposited at GPBS-1 was deposited some time after 21.8 ± 4.2 ka.

6.4 Discussion

The dataset used in this study enabled the mapping of features associated with the margins of GLP that were previously undetectable in other studies. This information provides new insight into lake levels, isostatic crustal adjustment, and ice sheet configuration during deglaciation.

Most approaches to shoreline mapping, even with GIS, generally rely upon a limited number of shoreline locations and elevations to reconstruct and correlate lake levels (e.g. Schaetzl et al., 2002; Johnson and Brennand, 2004). Furthermore, it has been argued that there is a considerable difference between top elevation of depositional landforms such as beach ridges, spits, and lags and the average elevation of the associated water-surfaces (Thompson, 1992). Thus, it is a challenge in isostatically dynamic environments to reconstruct paleo-lake levels to metre or sub-metre scale with any acceptable degree of certainty based on just a few widely dispersed correlative features. Indeed, LiDAR data used in this study show that, where well developed features exist, there is typically a flight of many shorelines spanning a relatively broad elevation interval at a given location. The shoreline features mapped here generated more than 40,000 data points clustered into four distinct populations, which support confident spatial correlation. The elevation populations suggest that four lake phases occurred in this area and that within those phases there were multiple stages representing both large scale and smaller lake level fluctuations (Fig. 6.6).

The highest phase ranges from 960 m to 990 m and is designated Phase I. This phase is poorly constrained and likely represents many water-surfaces that developed early during ice-sheet separation. Although we consider these features as part of GLP, it is conceivable that some of the shorelines may have been part of isolated lakes that developed adjacent to ice in upland valley areas (Liverman, 1991). As ice sheets retreated, lakes in the major valleys likely merged into a continuous body of water (i.e. GLP).

Phase II consists of a flight of shorelines that are well constrained by a population peak occurring between 890 m and 910 m. The range in elevation reflects, in part, the local elevation range of the shorelines at each location (typically 10 m-15 m; Fig. 6.7b) and in part results from

isostatic inclination of the landscape. The well-developed, yet narrow span of the shorelines represents the earliest unambiguous phase of GLP in this area. Although there are clearly some small scale lake level fluctuations, the narrow span of the distribution of elevations suggests that the large scale lake level remained stable. Stability is also suggested by strong geomorphic expression of these shoreline features in the field where well developed beach ridges, deltas, and spits are recognized. Lag deposits of sand, and gravel are common in these geomorphic features and often cover underlying glaciolacustrine and diamict units (Figs. 6.9 and 6.10). The relatively few data points falling between the populations assigned to Phase II and Phase III suggest that the transition of GLP Phase II to Phase III was abrupt, signifying a rapid lowering of lake level to a new stable position (e.g. Teller et al., 2002, Teller, 2005). This punctuated drop in lake level likely resulted from the abandonment of an unknown outlet and the establishment of a new, lower outlet probably the Pass Creek Outlet in Alberta (Mathews, 1980).

The multi-modal distribution of Phase III encompasses shorelines that span an elevation of 810-865 m. The multi-modal peaks are from well-developed, parallel shorelines (Fig. 6.7) traceable throughout the map area. Field visits at several strandlines south of Dawson Creek (near Highway 52), show well developed geomorphic expression in the form of benches, but limited sedimentologic evidence of extensive beaches. Sediments on the platforms of the benches typically consist of a thin, oxidized (<30 cm) silty-sand in the B-horizon (Brady and Weil, 1996) over glaciolacustrine silt and sand or diamict (probably till). The peaks indicate at least five, or possibly six, stages within Phase III and signify periodic regression and stabilization. These consistent and parallel shorelines suggest that GLP likely continued to exploit the same outlet during Phase III with the outlet incised to progressively lower elevations (c.f. Teller et al., 2002, Teller, 2005). Phase III is equivalent to Mathews (1980) Bessborough Stage (his Phase 2) as indicated by projecting the Bessborough shoreline elevation onto the cross-section in Fig. 6.8.

The shoreline features that represent Phase IV dominantly occur around the Swan Lake Basin between 724 m and 733 m. Shoreline features in Phase IVa typically are capped with well laminated sand (10-20 cm thick) and overlie glaciolacustrine sediments. Shorelines associated with Phase IVb can be traced to strandlines that essentially enclose modern Swan Lake suggesting these features developed as GLP retreated from the area and Swan Lake became an isolated basin.

It has been noted by others that there has been relative vertical crustal displacement in northeast British Columbia and northern Alberta from differential isostatic rebound following deglaciation (Tokarsky, 1967; Rutter, 1977; Mathews, 1978, 1980; Liverman, 1991; and Woolf, 1993; and Lemmen et al., 1994). This is confirmed in this study from the apparent slope of the polynomial surfaces generated from correlative shoreline features. Tokarsky (1967) suggested 0.3 m/km of rise to the northeast in the Grimshaw region of Alberta. Mathews (1980) predicted a general rise in elevation of 0.4 m/km towards the west and south and Woolf (1993) suggested that there could have been as much as 0.6 m/km of rise towards the south during the Clayhurst Phase of GLP. The isostatic adjustment suggested from this study is generally compatible with that suggested by Mathews (1980) and Woolf (1993). Results do indicate however, that the isostatic adjustment shifted through the various phases of the lake, a pattern consistent with the expected response of the crust as ice sheets retreat (Flint, 1971; Larsen, 1987, Teller, 2005). The cumulative modeled slope increases from Phase I to Phase II, then decreases through to Phase IV. If isostatic rise was constant, the cumulative relative slope of successive isobases (water surfaces) would decrease through time. Since this is not the case, it is suggested that the orientation of slope aspect may have flipped between Phase II and III. This is explained by isostatic uplift initiating in the northeast, but later outpaced by uplift in the southwest of the study area, implying that LIS initially retreated away from the CIS while the CIS remained extensive (Fig. 6.12). As the LIS thinned and retreated, the crust under the Interior Plains rebounded. In this scenario, the CIS would have either caused greater crustal depression in the mountains (very thick ice causing greater initial loading), or remained thick in the mountains well after the LIS retreated from the area. By the end of Phase III, the CIS would have thinned and rate of relative uplift in the Foothills and Rocky Mountains surpassed that of the Interior Plains. This history is consistent with the Late Wisconsinan retreat model of Bednarski and Smith (2007), but not with those of Bobrowsky (1989), Bobrowsky and Rutter, (1992) and Catto et al. (1996) that suggest the CIS was of limited extent during the Late Wisconsinan.

Four phases of GLP can be correlated with those identified by others (Fig. 6.13 and Fig. 6.14). The reconstructions presented here are remarkably similar to those established by Mathews (1978, 1980) from work in the 1950s and 1960s. His work is particularly noteworthy since it was completed prior to much of the infrastructure development in the area and without

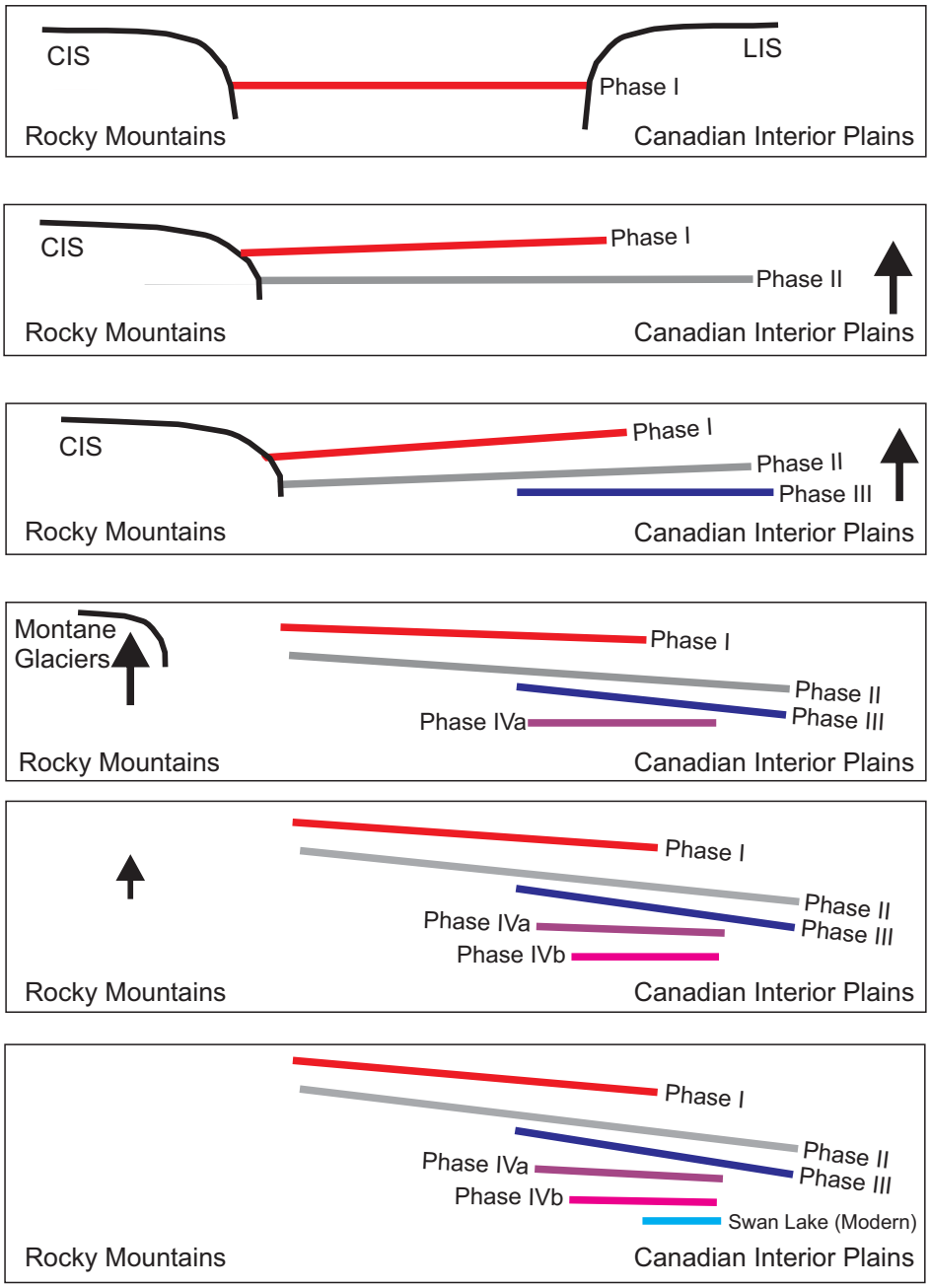

Figure 6.12. The slope of the isostatically adjusted surfaces though time. Phase I, GLP formed between the LIS and the CIS. Phase II, Canadian Interior Plains initially rose in response to ice unloading, causing shorelines to dip to the southwest. After Phase III isostatic uplift in the Rocky Mountains outpaced uplift in the Canadian Interior Plains (not to scale).

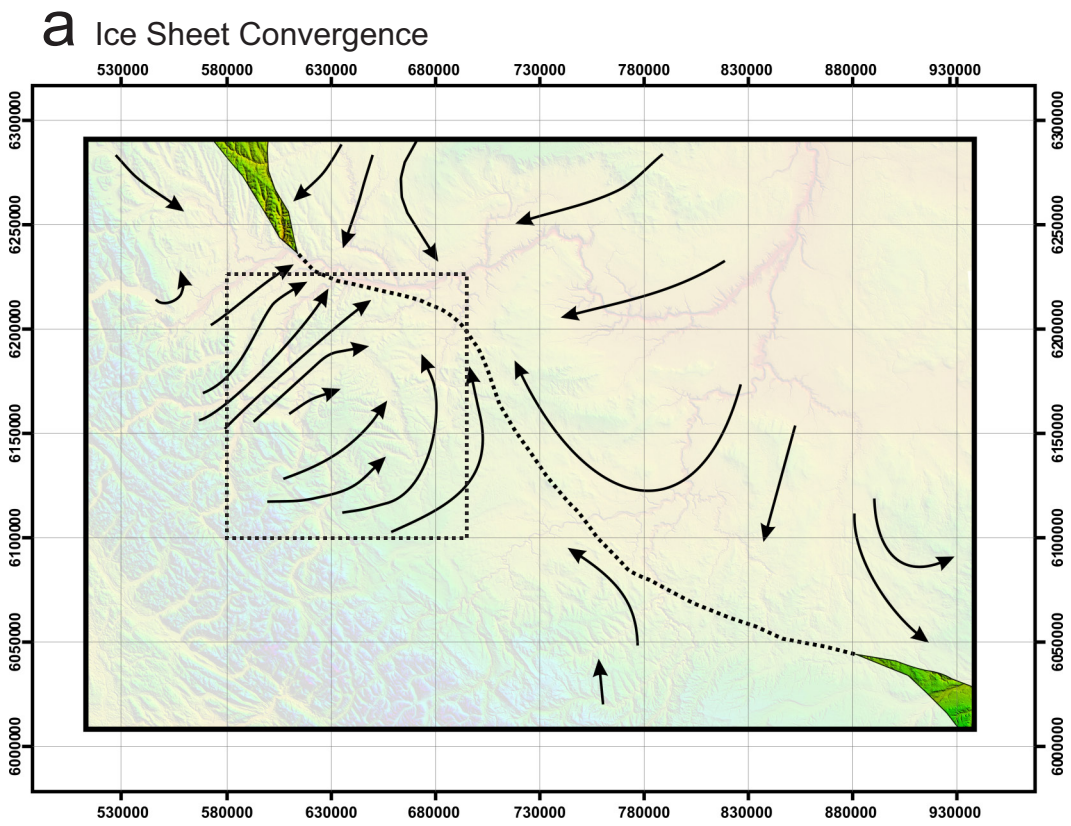

Figure 6.13. Possible ice sheet and GLP configuration in the Late Wisconsinan with isostatically corrected topography (study area is marked by the dashed black box) (ice margins modified from Mathews, 1980 and St Onge, 1972). a) Ice Sheet Convergence; b) Early Ice Sheet Separation c) Phase I: Both the CIS and the LIS continue to retreat and meltwater coalesces to form GLP; d) Phase II: The first phase with well established shorelines, was established around <16.0 ± 2.5 ka to 14.2 ± 0.5 ka yrs BP (from OSL ages). e) Upper Phase III: Equivalent to Bessbough Phase, a stable phase with an outlet at Pass Creek; f) Lower Phase III: Equivalent to Mathews' unnamed Phase 3; It is possible as the lake receded, a topographic high separated the Peace River Basin from the Smokey River Basin causing emergence of land around Grande Prairie; Phase IV: Lowest phase of GLP that occupied mainly the Peace River Basin.

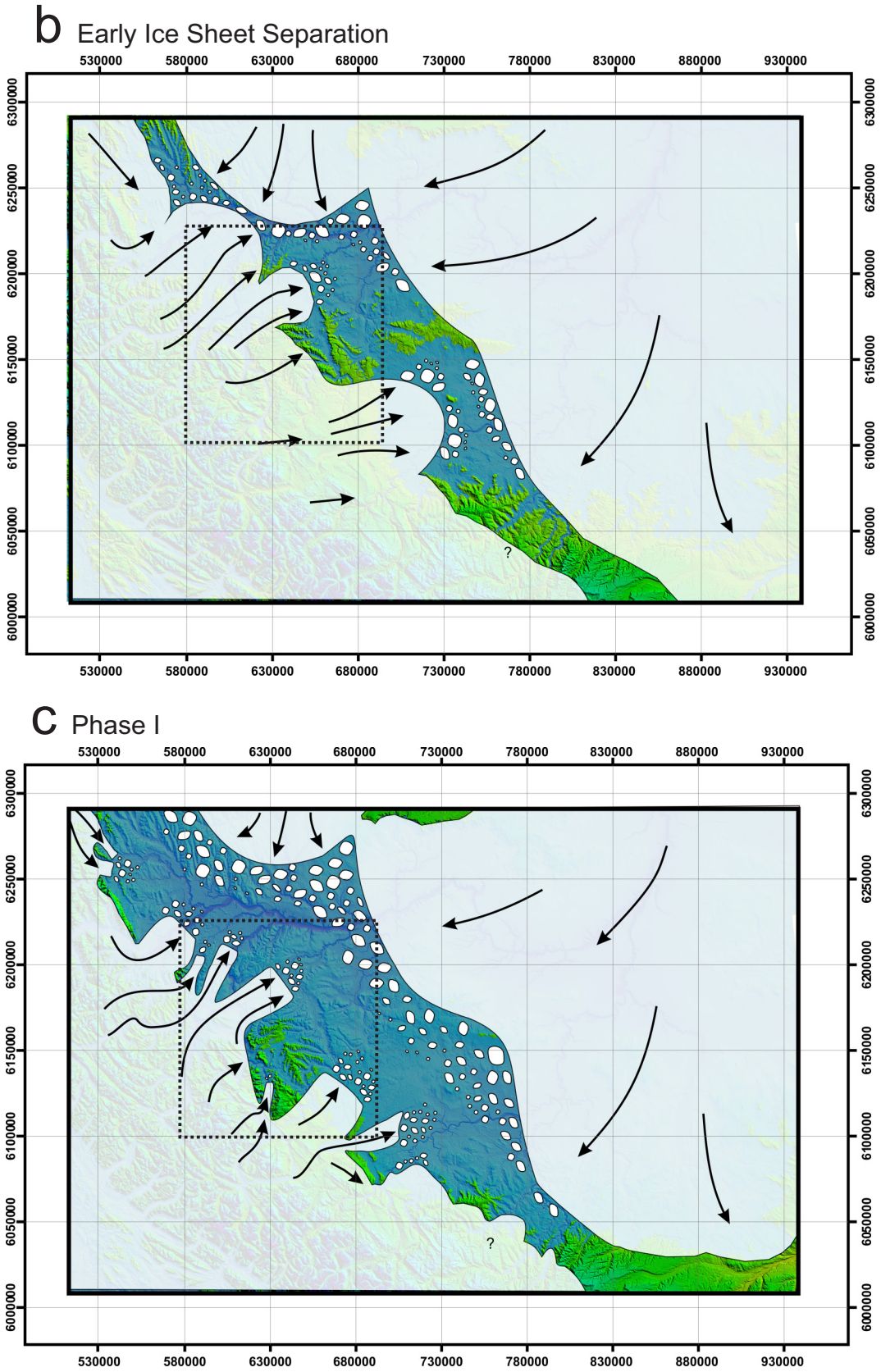

Figure 6.13. ***Continued***

d Phase II

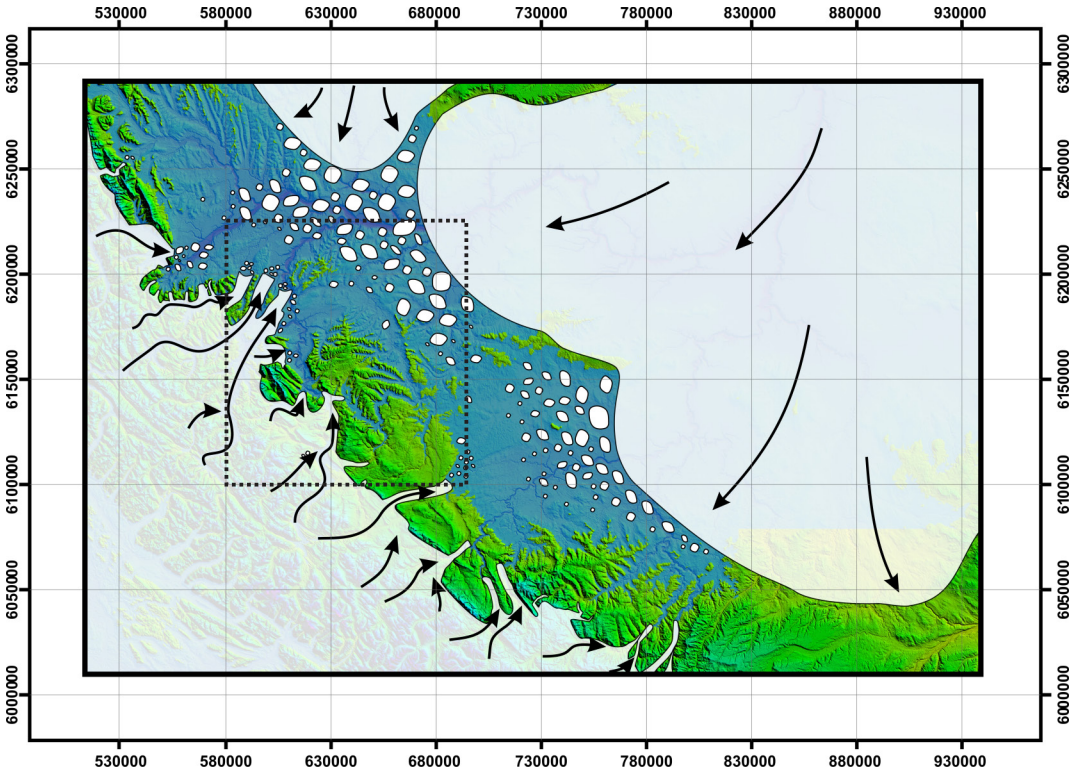

e Upper Phase III

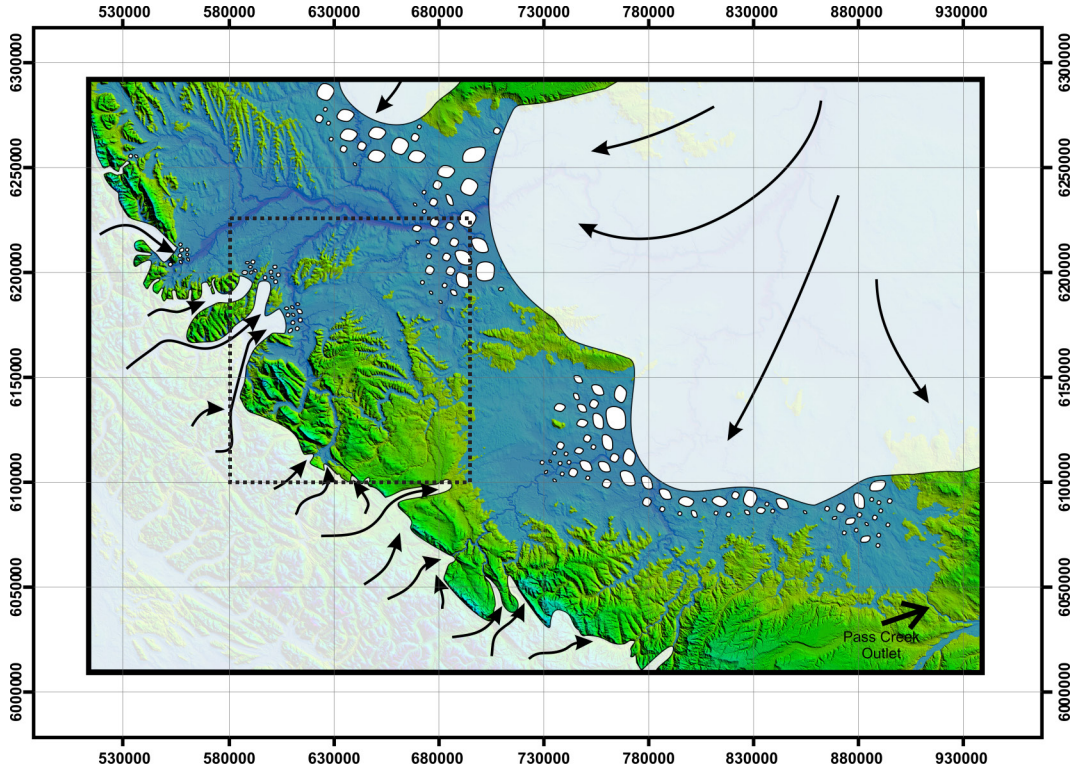

Figure 6.13. ***Continued***

f Lower Phase III

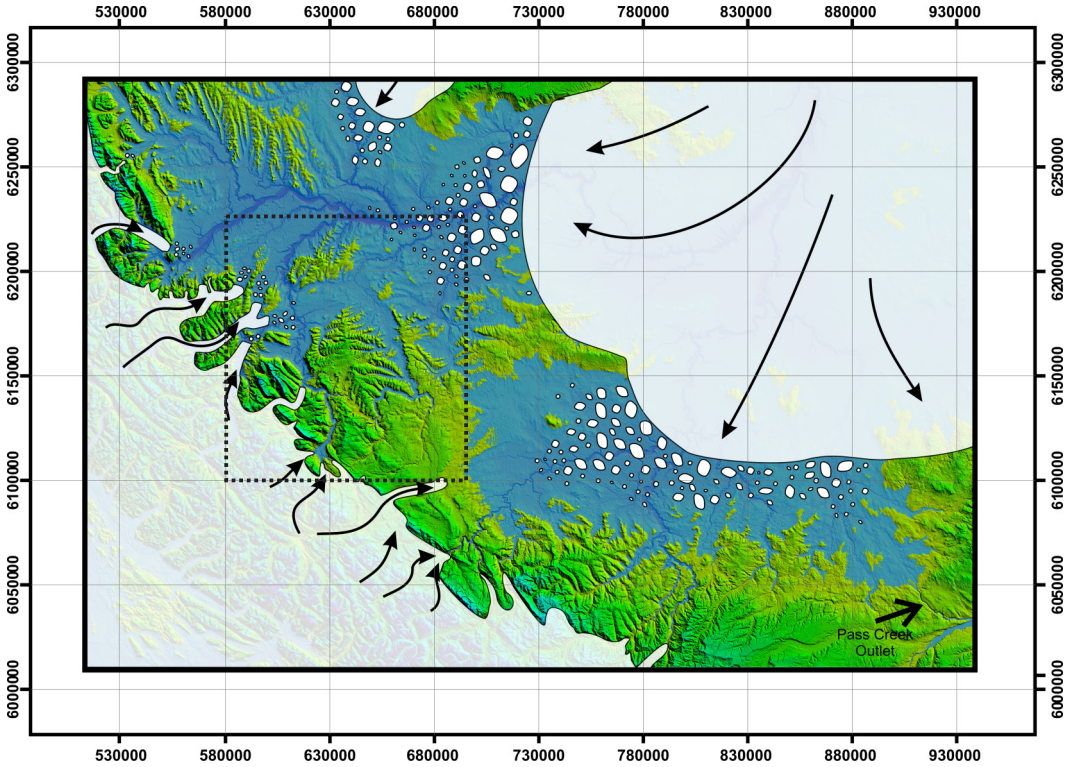

g Phase IV

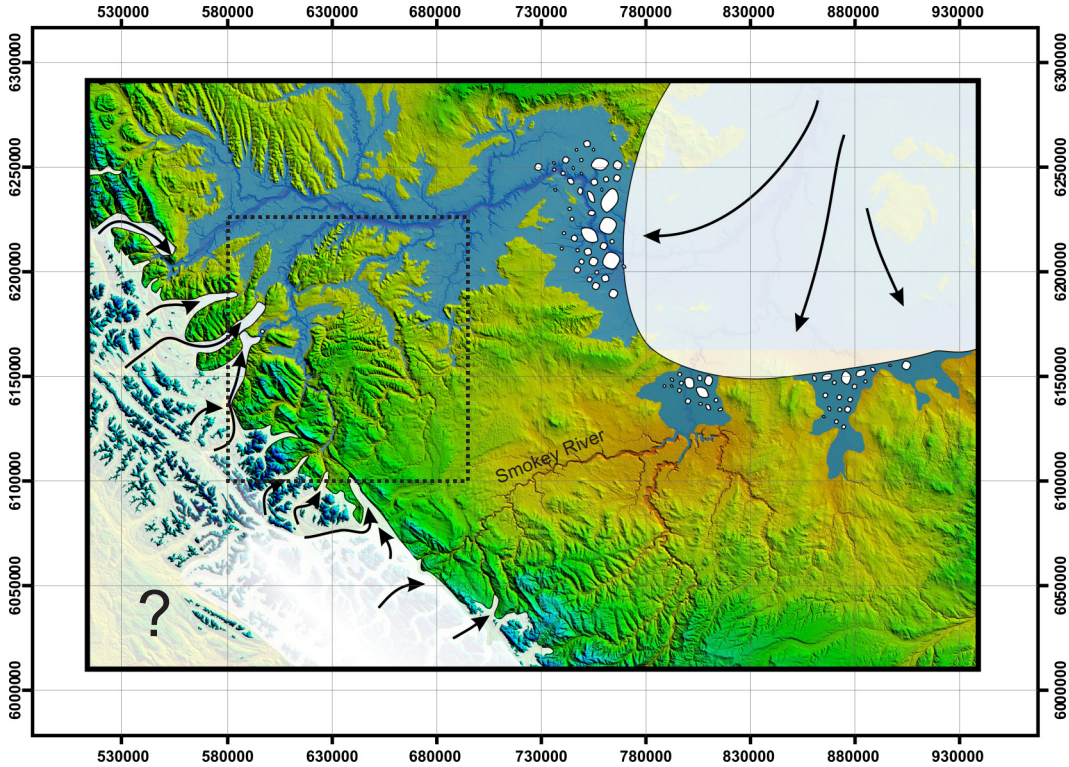

Figure 6.13. ***Continued***

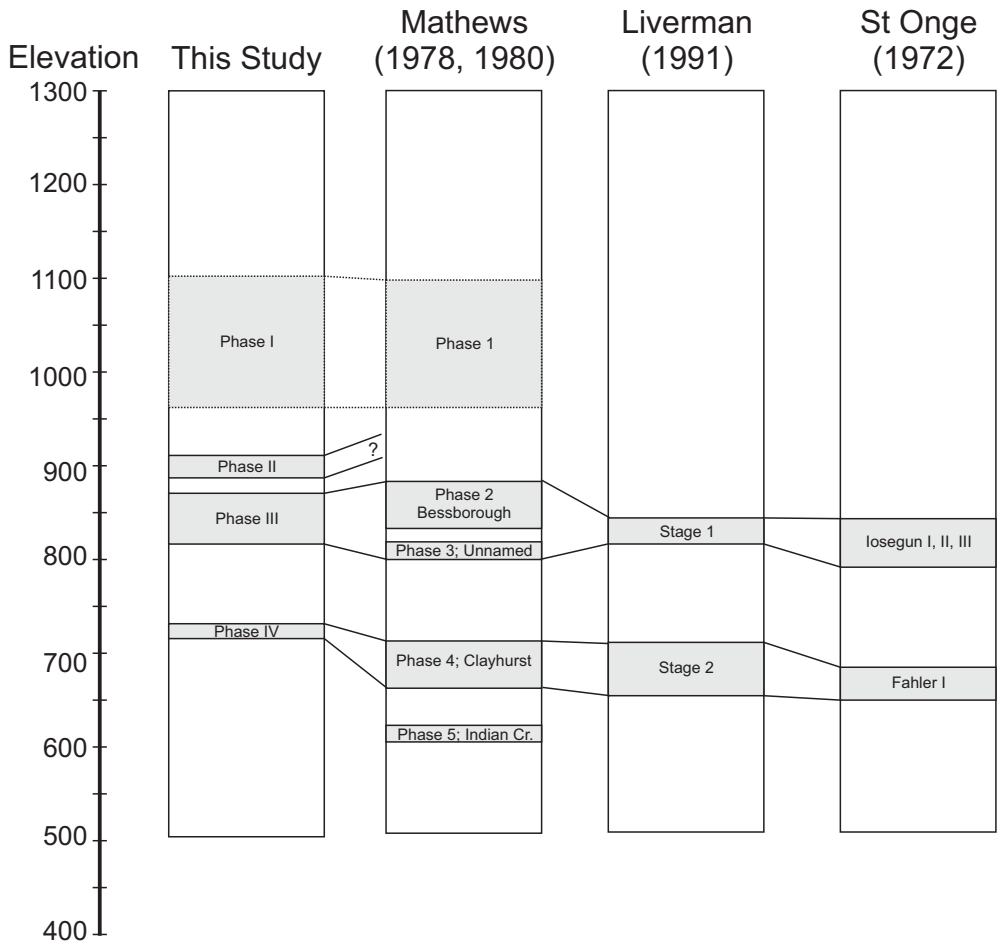

Figure 6.14. Phases of GLP from this study correlated with previous work.

the benefit of the many recent advancements in remote sensing and GIS.

Phase I from this study is relatively poorly constrained and encompasses a lake or many lakes that developed at high elevations, likely at the initial separation of the CIS and LIS. Though Figs. 6.13B and 6.13C show a single body of water, it is likely that small ice marginal lakes would have preceded the formation of a single large glacial lake. The basin would have continued to fill until a spillway was established. Mathews (1980) suggests that the spillway was likely located over the ice or to the north of the study area. Phase I is equivalent to Mathews' (1980) Phase 1 (Early ice diversion) where he uses the presence of glaciolacustrine sediments above 1130 m as evidence for a glacial lake. Glaciolacustrine deposits were also noted in this study at elevations as high as 1100 m in the Tumbler Ridge area (Fig. 6.1).

Phase II is not identified by Mathews (1980) and appears to be a previously undocumented phase. There is no spillway identified for this stage. Either it existed over ice, or it also occurred to the north of the study area. As ice retreated, it is likely that the Pass Creek spillway (Fig. 6.13e) was established rapidly, dropping Phase II to the initial level of Phase III (St Onge, 1972; Mathews 1980).

The upper shorelines of Phase III are likely equivalent to the Bessborough Stage (Phase 2; Mathews, 1980), Iosegun I and II of St Onge (1972), and probably also Stage 1 of Liverman (1991) (Fig. 6.14). The isostatically corrected lower shorelines of Phase III in this study appear to be equivalent to Mathews (1980) unnamed Phase 3, St Onge's (1972) Iosegun II and likely (at least in part) Iosegun III (Fig. 6.14). St Onge (1972) envisioned Iosegun III occurring after the Pass Creek spillway was abandoned, an event that we suggest did not happen until the end of Phase III. Phase III is also correlated here with the lower strandlines of Liverman's (1991) Stage 1 in the Grand Prairie area (Fig. 6.14). The range of strandlines identified in Phase III of this study suggests that the Bessborough Stage and the Unnamed Stage (Phase 3; Mathews, 1980) are part of the same lake and successive shorelines represent both the down cutting of the Pass Creek spillway and the retreat of the ice sheet. It is possible that, towards the end of Phase III, a topographic high emerged that separated the Peace River Basin from the Smokey River Basin (Grande Prairie) as suggested by Mathews (1980) (Fig. 6.13g). The Smokey River region of GLP may have drained during this period, though this remains conjecture (Fig. 6.13g).

Phase IV in this study is correlated here to the Clayhurst Stage (Phase 4; Mathews, 1980) and Liverman's (1991) Stage 2 (Fig. 6.14). Woolfe (1993) assigned the Fahler I Phase of St Onge

(1972) to Mathews' lower, Indian Creek Stage. The isostatically adjusted elevations of the Fahler Phase seems, however, to better correlate with the Phase IV/Clayhurst Stage. Using the isostatic adjustment from Phase IVa, the configuration of GLP in the Peace River Basin is consistent with Mathews (1980), but coincides poorly with St Onge's (1972) reconstruction in the Smokey River Basin. Using Mathews (1980) ice front configuration, this study suggests that the Smokey River Region was flooded much farther west than depicted by St Onge (1972). Either Grande Prairie remained submerged during Phase IV or isostatic adjustment determined from Phase IVa may not be valid southwest of the study area.

In this reconstruction, GLP during Phase II and III had water depths in excess of 300 m in some places. This deep water would have significantly affected the ice dynamics at the margins. Clean ice less than 330 m thick would be buoyant in fresh water deeper than 300 m (Benn and Evans, 1998). Buoyant ice with low tensile strength would encourage an active calving front (Powell, 1984). Rapid calving coupled with the reduced friction at the ice terminus, associated with buoyancy and the high pore-water pressure of basal sediments, would have enhanced the flow rates of both the CIS and the LIS.

The optical ages provide a limiting age range of <16.0 ± 2.5 to 10.5 ± 0.5 ka BP for Phase II. It is possible, however, that the 10.5 ± 0.5 BP age results from reworking of the sediments by paraglacial aeolian activity, in which case the development of the shoreline could be restricted to a period between <16.0 ± 2.5 ka and 14.2 ± 0.5 ka BP. Hartman (2005) summarized acceptable radiocarbon age dates associated with GLP using Arnold's (2002) criteria (Table 6.6). The optical ages are consistent with the range of ages that span approximately 17 to 12 ka cal yrs BP. The quartz ages presented here are similar to feldspar optical ages from sand dunes in the Grande Prairie region where sand is believed to have been deposited between ca. 18 ka and 12 ka ago; Wolf et al., 2004; Munyikwa et al., 2011). Of the 19 ages reported in these studies, 84 % of the optical ages occur between ca. 16 ka and 12 ka. If these ages are correct, the area east of Grande Prairie was not covered by LIS or GLP between ca. 16 ka and 12 ka. The discrepancy between the ages from shorelines (this study) and the sand dunes can be reconciled because: 1) the inherent limitations of the single aliquot optical dating method; and/or 2) GLP may have drained from Smokey River Basin before it drained from the Peace River Basin due to a topographic or ice sheet barrier.

Table 6.6. Radiocarbon dates related to GLP (from Hartman, 2005)

Location	Lat. and Long.	Dated Material	Dated Sediment	Possible Lake Phase	Age (C14 yrs BP)	Age (Cal C14 yrs BP)[1]	Original Ref.
Fort St John	56°10' N 120°44 W	Wood	Till-GLP Contact	Phase I	13,970 ± 170	17,149 ± 389	Catto et al, 1996
Watino	55°43' N 117°38 W	Bone	Postglacial Terrace	Post Dates GLP	11,200 ± 100	13,046 ± 253	Jackson and Pawson, 1984
Charlie Lake	56°17' N 120°56 W	Collagen (bone)	Cultural Layer	Lower Phase III or Younger	10,770 ± 120	12,691 ± 267	Fladmark et al. 1988
Charlie Lake	56°17' N 120°56 W	Collagen (bone)	Cultural Layer	Lower Phase III or Younger	10,450 ± 150	12,234 ± 413	Fladmark et al. 1988
Charlie Lake	56°17' N 120°56 W	Collagen (bone)	Cultural Layer	Lower Phase III or Younger	10,380 ± 160	12,122 ± 500	Fladmark et al. 1988
Tumbler Ridge	55°09' N 121°00 W	Collagen (bone)	Deltaic Sediment	Phase III	10,380 ± 100	12,204 ± 372	Woolf, 1993
Taylor	56°09' N 120°42 W	Bone	Postglacial Terrace	Post Dates GLP	10,240 ± 160	11,941 ± 588	Bobrowsky, et al 1991
Watino	55°43' N 117°38 W	Bone	Postglacial Terrace	Post Dates GLP	10,200 ± 200	11,895 ± 631	Churcher, 1984
Charlie Lake	55°43' N 117°38 W	Bone	Cultural Layer	Lower Phase III or Younger	10,100±210	11,854 ± 666	Driver, 1988

1 Radiocarbon ages calibrated using OxCal (Bronk Ramsey, 2001)

Optical dating has limitations. As noted earlier, GPBS-1 and GLP-04 probably contain grains that were not exposed to sufficient light to reset the luminescence clock. The resulting ages are too old and though the MAM model can aid in refining time since burial, it is likely that an alternative method such as single grain luminescence dating would be needed to distinguish age populations. This method is, however, cost prohibitive at this time for routine analysis. Calculated ages can also be too young for quartz grains if the analysis resulted in the inadvertent sampling of luminescence from traps that are thermally unstable. This happens when the desired fast component is significantly contaminated by luminescence from the medium or slow components. Additional optical dating of similar facies could further constrain the age of Phase II, or the quartz ages could be compared to feldspar ages from the same deposit.

Alternatively, ice sheet configuration may explain the age discrepancies. If a lobe of the LIS and/or topography separated the Smokey River Basin from the GLP basin, GLP may have drained from Smokey River Basin as early as the beginning of Phase II allowing exposed sediment to be affected by aeolian processes in the Grande Prairie region. This differential pattern remains unsubstantiated.

6.5 Conclusions

High resolution remote sensing techniques, such as LiDAR, reveal subtle geomorphological features that, when integrated into a GIS, offer derivative information that significantly aids in reconstructing landscape evolution. In this study, shoreline features were captured as elevation points and derived populations were used to define levels of glacial Lake Peace (GLP). This allowed for an estimate of cumulative isostatic adjustment and a reconstruction of lake and ice positions during the early phases of GLP, as well as correlation of these lake levels with previous work.

More than 44,000 data points were generated from the mapping of discrete shoreline features. The elevation of these data points group into four populations interpreted as major phases of GLP in the study area. Phase I ranges from 960 m and 990 m but is poorly constrained and likely represents many water planes but not necessarily a spatially continuous body of water. At some point during this phase these lakes may have merged to form a more or less continuous body of water between the LIS and the CIS referred to as GLP. This early phase

correlates with Mathews (1978, 1980) Phase 1. Phase II consists of a flight of shorelines between 890 m and 910 m. This well-developed flight of shorelines represents the earliest unambiguous phase of GLP. Phase II is a previously undocumented stage of GLP. Phase III is multi-modal and encompasses shorelines that span an elevation interval between 810 m and 865 m. The multi-modal peaks are from well-developed, parallel shorelines traceable throughout the map area. Phase III is correlated with Bessbough/Phase 2 (Mathews, 1978; 1980), Stage 1 of Liverman (1991), and Losegun I, II, and III of St Onge (1978). The shoreline features from Phase IV, between 724 m and 733 m, developed as GLP retreated from the area and Swan Lake became an isolated basin. This phase likely is correlated, in part, with Clayhurst/Phase 4 (Mathews, 1978; 1980), Stage 2 (Liverman, 1991), and Fahler I (St Onge, 1978).

The isostatic adjustments from this study are generally compatible with those suggested by Mathews (1980) and Woolf (1993) but indicate that isostatic adjustment shifted through time. Isostatically tilted shorelines increased from Phase I to Phase II, and then decreased through to Phase IV. Slope aspect appears to have changed between Phase II and III suggesting isostatic uplift began in the northeast, but was later outpaced by uplift in the southwest. This pattern suggests that LIS initially retreated away from the CIS, allowing the crust under the Interior Plains to rise. By the end of Phase III, the CIS thinned and the rate of relative uplift in the Foothills and Rocky Mountains surpassed that of the Interior Plains.

Reconstructions of lake and ice margins in this study are comparable with those of Mathews (1978, 1980). Phase I probably includes several ice marginal lakes that developed at the initial separation of the CIS and LIS before amalgamating into the initial phase of GLP. Phase II is not identified by Mathews (1980) and appears to be the first (and highest) unambiguous phase of GLP yet to be reported. As ice retreated in Phase II time, the Pass Creek spillway developed and rapidly dropped lake levels of Phase II down to the initial levels of Phase III. The range of strandlines identified in Phase III of this study suggests that the Bessborough Stage and the Unnamed Stage (Phase 3; Mathews 1978, 1980) are part of the same lake and successive shorelines represent both the down-cutting of the Pass Creek spillway and the retreat of the ice sheet. Phase IV is the lowest phase represented in the study area. Evidence of this phase is generally restricted to the Swan Lake area (Fig. 6.1) and may have formed when GLP retreated to the east and Swan Lake became an isolated lake basin. There is poor correlation between the Phase IV isostatically adjusted topography and Mathews (1980) and St Onge (1978) ice and lake

positions. Either Grande Prairie remained submerged during Phase IV, ice restricted drainage of the Peace River Basin while the Smokey River and adjacent basins drained to the east (Fig. 6.13G), or isostatic adjustments presented here are not valid for this phase southeast of the study area.

Three acceptable optical ages for Phase II provide limiting ages of 10.5 ± 0.5, 14.2 ± 0.5 and <16.0 ± 2.5 ka BP. If the 10.5 ± 0.5 ka BP age represents later reworking of the sediment by aeolian processes, these ages are consistent with radiocarbon age ranges for GLP (17 to 12 ka Cal yrs BP) from Hartman's (2005) summary. The Phase ll optical ages overlap with optical ages from sand dunes in the Grande Prairie region that stabilized between ca. 16 ka and 12 ka yrs ago. However, ice sheet reconstruction suggests that Grande Prairie would have emerged after the Phase II shorelines developed. This may suggest a limitation of the resolution of the single aliquot optical dating method. Alternatively, the transition from Phase II to Lower Phase III was relatively rapid (hence overlapping optical ages) and a topographic high likely emerged and separated the Smokey River from the Peace River basin, allowing the Smokey river basin to drain during Phase III.

6.6 References

Adamiec, G. and Aitken, M.J., 1998. Dose-rate conversion factors Update; Ancient TL, 16, 37-49.

Aitken, M.J., 1985. Thermoluminescence Dating; Academic Press, London, 359 pp.

Alley, N.F. and Harris, S.A., 1974. Pleistocene glacial lake sequences in the foothills, Southwestern Alberta, Canada; Canadian Journal of Earth Sciences, 11, 1220—1235.

Andrews, J.T., 1989. Postglacial emergence and submergence; In Fulton, R.J. (ed), Quaternary Geology of Canada, no. 1, Chapter 8, 546—562.

Ashley, G.M., Southard, J.B., and Boothroyd, J.C., 1982. Deposition of climbing-ripple beds: a flume simulation; Sedimentology, 29, 67—79.

Bednarski, J.M. and Smith, I.R., 2007. Laurentide and montane glaciations along the Rocky Mountain Foothills of northeastern British Columbia; Canadian Journal of Earth Science, 44, 445—457.

Benn, D.I. and Evans, D.J.A., 1998. Glaciers and Glaciation; Arnold, London, 734 pp.

Berger, G.W., 1988. Dating Quaternary events by luminescence; In Easterbrook, D.J. (ed), Quaternary Sediments, Geological Society of America Special Paper 227, 13—50.

Bobrowsky, P.T., 1989. Late Cenozoic geology of the northern Rocky Mountain Trench, British Columbia; unpublished PhD Thesis, University of Alberta, Edmonton, Alberta, 463 pp.

Bobrowsky, P.T.B. and Rutter, N.W., 1992. The Quaternary geological history of the Canadian Rocky Mountains; Géographie Physique et Quaternaire, 46, 5—50.

Bobrowsky, P.T., Catto, N.R., and Levson, V.M. 1991. Reconnaissance Quaternary geology investigations in Peace River District, British Columbia; British Columbia Ministry of Energy, Mines, and Petroleum Resources, Paper 1991-1, 345—358.

Brady, N.C. and Weil, R.R., 2008. The nature and properties of soils, 14th edition; Prentice Hall, New Jersey, 740 pp.

Bronk, R.C., 2001. Development of the radiocarbon calibration program OxCal. Radiocarbon, 43, 355—363.

Catto, N.R., Liverman, D.G.E., Bobrowsky, P.T., Rutter, N., and Mandryk, C.A.S., 1996. Laurentide, Cordilleran, and Montane glaciation in the western Peace River-Grand Prairie region, Alberta and British Columbia, Canada; Quaternary International, 32, 21—32.

Churcher, C.S., 1984. Faunal correlations of Pleistocene deposits in western Canada; In Mahaney, W.C. (ed), Correlation of Quaternary chronologies, Geo Books, Norwich, UK, 517 pp.

Clark, C.D. and Stokes, C.R., 2005. Paleo-Ice stream landsystem; In Evans, D.J.A. (ed), Glacial Landsystems; Hodder Arnold, London, 204—227.

Collinson, J.D. and Thompson, D.B., 1989. Sedimentary Structures, Second Edition; Chapman and Hall, New York, 207 pp.

Craig, B.G., 1965. Glacial Lake McConnell and the surficial geology of parts of Slave River and Redstone River map-areas, District of Mackenzie; Geological Survey of Canada, Bulletin 122, 33 pp.

Dawson, G.M., 1881. Report on exploration from Port Simpson on the Pacific Coast to Edmonton on the Saskatchewan; Geological Survey of Canada, Report of Progress, 1879-1880, Section B, 77 pp.

Dyke, A.S. and Prest, V.K., 1987. Late Wisconsinan and Holocene history of the Laurentide ice sheet; Geological Survey of Canada, Map 1702A, scale 1:5 000 000.

Dyke, A.S., Moore, A. and Robertson, L., 2003. Deglaciation of North America, Geological Survey of Canada, Open File 1574, CD-ROM.

Fisher, T.G., 1999. Sedimentology, stratigraphy, and geomorphology of Lake Calgary at Cochrane, Alberta, Canada; Canadian Journal of Earth Sciences, 36, 791—803.

Flint, R.F., 1971. Glacial and Quaternary Geology; John Wiley and Sons, New York, 892 pp.

Fladmark, K.R., Driver, J.C., and Alexander, D., 1988. The paleoindian component at Charlie Lake Cave (HbRf-39); American Antiquity, vol. 53, 371—384.

Fulton, R.J., 1969. Glacial lake history, Southern Interior Plateau, British Columbia; Geological Survey of Canada, Paper 69-37, 14 pp.

Gray, J.M., 1983. The measurement of relict shoreline altitudes in areas affected by glacio-isostasy, with particular reference to Scotland; In Shorelines and Isostasy, Smith, D.E. and Dawson, A.G. (eds), Institute of British Geographers, Special Publication 16, Academic Press, London, 97—127.

Hartman, G.M.D., 2005. Quaternary stratigraphy and geological history of the Charlie Lake (NTS 94A) map-area, British Columbia; Unpublished MSc thesis, Simon Fraser University, Burnaby, 166 pp.

Hartman, G.M.D. and Clague, J.J., 2008. Quaternary stratigraphy and glacial history of the Peace River valley, northeast British Columbia; Canadian Journal of Earth Sciences, 45, 549—564.

Hickin, A.S. and Best, M.E., 2013. Mapping the geometry and lithostratigraphy of a paleovalley with a time-domain electromagnetic technique in an area with small resistivity contrasts, Groundbirch, British Columbia, Canada; Journal of Environmental and Engineering Geophysics, 19, 119—135.

Hickin, A.S., Kerr, B. Turner, D.G., and Barchyn, T.E., 2008.Mapping Quaternary paleovalleys and drift thickness using petrophysical logs, northeast British Columbia, Fontas map sheet, NTS 94I; Canadian Journal of Earth Sciences, 45, 577—591.

Holland, S.S., 1976. Landforms of British Columbia, A physiographic outline; British Columbia Department of Mines and Petroleum Resources, Bulletin 48, 138 pp.

Huntley, D.J., Godfrey-Smith, D.I., and Thewalt, M.L.W., 1985. Optical dating of sediments; Nature, 313, 105—107.

Jackson, L.E. and Pawson, M., 1984. Alberta radiocarbon dates; Geological Survey of Canada, Paper 83-25, 27 pp.

Johnson, W.A., 1946; Glacial Lake Agassiz with special reference to mode of deformation of the beaches; Geological Survey of Canada, Bulletin 7, 20 pp.

Karrow, P.F., 2004. Algonquin-Nipissing shorelines, North Bay, Ontario; Geographie Physique et Quaternaire; 58, 297—304.

Larsen, C. E., 1987. Geological history of glacial Lake Algonquin and the Upper Great Lakes; US Geological Survey Bulletin, B1801, 36 pp.

Lemmen, D.S., Duk-Rodkin, A., and Bednarski, J.M., 1994. Late glacial drainage systems along the northwestern margin of the Laurentide Ice Sheet; Quaternary Science Reviews, 13, 805—828.

Leverington, D.W. and Teller, J.T., 2003. Paleotopographic reconstructions of the eastern outlets of glacial Lake Agassiz; Canadian Journal of Earth Sciences, 40, 1259—1278.

Leverington, D.W., Teller, J.T., and Mann, J.D., 2002. A GIS method for reconstruction of late Quaternary landscapes from isobase data and modern topography; Computer and Geosciences, 28, 631—639.

Lian, O.B., Hu, J., Huntley, D.J., Hicock, S.R., 1995. Optical dating of Quaternary organic-rich sediments from southwestern British Columbia and northwestern Washington State; Canadian Journal of Earth Sciences, 32, 1194—1207.

Lian, O.B. 2013. Optical Dating. In: Elias S.A. (ed.) The Encyclopedia of Quaternary Science, vol. 2 (2nd ed.), Elsevier, Amsterdam, 653—666.

Liverman, D.G., 1991. Sedimentology and history of a Late Wisconsinan glacial lake, Grande Prairies, Alberta, Canada; Boreas, 20, 241—257.

Mathews, W.H. 1978. Quaternary stratigraphy and geomorphology of Charlie Lake (94A) map area, British Columbia; Geological Survey of Canada, Paper 76-20, 25 pp.

Mathews, W.H., 1980. Retreat of the last ice sheets in northeastern British Columbia and adjacent Alberta; Geological Survey of Canada, Bulletin 331, 22 pp.

McCann, S.B. and Chorley, R.J., 1967; Trend surface mapping of raised shorelines; Nature, 215, 611—612.

McMechan, M.E., 1994. Geology and structure cross-section, Dawson Creek. British Columbia; Geological Survey of Canada, Map 1858A, scale 1:250 000.

Murray, A.S. and Roberts, R.G., 1998. Measurement of the equivalent dose in quartz using a regenerative-dose single aliquot protocol; Radiation Measurements, 29, 503—515.

Murray, A.S. and Wintle, A.G., 2000. Luminescence dating of quartz using an improved single-aliquot regenerative-dose protocol; Radiation Measurements, 32, 57—73.

Murray, A.S. and Wintle, A.G., 2000. The single aliquot regenerative dose protocol: Potential for improvements in reliability; Radiation Measurements, 37, 377—381.

Olley, J.M., Murray, A., Roberts, R.G., 1996. The effects of disequilibria in the uranium and thorium decay chains on burial dose rates in fluvial sediments; Quaternary Science Reviews, 15, 751—760.

Olley, J.M., Pietsch, T., and Roberts, R.G., 2004. Optical dating of Holocene sediments from a variety of geomorphic settings using single grains of quartz; Geomorphology, 60, 337—358.

Peltier, W.R. and Andrews, J.T., 1976. Glacio-isostatic adjustment 1 – The forward problem; Geophysical Journal of the Royal Astronomical Society, 46, 605—646.

Powell, R.D., 1984. Glacimarine processes and inductive lithofacies modelling of ice shelf and tidewater glacier sediments based on Quaternary examples; Marine Geology, 57, 1—52.

Prescott, J.R. and Hutton, J.T., 1994. Cosmic ray contributions to dose rate for luminescence and ESR dating: Large depth and long-term time variations; Radiation Measurements, 23, 497—500.

Prescott, J.R. and Hutton, J.T., 1995. Environmental dose rate and radioactive disequilibrium from sediment grains: New experimental data; Quaternary Science Reviews, 13, 439—448.

Reading, H.G. (ed), 1986. Sedimentary Environments and Facies; Blackwell, Oxford, 615 pp.

Reimchen, T.H.F., 1980. Surficial Geology, Dawson Creek, west of sixth meridian, British Columbia; Geological Survey of Canada, Map 1467A, 1:250 000 scale map.

Reimchen, T.H.F. and Rutter, N.W., 1972. Quaternary Geology, Dawson Creek, British Columbia (93P); Report of Activities, Part A, Geological Survey of Canada, Paper 72-1A, 176—177.

Rutter, N.W., 1976. Multiple glaciations in the Canadian Ropcky Mountains with special reference on north-eastern British Columbia; In Quaternary stratigraphy of North America; Mahaney, W.C. (ed.), Hutchinson and Ross, Stroudsburg. Pennsylvania, 409—440.

Rutter, N.W., 1977. Multiple glaciations in the area of Williston Lake, British Columbia; Geological Survey of Canada, Bulletin 273, 31 pp.

Sack, D., 2001. Shoreline and Basin configuration techniques in palaeolimnology; In Tracking environmental change using lake sediments, Volume 1: Basin Analysis, Coring, and Chronological Techniques; Last, W.M. and Smol, J.P. (editors), Kluwer Academic Publishing, Dordrecht, 49—71.

Smith, D.G., 1994. Glacial Lake McConnell: Paleogeography, age, duration, and associated river deltas, Mackenzie River basin, Western Canada; Quaternary Science Reviews, 13, 829—843.

St-Onge, D.A., 1972. Sequence of glacial lakes in north central Alberta; Geological Survey of Canada; Bulletin 213, 16 pp.

Teller, J.T., 1987. Proglacial lakes and the southern margin of the Laurentide Ice Sheet; In North American and adjacent oceans during the last deglaciation; Ruddiman, W.F. and Wright,

H.E. (eds), Geological Society of America, Decades of North American Geology, K-3, 39—69.

Teller, J.T., 1995. History and drainage of large ice-dammed lakes along the Laurentide Ice Sheet; Quaternary International, 28, 83—92.

Teller, J.T., 2005. Subaquatic landsystems: Large proglacial lakes; In Glacial Landsystems, Evans, D.J.A. (ed), Hodder Arnold, London, 348—371.

Teller, J.T., Leverington, D., and Mann, J, 2002. Freshwater outbursts to the ocean from glacial Lake Agassiz and climate change during the last deglaciation; Quaternary Science Reviews, 21, 879—887.

Thompson, T.A., 1992. Beach-ridge development and lake-level variation in southern Lake Michigan; Sedimentary Geology, 80, 305—318.

Tokarsky, O., 1967. Geology and groundwater resources of the Grimshaw/Cardinal Lake area, Alberta; unpublished MSc thesis, University of Alberta, 178 pp.

Webster, T.L., Murphy, J.B., Gosse, J.C., and Spooner, I., 2006. The application of liDAR-derived digital elevation model analysis to geological mapping: an example from the Fundy Basin, Nova Scotia, Canada; Canadian Journal of Remote Sensing, 32, 173—193.

Wintle, A.G. and Murray, A.S., 2006. A review of quartz optically stimulated luminescence characteristics and their relevance in single-aliquot regeneration dating protocol; Radiation Measurements, 41, 369—391.

Wolcott, R.I., 1970. Isostatic response to loading of the crust in Canada; Canadian Journal of Earth Sciences, 7, pages 716—727.

Wolcott, R.I., 1972. Late Quaternary vertical movements in eastern North America: quantitative evidence of glacio-isostatic rebound; Review of Geophysics and Space Physics, 10, 849—884.

Wolfe, S.A., Huntley, D.J. and Ollerhead, J., 2004. Relict Late Wisconsinan dune fields of northern great plains, Canada; Géographie physique et Quaternaire, 58, 323—336.

Woolf, K.E., 1993. Radiocarbon chronology for glacial Lake Peace; Unpublished MSc Thesis, Simon Fraser University, 93 pp.

Yang, Z. And Teller, J.T. 2012. Using LiDAR Digital Elevation Model data to map Lake Agassiz beaches, measure their isostatically-induced gradients, and estimate their ages; Quaternary International, 260, 32—42.

CHAPTER 7: GEOMORPHIC AND ECOLOGICAL AGE CONSTRAINTS FOR PARAGLACIAL TO BOREAL TRANSITION IN NORTHEASTERN BRITISH COLUMBIA

Adrian S. Hickin, Olav B. Lian, Alice Telka, and Victor M. Levson

This manuscript has not yet been submitted for publication

Abstract

The Late Wisconsinan deglaciation period was a time of rapid climate adjustment that resulted in the widespread transition from glacial and paraglacial conditions to settings favourable for plant and animal colonization. Establishing the timing of this transitional period in northeastern British Columbia provides constraints on the rate in which the biomes adapted during this interval of rapid climate change.

Preserved aeolian landforms (geomorphic) and macrofossil assemblages (biological) are complimentary proxies for interpreting climate amelioration. Paraglacial aeolian dunes in the Kiskatinaw Dune Field developed following the retreat of glacial Lake Peace which formed after the separation of the Cordilleran and Laurentide ice sheets. These parabolic sand dunes are vegetation anchored landforms that indicate plant colonization bio-morphologically influenced aeolian activity during stabilization. Optical dating established that stabilization occurred between 12.3 ± 0.7 and 10.6 ± 0.6 ka years BP, the same interval in which vegetation transitioned from Herb and Shrub Tundra to a Boreal Parkland and eventually Boreal Forest. Radiocarbon ages from macrofossil assemblages at the Flatbed River Section imply paraglacial conditions likely persisted to ca. 12 000 cal yrs BP after which Forest Tundra dominated. At that time, the Flatbed River was a dry floodplain that transitioned to a pond setting between 11 490 ± 206 and 11 226 ± 21 cal yrs BP. Open Spruce forests were established in the surrounding area by 11 207 ± 28 cal yrs BP marking the shift from Forest Tundra to Boreal Parkland. The site transitioned from pond to bog between 9964 ± 187 and 9789 ± 115 cal yrs BP and coincident with the onset of Boreal Forest conditions at the site.

Biome succession recorded at the Flatbed River section indicates that the site transitioned from a paraglacial setting to a boreal forest environment over ~2 ka (ca. 12 - 10 ka years ago). However, the change from tundra to forest conditions (which likely includes a lag period) took <600 years (ca. 12 - 11.4 ka years ago). This suggests that climate warming enabled a swift transition from cold dry tundra to more humid forest in only a few centuries.

7. 1 Introduction

The increased rate of climate change continues to be a significant issue, having human impact as well as ecological (IPCC, 2007). Some of the pivotal questions revolve around whether species will be able to adapt fast enough to survive (Visser, 2008) and what geomorphic processes might change as ecosystems adjust (Bull, 1991). Some insight can be gained by examining the late Wisconsinan deglacial period, also a time of rapid climate adjustment. Warming climate during this interval resulted in the widespread transition from harsh glacial and paraglacial conditions to settings more favourable for plants and animals to flourish. During this period the landscape experienced significant and rapid changes in geomorphic processes and biological diversity. The objective of this study is to establish the timing of the Late Wisconsinan transitional period in northeast British Columbia (Fig. 7.1), a region of early deglaciation along the northern Rocky Mountain Foothills between the margins of both the Laurentide and Cordilleran ice sheets. This study aims to constrain the timing of the climatic amelioration by determining: 1) the stabilization age of paraglacial sand dunes (geomorphic); and 2) timing of biome succession using macrofossils (biological) from an organic section.

Aeolian sand dunes provide an important geomorphic record of past wind regimes and paleoclimate (Wolfe et al., 2004, 2011). The activity and morphological form of active sand dunes has been attributed to the interplay between: 1) sediment supply; 2) sediment availability; and 3) wind transport capacity (Kocurek and Lancaster, 1999). The stabilization of dunes and the resulting preserved morphological form is, however, linked (i.e. bio-morphologically) to vegetation cover and biological growth rates (Lancaster and Baas, 1998; Durán and Herrmann, 2006; Barchyn and Hugenholtz, 2012a-c). Although not necessarily a direct link to climate (Hugenholtz et al., 2012), sand dune stabilization is a consequence of vegetation growth rates exceeding slipface depositional rates (Barchyn and Hugenholtz, 2012b). In some cases, the stabilizing of Late Wiconsinan sand dunes may imply more favourable climatic conditions for vegetation colonization (Wolfe et al., 2004, 2011; Barchyn and Hugenholtz, 2012a). Establishing stabilization ages for Late Wisconsinan sand dunes provides a minimum age for deglaciation and offers some insight into the amelioration of climate when vegetation proliferated. The advent of OSL dating (Huntley et al., 1985) has enabled the reliable determination of the absolute time elapsed since sand grains were buried. This method is very effective in aeolian environments because airborne grains in transport are very likely to be

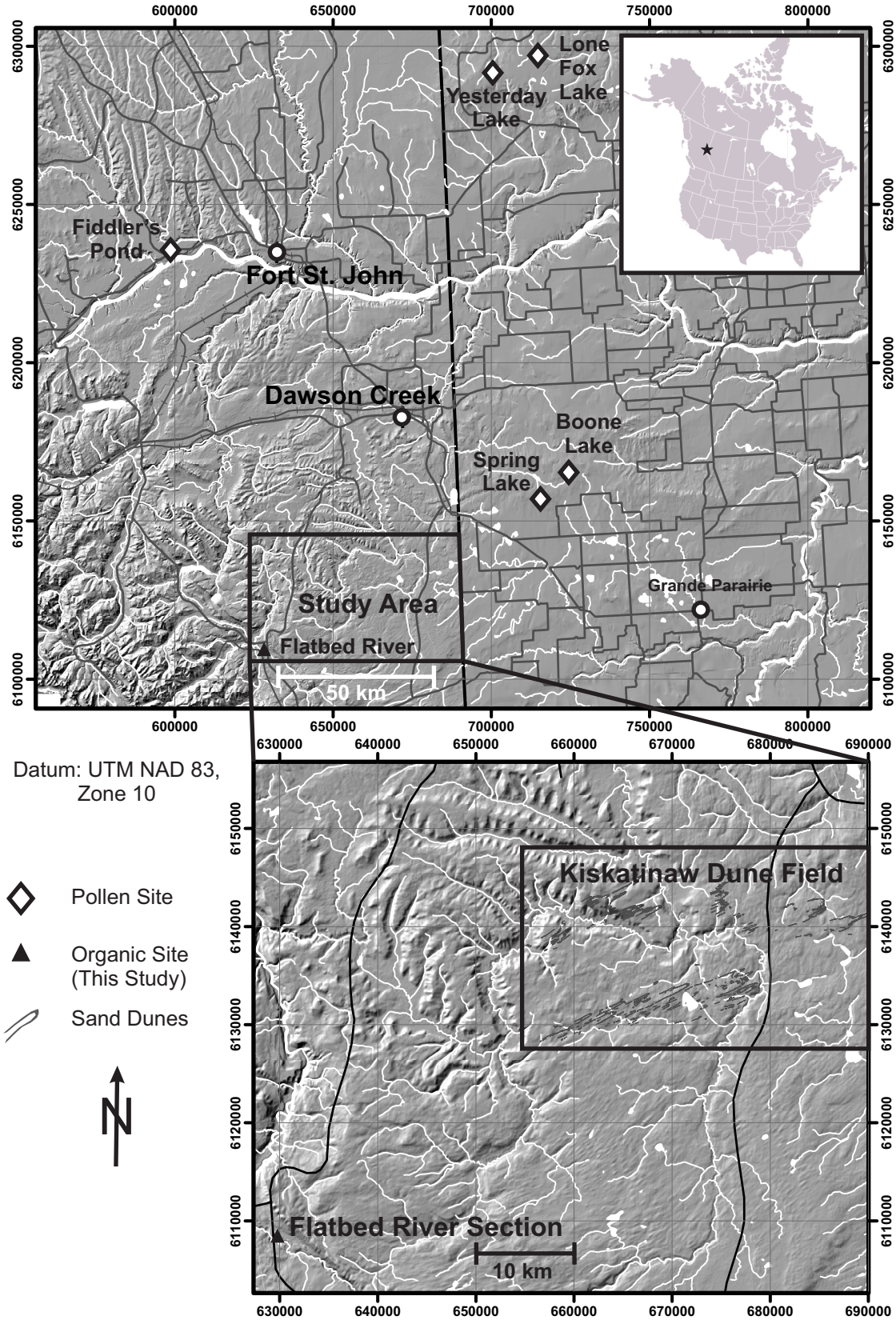

Figure 7.1. Location map of the study area.

exposed to sufficient solar radiation to reset the luminescence clock. Consequently, optical dating of sand grains from dunes provides an effective dating method in an environment with a paucity of organic material suitable for radiocarbon dating, as is common in an early deglacial/paraglacial setting (Wolfe et al., 2004, 2007, 2011; Mason et al., 2011; Munyikwa, et al., 2011; Stone and Thomas, 2013).

Paleoecological studies from Late Pleistocene macrofossils and pollen assemblages record the succession of biomes (Dyke, 2005) and provide a proxy for climatic change (Williams et al., 2004). Several studies from the area track the transition from tundra to woodland and boreal environments. Driver (1988) reports on macrofossil assemblages from the Charlie Lake cave with a Late Wisconsinan to early Holocene record that includes definitive evidence of human occupation (ca. 10,500 ^{14}C years BP; Fladmark et al., 1988). Most paleoecological studies in the region have, however, focused on pollen from lake cores (White and Mathewes, 1982; White et al., 1985; White and Mathewes, 1986; MacDonald, 1987a, 1987b). Dyke et al. (2004) and Dyke (2005) provide a regional summary of the paleovegetation succession for Canada, including this study area in 1000 year increments since 18 000 ^{14}C years BP (Fig. 7.2; Table 7.1). Dyke et al. (2004) suggests that, following deglaciation, the regional biomes progressed from Herb and Shrub tundra to Boreal Parkland, and eventually to the Boreal Forest (present biome).

7.2 Methods

7.2.1 Aeolian Landform Mapping

Aeolian landforms were delineated from a light detection and ranging (LiDAR) digital elevation model (DEM) in a geographic information system (GIS). The DEM was generated from a 1 m grid with a vertical resolution of approximately 20 cm. Only positive relief features are demarcated, though deflation features, such as windpits, blowout hollows, and deflation areas (as described by David, 1977) are prevalent throughout the landscape. The edge of most features is assumed to be the slope inflection between the inter-dune area and the positive relief aeolian landform (i.e. ridge, mound, dune, etc.). This edge is taken to mark the boundary between aeolian sand and the substrate (till or glaciolacustrine). In some cases, the downwind head of a dune or the outward facing slope of aeolian ridges grade into the inter-dune area of a hummocky landscape. Under these circumstances, the precise boundary is difficult to distinguish and is, therefore, subjectively delineated, an issue for all object based GIS

Table 7.1. Characteristics of Biomes (from Dyke, 2005)

Biome	Characteristics
Herb Tundra	A treeless area lacking shrubs and other small, prostrate willow and dominated by bare ground and herbs, typically sedge, grass, and sage with a variety of forbs; includes fellfield.
Shrub Tundra	A treeless area with nearly continuous cover of sedge, grass, sage, and forbs along with prostrate and semi-erect willows as well as one or more additional shrubs, chiefly dwarf birch, alder, and juniper, in increasing order of required warmth.
Alpine Tundra	Similar to herb or shrub tundra but occurring at high elevations.
Forest Tundra	A zone transitional between Shrub Tundra and Boreal Forest. That is, a continuous groundcover of herb and shrub vegetation with open stands of erect trees, typically spruce larch, and (or) poplar.
Boreal Forest	Nearly continuous cover of trees dominated by northern conifers, (mainly spruce, jackpine, larch, and fir) and northern hardwoods (mainly birch, aspen, poplar), broken by wetlands.
Boreal Parkland	Open stands of boreal forest trees growing in ground covers dominated by herb and (or) lichen. Includes the modern Aspen Parkland at the southern fringe of the western boreal forest in the Prairie Provinces and the lichen woodland (open spruce forest) of the eastern boreal forest, which grades to forest tundra.
Subalpine Forest	The conifer-dominated forest in montainous terrain of the Cordillera. Dominated by subalpine fir, Engelman spruce, Mountain hemlock, Lodgepole pine, and White bark pine in northern ranges; Limber pine, Bristlecone pine, and juniper farther south.

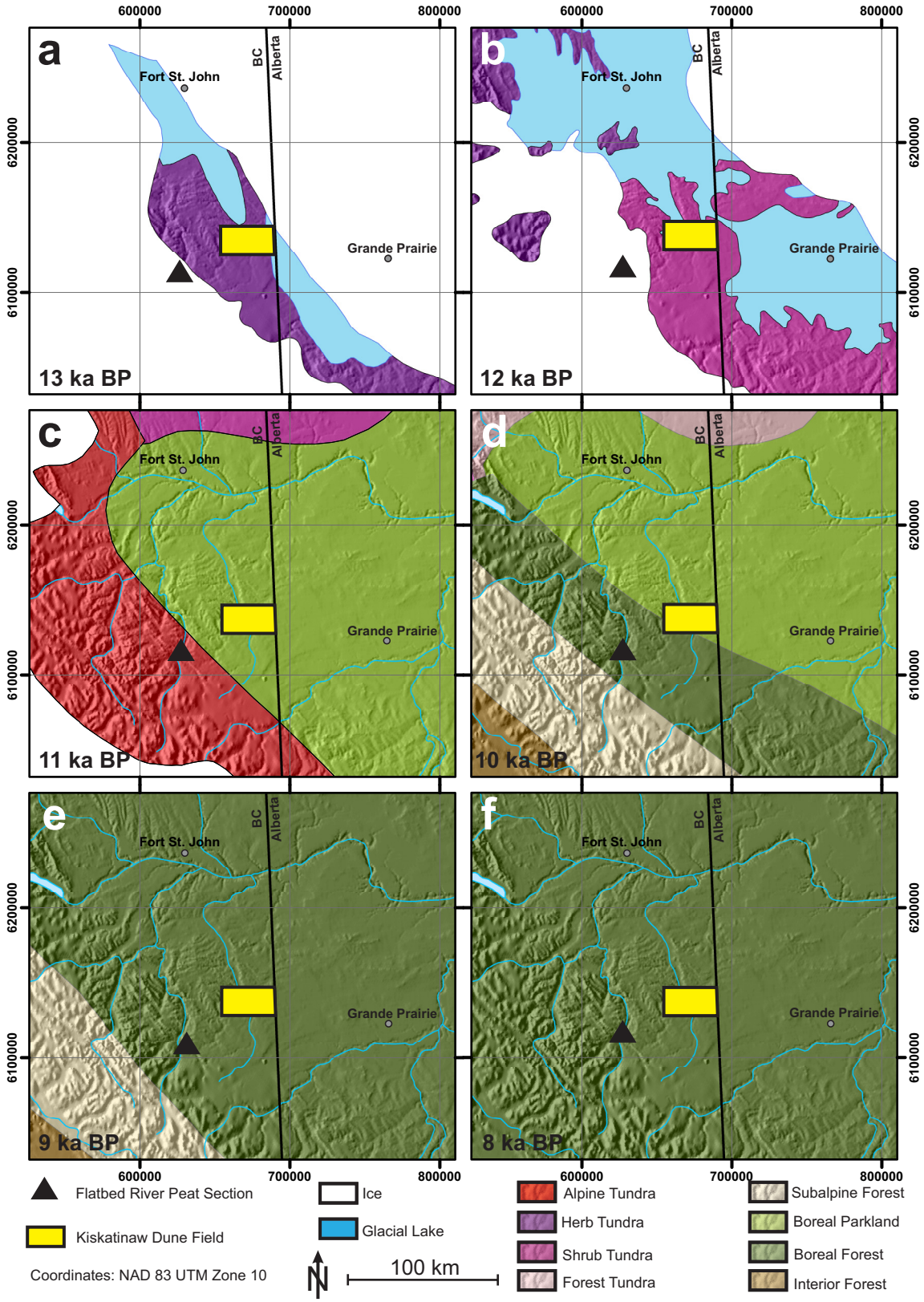

Figure 7.2. Regional vegetation history from ca. 13 ka to 8 ka (from Dyke et al., 2004); a) ~13 k ^{14}C yrs BP; b) 12 k ^{14}C yrs BP; c) 11 k ^{14}C yrs BP; d) 10 k ^{14}C yrs BP; e) 9 k ^{14}C yrs BP; f) 8 k ^{14}C yrs BP.

classification (c.f. Deng, 2007; Hugenholtz et al., 2012). In other cases degradation of the landform by subsequent erosion may have modified the form. Description of the morphological forms follows David (1977).

7.2.2 Organic Section

An organic profile was examined at a location on the north bank of the Flatbed River (Fig. 7.1). At this site, thick (>3m) organic strata overlie fluvial deposits in a terrace exposed by recent slope failure. The section was described and sampled for macrofossils. All samples were sent to PALEOTEC Services (Ottawa, Ontario) for macrofossil recovery and identification.

The procedure for isolating macrofossils for analysis involved the standard technique of sieving with warm tap water (Warner, 1990). For the overbank sands, a swirl technique was used to separate the organic content from the sand component. This technique involved gentle hose spraying the sides of a 1 L container of sediment creating a vortex of lighter organic material that was decanted into nested sieves. This procedure was repeated until all the observed organic material had been isolated. The compressed organics and dense peat were processed differently due to their compaction. These samples were soaked in warm water and the organic material floating on the surface was gently decanted into a 100 mesh Tyler sieve (mesh opening 0.15 mm). The remaining sample was sieved through nested 12, 20, 40 and 60 Canadian Standard Tyler series sieves (mesh openings 1.4 mm, 0.85 mm, 0.425 mm and 0.250 mm respectively). Since the material contained either organic peat peds or moss peds (Fig. 7.3) after the initial processing and examination of macrofossils, a more aggressive approach was utilized by hand massaging the peds. In many cases the peds could not be broken down entirely and many of the smaller crustaceans (commonly called water fleas, *Daphnia* resting eggs called ephippia), aquatic invertebrates such as Bryozoa (commonly called moss animals, bryozoan reproductive structures called statoblasts), aquatic insects such as chironomids (commonly called midges, larvae midge head capsules) and freshwater algae (commonly called stoneworts such as *Chara* and their reproductive structures called oogonia) are underrepresented in terms of enumeration. All material greater than 0.425 mm was examined using a binocular microscope and plant and insect fossil remains were isolated for identification and potential AMS radiocarbon dating. Microscopic digital photography of macrofossils was done using a digital

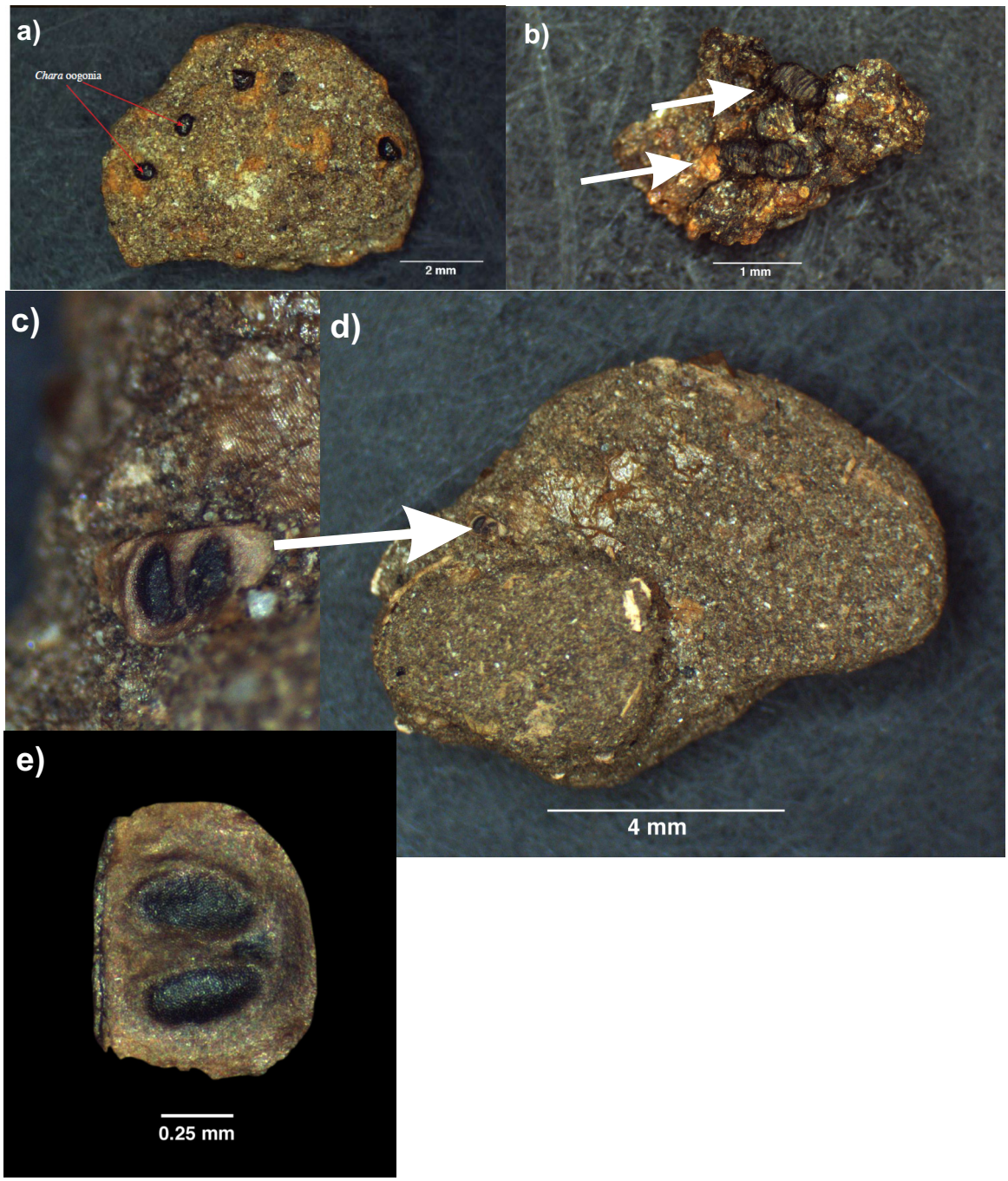

Figure 7.3. a) Peat ped from sample FBRP-06, (78 to 78.5 cm) with embedded Chara oogonia (black spheres); b) peat ped with embedded Chara oogonia (arrows; FBRP-08); c) close-up of embedded Daphnia ephippium in d) peat ped from FBRP-09; e) fossil ephippium of a water flea (Daphnia sp.; FBRP-09).

camera mounted on a binocular microscope.

7.2.3 Chronology

Six dune sand samples were collected for optical stimulated luminescence (OSL) age dating. An OSL age date provides an estimate of the time elapsed since sand grains were deposited and buried. It involves the measurement of an accumulation of ionized electrons in defects in the crystal lattice (traps) of a mineral grain (Huntley et al., 1985). The assumption is that the accumulate electrons in the crystal lattice traps will be vacated when the grain is exposed to sufficient energy such as light or heat. Exposure to sunlight will empty the traps and reset the luminescence clock. When the grain is deposited, buried, and consequently shielded from light, natural radiation from mineral grains immediately around the sample grain and from the sample grain itself, will be absorbed by the grain and stored. The rate at which the mineral grain absorbs radiation energy (dose rate) is proportional to the concentration of radio-isotopes and the intensity of cosmic rays at the site. The time elapsed since exposure to light is established by determining the laboratory dose of radiation that produces the same intensity of luminescence as did the environmental radiation (equivalent dose) and a measure of the environmental dose rate (Huntley et al., 1985). Time since burial is determined by dividing the equivalent dose by the dose rate.

Samples were collected from hand dug pits excavated to approximately 1.0 to 1.5 m deep. A 20 to 30 cm long aluminum pipe with a ~5 cm diameter was pounded in to the face of the pit wall. The pipe was then dug out from the pit wall, sealed with end caps and taped with grey duct tape. The cylinder was then marked to indicate the end farthest from the pit face.

The environmental dose absorbed by the sand grains prior to sampling comes from alpha (α), beta (β), and gamma (γ) radiation produced by decay of U, Th, their daughter products, and by ^{40}K. The environmental dose rate was determined by in-situ gamma-ray spectrometry (Table 7.2). From these data, dose rates in grays/thousand years (Gy/ka) were calculated using standard formulae (Aitken, 1985; Berger, 1988; Lian et al., 1995) and the dose-rate conversion factors of Adamiec and Aitken (1998). In each case, it is assumed that the U and Th decay chains have been in secular equilibrium since deposition of the sediment. This assumption generally has been found to be valid for well-drained mineral sediments (Prescott and Hutton, 1995; Olley et al., 1996). Water in the sediment matrix attenuates or absorbs

Table 7.2. K concentrations and U and Th equivalent concentrations (U_e and Th_e)[1] determined from i*n-situ* γ-ray spectrometry.

Sample name	K(%)	U_e(μg·g^{-1})	Th_e(μg·g^{-1})	γ dose rate (Gy·ka^{-1})
KDF1	0.618 ± 0.022	1.738 ± 0.132	3.176 ± 0.188	0.498 ± 0.018
KDF2	0.594 ± 0.021	1.694 ± 0.126	2.763 ± 0.177	0.467 ± 0.017
KDF3	0.593 ± 0.022	1.816 ± 0.132	3.093 ± 0.186	0.496 ± 0.018
KDF4	0.846 ± 0.029	2.106 ± 0.177	6.077 ± 0.261	0.733 ± 0.025
KDF5	0.728 ± 0.024	1.591 ± 0.134	3.340 ± 0.198`	0.516 ± 0.019
KDF6	0.629 ± 0.021	1.325 ± 0.124	3.063 ± 0.183	0.448 ± 0.017

[1] Equivalent concentrations, calculated from ^{214}Bi for U and ^{208}Tl for Th, assuming secular equilibrium in the respective decay chains

radiation differently from mineral matter, and therefore it is accounted for in the dose-rate calculations. The contribution of cosmic-rays can contribute significantly to the environmental dose rate, but its effect diminishes rapidly with burial depth. The contribution of cosmic rays was calculated using the method of Prescott and Hutton (1994).

Ages were determined from the luminescence of quartz grains using the single aliquot regenerative (SAR) protocol (Murray and Roberts, 1998; Murray and Wintle, 2000, 2003; Wintle and Murray, 2006). Aliquots were prepared and analyzed at the Luminescence Dating Laboratory at University of the Fraser Valley, British Columbia. The preparation and dating protocols are similar to those described by Hanson et al. (2012). Under controlled lighting conditions in the laboratory, approximately 150 g of sample were extracted for preparation after 2-3 cm of the light-exposed sediment was discarding from the end of the sample cylinder. The sand samples were treated with hydrochloric acid to dissolve carbonates and then sieved to isolate the 180-250 µm size fraction. Samples then were treated with concentrated hydrofluoric acid for 40 minutes to dissolve feldspar grains and to etch the outer surface of the quartz grains that had been affected by α radiation in the environment. Quartz grains were separated from other mineral grains using a sodium polytungstate solution with a density of 2.68 g/ml. Aliquots were then prepared by mounting 50-100 grains on 9.8 mm diameter aluminum discs using silicone oil as an adhesive.

Luminescence intensity was measured using a Risø TL/OSL DA-20 reader. Aliquots were stimulated using a 45 mW/cm^2 blue (470 ± 20 nm) light-emitting diodes. Ultraviolet emissions (~350 nm) were detected by a photomultiplier tube placed behind a 7.5 mm-thick Hoya U-340 optical filter. Laboratory irradiations were applied with a calibrated ^{90}Sr/^{90}Y β-source mounted on the reader that delivered 6.28 ± 0.12 Gy/min, 6.25 ± 0.12 Gy/min, 6.24 ± 0.11 Gy/min, 6.24 ± 0.11 Gy/min, 6.23 ± 0.11 Gy/min, and 6.23 ± 0.11 Gy/min for samples KDF-1 through KDF-6, respectively. The equivalent dose of each sample was determined using the standard SAR protocol of Murray and Wintle (2000), but with the inclusion of an infrared wash to remove any luminescence resulting from K-feldspar contamination (Olley et al., 2004; Wintle and Murray, 2006).

Radial plots (Galbraith et al., 1999; Galbraith, 2010), which display the distributions of equivalent dose (D_e) values of each aliquot about weighted mean values, were prepared for each sample. The central age model (CAM) of Galbraith et al. (1999) is appropriate for

determining the D_e for samples with overdispersion (i.e. observed variance is higher than the variance of the theoretical model) of less than 20% (indicating the aliquots consisting of grains that were sufficiently exposed to sunlight to reset the luminescence signal prior to burial). The CAM was appropriate for all samples. The validity of the SAR protocol for dating quartz from the study area was tested through dose recovery experiments on all samples (Roberts et al., 1999; Murray and Wintle, 2003). In each case the laboratory dose was sufficiently recovered, implying the quartz grains responded well to the technique and the method is suitable.

Select macrofossils were separated, identified and sent to the W.M. Keck Carbon Cycle Accelerator Mass Spectrometry (AMS) Laboratory at the University of California, Irvine for AMS radiocarbon age determination. Analysis was conducted using a 500 kV compact AMS unit from National Electrostatics Corporation using protocols described by Southon et al. (2004). In order to compare radiocarbon ages with Optical ages, all reported radiocarbon ages were calibrated using the OxCal online routine version 4.2 and the IntCal09 calibration curve (Bronk Ramsey 1994, 2001; Reimer et al. 2009). Samples containing suitable material for dating were isolated, weighed and photographed. Prior to submission isolated material was inspected and in some cases cleaned using an ultra-sonic bath. The dried material was packaged using freshly cut, small square pieces of aluminum foil, folded into small packets and placed in labeled plastic sterilized 3.5 cm diameter covered petri dishes for shipment to Keck Carbon Cycle AMS Laboratory. Throughout the entire process new latex disposable gloves were worn and only non-carbon instruments or material were used (glass beakers, glass petri dishes, stainless steel forceps, and aluminum foil).

7.3 Results

7.3.1 Kiskatinaw Dune Field

The Kiskatinaw Dunes Field is a tract of aeolian landforms that extends for more than 35 km from the East Kiskatinaw River (west) to, and probably beyond the British Columbia-Alberta border (east) (Fig. 7.1). The local terrain is irregular and the dunes appear to have migrated across the landscape with little impedance from the local topography. The dominant forms are hummock dunes (Pye and Tsoar, 1990) and composite or singular parabolic dunes typically showing significant elongation (David, 1977). These dunes are considered by Livingstone and Warren (1996) to be a type of anchored (vegetative) dune class. Dune ridges (arms) and

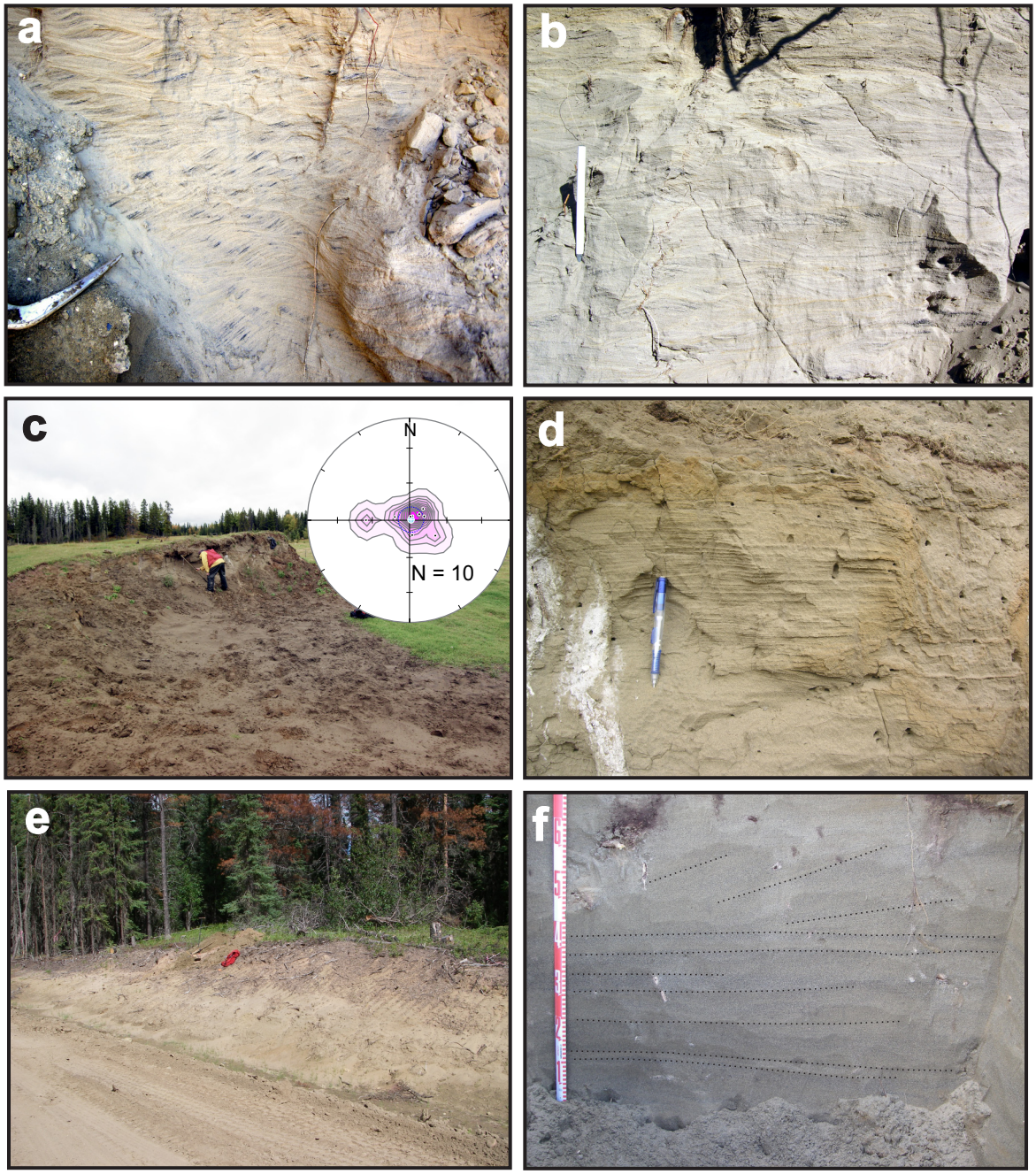

Figure 7.4. a) and b) Climbing ripple and cross-laminated silty sand from an exposure on the West Kiskatinaw River (black grains are coal fragments). These glaciolacustrine sediments are likely the source material for the Kiskatinaw Dune Field; c) an exposed dune mound from dune Area B (see Fig. 7b) and contoured stereo net showing poles to planes of the strata (near horizontal); d) a close up of horizontal to shallow dipping laminated medium sand from dune shown in Fig. 7.4c; e) low ridge from an elongated dune at sample site KDF-6 (Fig. 7.8); horizontally laminated medium sand overlain by planar cross stratified medium sand from within the arm of an elongated dune ridge at KDF-2 (see Fig. 7.9).

parabolic forms have consistent orientation indicative of unidirectional (Pye and Tsoar, 1990) winds blowing from the southwest (~245°—255°) to the northeast (~65°—75°). The source sand for the dunes is glaciolacustrine sediments (glacial Lake Peace) from within the river valleys (Figs. 7.4a and 7.4b). The aeolian dunes and ridges (Figs. 7.4c-7.4f) typically consist of well sorted medium sand. The internal stratigraphic architecture was only observed in a few locations and in the shallow (~1 m) pits dug to collect OSL samples. In most cases the internal structure is dominated by low angle laminated sand (Fig. 7.4c and 7.4d), with minor (40 cm thick) planar cross-beds (noted in the arm of a dune at KDF-2, Fig. 7.4f). Numerous deflation features are noted on the LiDAR DEM, which suggest that a veneer of loess or sand may be present. Field observations, however, indicate that silty sand only occurs in the upper 10-15 cm of most soil profiles. The dominant substrate in the area is clay-rich till. There are four distinct dune clusters in the Kiskatinaw Dune Field (Fig. 7.5).

7.3.1.1. Area A

Area A is located adjacent to the East Kiskatinaw River valley (Fig. 7.6a). On the South side of the valley the dunes are generally poorly developed and form composite elongated parabolic dunes with border and dune ridges. These features originate at a gully and track to the northeast where the dunes appear to plunge over the incised edge of the valley (Fig. 7.6b). The composite dunes show both superposed (arranged along a common axis) and in-succession (arms of individual dunes form one common ridge in an off-set position). On the north side of the West Kiskatinaw River, dunes track obliquely across gullies. On the downwind side of some gullies, aeolian sediments have accumulated and formed sand sheets with sand tongues that nourished smaller parabolic dunes (Fig. 7.6c). At the northeastern end of the dune cluster, distinct ridges are well developed and form serrated composite parabolic dunes. Some dune heads are sharp (Fig. 7.6d) whereas others have aprons that grade into the surrounding terrain (Fig. 7.6e).

7.3.1.2. Area B

The main portion of dune Area B occurs near the confluence of the East and West Kiskatinaw rivers (Figs. 7.5 and 7.7a). Aeolian features in this cluster are dominantly dune hummocks and subtle ridges that form several km-scale, generally u-shaped aeolian complexes

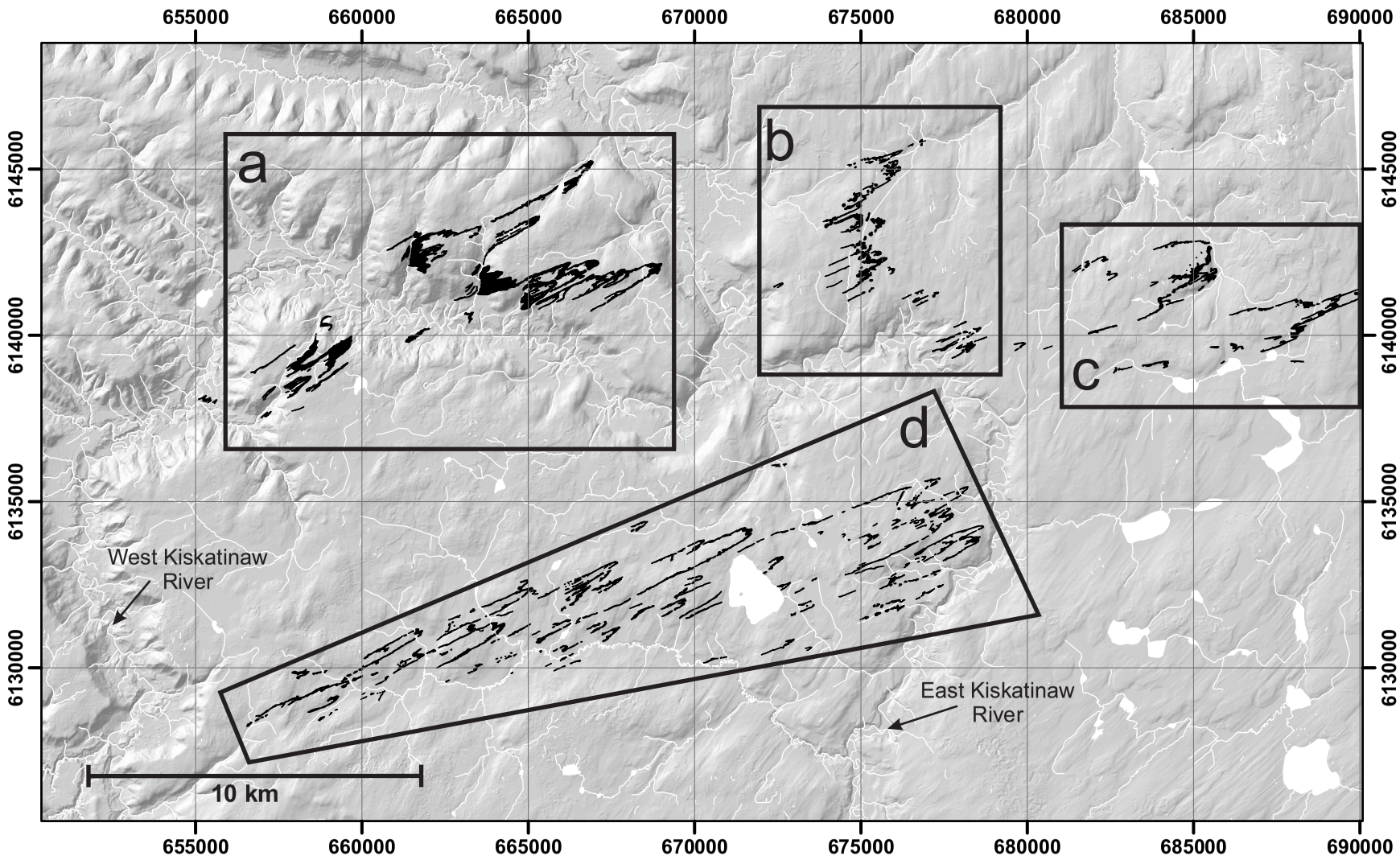

Figure 7.5. Four clusters of dunes (a-d) make up the Kiskatinaw Dune Field.

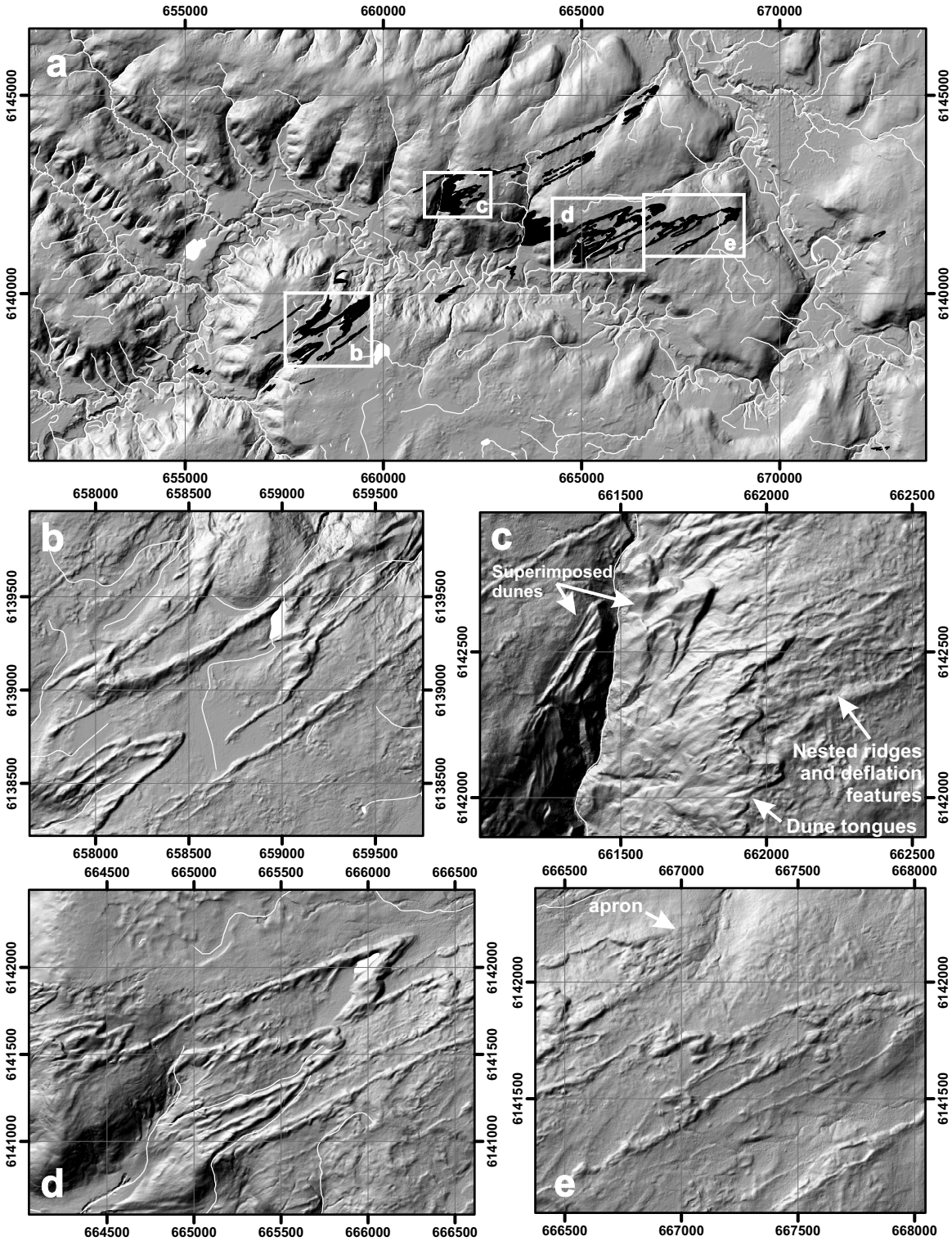

Figure 7.6. a) Dune Area A (all images have 2x vertical exaggeration); b) composite parabolic dunes; c) sand accumulation and emerging dune along a gully; d) composite parabolic and zig-zag dunes with prominent dune heads; e) zig-zag dunes with well developed aprons rather than ridged dune heads.

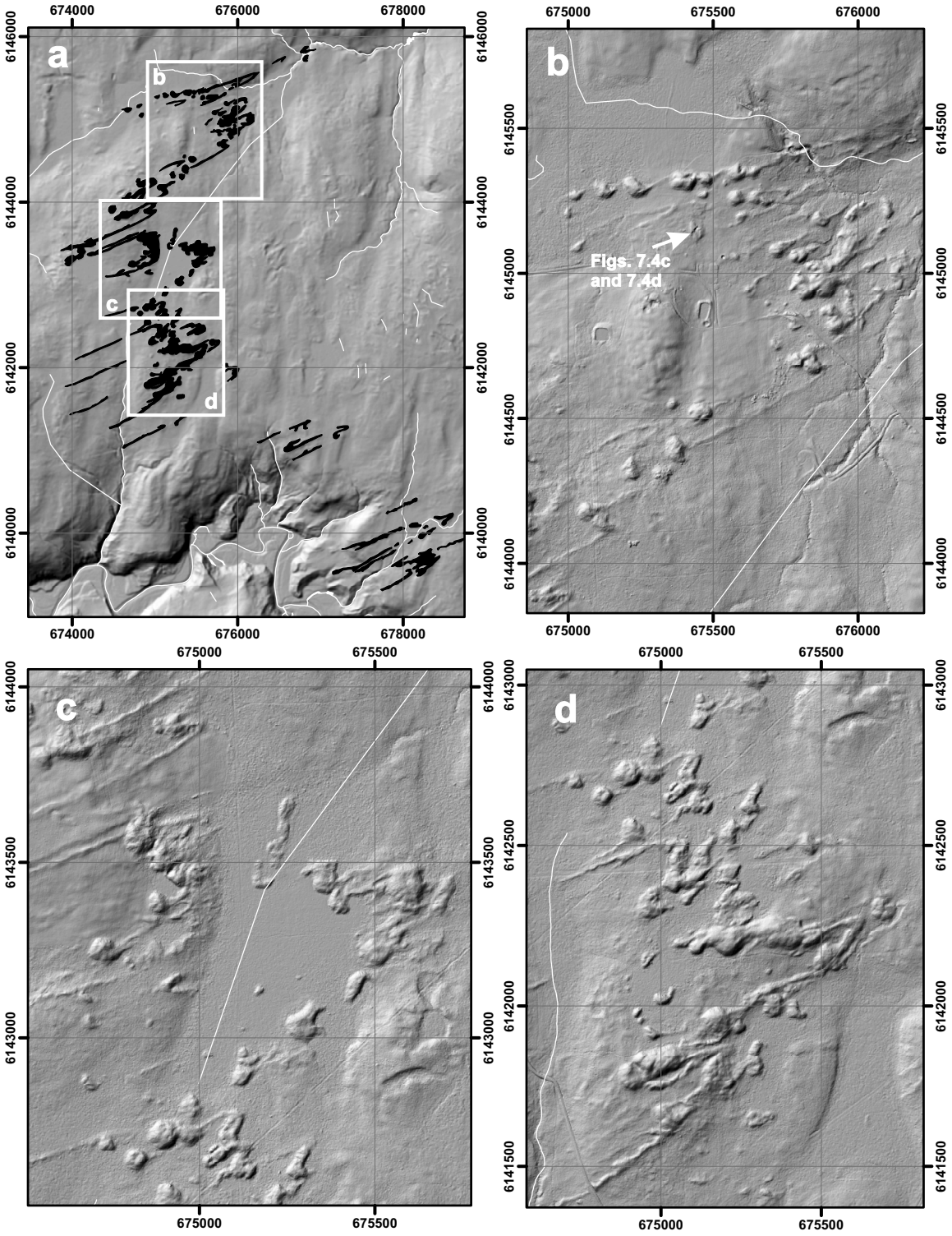

Figure 7.7. a) Dune Area B (all images have 2x vertical exaggeration); b) dunes hummocks connected by subtle ridges; c and d) dune hummocks that form a eroded composite dune head.

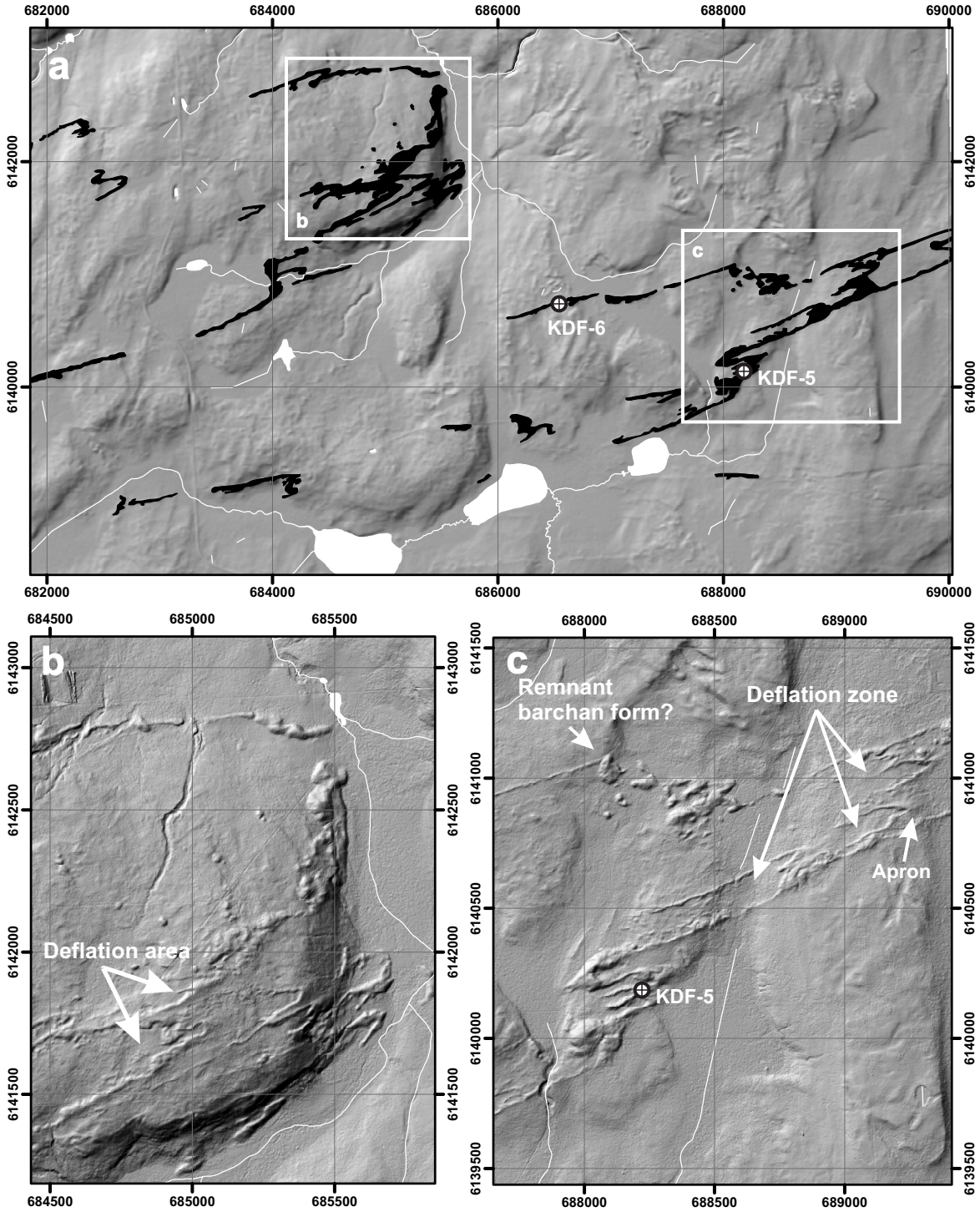

Figure 7.8. a) Dune Area C (all images have 2x vertical exaggeration); b) Large (km-scale) u-shaped dune complex; c) Large (km-scale) u-shaped dune complex with subsequently remobilized head (not currently active). The luminescence stabilization age from a ridge on the southern shoulder is 10.6 ± 0.6 ka BP (KDF-5) and the northern arm is 11.0 ± 1.0 ka BP (see Fig. 7.8a for location).

(Figs. 7.7b-d). These hummocks are probably the remnants of better developed dune forms that were modified and disarticulated by post stabilization erosion (i.e. blowouts).

7.3.1.3. Area C

Dune Area C occurs in the eastern edge of the study area (Fig. 7.5). It consists of two composite dune complexes (Fig. 7.8a-c). The western complex (Fig. 7.8b) consists of a large (km-scale) generally u-shaped ridge with a poorly developed, but prominent head along the crest of an escarpment. The dune head consists of en echelon arrangement of a zig-zag ridge or hummocks. The lateral ridges (arms) on the north side of the complex are subtle and low (2 m). On the south side of the complex the arm is poorly defined but is marked by a low relief sand apron (blanket) with a well developed deflation area (Fig. 7.8b). Several well developed discrete parabolic dunes occur at the base of the escarpment.

The eastern complex (Fig. 7.8c) has a u-shape similar to the western complex, but the central part of the head of the dune may have been reactivated and extended downwind. The main arms of the complex consists of long (~2 km), low relief (<3m) ridges, the northern of which was dated by KDF-6. Where the u-shaped head originally occurred (forms two shoulders), the ridges develop more relief, but the forms are ambiguous. Several poorly developed parabolic forms are preserved on the northern shoulder (Fig. 7.8c). On the southern shoulder the ridges are part of a series of poorly developed parabolic dunes. These ridges were dated by KDF-5. Where the head of the dune has reactivated, there are well developed lateral arms, but the heads are marked by a subtle downwind apron behind which is a well developed deflation zone.

7.3.1.4. Area D

Dune Area D is relatively large, covering more than 25 km (Fig. 7.9a). Narrow ridges (dune arms) are the dominant aeolian form and some dune arms extend for over 15 km. In general, this dune cluster resembles the so called “Cree Lake” type dune ridges of David (1977). Many ridges occur in isolation (no head) suggesting they represent stabilized relict dune arms. In the western (proximal) part of the dune cluster, well developed parabolic heads are common and typically occur as single or paired parabolic landforms (Fig. 7.8c). Dune heads typically have well developed ridges and clear parabolic form. In the central and eastern part of the cluster, composite dunes are more common and dune heads less well defined. In some cases large

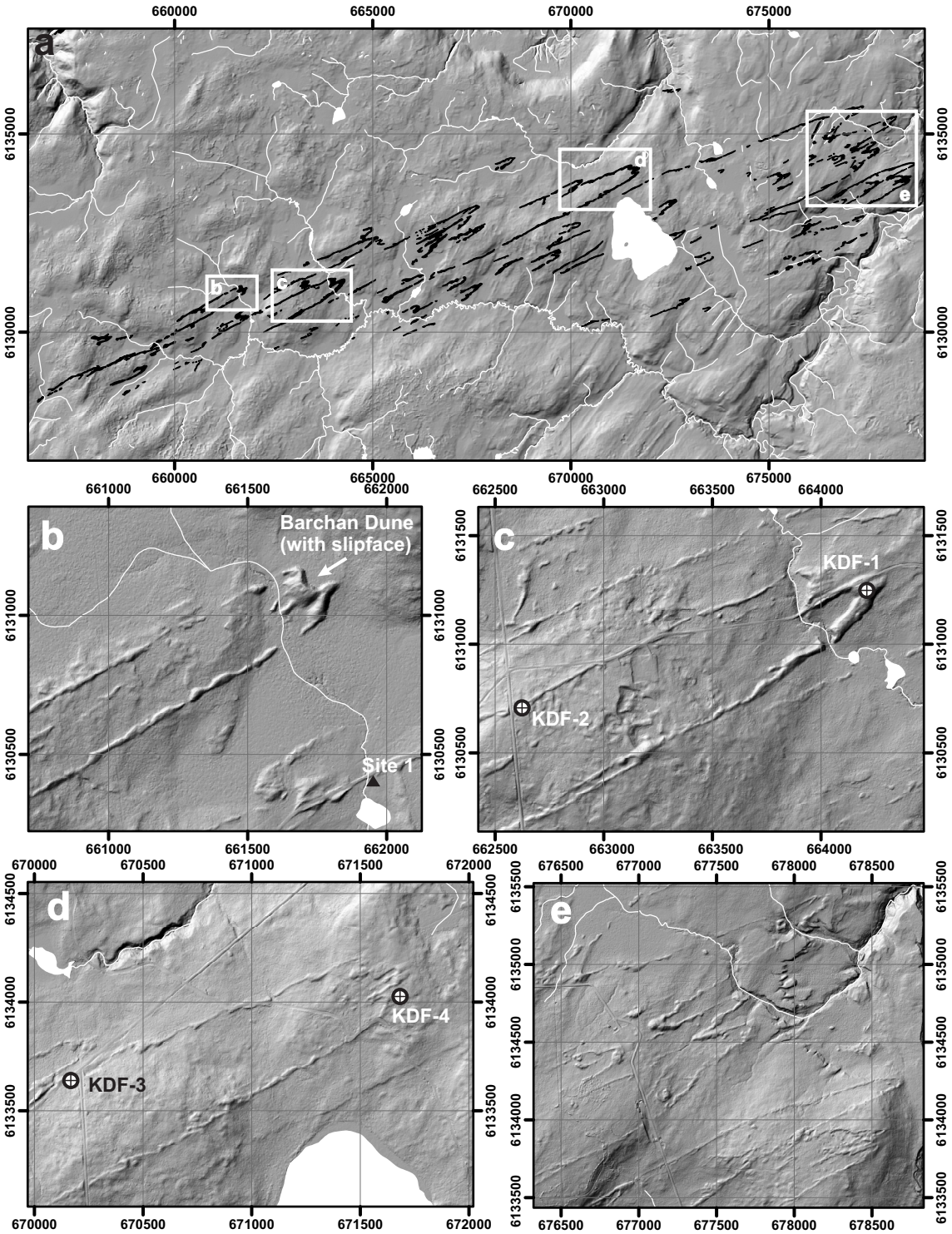

Figure 7.9. a) Dune Area D (all images have 2x vertical exaggeration); b) a barchan dune with trailing arms partially preserved; c) elongated twined parabolic dune (optical ages: KDF-1 = 10.8 ± 0.6 ka BP; KDF-2 = 12.3 ± 0.7 ka BP); d) elongated parabolic dune with in succession arrangement (David, 1977) (optical ages: KDF-4 = 8.7 ± 0.5 ka BP; KDF-3 = 11.3 ± 0.7 ka BP); e) elongated parabolic dunes complex at the downwind (east) region of Dune Area D.

Table 7.3. OSL sample site for the Kiskatinaw Dune Field.

Sample	Depth (cm)	Easting	Northing	Location on Dune
KDF-1	100	664215	6131260	Head
KDF-2	120	662573	6130692	Arm
KDF-3	105	670194	6133138	Arm
KDF-4	85	671684	6134020	Head
KDF-5	90	688205	6140190	Head
KDF-6	125	686542	6140750	Arm

Universal Transverse Mercator North American Datum 83

Table 7.4. Sample depth below the ground surface (d), equivalent dose (D_e), cosmic-ray dose rate (D_c), total dose rate (D_T), and apparent optical age.

Sample name	*d* (cm)	D_e (Gy)[1]	D_c (Gy·ka^{-1})	D_T (Gy·ka^{-1})	Optical age (ka)
KDF-1	100	15.8 ± 0.6	0.18	1.46 ± 0.08	10.8 ± 0.6
KDF-2	120	16.1 ± 0.5	0.04	1.26 ± 0.07	12.3 ± 0.7
KDF-3	105	16.0 ± 0.6	0.17	1.44 ± 0.10	11.3 ± 0.7
KDF-4	85	16.8 ± 0.7	0.18	1.99 ± 0.12	8.7 ± 0.5
KDF-5	90	15.3 ± 0.6	0.18	1.54 ± 0.09	10.6 ± 0.6
KDF-6	125	15.3 ± 0.8	0.17	1.37 ± 0.08	11.0 ± 1.0

[1]Values were calculated using the CAM routine with outlier points removed.

Notes: uncertainties are analytical only, and are reported as ±1 standard deviation. The "as-collected" water contents were used in each case for the dose rate calculation.

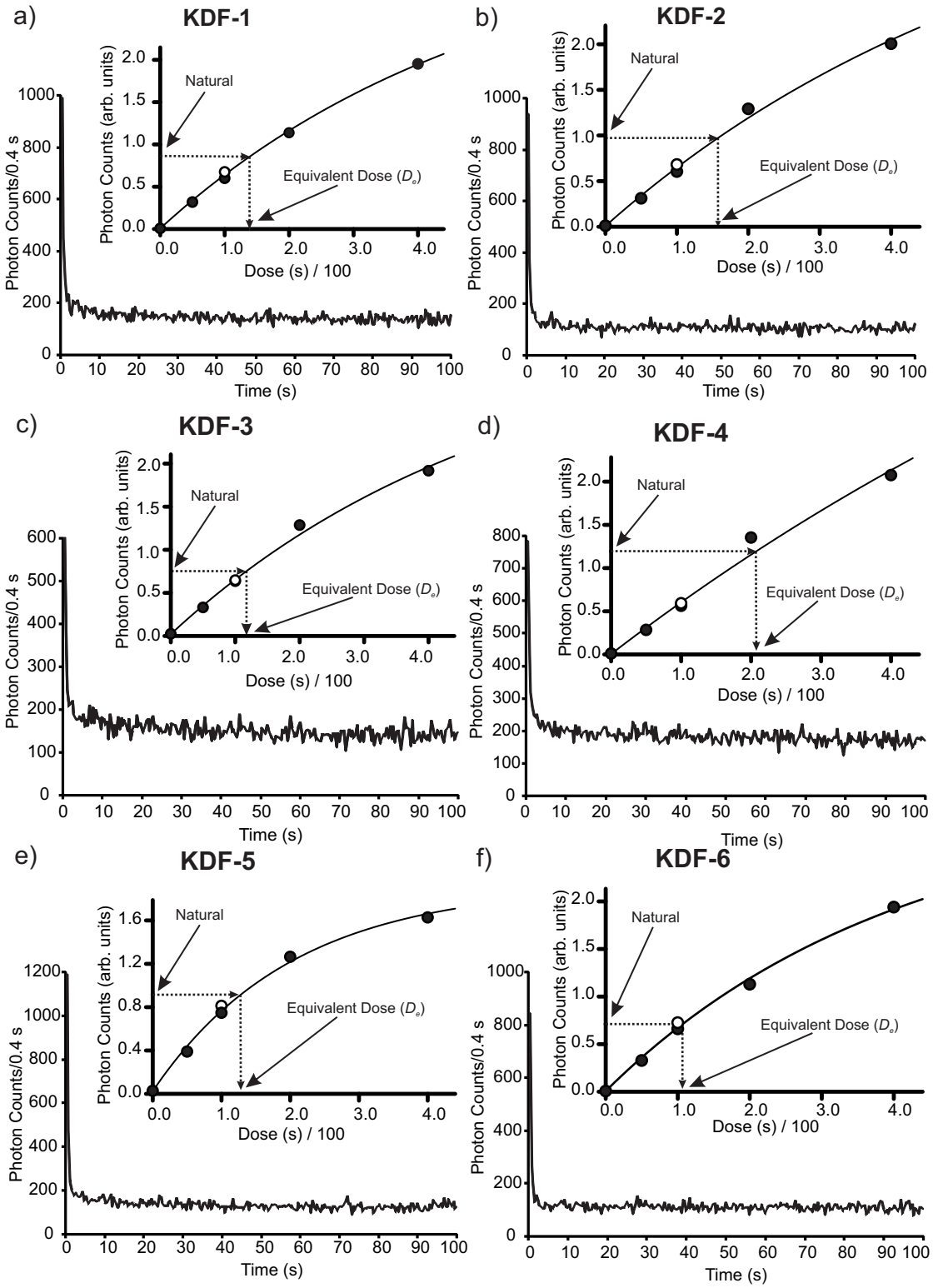

Figure 7.10. Dose response curves with example of a typical shine-down curve. The open circle on the growth curve is a duplicate dose point used to determine the recycling ratio. Since it is close to unity in these samples, the test dose procedures has successfully corrected for sensitivity changes. a) KDF-1; b) KDF-2; c) KDF-3; d) KDF-4; e) KDF-5; and f) KDF-6.

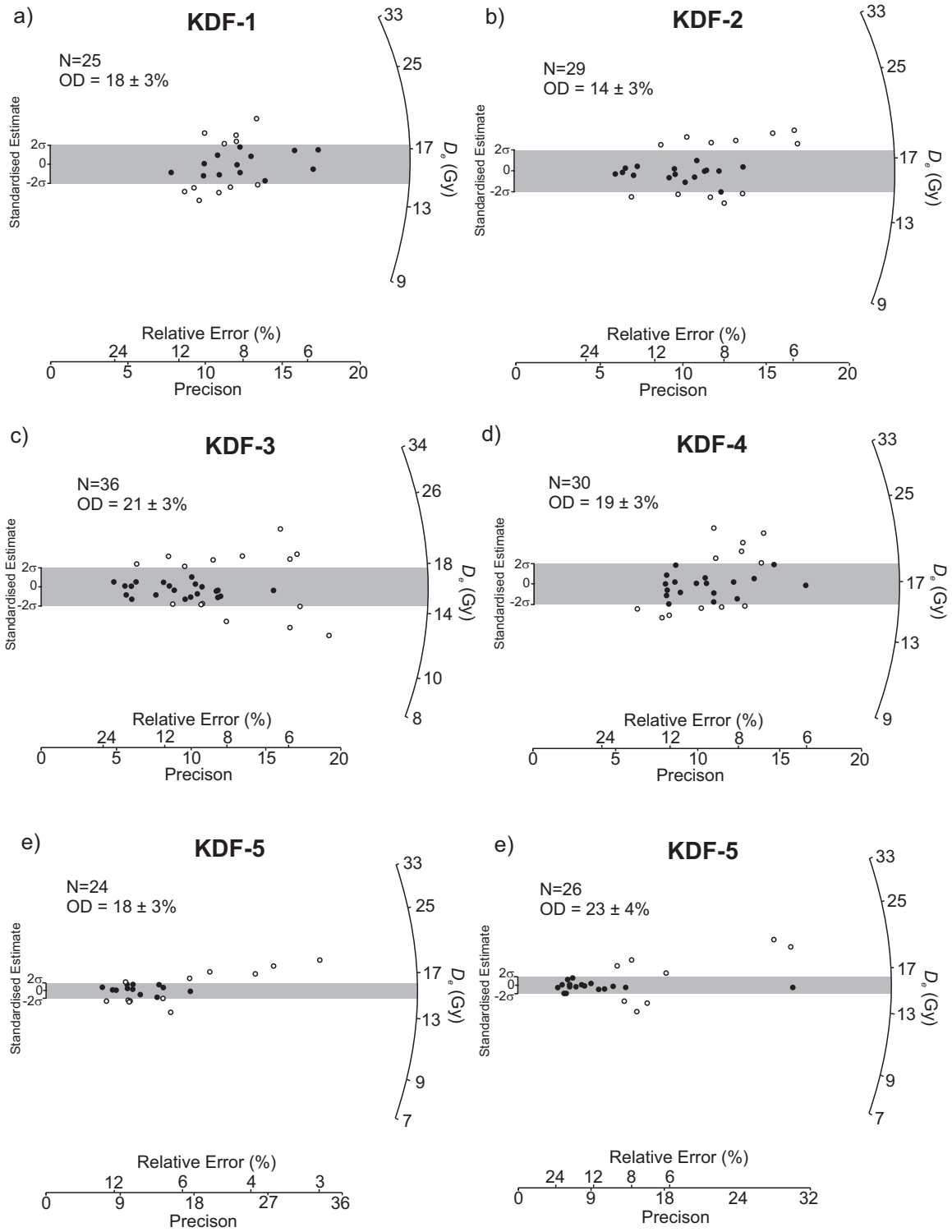

Figure 7.11. Radial Plots with central age modeled. The grey region on the radial plots represents the weighted-mean equivalent dose value of all the data. OD = Overdispersion; N = number of aliquots. a) KDF-1; b) KDF-2; c) KDF-3; d) KDF-4; e) KDF-5; and f) KDF-6.

deflation areas define the interior of the dune forms, whereas low ridges and amorphous aprons downwind of the dune head have developed (Figs. 7.9d and 7.9e)

7.3.1.5 OSL Dating

The six luminescence (Table 7.3) samples returned ages that range from 12.3 ± 0.7 ka to 8.7 ± 0.5 ka (uncertainty at 1σ; Table 7.4; Fig. 7.10 and 7.11). KDF-2 from the arm of a dune in Area D is the oldest stabilization age (12.3 ± 0.7 ka). KDF-1 was sampled from head the same, or possibly an adjacent dune approximately 1.7 km downwind and returned an age of 10.8 ± 0.6 ka. Sample KDF-3 and KDF-4 are from a different dune in Area D, downwind of KDF-1 and KDF-2. The arm of this dune returned an age of 11.3 ± 0.7 ka (KDF-3) where as the head of this dune returned the youngest age of 8.7 ± 0.5 ka (KDF-4). This young age is possibly the result of the reactivation of this dune from a blowout. KDF-5 (dune shoulder) and KDF-6 (dune arm) are from Area C and returned ages 10.6 ± 0.6 ka and 11.0 ± 1.0 ka, respectively.

7.3.2 Organic Sections

The organic section is located several metres above the modern Flatbed River on the edge of a terrace (easting: 629628, northing: 6108289; datum: NAD 83; Fig. 7.1). The section, exposed by a recent slope failure, consists of (bottom to top) 50 cm of pebble to cobble gravel, 78 cm of massive medium to fine sand, 8 cm of compressed, laminated organics and fine sand, and 211 cm of felted, fibric dense peat (Fig. 7.12a-e). A moist sphagnum bog currently occupies the top of the terrace.

Thirty-four bulk samples collected from the site were submitted to PALEOTEC Services for macrofossil identification and selected sample submission for AMS radiocarbon dating. Of the 34 samples submitted, only the basal 15 were analyzed in this study (Table 7.5 and 7.6). The samples consist of an overbank deposit (FBRP-01 to FBRP-06), compressed organics (FBRP-07 to FBRP-12), and dense peat (FBRP-13 to FBRP-15) (for detailed report see Appendix C).

7.3.2.2.1 Overbank Sand

7.3.2.2.1.1 FBRP-01; 50-80 cm; 9195 ± 25 yr BP (10 366 ± 115 cal yrs BP)

Overall, the preservation of the plant and animal macrofossils in the overbank sand is poor, but organic remains were recovered (Figs 7.13a-g). Some plant remains were difficult to

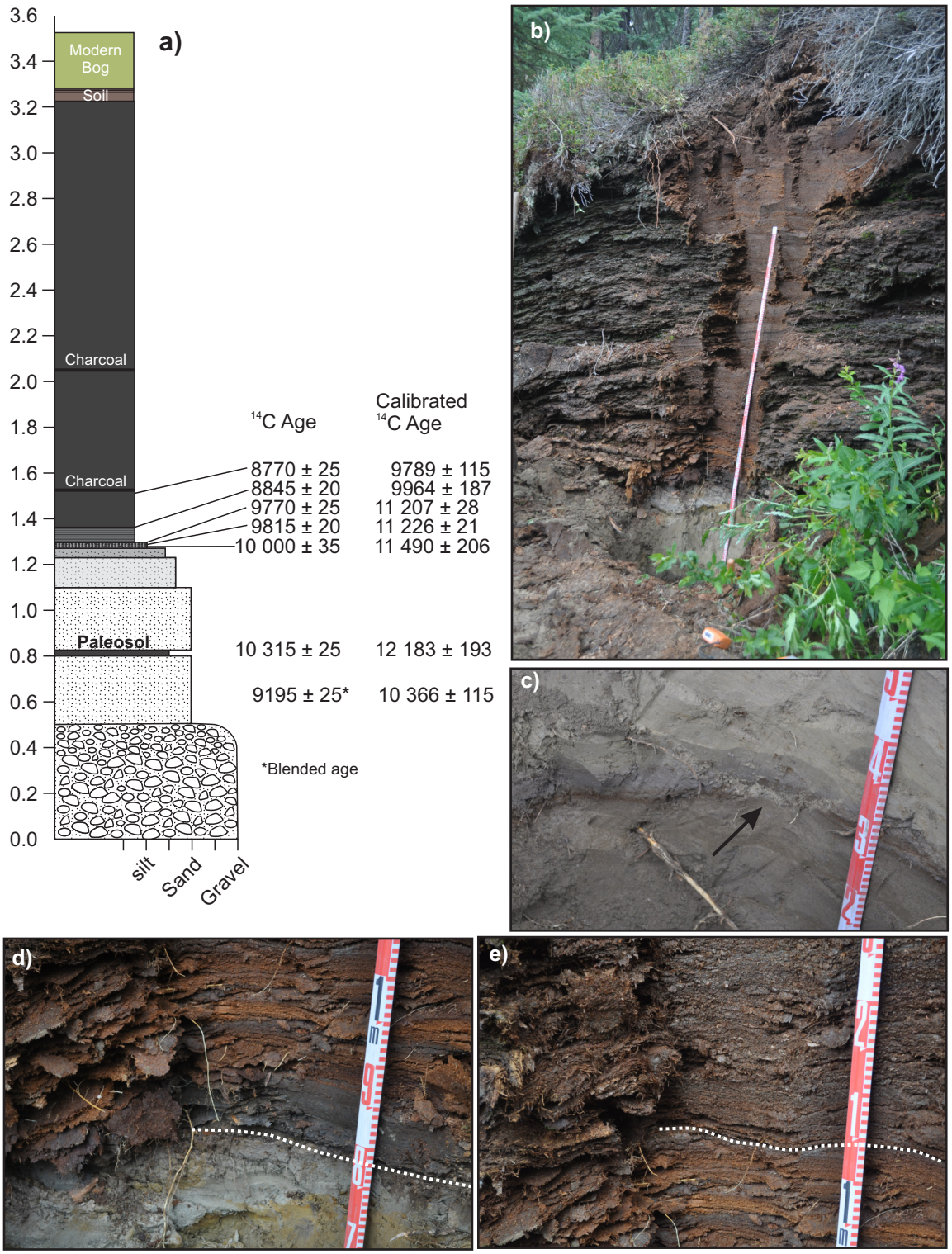

Figure 7.12. Organic section from the Flatbed River; a) summary stratigraphic log with radiocarbon dates; and b) photograph of the overbank and organic portion of the section; Overbank sand with paleosol (arrow) dated at 10 315 ± 25 14C yrs BP (12 183 ± 193 cal yrs BP); d) contact between overbank sand and compressed organics; e) contact between compressed organics and dense peat.

Table 7.5. Relative abundance of plant macrofossils from the Flatbed Peat Site (+ = taxon present, ++ = taxon common, +++ = taxon abundant).

PLANT MACROFOSSILS:	FBRP 1 50-80 cm	FBRP 2 80-82 cm	FBRP 3 82-110 cm	FBRP 4 110-122 cm	FBRP 5 122-128 cm	FBRP 6 128-128.5 cm	FBRP 7 128.5-128.7 cm	FBRP 8 128.7-128.9 cm	FBRP 9 129-130 cm	FBRP 10 130-132 cm	FBRP 11 132-134 cm	FBRP 12 136 cm	FBRP 13 145 cm	FBRP 14 150-152 cm	FBRP 15 155-156 cm
Algal remains:															
Characeae															
Chara sp.	+			+	+	++	+	+++	+	+	+	+			
Non Vascular Plants															
Bryophytes ....."mosses"	+			+			+		+	++	++	++	+++	+++	+++
Vascular Plants:															
Pinaceae ....."pine family"															
Pinus contorta Dougl. ex Loud.				+											
Picea sp.	+											+		++	+
Typhaceae....."Cat-tail family"															
Typha latifolia L.						+			+	+	+				
Sparganiaceae ....."bur-reed family"															
Sparganium hyperboreum type									+						
Potamogetonaceae .."pondweed family"															
Potamogeton richardsonii (A.Benn.) Rydb.									+	+	+				
Potamogeton compressus L.							+								
Potamogeton sp.						+			+	+	+	+			
Potamogeton spp.								+							
Potamogeton? sp.	+														
Ruppia cirrhosa (Petagna) Grande						+									
Najadaceae															
Najas flexilis (Willd.) Rostk. & W.L.E.Schmidt							+	+	+	++	++				
Cyperaceae ....."sedge family"															
Carex lenticular type											+	+			
Carex trigonous type								+			+				
Schoenoplectus tabernaemontani (C.C. Gmel.) Palla								+	+						
Scirpus sp.												+			
Scirpus small type												+			
Eleocharis palustris-uniglumis type						+									

Table 7.5. ***continues***

PLANT MACROFOSSILS:	FBRP 1 50-80 cm	FBRP 2 80-82 cm	FBRP 3 82-110 cm	FBRP 4 110-122 cm	FBRP 5 122-128 cm	FBRP 6 128-128.5 cm	FBRP 7 128.5-128.7 cm	FBRP 8 128.7-128.9 cm	FBRP 9 129-130 cm	FBRP 10 130-132 cm	FBRP 11 132-134 cm	FBRP 12 136 cm	FBRP 13 145 cm	FBRP 14 150-152 cm	FBRP 15 155-156 cm
Salicaceae ....."willow family"															
Salix sp.									+		+	+			
Betulaceae ....."birch family"				+											
Betula occidentalis ?	+														
Betula medium shrub/small tree type														+	+
Betula arboreal type															+
Chenopodiaceae ...."goosefoot family"															
Chenopodium capitatum?								+	+						
Caryophyllaceae ..."pink family"															
Symphoricarpos albus (L.) S.F.Blake												+			
Ceratophyllaceae .."hornwort family"															
Ceratophyllum demersum L.										+					
Nymphaeaceae ....."water lily family"															
Nuphar sp.														+	
Rosaceae ....."rose family"															
Potentilla sp.							+					+			
Haloragaceae ....."water milfoil family"															
Hippuris vulgaris L.									+						
Ericaceae ....."heath family"															
Arctostaphylos uva-ursi (L.)Spreng.											+				
Gentianaceae ....."gentian family"															
Menyanthes trifoliata L.										+	+				+
Lamiaceae ....."mint family"															
Mentha sp										+		+			

Table 7.5. ***continues***

PLANT MACROFOSSILS:	FBRP 1 50-80 cm	FBRP 2 80-82 cm	FBRP 3 82-110 cm	FBRP 4 110-122 cm	FBRP 5 122-128 cm	FBRP 6 128-128.5 cm	FBRP 7 128.5-128.7 cm	FBRP 8 128.7-128.9 cm	FBRP 9 129-130 cm	FBRP 10 130-132 cm	FBRP 11 132-134 cm	FBRP 12 136 cm	FBRP 13 145 cm	FBRP 14 150-152 cm	FBRP 15 155-156 cm
Unidentifiable plant taxa															
Other:															
carbonates	+++														
wood/twig	+			+	+			+				+			
charcoal	+											+		+	+
peat/moss peds	+						++	++	++	++	++	+		++	++
deciduous leaf	+														
reworked late Tertiary or Cretaceous coal	++	++	+		+	+									
modern roots/rhizomes	+	+												+	
sand cemented peds		+	+	+	+	+									
modern/aged ECM's			+	+	+										
woody herbaceous stems									+						
aquatic herb plant stems									+	++	++				
fungal spores (*Glomus* ? sp.)															+

Table 7.6. Relative abundance of animal macrofossils from the Flatbed Peat Site (+ = taxon present, ++ = taxon common, +++ = taxon abundant).

Animal Macrofossils:	FBRP 1 50-80 cm	FBRP 2 80-82 cm	FBRP 3 82-110 cm	FBRP 4 110-122 cm	FBRP 5 122-128 cm	FBRP 6 128-128.5 cm	FBRP 7 128.5-128.7 cm	FBRP 8 128.7-128.9 cm	FBRP 9 129-130 cm	FBRP 10 130-132 cm	FBRP 11 132-134 cm	FBRP 12 136 cm	FBRP 13 145 cm	FBRP 14 150-152 cm	FBRP 15 155-156 cm
PORIFERA ....."sponges"															
HAPLOSCLERINA															
Spongillidae															
Spongilla type									+			+			
PLATYHELMINTHES															
TUBELLARIA ....."flatworms"							+								+
BRYOZOA															
Cristatella mucedo L.							+		+	+	+	+			
Plumatella sp.							+			+		+		+	
ANNELIDA															
HIRUDINEA ....."leeches"						+									
ARTHROPODA															
INSECTA															
HEMIPTERA ....."bugs"							+								
Cicadellidae ....."leafhoppers"						+									
COLEOPTERA ....."beetles"	+			+	+	+		+	+	+		+			+
Dytiscidae .."predaceous diving beetles"															
Hydroporus sp.											+				
Colymbetes sp.										+	+	+	+		
Acilius semisulcatus Aubé									+			+			
Acilius sp.										+	+			+	
Hydrophilidae ..."water scavenger beetles"															
Cercyon sp.								+							
Staphylinidae ....."rove beetles"					+										
Olophrum sp.	+														
Scarabaeidae ....."scarab beetles"															
Aegialia sp.	+				+										
Helodidae ....."marsh beetles"															
Cyphon sp.															+
Byrrhidae ....."pill beetles"		+													
Simplocaria sp.			+			+									
Morychus sp.	+	+				+									
Cytilus alternatus (Say)						+									
Chrysomelidae ....."leaf beetles"	+														
Donaciinae										+	+				
Curculionidae ....."weevils"	+	+		+	+	+								+	
Lepidophorus lineaticollis Kirby						+									
Isochnus sp.	+														

Table 7.6. ***continues***

Animal Macrofossils:	FBRP 1 50-80 cm	FBRP 2 80-82 cm	FBRP 3 82-110 cm	FBRP 4 110-122 cm	FBRP 5 122-128 cm	FBRP 6 128-128.5 cm	FBRP 7 128.5-128.7 cm	FBRP 8 128.7-128.9 cm	FBRP 9 129-130 cm	FBRP 10 130-132 cm	FBRP 11 132-134 cm	FBRP 12 136 cm	FBRP 13 145 cm	FBRP 14 150-152 cm	FBRP 15 155-156 cm
TRICHOPTERA ....."caddisflies"	+														
DIPTERA ....."flies"										+					
Tipulidae ....."crane flies"															
Tipula sp.							+								
Chironomidae ....."midges"				+		+	+		+	+	+	++		+	
HYMENOPTERA ....."wasps and ants"															
Ichneumonidae											+				
Formicidae ....."ants"															
Myrmica sp.	+														
CRUSTACEA															
Cladocera ....."water fleas"															
Daphnia sp.	+			+		+	++	++	+++	+	+	+++			
Simocephalus sp.						+	+	+	+						
Ostracoda ....."ostracodes"	+														
ARACHNIDA															
Oribatei ....."oribatid mites"											+			+	
Hydrozetidae															
Hydrozetes sp.				+	+	+			+	+		+			
MOLLUSCA															
Gastropoda ....."snails, limpets"															
conical vertical snails	+++														
discoidal horizontal snail				+											
Other:															
immature mandibles															+

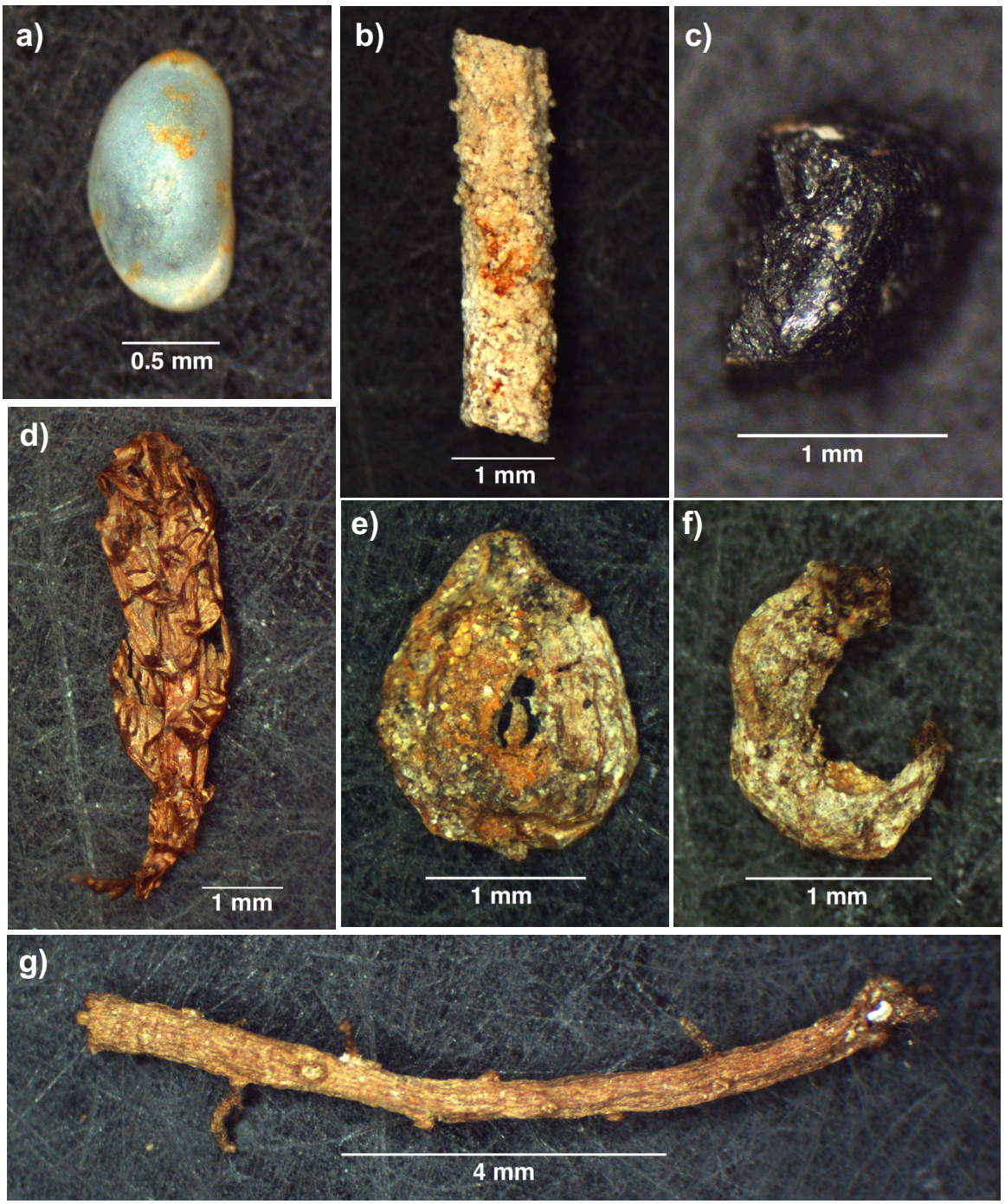

Figure 7.13. Examples of fossils recovered from FBRP-01. a) ostracode valve; b) calcium carbonate cylinder; c) Cretaceous reworked coal; d) moss; e) unknown seed (Potamogeton?); e) unknown partial seed; g) aged rhrizome. Note the poor preservation of the seeds and Fe staining (rust-coloured precipitate) on the fossils.

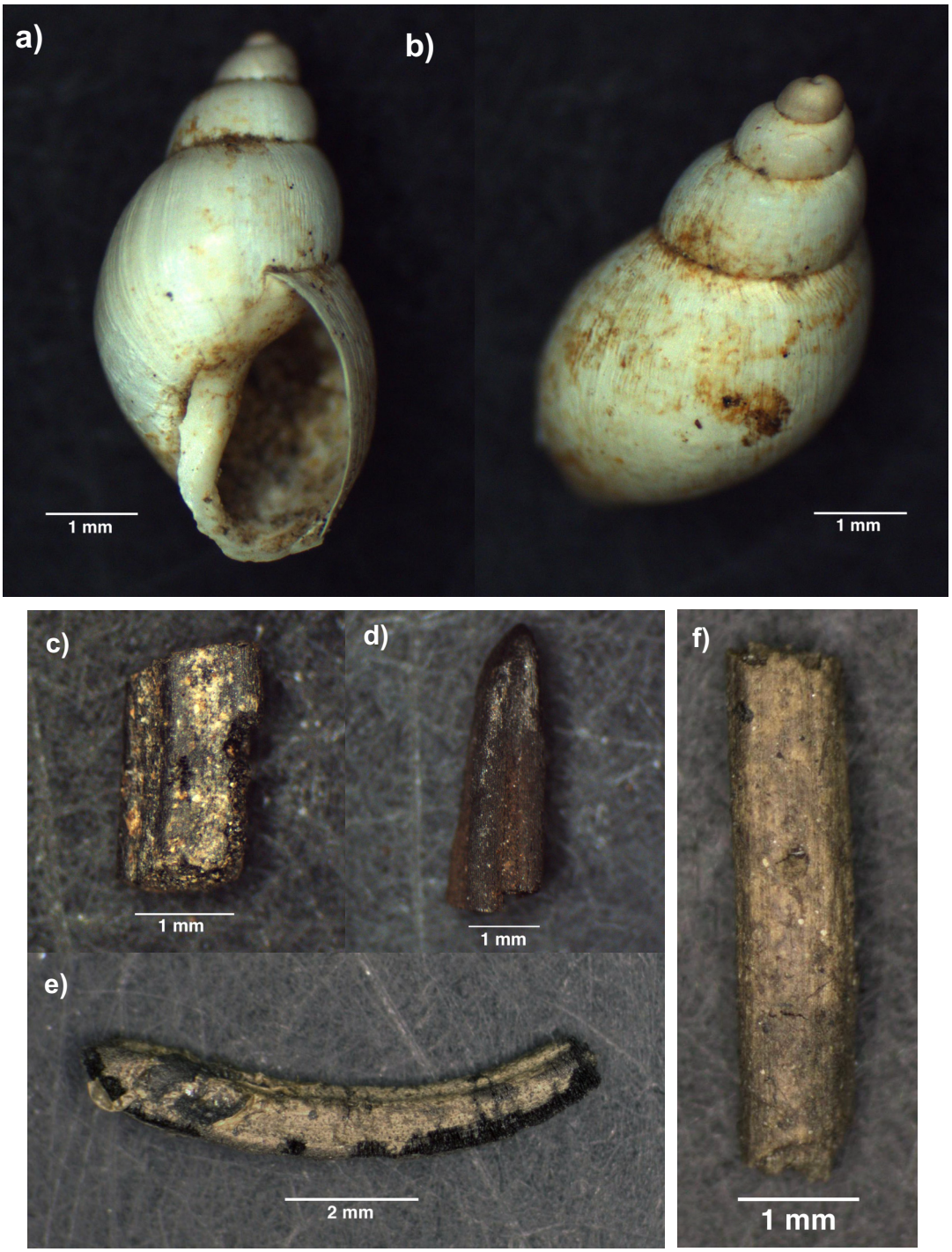

Figure 7.14. a and b) Opposite views of a conical (vertical coiled) snail from FBRP-01; Spruce (*Picea* sp.) macrofossil needle fragments from c) FBRP-01; d) FBRP-12; and e): FBRP-14 (charred). Charred and not charred spruce needle fragments from FBRP-14; f) a macrofossil fragment of a two-needle pine, *Pinus contorta* from sample FBRP-04. *Pinus contorta* occurs on a wide range of soils and sites, including wet depressions and easily colonizes recently burned areas (Farrar, 1999).

identify (e.g. Figs. 7.13e and 7.13f) and many of the macrofossils have iron staining (rust-coloured precipitate) on the surfaces, likely the result of deposition in an oxygen-deprived aquatic environment containing iron bacteria. Many calcium carbonate, hollowed, tubular-shaped precipitates occur in FBRP-01 (Fig. 7.13b) attesting to the hard water environment of the overbank deposits.

The basal sample, FBRP-01, 50-80 cm, is unlike the other samples examined because it contains abundant molluscs (Figs. 7.14a-b) with approximately 300 conical (vertical coiled) isolated snails varying in size from 5 mm to 2 cm. Snails are commonly found along the shallow edges of freshwater ponds, lakes and streams with some species being found in temporarily wet areas. Snails are grazers feeding on organic material that accumulates on plants, rocks or soft bottom sediments. They are ubiquitous in calcareous sediments which indicate deposition in non-acidic waters (Miller and Tevesz, 2001). Ostracods (valves) are also present (Fig. 7.13a). Ostracods prefer carbonate buffered water bodies and are benthic organisms of lakes, ponds, and streams and generally do not live in high energy environments. Being detritus feeders, ostracodes prefer an organic rich, well defined, clay to fine silt textured sediment at the sediment-water interface (Delorme, 1990).

Almost all of the beetle fossils are thin and pitted, typical of sand deposited floodplain environments in which the beetle chitin has been impacted by saltating mineral grains. As such, identification of the beetle parts was difficult since key indicators such as setigerous punctures could not be differentiated from the pits created by sand mineral grains. Identifications could only be made to the generic level and in some cases only to Family. Many of the beetle (Order Coleoptera) fossils in this sample live in sandy floodplains that have sparsely vegetated areas. They include the pill beetle, *Morychus* sp. and scarab beetle, *Aegialia*. The rove beetle, *Olophrum* sp. live in poorly drained sites being found in emergent subaquatic vegetation (particularly *Carex*), growing in shallow water (Campbell, 1983). The tiny flea beetle, *Isochnus* is associated primarily with riparian habitats with the leaf mining larvae feeding on willow (*Salix*) and poplar (*Populus*) (Anderson, 1989).

Plant macrofossils in FBRP-01 are not as abundant as the animal fossils. Submergent aquatic plants typical of ponds are absent. The tentative identification of pondweed (*Potamogeton?*) is based on the poorly preserved achenes and is questionable since no

pondweed remains occur in any of the five overbank bank samples examined. Although low in number, aquatic algae remains (oogonia) of stonewort (*Chara* sp.) along with mosses (Fig, 7.13d) occur in this sample. Stoneworts usually grow in shallow water and in general prefer waters of moderate to high alkalinity (Wood and Imahori, 1965). A few spruce (*Picea* sp.) needles (charred and not charred; Fig. 7.14c) were isolated in this sample suggesting spruce was growing in the vicinity of the Flatbed Peat site. A Shrub/small tree nutlet of water birch, *Betula occidentalis(?)* also occurs in this sample. Although a definitive species could not be determined, water birch is a tall shrub/small tree growing up to 10 m high with dense, pure thickets being common. It grows on moist soils along streams mixed with poplars, willow and alders (Farrar, 1995).

A sample of chitinous beetle and ant parts yielded a ^{14}C date of 9195 ± 25 yr BP (UCIAMS-118712). This date is approximately 1120 ^{14}C yr BP younger than the date obtained from the sample directly above (FBRP-02, 80-82 cm; 10 315 ± 25 ^{14}C yr BP, UCIAMS-117268). The age discrepancy can be explained in part by: 1) the 30 cm sampling interval for FBRP-01 likely included a large time interval than FBRP-02, a 2 cm point sample, and 2) FBRP-01 contained both beetles and ant parts (*Myrmica* sp.), the latter having the ability to burrow quite deeply into sand deposits thus potentially providing a blended AMS age of 'younger' ants combined with the more in situ beetle remains. FBRP-01 contains abundant reworked late Tertiary/Cretaceous coal (Fig. 7.13c).

7.3.2.2.1.2 FBRP-02, 80-82 cm; 10315 ± 25 ^{14}C yr BP (12 183 ± 193 cal yrs BP)

The content of sample FBRP-02 is similar to that of FBRP-01, with abundant reworked late Tertiary/Cretaceous coal and many cemented peds with iron staining (rust-coloured precipitate) and modern rhizomes. No plant macrofossils were seen in this sample implying a floodplain environment that is sparsely vegetated or the more delicate plant macrofossils could not survive in this harsh depositional environment.

Many of the beetle fossils in this sample, as in FBRP-01 are thin and pitted. Pill beetles (Family Byrrhidae) including *Morychus* sp. were AMS ^{14}C dated, providing an age of 10315 ± 25 ^{14}C yr BP (UCIAMS-117268). Byrrhid pill beetles usually occur in sandy settings, such as shorelines, where they may be found under debris (Triplehorn and Johnson, 2005). The pill

beetle *Morychus* can usually be found under stones and mosses in sandy areas near shorelines (Johnson, 1986).

7.3.2.2.1.3 FBRP-03, 82-110 cm

This sample is identical to FBRP-02 in terms of fossil content. Reworked coal, iron-stained, sand-cemented peds and modern rhizomes occur in this sample along with pill beetle, *Morychus* sp. Plant macrofossils are absent.

7.3.2.2.1.4 FBRP-04, 110-122 cm

Beetle fossils in this sample are rare with miscellaneous fragments of sternites and leg fragments (femur and tibia) being recovered. Other insect fossils are minimally represented (e.g. one head capsule of larva midge; Family Chironomidae). Crustaceans of the water flea (*Daphnia sp*) ephippia, oribatid mites (*Hydrozetes* sp.) and discoidal horizontal snails (Gastropoda) are equally present in low numbers. *Daphnia* are often found in open water where they feed on planktonic algae and diatoms (Korhola and Rautio, 2001). Species of the mite *Hydrozetes* occur in freshwater lakes, ponds, bog pools and in very wet fens where they are found often in great densities (Solhøy, 2001).

Plant macrofossils in FBRP-04 are not abundant but are significant compared to the other overbank samples examined. Macrofossil needle fragments of lodgepole pine (*Pinus contorta*) (Fig. 7.14f) and charred and not charred spruce (*Picea* sp.) needle fragments are present in this sample. Lodgepole pines are medium-sized trees that grow up to 30 m high and 60 cm in diameter and live to 200 years of age. They can be found on a wide range of soils and sites, including wet depressions. Due to their abundant seed supply in closed cones, lodgepole pine is able to colonize recently burned areas and most stands are of fire origin (Farrar, 1995). Spruce usually grows on well-drained sites with most species being shade-tolerant. Birch (*Betula sp.*) also occurs in this sample. The preservation of the one nutlet is very poor but it likely represents water birch as seen in FBRP-01. Thus pine, spruce and birch were growing in the vicinity of Flatbed Peat Site at the time FBRP-04 was deposited.

Although low in number, aquatic algae remains (oogonia) of stonewort (*Chara* sp.) along with mosses occur in this sample.

7.3.2.2.1.5 FBRP-05, 122-128 cm

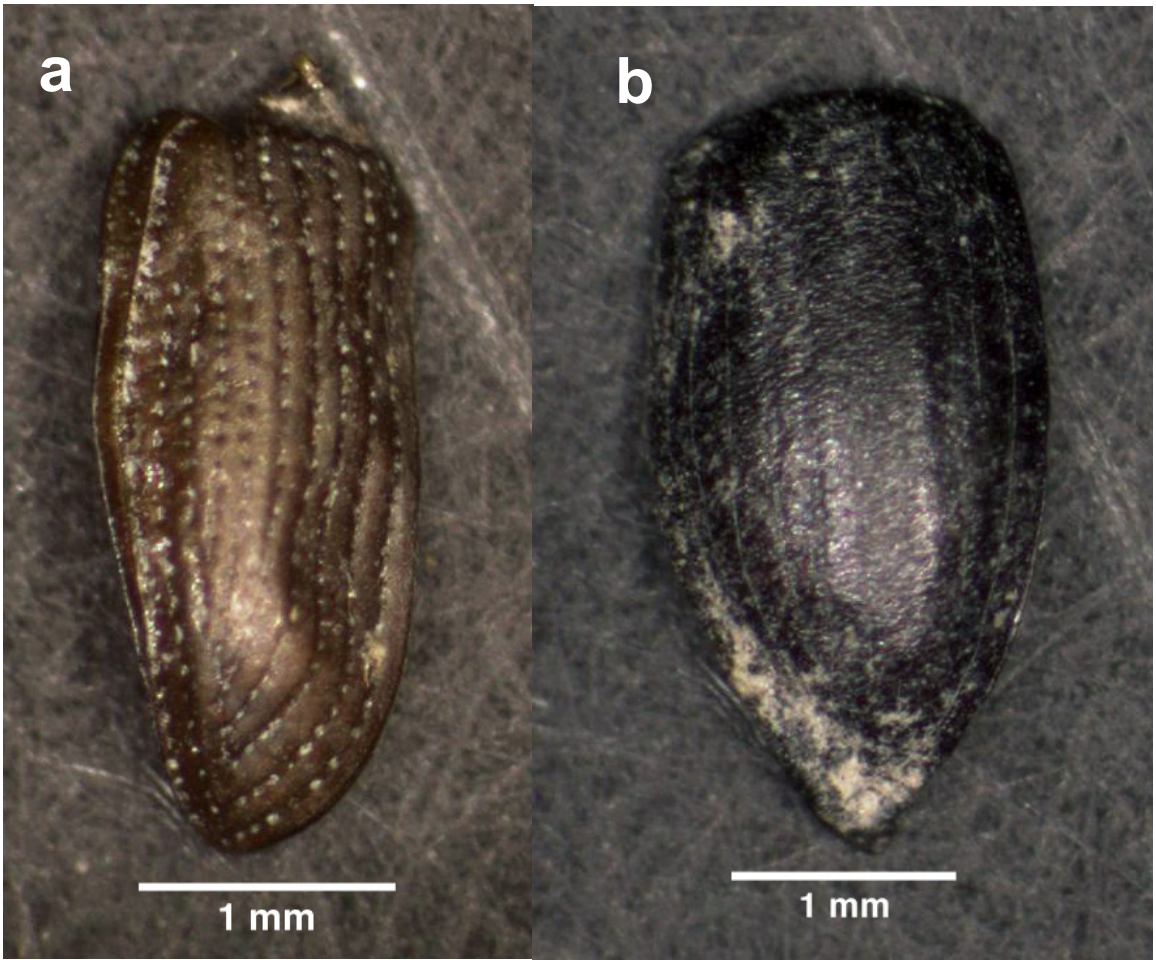

Figure 7.15. a) Fossil elytron from an *Aegialia* Sp. beetle (FBRP-05); b) fossil elytron of *Cytilus alternatus* fro sample FBRP-06. This elytron is one of three that were dated along with other beetle parts including *Morychus* elytron, *Lepidophorus lineaticolis* pronota, that yielded an age of 10 000 ± 35 ^{14}C yrs BP (11 490 ± 206 cal yrs BP).

FBRP-05 sample contains very few macrofossils. Rare beetle fossils include rove beetles (Family Staphylinidae), scarab beetle *Aegialia* sp. (Family Scarabaeidae) and weevils (Family Curculionidae). Species of *Aegialia* are primarily psammophiles, living on stream deposited sand bars, wind deposited sand dunes, or in other very sandy substrates (Gordon and Cartwright, 1988; Fig. 7.15a). Weevils in general feed on host-specific plants or shrubs. A couple of oribatid mites of *Hydrozetes* also occur in this sample.

Vascular plant macrofossils are absent in FBRP-05. Only algae remains (*Chara* sp. oogonia) of stoneworts are present in small numbers. This sample contains reworked Cretaceous coal along with many sand-cemented peds with iron staining (rust-coloured precipitate) and modern rhizomes. Some small degraded wood or twig fragments occur in FBRP-05.

7.3.2.2.1.6 FBRP-06, 128-128.5 cm; 10 000 ± 35 yr BP (11 490 ± 206 cal yrs BP)

The sands in this sample are at the contact between the underlying overbank deposit and compressed organics containing both sand and organic material (Fig. 7.12d). Beetle parts including *Cytilus alternatus* (half head, 3 elytra, Fig. 7.15b), *Morychus* sp. (elytron-1), *Lepidophorus lineaticolis* (pronotum-1, head-1) and miscellaneous sternites and legs weighing 1.61 mg were dated yielding ^{14}C age of 10000 ± 35 yr BP (UCIAMS-117269). The pill beetle *Cytilus alternatus*, although it lives in the vicinity of water, is often collected in sandy sites among the cover of mosses and grasses. They are obligate moss feeders. Fossils of another pill beetle, *Morychus* sp. and the weevil *Lepidophorus lineaticollis* indicate prevalence of dry local conditions. *Morychus* live in sandy places along river banks and are often found in the sparsely vegetated areas of large floodplains. *Lepidophorus lineaticollis* lives among willows and alders along sandy shorelines of rivers, at dry sites within forests and dry tundra conditions (Anderson, 1997). This sample contains a fossil head of a leafhopper (Family Cicadellidae) not seen in other samples examined. They feed on grasses suggesting some grasses are present in the environment even if no delicate macrofossils of grasses were isolated. Crustaceans of the water flea (*Daphnia* sp.) ephippia, and oribatid mites (*Hydrozetes* sp.) are present in this sample. *Daphnia* are often found in open water where they feed on planktonic algae and diatoms (Korhola and Rautio, 2001). Species of the mite *Hydrozetes* occur in freshwater lakes, ponds, bog pools, and in very wet fens where they are found often in great densities (Solhøy, 2001).

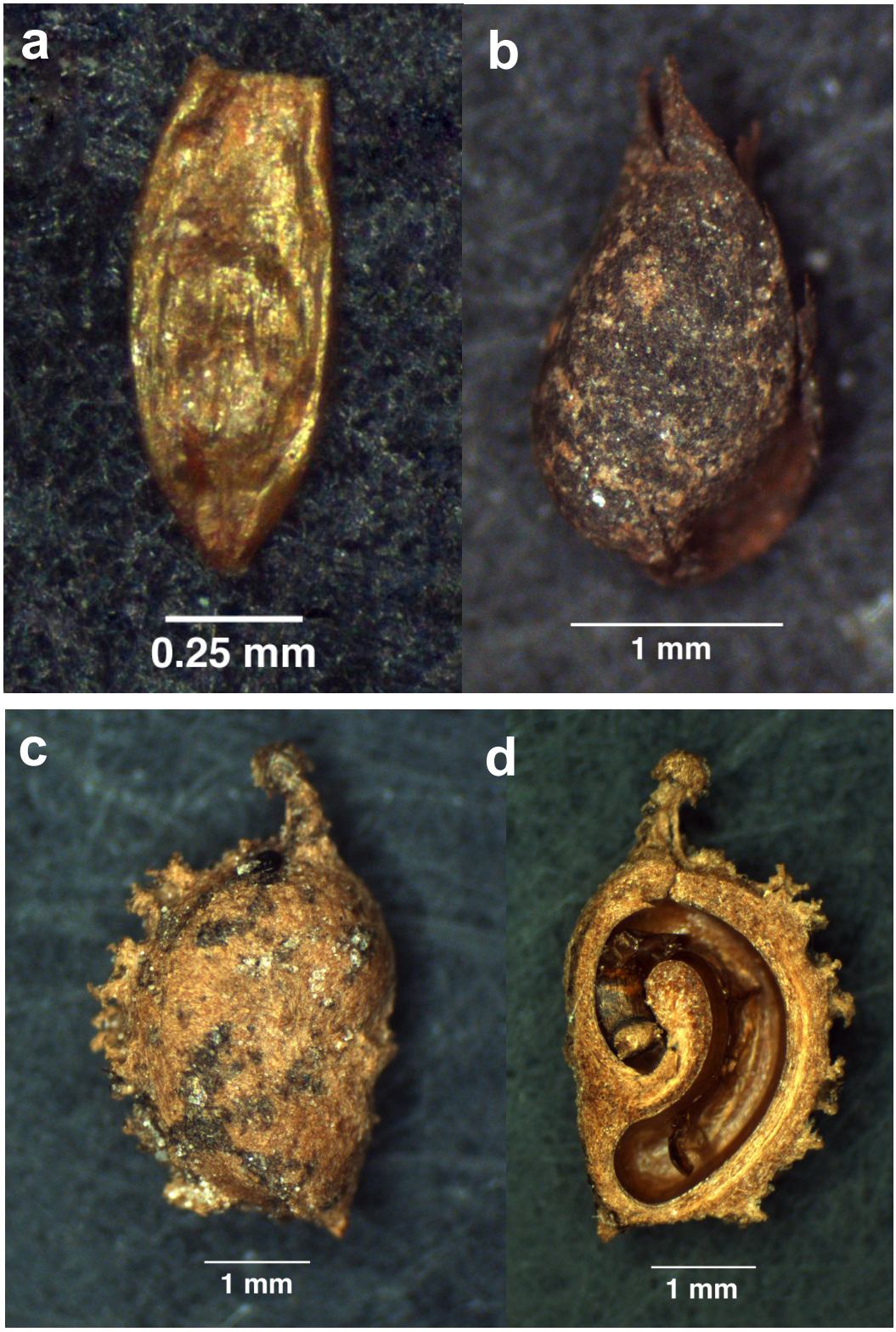

Figure 7.16. a) fossil achene of *Typha latifolia* (Cattails) from sample FBRP-06.; b) fossil fruit of *Ruppia cirrhosa* (ditch grass) from FBRP-06; c) macrofossil achene of flatstem pondweed from FBRP-07; d)cross-section of same achene.

Plant macrofossils in this sample are poorly preserved and in many cases the outer seed coat has been lost with only embryos (inner contents of seeds) being observed. Embryos of pondweed (*Potamogeton* sp.) and both seeds and embryos of the sedge family, *Eleocharis palustris-uniglumis* type occur in this sample along with cattail, *Typha latifolia* (Fig. 7.16a) and ditch-grass, *Ruppia cirrhosa* (Fig. 7.16b). Species of *Potamogeton* usually grow completely submerged and attached to the bottom of ponds at depths of up to 3 m. Ditch-grass, another submergent aquatic plant inhabits shallow alkaline waters (Porsild and Cody, 1980). Both cattail and *E. palustris-uniglumis* type are emergent and live in shallow water along margins of water bodies with cattail being an aquatic or marsh herb found in swampy ground and shallow water (Scoggan, 1978). Quite a few oogonia of stoneworts (*Chara* sp.) occur in this sample. Their numbers are under-represented since many oogonia were seen embedded in peat peds (Fig. 7.3). Stoneworts usually grow in shallow water and in general prefer waters of moderate to high alkalinity (Wood and Imahori, 1965).

The combined plant macrofossil and animal fossils suggest dry local conditions with a shallow aquatic environment of a pond or temporary pool that is alkaline.

7.3.2.2.2 Compressed Organics

7.3.2.2.2.1 FBRP-07, 128.5-128.7 cm; 9815 ± 20 yrs BP (11 226 ± 21 cal yrs BP)

This small volume (~10 ml) sample contains similar plant macrofossils as seen in FBRP-06 with animal macrofossils portraying a shallow aquatic environment. Invertebrate bryozoans (moss animals) of both *Cristatella mucedo* and *Plumatella* sp. occur in this sample. Species of the freshwater *Plumatella* and *C. mucedo* occur primarily in still or slow-flowing waters feeding on protozoans, bacteria and organic matter. Absent from this sample are fossil beetles. Instead aquatic insects such as larvae midge (Chironomidae) head capsules are common with minor occurrences of adult crane flies (*Tipula* sp.). Larvae of midges can be found in almost any aquatic or semiaquatic habitat. Most crane flies are associated with moist environments, the adults usually being found in low, leafy vegetation along streams or around ponds in wooded areas (Wiggins, 1984). Many cladoceran crustaceans (water fleas) occur in this sample. Species of *Daphnia* and *Simocephalus* are often found in open water where they feed on planktonic algae and diatoms. It should be noted that this sample, as well as other compressed organic samples examined contain peat peds that could not be broken down. As such, small fossils are under-

represented in terms of numbers. They include bryozoans, larvae midge head capsules and cladoceran ephippia.

Plant macrofossils in this sample include algal stoneworts (*Chara* sp.), flatstemmed pondweed (*Potamogeton compressus*) (Figs. 7.16c and 7.16d), and water nymph (*Najas flexilis*). The submergent flatstem pondweed is found in shallow ponds, lakes and slow-moving waters, 1 to 2.5 m deep (Brayshaw, 1985). Water nymph is a completely submersed annual plant found in clear, lowland freshwater bodies such as ponds, lakes, and slow-moving streams to depths of four meters. It can grow in water rich in lime and can tolerate brackish water.

A bulk AMS date from this sample yielded a ^{14}C age 9815 ± 20 (UCIAMS-46468).

7.3.2.2.2.2 FBRP-08, 128.7-128.9 cm

This small point sample (vol. ~18 ml) is similar to FBRP-07 in that it contains mostly aquatic macrofossils. Aquatic animal macrofossils in this sample include insect larvae midge head capsules and many cladoceran ephippia. Their numbers are underrepresented since many were observed in peat peds that could not be broken down (Fig. 7.3). Sample FBRP-07 (128.5-128.7 cm), FBRP-08, (128.7-128.9 cm), FBRP-09 (129-130 cm), and FBRP-12, (136 cm) contain the highest number of *Daphnia* ephippia (174, 299, 584 and 499 respectively; Appendix C). Note the sample volumes processed vary for these samples (10 ml, 18 ml, 110 ml, and 50 ml respectively). Most *Daphnia* are cyclical parthenogens in that natural populations are composed of females who clonally reproduce until conditions within the pond deteriorate (e.g. overcrowding, declining water levels, lack of food or oxygen depletion). It is under stressful environmental conditions when males are produced along with haploid eggs which the males fertilize giving rise to resting eggs (ephippia). In ponds that dry completely, ephippia can lie dormant, even in freezing temperatures until conditions become favorable. They have been known to survive in dormancy for more than twenty years in sediment (Korhola and Rautio, 2001). The large numbers of Daphnia ephippia in these samples indicate that something in the environment has changed. For FBRP-08, the deposit is comprised of compressed organic/mineral (sand) suggesting sands have been flushed into the pond (i.e. a disturbed environment).

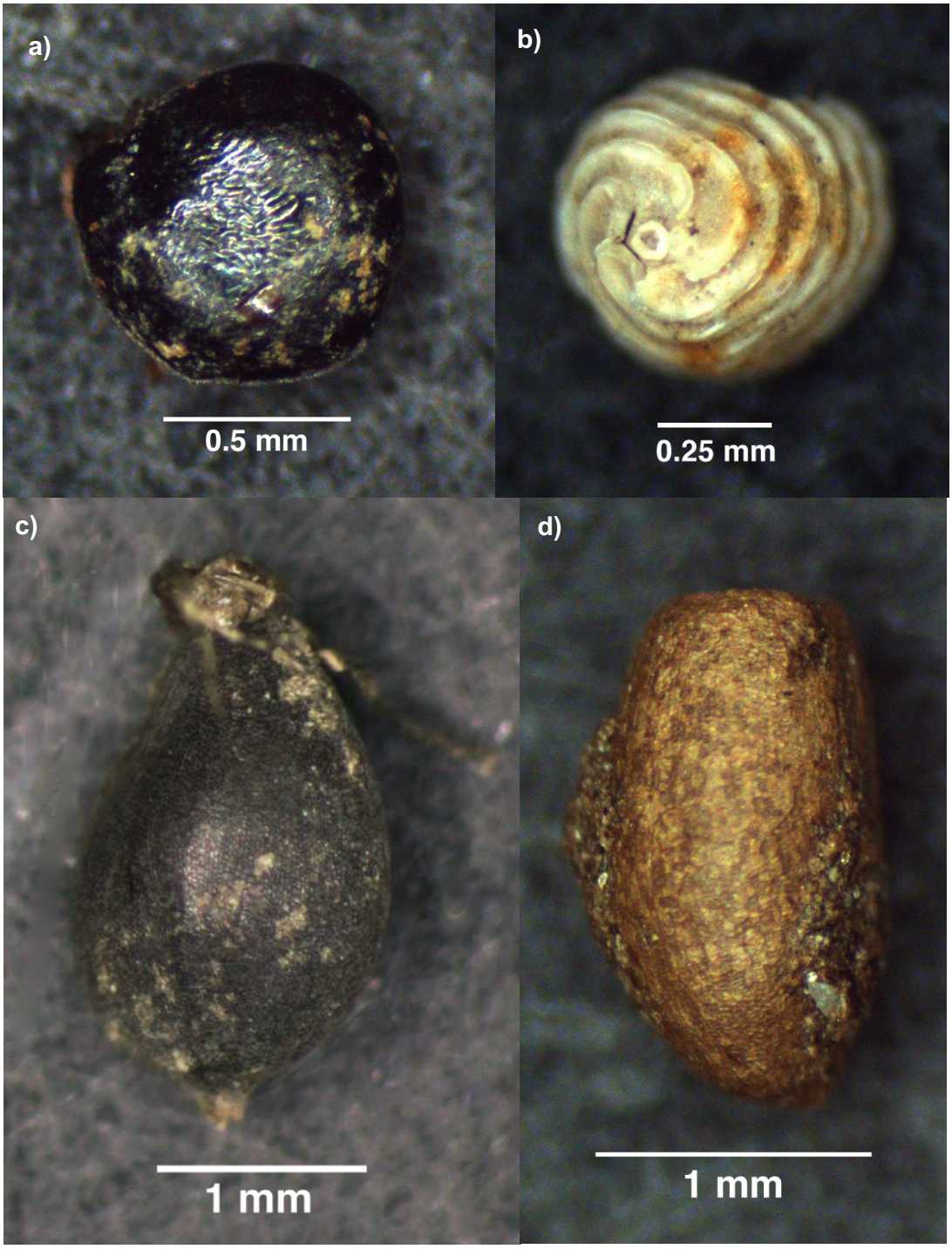

Figure 7.17. a) fossil seed likely of strawberry-blite (Chenopodium catpitatum?) from FBRP-08. Chenopodium seeds are abundant in this sample and not seen in other samples examined; b) Chara oogonium with calcium carbonate coating (FBRP-08); c) fossil achene of Schoenoplectus tabernaemontani (FBRP-09). Four achenes weighing 3.37 mg were dated yielding an age of 9770 ± 25 ^{14}C yr BP (11 207 ± 28 cal yrs BP); d) fossil fruit of mare's-tail (Hippuris vulgaris) from sample FBRP-09.

This sample also contains the water scavenger beetle, *Cercyon* sp. which occurs in decomposing organic matter, often in wet to very wet habitats near water and is almost semiaquatic (Smetana, 1978).

Plant macrofossils in this sample are dominated by aquatic plants including submergents and emergents. Submergent plants include two species of pondweed (*Potamogeton* sp.) and water nymph (*Najas flexilis*). Emergent aquatic plant of softstem bulrush, *Schoenoplectus tabernaemontani* is bordering the shoreline of the pond. It can be found in marshes, lakeshores and streams in the lowland, steppe and montane zones throughout British Columbia. *Carex* (trigonous type) occur in this sample. The grass-like sedges are common, widespread plants that can be found in a variety of habitats including shallow water margins, meadows, grassy/moist slopes, turfy places etc. Although a species determination could not be made on the goosefoot seeds in this sample it is likely strawberry-blite, *Chenopodium capitatum?* (Fig. 7.17a). This annual herb grows in mesic to dry disturbed areas and is common throughout British Columbia. This annual herb can grow to be 20 to 100 cm tall and is found at low to medium elevation throughout British Columbia (Mackinnon et al., 1999). It is weedy in habitat and often colonizes clearings and disturbed sites. It is often associated with burned-over areas (Porsild and Cody, 1980).

Algae remains of stonewort *Chara* sp. peak in abundance in this sample (769 oogonia) with many of the oogonia not counted but observed in peat peds that could not be broken down (Fig. 7.3b). Charophytes are rapid colonizers of new or temporary water bodies. This advanced form of algae is often mistaken for higher vascular plants. Dense growths, attached but not rooted, may cover the entire bottom of pond or lake (Fig. 7.17b). *Chara* algae usually grow in shallow water but where water is clear, are found at depths of 6 meters or more (Wood and Imahori, 1965). They are able to grow at deeper levels than many of the vascular plants. Species of *Chara* prefer waters of moderate to high alkalinity. It often collects a coating of lime, and exudes the smell of hydrogen sulfide. Its affinity for lime has resulted in the name of stonewort.

In summary, the paleoenvironment locally is a shallow aquatic pond dominated by stoneworts that are rapid colonizers of new or temporary water bodies. There are a few submergent and emergent aquatic plants however stoneworts dominate. The environment is disturbed as evidenced by the high number of *Daphnia* ephippia and the occurrence of

Chenopodium capitatum?, a herb that colonizes clearings and disturbed sites. This plant grows in mesic to dry disturbed areas.

7.3.2.2.2.3. FBRP-09, 129-130 cm; 9770 ± 25 yr BP (11 207 ± 28 cal yrs BP)

All the animal macrofossils in this sample are aquatic inhabitants. They include freshwater sponges (*Spongilla* type), bryozoans *Cristatella mucedo*, cladoceran *Daphnia* and oribatid mites of *Hydrozetes* sp. Sponges generally require relatively clean-water habitats in order to maintain the filtering of their water processing system (Frost, 2001). *Cristatella mucedo* live in lakes, ponds, and slow streams being found on most substrates in standing or lightly streaming water. *Daphnia* ephippia are abundant in this sample. They are often found in open water where they feed on planktonic algae and diatoms (Korhola and Rautio, 2001). Insect fossils include the head capsules of midges (Chironomidae) and predaceous diving beetle *Acilius semisulcatus*. This aquatic beetle occurs in standing water in forested regions. Western and northern boreal populations are found in permanent ponds and are common in beaver ponds and small fishless lakes (Larson et al., 2000).

Stoneworts that dominated the pond in FBRP-08 have been taken over by aquatic vascular plants in FBRP-09. Emergent aquatic plants living near the shoreline include cattail (*Typha latifolia*), northern bur-reed (*Sparganium hyperboreum* type), softstem bulrush, (*Schoenoplectus tabernaemontani*) (Fig. 7.17c), and mare's-tail Hippuris vulgaris (Fig. 7.17d). Submersed aquatic plants include pondweeds (*Potamogeton richardsonii*) (Figs. 7.18a-c) and water nymph (*Najas flexilis*). Richard's pondweed, *P. richardsonii* is found in shallow to deep clear lake waters, 0.5 to 3.5 m deep, often where slightly alkaline, or in slow moving rivers (Brayshaw, 1985). One persistent bud of willow (*Salix* sp.) occurs in this sample (Fig. 7.18d).

Macrofossils achenes of softstem bulrush, (*Schoenoplectus tabernaemontani*) (Fig. 7.17c) have been AMS dated from this interval yielding a ^{14}C age of 9770 ± 25 yr BP (UCIAMS-117270).

In summary, the evidence from plant and animal macrofossils indicates the pond was a standing water body with clear-water, slightly alkaline in a forested region. Although evidence of trees is absent except for willow, the predaceous diving beetle, *Acilius semisulcatus* suggests the region was forested.

7.3.2.2.2.4. FBRP-10, 130-132 cm

Figure 7.18. a, b, and c) fossil achene from Richard's pondweed (Potamogeton richardsonii) from FBRP-09; d) fossil of willow (Salix sp.) persistent bud from FBRP-09; e) a well preserved fossil achene enclosed in perigynium (outer seed coat) of Richard's pondweed, Potamogeton richardsonii (FBRP-10); f) fossil achene of Ceratophyllum demersum (FBRP-10).

The plant and animal macrofossil assemblage in this sample is identical to those found in FBRP-09 with a few new elements. Beetle fossils include the aquatic predaceous diving beetles *Acilius* sp. and *Colymbetes* sp. and long-horned leaf beetle, *Donacia* sp. Species of adult *Donacia* typically feed on the emergent leaves and flowers of a wide variety of aquatic emergent plant species. Richard's pondweed occurs in this sample (Fig. 7.18e) with the common hornwort, *Ceratophyllum demersum* (Fig. 7.18f). *C. demersum* grows entirely submersed without anchored roots (free-floating) in still or very slow-moving water (often in hard water lakes, ponds, and quiet streams) with stems reaching 1-3 m in length. The aquatic emergent buckbean, *Menyanthes trifoliata* is common throughout British Columbia where it is found in bogs, fens, marshes, shallow ponds and lakesides in the lowland, steppe and montane zones. One notable difference in this sample is the abundance of Bryophytes (mosses) compared to samples examined in the lower Flat Bed Peat site. This sample also contains many aquatic plant stems and leaves (Fig. 7.19a-b).

The combined plant and animal macrofossil evidence indicates the pond, during deposition of sample FRBP-10, is the same as FBRP-09. It is a still standing body of water, slightly alkaline in a forested region.

7.3.2.2.2.5. FBRP-11, 132-134 cm

Floral and faunal elements in this sample continue to be the same as in FBRP-09 and FBRP-10 samples. Aquatic insect fossils dominate the faunal assemblage. They include predaceous diving beetles, *Hydroporus* sp., *Colymbetes* sp. (Fig. 7.20a) and *Acilius* sp. along with the long-horned leaf beetle of Family Donaciinae. Although a species identification on *Acilius* could not be made based on the small elytron fragment isolated in this sample, it likely belongs to *A. semisulcatus*. Larvae head capsules of midges (Chironomidae) occur as well as cladoceran (*Daphnia* sp.) ephippia. Well-preserved moss animals statoblasts of *Cristatella mucedo* are also present (Fig. 7.20b-c). *C. mucedo* live in lakes, ponds, and slow streams being found on most substrates in standing or lightly streaming water. They are least adapted to siltation or high turbidity because of their gelatinous colony structure (Bushnell, 1973).

Plant macrofossils in FBRP-11 comprise both emergent and submergent aquatic plants. There are abundant aquatic herb plant stems and leaves (40% by volume) with some leaves of Richard's pondweed (*P. richrdsonii*) (Fig. 7.21a-b). Only two achenes of pondweed exist in this

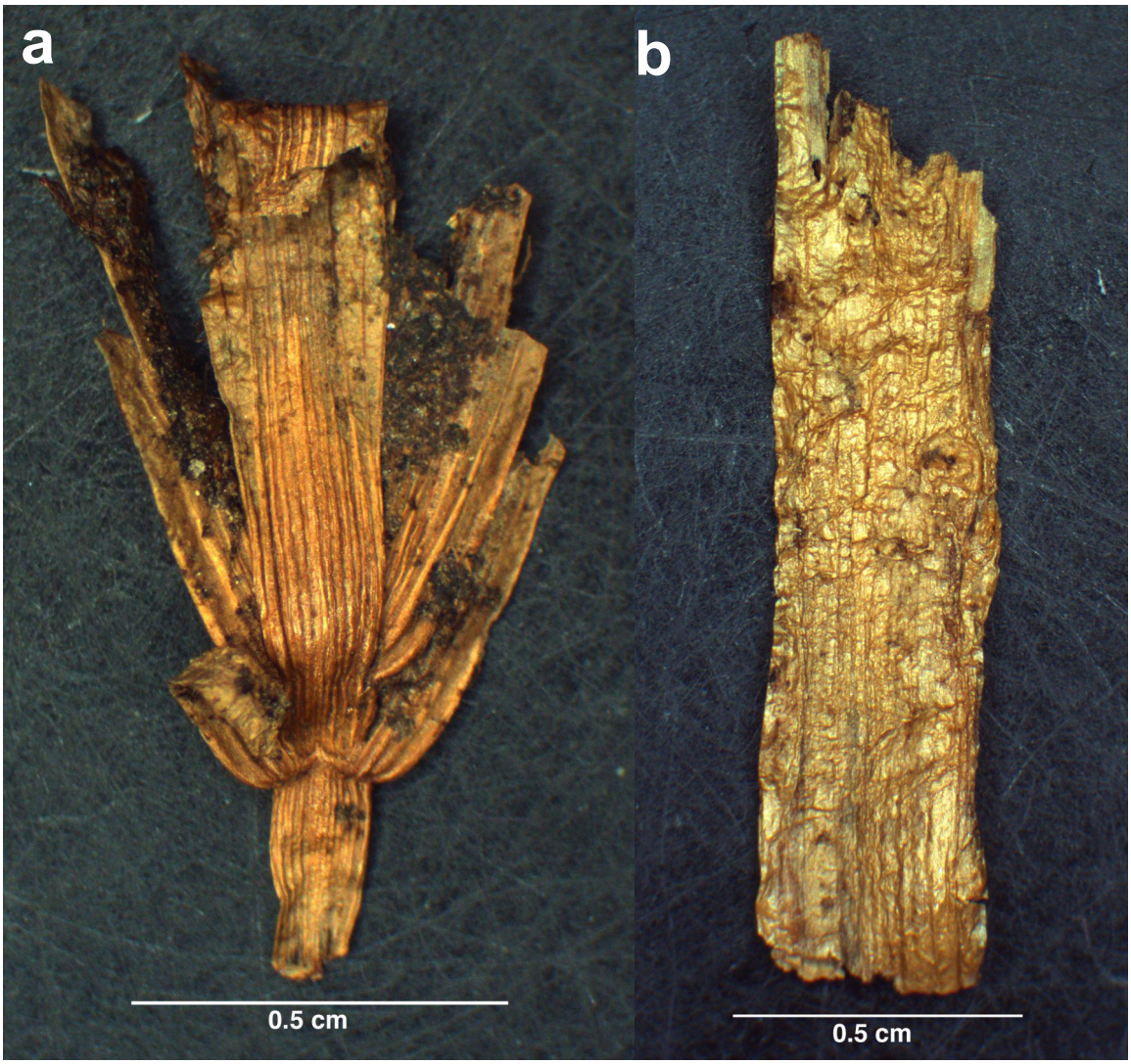

Figure 7.19. Aquatic plant fragments from FBRP-10.

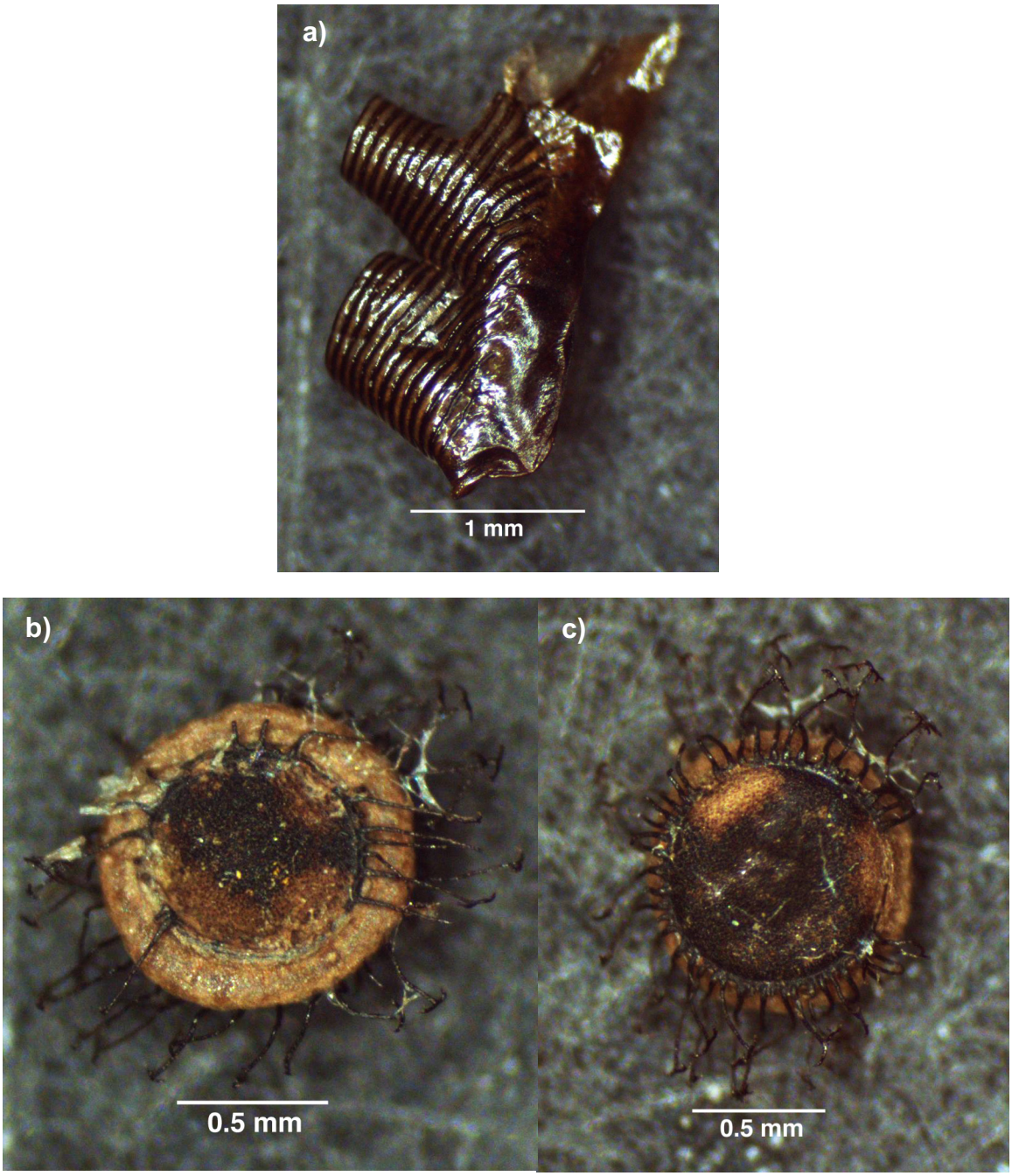

Figure 7.20. Fossil fauna from FBRP-11; a) fossil elytron fragment of a predaceous diving beetle (*Colymbetes* sp.); b and c) fossil statoblast of *Cristella mucedo*.

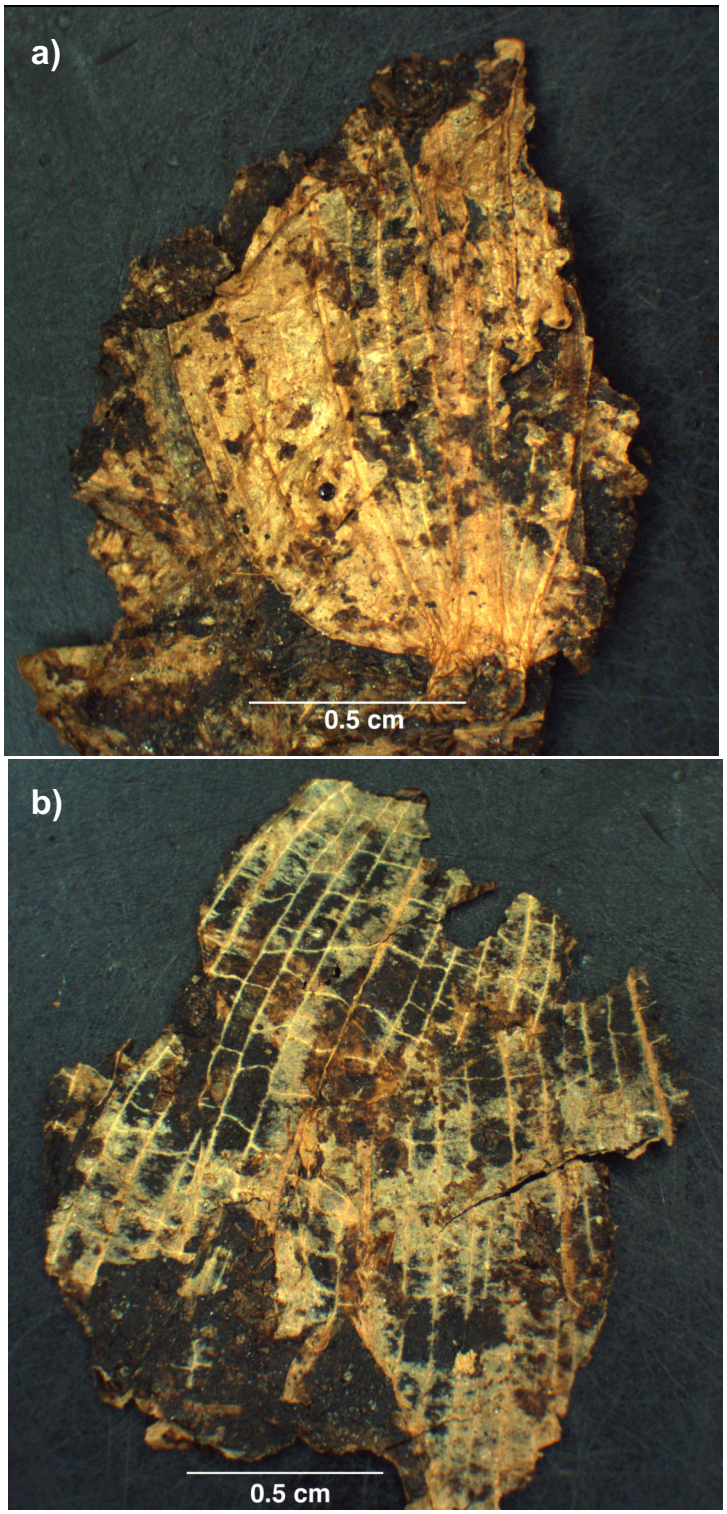

Figure 7.21. Aquatic plants from FBRP-11; a) pondweed (*Potamogeton richardsonii*) leaf from felted peat layers; b) pondweed, *Potamogeton richardsonii?* From embedded leaf in felted peat layers.

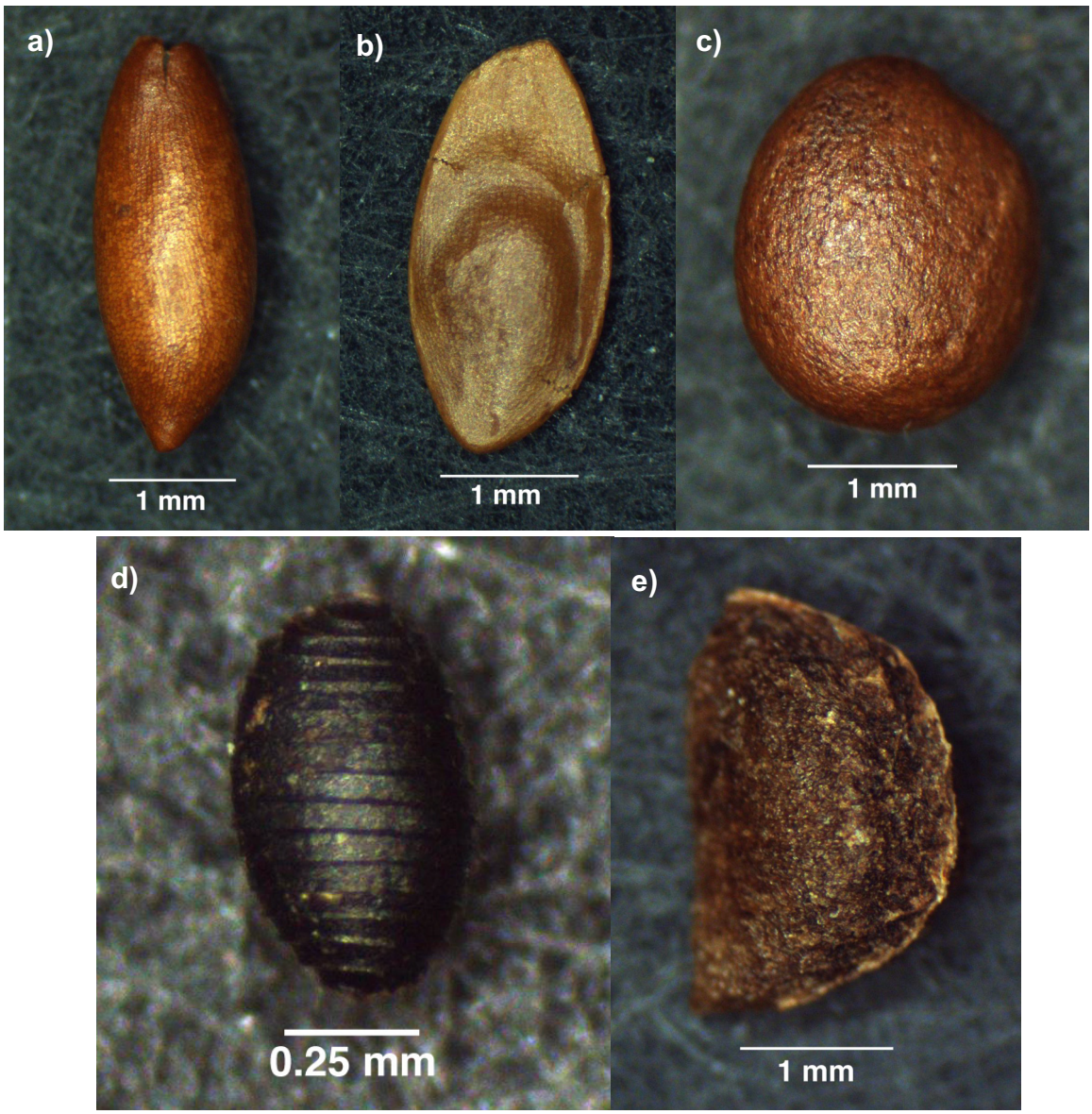

Figure 7.22. Plant macrofossils from FBRP-11; a) fossil seed of water nymph (*Najas flexilis)*; b) flattened fossil seed of *Najas flexilis*; c) fossil seed of buckbean (*Menyanthes trifoliate*); d) freshwater algae stonewort (*Chara* sp.) oogonium; e) fossil seed of bearberry, *Arctostaphylos uva-ursi*.

sample and water nymphs (*Najas flexilis*) are more abundant (36 seeds) (Figs. 7.22a-b). Water nymph is a completely submersed annual plant found in clear, lowland freshwater bodies such as ponds, lakes, and slow-moving streams to depths of four meters. It can grow in lime-rich water and can tolerate brackish water. Emergents include cattails (*Typha latifolia*) and buckbeen (*Menyanthes trifoliata*) (Fig. 7.22c). Algae remains of stonewort, *Chara* sp. oogonia (Fig. 7.22d) occur in this sample but are lower in number (n=59) compared to FBRP-08 which had the highest number (n=769). Species of *Chara* prefer shallow waters of moderate to high alkalinity.

Evidence of shrubs or trees is rare with persistent buds of willow (*Salix* sp. ,n=7) and a single seed of common bearberry/kinnikinnick (*Arctostaphylos uva-ursi*, Fig. 7.22e). Bearberry is a prostrate, many branched shrub that grows on sandy and well-drained exposed sites, dry rocky slopes, dry forest and clearings. It is common and widespread, from low elevations to alpine tundra throughout interior and northern British Columbia (MacKinnon et al., 1999). Mosses are abundant in this sample (20% by volume) as seen in FBRP-10 and continue to increase in volume in overlying samples.

7.3.2.2.2.6. FBRP-12, 136 cm; 8845 ± 20 yr BP (9964 ± 187 cal yrs BP)

Animal macrofossils in this sample portray the same environment as seen in FBRP-11 of a shallow pond. There are freshwater sponges (*Spongilla* type), some moss animals of *Cristatella mucedo* and *Plumatella* sp., many midge (Chironomidae) head capsules (n=220) and some oribatid mites of *Hydrozetes* sp. Aquatic beetles include predaceous diving beetles, *Colymbetes* sp. and *Acilius semisulcatus* (Fig. 7.23a). This aquatic beetle occurs in standing water in forested regions. Western and northern boreal populations are found in permanent ponds and are common in beaver ponds and small fishless lakes (Larson et al., 2000).

Plant macrofossils of aquatic plants have declined in FBRP-12, especially submergent aquatics with only one achene of pondweed (*Potamogeton* sp.) observed. Instead, some emergents exist (bulrush, *Scirpus* sp.) and mosses (Bryophytes) proliferate. Macrofossil remains of trees and shrubs are present including charred and not charred needle fragments of spruce (*Picea* sp.) (Fig. 7.14d). Shrub remains include willow (*Salix* sp.) and common snowberry, (*Symphoricarpos albus*; Fig. 7.23b). Snowberry is an erect, branching shrub (0.5-1.5 m tall) that grows in open forest, thickets, or dry rocky slopes. It is most abundant in dry habitats but also can be found on moist sites, especially well-drained floodplains (MacKinnon et al., 1999). Five

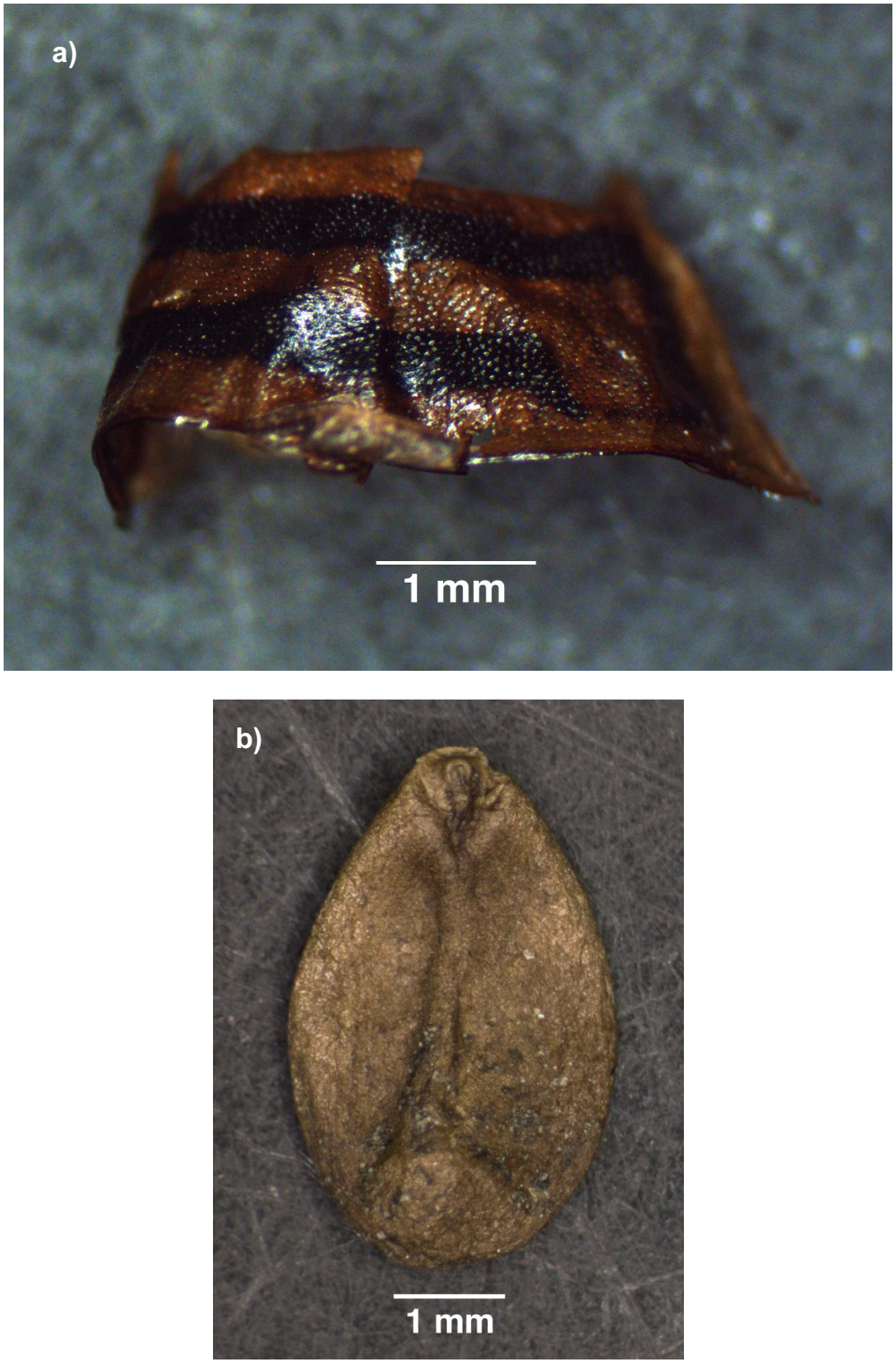

Figure 7.23. a) fossil pronotum of *Acilius semisulcatus* from FBRP-12; b) fossil seed of snowberry (*Symphoricarpos albus*) from FBRP-12. Five seeds weighing 6.47 mg were dated yielding an age of 8845 ± 20 ^{14}C yr BP (UCIAMS-117271).

seeds of *S. albus* weighing 6.47 mg were dated by yielding an age of 8845 ± 20 ^{14}C yr BP (UCIAMS-117271).

In summary, the macrofossil evidence suggests the pond is a much shallower depression during deposition of sample FRBP-12 and the site is poorly drained allowing mosses to become more dominate. Spruce is growing locally suggesting an open forested area at Flatbed Peat site.

7.3.2.2.3 Compacted Dense Peat

The following samples are from autochthonous moss peat deposits which typically have low recovery of plant and insect macrofossils. Their occurrence in these samples, however, indicates the plants and insects were growing or living locally.

7.3.2.2.3.1. FBRP-13, 145 cm

Felted layers of compacted mosses in this sample (Fig. 7.24) were difficult to break down. As such, there were many small moss peds that had to be teased apart using two forceps. By volume, mosses dominate (99%) the floral assemblage. Modern roots permeate the felted moss 'sheets'. Vascular plant remains are absent and elytral fragments of predaceous diving beetles (*Colymbetes* sp.) are the only animal macrofossil in this sample.

Based on the scant macrofossils in this sample, the paleoenvironment was a poorly drained, wet depression dominated by mosses.

7.3.2.2.3.2. FBRP-14, 150-152 cm; 8770 ± 25 yr BP (9789 ± 115 cal yrs BP)

Similar to FBRP-13, felted layers of compacted moss are abundant (99% by volume). Some aquatic animal macrofossils are present along with the predaceous diving beetle, *Acilius* sp. Seeds of water lily, *Nuphar* sp., are unique to this sample, possibly referred to yellow pond lily, *Nuphar polysepala*. It is an aquatic submergent with leaves mostly floating, occasionally immersed or submersed. It prefers slow, shallow water but is also common in ponds, lakes, and sluggish streams. Conifer remains of seeds and charred and not charred spruce (*Picea* sp.) needles are fairly abundant along with charcoal. Birch (*Betula* sp. nutlet) of medium shrub/small tree also occurs in this sample.

Charred and not charred spruce needle fragments from FBRP-14 (Fig. 12c) were dated yielding an age of 8770 ± 25 *14*C yr BP (UCIAMS-117272).

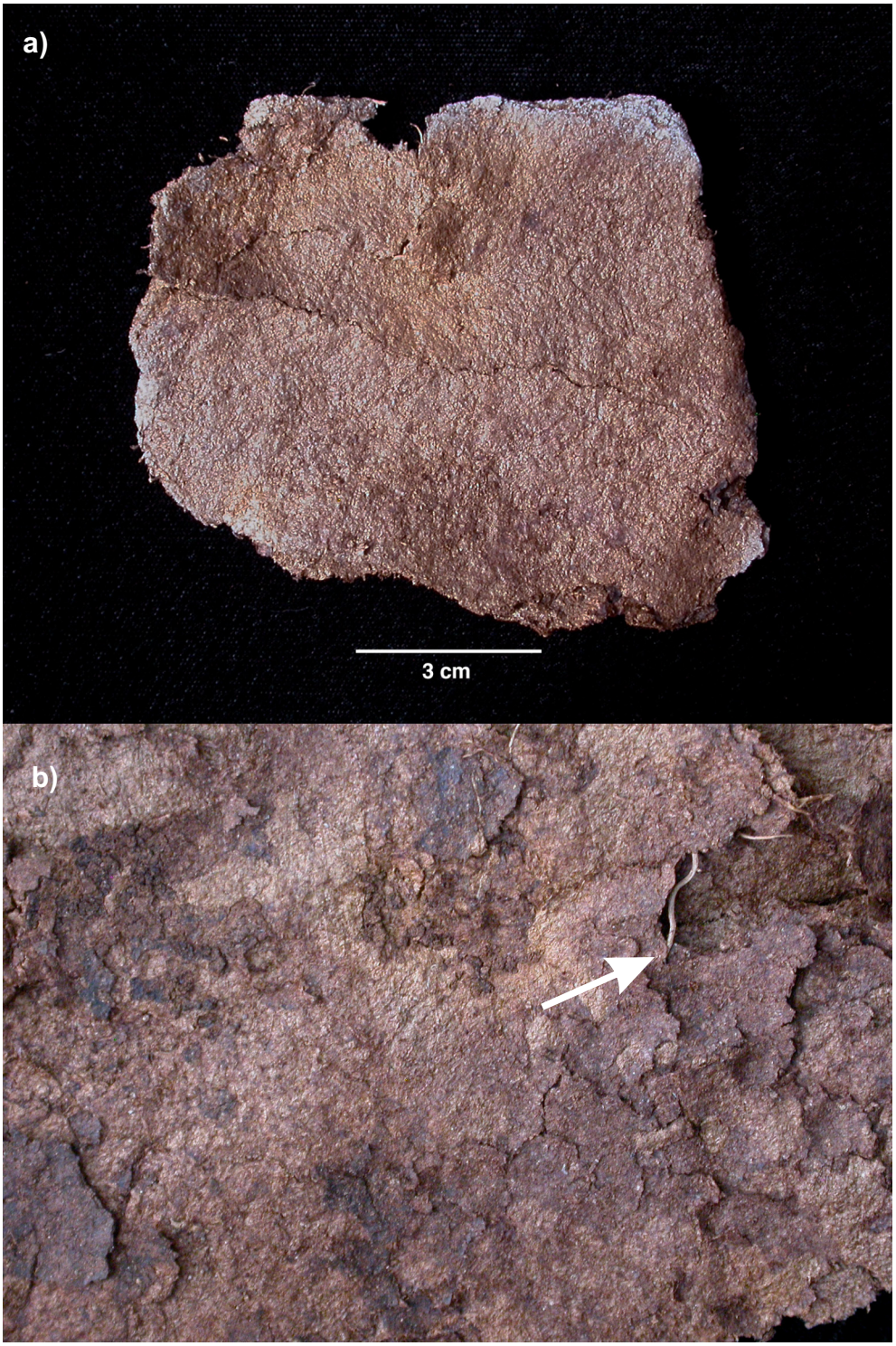

Figure 7.24. Moss from FBRP-13; a) felted, thin sheet, of compacted mosses; b) close-up of the moss sheet with modern root contamination (arrows).

In summary, macrofossil evidence such as the presence of water lily and some aquatic insects suggests the environment is a shallow water body (wet depression) of a poorly drained site abundant in mosses. Spruce are growing locally (open forest) with evidence of a fire occurring near the site.

7.3.2.2.3.3. FBRP-15, 155-156 cm

Mosses continue to dominate the floral assemblage (99% by volume). The felted, compact moss expanded three-fold upon addition of water for processing. Predaceous diving beetles that were present in many of the previous samples are absent. Beetle fossil remains include an elytron of marsh beetle, *Cyphon* sp. Species of *Cyphon* are always found near water, generally occurring on vegetation in damp sites. Plant macrofossils include spruce trees (*Picea* sp.) and birches (*Betula* sp.) of the medium shrub/small tree type and arboreal birch. The emergent buckbean (*Menayanthes trifoliata*) occurs in this sample. Buckbean, is common throughout British Columbia being found in bogs, fens, marshes, shallow ponds and lakesides in the lowland, steppe and montane zones.

7.4 Discussion

The dune forms and luminescence stabilization ages complement the flora and fauna radiocarbon ages. The inferred biome succession and ages provide temporal constraints on the transition from cool arid conditions to woodland and boreal ecosystems. The following discussion examines the climatic implications of: 1) dune forms and their ages; 2) macrofossil assemblages and their ages; and 3) integration of the two data sets.

Stabilized Late Wisconsinan/Early Holocene relict sand dunes are relatively common in northwestern Canada (David, 1977; Muhs and Wolfe, 1999, Wolfe et al., 2007). Several studies have identified or described Late Wisconsinan sand dunes in northeastern British Columbia and northwestern Alberta (Odynsky, 1958; Henderson 1959; David, 1977; Halsey et al., 1990; Halsey and Catto, 1994; Wolfe et al., 2004; Paulen and Plouffe, 2007; Trommelen and Smith, 2007; Wolfe et al., 2007; Smith, 2009; Munyikwa et al., 2011). In most cases the dunes occur in discrete fields (David, 1977; Wolfe et al, 2004; e.g. Grande Prairie), are associated with glaciofluvial terraces or sandy glaciolacustrine plains, and have classic parabolic, composite parabolic forms (e.g. twinned), or transverse forms. The dunes preserved in the Kiskatinaw

Dune Field are mainly parabolic forms. Parabolic dunes are associated with unidirectional wind, limited sediment supply and the presence of vegetation that exerts a significant bio-morphological control on form. Vegetation impedes dune activity and differential plant growth rates and variation in sand flux across the dune results in uneven (though systematic) dune stabilization (Pye and Tsoar, 1990). Typically, dune edges stabilize first resulting in preserved trailing arm ridges as the head of the dune advances. Unlike most of the dunes documented in northeast British Columbia and northern Alberta, dunes in the Kiskatinaw Dune field are distinct as they: 1) form composite dune waves or chains; or 2) are highly elongated.

The composite dune waves or chains (David, 1977) occur as discrete belts that are separated by several kilometres (Fig. 7.5). They probably reflect periodic exposure of sandy glaciolacustrine deposits that nourish pulses of dune activity. These compound landforms probably initiated as individual, (likely barchan) dunes close to primary (i.e. sandy glaciolacustrine deposits) or secondary (i.e. sand accumulations from the gully in Fig. 7.6c) sediment supply, but as the dunes develop and migrate individual dunes coalesced and formed chains (McKee, 1979). Barchyn and Hugenholtz (2012c) have shown in modelled simulations that as dunes collide stabilization time decreases. This may explain, in part, the preservation of the compound forms. The resulting complexes likely advanced down wind through blowouts (i.e. common parabolic dune propagation; Pye and Tsoar, 1990; Bailey and Bristow, 2004) and by shedding barchanoid forms that later stabilized to vegetated parabolic forms (Wolfe and Hugenholtz, 2009).

Most of the dunes in Area D are highly elongate parabolic dunes or dune ridges (relict dune arms). The forms are similar to the so called “Cree Lake” type dune ridges of David (1977). In the Cree Lake region David (1977) recognizes highly elongate individual parabolic dunes but also identifies composite parabolic dunes developed from a common arm with an “in succession” arrangement similar to the ridges in Area D (Fig. 7.9d). He also notes that the Cree Lake dunes formed from a very limited sediment supply on a hard, non-deflatable bedrock surface. This is likely a similar case in the Kiskatinaw Field where primary sediment is supplied from a small area in the West Kiskatinaw River Valley where silt- and clay-rich till (cohesive sediment) forms the substrate and would behave as a surface of limited erodiblity, contributing little to the dunes in the way of sediment supply (Kok et al., 2012).

The barchan origin of the parabolic dunes is evident from some dune forms that have stabilized in a transitional state (e.g. 7.9b). The transformation from barchan to parabolic dunes is a well documented and modelled phenomenon (e.g. Tsoar and Blumberg, 2002; Durán and Herrmann, 2006; Wolfe and Hugenholtz, 2009; Reitz et al., 2010; Barchyn and Hugenholtz, 2012c) and occurs when the colonizing vegetation impedes dune activity. The forms that dominate will depend on effective sediment transport and vegetation growth rates. Under mobile conditions, (i.e. high sediment transport accompanied by low vegetation growth rates) barchan and transverse dunes are predicted. Conversely, parabolic dunes are more likely to develop under stabilizing conditions such as humid, calm circumstances (Lancaster 1988; Barchyn and Hugenholtz, 2012c). Therefore, if a paraglacial setting transitions to a warmer, wetter climate, it would be expected that mobile conditions would shift to a stabilizing scenario as vegetation becomes more prolific (Wolfe and Hugenholtz, 2009). It is speculated that the highly elongated dunes represent a terminal parabolic form (Fig. 1e of Durán and Herrmann, 2006). If the transformation of the barchan dune to a parabolic dune is allowed to progress to completion without being stabilized in a transitional state, a highly elongated parabolic form would likely be the terminal shape. This may be why many of these dunes have amorphous aprons at the head of the dune rather than a dune head ridge. This would imply that vegetation colonization was sufficient to stabilize the arm of the dunes as they advanced, but dune geometry at the propagating head was such that the dune could continue to advance.

The luminescence ages imply that the dunes stabilized between ca. 12-10 ka. The weighted mean (Ludwig, 2012) stabilizing age for the Kiskatinaw field is 11.1 ± 0.9 ka (n= 5; 8.7 ± 0.5 ka from KDF-4 is probably a younger reactivation event and is not included), younger than the weighted mean stabilization age of 12.8 ± 0.6 ka (n=33) (i.e. samples from <2m) for dunes in Alberta and elsewhere in northeast British Columba (Table 7.7; Fig. 7.25a). The data suggests that the Kiskatinaw field stabilized later than other fields that developed between the Laurentide and Cordilleran ice sheets. The Cordilleran ice sheet likely persisted in the region after the Laurentide Ice sheet retreated into Alberta (Mathews, 1980). Cold katabatic winds from the Cordilleran Ice Sheet (likely present in the mountains and foothills) may have delayed local climatic amelioration, thereby delaying sustained stabilization of the Kiskatinaw Dunes. This is consistent with the interpretation Dyke et al. (2004) for biome successions in this area.

Table 7.7. ***Optical ages from sand dunes in Alberta and British Columbia.***

Location	Latitude	Longitude	Easting	Northing	Zone	Depth	Mineral	OSL Age (ka)	Reference
Lac la Biche	54° 58' 23"	112° 06' 35"	428087	6036723	12	0.8	K-Feldspar	12.6 ± 0.6	Wolfe et al., 2004
Hondo	55° 05' 18"	114° 02' 58"	688299	6108599	11	1.0	K-Feldspar	14.2 ± 0.7	Wolfe et al., 2004
Decrene	55° 06' 47"	114° 09' 12"	681559	6111073	11	1.0	K-Feldspar	14.8 ± 0.9	Wolfe et al., 2004
Chisholm	54° 50' 50"	114° 10' 36"	681265	6081444	11	1.0	K-Feldspar	15.3 ± 0.8	Wolfe et al., 2004
Nelson Lake	54° 29' 07"	114° 17' 07"	675851	6040908	11	1.0	K-Feldspar	14.5 ± 0.9	Wolfe et al., 2004
Holmes Crossing	54° 17' 55"	114° 51' 23"	639495	6018866	11	1.0	K-Feldspar	14.9 ± 1.0	Wolfe et al., 2004
Fort Assiniboine	54° 25' 33"	114° 29' 15"	662991	6033809	11	2.5	K-Feldspar	14.5 ± 1.0	Wolfe et al., 2004
Edson	53° 29' 31"	116° 37' 30"	524879	5927063	11	1.5	K-Feldspar	14.0 ± 0.8	Wolfe et al., 2004
Bear River	55° 05' 20"	118° 48' 09"	384958	6106167	11	1.0	K-Feldspar	13.7 ± 1.0	Wolfe et al., 2004
	55° 05' 16"	118° 48' 35"	384494	6106055	11	5.0	K-Feldspar	13.5 ± 1.0	Wolfe et al., 2004
Stony Plain	53° 24' 09"	113° 45' 04"	317114	5920573	12	1.0	K-Feldspar	12.0 ± 0.6	Wolfe et al., 2004
	53° 23' 25"	113° 40' 53"	321697	5919037	12	1.0	K-Feldspar	13.4 ± 0.8	Wolfe et al., 2004
	53° 26' 48"	113° 48' 20"	313689	5925626	12	1.2	K-Feldspar	6.2 ± 0.6	Wolfe et al., 2004
Battle River	52° 34' 47"	113° 37' 02"	322673	5828737	12	1.0	K-Feldspar	12.8 ± 0.6	Wolfe et al., 2004
	52° 34' 47"	113° 37' 02"	322673	5828737	12	4.0	K-Feldspar	11.3 ± 0.5	Wolfe et al., 2004
Rocky Mountain House	52° 22' 17"	115° 00' 30"	635588	5804213	11	1.1	K-Feldspar	<11.6 ± 0.8	Wolfe et al., 2004
	52° 22' 17"	115° 00' 30"	635588	5804213	11	6.0	K-Feldspar	12.4 ± 0.8	Wolfe et al., 2004
Lodgepole	53° 06' 54"	115° 14' 39"	617516	5886504	11	3.0	K-Feldspar	14.1 ± 1.8	Wolfe et al., 2004
Windfall	54° 11' 56"	116° 08' 00"	556538	6005997	11	1.7	K-Feldspar	15.7 ± 1.6	Wolfe et al., 2004
Economy Creek	55° 03' 54"	118° 12' 50"	422477	6102698	11	1.3	K-Feldspar	11.8 ± 0.7	Wolfe et al., 2004
Grovedale	55° 02' 57"	118° 44' 37"	388606	6101652	11	1.3	K-Feldspar	14.9 ± 1.0	Wolfe et al., 2004
Pipestone	55° 03' 16"	119° 13' 16"	358123	6103105	11	1.1	K-Feldspar	14.2 ± 0.9	Wolfe et al., 2004
Watino	55° 43' 24"	117° 32' 12"	466291	6175419	11	1.2	K-Feldspar	12.9 ± 0.8	Wolfe et al., 2004
Redwater	53° 56' 24"	112° 57' 05"	371911	5978610	12	1.2	K-Feldspar	11.7 ± 0.6	Wolfe et al., 2004
Beaverhill Creek	53° 51' 50"	112° 54' 05"	374966	5970054	12	1.0	K-Feldspar	12.5 ± 0.7	Wolfe et al., 2004
Sandy Lake	54° 58' 23"	114° 33' 54"	655852	6094506	11	1.5	K-Feldspar	10.5 ± 0.5	Wolfe et al., 2004
High Level	58° 25' 21"	116° 45' 39"	513970	6475775	11	1.1	K-Feldspar	13.4 ± 1.2	Wolfe et al., 2007
	58° 24' 01"	116° 17' 31"	541384	6473494	11	1.1	K-Feldspar	11.7 ± 1.0	Wolfe et al., 2007
	58° 15' 15"	116° 50' 38"	509162	6457019	11	1.1	K-Feldspar	10.3 ± 0.9	Wolfe et al., 2007
	58° 07' 02"	117° 10' 37"	489575	6441775	11	1.3	K-Feldspar	11.0 ± 1.0	Wolfe et al., 2007
Fontas River	58° 13' 49"	120° 55' 50"	621525	6456214	10	1.1	K-Feldspar	12.7 ± 1.0	Wolfe et al., 2007
	58° 13' 52"	120° 56' 16"	621098	6456294	10	1.1	K-Feldspar	11.7 ± 1.0	Wolfe et al., 2007
	58° 16' 07"	121° 06' 03"	611407	6460187	10	1.1	K-Feldspar	13.9 ± 1.2	Wolfe et al., 2007
Hondo	55° 06' 21"	114° 00' 05"	691273	6110688	11	2.5	K-Feldspar	15.4 ± 1.1	Munyikwa et al., 2011
	55° 06' 21"	114° 00' 05"	691273	6110688	11	0.5	K-Feldspar	14.9 ± 1.1	Munyikwa et al., 2011
	55° 06' 41"	114° 00' 22"	690946	6111309	11	2.4	K-Feldspar	13.2 ± 1.2	Munyikwa et al., 2011
	55° 08' 45"	114° 01' 12"	689901	6115104	11	10.0	K-Feldspar	18.2 ± 1.2	Munyikwa et al., 2011
	55° 08' 45"	114° 01' 12"	689901	6115104	11	7.6	K-Feldspar	20.3 ± 1.8	Munyikwa et al., 2011
	55° 08' 45"	114° 01' 12"	689901	6115104	11	2.5	K-Feldspar	13.3 ± 1.2	Munyikwa et al., 2011
Holmes Crossing	54° 17' 28"	114° 52' 14"	638582	6018018	11	2.6	K-Feldspar	18.3 ± 1.2	Munyikwa et al., 2011
	54° 17' 28"	114° 52' 14"	638582	6018018	11	1.0	K-Feldspar	13.5 ± 1.0	Munyikwa et al., 2011
	54° 12' 07"	114° 52' 13"	638905	6008098	11	2.8	K-Feldspar	15.3 ± 1.3	Munyikwa et al., 2011
Fort Assiniboine	54° 22' 10"	114° 38' 21"	653354	6027206	11	3.0	K-Feldspar	14.6 ± 1.7	Munyikwa et al., 2011
	54° 22' 46"	114° 38' 06"	653593	6028342	11	3.0	K-Feldspar	15.0 ± 1.3	Munyikwa et al., 2011
	54° 22' 46"	114° 38' 06"	653593	6028342	11	1.0	K-Feldspar	13.1 ± 0.9	Munyikwa et al., 2011
Lac La Biche	54° 59' 25"	114° 09' 12"	682110	6097445	11	2.0	K-Feldspar	14.7 ± 1.6	Munyikwa et al., 2011

Datum: NAD 83

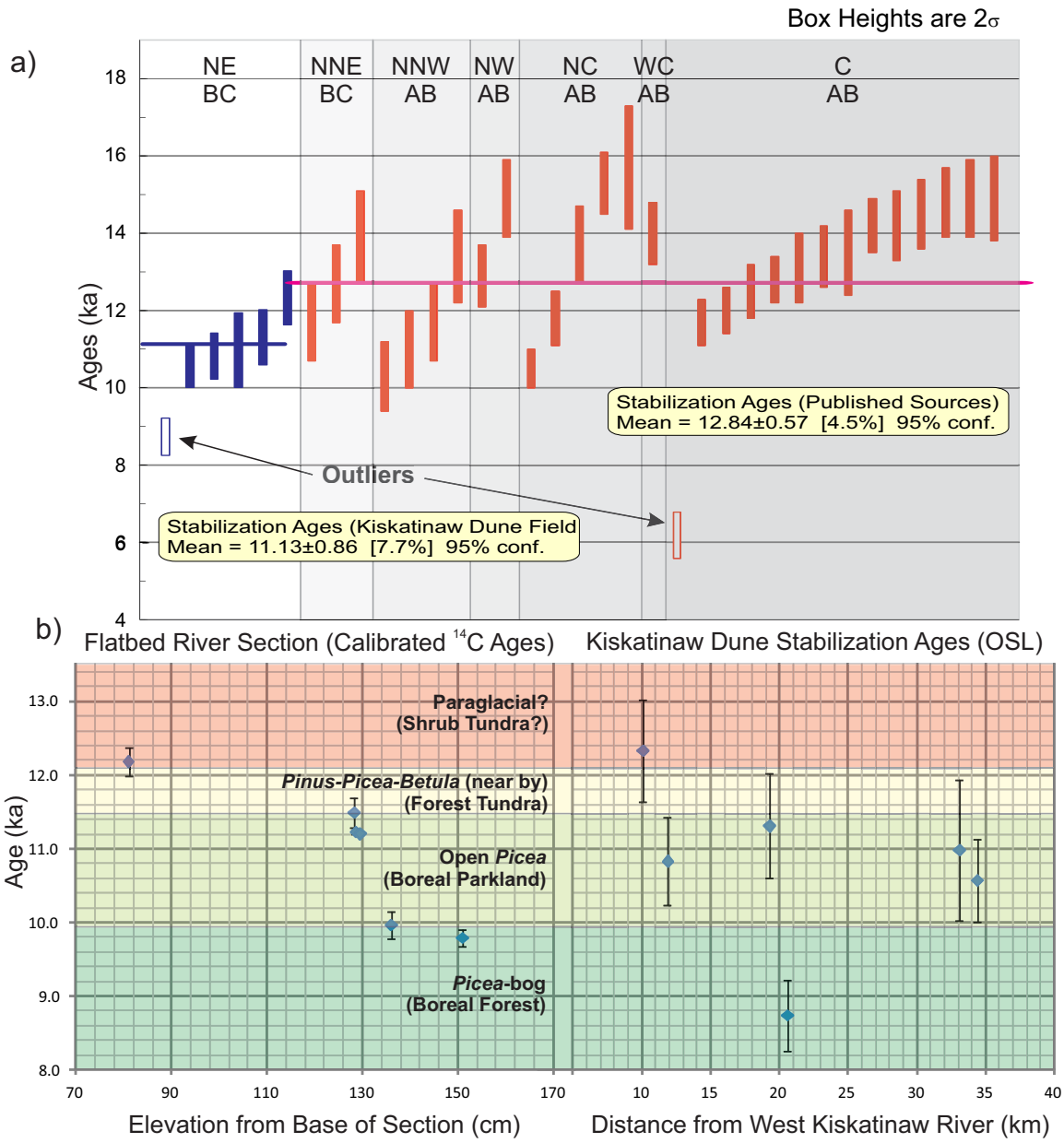

Figure 7.25. a) Comparison of dune stabilization ages from the Kiskatinaw Dune Field (blue) and other published ages (red; from Wolfe et al. 2004; Wolfe et al., 2007 and Munyikwa et al., 2011; all K-Feldspar ages). Stabilization ages are considered to be from those samples collected from a depth of < 2m (arbitrary) below surface (NE BC = Northeast British Columbia; NNE BC = Northern Northeast British Columbia; NNW AB = Northern Northwest Alberta; NW AB = Northwest Alberta; NC AB = North-central Alberta; WC AB = West-central Alberta; C AB = Central Alberta; see Table 7.7); b) Comparison of the radiocarbon ages and the interpreted biome (following Dyke's, 2005 classification) from the Flatbed River Section and the stabilization ages for the Kiskatinaw Dune Field.

They imply that the Alpine Tundra biome persisted in the foothills after Boreal Parkland succeeded tundra in central Alberta (Fig. 7.2).

The Flatbed organic section records the transition from an active floodplain to a permanent pond, and eventually to a spruce bog. During the floodplain stage, Lodgepole pine (*Pinus contorta)* and spruce (*Picea* sp.) were present near but not right on the floodplain (probably representing a nearby woodland setting). A spruce dominated open forest was established locally by 9770 ^{14}C yrs BP (11 207 ± 28 cal yrs BP) where the site supports a mainly aquatic ecosystem. By 8770 ^{14}C yrs BP (9789 ± 115 cal yrs BP) the site became a boreal spruce bog.

The overbank deposits contain mostly beetles typical of sparsely vegetated sandy floodplains. They include byrrhids of *Morychus* and *Cytilus alternatus*, scarab beetle, *Aegialia* and weevil *Lepidophorus lineaticollis*. These beetles indicate prevalence of dry local conditions. There is, however, evidence that the site is periodically flooded and a wet depression or shallow bodies of water (pools, ponds and slow flowing streams) were common. Conical snails along with ostracodes imply a carbonate-rich environment within a low energy water environment. The scant recovery of plant macrofossils suggests vegetation cover was sparse. Algal aquatic remains of stonewort (*Chara* sp.) indicate they were growing in the shallow water bodies. Lodgepole pine (*Pinus contorta)* and spruce (*Picea* sp.) were present around 10,000 BP (11 490 ± 206 cal yrs BP) and were probably living in the region of the Flatbed Peat site but not immediately on the floodplain.

The compressed organic samples represent a shallow, permanent pond with many of the aquatic plants having an affinity for hard water. Aquatic emergent plants growing near the shoreline include cattail (*Typha latifolia*), softstem bulrush (*Schoenoplectus tabernaemontani*) sedges *Eleocharis palustris-uniglumis* type, northern bur-reed (*Sparganium hyperboreum* type), and mare's-tail (*Hippuris vulgaris*). Plants growing submerged in the pond include flatstemmed pondweed (*Potamogeton compressus*) and Richard's pondweed (*Potamogeton richrdsonii*), ditch-grass (*Ruppia cirrhosa*) and water nymph (*Najas flexilis*). Algal remains of stonewort (*Chara* sp.) peak in abundance in FBRP-08. Charophytes are rapid colonizers of new water bodies but their numbers decline as submergents aquatic plants increase in FBRP-09. Aquatic animals typical of what was a freshwater habitat include moss inhabiting animals, *Cristatella mucedo* and *Plumatella* sp., larvae midges (*Chironomidae*), water fleas (*Daphnia*), oribatid mites

(*Hydrozetes* sp.) and snails (Gastropoda). Aquatic insects of predaceous diving beetles and water scavenger beetles dominate the pond. They include *Hydroporus* sp., *Colymbetes* sp., *Acilius semisulcatus* and *Cercyon* sp. Of particular importance is the predaceous diving beetle, *Acilius semisulcatus*. This aquatic beetle occurs in standing water in forested regions with western and northern boreal populations being found in permanent ponds. The presence of this beetle suggests that by FBRP-09 time (9770 ± 25 yr BP or 11 207 ± 28 cal yrs BP), the site was locally an open spruce forest. By FBRP-12 time (8845 ± 20 yr BP or 9964 ± 187 cal yrs BP), the pond was much shallower (possibly a shallow depression) and the site was poorly drained allowing mosses to become more dominant. Over the next 75 ^{14}C yr with peat development, the site was mostly covered by aquatic mosses with some emergents (water lily, *Nuphar* sp. and buckbean, *Menyanthes trifoliata*) growing in a poorly drained site of a wet depression. Spruce (*Picea* sp.) was well established by 8770 ± 25 yr BP (9789 ± 115 cal yrs BP).

White et al. (1985) and White and Mathewes (1986) examined the pollen record in sediment cores from Boone and Spring lakes east of the study area in Alberta (Fig. 7.1). They reported that paraglacial conditions following deglaciation persisted to about 12 000 ^{14}C years BP supporting shrub-herb tundra. From 12 000 to 11 700 ^{14}C year BP, the vegetation consisted of open, sedge-dominated cover with chenopodineae (Goosefoot), grasses and other herbs. Poplar became more wide spread towards the end of this phase and open poplar woodlands dominated from 11 700 to 11 500 ^{14}C yrs BP. Vegetation then began to change rapidly between 11 500 to 11 300 ^{14}C yrs BP. During this phase the region is described as a deciduous grassland-parkland with fir, spruce and possibly pine as minor regional elements. Spruce and pine forests became established by 11 150 ^{14}C years BP marking the transition to boreal conditions.

MacDonald (1987a) examined pollen from lake sediment cores from Lone Fox Lake and Yesterday Lake in Alberta (Fig. 7.1), north of the area studied by White and Mathewes (1986). MacDonald (1987a) identified an *Aremisia-Gramineae-Salix* zone between ~11 000 to 9800 ^{14}C yrs BP that transitioned to more boreal conditions in his *Picea* zone (~ 9800 to 8800 ^{14}C yrs BP). This was followed by a *Picea-Betula* zone (~8000 to 7000 ^{14}C yrs BP) and *Pinus-Picea* (~7000 ^{14}C yrs BP to present). Vertebrate fossils at the Charlie Lake Caves near Fort St John (Driver, 1988) indicate an open woodland forest in the area between ~10 700 to 10 000 ^{14}C yrs BP. Fauna from ~10 000 to 9000 ^{14}C yrs BP indicate evidence of boreal forest and grasslands. The biome succession and timing at the Flatbed River site is consistent with the interpretations of

MacDonald (1987a) and Driver (1988), but occurs slightly later than the Boone and Spring lake sites (White et al., 1985; White and Mathewes, 1986), supporting the notion that the succession to Boreal conditions was delayed along the foothills.

To examine the relationship between dune stabilization and vegetation succession, their ages are compared (Fig. 7.25b). Kiskatinaw Dunes initially stabilized in the Shrub Tundra setting (KDF-2; 12.3 ± 0.7 ka). Four of the six stabilization ages, however, occur between 11.3 ± 0.7 ka and 10.6 ± 0.6 ka (~<1000 year spread), coincident with the Boreal Parkland phase (Fig. 7.25b). In fact, almost all the dunes in Northeastern British Columbia and Alberta stabilized during this period (Fig. 7.25b). The outliers fall within the Boreal phase and represent minor local aeolian activity. As the vegetation transitioned from Shrub Tundra to forests, the dunes stabilized. The transition from Forest Tundra to Boreal Parkland probably marks the major climatic shift away from paraglacial conditions. The bio-geomorphic response (i.e. dune stabilization) is delayed relative to the climate signal by 100-2000 years. Although much of the uncertainty is associated with the precision of the luminescence dating method, undoubtedly some of the delay reflects causal geomorphic response to the proliferation of vegetation (Bullard et al., 1997; Hugenholz and Wolfe, 2005). Nonetheless, at the resolution of luminescence dating, aeolian activity, as a geomorphic agent, declined as Boreal Parkland expanded. The age of dune stabilization is therefore a useful geomorphic indicator of regional biome succession which is interpreted to imply climatic amelioration.

7.5 Conclusion

Preserved aeolian landforms (geomorphic) and macrofossil assemblages (biological) are complimentary proxies for interpreting climate amelioration during late Wisconsinan deglaciation. Aeolian dunes in the Kiskatinaw Dune field likely were initiated in a paraglacial setting, sourced from sediments associated with an early phase of glacial Lake Peace, the ice-marginal lake that occupied the region following initial separation of the Cordilleran and Laurentide ice sheets. The preserved, mainly parabolic sand dunes are vegetation anchored aeolian landforms. They are indicative of plant colonization, adequate enough to bio-morphologically influence aeolian activity and ultimately stabilize the dune field. The stabilization occurred between 12.3 ± 0.7 and 10.6± 0.6 ka years BP. This period is the same interval in which vegetation transitioned from Herb and Shrub tundra to a Boreal Parkland and

eventually Boreal Forest. The macrofossil assemblages at the Flatbed River Section support this assertion and provide temporal control from radiocarbon ages. Paraglacial conditions likely persisted to ca. 12 183 ± 193 cal yrs BP after which a Forest Tundra dominated. Locally, the Flatbed River floodplain transitioned to a pond setting between 11 490 ± 206 and 11 226 ± 21 cal yrs BP. Open Spruce forests were well established by 11 207 ± 28 cal yrs BP suggesting that this ages approximates the shift from Forest Tundra to Boreal Parkland. The site transitioned from pond to bog between 9964 ± 187 and 9789 ± 115 cal yrs BP marking the onset of Boreal Forest conditions at the site.

Optical ages and geomorphology of the Kiskatinaw Sand Dunes and radiocarbon age control on biome succession recorded at the Flatbed River section indicate that the region transitioned from a paraglacial setting to a boreal forest environment, similar to the modern setting, over a time span of ~2 ka (ca. 12 - 10 ka years ago). The shift from tundra to forested conditions (driven by climate change), however, was probably much more rapid taking <600 years (ca. 12 - 11.4 ka years ago) and likely includes a lag between climate change and vegetation adaptation. This period, therefore, represents a time of very rapid climate warming with significant ecological response, useful for examining modern climate change implications.

7.6 References

Aitken, M.J., 1985. Thermoluminescence Dating; Academic Press, London, 359 pp.

Adamiec, G. and Aitken, M.J., 1998. Dose-rate conversion factors update; Ancient TL, 16, 37—49.

Anderson, R.S., 1989. Revision of the subfamily Rhynchaeninae in North America (Coleoptera: Curculionidae); Transactions of the American Entomological Society, 15: 207—312.

Anderson, R.S., 1997. Weevils (Coleoptera: Curculionoidea, excluding Scolytinae and Platypodinae) of the Yukon; In H.V. Danks and J.A. Downes (eds). Insects of the Yukon; 523—556.

Bailey, S.D., and Bristow, C.S., 2004. Migration of parabolic dunes at Aberffraw, Anglesey, north Wales; Geomorphology, 59, 165—174.

Barchyn, T.E. and Hugenholtz, C.H., 2012a. Aeolian dune field geomorphology modulates the stabilization rate imposed by climate; Journal of Geophysical Research, 117, doi:10.1029/2011JF002274.

Barchyn, T.E. and Hugenholtz, C.H., 2012b. A process-based hypothesis for barchans-parabolic transformation and implication for dune activity modelling; Earth Surface Processes and Landforms, 37, 1456—1462.

Barchyn, T.E. and Hugenholtz, C.H., 2012c. Predicting vegetation-stabilized dune field morphology; Geophysical Research Letters, 39, doi: 10.1029/2012GL052905.

Berger, G.W. 1988. Dating Quaternary events by luminescence; In Easterbrook, D.J. (ed). Quaternary sediments; Geological Society of America Special Paper 227, 13—50.

Brayshaw, T.C., 1985. Pondweeds and bur-reeds, and Their Relatives: Aquatic Families of Monocotyledons in British Columbia; Occasional Papers of the British Columbia Provincial Museum. No. 26, 167 pp.

Bronk Ramsey, C., 1994. Analysis of Chronological Information and Radiocarbon Calibration: The Program OxCal; Archaeological Computing Newsletter, 41, 11—16.

Bronk Ramsey, C., 2001. Development of the radiocarbon calibration program OxCal; Radiocarbon, 43, 355—363.

Bull, W.A., 1991. Geomorphic response to climatic change; Oxford University Press, New York, 326 pp.

Bullard, J.E., Thomas, D.S.G., Livingstone, I., and Wiggs, G.F.S., 1997. Dune field activity and interactins with climate variability in the southwest Kalahari Desert; Earth Surface Processes and Landforms, 22, 165—174.

Bushnell, J.H., 1973. The freshwater Ectoprocta: A zoogeographical discussion; In: Larwood, G.P. and Abbott, M.B. (eds.). Living and Fossil Bryozoa: Recent Advances in Research; Academic Press, London, 503—521.

Campbell, J.M., 1983. A Revision of the North American Omaliinae (Coleoptera: Staphylinidae). The genus *Olophrum* Erichson; Canadian Entomologist, 115, 577—622.

David, P.P., 1977. Sand dune occurrences of Canada: A theme and resource inventory study of eolian landforms of Canada; Department of Indian Affairs and Northern Development, National Parks Branch, Contract no. 74-230, 183 pp.

Delorme, L.D., 1990. Freshwater Ostracodes. In B.G. Warner (ed). Methods in Quaternary Ecology, Geoscience Canada Reprint Series 5, Geological Association of Canada, St. John's, Newfoundland, 93—112.

Deng, Y., 2007. New trends in digital terrain analysis: landform definition, representation, and classification; Progress in Physical Geography, 31, 405—419.

Driver, J.C., 1988. Late Pleistocene and Holocene vertebrate and paleoenvironments from Charlie Lake Caves, northeast British Columbia; Canadian Journal of Earth Sciences, 25, 1545—1553.

Durán, O. and Herrmann, H.J., 2006. Vegetation against dune mobility; Physical Review Letters, 97, 1—4, DOI: 10.1103/PhysRevLett.97.188001.

Dyke, A.S., 2005. Late Quaternary vegetation history of northern North America based on pollen, macrofossils, and faunal remains; Géographie Physique et Quaternaire, 59, 211—262.

Dyke, A.S., Giroux, D., and Robertson, L., 2004. Paleovegetation maps of northern North America 18 000 to 1 000 BP; Geological Survey of Canada, Open File 4682.

Farrar, J.L., 1995. Trees in Canada; Fitzhenry and Whiteside Limited and Canadian Forest Service, Natural Resources Canada, 502 pp.

Fladmark, K.R., Driver, J.C., and Alexander, D., 1988. The paleoindian component at Charlie Lake Cave (HbRf 39), British Columbia; American Antiquity, 53, 371—384.

Frost, T.M., 2001. Freshwater Sponges. In: Smol, J.P., H.J.B. Birks and W.M. Last (eds.). Tracking environmental change using lake sediments. Vol. 3: Terrestrial, algal, and siliceous indicators; Kluwer Academic Publishers, Dordrecht, The Netherlands, 67—80.

Galbraith, R.F., 2010. On plotting OSL equivalent doses; Ancient TL, 28, 1—9.

Galbraith, R.F., Roberts, R.G., Laslett, G.M., Yoshida, H., and Olley, J.M., 1999. Optical dating of single and multiple grains of quartz from Jinmium rock shelter, northern Australia. Part I: experimental design and statistical models; Archaeometry, 41, 339—364.

Gordon, R.D. and O. L. Cartwright, 1988. North American representatives of the tribe Aegialiini (Coleoptera: Scarabaeidae: Aphodiinae); Smithsonian Contributions to Zoology, No. 461, 37 pp.

Halsey, L.A. and Catto, N.R., 1994. Geomorphology, sedimentary structures and genesis of dome dunes in western Canada; Géographie Physique et Quaternaire, 48, 97—105.

Halsey, L.A., Catto, N.R., and Rutter, N.W., 1990. Sedimentology and development of parabolic dunes, Grande Prairie dune field, Alberta; Canadian Journal of Earth Sciences, 27, 1762—1772.

Hanson, M.A., Lian, O.B., Clague, J.J., 2012. The sequence and timing of large late Pleistocene floods from glacial Lake Missoula; Quaternary Science Reviews, 31, 67—81.

Henderson, E.P., 1959. Surficial Geology of Sturgeon Lake Map-Area, Alberta; Geological Survey of Canada, Ottawa Memoir 303, 170 pp.

Hugenholtz, C.H., Levin, N., Barchyn, T.E., Baddock, M.C., 2012. Remote sensing and spatial analysis of aeolian sand dunes: review and outlook; Earth-Science Reviews, 111, 319—334.

Huntley, D.J., Groodfrey-Smith, D.I., and Thewalt, M.L.W., 1985. Optical dating of sediment; Nature, 303, 105—107.

IPCC, 2007. Summary for policymakers; In Solomon, S., Qin, D., Manning, M., Chen, Z., and Marquis M., (eds). Climate change 2007: the physical science basis. Contribution of working group I to the fourth assessment report of the intergovernmental panel on climate change; Cambridge University Press. Cambridge, UK, 1–18.

Johnson, P.J., 1986. Taxonomic notes, new records, and a key to the adults of North America Byrrhidae (Coleoptera); Proceedings of the Entomological Society of Washington, 93, 322—332.

Kocurek, G. And Lancaster, N., 1999. Aeolian system sediment state: theory and Mojave Desert Kelso dune field example; Sedimentology, 46, 505—515.

Kok J.F., Parteli E.J.R., Michaels, T.I., and Bou Karam, D. 2012. The physics of wind-blown sand and dust; Reports on Progress in Physics, 75, 106901.

Korhola, A. and M. Rautio, 2001. Cladocera and other Branchipod Crustaceans. In: Smol, J.P., Birks H.J.B., and Last W.M. (eds.). Tracking environmental change using lake sediments. Vol. 4: Zoological indicators; Kluwer Academic Publishers, Dordrecht, The Netherlands, 5-41.

Lancaster, N. 1988. Development of linear dunes in south-western Kalahari, southern Africa; Journal of Arid Environments, 14, 233—244.

Lancaster, N. and Baas, A., 1998. Influence of vegetation cover on sand transport by wind: Field studies at Owens Lake, California; Earth Surface Processes and Landforms, 23, 69—82.

Larson, D.J., Alarie, Y. and R.E. Roughley, 2000. Predaceous Diving Beetles (Coleoptera: Dytiscidae) of the near Arctic region, with emphasis on the fauna of Canada and Alaska; NRC Research Press, Ottawa, Ontario, Canada. 982 pp.

Lian, O.B., Hu, J., Huntley, D.J., Hicock, S.R. 1995. Optical dating of Quaternary organic-rich sediments from southwestern British Columbia and northwestern Washington State; Canadian Journal of Earth Sciences, 32, 1194—1207.

Livingstone, I. and Warren, A., 1996. Aeolian geomorphology: An introduction; Longman Singapore Publishers Ltd., Singapore, 177 pp.

Ludwig, K.R., 2012. User's Manual for Isoplot 3.75: A geochronological toolkit for Excel; Special Publication No. 5, Berkeley Geochronology Centre, 73 pp.

MacDonald, G.M., 1987a. Postglacial development of the subalpine-Boreal transition forest of western Canada; Journal of Ecology, 75, 303—320.

MacDonald, G.M., 1987b. Postglacial vegetation history of the Mackenzie River Basin; Quaternary Research, 28, 245—262.

MacKinnon, A., Pojar, J. and R. Coupé (Eds.), 1999. Plants of Northern British Columbia; Lone Pine Publishing, Vancouver, B.C., 351 pp.

Mason, J.A., Swinehart, J.B., Hanson, P.R., Loope, D.B, Goble, R.J., Miao, X., and Schmeisser, R., 2011. Late Pleistocene dune activity in the central Great Plains, USA; Quaternary Science Reviews, 30, 3858—3870.

Mathews, W.H., 1980. Retreat of the last ice sheet in northeastern British Columbia and adjacent Alberta; Geological Survey of Canada, Bulletin 331, 22 pp.

McKee, E.D., 1979. A study of global sand seas; U.S. Geological Survey Professional Paper, no. 1052, 429 pp.

Miller, B.H. and Tevesz, M.J.S., 2001. Freshwater Molluscs. In Smol, J.P., Birks H.J.B. and Last W.M. (ed). Tracking environmental change using lake sediments. Vol. 4: Zoological indicators; Kluwer Academic Publishers, Dordrecht, The Netherlands, 153-171.

Muhs, D.R. and Wolfe, S.A., 1999. Sand dunes of the northern Great Plains of Canada and the United States; In: Lemmen, D.S. and Vance, R.E. (eds), Holocene climate and environmental change in the Palliser Tiangle: A geoscientific context evaluating the impacts of climate change on the southern Prairies; Geological Survey of Canada, Bulletin 534, 183—197.

Munyikwa, K., Feathers, J.K., Rittenour, T.M., and Shimpton, H.K., 2011. Constraining the Late Wisconsinan retreat of the Laurentide ice sheet from western Canada using luminescence ages from postglacial Aeolian dunes; Quaternary Chronology, 6, 407—422.

Murray, A.S. and Roberts, R.G., 1998. Measurement of the equivalent dose in quartz using a regenerative-dose single aliquot protocol; Radiation Measurements, 29, 503—515.

Murray, A.S. and Wintle, A.G., 2000. Luminescence dating of quartz using an improved single-aliquot regenerative-dose protocol; Radiation Measurements, 32, 57—73.

Murray, A.S. and Wintle, A.G., 2003. The single aliquot regenerative dose protocol: Potential for improvements in reliability; Radiation Measurements, 37, 377—381.

Odynsky, W., 1958. U-shaped dunes and effective wind direction in Alberta; Canadian Journal of Soil Science, 38, 56—62.

Olley, J.M., Murray, A., and Roberts, R.G., 1996. The effects of disequilibria in the uranium and thorium decay chains on burial dose rates in fluvial sediments; Quaternary Science Reviews, 15, 751—760.

Paulen, R.C. and Plouffe, A., 2007. Surficial Geology of the La Crête Area (NTS 84K/SE); Alberta Energy and Utility Board, EUB/AGS Map 412, and Geological Survey of Canada, Open File 5526.

Porsild, A.E. and Cody, W.J., 1980. Vascular Plants of Continental Northwest Territories, Canada; National Museum of Natural Science Publication, National Museums of Canada, 667 pp.

Prescott, J.R. and Hutton, J.T., 1994. Cosmic ray contributions to dose rate for luminescence and ESR dating: Large depth and long-term time variations; Radiation Measurements, 23, 497—500.

Prescott, J.R. and Hutton, J.T., 1995. Environmental dose rate and radioactive disequilibrium from sediment grains: New experimental data; Quaternary Science Reviews, 13, 439—448.

Pye, K. and Tsoar, H., 1990. Aeolian sand and sand dunes; Unwin Hyman, London, 396 pp.

Reimer, P.J., Baillie, M.G.L., Bard, E., Bayliss, A., Beck, J.W., Blackwell, P.G., Bronk Ramsey, C., Buck, C.E., Burr, G.S., Edwards, R.L., Friedrich, M., Grootes, P.M., Guilderson, T.P., Hajdas, I., Heaton, T.J., Hogg, A.G., Hughen, K.A., Kaiser, K.F., Kromer, B., McCormac, F.G., Manning, S.W., Reimer, R.W., Richards, D.A., Southon, J.R., Talamo, S., Turney, C.S.M., van der Plicht, J., and Weyhenmeyer, C.E. (2009). IntCal09 and Marine09 radiocarbon age calibration curves, 0-50,000 years cal BP; Radiocarbon, 51, 1111—1150.

Reitz, M.D., Jerolmack, D.J., Ewing, R.C., Martin, R.L., 2010. Barchan-parabolic dune patter transition from vegetation stability threshold; Geophysical Research Letters, 37, L19402, doi:10.1029/2010GL044957

Roberts, R.G., Galbraith, R.F., Olley, J.M., Yoshida, H., and Laslett, G.M., 1999. Optical dating of single and multiple grains of quartz from Jinmium rock shelter, northern Australia. Part II: results and implications; Archaeometry, 41, 365—395.

Scoggan, H.J., 1978. The flora of Canada. Part 2-Pteridophyta, Gymnospermae, Monocotyledoneae; National Museum of Natural Sciences, Publications in Botany, 7, National Museums of Canada Publisher, 545 pp.

Smetana, A., 1978. Revision of the Subfamily Sphaeridiinae of America north of Mexico (Coleoptera: Hydrophilidae); Memoirs of the Entomological Society of Canada, 105, 292 pp.

Smith, I.R., 2009. Surficial Geology, Kahntah River, British Columbia; Geological Survey of Canada, Open File 5540.

Solhøy, T, 2001. Oribatid Mites. In: Tracking environmental change using lake sediments. Vol. 4: Zoological indicators; in: Smol, J.P., Birks H.J.B., and Last W.M. (eds.), Kluwer Academic Publishers, Dordrecht, The Netherlands, 81-104.

Southon, J., Santos, G.M., Druffel-Rodriguez, K., Druffel, E., Trumbore, S., Xu, X., Griffith, S., Ali, S., and Mazon, M. 2004. The Keck Carbon Cycle AMS Laboratory, University of California, Irvine: two installations, initial operation, and a background surprise; Radiocarbon, 46, 41—49.

Stone, A.E.C. and Thomas, D.S.G., 2013. Casting new light on late Quaternary environmental and palaeohydrological change in the Namib Desert: A review of the application of optically stimulated luminescence in the region; Journal of Arid Environments, 93, 40—58.

Triplehorn, C.A. and Johnson, N.F., 2005. Borror and DeLong's introduction to the study of insects, 7th ed., Brooks Cole Publishers, 864 pp.

Trommelen, M. and Smith, I.R., 2007. Surficial geology, Dazo Creek, British Columbia; Geological Survey of Canada, Open File 5527.

Tsoar, H., and Blumberg, D., 2002. Formation of parabolic dunes from barchans and transverse dunes along Israel's Mediterranean coast; Earth Surface Processes and Landforms, 27, 1147—1161.

Visser, M.E., 2008. Keeping up with warming world; assessing the rate of adaptation to climate change; Proceedings of the Royal Society B, 275, 649—659.

Warner, B.G. (ed), 1990. Methods in Quaternary ecology; Geological Association of Canada, St. John's, Newfoundland, 170 pp.

White, J.M. and Mathewes, R.W., 1982. Holocene vegetation and climate change in the Peace River district, Canada; Canadian Journal of Earth Sciences, 19, 555—570.

White, J.M. and Mathewes, R.W., 1986. Postglcial vegetation and climate change in the upper Peace River district, Alberta; Canadian Journal of Botany, 64, 2305—2318.

White, J.M., Mathewes, R.W., and Mathews, W.H., 1985. Late Pleistocene chronology and environment of the “ice-free corridor” of northwestern Alberta; Quaternary Research, 24, 173—186.

Wiggins, G.B., 1984. Trichoptera. In: Merritt, R.W and Cummins, K.W., Kendall (eds.). An introduction to the aquatic insects of North America, 2nd edition; Hunt Publishing Company, Dubuque, Iowa, 271—347.

Williams, J.W., Shuman, B.N., Webb, T., III, Bartlein, P.J., and Leduc, P., 2004. Late-Quaternary vegetation dynamics in North America: Scaling from taxa to biomes; Ecological Monographs, 74, 309—334.

Wintle, A.G. and Murray, A.S., 2006. A review of quartz optically stimulated luminescence characteristics and their relevance in single-aliquot regeneration dating protocol; Radiation Measurements, 41, 369—391.

Wolfe, S.A. and Hugenholtz, C.H., 2009. Barchan dune stabilized under recent climate warming an the northern Great Plains; Geology, 37, 1039—1042.

Wolfe, S.A., Huntley, D.J., and Ollerhead, J., 2004. Relict Late Wisconsinan dune fields of the northern Great Plains, Canada; Géographie Physique et Quaternaire, 58, 323—336.

Wolfe, S., Bond, J., and Lamothe, M., 2011. Dune stabilization in central Yukon in relation to early Holocene environmental change, northwest North America; Quaternary Science Reviews, 30, 324—334.

Wolfe, S.A., Paulen, R.C., Smith, I.R., and Lamothe, M., 2007. Age and paleoenvironmental significance of Late Wisconsinan dune Fields in the Mount Watt and Fontas River map areas, northern Alberta and British Columbia; Geological Survey of Canada, Current Research, 2007-B4, 10 pp.

Wood, R.D. and K. Imahori, 1965. Monograph of the Characeae, Vol. 1; Cramer, Wertheim, 904 pp.

CHAPTER 8: USING GROUND-PENETRATING RADAR AND CAPACITIVELY COUPLED RESISTIVITY TO INVESTIGATE 3-D FLUVIAL ARCHITECTURE AND GRAIN-SIZE DISTRIBUTION OF A GRAVEL FLOODPLAIN IN NORTHEAST BRITISH COLUMBIA, CANADA

Adrian S. Hickin, Benjamin Kerr, Tom E. Barchyn and Roger C. Paulen

A version of this chapter was published in the Canadian Journal of Sedimentary Research, 2009.

Citation:

Hickin, A.S., Kerr, B., Barchyn. T.E. and Paulen, R.C., 2009. Using ground-penetrating radar and capacitively coupled resistivity to investigate 3-D fluvial architecture and grain-size distribution of a gravel floodplain in northeast British Columbia, Canada; Journal of Sedimentary Research, vol. 79, pages 457—477.

Abstract

This study combines ground-penetrating radar (GPR) and capacitively coupled resistivity (CCR) for geophysical architecture-analysis of a bar platform and channel bend on the floodplain of a poorly organized wandering gravel-bed river. An important objective of fluvial architectural analysis is linking fluvial style with preserved subsurface sedimentology. Most architectural analysis, however, relies on opportunistic outcrops with locations or orientations that may not provide appropriate data. GPR is a well-established geophysical method that images reflections interpreted to represent bed geometry and bounding surfaces and is therefore ideal for imaging fluvial architecture. Unfortunately, grain-size information, which is integral to architectural classification, is more elusive using GPR. Resistivity data can be used as a proxy for sediment grain size. When GPR and CCR are combined they offer an effective tool for geophysical fluvial architectural analysis.

Five trenches provided direct observation of the subsurface sedimentology and are used to calibrate the two geophysical methods. Eight radar facies and one radar element are classified from the GPR survey and grouped into four categories: horizontal and subhorizontal, laterally continuous reflections (Group 1), clinoform reflections (Group 2), discontinuous reflections (Group 3), and concave-up elements (Group 4). The 2-D resistivity data are combined in a GIS to establish a 3-D resistivity model for the upper 5 m of the floodplain. Resistivity values correlate well with grain size and are categorized into fine-grained (< 400 ohm-m), sand-size (400 to 800 ohm-m) and gravel-sized (> 800 ohm-m) sediments. In general, resistivity values indicate coarse sediment in the bar platform and sand to fine-grained material in the main channel and subordinate depressions. Resistivity profiles were extracted from the 3-D model along the GPR lines so that resistivity values could be directly compared to radar facies. The shape and spread of the resistivity distributions provide dominant grain size as well as an indication of sediment sorting for individual radar facies. In some cases, the same radar facies is associated with markedly different grain sizes, indicating different architectural elements (i.e., horizontally bedded gravel verses horizontally bedded sand or fine-grained sediment). This demonstrates the utility of combining GPR and CCR, insomuch as radar architecture alone is not diagnostic of fluvial architectural elements.

In this case study, the bar platform and channel bend have a planform that might suggest a meandering fluvial style. However, GPR-CCR results indicate that the dominant depositional

process across the bar platform was vertical accretion of gravel sheets, an architecture more consistent with a wandering gravel-bed fluvial style. Lateral migration was limited to the outer downstream margin of the platform, a location dominated by a mix of sand and gravel. Coarse gravel likely occupies the base of the main channel, with fine-grained sediment contributing to the remainder of the channel fill. A four-phase history is presented where the initial phase of development involves vertical accretion and migration of stacked gravel-sheets during floods, forming the core of the bar platform. After flooding subsides and the interior bar emerges, the channel becomes established and lateral migration becomes the dominant depositional process. The evolution concludes with avulsion and eventual abandonment of the channel.

8.1 Introduction

This case study combines ground-penetrating radar (GPR) with capacitively coupled resistivity (CCR) to examine the subsurface architectural structure and grain-size distribution of several discrete morphostratigraphic units on a natural floodplain. Brierley (1991) uses the term morphostratigraphic unit to describe floodplain surface features, and differentiates individual units by their 3-D surface geometry in association with their sedimentary characteristics (e.g., bar platforms and channels). Linking fluvial morphostratigaphic units with preserved subsurface sedimentology from vertical profiles has been criticized in the past (Allen 1983; Bridge 1985; Brierley 1989). Miall (1996) addressed this criticism through architectural-element analysis, a method that involves mapping the 2D- and 3-D character of fluvial deposits. Sediment architecture (i.e., bed and bounding-surface geometry) and grain size are integral to Miall's method, in that these characteristics define the classification terminology (e.g., gravel bars and bedforms– GB, sandy bedforms – SB, laminated sand sheet- LS). Any indirect methodology developed for fluvial-architecture analysis needs to address both of these fundamental parameters. The methodology presented in this study utilizes radar for imaging the subsurface architecture and CCR data as a proxy for sediment grain size.

Direct observations of sedimentary architecture and distribution of lithofacies within fluvial deposits is often difficult, relying on opportunistic natural exposures or destructive investigative techniques such as trenching or excavation (e.g., commercial sand and gravel operations). Consequently, there is a deficiency of work linking surface processes to the preserved deposits. The application of high-resolution geophysical surveys has enabled considerable advancement in addressing this deficiency. Mesoscale and macroscale fluvial architecture (Miall, 1996) has been routinely imaged by GPR (e.g., Gawthorpe et al., 1993; Huggenberger, 1993; Stephens, 1994; Beres et al., 1995; Bridge et al., 1995; Bristow, 1995; Olsen and Andreasen, 1995; Leclerc and Hickin, 1997; Roberts et al., 1997; Bridge et al., 1998; Beres et al., 1999; Vandenberghe and van Overmeeren, 1999; Neal, 2004; Wooldridge and Hickin, 2005; Bersezio et al., 2007; Kostic and Aigner, 2007, Mumpy et al., 2007). GPR measures the travel time of electromagnetic waves that reflect off horizons of contrasting dielectric properties (Davis and Annan, 1989) yielding vertical profiles that depict architectural features (Jol and Smith, 1991).

Although GPR investigations have made significant contributions to the understanding of sedimentary architecture, without considerable data processing (Moysey et al., 2006) GPR is unable to effectively resolve sediment grain size. This information is critical in architectural analysis and the development of 3-D facies models (Miall, 1985; Miall, 1996). Ground-based resistivity is a technique that can partially fulfill this role. Resistivity surveys inject current into the ground using two current electrodes. The difference in voltage between two voltage electrodes is subsequently measured, from which the apparent resistivity can be calculated. The effectiveness of a survey is dependent on geological complexity, ground conditions, method (e.g., electrical resistivity, capacitively coupled resistivity, or electromagnetic induction), and electrode configuration. The target depth of investigation can be manipulated by varying the spacing of the transmitter and receiver electrodes. With multiple receiver electrodes set at various distances from the transmitter electrodes, a vertical geometric model (i.e., a pseudosection) of the electrical structure of the subsurface can be produced (Edwards, 1977). The electrical structure of the substrate is closely related to porosity, pore fluids (e.g., content, composition, and temperature), grain size, and mineralogy (Archie, 1942; Best et al., 2005). In general, clay and silt tend to be more conductive (low resistivity) whereas sand and gravel are more resistive (Reynolds, 1987; Reynolds, 1997; Best et al., 2006). Traditional resistivity data are acquired through techniques where electrodes are hammered into the ground. Modern surveys generally involve many electrodes controlled from a single location, which significantly increases the speed of data collection. However, the process still requires the electrodes to be manually placed, resulting in time-consuming and labour-intensive surveys. Alternatively, capacitively coupled resistivity (CCR) surveys use electric dipoles that are not grounded, but towed across a survey area. The dipole transmitter capacitively injects current into the ground and the dipole receiver detects the voltage, again through capacitive coupling. This technology enables the rapid collection of shallow, high-resolution data over large areas in a relatively short period of time. The depth of investigation in CCR is more limited than conventional resistivity because there is a larger skin depth effect associated with the relatively high frequency (16 kHz) at which CCR operates. Skin depth is the depth within a conductor (in this case the ground) at which the amplitude of a time-varying electric or magnetic field is 37% of the amplitude of the electric or magnetic field at the surface of the conductor. CCR is further depth limited by the

maximum distance over which the dipole receiver can detect the signal from the dipole transmitter.

8.2 Study Area

This study was conducted at Scobie Ranch, on the floodplain of Halfway River in northeastern British Columbia, Canada. Halfway River originates in the Rocky Mountains and flows south to Peace River (Fig. 8.1). In this area, Halfway River is best described as a poorly organized wandering gravel-bed river, as defined by Church, (1983) and Nanson and Knighton, (1996) (Fig. 8.2). The floodplain has been cleared for agricultural activities, and the open fields allow an unimpeded survey. Thus, it is an ideal site for imaging the radar architecture and testing the utility of CCR for determining 3-D grain-size distribution.

Two hydrometric-station records are available from Environment Canada for the lower Halfway River. One station is located upstream (north) of Graham River, the other downstream (south) of the confluence of the Graham, near Peace River (Fig. 8.1). The northern station (07FA003) has data between 1977 and 1995 but is currently inactive; the southern station (07FA006) has a record that includes data from 1984 to 2005 (Fig. 8.3). The records show similar trends, although the southern station has higher discharges with the addition of Graham River to the Halfway River catchment. Peak annual discharge is driven by snowmelt during the spring and early summer. The records indicate that flood events are crudely cyclical with relatively high mean discharge (averaged over a month) occurring every 5-6 years.

A series of five sequential aerial photographs (1963, 1978, 1987, 1992, and 1999) yield a 37-year record of change in the Halfway River planform near the study area (Fig. 8.4). Although the features studied here have remained stable for this period, the bars and channels developed since 1963 represent analogues for morphostratigraphic units preserved on the floodplain.

The main channel has distinctly sinuous meanders, and lateral bars are present. However, the many semipermanent vegetated and nonvegetated bars and islands with secondary channels are more typical of wandering gravel-bed rivers (Church, 1983; Carson, 1984a, 1984b, 1984c; Schumm, 1985; Desloges and Church, 1987; Brierley and Hickin, 1991; Nanson and Knighton, 1996). Main channel migration tends to be variable and characterized by phases of rapid shifting. As the dominant channel becomes choked with sediment, it avulses and occupies

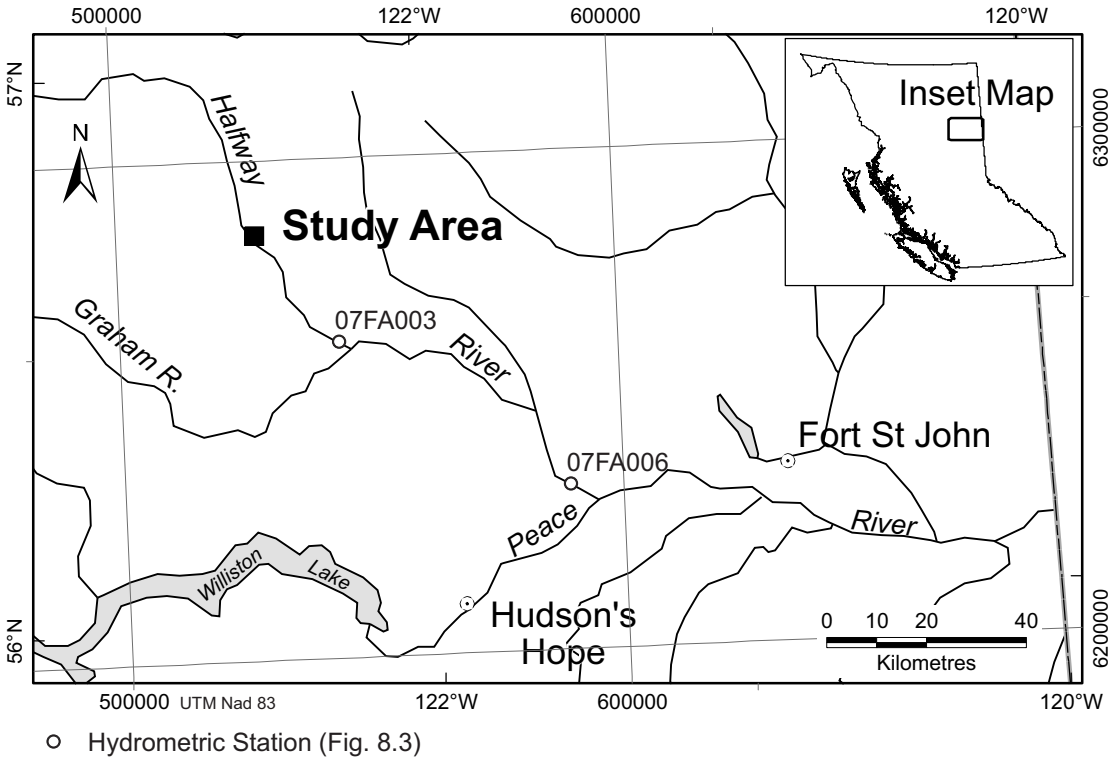

Figure 8.1. The study area is located at the Scobie Ranch on the Halfway River floodplain in northeast British Columbia.

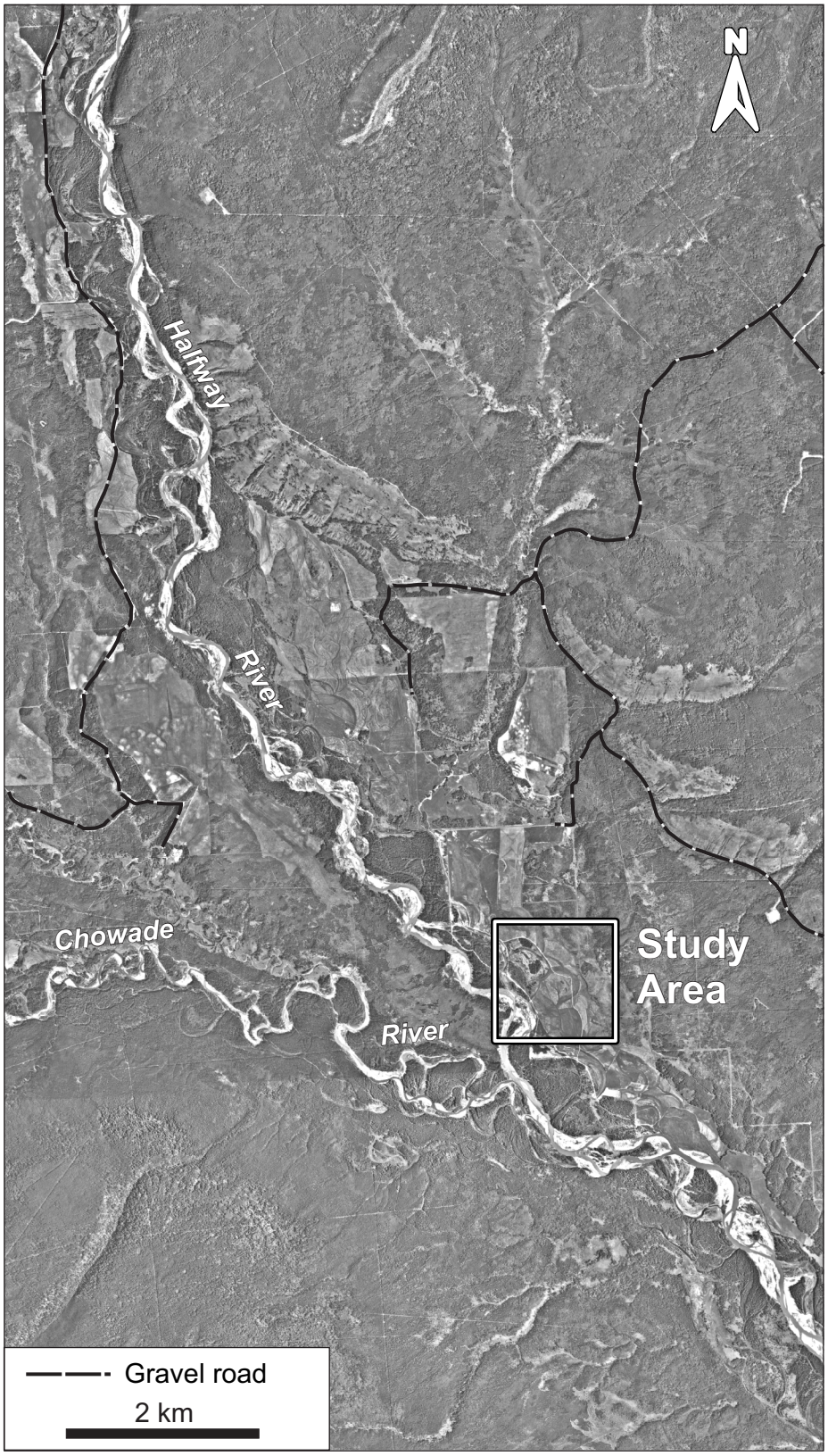

Figure 8.2. This reach of the Halfway River is best described as a poorly organized wandering gravel-bed river. The study area is outlined.

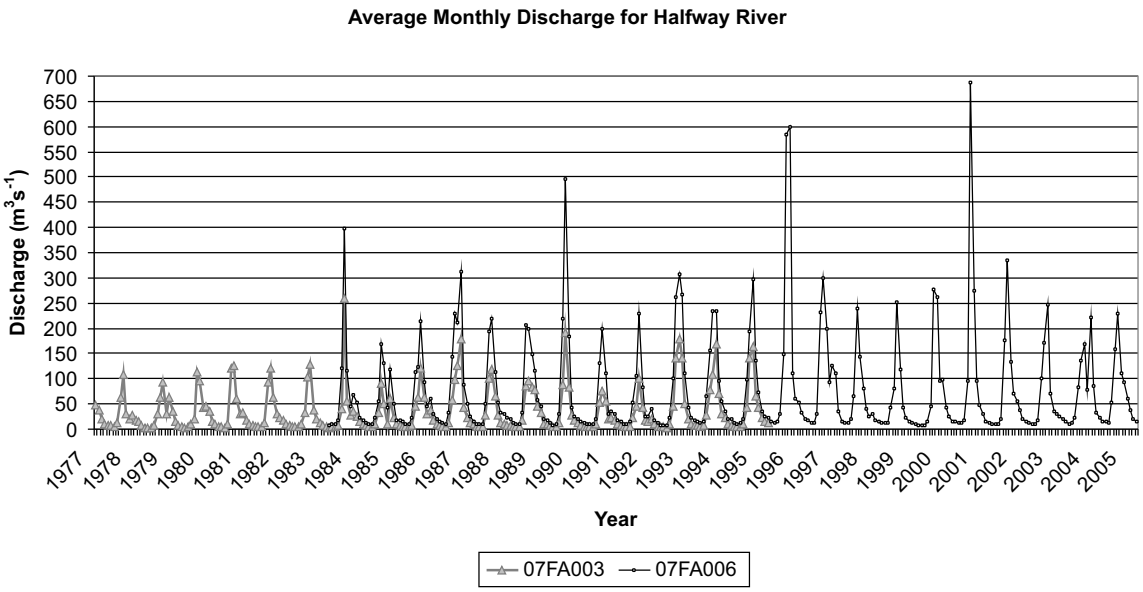

Figure 8.3. Two hydrographs show the mean average monthly discharge of the Halfway River. Station 07FA003 is located downstream of the study area but above the confluence of the Graham and Halfway rivers. Station 07FA006 is located below the confluence towards the Peace River (Fig. 8.1).

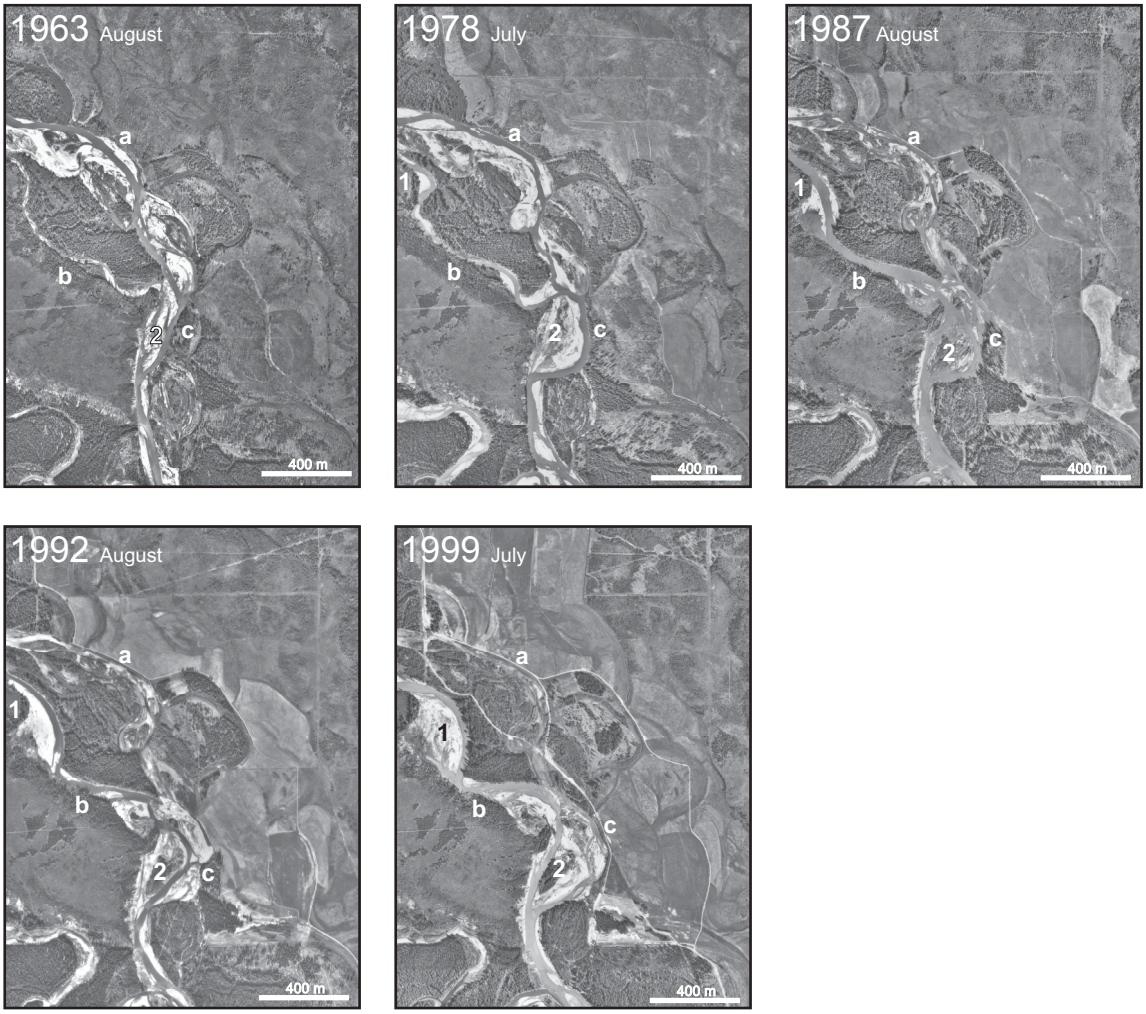

Figure 8.4. Five aerial photographs of the Scobie Ranch show the evolution of the floodplain of the Halfway River in the study area (box indicates area in Fig. 8.2). The numbers refer to bars, and letters to channels. From 1963 to 1987 subordinate channel b became the main channel when channel a was reduced to a subordinate status and eventually abandoned by 1999. Lateral bar 1 developed from the eastward migration of channel b. Bar 2 developed from a small lateral bar into a compound bar as channel c migrated to the east. Channel c eventually became choked with sediment by 1992 and avulsed to a western position by 1999, dissecting bar 2. The former positions of channel c were subsequently reduced to subordinate status after 1999.

new or subordinate channels (presumably during flood), abandoning the former thalweg (Fig. 8.4).

The Halfway River planform is indicative of a system dominated by bed-load transport (Schumm 1985). Evidence of sheeted gravel transport is preserved on bar tops (bar 2, Figs. 8.4 and 8.5). Sheets of gravel with prograding slip-faces were observed and left in place when transport capacity of the stream decreased during waning flow (Ferguson and Werritty 1983). Abundant channels dissect bar 2, and channel bottoms contain imbricated cobble gravel. In places the channels have been infilled with fine-grained organic mud (Fig. 8.5F).

The focus of the study is a former channel bend and an associated interior bar platform (Fig. 8.6). The main channel appears to have been an eastward-migrating river bend that eroded into the pre-existing floodplain. The interior bar has two subtle, positive topographic regions and four poorly defined topographic lows that are interpreted as bar platforms and subordinate ridges and swales, respectively. The western platform stands approximately 1.0 m above the eastern platform, separated by a topographic low that is indistinct to the northwest but narrows and deepens to form a channel where it meets the main river bend (between GPR Lines 4 and 5; Fig. 8.6).

8.3 Methods

The study, conducted in the winter 2006, consisted of three components: (1) trenching; (2) GPR survey; and (3) CCR survey. Five sites were trenched with an excavator to depths between 3.2 and 4.5 m. Trenches were located near GPR lines on three of the main morphostratigraphic units (Fig. 8.6). At each location, lithofacies were described and photographed. Bulk samples were collected from the gravel component at four of the trenches. Grain-size analysis was conducted on the samples following procedures outlined by the Canadian Standards Association (ASTM C 136-06). The proportion of oversized clasts (> 75 mm; Modified Unified Classification System for Soils) were estimated in the field and incorporated into the normalized proportions.

The GPR survey was conducted using a Sensors & Software's pulseEKKO IV GPR system with a 400 V transmitter and 100 MHz antennae. The survey was conducted following procedures and survey design described in Sensors & Software (1996). Antennae were oriented perpendicular to the direction of travel with a fixed separation of 1.0 m and traces collected at

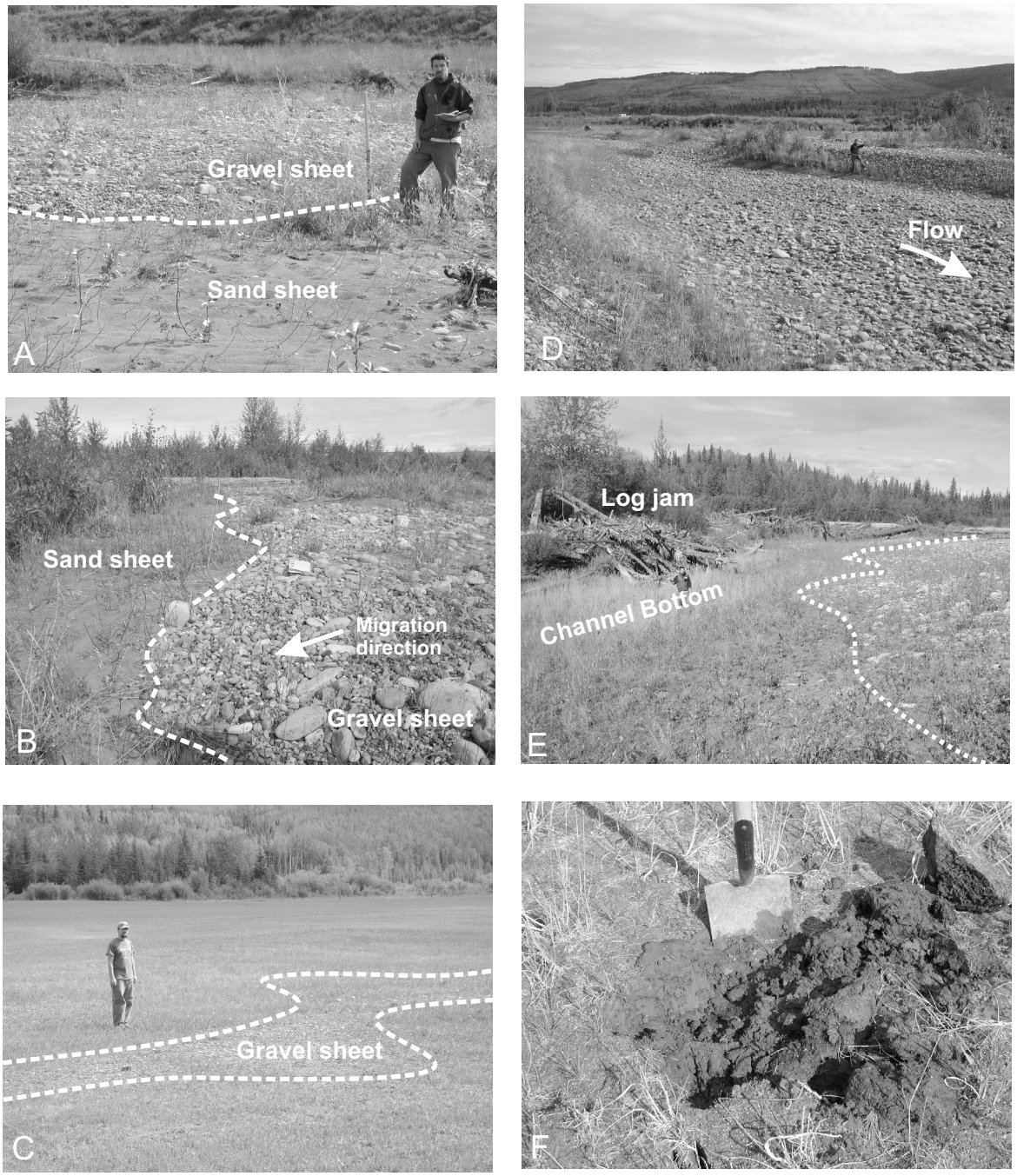

Figure 8.5. Bar 2 (see Fig. 8.4) is a likely analog for the development of the features in this study. A, B) Migrating gravel sheets preserved on the top of bar 2. C) Gravel sheet preserved on top of the bar platform in Fig. 8.6. D) Channel c is an abandoned channel of the Halfway River. E) The active channel in 1992 is now vegetated with organic mud overlying gravel. F) The organic mud in the former active channel.

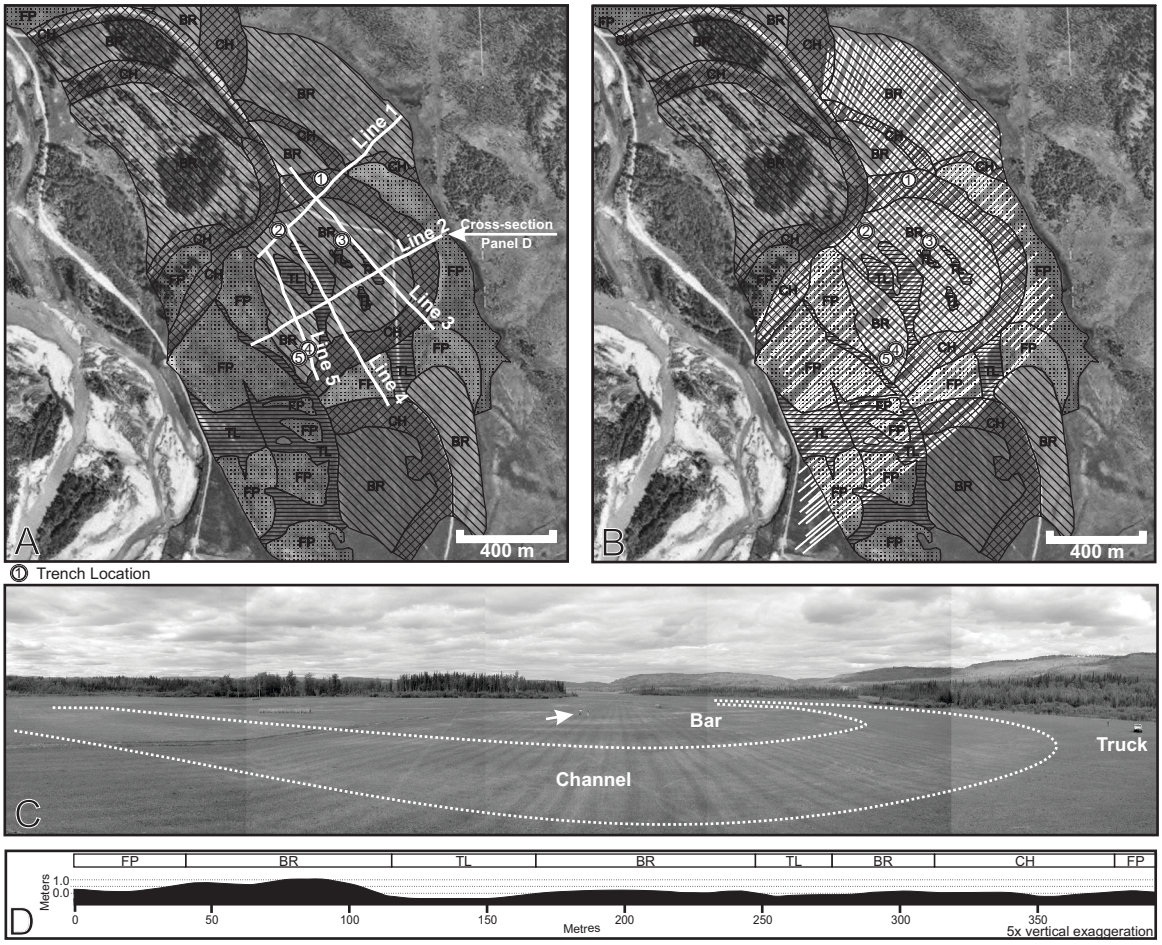

Figure 8.6. The GPR and CCR surveys were conducted over a bar platform and channel bend. The numbers indicate trench locations, and the letters refer to morphostratigraphic units (BR = bar, CH = channel, TL = local topographic low, FP = undifferentiated floodplain). A) GPR survey lines (shown in white). B) The CCR survey lines (shown in white). C) Bar and channel viewed from the southeast end of Line 3 towards the northwest (arrow indicates people for scale). D) Topographic profile with morphostratigraphic units along GPR Line 2.

0.5 m intervals. The survey consists of five lines, two of which are oriented southwest-northeast (Lines 1 and 2) and three lines are oriented approximately northwest-southeast (Lines 3 – 5), orthogonal to Lines 1 and 2 (Fig. 8.6). Lines were spatially located with a hand-held global-positioning system (GPS) every 10 to 20 m. A velocity of 0.132 m/ns is used to convert the time scale to a depth scale, estimated from the mean of two common-midpoint surveys (CMP) collected at locations within the interior bar. Processing includes dewowing the saturation signal (removal of low frequency component of the signal), applying an automatic gain control (set at 1000) to enhance later arrivals, and applying topographic trace adjustment to account for subtle changes in elevation. Filters were set with trace-to-trace averaging at 4 and down the trace averaging at 7 to enhance the signal-to-noise ratio (Sensors & Software, 1996).

Radar facies and element interpretations are based on the principles of radar stratigraphy (Beres and Haeni, 1991; Jol and Smith, 1991) derived from seismic stratigraphy (Mitchum et al., 1977). Radar facies are defined as mappable 2-D units composed of reflections whose internal reflection configuration, continuity, amplitude, polarity, spacing, and external 2-D geometry differ from adjacent units (Jol and Smith 1991). The resolution of a GPR survey is dependent on the central operating frequency of the antenna. The scale of bedding, bounding surfaces, and the resulting radar facies resolved in a given survey are therefore also dependent on the central operating frequency (Woodward et al., 2003). Closely related radar facies can be combined to form radar elements in much the same way lithofacies combine to form architectural elements (Miall, 1978, 1985, 1996). Genetic interpretation of the radar facies for wandering gravel-bed rivers follows Wooldridge and Hickin, (2005).

The CCR survey was conducted with an OhmMapper™ instrument configured with five, 5 m dipole receivers and a dipole transmitter with a 5 m rope length, arranged in a dipole-dipole array (Geometrics, 2001) (Fig. 8.7). Readings were collected continuously at 0.5 second intervals, travelling at approximately 6 to 10 km/h with receivers spaced at n = 1.0, 1.5, 2.0, 2.5, and 3.0 (n is equal to the dipole length). This resulted in a vertical pseudosection of approximately 5 m depth. Lines were spaced approximately 10 m apart, and positional data were continually acquired with a hand-held GPS (estimated accuracy of ± 5m). Topographic data from a high-resolution light detection and ranging survey (LiDAR) were incorporated into each line. The raw CCR data were uploaded into Geometric's MagMap2000™ software and individual lines exported in a format compatible with inversion software (RES2DINV™; Griffiths and Barker 1993;

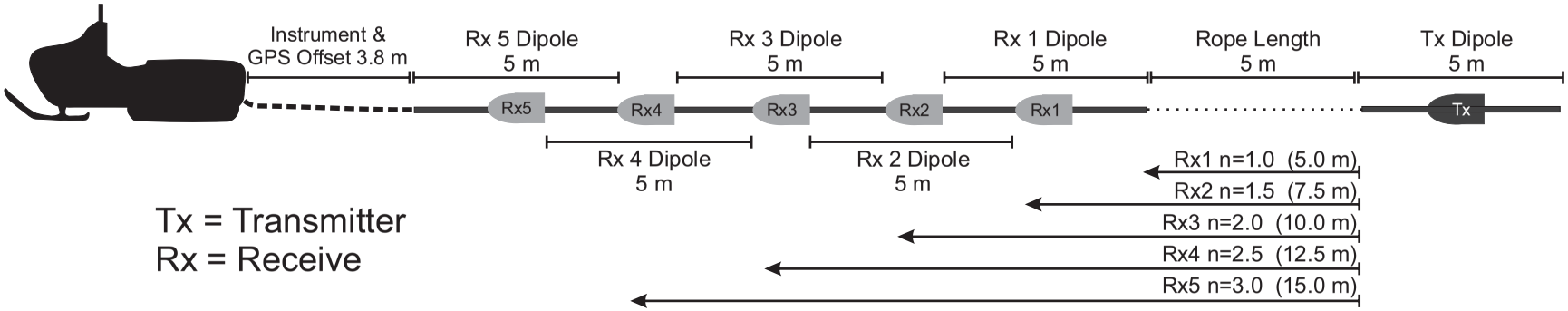

Figure 8.7. OhmMapper configuration with five dipoles and a transmitter (modified from Geometrics, 2001) scale). D) Topographic profile with morphostratigraphic units along GPR Line 2.

Loke and Barker 1996). Lines were inspected and poor data points removed. RES2DINV™ provides a 2-D resistivity inversion of the subsurface for data obtained from electrical imaging surveys (deGroot-Hedlin and Constable, 1990; Griffiths and Barker, 1993; Loke and Barker, 1996). Robust inversion was chosen because this method enhances sharp boundaries (Claerbout and Muir, 1973). A soft user-defined boundary was included at 1.25 m with a boundary weight factor of 50. This enables the inversion software to invoke a sharp boundary near the defined depth, but does not force the boundary if not supported by data. The weight factor reflects the rigor with which the inversion incorporates the boundary (Geotomo Software, 2006). With the above configurations, the model generated low-resistivity values in the channels where fine-grained sediments were noted in trenches or at surface. The inversion process was iterative, and parameters were altered systematically until the software generated a geologically reasonable model that was consistent with field observations. Once the parameters were optimized, batch inversions were performed on all lines.

A 3-D resistivity model was generated using Golden Software's Voxler ™ (Golden Software, 2006) and Geospatial Analyst in ArcMap™. Point data from all of the 2-D resistivity inversions were extracted from RES2DINV™ as x, y, z location data and a resistivity attribute value, and imported into Voxler™. Data distribution is dense along lines, sparse between lines, and offset vertically by the magnitude of the surface relief (i.e., points are at constant depth below surface, not at constant elevation). In order to generate elevation slices, data were imported into Voxler™ and the resistivity values interpolated vertically using a prolate ellipsoidal search radius with a 2.0 m major axis, a 1.0 m minor axis, and an inverse distance weighting algorithm. The interpolation produced columns of voxles (i.e., a 3-D equivalent of a pixel) with cell dimensions 1.0 m x 1.0 m x 0.4 m (x, y, z) and a resistivity value. This interpolation increases the vertical density of data points from five per column to as many as twelve per column. Depth slices at constant elevations were extracted from the Voxler ™ model at 0.40 m intervals and imported into ArcMap™. The data distribution of each at 0.40 m elevation slice was investigated with the aid of semivariograms and histograms in Geostatistical Analyst. To increase the data density to an evenly spaced 2 m grid, data are interpolated between points in the x-y plane. All depth slices were then reintroduced into Voxler™ resulting in a point cloud which provides a 3-D resistivity model.

The relationship between radar facies and resistivity required vertical resistivity profiles to be extracted from the final Voxler™ model along the GPR lines. Resistivity point data and images of the interpreted GPR profiles were also introduced into ArcMap™ and each radar facies digitized into polygons. The polygons were then overlaid onto the resistivity profiles and point values falling within each polygon counted and frequency distribution curves generated and analyzed.

8.4 Results and Interpretation

8.4.1 Trenching

Five trenches were dug for this study: Trench 1 in the abandoned channel and trenches 2-5 on the interior bar platform (Figs. 8.6 and 8.8; Table 8.1). Trench 1 (3.3 m deep) consists of three units. Unit 1 (lower) is at least 2.0 m thick, massive, poorly sorted, matrix-supported pebble to cobble gravel with a lower contact below the bottom of the trench. Clasts are subangular to well rounded. The matrix is medium sand to coarse granular sand with some silt. Unit 2 (middle) is a 0.6-m-thick, well-sorted, laminated to thin- bedded silty fine sand with dish-shaped lenses of medium sand and both disseminated and layered organic detritus (0.01-0.02 m thick). The lower contact is sharp and undulatory. Unit 3 (upper) is 0.7 m thick and consists of laminated very fine sandy silt with organic detritus. The lower contact is indistinct and gradational over 0.1 m.

Trench 2 (3.6 m deep) is located on the upstream portion of the lower interior bar and consists of three units. Unit 1 (lower) is at least 0.5 m thick clast-supported, massive, poorly sorted, cobble to boulder gravel with a medium to coarse sand matrix and rare pockets of matrix-supported gravel. Many clasts exceed 0.3 m in diameter. A boulder lag occurs at the top of the unit. The lower contact is below the bottom of the pit. Unit 2 (middle) is a 2.85-m-thick, well-stratified, medium-bedded, clast-supported pebble to cobble gravel with minor sand lenses less than 0.1 m thick. Individual beds are horizontal to gently westward-dipping and generally massive. Beds alternate between open-framework, well-sorted, pebble gravel and moderately sorted, pebble to cobble gravel with a medium to coarse sand matrix. Minor westward-dipping planar cross-beds occur. The lower contact is indistinct but marked by a grain size shift, and the boulder lag in the underlying unit. Unit 3 (upper) is 0.25 m thick and consists of laminated, very fine sand and silt with a sharp lower contact.

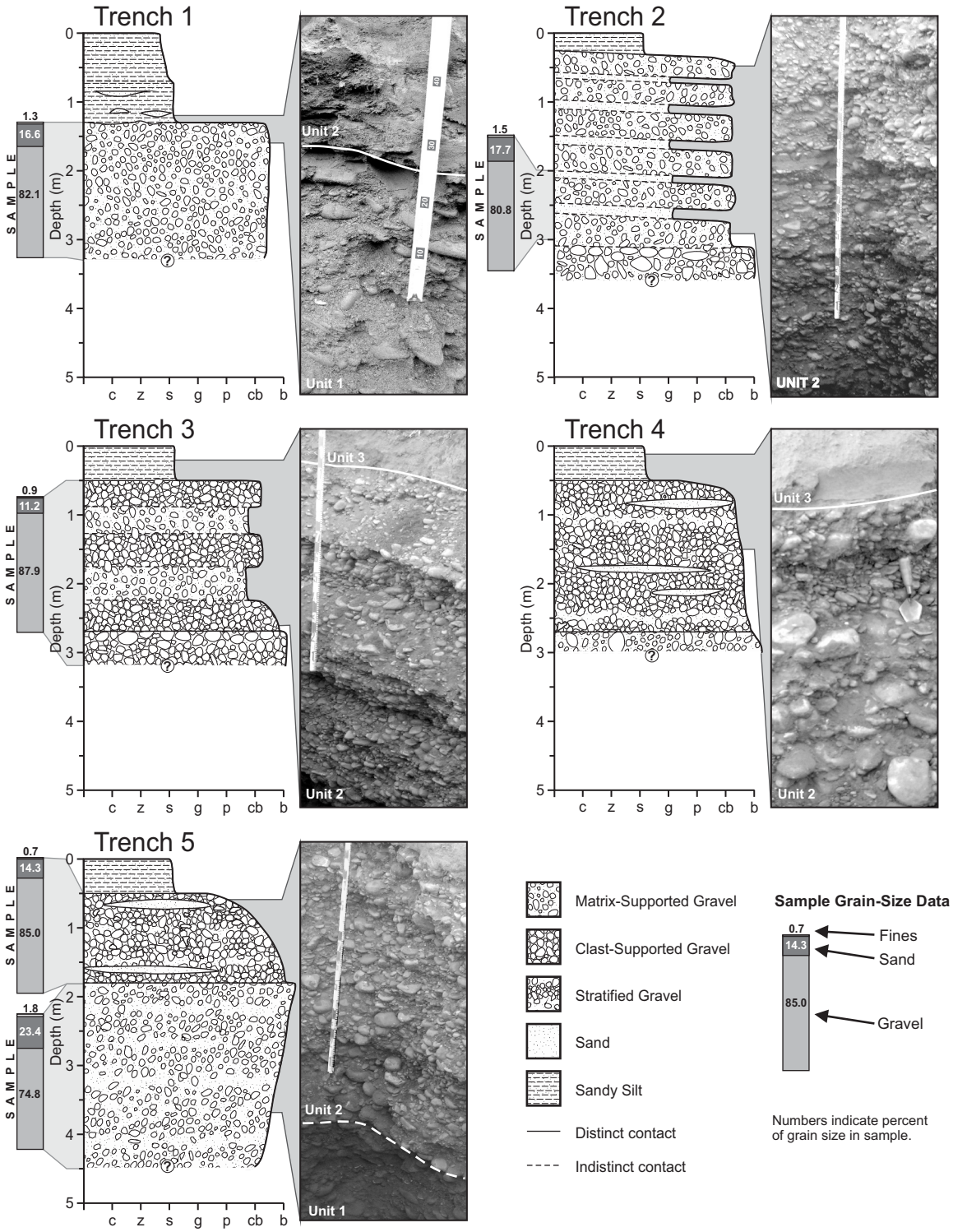

Figure 8.8. Trench stratigraphy of the bar platform and channel (locations in Fig. 8.6).

Table 8.1. Summary of Trench Data

Testpit	Depth (m)	Lithofacies (Modified from Miall 1996)
	0-0.7	Fl
	0.7-1.3	Fl, Sm
1	1.3-3.3	Gmm
	0-0.25	Fl
	0.25-3.1	Gcm, Gcp, Sm
2	3.1-3.6	Gcm, Gmm
	0-0.5	Fl
	0.5-2.7	Gcp, Gmp
3	2.7-3.2	Gmm
	0-0.5	Fl, Sr
	0.5-2.7	Gcm, Sm, Gcg
4	2.7-3	Gmm, Gmi
	0-0.5	Fl
	0.5-1.8	Gcm, Gcp, Sm
5	1.8-4.5	Gmm, Gmi

Fl: Fines; laminated	Gcm: Gravel; clast supported; massive
	Gcp: Gravel; clast supported; planar stratified
Sm: Sand; massive	Gcg: Gravel; clast supported; graded
Sr: Sand; rippled	Gmm: Gravel; matrix supported; massive
	Gmp: Gravel; matrix supported; planar stratified
	Gmi: Gravel; matrix supported; inverse grading

Trench 3 (3.2 m deep) is located on the interior bar between Trench 2 and the channel, and also reveals three units. Unit 1 (lower) is 0.5 m thick and consists of massive, poorly sorted, matrix- and clast-supported, cobble gravel with rare boulders greater than 0.5 m in diameter. Clasts are slightly more angular than those in the overlying unit. A poorly developed boulder lag occurs at the top of the unit. The lower contact is below the bottom of the pit. Unit 2 (middle) is a 2.2-m-thick, horizontally stratified, thick-interbedded, clast- and matrix-supported, pebble to small cobble gravel. The matrix within the clast-supported beds is coarse sand, whereas the matrix within the matrix-supported beds is medium-grained sand. The lower contact is sharp and marked by the boulder lag. Unit 3 (upper) is a 0.5-m-thick laminated silty, very fine sand with a sharp lower contact.

Trenches 4 and 5 are located on the unit bar west of the interior bar and have consistent stratigraphies also involving three units. Unit 1 (lower) is 0.3 m in Trench 4 and 2.7 m thick in Trench 5 with the lower contact occurring below the bases of the trenches. More of the unit was exposed in Trench 5, where it consists of a coarsening-upwards, crudely stratified cobble gravel. Unit 2 (middle) is 2.2 and 1.3 m thick in trenches 4 and 5, respectively. The unit is a thick-bedded, moderately stratified to massive, clast-supported, large pebble to cobble gravel with a medium-sand matrix. The beds dip gently ($<10^{o}$) to the south and west in each trench, respectively. The gravel is interbedded with dish-shaped lenses of medium sand, 0.05 to 0.1 m thick, and is laterally continuous for up to 1.0 m. The lower contact is sharp, marked by an increase in clast size with depth. Unit 3 (upper) in both sections is 0.5 m thick and consists of massive and rippled laminated silty, very fine sand with a sharp lower contact.

8.4.2 Ground-Penetrating Radar

The radar profiles typically contain laterally continuous reflections in the upper five meters and abundant diffractions in the lower portions of the profiles (e.g., Figs. 8.9 and 8.10). Aggressive filtering was applied to enhance the continuous reflection without overly obscuring dipping reflections, though the dipping reflections were affected. Interpretation of the filtered data resulted in the differentiation of eight radar facies, one radar element (Table 8.2), and several major bounding reflections. The facies and the element constitute four groups: (1) continuous, horizontal to subhorizonal reflections; (2) clinoform reflections; (3) discontinuous

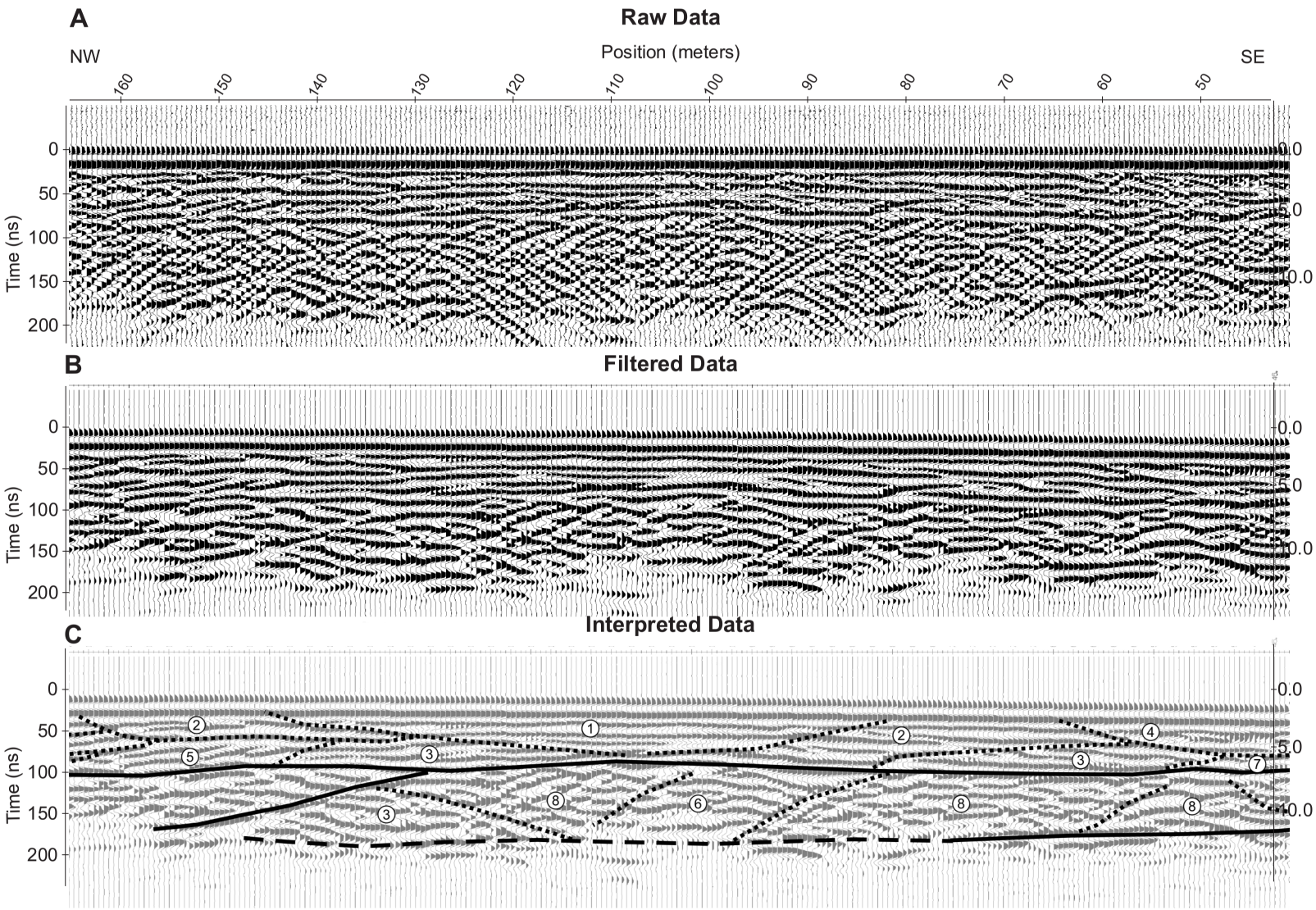

Figure 8.9. A portion of GPR Line 5 located across the bar platform. A) Raw data; B) filtered data; C) interpreted data (see Table 8.2).

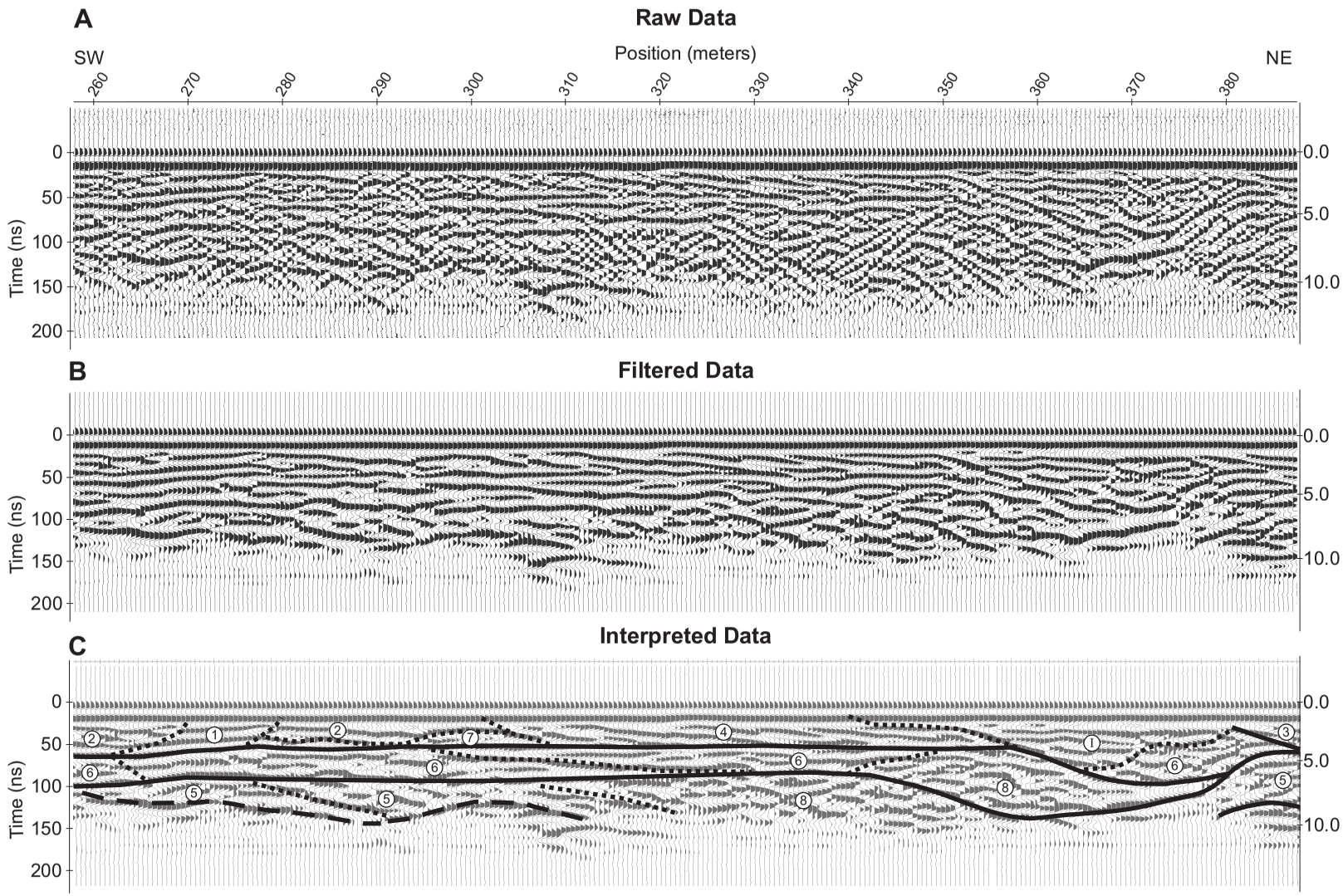

Figure 8.10. A portion of GPR Line 2 located at the transition from the bar platform to the channel. A) raw data; B) filtered data; C) interpreted data (see Table 8.2).

Table 8.2. Four Groups of Radar Facies and their interpretation.

Group	Catagory	Description	Interpretation	Schematic Example
1 Continuous Horizontal to Subhorizontal,	Facies 1	Laterally continuous (10-70 m), parallel, even, uniform, horizontal to subhorizontal reflections.	Well stratified, horizontal bedding - Vertical accretion, horizontal component of cross-bedding.	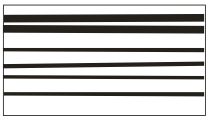
	Facies 2	Laterally continuous (10-70 m), non-uniform, subhorizontal (0° - $<10^o$) to weakly hummocky, parallel to subparallel reflections.	Moderately stratified subhorizontal to slightly inclined bedding - Vertical accretion, downstream accretion, horizontal component of cross-bedding.	
2 Clinoform	Facies 3	Laterally continuous (15-60 m), low-angle (1°-20°), sigmoidal to divergent reflections.	Well to moderately stratified, dipping bedding - Lateral or downstream accretion, migrating bar or bedform, prograding channel fill.	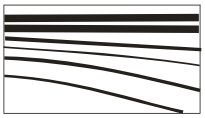
	Facies 4	Moderately continuous (5-30 m), inclined (5°-20°), shingled reflections.	Well to moderately stratified dipping bedding - Lateral accretion, slipface of migrating bedform.	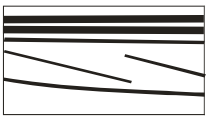
	Facies 5	Short (5 - 10 m), oblique, tangential or parallel, inclined (15°-30°) reflections.	Moderately to poorly stratified dipping bedding - Lateral accretion, slipface of migrating bedforms, cutbank colluvium.	
3 Discontinuous	Facies 6	Discontinuous (5-15 m), hummocky or disrupted reflections.	Crudely stratified to massive deposit obscured by diffractions	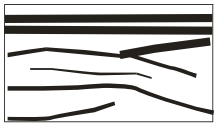
	Facies 7	Discontinuous (5-10 m), random, chaotic reflections.	Crudely stratified to massive deposit obscured by diffractions	
	Facies 8	Discontinuous, abundant diffracted reflections	Abundant point source diffraction from objects such as large cobbles, boulders, or logs.	
4 Concave-up Lower Boundary	Element I	Small- to medium-scale (10-30 m), concave-up lower bounding surface, internal reflection geometry includes onlap, mounded onlap, divergent, prograding, chaotic, or complex fills.	Sediment-filled chute or channel	

reflections; and (4) concave-up elements. 3-D facies relationships are established where the survey lines cross.

8.4.2.1 Group 1

Group 1 includes two facies, both of which are represented by continuous, laterally extensive, horizontal, subhorizontal, or slightly inclined (< 5°) reflections. Facies 1 has evenly spaced parallel reflections with a uniform frequency between traces. Facies 2 differs from Facies 1 in that individual traces produce reflections of less uniform frequency and tend to be subparallel to slightly hummocky, perhaps the result of constructive/destructive interference or from filtering. These facies dominate the upper 2-3 m of the GPR profiles in the interior bars, secondary channels, but are less common in the main channel.

Interpretation: These facies are interpreted to be well-stratified horizontally to subhorizontally bedded sediments, suggesting vertical accretion (Wooldridge and Hickin 2005), downstream accretion (Miall 1996), or possibly the horizontal component of cross bedding (Wright 1959).

8.4.2.2 Group 2

The second group includes the various clinoform reflections. Facies 3 consists of laterally continuous reflections with constant, divergent or sigmoidal dip patterns. It consistently occurs within the inner bend of the main channel, dipping towards the channel center. Facies 3 also occurs throughout the bar platform with various dip directions. Facies 4 is generally rare, characterized by a shingled pattern, and tends to dip steeper, and is less laterally extensive, than Facies 3. Facies 4 is most notable in Line 2 and 3 at the transition from bar to channel on the inner bank, dipping towards the channel. Facies 5, also rare, has the shortest reflection length and the steepest apparent dip. It occurs on the cutbank side of the channel, dipping towards the channel center, at the base of the channel in Line 4, and in the upper 5 m of Line 5, dipping towards the bar head.

Interpretation: These facies are interpreted as well-stratified dipping beds. Where facies 3 occurs in the channel, it may represent lateral migration (Willis 1989; Miall 1996) and channel fill (Bristow 1993); elsewhere it may represent lateral or downstream accretion or bar-margin slip faces (Wooldridge and Hickin 2005). Facies 4 represents lateral accretion. At the cutbank edge,

Facies 5 may represent colluvial material while elsewhere it may represent the slip faces of migrating bedforms (Miall 1994).

8.4.2.3 Group 3

Group three includes discontinuous reflections. These facies form a continuum of reflection patterns, and their classification is relatively arbitrary but focuses on the dominant pattern. Facies 6 is the most coherent of the group and consistently occurs in the base of the main channel. Facies 7 consists of random or chaotic reflections, and Facies 8 consists of diffractions or lenticular reflections. Collectively these discontinuous facies dominate the lower 5 m of all the profiles.

Interpretation: All of these facies are associated with various concentrations of diffractions in the raw data. Facies 6 and 7 are interpreted as a continuum of crudely stratified to massive deposits. Facies 8 represents a high density of point sources such as cobbles, boulders, or buried logs.

8.4.2.4 Group 4

Group 4 is represented by Element I. A radar element consists of an association of radar facies in the same way fluvial architectural elements consist of an association of lithofacies (Miall 1996). Element I is defined as a small- to medium- scale feature with a concave-up lower bounding reflection and a variety of internal reflection configurations. This facies is most common in the upper 5 m of the bar platform and within the upper portion of the channel.

Interpretation: This element is interpreted as filled channels, chutes, or scour-and-fill deposits.

8.4.2.5 3-D Facies Relationships

At the intersection of GPR lines, a 3-D interpretation of the facies is made (Figs. 8.11 and 12). Because Facies 1 typically occurs adjacent to either another Facies 1 or Facies 2, the orientation of the reflectors is generally horizontal to subhorizontal in 3-D. These are the dominant facies pairing in the upper portion of the profiles across the bar platforms (Fig. 8.12). There are several exceptions; Facies 1 and 2 occur with dipping reflections in rare cases and therefore represent the horizontal component of cross-bedding (Miall 1996). A poorly developed Facies 2 occurs with a portion of Facies 6, implying that stratification was resolved in

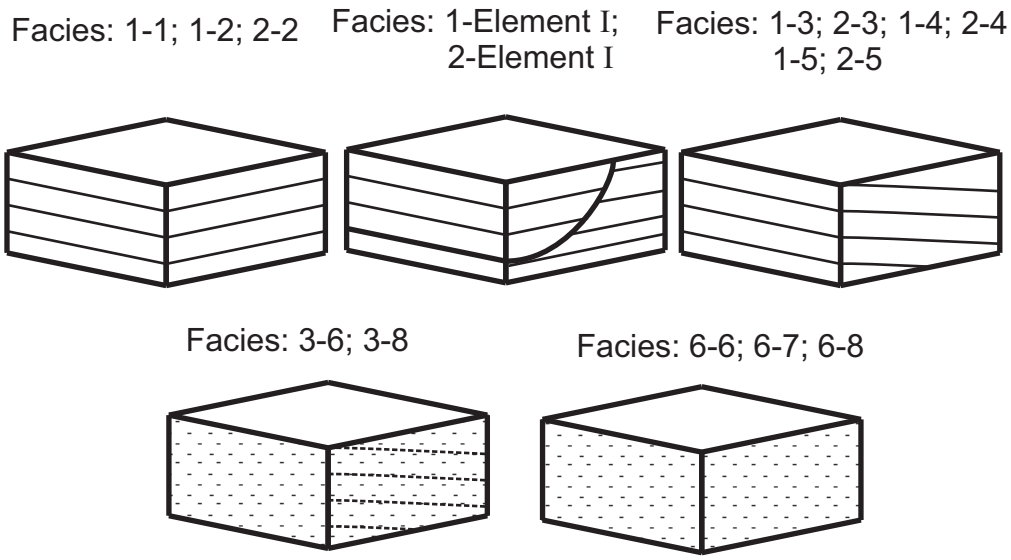

Figure 8.11. Radar facies pairings and 3-D reflection orientations from the intersection of GPR lines.

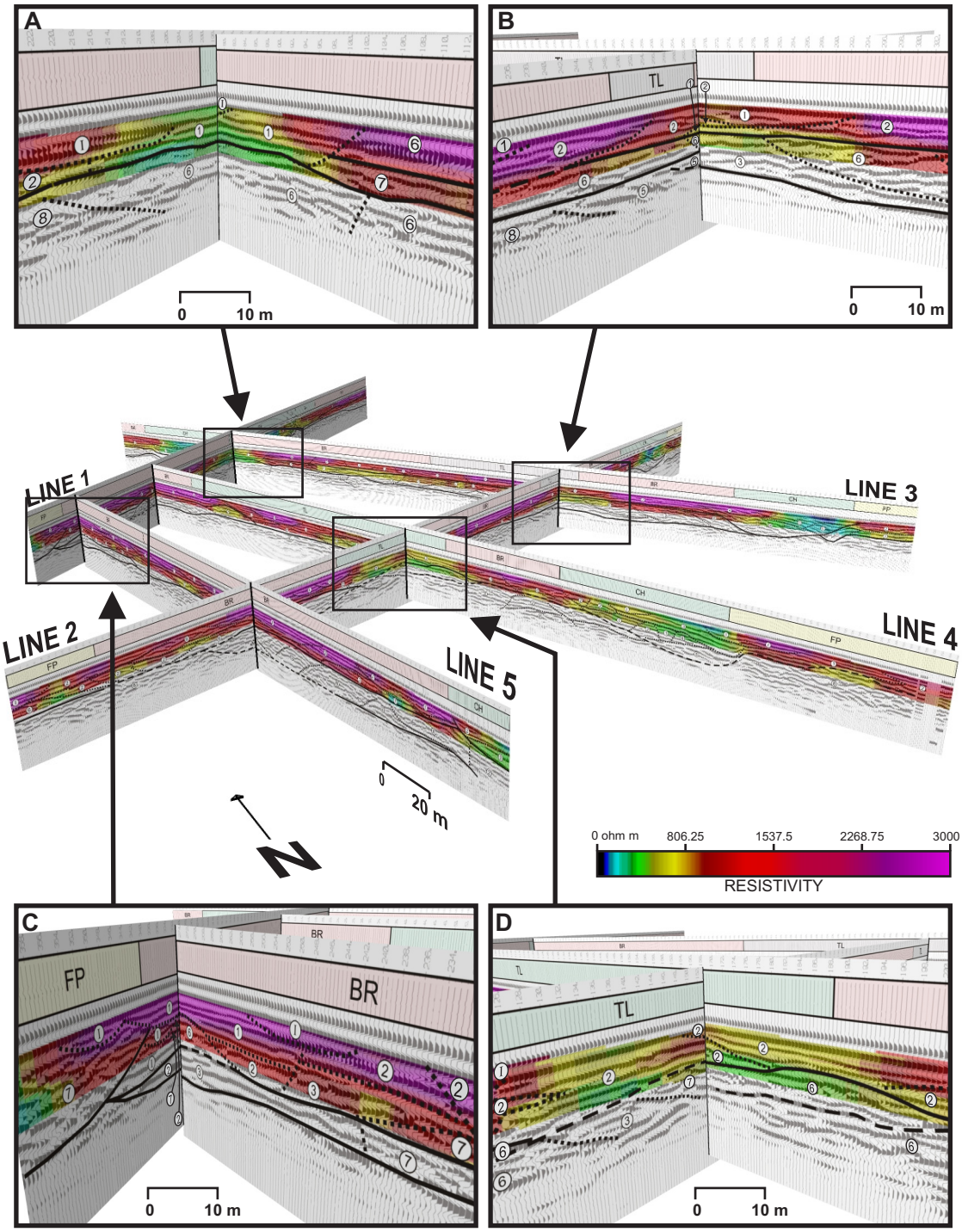

Figure 8.12. Resistivity data from the 3-D model overlaid onto the GPR lines. The numbers refer to radar facies from Table 8.2, the dashed lines are facies boundaries, and the solid lines are storey boundaries. A) Upstream margin of bar platform and channel. B) Small subtle topographic low on bar platform. C) Upstream margin of bar platform. D) Well developed topographic low within bar platform.

only one direction. Other pairings include Facies 3 commonly with Facies 6 and 8, suggesting that crudely stratified dipping beds are resolved in only one direction, and obscured by diffractions in the other. Facies 3 is also paired with Facies 5; reflectors that dip along orthogonal survey lines indicate that each line captured the apparent dip of inclined reflectors. The remaining facies combinations dominate the lower portion of most profiles and include discontinuous reflections in both directions, indicating that these units are crudely stratified, massive, or obscured by diffractions in 3-D.

8.4.2.6 Bounding Reflections

A boundary is identified in the top 3-5 m of all the profiles, marked by the transition from the more coherent facies (Facies 1-4) to the more discontinuous (Facies 6-8; Figs. 8.9-8.12). In some places a strong, laterally continuous (> 100 m) reflection is associated with this facies shift. However, elsewhere the boundary is inferred from the change in reflection geometry. This surface is interpreted as a boundary between two stories: a deposit of a single channel bar and adjacent channel fill (Bridge and Mackey 1993). The boundary separates deposits interpreted to be moderate to well stratified from crudely stratified, massive, or very coarse deposits. The lower story may represent basal channel sediments, overlain by sheeted bar-platform sediments of the upper story (Mackin 1937; Allen 1963; Walker 1979). Alternatively, the two stories may not be contemporary and therefore represent different generations of floodplains.

8.4.3 Resistivity

The 3-D resistivity model allows a thorough investigation of the distribution of resistivity values. The resistivity values are comparable to those expected for clay, silt, sand, and gravel from ground electromagnetic (EM) survey methods reported by Palacky and Stevens (1990). However, the values are considerably higher than those reported from an airborne EM survey of buried sand and gravel in northeast British Columbia (Best et al., 2006). The resistivity values for fine-grained sediments are comparable to values suggested by Reynolds (1997), but the values he suggests for sand and gravel are much lower than those found in this study. This may be a function of the sediment characteristics or be related to ice in the interstices of the coarse-grained deposit. Based on trench data and surface observations on the morphostratigraphic units, general grain-size prediction can be inferred from the resistivity data. Resistivity values below 400 ohm-m correspond to fine-grained sediments (clay, silt, and fine sand), values

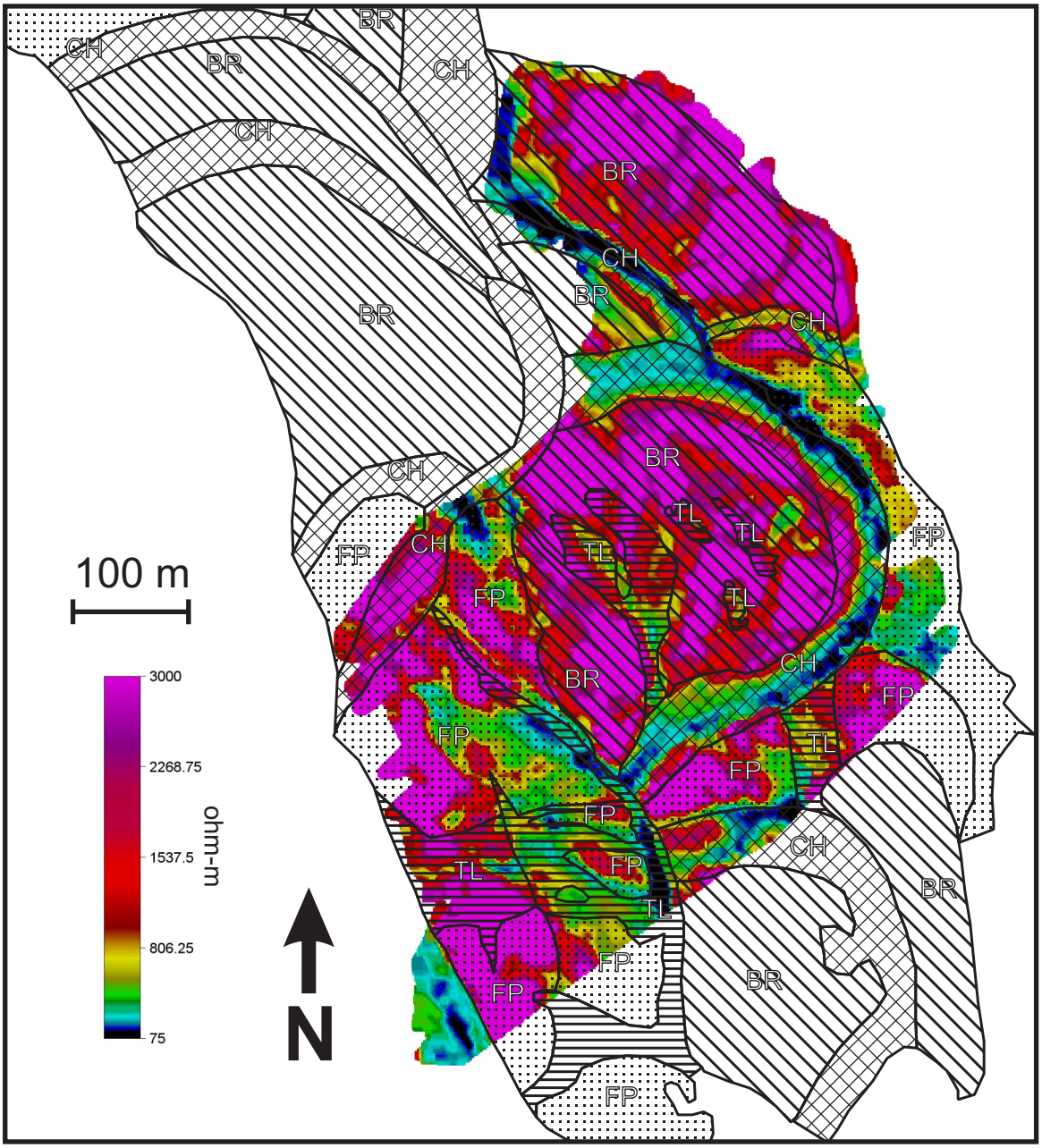

Figure 8.13. The surface resistivity correlates well with the morphostratigraphic units derived from the aerial photographs (BR = bar, CH = channel, TL = local topographic low, FP = undifferentiated floodplain).

between 400 and 800 ohm-m represent medium-grained sediments (sand), and values greater than 800 ohm-m are correlative with coarse-grained sediments (gravel).

Surface resistivity values representing a depth of approximately 0.40 m below the surface correspond well with the morphostratigraphic units mapped from aerial photographs (Fig. 8.13). Although there are some exceptions, most bar and undifferentiated floodplain features correspond with high resistivity values (> 800 ohm-m) and therefore with coarse sediment. Most depressions and channels, with low resistivity values (< 300 ohm-m), imply sand or fine-grained material. Only the upper portions of major channel features exhibit values less than 100 ohm-m, suggesting fine-grained sediment. In 3-D, the higher resistivity values (> 800 ohm-m) cluster into bodies, connect at the surface, but have an undulating, “basin and dome”-like morphology (Ramsey 1967) at depth surrounded by lower resistivity values at the base of the model.

Two-dimensional resistivity pseudosections were extracted from the 3-D model along the same lines as the GPR survey (Figs. 8.12 and 8.14). Generally, the profiles show high resistivity values in the upper 2-3 m of areas classified as bar or floodplain morphostratigraphic units, suggesting 2-3 m of coarse sediment, consistent with trench data. The upper 2-3 m in areas classified as topographic lows or channel morphostratigraphic units commonly have low values, suggesting sand or fine-grained channel fill. The lowest resistivity values occur within the main channel scar, again suggesting fine-grained channel fill. However, low values in the channel (though slightly higher than the surface measurements) commonly persist to the base of the profile, suggesting fine-grained sediments at depth, which is inconsistent with the trench data that show gravel in the base of the channel scar (Fig. 8.8). This discrepancy is in part related to skin-depth effect, but more importantly the conductive surface material (fine-grained sediment) provides a preferential path for current to flow, essentially blocking current from flowing into deeper units (Geometrics, 2001). Resistivity values for sediments deeper than 2 m below the fine-grained channel fill are, consequently, suspect.

There are exceptions to these generalizations. For example, in Line 3 there is no significant change in the high resistivity values in the upper 2 m from the bar across the poorly developed topographic low and back to the bar. In Line 4, high resistivity values characterize the northwest portion of the topographic low, although resistivity decreases to the southeast as this topographic low passes into a more developed channel. This suggests that the low values are more likely to occur where depressions and channel features are better developed.

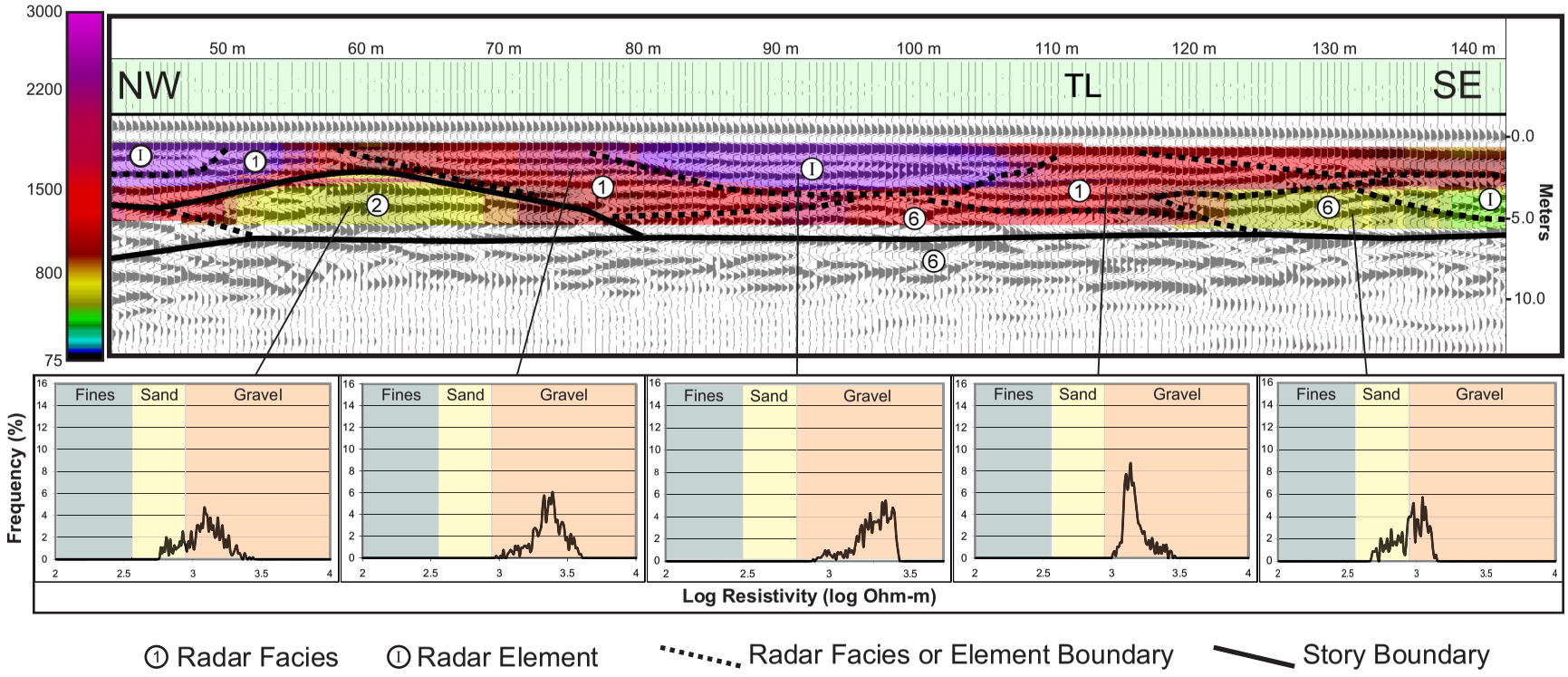

Figure 8.14. Example of combined the GPR and CCR from a portion of GPR Line 4 with resistivity distributions and corresponding grain size for several GPR facies.

8.4.4 Combined GPR and Resistivity

The GPR and CCR surveys are directly combined to explore the relationship between the radar facies and distribution and magnitude of resistivity values within each facies. The shape of the distributions can indicate sorting, and the magnitude of the resistivity values is used as a proxy for grain size (Fig. 8.14). Narrow distributions with consistent resistivity values are taken to represent well-sorted material, and wide distributions represent more poorly sorted material. Overall there is reasonable visual correlation between facies and resistivity, with sharp changes in resistivity roughly coinciding with facies boundaries (Fig. 8.14). This was encouraging, insomuch as the facies boundaries are determined independently of the resistivity data.

The distribution of resistivity values within individual facies polygons are classified into seven general shapes (Fig. 8.15): (a) log-normal low variability; (b) log-normal moderate variability; (c) log-normal highly variable; (d) log-skewed left; (e) log-skewed right; (f) log-bimodal; and (g) log-multimodal.

Shapes a, b, and c all have log-normal distributions but with progressively larger standard deviations. This is interpreted as indicating good sorting in a, moderate sorting in b, and poor sorting in c. Shapes d and e have positively and negatively skewed patterns, respectively. Shape d has a relatively narrow region of dominant resistivity values flanked by subordinate lower values whereas shape e is flanked by subordinate higher values. These distributions represent a dominant grain size with subordinate finer-grained or coarser-grained material, respectively. Alternatively, these shapes may result from the poor fit of the GPR facies to the resistivity data, erroneously incorporating values from adjacent units. Shapes f and g include distributions with two or more distinctive peaks. Bimodal Shape f represents two dominant grain-sizes and can have a wide range or a relatively narrow range of resistivity values. Multimodal Shape g generally spans a wide range of resistivity values, indicating poor sorting.

The dominant grain size for each polygon uses the surface grain-size classes noted earlier (i.e. < 400 ohm-m = fine-grained; 400-800 ohm-m = sand; > 800 ohm-m = gravel). Grain size for each polygon is assigned by noting where the largest area under the log-transformed frequency curve falls on the resistivity spectrum (e.g., Fig. 8.14). If a distribution spans more than one class, the polygon is considered to be composed of a mix of sediment. A summary of the grain size, sorting, and associated radar architecture is presented in Table 8.3.

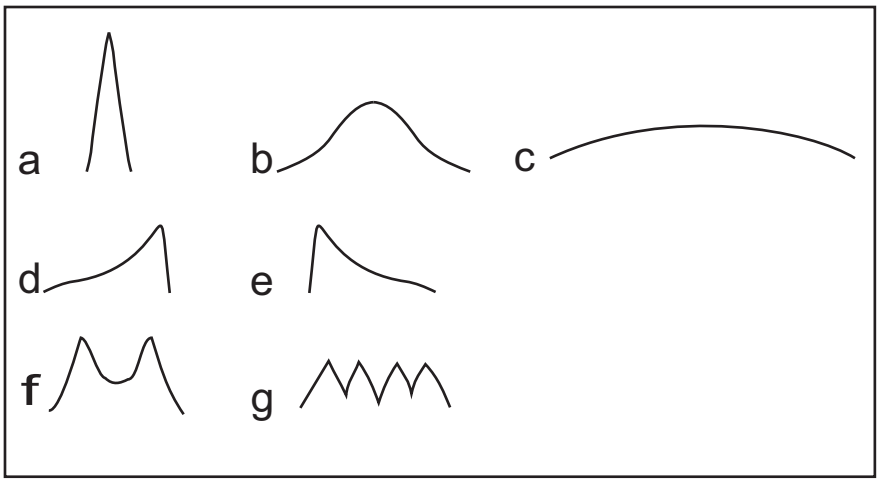

Figure 8.15. Simplified Resistivity-value distribution shapes used as a proxy for grain size and sorting for each radar facies polygons (Table 8.3). a) log-normal low variability; b) log-normal moderate variability; c) log-normal highly variable; d) log-skewed left; e) log-skewed right; f) log-bimodal; and g) log-multimodal.

Table 8.3. Combined radar facies and the distribution of resistivity values were interpreted in terms of grain size, sorting, and architecture.

Radar Facies	Grain-size and Sorting from Resistivity Distribution	Architectural and grain-size Interpretation	No. by Radar Facies
1	Moderately sorted coarse-grained unit	Horizontally stratified gravel	8
1	Moderate to well sorted coarse-grained unit	Horizontally stratified gravel	3
1	Well sorted medium-grained unit	Horizontally stratified sand	3
1	Two distinct coarse-grained units	Horizontally stratified gravel	2
1	Moderately sorted coarse-grained unit	Horizontally stratified sand and gravel	1
1	Poorly sorted fine- to coarse-grained unit	Horizontally stratified fines, sand, and gravel	1
1	Two distinct medium- to coarse-grained units	Horizontally stratified sand and gravel	1
1	Well sorted coarse-grained unit	Horizontally stratified gravel	1
1	Well sorted medium- to coarse-grained unit	Horizontally stratified sand and gravel	1
2	Poorly sorted medium- to coarse-grained unit	Subhorizontally stratified sand and gravel	10
2	Well sorted coarse-grained unit	Subhorizontally stratified gravel	8
2	Moderately sorted coarse-grained unit	Subhorizontally stratified gravel	7
2	Poorly sorted coarse-grained unit	Subhorizontally stratified gravel	4
2	Poorly sorted fine- to coarse-grained unit	Suborizontally stratified fines, sand, and gravel	3
2	Moderate to well sorted medium-grained unit	Subhorizontally stratified sand	2
2	Moderate to well sorted medium- to coarse-grained unit	Subhorizontally stratified sand and gravel	1
2	Moderately sorted fine- to medium-grained unit	Subhorizontally stratified fines and sand	1
2	Moderately sorted fine-grained unit	Subhorizontally stratified fines	1
2	Moderately sorted medium- to coarse-grained unit	Subhorizontally stratified sand and gravel	1
2	Moderately sorted medum-grained unit	Subhorizontally stratified sand	1
2	Poorly sorted fine- to medium-grained unit	Subhorizontally stratified fines and sand	1
2	Two distinct coarse-grained unit	Subhorizontally stratified gravel	1
2	Two distinct coarse-grained units	Subhorizontally stratified gravel	1
2	Two distinct fine-grained unit	Subhorizontally stratified fines	1
2	Two distinct medium-grained units	Subhorizontally stratified sand	1
2	Well sorted medium-grained unit	Subhorizontally stratified sand	1
3	Poorly sorted fine- to coarse-grained unit	Dipping stratified fines, sand, and gravel	5
3	Moderately sorted coarse-grained unit	Dipping stratified gravel	3
3	Poorly sorted medium- to coarse-grained unit	Dipping stratified sand and gravel	2
3	Moderately sorted fine- to medium-grained unit	Dipping stratified silty fine sand	1
3	Poorly sorted fine- to medium-grained unit	Dipping stratified fines and sand	1
4	Moderately sorted coarse-grained unit	Dipping stratified gravel	1
4	Moderately sorted medium- to coarse-grained unit	Dipping stratified sand and gravel	1
4	Two distinct coarse-grained unit	Dipping stratified gravel	1
5	Poorly sorted coarse-grained unit	Dipping moderately stratified gravel	1
5	Poorly sorted fine- to medium-grained unit	Dipping crudely stratified fines and sand	1
5	Well sorted medium-grained unit	Dipping crudely startified sand	1
6	Poorly sorted medium- to coarse-grained unit	Massive to crudely stratified sand and gravel	9
6	Poorly sorted coarse-grained unit	Massive to crudely stratified gravel	2
6	Poorly sorted fine- to coarse-grained unit	Massive to crudely stratified fines, sand, and gravel	2
6	Moderately sorted coarse-grained unit	Massive to crudely stratified gravel	1
6	Moderately sorted fine- to medium-grained unit	Massive to crudely stratified fines	1
6	Moderately sorted fine- to medium-grained unit	Massive to crudely stratified fines and sand	1
6	Two distinct coarse-grained unit	Massive to crudely stratified gravel	1
6	Well sorted coarse-grained unit	Massive to crudely stratified gravel	1
6	Well sorted fine- to medium-grained unit	Massive to crudely stratified fines and sand	1
7	Poorly sorted medium- to coarse-grained unit	Massive sand and gravel	4
7	Poorly sorted fine- to coarse-grained unit	Massive fines, sand, and gravel	2
7	Moderately sorted medium-grained unit	Massive sand	1
7	Poorly sorted coarse-grained unit	Massive gravel	1
7	Well sorted medium- to coarse-grained unit	Massive sandy gravel	1
8	Moderately sorted coarse-grained unit	Massive gravel (boulders?)	1
8	Poorly sorted fine- to coarse-grained unit	Massive sand and gravel (boulders?)	1
8	Well sorted medium-coarse grained unit	Massive sand and gravel (boulders?)	1
Element I	Well sorted coarse-grained unit	Gravel channel fill	7
Element I	Moderately to well sorted coarse-grained unit	Gravel channel fill	6
Element I	Moderately sorted coarse-grained unit	Gravel channel fill	4
Element I	Poorly sorted fine- to coarse-grained unit	Fines, sand, and gravel channel fill	4
Element I	Moderately sorted medium- to coarse-grained unit	Sand and gravel channel fill	2
Element I	Poorly sorted fine- to medium-grained unit	Fines and sand channel fill	2
Element I	Poorly sorted medium- to coarse-grained unit	Sand and gravel channel fill	2
Element I	Moderately sorted medium-grained unit	Sand channel fill	1
Element I	Poorly sorted coarse-grained unit	Gravel channel fill	1

A resisitivity drop consistently occurs across the major bounding reflection (story boundary) noted in the GPR survey. This sharp resistivity drop is coincident with the transition between the horizontal to subhorizontal radar facies (Group 1) and the more discontinuous facies below. As previously noted, this story boundary occurs between well-stratified upper gravel and the poorly sorted lower gravel observed in the trenches.

8.5 Discussion

8.5.1 The Case Study

The objective of this study is to develop a methodology of combining sedimentology, GPR, and CCR for geophysical architecture analysis in fluvial environments. The trenches provide direct observation of the preserved lithofacies in the morphostratigrapic units and stratigraphies for the channel and bar platform on which to base the interpretation of the radar and resistivity data. The trench data are summarized in two idealized vertical sections (Fig. 8.16): one represents the channel fill, the other the interior bar platform. The lower gravel portion of the channel-fill succession represents bedload transported in an active channel (e.g., Fig. 8.5D). This is overlain by laminated silty fine sand deposited mainly from suspension during waning flow or from periodic flooding of the abandoned channel. The upper laminated organic-rich fine sand and silt represents deposition in standing water following channel abandonment. This stratigraphy is consistent with the unstable or abandoned channels of wandering gravel-bed rivers, described by Desloges and Church (1987) and Brierley and Hickin (1992)

The lower portion of the interior bar consists of poorly sorted cobble to boulder gravel capped by a boulder lag. This unit is interpreted as a high-energy gravel deposit that was subsequently winnowed. This unit is overlain by horizontal to gently inclined, well-stratified pebble to cobble gravel interpreted to be stacked gravel-bedload sheets (Fig. 8.5B) (Whiting et al. 1988; Ashmore 1991;). The upper unit consists of laminated sandy silt deposited mainly from suspension as overbank sediments. This fining-upward sequence is consistent with bar and floodplain stratigraphy of a wandering gravel-bed river (Allen 1983; Desloges and Church 1987; Brierley 1991; Nanson and Knighton 1996; Passmore and Macklin 2000).

The processed GPR data reveal two domains: the upper portion, dominated by Groups 1, 2, and 4 radar facies, and the lower, dominated by Group 3 facies (Table 8.2). In the upper domain, Groups 1 and 4 are common across the bar core, indicating that the bar platform is

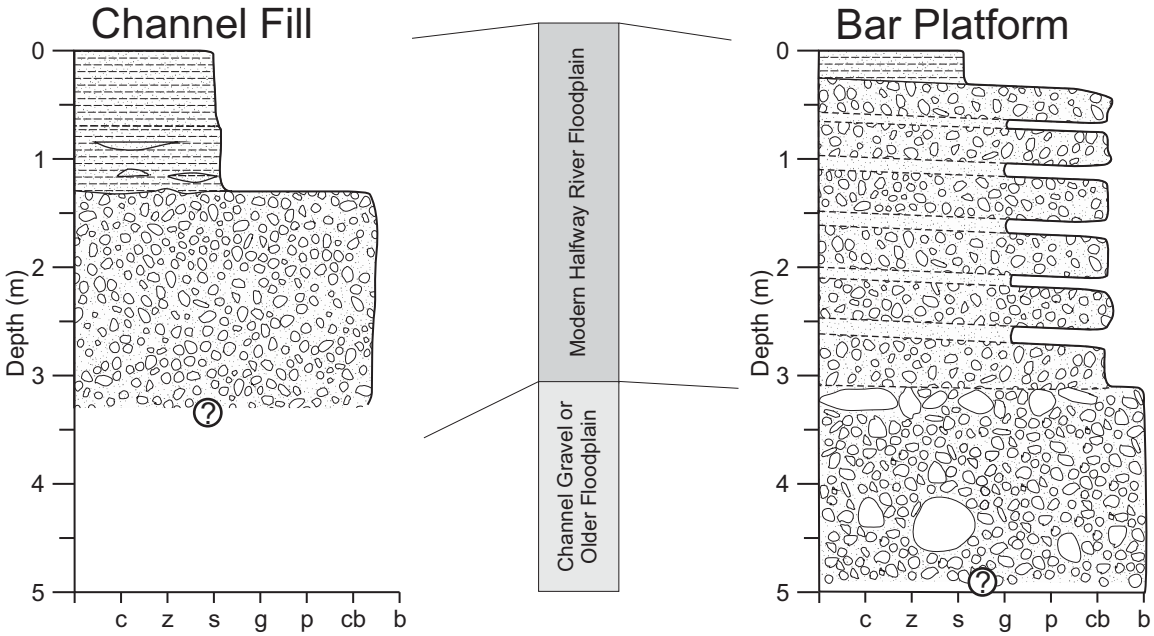

Figure 8.16. Two idealized vertical sections representing the stratigraphy of the channel fill and the bar platform from trench data.

dominated by well-stratified, horizontal to subhorizontal sediments occasionally dissected by channels (Element I). Resistivity values for facies in the bar core are typically high, and have relatively narrow distributions, suggesting that gravel is the dominant grain size (consistent with trench data). Therefore, the prevailing depositional process across the bar platform was vertical accretion of gravel sheets. Sheeted deposits are well documented in modern and ancient braided and wandering rivers (Smith, 1974; Ferguson and Werritty, 1983; Desloges and Church, 1987; Roberts et al., 1997; Wooldridge and Hickin, 2005; Passmore and Macklin, 2007).

The main topographic low that dissects the bar platform has architecture similar to that of the adjacent bar core, but resistivity values are lower and more varied where it forms a distinct channel (intersection of Lines 2 and 4; Fig. 8.12D). The resistivity predicts finer-grained sediment in this area despite a GPR signature consistent with the rest of the bar. This portion of the topographic low is therefore interpreted as a different architectural element, a subordinate channel with subhorizontally stratified sand or a mix of fines, sand, and gravel fill.

The transition from bar to channel in the upper portion of Lines 2 and 3 shows that the dominant depositional process was lateral accretion of moderately to poorly sorted or mixed sand and gravel (Facies 4). This suggests that the bar platform transitions from vertical accretion in the core to lateral and downstream migration on the mid to downstream section of the outer-platform margin. The radar facies within the main channel show consistency. Facies 6 or 8 typically occur in the base of the channel, indicating massive deposits or coarse sediment (abundant point sources), such as cobbles and boulders. Unfortunately, the base of the channel is below the maximum depth of reliable CCR data, so it is speculated that these facies represent basal-channel gravel. Where Facies 3 occurs in the upper 2-3 m on the inner bank of the channel (e.g. Fig. 8.9c), dipping towards the channel center, resistivity values are indicative of sand. Here, Facies 3 represents channel fill dominated by lateral progradation from the bar platform into the main channel. The remainder of the channel consists of fine-grained subhorizontal (Facies 2) channel fill and Element I, small channels, chutes, or scours with fine-grained sediment fill. The GPR signature alone is insufficient to differentiate Facies 2 in the bar core from Facies 2 in the channel fill, but the inclusion of resistivity data enables these facies to be separated into different architectural elements.

Geomorphology alone might lead this morphostratigraphic assemblage to be classified as a laterally migrating channel bend consistent with the classic meander model. The GPR-CCR

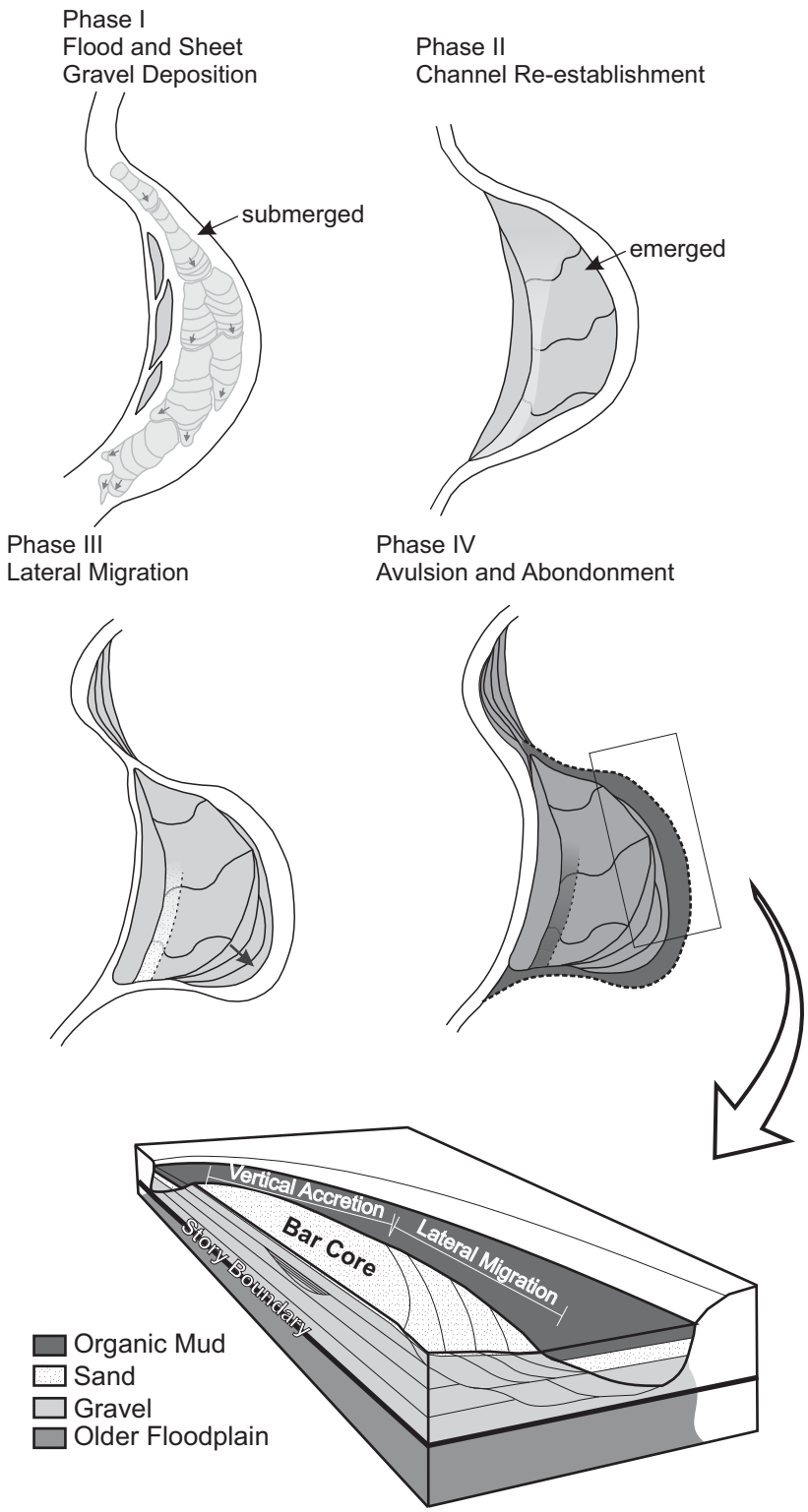

Figure 8.17. The evolution of the bar and channel based on the combined sedimentology, GPR, and CCR data.

surveys reveal instead that this channel bend essentially is an avulsion feature, and a four-phase model is invoked to explain the radar facies and resistivity model (Fig. 8.17). The bulk of gravel transport and deposition occurs during flood stages. Sheets of gravel are transported as bedload along the bar surface during peak discharge (Phase I). As stream power declines and flow wanes, the gravel sheets essentially freeze in place and suspended sediment is deposited over the sheeted gravel. As water levels drop, the gravel bodies emerge as an interior bar (Phase II). The main channel becomes established as a river bend, and the sheeted gravel becomes the core of the bar platform. Clinoforms common on the mid to downstream margin of the bar platform (Facies 4) suggest that once the main channel became established, lateral migration and reworking of the existing floodplain commenced (Phase III). The final phase is marked by avulsion and abandonment of the channel (Phase IV). During this phase, periodic flooding or water stagnation results in the slow accumulation of organic mud. The discrepancy between planform and expected architecture reinforces an important caution: landform genesis can be established reliably only if the 3-D internal structure and composition are known.

8.5.2 Methodology

When combined, outcrop data (trenching), GPR, and CCR are effective subsurface investigative tools. Outcrop data provide sedimentological and stratigraphic context, which in turn is used to calibrate the geophysical data. Indirect geophysical methods require, or at least benefit from, calibration from direct observation because most geophysical techniques produce non-unique solutions. Hence, geophysical interpretations are more reliable when developed from observation. Geophysics does, however, extend investigation beyond exposed outcrop and can be an efficient and powerful tool for subsurface investigation.

The OhmMapper™ instrument is a practical resistivity tool, and the data effective for estimating the grain size in the upper 5 m of the floodplain. The data collection is relatively simple and efficient. The inverted data produce geologically plausible pseudosections that are generally compatible with surface and trench observations. The procedure for incorporating the 2-D resistivity pseudosection into a coherent 3-D subsurface model combines geophysical inversion software with established geospatial techniques and offers a relatively cost-effective method of generating a versatile 3-D resistivity model. The GIS platforms and tools used are

neither specialized nor proprietary geophysical modelling software, but instead are common, commercial GIS products.

The approach presented in this study is relatively novel and is considered a foundation on which to build. Improvements will undoubtedly benefit future studies. For example, the GPR data are aggressively filtered to enhance reflections obscured by diffractions. More sophisticated processing, such as migration, is more effective at revealing coherent dipping reflections or those obscured by diffractions. Additional processing may therefore clarify some GPR data (Neal, 2004). Multi-frequency GPR may also enhance the interpretation of radar facies. Because the resolution of GPR is dictated by the central operating frequency of the survey, interpretation of radar facies as fluvial lithofacies or architectural elements benefits from multi-frequency surveys along each line (Wooldridge and Hickin, 2005; Mumpy et al., 2007). The correlation between resistivity values and grain size are essentially empirical in this study. Direct, in situ measurement of the resistivity values with respect to lithofacies would quantify the resistivity results, thereby improving the prediction of grain size from resistivity data. These data can be incorporated directly into the inversion parameters, refining the model. Addressing conductive surface sediment, such as in the main channel, will improve the model. Resistivity values below the fine-grained channel fill were not indicative of gravel in the channel bottom as was observed in the trenches. This inconsistency may be addressed by adjustment and fine-tuning the inversion parameters or by changing instrument configuration to extend the depth of the pseudosection (e.g., using 10 m dipoles). Addressing conductive surface sediments will be particularly important in future surveys where thick, fine-grained deposits are substantial fluvial-architecture elements (e.g., overbank environments). In terms of direct comparison of GPR and CCR data, the scale and resolution of the two geophysical techniques used in this study are not entirely compatible. The radar facies established with the 100 MHz antenna resolved mesoscale features, whereas the resolution of the resistivity data is more comparable to the mesoscale to macroscale features (Miall 1996). Some error was introduced because of this discrepancy in scale. Integrating the GPR facies boundaries and bounding surfaces directly into the inversions parameters would enhance the fit of two data sets.

Despite these considerations, this study confirms the utility of combining GPR and CCR for indirect fluvial architectural analysis. Because this study was conducted on a poorly developed wandering gravel-bed river, the logical next step is to apply the methodology to

morphostratigraphic units in end-member river planforms preferably with historic records in order to establish a link between fluvial style and preserved subsurface elements. The method will also benefit studies relating subsurface features that produce GPR reflections and host material (volumes) with contrasting electrical properties (e.g., subsurface contamination, buried cavities, and coal and stratiform-mineral exploration).

8.6 Conclusion

This study directly combines GPR and CCR to image fluvial architecture and grain-size distribution of a bar platform and channel on the floodplain of a poorly organized wandering gravel-bed river. Although GPR is routinely used to image fluvial architecture, most GPR studies do not include grain size in the radar-facies evaluation. This information is critical to fluvial architectural analysis, insomuch as architecture and grain size are integral to the classification terminology proposed by Miall (1996). This study demonstrates that CCR adds a grain-size proxy to traditional GPR studies essential for geophysical fluvial architectural analysis. The methodology presented here uses field observations to calibrate the geophysical data. Trenches provide lithofacies and stratigraphy from which geophysical interpretation and inversion parameters are based. The reflectors imaged in a 100 MHz GPR survey are taken to represent bed orientation and major bounding surfaces. The resulting radar facies are interpreted as mesoscale and small macroscale fluvial-architecture units. The inverted and modelled CCR data are used as a proxy for grain size, where high values correspond with coarse sediment and lower values with fine-grained material. The direct comparison of resistivity values with the GPR facies reveals that GPR architecture is not independent of grain size and that GPR facies may be common to both a coarse-grained and a fine-grained unit, in which case they represent separate fluvial architectural elements. The combination of GPR and CCR is, therefore, more appropriate for comprehensive geophysical architectural analysis.

In this case study, the geomorphology of a bar platform and channel scar suggest a laterally migrating channel bend, consistent with the classic meander model. However, the geophysical surveys in conjunction with direct subsurface observations indicate vertical accretion of gravel sheets is the dominant depositional process on the bar platform, an architecture associated with braided and wandering fluvial styles. Lateral migration is restricted to the outer, mid to downstream section of the platform, likely initiated after the bar emerged

and the channel established. This study reiterates cautions raised by Brierley and Hickin (1991) that depositional process, and therefore architecture, may not always be functions of planform and that one may not be used to predict the other.

8.7 Acknowledgments

The authors would like to thank Al Scobie for allowing access to his property and for providing an excavator for trenching. Mike Fournier is thanked for his assistance with drafting some of the figures. Funding for this project was provided by the British Columbia Ministry of Energy, Mines and Petroleum Resources as part of the Northeast British Columbia Aggregate and Surficial Geology Mapping Program. An earlier version of this manuscript benefited from review by Ted Hickin and Mel Best. The authors would like to extend their appreciation to Marc Gouw, an anonymous reviewer, Associate Editor Whitney Autin, and Editor Paul McCarthy for their constructive comments that improved the manuscript.

8.8 References

Allen, J.R.L., 1963, The classification of cross-stratified units, with notes on their origin: Sedimentology, v. 2, p. 93-114.

Allen, J.R.L., 1983, Studies in fluviatile sedimentation: bars, bar complexes and sandstone sheets (low-sinuosity braided streams) in the Browstones (L. Devonian), Welsh borders: Sedimentary Geology, v. 33, p. 237-293.

Archie G.E., 1942, The electrical resistivity log as an aid in determining some reservoir characteristics: Transactions of the American Institute of Mining, Metallurgical, and Petroleum Engineers, v. 146, p. 54-67.

Ashmore, P.E., 1991, How do gravel-bed rivers braid?: Canadian Journal of Earth Sciences, v. 28, p. 326-341.

Beres, M., and Haeni, F.P., 1991, Application of ground-penetrating-radar methods in hydrogeologic studies: Ground Water, v. 29, p. 375-386.

Beres, M., Green, A., Huggenberger, P., and Horstmeyer, H., 1995, Mapping the architecture of glaciofluvial sediments with 3-D Georadar: Geology, v. 23, p. 1087-1090.

Beres M., Huggenberger P., Green A., and Horstmeyer H., 1999, Using two- and three-dimensional georadar methods to characterize glaciofluvial architecture: Sedimentary Geology, v. 129, p. 1-24.

Bersezio, R., Giudici, M., and Mele, M., 2007, Combining sedimentology and geophysical data for high-resolution 3-D mapping of fluvial architectural elements in the Quaternary Po plain (Italy): Sedimentary Geology, v. 202, p. 230-248.

Best, M.E., Levson, V.M., and McConnell, D., 2005, Sand and gravel mapping in Northeast British Columbia using airborne electromagnetic surveying methods, in Summary of Activities 2004, British Columbia Ministry of Energy and Mines, p. 1-6.

Best, M.E., Levson, V.M., Ferbey, T., and McConnell, D., 2006, Airborne electromagnetic mapping for buried Quaternary sands and gravels in Northeast British Columbia, Canada: Journal of Environmental & Engineering Geophysics, v. 11, p. 17-26.

Bridge, J.S., 1985, Paleochannel patterns inferred from alluvial deposits: a critical evaluation: Journal of Sedimentary Petrology, v. 55, p. 579-589.

Bridge, J.S., and Mackey, S.D., 1993, A revised alluvial stratigraphy model, in Marzo, M., and Puigdefabregas, C., eds., Alluvial Sedimentation: International Association of Sedimentologists Special Publication 17, p. 319–336.

Bridge, J.S., Alexander, J., Collier, R.E.L., Gawthorpe, R.L., and Jarvis, J., 1995, Ground-penetrating radar and coring used to study the large-scale structure of point-bar deposits in three dimensions: Sedimentology, v. 42, p. 839-852.

Bridge J.S., Collier, R.E.L., Alexander, J., 1998, Large-scale structure of Calamus River deposits (Nebraska, USA) revealed using ground-penetrating radar: Sedimentology, v. 45, p. 977-986.

Brierley, G.J., 1989, River planform facies models: the sedimentology of braided, wandering, and meandering reaches of the Squamish River, British Columbia: Sedimentary Geology, v. 61, p. 17-35.

Brierley, G.J., 1991, Bar sedimentology of the Squamish River, British Columbia: Definition and application of morphostratigraphic units: Journal of Sedimentary Petrology, v. 61, p. 211-225.

Brierley, G.J., and Hickin, E.J., 1991, Channel planform as a non-controlling factor in fluvial sedimentology: The case of the Squamish River floodplain, British Columbia: Sedimentary Geology, v. 75, p. 67-83.

Brierley, G.J., and Hickin, E.J., 1992, Floodplain development based on selective preservation of sediments, Squamish River, British Columbia: Geomorphology, v. 4, p. 381-391.

Bristow, C.S., 1993, Sedimentary structures exposed in bar tops in the Brahmaputra River, Bangladesh, in Best, J.L., and Bristow, C.S., eds., Braided Rivers: Geological Society of London, Special Publication 75, p. 277-289.

Bristow, C.S., 1995, Facies analysis in the Lower Greensand using ground-penetrating radar: Geological Society of London, Journal, v. 152, p. 591–598.

Carson, M.A., 1984a, The meandering-braided river threshold: a reappraisal: Journal of Hydrology, v. 73, p. 315-334.

Carson, M.A., 1984b, Observations on the meandering-braided river transition, the Canterbury Plains, New Zealand: New Zealand Geographer, v. 40, p. 12-17.

Carson, M.A., 1984c, Observations on the meandering-braided river transition, the Canterbury Plains, New Zealand: New Zealand Geographer, v. 40, p. 89-99.

Church, M.A., 1983, Pattern of instability in a wandering, gravel-bed channel, in Collinson, J.D., and Lewin, J., eds., Modern and Ancient Fluvial Systems: International Association of Sedimentologists, Special Publication 6, p. 169-180.

Claerbout, J.F., and Muir, F., 1973, Robust modeling with erratic data: Geophysics, v. 38, p. 826-844.

Davis, J.L., and Annan, A.P., 1989, Ground-penetrating radar for high resolution mapping of soil and rock stratigraphy: Geophysical Prospecting, v. 37, p. 531-551.

deGroot-Hedlin, C., and Constable, S., 1990, Occam's inversion to generate smooth, two-dimensional models from magnetotelluric data: Geophysics, v. 55, 1613-1624.

Desloges J.R., and Church, M.A., 1987, Channel and floodplain facies in a wandering gravel-bed river, in Ethridge, F.G., Flores, R.M., Harvey, M.D., eds., Recent Developments in Fluvial Sedimentology: SEPM, Special Publication 39, p. 99-109.

Edwards, L.S., 1977, A modified pseudosection for resistivity and induced-polarization: Geophysics, v. 42, p. 1020-1036.

Ferguson, R.I., and Werritty, A., 1983, Bar development and channel changes in gravelly River Feshie, Scotland, in Collinson, J.D., and Lewin, J., eds., Modern and Ancient Fluvial Systems: International Association of Sedimentologists, Special Publication 6, p. 181-193.

Gawthorpe, R.L., Collier, R.E.L., Alexander, J., Bridge, J.S., and Leeder, M.R., 1993, Ground penetrating radar: application to sandbody geometry and heterogeneity studies, in North, C.P., and Prosser, D.J., eds., Characterization of Fluvial and Aeolian Reservoirs: Geological Society of London, Special Publication 73, p. 421-432.

Geometrics Inc., 2001, OhmMapper TR1 Operation Manual: Geometrics Inc, San Jose, California, 147 p.

Geotomo Software, 2006. RES2DINV Rapid 2D Resistivity and IP Inversion: Geoelectrical Imaging 2D and 3D. Terraplus Inc., Richmond Hill, Ontario, 132 p.

Golden Software, 2006, Voxler 3D Data Visualization: Golden Software Inc., Golden, Colorado, 52 p.

Griffiths, D.H., and Barker, R.D., 1993, Two-dimensional resistivity imaging and modelling in areas of complex geology: Journal of Applied Geophysics, v. 29, p. 211-226.

Huggenberger P., 1993, Radar facies: recognition of facies patterns and heterogeneities within Pleistocene Rhine gravels, NE Switzerland, in Best, J.L., and Bristow, C.S., eds., Braided Rivers: Geological Society of London, Special Publication 75, p. 163–176.

Jol, H.M., and Smith, D.G., 1991, Ground penetrating radar of northern lacustrine deltas: Canadian Journal of Earth Sciences, v. 28, p. 1939-1947.

Kostic, B., and Aigner, T., 2007, Sedimentary architecture and 3D ground-penetrating radar analysis of gravelly meandering river deposits (Neckar Valley, SW Germany): Sedimentology, v. 54, p. 789–808.

Leclerc, R.F., and Hickin, E.J., 1997, The internal structure of scrolled floodplain deposits based on ground-penetrating radar, North Thompson River, British Columbia: Geomorphology, v. 21, p. 17–38.

Loke, M.H., and Barker, R.D., 1996, Rapid least-squares inversion of apparent resistivity pseudosections by a quasi-Newton method: Geophysical Prospecting, v. 44, p. 131-152.

Mackin, J.H., 1937, Erosional history of Big Horn Basin, Wyoming: Geological Society of America, Bulletin, v. 48, p. 813-894.

Miall, A.D. ed., 1978, Fluvial Sedimentology: Canadian Society of Petroleum Geologists, Memoir 5, 858 p.

Miall, A.D., 1985, Architectural-element analysis: a new method of facies analysis applied to fluvial deposits: Earth-Science Reviews, v. 22, p. 261-308.

Miall, A.D., 1994, Reconstructing fluvial macroform architecture from two-dimensional outcrops: examples from the Castlegate Sandstone, Book Cliffs, Utah: Journal of Sedimentary Research, v. B64, p. 146-158.

Miall, A.D., 1996, The Geology of Fluvial Deposits; Sedimentary Facies, Basin Analysis and Petroleum Geology: Berlin, Springer-Verlag, 582 p.

Mitchum, R.M. Jr., Vail, P.R., and Sangree, J.B., 1977, Seismic stratigraphy and global changes of sea level, part 6: stratigraphic interpretation of seismic reflection patterns in depositional sequences, in Payton, C.E., ed., Seismic Stratigraphy – Applications to Hydrocarbon Exploration: American Association of Petroleum Geologists, Memoir 26, p. 117–133.

Moysey, S., Knight, R.J., and Jol, H.M., 2006, Texture-based classification of ground-penetrating radar images: Geophysics, v. 71, p. 111-118.

Mumpy, A.J., Jol, H.M., Kean, W.F., and Isbell, J.L., 2007, Architecture and sedimentology of an active braid bar in the Wisconsin River based on 3-D ground penetrating radar, in Baker, G.S., and Jol, H.M., eds., Stratigraphic Analysis using GPR: Geological Society of America, Special Paper 432, p. 111-131.

Nanson, G.C., and Knighton, A.D., 1996, Anabranching rivers: their cause, character and classification: Earth Surface Process and Landforms, v. 21, p. 217–239.

Neal, A., 2004, Ground-penetrating radar and its use in sedimentology: principles, problems and progress: Earth-Science Reviews, v. 66, p. 261–330.

Olsen, H., and Andreasen, F., 1995, Sedimentology and ground-penetrating radar characteristics of a Pleistocene sandur deposit: Sedimentary Geology, v. 99, p. 1–15.

Palacky, G.J., and Stevens, L.E., 1990, Mapping of Quaternary sediments in northeastern Ontario using ground electromagnetic methods: Geophysics, v. 55, p. 1595-1604.

Passmore, D.G., and Macklin, M.G., 2000, Late Holocene channel and floodplain development in a wandering gravel-bed river: The River South Tyne at Lambley, Northern England: Earth Surface Processes and Landforms, v. 25, p. 1237-1256.

Ramsay, J.G., 1967, Folding and Fracturing of Rocks: New York, McGraw-Hill, 568 p.

Reynolds, J.M., 1987, The role of surface geophysics in the assessment of regional groundwater potential in northern Nigeria, in Culshaw, M.G., Bell, F.G., Cripps, J.C., and O'Hara, M., eds., Planning and Engineering Geology: Geological Society of London, Engineering Group, Special Publication 4, p. 185-190.

Reynolds, J.M., 1997, An Introduction to Applied and Environmental Geophysics: New York, John Wiley & Sons, 796 p.

Roberts, M.C., Bravard, J.P., and Jol, H.M., 1997, Radar signatures and structure of an avulsed channel: Rhône River, Aoste, France. Journal of Quaternary Science, v. 12, p. 35-42.

Schumm, S.A., 1985, Patterns of alluvial rivers: Annual Review of Earth and Planetary Sciences, v. 13, p. 5-27.

Sensors & Software, 1996, PulseEKKO IV User's Guide: Sensors & Software Inc. Mississauga, Ontario, 59 p.

Smith, N.D., 1974, Sedimentology and bar formation in the upper Kicking Horse River, a braided outwash stream: Journal of Geology, v. 82, p. 205-223.

Stephens, M., 1994, Architectural element analysis within the Kayenta Formation (Lower Jurassic) using ground-probing radar and sedimentological profiling, southwestern Colorado: Sedimentary Geology, v. 90, p.179-2.

Vandenberghe, J., and van Overmeeren, R. A., 1999, Ground penetrating radar images of selected fluvial deposits in the Netherlands: Sedimentary Geology, v. 128, p. 245–270.

Walker, R.G., ed., 1979, Facies Models: Geological Association of Canada, Geoscience Canada, Reprint Series 1, 211 p.

Whiting, P.J., Dietrich, W.E., Leopold, L.B., Drake, T.G., and Shreve, R.L., 1988, Bedload sheets in heterogeneous sediments: Geology, v. 16, p. 105-108.

Willis, B.J., 1989, Paleochannel reconstruction from point bar deposits: a three-dimensional perspective: Sedimentology, v. 36, p. 757-766.

Woodward, J., Ashworth, P.J., Best, J.L., Sambrook Smith, G.H., and Simpson, C.J., 2003, The use and application of GPR in sandy fluvial environments: methodological considerations, in Bristow, C.S., and Jol, H.M., eds., Ground Penetrating Radar in Sediments: Geological Society of London, Special Publication 211, p. 127-142.

Wooldridge, C.L., and Hickin, E.J., 2005, Radar architecture and evolution of channel bars in wandering gravel-bed rivers: Fraser and Squamish rivers, British Columbia, Canada: Journal of Sedimentary Research, v. 75, p. 844-860.

Wright, M.D., 1959, The formation of cross-bedding by a meandering or braided stream: Journal of Sedimentary Petrology, v. 29, p. 610-615.

CHAPTER 9: SUMMARY

The preceding chapters presented a series of investigations that contribute to the understanding of the origin of the modern landscape in northeastern British Columbia. In the following discussion key components from these papers are used to summarize how the landscape has evolved.

Bedrock topography is an important component of the landscape and represents a topographically complex base to the Quaternary section in northeast British Columbia. Bedrock topography was modelled in Chapters 2 and 3 using petrophysical logs, water well drillers' logs, and ground based geophysics. These models imply that the difference in elevation between the bedrock surface and the ground surface (modern topography) is highly variable and where depths from surface to bedrock are substantial, sediment filled paleovalleys are interpreted. The resolution of these models is, however, limited to the quality and density of the subsurface data. Nonetheless, the methods developed here were successful in depicting major depressions that represent paleovalleys.

In general, bedrock topography is primarily controlled by major bedrock tectonic structures in northeast British Columbia. The regional structures reflect major uplift and mountain building events in the Rocky Mountain Foreland Belt which contrasts with the subdued relief of the relatively stable Western Canadian Sedimentary Basin. For most of the region, near surface bedrock consists mainly of Cretaceous age sedimentary units (Thompson, 1977; McMechan 1994; Massey et al., 2005). These units are generally flat lying to inclined, and gently dipping to the west in the Canadian Interior Plains. Towards the Foothills, however, these units dip to the east and become more profoundly folded, eventually thrusting to the east in the Rocky Mountains. Nevertheless, the regional slope of the bedrock surface consistently dips towards the east-northeast, away from the mountains. Continental ice sheets nourished from eastern sources, such as the Late Wisconsinan (MIS 2) Laurentide Ice sheet (LIS), flowed to the southwest from the Keewatin Ice Centre in north-central Canada and, therefore, advanced up the regional slope (Mathews, 1980). This has significant implications for fluvial processes as the advancing ice episodically blocked and reorganized east draining rivers and caused the formation of ice marginal glacial lakes that changed local base levels. Cordilleran and mountain ice sheets that extended onto the interior plains flowed down the regional slope.

In the Fort Nelson Lowlands Physiographic Region (Bostock, 1948; Holland, 1976), the nearly flat lying Fort St John Group underlies deep, wide paleovalleys that are interpreted to have significant antiquity, and are probably pre-Quaternary in age. Though these paleovalleys are entirely masked by thick unconsolidated valley-fill today, these major topographic features would have had a significant role in controlling ice flow, particularly during early glacial advance when ice was thin and therefore influenced by local relief (ca. 200 m). Though the major paleovalleys initially exerted appreciable control on ice flow, they would have become less significant as ice thickened or sediment filled these depressions. Abundant streamlined surface landforms in the Fort Nelson Lowlands suggest that at the late glacial maximum, the LIS flowed across the area unimpeded by topography, though flow trajectory may have experienced minor deviation from major topographic features such as the Etsho Plateau (e.g. Bednarski, 2008; Trommelen et al., 2008; Demchuk, 2010).

In the Dawson Creek and Fort St John areas (part of the Alberta Plateau Physiographic Region; Bostock, 1948; Holland, 1976), paleovalleys are typically coincident with modern valleys (Hickin, 2011; Hickin and Best, 2012, 2013). Paleovalleys in this setting are generally narrower than those in the Fort Nelson region (Hickin et al., 2008) and host important Quaternary sedimentary records. Major paleovalleys influenced late ice flow of the Laurentide (LIS) and Cordilleran (CIS) ice sheets, however, ice flow indicators outside the main valleys and at high elevations confirm that during late glacial maximum, ice flow was topographically independent.

Numerous stratigraphic exposures, including sections from the Murray and Pine river valleys, host a relatively complete late Quaternary record. The sections contain sediments deposited before the penultimate glacial interval (possibly MIS 4; early Wisconsinan) and include deposits from the middle Wisconsinan (MIS 3; interglacial equivalent to the Olympic non-glacial climatostratigraphic interval), Late Wisconsinan (MIS 2; equivalent to Fraser Glaciation) and Holocene (Ryder and Clague, 1989). The oldest unconsolidated deposits reported in the region include quartzite-rich fluvial gravel that caps upland regions. These are likely equivalent to Tertiary age gravels identified in the Clear and Chinchaga hills in Alberta (Mathews 1978; Liverman, 1989). A quartzite gravel was also encountered under till on the small escarpment on the east side of the Dawson Creek map sheet (NTS 93P; north of location S7 in Figure 5.2) and may be equivalent to the Tertiary deposits. Without reliable dates or fossils, however, this remains speculative. The quartzite gravel units are thought to represent

large fluvial systems that developed on a peneplain that extended from the Rocky Mountains across the Canadian Interior Plains. These deposits may be associated with the Tertiary Bell River system proposed by McMillan (1973) and are thought to have transported sediments from western Canada to the Labrador Shelf (Duk-Rodkin and Hughes, 1994).

The stratigraphically lowest unit from the Murray-Pine river valleys is an undated fluvial unit tentatively assigned to MIS 5, but it may be equivalent to the Tertiary deposits noted above. The fluvial style of this unit is difficult to ascertain as the sediment is highly deformed, but the unit is interpreted to have a non-glacial origin.

Sediments representing the penultimate glaciation are assigned to MIS 4 (Early Wisconsinan) although an older glacial period can't be completely discounted. This package of sediments includes an advance phase glaciofluvial unit overlain by a glacial sedimentary complex and a retreat phase glaciolacustrine deposit. A luminescence age from the advance phase glaciofluvial unit returned a limiting age of <128 ± 5 ka BP (i.e. the unit is younger than 128 ± 5 ka BP).

The penultimate glacial sediments are overlain by a MIS 3 (Middle Wisconsinan) non-glacial fluvial unit. This unit is confidently assigned to MIS 3 (equivalent to the Olympic non-glacial interval) based on two radiocarbon ages (27 760 ± 230 ^{14}C yrs BP or 32 039 ± 640 cal yrs BP; 30 380 ± 300 ^{14}C yrs BP or 35 355 ± 828 cal yrs BP) and an optical age (22.7 ± 1.0 ka BP).

Six units constitute the Late Wisconsinan (MIS 2) succession, equivalent to the Fraser glacial climatostratigraphic interval. The lowest unit is an advance phase glaciofluvial deposit. This unit is overlain by glaciolacustrine deposits that are thickest (> 100 m) towards the Peace River valley. These sediments were deposited in glacial Lake Mathews and are recognized regionally (Hartman and Clague, 2008). Advance phase alluvial, subaqueous fan, and/or gravity flow deposits occur discontinuously, but stratigraphically above or within the glacial Lake Mathews sediments. These deposits represent unstable valley slopes and fan development as glaciers advanced down valleys into glacial Lake Mathews. Full glacial conditions are represented by a diamict interpreted to be till. Retreat phase sediments include glaciolacustrine deposits associated with glacial Lake Peace and glaciofluvial deposits that formed deltas and terraces during stable phases of glacial Lake Peace (GLP). GLP likely occupied the area between ca. 17-12 ka yrs ago (Catto, 1996) which is consistent with the <16.0 ± 2.5 to 14.2 ± 0.5 ka BP optical ages determined for the Phase II shorelines in this study.

Aeolian deposits occur at the top of the stratigraphic column and span from Late Quaternary to Holocene time. What is interpreted to be loess in the Coldstream valley was optically dated to 8.7 ± 0.3 ka BP. Stabilization ages from stratigraphically equivalent aeolian dunes in the Kiskatinaw Dune Field were optically dated at ca. 12 ka to 10 ka (based on optical dates of 12.3 ± 0.7 ka, 11.3 ± 0.7 ka, 11.0 ± 1.0 ka, 10.8 ± 0.7 ka, and 10.6 ± 0.6 ka; uncertainty at 1σ) with minor reactivations occurring as young as 8.7 ± 0.5 ka.

This Late Wisconsinan stratigraphy can be correlated with sections in the Peace River Valley in British Columbia (Hartman and Clague, 2008) and Alberta (Morgan et al., 2012) and can be tracked out of the valleys on to interfluves. It is asserted here that surface till and glacial landforms in the Dawson Creek area have a Late Wisconsinan origin, contrary to the pre-Late Wisconsinan origin suggested by Reimchen (1980), Bobrowsky and Rutter (1992), and Catto et al. (1996).

It has been argued by Reimchen and Rutter (1972), Reimchen (1980), Bobrowsky (1989), Bobrowsky and Rutter (1992) and Catto et al. (1996) that an extensive CIS in the region was restricted to an Early Wisconsinan (MIS 4) or older event and that the Late Wisconsinan CIS was of limited extent. They suggested that the maximum montane glaciation postdated the Laurentide advance (Reimchen and Rutter, 1972) and the maximum extent of the CIS (and possibly coalescence) occurred in a previous glaciation. Liverman et al. (1989), however, concluded that only one Laurentide glacial event is recorded at Watino, Alberta (~175 km east of the study area) and is of a late Wisconsinan age. Studies included in this thesis favour the model proposed by Mathews (1980) and support an extensive Late Wisconsinan western sourced ice sheet that coalesced with the LIS. This is based on: 1) local stratigraphy that indicates surface till and glacial landforms are Late Wisconsinan (MIS 2); 2) a continuous field of streamlined landforms indicating a major lobe of western sourced ice, flowing east, was deflected by the LIS; and 3) the western sourced ice lobe post-dates the maximum advance of the LIS and is, therefore, of Late Wisconsinan age (MIS 2), and 4) the radiocarbon and optical luminescence chronology described above.

The LIS reached its maximum extent in the Late Wisconsinan (Liverman, 1989) and deposited till with eastern provenance clasts in British Columbia. Landforms occurring on the surface in the Dawson Creek region, however, record eastern ice flow all the way to the Alberta border. This implies that western sourced ice flowed east over the region previously occupied by

the LIS. The landforms record deflection that could have only occurred if the LIS impeded eastern flow (coalescence). This sequence is also supported by diamict properties (grain-size, clast lithology, and geochemistry) in a section from the East Kiskatinaw River valley. Diamict at the base of the section has LIS affinity but becomes more like CIS diamict up section. Furthermore, irregular postglacial isostatic adjustment (based on shorelines from glacial Lake Peace) imply initial unloading in the east, as the LIS thinned and retreated but CIS persisted (and/or thickened) in the west. Later isostatic adjustment reflects unloading in the west as the CIS diminished. Dune stabilization and biome succession also indicates that climate ameliorated earlier in central Alberta than in the Interior Plains in northeast British Columbia (Dyke, 2005), perhaps because the Cordilleran or Montane ice remained in the foothills after the LIS retreated to the east in Alberta, influencing local climate along the foothills.

The modern landscape is a geomorphic collage that developed from a variety of processes acting at different times and places within the region. In order to understand the history of a landscape, landsystems (landforms and their sediments and associated geomorphic processes) need to be identified and placed in a morphostratigraphic sequence. Digital elevation models (DEMs) from data such as light detecting and ranging (LiDAR) surveys provide high resolution imagery of landform assemblages that can be used to interpret landsystems in previously glaciated regions (Evans, 2005). The following settings are recorded in the Dawson Creek area: 1) glacial; 2) deglacial; 2) large proglacial lake; 4) paraglacial; and 5) modern Boreal Forest.

The preserved landforms related to the active Late Wisconsinan glacial phase in the Dawson Creek area are mainly represented by streamlined landforms (e.g. Fig. 4.3) composed of till. Streamlined landforms from the Dawson Creek area are all associated with the CIS and their orientations imply that ice sourced from the west flowed from the mountains onto the interior plains. The dominant flow trajectory is generally northeast towards the Peace River valley, however, deflection to a northerly trajectory resulted from coalescence.

It is likely that the subglacial dynamics at a local scale varied spatially as well as temporally. For example, streamlined landforms with a low length/width (l/w) ratio occur on a low escarpment on the east side of the Dawson Creek study area. This belt of streamlined features separates elongated streamlined landforms to the east and west. In Chapter 5, subglacial bed conditions in this area were examined using the orientation of electrical anisotropy. This study evaluated and compared the orientation of electrical anisotropy with the

orientation of streamlined landforms. The study revealed that the principle axis of the resistivity ellipse is perpendicular to ice flow in highly elongated streamlined landforms (length/width >3) and parallel to ice flow in landforms with l/w <3. Electrical anisotropy in till may result from the alignment of sediment particles and, like pebble fabrics, electrical anisotropy may be parallel or transverse to ice flow depending on strain responses to local stress fields. The orientation of electrical anisotropy may be explained in terms of the deforming bed mosaic concept. This theory predicts elongated streamlined landforms are produced from highly deformable till that takes up the stress from extensional flowing ice. Landforms with lower elongation ratios form where stiffer subglacial beds occur. A stiffer bed would begin to behave as a so called "sticky-spot" (Stokes et al., 2007), where increased drag/friction results in a shift from extensional to compressional ice flow. Under compressional flow, subglacial sediment particles will rotate towards a transverse fabric. The anisotropy would, therefore, correspond with the sediment fabric. Another possible explanation for the apparent rotation of resistivity ellipses in landforms with low l/w ratios may reflect modification of the subglacial sediment fabric during ice stagnation and the development of crevasse squeeze ridges. Many of the low elongated ratio landforms in this study were ornamented with rectilinear ridges. The electrical anisotropy on these low ratio landforms may therefore be coincident with the strain ellipse associated with stress from stagnant ice as the sediment was squeezed into subglacial crevasses.

As the glacial interval transitioned to the deglacial phase, the ice sheets separated and GLP formed. At Initial separation the CIS, no longer buttressed by the LIS, flowed unimpeded to the northeast (recorded by streamlined landforms in the Redwillow area). Hummocky terrain in defuse zones was superimposed on streamlined landforms and represents stagnant ice. Recessional moraines, typical of actively retreating ice margins are absent in the Dawson Creek area indicating that the dominant deglacial mechanism was probably ice sheet collapse rather than actively retreat.

The formation of GLP had a significant impact on ablation, ice sheet slope, and flow rates (cf. Stokes and Clarke, 2003). The inability to sustain an ice shelf in a deep fresh water lake (Patterson, 1994) would result in rapid calving of the ice front causing substantial ablation. This in turn would have likely increased ice slope, which, when accompanied by saturated (lubricated) subglacial sediments and reduced friction at the ice terminus, would increase flow velocity. This may explain, in part, the well developed highly elongated flutes common on the

east side of the Dawson Creek study area. The increase in rapid ablation would have depleted the ice reservoir and may have been a factor in the collapse of this part of the ice sheet. This landform assemblage is consistent with local readvance, local ice streaming (Stokes and Clark, 2003) or glacier surging (Evans and Rea, 2005). If the landforms represent a local readvance, it is restricted to a relatively small region. The lack of a characteristic convergent flow pattern and shear moraines, does not support the ice stream model, however, the setting is consistent with a Dubawnt style ice stream (ice margin in a proglacial lake) and the highly elongated streamlined features, discordant to other streamlined features, make this landsystem an attractive interpretation. However, the highly elongated streamlined landforms and the abundant ice–squeeze hummocky stagnant ice moraine are consistent with a surging glacier landsystem (Evans and Rea, 2005). More detailed work is necessary to clarify the specific landsystem associated with this landform assemblage.

GLP continued to occupy the Dawson Creek area after the glaciers retreated into the foothills and mountains. Shoreline features are well preserved and enable the reconstruction of lake and ice positions during the early phases of GLP (Fig. 6.13). Four phases are distinguished in the Dawson Creek area. Phase I ranges in elevation between 990 m and 960 m asl and likely represents several independent ice marginal lakes. These lakes merged to form a more or less continuous body of water between the LIS and the CIS. Phase II consists of a flight of shorelines between 910 m and 890 m asl, the earliest unambiguous phase of GLP. As ice retreated in Phase II time, the Pass Creek spillways in Alberta developed and lake levels dropped to the initial levels of Phase III. Phase III shorelines span an elevation interval between 865 m and 810 m. This Phase is equivalent to both the Bessborough Stage and the Unnamed Stage of Mathews (1978, 1980). The successive shorelines represent both the down-cutting of the Pass Creek spillway and the retreat of the LIS. Phase IV, between 733 m and724 m, developed as GLP retreated from the area and Swan Lake became an isolated basin.

Paraglacial conditions, that would have occurred in immediate post-glacial times (Church and Ryder, 1972), shifted to a boreal setting during the early Holocene. The transition is marked by climate warming and the establishment and proliferation of plants and animals. Aeolian dunes in the Kiskatinaw Dune field were likely active as barchan-like dunes in the paraglacial setting. However, the preserved, mainly parabolic sand dunes in the field are indicative of plant colonization adequate enough to bio-morphologically influence aeolian activity and ultimately

stabilize the dune field. Stabilization occurred between 12.3 ± 0.7 and 10.6 ± 0.6 ka years BP. Around the same time, the Herb and Shrub Tundra/Tundra Forest biome in the area evolved to Boreal Parkland and eventually to Boreal Forest. Radiocarbon ages from macrofossil assemblages at the Flatbed River Section provide some temporal control for these transitions. Paraglacial conditions likely persisted to ca. 12 183 ± 193 cal yrs BP after which a Forest Tundra dominated. Locally, the Flatbed River floodplain transitioned to a pond setting between 11 490 ± 206 and 11 226 ± 21 cal yrs BP. Open Spruce forests, established by 11 207 ± 28 cal yrs BP, mark the shift from Forest Tundra to Boreal Parkland. The site transitions from pond to bog between 9964 ± 187 and 9789 ± 115 cal yrs BP marking the onset of Boreal Forest conditions at the site.

Although modern geomorphic processes are dominantly erosional, some rivers at the edge of the foothills are under a state of limited aggradation. Most of the relief in the Dawson Creek area is the result of post-glacial river incision. Slope failures and landslides are common (Severin, 2004) in these steep sided river valleys. Fluvial deposition is limited and planforms are generally valley controlled. Yet, braided and wandering gravel bed planforms are common where they emerge from the foothills. The final study in the thesis is a case study that examines the architecture of a modern river planform. The study directly combines two geophysical techniques, ground penetrating radar (GPR) and capacitively coupled resistivity (CCR), to image the fluvial architecture and grain-size distribution of a bar platform and channel on the floodplain of a poorly organized wandering gravel-bed river. The GPR survey provides bed orientation and major bounding surfaces and CCR data are used as a proxy for grain size. The geomorphology of a bar platform and channel scar suggest a laterally migrating channel bend, consistent with the classic meander model. However, the geophysical surveys in conjunction with direct subsurface observations indicate that vertical accretion of gravel sheets is the dominant depositional process, which is the sedimentary architecture more typically associated with braided and wandering fluvial styles. Lateral migration is restricted to the outer, mid to downstream section of the planform, and likely initiated after the bar emerged and the channel established. A key finding of the study is that depositional process, and therefore architecture may not always be a function of planform and that one may not be used to predict the other.

Although this thesis makes contributions to the understanding of the landscape and Quaternary history of the Dawson Creek area, there remain many avenues of additional research. Paleovalleys host important resources such as groundwater and natural gas.

Continuing accurate mapping of the geometry of paleovalleys and establishing the geological framework for their valley fill successions has important practical applications. Integrating multiple geophysical methods is an approach that will likely provide important subsurface information between reference points (i.e. wells and exposures). Combining electromagnetic data with shallow seismic data, through a method similar to that presented in Chapter 8, has promising potential for establishing the internal stratigraphy of paleovalleys for hydrogeological studies.

Electrical anisotropy has intriguing implications as a proxy for sediment fabrics. If this technique can be established as a suitable alternative to the time consuming collection of pebble fabric data, it may offer a cost effective and efficient method for routinely gathering this type of information. The method is, however, in its infancy and requires considerable testing in a variety of environments before it can be accepted as a reliable proxy. Much will be gained by confirming the specific controls on electrical anisotropy. Additional studies on the effects of parameters such as clay and mineral grain alignment, pore geometry, fissility and fracture geometry, and fluid chemistry may all contribute to a better understanding of what electrical anisotropy is measuring.

Quaternary stratigraphic studies have benefited greatly by the advent of optical dating. Not only has this technique extended absolute age dating back beyond the limits of traditional radiocarbon dating, it has enabled the estimation of the time elapsed since sediments, exposed to sunlight, were buried in environments where organics are absent (a common occurrence in glacial studies). Expanding and refining optical ages in other stratigraphic studies in the Peace region may lead to the reconciliation of incompatible models.

High resolution digital elevation models (DEMs) from LiDAR technology have also greatly advanced the ability to detect and image landforms to submeter-scale even under the canopy of trees. This has allowed for better analysis of landform assemblages and their relationship to past environments. The continued expansion of regional LiDAR coverage will undoubtably reveal subtle features that will change our understanding of the history and evolution of landscapes. Identifying critical features such as ice flow indicators, ice marginal landforms, and lake outlets, will help refine the glacial and deglacial history of terrestrial settings. Combined with

References

Bostock, H.S. 1948. Physiography at the Canadian Cordillera with special reference to the area north of the fifty-fifth parallel; Geological Survey of Canada, Memoir 247, 106 p.

Bednarski, J.M. 2008. Landform assemblages produced by the Laurentide Ice Sheet in northeastern British Columbia and adjacent Northwest Territories — constraints on Glacial Lakes. Canadian Journal of Earth Sciences, 45, 593 – 610.

Bobrowsky, P.T.B. and Rutter, N.W., 1992. The Quaternary history of the Canadian Rocky Mountains; Géographie Physique et Quaternaire, v. 46, p. 5—50.

Ballantyne, C.K., 2005. Paraglacial landsystems; In: Evans, D.J.A. (ed), Glacial Landsystems. Holder Arnold, London, p. 432—461.

Catto, N.R., Liverman, D.G.E., Bobrowsky, P.T., Rutter, N., and Mandryk, C.A.S., 1996. Laurentide, Cordilleran, and Montane glaciation in the western Peace River-Grand Prairie region, Alberta and British Columbia, Canada. Quaternary International, v. 32, p. 21—32.

Church, M. and Ryder, J.M., 1972. Paraglacial sedimentation: consideration of fluvial processes conditioned by glaciation; Geological Society of America Bulletin, v. 83, p. 3059—3072.

Colgan, P.M., Mickelson, D.M., and Cutler, P.M., 2005. Ice-marginal terrestrial landsystem: Southern Laurentide ice sheet margin; in Evans, D.J.A. (ed), Glacial Landsystems. Holder Arnold, London, p. 111—142.

Demchuk, T.E., 2010. Surficial Geology of the Komie Creek map area and an investigation of an ice-contact glaciofluvial delta, northeast British Columbia (NTS 94P/05); unpublished MSc Thesis, University of Victoria, 266 p.

Duk-Rodkin, A. and Hughes, O.L. 1994. Tertiary-Quaternary drainage of the pre-glacial Mackenzie Basin; Quaternary International, v. 22/23, p. 221—241.

Dyke, A.S., 2005. Late Quaternary vegetation history of northern North America based on pollen, macrofossils, and faunal remains; Géographie Physique et Quaternaire, 59, 211—262.

Evans, D.J.A., 2005a. Glacial Landsystems. Holder Arnold, London, 532 pages.

Evans, D.J.A., 2005b. Ice-marginal terrestrial landsystens: Active temperate glacier margin; In: Evans, D.J.A. (ed), Glacial Landsystems. Holder Arnold, London, p. 12—43.

Evans, D.J.A. and Rea, B.R., 2005. Surging glacier landsystem; In: Evans, D.J.A. (ed), Glacial Landsystems. Holder Arnold, London, p. 259—288.

Hickin, A.S., 2011. Preliminary bedrock topography and drift thickness of the Montney Play ; British Columbia Ministry of Energy, Mines and Petroleum Resources, Energy Open File 2011-1 and Geoscience BC, Report 2011-07.

Hickin A.S. and Best M.E., 2012. Stratigraphy and proposed geophysical survey of the Groundbirch paleovalley: a contribution to the collaborative Northeast British Columbia Aquifer Project,; In Geoscience Reports 2012, British Columbia Ministry of Energy and Mines, p. 91—103.

Hickin A.S. and Best M.E., 2013. Mapping the geometry and Lithostratigraphy of a paleovalley with a time-domain electromagnetic technique in an area with small resistivity contrasts, Groundbirch British Columbia, Canada. Journal of Environmental and Engineering Geophysics, v. 18, p. 119—135.

Hickin, A.S., Kerr, B., Turner, D.G., and Barchyn, T.E., 2008. Mapping Quaternary paleovalleys and drift thickness using petrophysical logs, northeast British Columbia, Fontas map sheet, NTS 94I; Canadian Journal of Earth Sciences, v. 45, p. 577—591.

Holland, S.S. 1976. Landforms of British Columbia A Physiographic Outline; British Columbia Department of Mines and Petroleum Resources, Bulletin 48, 138 p.

Liverman, D.G.E. 1989. The Quaternary Geology of the Grande Prairie area, Alberta; unpublished PhD thesis, University of Alberta, Edmonton, 360 p.

Massey, N.W.D., MacIntyre, D.G., Desjardins, P.J., and Cooney, R.T., 2005. Digital geology map of British Columbia; BC Ministry of Energy Mines and Petroleum Resources, British Columbia Geological Survey GeoFile 2005-1.

Mathews, W.H. 1978. Quaternary stratigraphy and geomorphology of Charlie Lake (94A) map-area, British Columbia; Geological Survey of Canada, Paper 76-20, 25 p.

McMechan, M.E., 1994, Geology and structure cross-section, Dawson Creek, British Columbia; Geological Survey of Canada, Map 1858A.

McMillan, J.N. 1973. Shelves of the Labrador Sea and Baffin Bay, Canada; In: The future petroleum provinces of Canada: Their geology and potential; p. 473—517.

Mercier, D., 2008. Paraglacial and paraperiglacial landsystems: concepts, temporal scales and spatial distribution; Géomorphologie: relief processus, environnement, v. 4, p. 223—234.

Miall, A.D. 2006. The geology of fluvial deposits: Sedimentary facies, basin analysis, and petroleum geology; Springer, New York, 582 p.

Morgan, A.J., Paulen, R.C., Slattery, S.R., and Froese, C.R., 2012. Geological Setting for Large Landslides at the Town of Peace River, Alberta (NTS 84C). Energy Resource Conservation Board/Alberta Geological Survey, Open File Report 2012-04, 33 p.

Patterson, W.S.B. 1994. The physics of glaciers, 3rd edition. Butterworth Heinemann, New York, 481 p.

Reimchen, T.H.F., 1980. Surficial Geology, Dawson Creek, west of sixth meridian, British Columbia; Geological Survey of Canada, Map 1467A, 1:250 000 scale map.

Ryder and Clague, 1989. British Columbia (Quaternary stratigraphy and history, Cordilleran Ice Sheet); in Fulton, R.J. (ed), Chapter 1, Quaternary Geology of Canada and Greenland; Geological Survey of Canada, Geology of Canada, vol. 1, p. 48—58.

Severin, J.M., 2004. Landslides in the Charlie Lake map sheet, Fort St. John; unpublished Msc thesis, University of British Coilumbia, Vancouver, 395 p.

Stokes, C.R. and Clark, C.D. 2003. The Dubawnt Lake palaeo-ice stream: evidence for dynamic ice sheet behaviour on the Canadian Shield and insights regarding the controls on ice-stream location and vigour; Boreas, v. 32, p. 263–279.

Stokes, C.R., Clark, C.D., Lian, O.B., Slawek, T., 2007. Ice stream sticky spots: A review of their identification and influence beneth contemporary and paleo-ice streams; Earth-Science Reviews, v. 81, 217—249.

Teller, J.T., Subaqueous landsystems: Large proglacial lake; In: In: Evans, D.J.A. (ed), Glacial Landsystems. Holder Arnold, London, p. 348—371.

Thompson, R.I. 1977. Geology of Beatton River, Fontas River and Petitot River map areas, northestern British Columbia; Geological Survey of Canada, Paper 75-11.

Trommelen, M.S., Levson, V.M., and Smith, I.R. 2008. Quaternary stratigraphy of the Prophet River. Canadian Journal of Earth Sciences, 45, 565 – 575.

Appendix

Appendix A: Bedrock Topography Database (Dawson Creek-Fort St John)
Includes all data and interpretation of bedrock topography for the Montney Play area.

Appendix B: Till Geochemistry
Major oxide and elemental geochemistry from diamict samples

Appendix C: PALEOTEC Macrofossil Report
Macrofossil report from the Flatbed River Section